

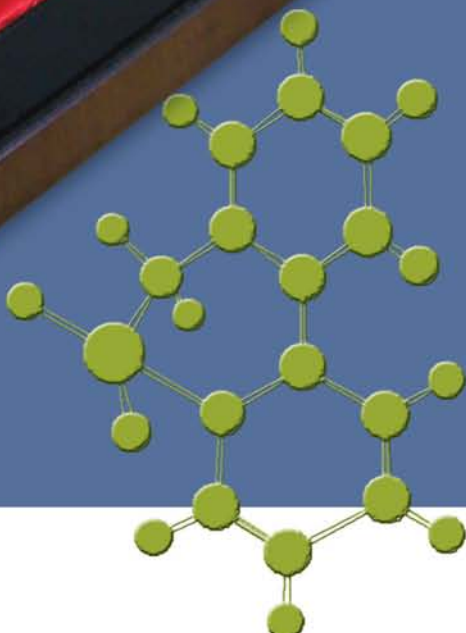
# ORGANIC ELECTRONICS

## Materials, Processing, Devices and Applications

Edited by Franky So



CRC Press  
Taylor & Francis Group



# **ORGANIC ELECTRONICS**

## **Materials, Processing, Devices and Applications**



# ORGANIC ELECTRONICS

## Materials, Processing, Devices and Applications

Edited by Franky So



CRC Press  
Taylor & Francis Group  
Boca Raton London New York

---

CRC Press is an imprint of the  
Taylor & Francis Group, an **informa** business

CRC Press  
Taylor & Francis Group  
6000 Broken Sound Parkway NW, Suite 300  
Boca Raton, FL 33487-2742

© 2010 by Taylor and Francis Group, LLC  
CRC Press is an imprint of Taylor & Francis Group, an Informa business

No claim to original U.S. Government works

Printed in the United States of America on acid-free paper  
10 9 8 7 6 5 4 3 2 1

International Standard Book Number: 978-1-4200-7290-7 (Hardback)

This book contains information obtained from authentic and highly regarded sources. Reasonable efforts have been made to publish reliable data and information, but the author and publisher cannot assume responsibility for the validity of all materials or the consequences of their use. The authors and publishers have attempted to trace the copyright holders of all material reproduced in this publication and apologize to copyright holders if permission to publish in this form has not been obtained. If any copyright material has not been acknowledged please write and let us know so we may rectify in any future reprint.

Except as permitted under U.S. Copyright Law, no part of this book may be reprinted, reproduced, transmitted, or utilized in any form by any electronic, mechanical, or other means, now known or hereafter invented, including photocopying, microfilming, and recording, or in any information storage or retrieval system, without written permission from the publishers.

For permission to photocopy or use material electronically from this work, please access [www.copyright.com](http://www.copyright.com) (<http://www.copyright.com/>) or contact the Copyright Clearance Center, Inc. (CCC), 222 Rosewood Drive, Danvers, MA 01923, 978-750-8400. CCC is a not-for-profit organization that provides licenses and registration for a variety of users. For organizations that have been granted a photocopy license by the CCC, a separate system of payment has been arranged.

**Trademark Notice:** Product or corporate names may be trademarks or registered trademarks, and are used only for identification and explanation without intent to infringe.

---

**Library of Congress Cataloging-in-Publication Data**

---

Organic electronics : materials, processing, devices and applications / editor, Franky So.  
p. cm.  
“A CRC title.”  
Includes bibliographical references and index.  
ISBN 978-1-4200-7290-7 (hard back : alk. paper)  
1. Organic electronics. 2. Electronic devices--Materials. 3. Electronic polymers. I. So,  
Franky. II. Title.

TK7871.15.P6O74 2010  
621.381--dc22

2009030895

---

Visit the Taylor & Francis Web site at  
<http://www.taylorandfrancis.com>

and the CRC Press Web site at  
<http://www.crcpress.com>

---

# *Contents*

---

Preface.....	vii
Editor.....	ix
Contributors.....	xi

## **Part I Materials and Processing**

1. **π-Conjugated Polymers for OLEDs** ..... 3  
*Muthusamy Tamilvanan and Sung-Ho Jin*

2. **Organic Vapor-Phase Deposition** ..... 27  
*Max Shtein*

## **Part II Device Physics**

3. **Charge Transport and Injection in Amorphous Organic Semiconductors** ..... 61  
*S. C. Tse, C. H. Cheung, and S. K. So*

4. **Magnetic Field Effects in Organic Semiconducting Materials and Devices** ..... 111  
*Bin Hu and Liang Yan*

5. **Interface in Organic Semiconductor Devices: Dipole, Doping, Band Bending, and Growth** ..... 141  
*Yongli Gao*

6. **Interfaces in Organic Electronic Devices—New Insights to Traditional Concepts** ..... 181  
*Man-Keung Fung, Chun-Sing Lee, and Shuit-Tong Lee*

7. **The Role of Homolytic Reactions in the Intrinsic Degradation of OLEDs** ..... 211  
*Denis Y. Kondakov*

8. **Materials and Interface Engineering in Organic Light-Emitting Diodes** ..... 243  
*Fei Huang and Alex K.-Y. Jen*

## Part III Organic Electronic Devices

<b>9. Microcavity Effects in Organic Light-Emitting Devices.....</b>	265
<i>Chung-Chih Wu and Hao-Wu Lin</i>	
<b>10. Vertical-Type Organic Transistors .....</b>	293
<i>Yasuyuki Watanabe, Masakazu Nakamura, and Kazuhiro Kudo</i>	
<b>11. Routes toward High-Efficiency Polymer Solar Cells .....</b>	319
<i>Yang Yang, Yan Yao, and Gang Li</i>	
<b>12. Mixed Molecular Heterojunction Photovoltaic Cells .....</b>	359
<i>Jiangeng Xue</i>	
<b>13. Development of Polymer Semiconductors for Field-Effect Transistor Devices in Displays .....</b>	393
<i>Rick Hamilton, Martin Heeney, Thomas Anthopoulos, and Iain McCulloch</i>	

## Part IV Applications

<b>14. OLED Materials and Device Architectures for Full-Color Displays and Solid-State Lighting.....</b>	433
<i>Tukaram K. Hatwar, Marina E. Kondakova, David J. Giesen, and Jeffrey P. Spindler</i>	
<b>15. Organic Light-Emitting Diodes and Photodetectors for Optical Communication.....</b>	511
<i>Yutaka Ohmori</i>	
<b>16. Organic Light-Emitting Diodes in Chemical and Biological Sensors.....</b>	529
<i>Ruth Shinar, Yuankun Cai, and Joseph Shinar</i>	
<b>Index .....</b>	551

---

## Preface

---

Research in organic semiconductors has long been a subject of scientific interest for many chemists. Initially, physicists and engineers did not consider organic semiconductors to have any technological significance because of the lack of control of material purity and structural ordering when compared to their inorganic counterparts such as silicon or gallium arsenide. I remember giving a talk on organic semiconductor devices at an IEEE conference in the late 1980s while I was still a graduate student, when somebody came to me after the presentation and said “you are still talking about that plastic stuff.” I felt as though I did not belong there because people were not interested in “stuff” made primarily from carbon. Twenty years later, the world has changed and so has scientific research. Ever since the invention of organic light-emitting diodes (OLEDs) by Tang and Van Slyke in the late 1980s, research in the field of organic semiconductors has flourished. The number of citations to the original OLED paper published in *Applied Physics Letters* by Tang and Van Slyke alone has exceeded 5000. There are many consumer products such as mobile phones and MP3 players that have OLED displays. Sony introduced an 11 in. OLED television into the market in 2008. Since then, many electronic companies have been pursuing OLEDs as the next generation displays for televisions. Moving forward, organic semiconductors may soon be used in a variety of consumer products. Applications other than OLEDs will probably be organic thin film transistors used in devices such as back-plane transistors for e-book displays. Further down the road, another important application might be the third-generation organic photovoltaics.

Given the rapid development in this field, a book covering various aspects of organic semiconductors from materials processing, physics of organic semiconductors, and organic electronic devices to applications is much needed. I have invited 16 experts in the field to contribute chapters to this book. This book has been divided into four parts. Part I covers materials and processing. Professor Sung-Ho Jin and coworkers present the latest developments of conjugated polymers for organic devices and Professor Max Shtein presents the latest developments of organic vapor phase deposition to fabricate organic nanostructures. Part II covers the physics of organic semiconductors. In device physics, Professor S.K. So and coworkers present charge transport and injection in organic semiconductors and Professor Bin Hu and coworkers present their work on spin injection. In the area of interface physics, Professor Yongli Gao discusses the energy alignment and doping effect in organic semiconductors, and Professor C.S. Lee and coworkers present their results on the effect of interface physics on devices. In the area of device degradation, Dr. Denis Kondakov presents his results on the physics and

chemistry of OLED degradation. In the area of device engineering, Professor Alex Jen and coworkers present recent developments on interface engineering. Part III covers novel organic electronic devices. In the area of OLEDs and photovoltaics, Professor C.C. Wu presents his work on microcavity effects on OLEDs, Professor Yasuyuki Watanabe and coworkers present their work on vertical-type organic transistors, Professor Yang Yang and coworkers present the latest developments on polymer solar cells, Professor Jiangeng Xue presents his latest work on small molecule solar cells, and Professor Iain McCulloch and coworkers present their work on polymer thin film transistors. Part IV covers the applications of organic electronic devices. Dr. T.K. Hatwar and coworkers present their work on OLEDs for displays and lighting, Professor Yutaka Ohmori presents his work on OLEDs and organic photodetectors for optical communication, and Professor Joseph Shinar and coworkers present their work on OLEDs for biosensors.

I believe that this book can serve as a research update as well as a reference tool for scientists and engineers in the field of organic semiconductor materials and devices. I hope the information presented in this book serves as a base to further develop new sciences and technologies based on organic semiconductors. Finally, I would like to thank all the authors for their contributions to this book.

**Franky So**  
*University of Florida*

---

## *Editor*

---

**Franky So** received his BA in physics from Hamilton College, his MS in materials science from the Massachusetts Institute of Technology, and his PhD in electrical engineering from the University of Southern California. After his graduation in 1991, he worked as a research scientist at the Hoechst Celanese Research Division studying high-speed polymer electro-optical modulators and organic light-emitting diodes (OLEDs). In 1993, he joined the Motorola Phoenix Corporate Laboratories and worked to develop OLEDs for flat-panel displays. He later became the program manager responsible for the development of OLED technology. During his tenure at Motorola, he received the Distinguished Innovator Award and the Master Innovator Award. In 2001, So joined OSRAM Opto-Semiconductors and became the head of materials and devices research. He was responsible for managing the OLED R&D activities for flat-panel displays as well as solid state lighting. In the summer of 2005, he joined the faculty in the Department of Materials Science and Engineering at the University of Florida. He currently works as an associate professor in the department. His research interests include electronic properties of organic semiconductor thin films, charge transport properties, device physics, organic-based light-emitting devices, organic photovoltaics, and organic sensors.

Dr. So is currently an associate editor of the *IEEE Journal of Display Technology* and the journal *Materials Science and Engineering Reports*. Dr. So holds more than 50 issued patents and is a Fellow of the SPIE.



---

## *Contributors*

---

**Thomas Anthopoulos**

Department of Physics  
Imperial College  
London, United Kingdom

**Yuankun Cai**

Ames Laboratory—U.S. Department  
of Energy  
Iowa State University  
Ames, Iowa

and

Department of Physics and  
Astronomy  
Iowa State University  
Ames, Iowa

**C. H. Cheung**

Department of Physics  
Hong Kong Baptist University  
Hong Kong SAR, China

**Man-Keung Fung**

Department of Physics and  
Materials Science  
City University of Hong Kong  
Kowloon Tong, Hong Kong SAR,  
China

**Yongli Gao**

Department of Physics and  
Astronomy  
University of Rochester  
Rochester, New York

**David J. Giesen**

Display Technology Unit  
Research and Development  
Eastman Kodak Company  
Rochester, New York

**Rick Hamilton**

Department of Chemistry  
Imperial College  
London, United Kingdom

**Tukaram K. Hatwar**

Display Technology Unit  
Research and Development  
Eastman Kodak Company  
Rochester, New York

**Martin Heeney**

Departments of Chemistry  
Imperial College  
London, United Kingdom

**Bin Hu**

Department of Materials Science  
and Engineering  
University of Tennessee  
Knoxville, Tennessee

**Fei Huang**

Department of Materials Science  
and Engineering  
Institute of Advanced Materials and  
Technology  
University of Washington  
Seattle, Washington

**Alex K.-Y. Jen**

Department of Materials Science  
and Engineering  
Institute of Advanced Materials and  
Technology  
University of Washington  
Seattle, Washington

**Sung-Ho Jin**

Department of Chemistry Education  
and Interdisciplinary Program  
of Advanced Information and  
Display Materials  
Pusan National University  
Busan, South Korea

**Denis Y. Kondakov**

OLED Materials and Architecture  
Research and Development  
Eastman Kodak Company  
Rochester, New York

**Marina E. Kondakova**

Display Technology Unit  
Research and Development  
Eastman Kodak Company  
Rochester, New York

**Kazuhiro Kudo**

Faculty of Engineering  
Chiba University  
Chiba, Japan

**Chun-Sing Lee**

Department of Physics and  
Materials Science  
City University of Hong Kong  
Kowloon Tong, Hong Kong SAR,  
China

**Shuit-Tong Lee**

Department of Physics and  
Materials Science  
City University of Hong Kong  
Kowloon Tong, Hong Kong SAR,  
China

**Gang Li**

Department of Materials Science  
and Engineering  
University of California-Los Angeles  
Los Angeles, California

and

Solarmer Energy Inc.  
El Monte, California

**Hao-Wu Lin**

Department of Materials Science  
and Engineering  
National Tsing Hua University  
Hsin-Chu, Taiwan

**Iain McCulloch**

Department of Chemistry  
Imperial College  
London, United Kingdom

**Masakazu Nakamura**

Faculty of Engineering  
Chiba University  
Chiba, Japan

**Yutaka Ohmori**

Center for Advanced Science and  
Innovation  
Osaka University  
Suita, Osaka, Japan

**Joseph Shinar**

Ames Laboratory—U.S. Department  
of Energy  
Iowa State University  
Ames, Iowa

and

Department of Physics and  
Astronomy  
Iowa State University  
Ames, Iowa

**Ruth Shinar**

Microelectronics Research Center  
Iowa State University  
Ames, Iowa

and

Department of Electrical and  
Computer Engineering  
Iowa State University  
Ames, Iowa

**Max Shtein**

Department of Materials Science  
and Engineering  
University of Michigan  
Ann Arbor, Michigan

**S. K. So**

Department of Physics  
Hong Kong Baptist University  
Hong Kong SAR, China

**Jeffrey P. Spindler**

Display Technology Unit  
Research and Development  
Eastman Kodak Company  
Rochester, New York

**S. C. Tse**

Department of Physics  
Hong Kong Baptist University  
Hong Kong SAR, China

**Muthusamy Tamilvanan**

Department of Chemistry Education  
and Interdisciplinary Program  
of Advanced Information and  
Display Materials  
Pusan National University  
Busan, South Korea

**Yasuyuki Watanabe**

Center for Frontier Science  
Chiba University  
Chiba, Japan

**Chung-Chih Wu**

Department of Electrical  
Engineering  
National Taiwan University  
Taipei, Taiwan

**Jiangeng Xue**

Department of Materials Science  
and Engineering  
University of Florida  
Gainesville, Florida

**Liang Yan**

Department of Materials Science  
and Engineering  
University of Tennessee  
Knoxville, Tennessee

**Yang Yang**

Department of Materials Science  
and Engineering  
University of California-Los Angeles  
Los Angeles, California

**Yan Yao**

Department of Materials Science  
and Engineering  
University of California-Los Angeles  
Los Angeles, California



# **Part I**

# **Materials and Processing**



# 1

---

## *π-Conjugated Polymers for OLEDs*

---

Muthusamy Tamilvanan and Sung-Ho Jin

### CONTENTS

1.1	Introduction .....	3
1.2	Synthesis and Characterization of PPV and PFV Derivatives.....	5
1.3	Optical and Electroluminescence Properties of PPV and PFV Derivatives .....	9
1.4	Summary and Conclusion .....	20
	Acknowledgments .....	23
	References.....	23

---

### 1.1 Introduction

The development of  $\pi$ -conjugated polymers is one of the most challenging topics in polymer chemistry. These  $\pi$ -conjugated materials are suitable for the preparation of the emissive and charge-transporting layers of organic light-emitting diodes (OLEDs), polytronics, and organic solar cells. The  $\pi$ -conjugated electroluminescent (EL) polymers have been very active due to their film-forming abilities via spin coating and their tunable luminescence properties, which makes them an excellent choice in both single- and multilayer OLEDs. Polymer light-emitting diodes (PLEDs) have many advantages, including self-emission, low operating voltage, fast switching time, easy fabrication at low cost, and potential in full-color flat-panel displays and flexible displays compared to other displays.<sup>1–3</sup> The efficiency of the OLEDs is determined by the amount of charge-carrier injection, the probability of charge capture, and the balance between the injection rates of electrons and holes from opposite contacts into the OLEDs.<sup>4–6</sup> In simple OLEDs, the emissive layer would be sandwiched between two electrodes. At the cathode, the electrons are injected into the lowest unoccupied molecular orbital (LUMO); at the anode, the holes are injected into the highest occupied molecular orbital (HOMO). The two charges move through the layer under the applied bias and if they meet on the same molecule, they can

form an exciton, which may decay thus emitting a light the color of which is governed by the HOMO–LUMO energy gap of the material. To have efficient OLEDs, it is necessary to have balanced charge injection and transport, to capture all the injected charges to form excitons, and to have radiative decay of all the excitons formed. A balance of the rates in the injection of electrons and holes from opposite contacts into the OLEDs is crucial to achieving high EL efficiency.<sup>7</sup> The use of metal with a low work function as cathode, such as calcium, magnesium, or lithium, can lower the charge-injection barrier at the cathode to improve the luminous efficiency by balancing the injected electrons and holes.<sup>8–10</sup> However, these metals have high chemical reactivity to oxygen and moisture that limits their practicality. This method could also space charges and tunneling of accumulated holes<sup>11,12</sup> and subsequently increase the turn-on voltage. Another strategy to improve the efficiency of the device is to use a blend of electron-transport material and an EL polymer. The inevitable drawback of this approach is that there may be phase separation<sup>13,14</sup> between two different kinds of materials, which could accelerate the rate of recrystallization and aggregate formation generated by the heat formed during the separation of OLEDs. Therefore, to improve the luminance efficiency of PLEDs, many research groups have used a combination of electron and/or hole transport materials or they have attached electron and/or hole transport moieties on the side chain of the polymer backbone or on the main chain of the polymer.<sup>15,16</sup> Among the various types of  $\pi$ -conjugated polymers reported, poly(*p*-phenylenevinylenes) (PPVs),<sup>17–19</sup> poly(dialkylfluorenes) (PFs),<sup>20,21</sup> polythiophenes (PThs),<sup>22</sup> and their derivatives exhibit the most promise for PLED applications and have been used widely. Various techniques have been proposed to improve the performance of PLEDs by modifying the chemical structure of the polymer with bulky phenyl side groups, or PPV-based alternating copolymers containing the conjugated phenylenevinylene segments and nonconjugated spacers.<sup>23–25</sup> These bulky side groups interrupt conjugation length and interfere with the packing of the polymer chain, which results in the formation of amorphous PPVs. Similarly, PFs containing two planarized benzene rings per monomeric unit have many advantages such as chemical and thermal stability, high photoluminescence (PL) quantum efficiency, and ease of property tuning by copolymerization with various monomers. However, the main drawback of PFs is their tendency to form aggregates or keto defects with long wavelength as a result of heating or current application during device fabrication or operation.<sup>26–30</sup> In an attempt to solve these problems, many research groups have introduced fluorene substituents into the carbon 9-position of the fluorene main chain to produce spirobifluorene segments.<sup>31,32</sup> In such spiro-segments, the bifluorenes are orthogonally arranged and the resulting polymer chains are twisted at an angle of 90° at each spiro-center. This structural feature was expected to reduce the probability of interchain interactions and to prevent close packing of the polymer chains. In addition, the spirobifluorene-annulated segment was expected to enhance the rigidity of the polymer backbone, leading to a significant increase both in the glass transition temperature

and in the thermal stability of these polymers. However, spirobifluorene-segmented homopolymers exhibit poor solubility in common organic solvents, which makes it difficult to fabricate devices. One strategy to solve the defects of spirobifluorene-segmented polymers is to introduce long-chain alkyloxy substituents into the spirobifluorene units in order to improve the solubility of the resulting polymers. Another approach via chemical modification is the introduction of vinylene-repeating units along the spirobifluorene main chain by Gilch polymerization in order to reduce the rigidity of the polymer chain and increase the level of amorphous morphology, which improves the performance of PLEDs and the tuning of the electro-optical properties. The EL polymers synthesized in our group have been carried out by the Gilch polymerization. Various polymerization methods for the synthesis of EL polymers have been developed, such as the Wittig reaction,<sup>33</sup> the Heck reaction,<sup>34</sup> the Suzuki coupling,<sup>35</sup> the Ni(0)-mediated Yamamoto coupling reaction,<sup>36</sup> and the Gilch polymerization.<sup>37</sup> Among them, the Gilch polymerization offers a number of important advantages for the introduction of vinylene units along the polymer backbone with high molecular weight and low polydispersity, and allows for easy purification.<sup>38</sup>

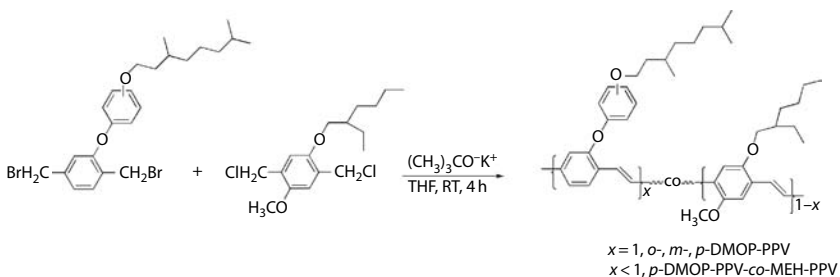
In recent years, our research work has been focused on the synthesis of novel PPV and poly(9,9-dialkylfluorenyl-2,7-vinylene) (PFV) derivatives for PLEDs. In this chapter, we have been able to provide the results of recently synthesized PPV and PFV derivatives with their PLED applications.

---

## 1.2 Synthesis and Characterization of PPV and PFV Derivatives

We have reported the synthesis and characterization of the color-tunable PPV derivatives and their copolymers as obtained by the molecular design.<sup>39</sup> To control emission colors, 3,7-dimethyloctyloxy groups were introduced into the *ortho*-, *meta*-, and *para*-positions of the phenoxy-substituted PPV backbone. Scheme 1.1 outlines the synthesis of the poly[2-{2-[(3,7-dimethyloctyl)oxy]phenoxy}-1,4-phenylenevinylene] (DMOP-PPV) and DMOP-PPV-*co*-MEH-PPV. The polymerization of bis(bromomethyl)benzene derivatives was performed with an excess of potassium *tert*-butoxide in cooled dry THF under N<sub>2</sub> atmosphere. The copolymerization was carried out with various initial monomer concentrations of 1,4-bis(chloromethyl)-2-[(2'-ethylhexyl)oxy]-5-methoxybenzene following a method similar to homopolymerization.

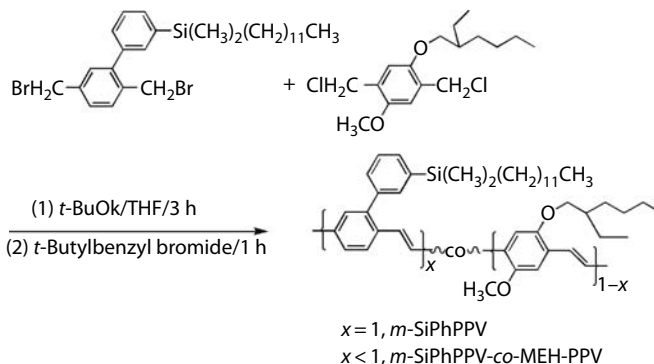
We have also reported a new series of asymmetric and color-tunable PPV derivatives, including copolymers, that were developed in order to overcome the phase separation in polymer-blending systems with MEH-PPV units.<sup>40</sup> In order to improve the performance of PLEDs, the bulky dimethyldodecylsilylphenyl group was introduced into the *meta*-position of the phenyl substituent, which inhibits the intermolecular interaction between the

**SCHEME 1.1**

Synthesis of alkyloxyphenoxy-substituted PPVs.

resulting polymer chains. Scheme 1.2 outlines the synthesis of *m*-SiPhPPV and copolymers, *m*-SiPhPPV-*co*-MEH-PPVs, with various monomer feed ratios. The insertion of a long-chain dodecyldimethylsilylphenyl group as the side chain of a PPV backbone yields unique properties, which include good flexibility, solubility, adhesion to the substrate and electrodes, and improved performances of the devices. The homopolymerization of the monomer and the copolymerization with 1,4-bis(chloromethyl)-2-(2-ethylhexyloxy)-5-methoxybenzene were performed as described earlier.<sup>39</sup> The resulting EL polymers, *m*-SiPhPPV, and copolymers, *m*-SiPhPPV-*co*-MEH-PPVs, were completely soluble in common organic solvents, such as chloroform, chlorobenzene, toluene, THF, and xylene.

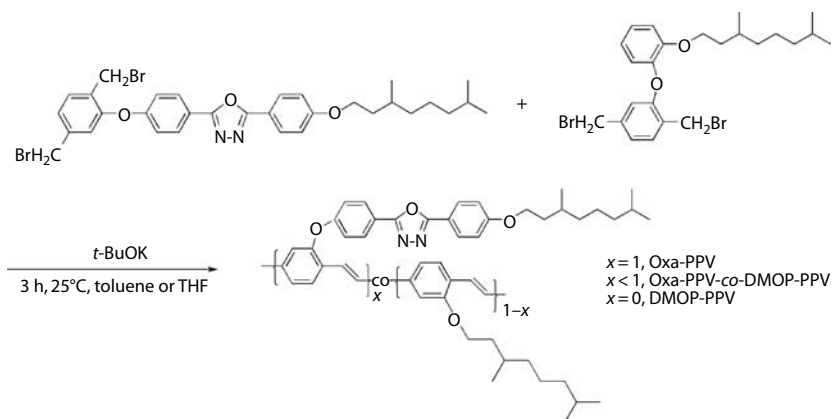
To improve the luminance efficiency of PLEDs, many research groups have attached electron and/or hole transport moieties on the side chain of the polymer backbone or on the main chain of the polymer. Therefore, we reported a new series of multifunctional high-brightness and luminance-efficient EL polymers, poly[2-[4-[5-(4-(3,7-dimethyloctyloxy)phenyl)-1,3,4-oxadiazole-2-yl]phenyloxy]-1,4-phenylenevinylene] (Oxa-PPV), DMOP-PPV,

**SCHEME 1.2**

Synthesis of silylphenyl-substituted PPVs.

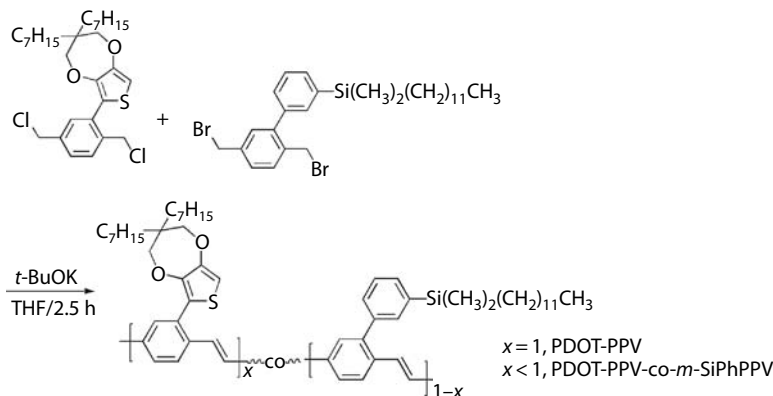
and their corresponding random copolymers, poly[[2-{4-[5-(4-(3,7-dimethyloctyloxy)phenyl)-1,3,4-oxadiazole-2-yl]phenoxy}-1,4-phenylenevinylene]-co-[2-{2-[ (3,7-dimethyloctyl)oxy]phenoxy}-1,4-phenylenevinylene]} (Oxa-PPV-*co*-DMOP-PPV) with electron-deficient 1,3,4-oxadiazole unit on side groups were synthesized through the Gilch polymerization method.<sup>41</sup> One of the most widely used electron-transport moieties are aromatic 1,3,4-oxadiazole-based compounds with high electron affinities, which facilitate electron transport and injection. For such a purpose, we designed and synthesized PPV derivatives containing 1,3,4-oxadiazole pendant groups. The synthetic routes for Oxa-PPV and Oxa-PPV-*co*-DMOP-PPV are depicted in Scheme 1.3. Homopolymerization of the monomer was performed with an excess of potassium *tert*-butoxide in dry toluene under N<sub>2</sub> atmosphere. To improve the performance of PLEDs and to tune the electro-optical properties of Oxa-PPV, we copolymerized 2-[4-[2,5-bis(bromomethyl)phenoxy]phenyl-5[4-[3,7-imethyloctyl]oxy]phenyl]-1,3,4-oxadiazole with various feed ratios of 1,4-bis(bromomethyl)-2-[2-[3,7-dimethyloctyl]oxy]phenoxy]benzene in THF. During the polymerization, the viscosity of the reaction mixture was increased without any precipitation and intense fluorescent light was observed. The good solubility behavior of the EL polymers, Oxa-PPV and Oxa-PPV-*co*-DMOP-PPV, is due to the easy and free rotation between the PPV backbone and the side chain 1,3,4-oxadiazole units, which was linked via oxygen atom and bent type 3,7-dimethyloctyloxy substituent into the phenoxy side group on DMOP-PPV.

More recently, we have synthesized a new series of multifunctional EL polymers, poly[1,4-{2-(3,3'-diheptyl-3,4-propylenedioxythiophene-2-yl)}phenylenevinylene] (PDOT-PPV), which is a series of fully conjugated PPV derivatives with a PDOT moiety as a pendant group.<sup>42</sup> The polymerization of the monomers is outlined in Scheme 1.4. The homo- and copolymerization of monomers was performed by the Gilch polymerization



SCHEME 1.3

Synthesis of oxadiazole-substituted PPVs.

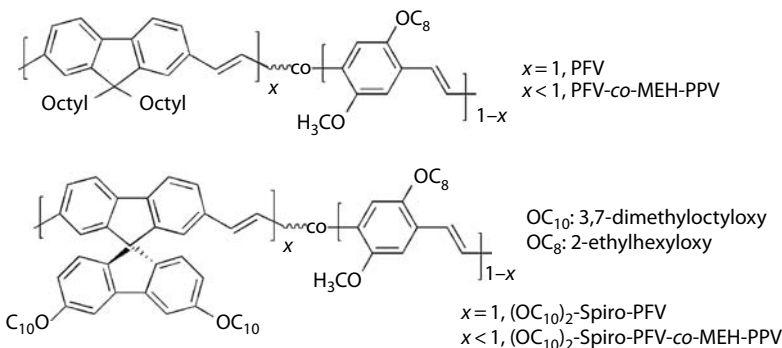


### SCHEME 1.4

## Synthesis of PDOT-substituted PPVs.

with an excess of potassium *tert*-butoxide in THF in an ice bath under N<sub>2</sub> atmosphere.

Fluorene-based EL polymers have many advantages such as the easy introduction of substituents at the C-9 position, high PL and EL efficiencies, thermal and chemical stabilities, and tuning the emission colors by controlling the coplanarity or copolymer system. The electronic and optical properties of EL polymers are governed by modifying the chemical structure of the backbone. In order to adjust the HOMO and LUMO energy levels and the formation of amorphous morphology of the fluorene-based EL polymers, we first synthesized PFV and its copolymers via the Gilch polymerization.<sup>43</sup> Scheme 1.5 shows the chemical structures of PFV, PFV-*co*-MEH-PPV, (OC<sub>10</sub>)<sub>2</sub>-Spiro-PFV, and (OC<sub>10</sub>)<sub>2</sub>-Spiro-PFV-*co*-MEH-PPV. The resulting EL polymers, PFV, PFV-*co*-MEH-PPV, (OC<sub>10</sub>)<sub>2</sub>-Spiro-PFV, and



### SCHEME 1.5

Chemical structures of PFV, PFV-*co*-MEH-PPV, (OC<sub>10</sub>)<sub>2</sub>-Spiro-PFV, and (OC<sub>10</sub>)<sub>2</sub>-Spiro-PFV-*co*-MEH-PPV.

(OC<sub>10</sub>)<sub>2</sub>-Spiro-PFV-*co*-MEH-PPV were completely soluble in various organic solvents such as chloroform, chlorobenzene, toluene, and xylene. The good solubility of these polymers is an important requirement for PLED fabrication and can be attributed to the dialkyl side chains at the C-9 position in PFV units and three branched alkyloxy side chains attached to the Spiro-PFV units and the PPV-repeating units along the polymer backbone. This structural feature inhibits chain packing and thus minimizes  $\pi-\pi^*$  intermolecular interactions. The glass transition temperatures of the PFV derivatives were found to be in the range of 169°C–222°C; these values are higher than those of dialkyloxy-substituted PPVs<sup>44</sup> and poly(9,9-dialkylfluorene)s.<sup>45,46</sup>

Table 1.1 summarizes the polymerization results, molecular weights, and thermal characteristics of the resulting polymers.

---

### 1.3 Optical and Electroluminescence Properties of PPV and PFV Derivatives

Homopolymers with *ortho*-, *meta*-, and *para*-positions of 3,7-dimethyloctyloxy substituent in phenoxy side group show almost the same absorption maxima at about 451, 455, and 464 nm. As the 3,7-dimethyloctyloxy group is linked from *para*- to *ortho*-position of the phenoxy side group, the effective conjugation length is shortened by steric hindrance between 3,7-dimethyloctyloxyphenoxy side group and vinylic protons because of the distortion of coplanarity of the polymer backbones. The maximum absorption spectra of the copolymers are more redshifted than those of *o*-, *m*-, and *p*-DMOP-PPV. The emission peaks of the *o*-, *m*-, and *p*-DMOP-PPV are broader and the maximum peaks were observed at 549, 560, and 585 nm, respectively, with a shoulder at about 518–540 nm. As the MEH-PPV contents were increased, the emission peaks of the copolymers were redshifted from 549 to 600 nm. Such a redshift of the copolymer system could be attributed to the intramolecular energy transfer from the high band gap of the *p*-DMOP-PPV segment to the low band gap of the MEH-PPV segment of the copolymers. The PLED performances of *o*-, *m*-, and *p*-DMOP-PPV, and *p*-DMOP-PPV-*co*-*m*-SiPhPPV have been studied. Figure 1.1 shows the current density–voltage–luminance (*J*–*V*–*L*) characteristics of the ITO/PEDOT:PSS/homopolymer (Figure 1.1a) or copolymer (Figure 1.1b)/Al devices. The PEDOT:PSS buffer layer was coated to achieve the high luminous efficiency and low turn-on voltage. The turn-on voltage of light emission varied from approximately 1.8 V for *p*-DMOP-PPV-*co*-MEH-PPV (3:7) to 4.5 V for homopolymers. The brightness of *o*-, *m*-, and *p*-DMOP-PPV reaches about 1845, 770, and 316 cd/m<sup>2</sup>, respectively, at 10 V. The brightness of *p*-DMOP-PPV-*co*-MEH-PPV (7:3) is 7000 cd/m<sup>2</sup> at 10 V, which is much higher than those of *o*-, *m*-, and *p*-DMOP-PPV. The

**TABLE 1.1**

Polymerization Results, Weight Average Molecular Weight ( $M_w$ ), and Polydispersity of the Polymers

Polymer	Yield (%)	$M_w^a \times 10^4$	PDI <sup>a</sup>
<i>o</i> -DMOP-PPV	70	24	2.81
<i>m</i> -DMOP-PPV	74	25	2.93
<i>p</i> -DMOP-PPV	65	12	2.46
<i>p</i> -DMOP-PPV- <i>co</i> -MEH-PPV (70:30) <sup>b</sup>	71	73	4.28
<i>p</i> -DMOP-PPV- <i>co</i> -MEH-PPV (50:50) <sup>b</sup>	66	26	3.65
<i>p</i> -DMOP-PPV- <i>co</i> -MEH-PPV (30:70) <sup>b</sup>	70	31	2.24
<i>m</i> -SiPhPPV	75	96	3.40
<i>m</i> -SiPhPV- <i>co</i> -MEH-PPV (90:10) <sup>c</sup>	80	27	1.92
<i>m</i> -SiPhPV- <i>co</i> -MEH-PPV (75:25) <sup>c</sup>	82	83	2.0
<i>m</i> -SiPhPV- <i>co</i> -MEH-PPV (20:80) <sup>c</sup>	85	54	1.86
MEH-PPV	80	80	2.67
Oxa-PPV	46	9.7	1.4
Oxa-PPV- <i>co</i> -DMOP-PPV (84:16) <sup>d</sup>	53	69	4.9
Oxa-PPV- <i>co</i> -DMOP-PPV (64:36) <sup>d</sup>	60	38	6.5
Oxa-PPV- <i>co</i> -DMOP-PPV (51:49) <sup>d</sup>	57	35	7.8
Oxa-PPV- <i>co</i> -DMOP-PPV (28:72) <sup>d</sup>	55	59	8.6
Oxa-PPV- <i>co</i> -DMOP-PPV (7.93) <sup>d</sup>	40	39	5.9
PDOT-PPV	59	22.0	5.3
PDOT-PPV- <i>co</i> - <i>m</i> -SiPhPPV (73:27) <sup>e</sup>	75	31.2	5.0
poly(PDOT-PV- <i>co</i> - <i>m</i> -SiPhPPV (53:47) <sup>e</sup>	60	23.2	5.2
poly(PDOT-PV- <i>co</i> - <i>m</i> -SiPhPPV (34:66) <sup>e</sup>	75	36.7	5.8
(OC <sub>10</sub> ) <sub>2</sub> -Spiro-PFV	70	4.3	2.8
(OC <sub>10</sub> ) <sub>2</sub> -Spiro-PFV- <i>co</i> -MEH-PPV (95:5) <sup>f</sup>	75	12.6	1.8
(OC <sub>10</sub> ) <sub>2</sub> -Spiro-PFV- <i>co</i> -MEH-PPV (85:15) <sup>f</sup>	80	12.5	1.9
(OC <sub>10</sub> ) <sub>2</sub> -Spiro-PFV- <i>co</i> -MEH-PPV (80:20) <sup>f</sup>	80	23.5	2.3
(OC <sub>10</sub> ) <sub>2</sub> -Spiro-PFV- <i>co</i> -MEH-PPV (40:60) <sup>f</sup>	80	31.9	2.7

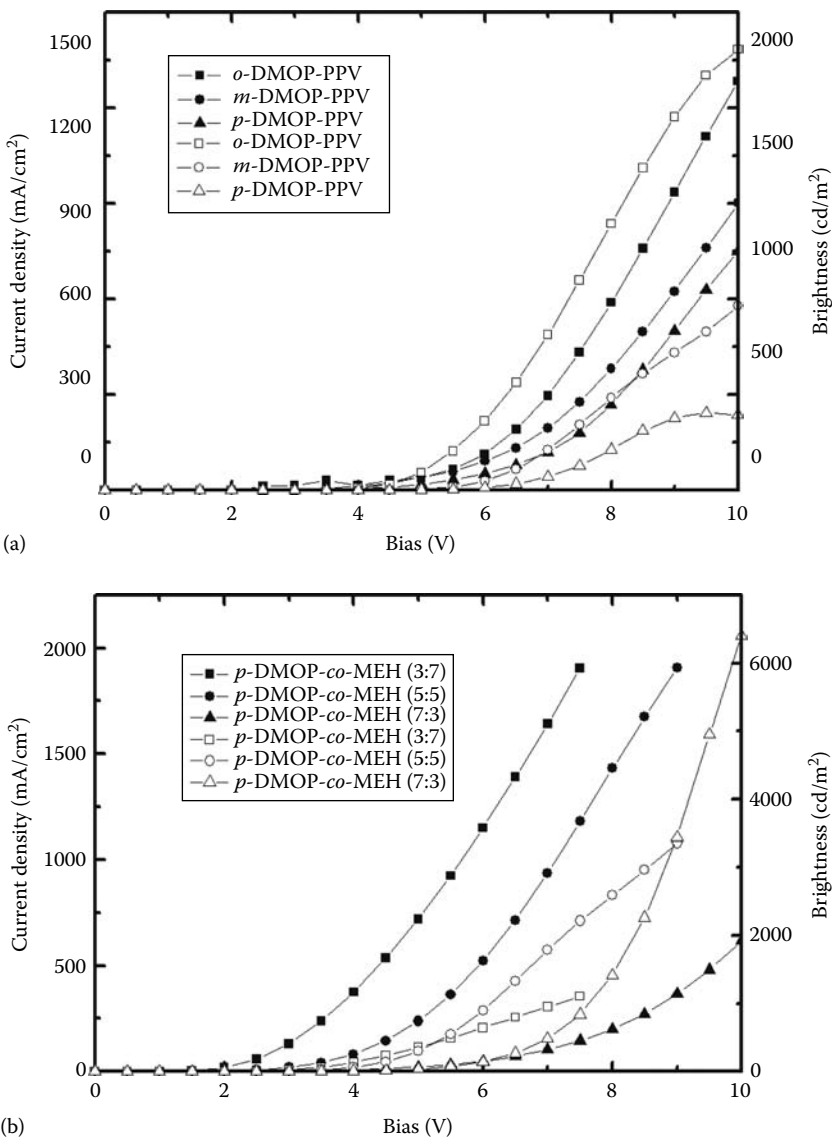
<sup>a</sup> Mw and PDI of the polymers were determined by GPC using polystyrene standards.

<sup>b</sup> Initial monomer feed ratios.

<sup>c,e,f</sup> Composition was determined from <sup>1</sup>H-NMR spectroscopy.

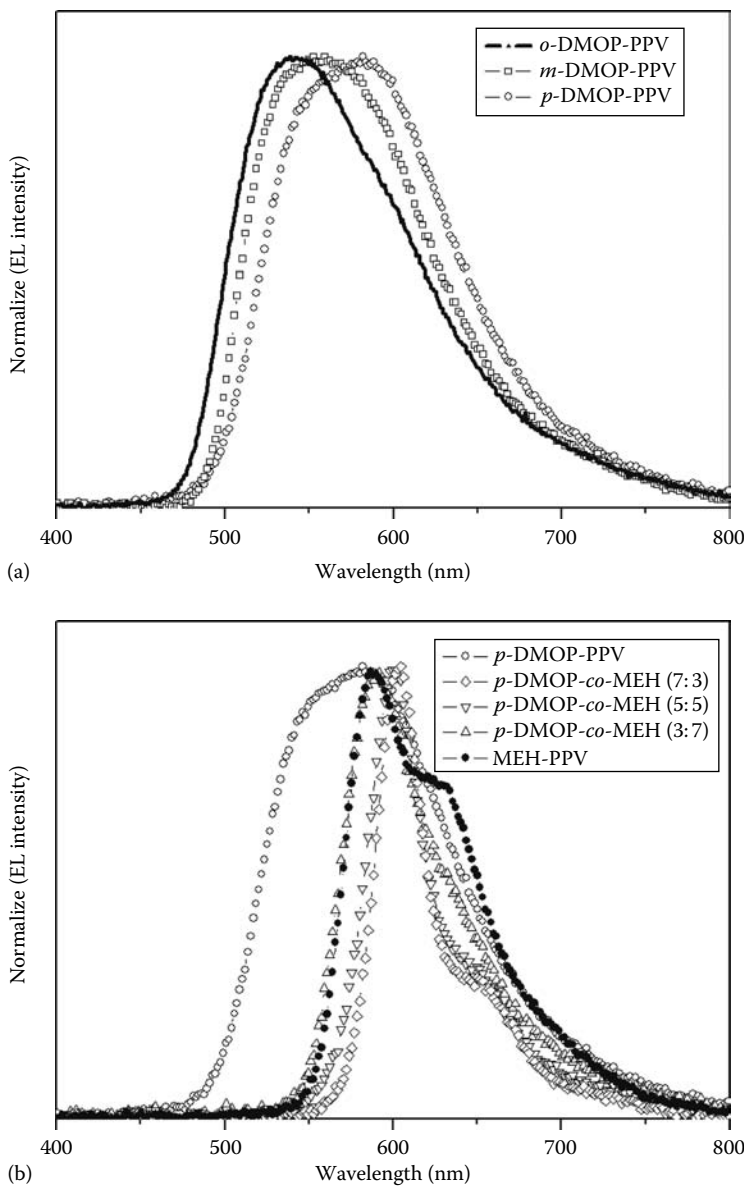
<sup>d</sup> Composition ratio was determined from the ratios of phenyl protons on 1,3,4-oxadiazole and methylene next to oxygen atom.

highest brightness of the *p*-DMOP-PPV-*co*-MEH-PPV (7:3) is attributed to the lower band offset between the LUMO energy level and the Al electrode than those of homopolymers resulting in an easy injection for the electron. The EL spectra of *o*-DMOP-PPV, *m*-DMOP-PPV, and *p*-DMOP-PPV were essentially identical to the PL spectra of the resulting polymers. This result indicates that the EL of the device occurs at the same emission center of PL in the polymer-emitting layer. EL spectra were also found to be redshifted when going from *o*-DMOP-PPV to *p*-DMOP-PPV-*co*-MEH-PPV similarly to

**FIGURE 1.1**

Voltage–current density ( $V$ – $I$ ) (close) and voltage–luminescence ( $V$ – $L$ ) (open) characteristics of ITO/PEDOT/homopolymers (a) and copolymers (b)/Al devices. (Reprinted from Jin, S.-H. et al., *Chem. Mater.* 14, 5090, 2002. With permission.)

the PL and absorption spectra. The sharper emission colors are an important parameter for realizing full color displays. In comparison to MEH-PPV, the copolymer  $p$ -DMOP-PPV-*co*-MEH-PPV (Figure 1.2b) shows narrow emission peaks with a full width at half-maximum (FWHM) approaching

**FIGURE 1.2**

EL spectra of ITO/PEDOT/homopolymer (a) and copolymer (b)/Al devices. (Reprinted from Jin, S.-H. et al., *Chem. Mater.* 14, 5090, 2002. With permission.)

40 nm. This phenomenon is good coinciding with the explanation of higher external PL quantum efficiency. Due to the inhibition, the intermolecular interaction by 3,7-dimethyloctyloxyphenoxy groups in solid state, the

emission spectra of the *p*-DMOP-PPV-*co*-MEH-PPV is much narrower than that of MEH-PPV.

In the case of asymmetric and color-tunable PPV derivatives with a dimethyldodecylsilylphenyl pendant group, the maximum absorption of *m*-SiPhPPV, *m*-SiPhPPV-*co*-MEH-PPV (75:25 wt %), and MEH-PPV thin films was found at 435, 464, and 510 nm with an onset absorption at 535, 600, and 590 nm, respectively. The absorption and emission maxima of the *m*-SiPhPPV copolymers and MEH-PPV are summarized in Table 1.2. The redshift of the maximum absorption in *m*-SiPhPPV-*co*-MEH-PPV (75:25 wt %) is probably due to the introduction of MEH-PPV and the extension of the polymer main chain. The maximum emission peaks of the *m*-SiPhPPV, *m*-SiPhPPV-*co*-MEH-PPV (75:25 wt %), and MEH-PPV were observed at 525, 594, and 592 nm, which corresponds to green and orange-red light, respectively. The maximum PL spectrum of the *m*-SiPhPPV-*co*-MEH-PPV (75:25 wt %) is similar to that of MEH-PPV. This indicates that the energy transfer in copolymer systems occurs from the *m*-SiPhPPV segment to the MEH-PPV part of the copolymers. The PLED performances of *m*-SiPhPPV, *m*-SiPhPPV-*co*-MEH-PPV, and MEH-PPV have been studied with ITO/PEDOT/polymer/Al:Li devices and are summarized in Table 1.3. The turn-on voltage

**TABLE 1.2**

Absorption, PL, and EL Data of *m*-SiPhPPV, Copolymers, and MEH-PPV

Polymers	Abs <sub>max</sub> (nm)	PL <sub>max</sub> (nm)	EL <sub>max</sub> (nm)
<i>m</i> -SiPhPPV	435	525	528
<i>m</i> -SiPhPV- <i>co</i> -MEH-PPV (90:10)	434	588	589
<i>m</i> -SiPhPV- <i>co</i> -MEH-PPV (75:25)	464	594	595
<i>m</i> -SiPhPV- <i>co</i> -MEH-PPV (20:80)	505	598	590
MEH-PPV	510	592	590

Source: Reprinted from Jin, S.-H. et al., *Chem. Mater.*, 14, 643, 2002. With permission.

**TABLE 1.3**

PLED Performance of the Resulting Polymers in ITO/PEDOT/Polymer/Al:Li Devices

Polymer	Turn-On (V)	L <sub>a</sub> <sup>a</sup> <sub>max</sub> (cd/m <sup>2</sup> , V)	LE <sub>b</sub> <sup>b</sup> <sub>max</sub> (lm/W)
<i>m</i> -SiPhPPV	14	570 (43 V)	0.08
<i>m</i> -SiPhPV- <i>co</i> -MEH-PPV (90:10)	5.5	4,920 (18 V)	0.74
<i>m</i> -SiPhPV- <i>co</i> -MEH-PPV (75:25)	2.3	19,180 (12 V)	2.9
<i>m</i> -SiPhPV- <i>co</i> -MEH-PPV (20:80)	1.9	17,200 (10.5 V)	1.74
MEH-PPV	2.0	4,450 (7.8 V)	0.89

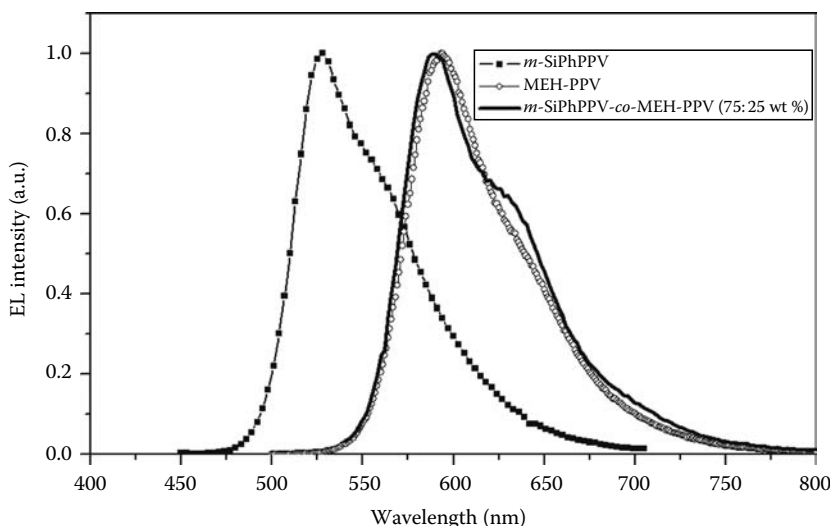
Source: Reprinted from Jin, S.-H. et al., *Chem. Mater.*, 14, 643, 2002. With permission.

<sup>a</sup> Maximum luminescence.

<sup>b</sup> Maximum power efficiency.

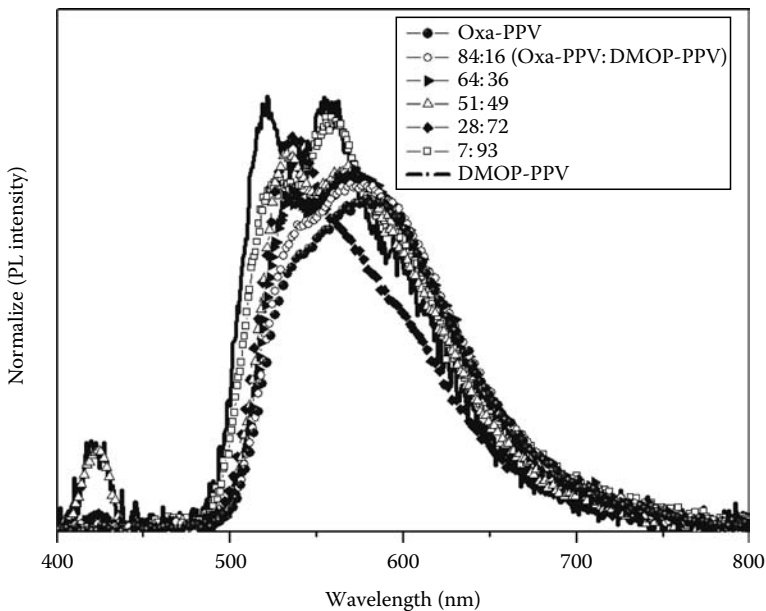
of *m*-SiPhPPV, *m*-SiPhPPV-*co*-MEH-PPV, and MEH-PPV devices were 14, 2.3, and 2.0 V, respectively. The higher turn-on voltage of *m*-SiPhPPV is due to the higher energy barrier between the ITO and HOMO state of *m*-SiPhPPV, which results in a dramatic decrease of hole injection. The EL maximum peak of *m*-SiPhPPV-*co*-MEH-PPV (75:25 wt %) is about 67 nm redshifted relative to that of *m*-SiPhPPV. The maximum brightness of the *m*-SiPhPPV-*co*-MEH-PPV (75:25 wt %) is about 19,180 cd/m<sup>2</sup> at 12.6 V with a current density of about 1.06 A/cm<sup>2</sup>. The half lifetime of a single-layer device of *m*-SiPhPPV-*co*-MEH-PPV (75:25 wt %) at 1000 cd/m<sup>2</sup> is about 120 h in N<sub>2</sub> at room temperature. The maximum power efficiency was 2.9 lm/W with 10 mA/cm<sup>2</sup> at 9.6 V. The EL spectrum of *m*-SiPhPPV, *m*-SiPhPPV-*co*-MEH-PPV, and MEH-PPV in ITO/PEDOT/polymer/Al:Li device is shown in Figure 1.3. The maximum emission peaks of the *m*-SiPhPPV, *m*-SiPhPPV-*co*-MEH-PPV (75:25 wt %), and MEH-PPV were observed at 525, 594, and 592 nm, which corresponds to green and orange-red light, respectively.

The absorption spectrum of Oxa-PPV exhibited two peaks at 441 and 303 nm, which were contributed from  $\pi$ -conjugated main chains and 1,3,4-oxadiazole units, respectively. With the increase in DMOP-PPV content, absorption maximum peak of the 1,3,4-oxadiazole units was decreased and the absorption  $\lambda_{\text{max}}$  of  $\pi-\pi^*$  transition of conjugated main chains was statistically increased. The emission spectra of Oxa-PPV, DMOP-PPV, and Oxa-PPV-*co*-DMOP-PPV in thin films are shown in Figure 1.4. When the



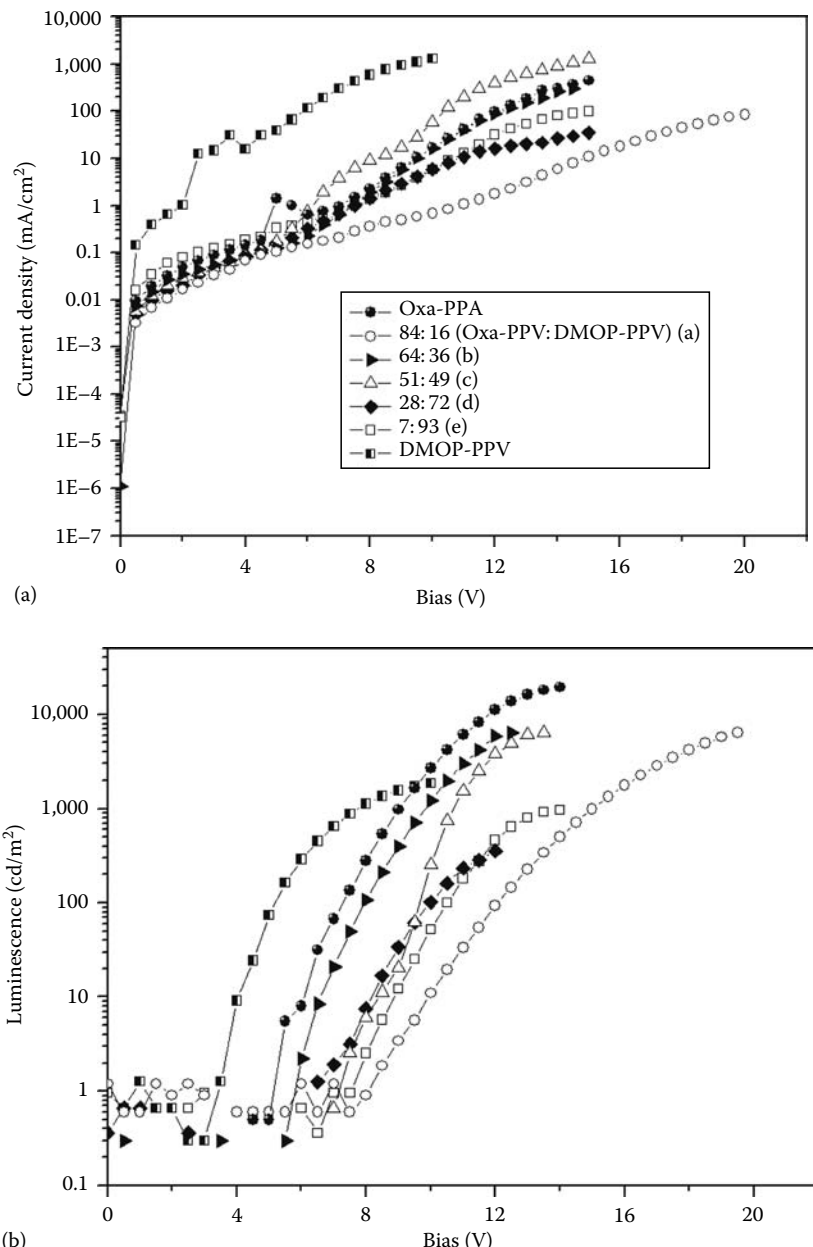
**FIGURE 1.3**

EL spectra of an ITO/PEDOT/polymer/Al:Li devices. (Reprinted from Jin, S.-H. et al., *Chem. Mater.*, 14, 643, 2002. With permission.)

**FIGURE 1.4**

PL spectra of Oxa-PPV, DMOP-PPV, and DMOP-PPV-*co*-Oxa-PPV in solid state. (Reprinted from Jin, S.-H. et al., *J. Am. Chem. Soc.*, 126, 2474, 2004. With permission.)

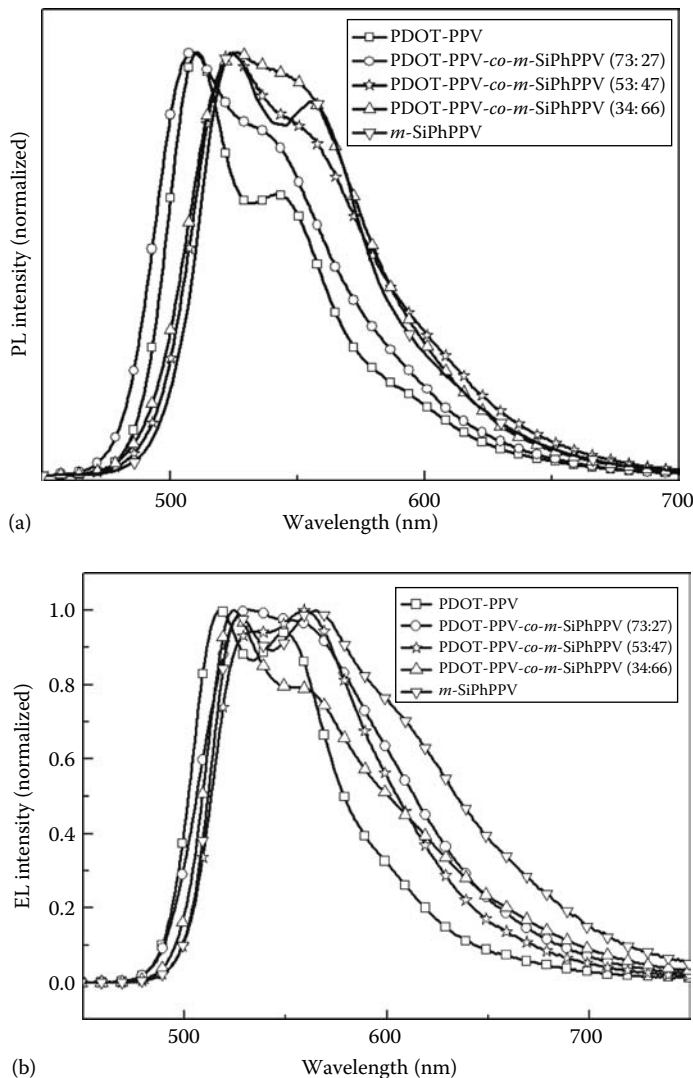
polymer films were excited at maximum absorption wavelength of each polymer, two emission peaks of DMOP-PPV were observed at 520 and 539 nm. However, as Oxa-PPV content was increased in copolymer systems, the emission peak was redshifted from 520 to 573 nm. Photoluminescence excitation (PLE) spectra of Oxa-PPV, DMOP-PPV, and Oxa-PPV-*co*-DMOP-PPV were monitored at the  $\lambda_{\text{max}}$  of the emission spectrum of each polymer. The PLE spectra of Oxa-PPV, DMOP-PPV, and Oxa-PPV-*co*-DMOP-PPV are similar to the absorption spectrum. These phenomena indicated that the efficient energy transfer occurs from 1,3,4-oxadiazole units to the PPV main chain. PLED performance of Oxa-PPV is higher than those of DMOP-PPV and Oxa-PPV-*co*-DMOP-PPV. This is due to better electron injection and charge balance between holes and electrons, as well as efficient intramolecular energy transfer from 1,3,4-oxadiazole units to PPV backbones. The maximum EL peak of Oxa-PPV is redshifted by 18 nm compared to the PL spectrum. This change in EL spectrum might be due to the injected current density, which results in an extended effective conjugation length. The emission colors of Oxa-PPV and DMOP-PPV at the Commission International de l'Eclairage (CIE) coordinates of  $x=0.50$ ,  $y=0.47$  and  $x=0.36$ ,  $y=0.55$  exhibits yellowish-orange and green light, respectively. By adjusting the feed ratios of Oxa-PPV in copolymers, the emission colors could be tuned from

**FIGURE 1.5**

Current density–voltage–luminescence ( $J$ – $V$ – $L$ ) characteristics of ITO/PEDOT/polymer/Al devices. (Reprinted from Jin, S.-H. et al., *J. Am. Chem. Soc.*, 126, 2474, 2004. With permission.)

green to yellowish-orange. The voltage–luminance (a) and current density–luminance efficiency (b) characteristics of ITO/PEDOT/polymer/Al devices are shown in Figure 1.5. The turn-on voltages of ITO/PEDOT/DMOP-PPV/Al and ITO/PEDOT/Oxa-PPV/Al devices are about 2.5 and 5 V, respectively. The copolymers showed a turn-on voltage similar to that of Oxa-PPV. The luminescence intensities of Oxa-PPV, DMOP-PPV, and Oxa-PPV-*co*-DMOP-PPV are increased exponentially with an increased voltage. The maximum luminescence of DMOP-PPV is 1840 cd/m<sup>2</sup> at 10 V. However, the maximum luminescence of copolymers increased dramatically with increasing the feed ratios of Oxa-PPV, and the maximum luminescence of Oxa-PPV-*co*-DMOP-PPV (84:16), Oxa-PPV-*co*-DMOP-PPV (64:36), and Oxa-PPV-*co*-DMOP-PPV (51:49) is about 6500 cd/m<sup>2</sup>. Oxa-PPV with Al electrode shows the maximum luminescence of 19,395 cd/m<sup>2</sup> at 14 V. Figure 1.5b shows the luminance efficiency of Oxa-PPV, DMOP-PPV, and Oxa-PPV-*co*-DMOP-PPV as a function of the current density. As the 1,3,4-oxadiazole content in the copolymers was increased, the luminance efficiency of Oxa-PPV-*co*-DMOP-PPV (84:16) was 41 times higher than that of DMOP-PPV and reached about 10 cd/A at 1760 cd/m<sup>2</sup> and 17 mA/cm<sup>2</sup>. The luminance efficiency of Oxa-PPV containing 1,3,4-oxadiazole side groups exhibited up to 21.1 cd/A at 5930 cd/m<sup>2</sup> and 29 mA/cm<sup>2</sup> using Al electrode, and 88 times higher than that of DMOP-PPV. The highest luminance efficiency of copolymers with the relatively low current density was due to the high LUMO energy level compared to conventional PPV derivatives. The barrier heights of Oxa-PPV and Oxa-PPV-*co*-DMOP-PPV (84:16) were found to be 1.09 and 1.1 eV at the interface of the Al/LUMO state for electron injection. Thus, easily injected electrons were recombined with the holes in emitting layers to give high luminance efficiency. The Oxa-PPV system also seems to form another charge transport channel (mainly for electrons) via wavefunction overlapping of  $\pi$ -electrons along the 1,3,4-oxadiazole pendants itself as well as original transport (mainly for holes) along the PPV backbone. In fact, the suggestion of new  $\pi$ -electron channels was strongly supported by the observation of broad spectral feature around 300 nm in the absorption spectrum of Oxa-PPV, which reflects  $\pi$ -electron wavefunction overlapping along the 1,3,4-oxadiazole units. Therefore, we consider that the excellent PLED performance of Oxa-PPV was also attributed to enhanced electron transport along new transport channels as well as easier electron injection in this system. Accordingly, introduction of 1,3,4-oxadiazole units into the PPV backbone via oxygen linkage and asymmetric molecular design of Oxa-PPV and Oxa-PPV-*co*-DMOP-PPV are responsible for the outstanding device performance.

The PL emission spectra of PDOT-PPV, PDOT-PPV-*co*-*m*-SiPhPPV, and *m*-SiPhPPV in the thin film state are shown in Figure 1.6a. The PL emission spectrum of PDOT-PPV shows two peaks centered at 511 and 542 nm as well as a weak shoulder centered at about 578 nm. As the *m*-SiPhPPV content in PDOT-PPV-*co*-*m*-SiPhPPV was increased, the intensity of the shoulder peaks in the PL emission increased consistently. We fabricated PLEDs with two different

**FIGURE 1.6**

PL spectra (a) and EL spectra (b) of the ITO/PEDOT/polymer/Alq<sub>3</sub>/LiF/Al device. (Reprinted from Jeon, H.-S. et al., *Macromolecules*, 40, 4794, 2007. With permission.)

cathode structures based on PDOT-PPV, PDOT-PPV-*co*-*m*-SiPhPPV, and *m*-SiPhPPV and compared them with ITO/PEDOT:PSS/polymer/cathodes. The cathodes were either bilayer of LiF (0.5 nm)/Al (200 nm) (cathode 1) or triple layer of Alq<sub>3</sub>/LiF/Al (cathode 2) with a 15 nm Alq<sub>3</sub> layer between the emitting and electron-injection layers as an electron-transport layer for improved PLED performance.

Figure 1.6b shows the EL spectra of PDOT-PPV, PDOT-PPV-*co*-*m*-SiPhPPV, and *m*-SiPhPPV for cathode 2 devices. The EL spectra of the PLEDs were almost identical to their PL spectra as shown in Figure 1.6a. This confirms that the EL emission of cathode 2 devices originates in the EL polymers and that the Alq<sub>3</sub> layer serves as an electron-transport layer. The maximum emission peak of PDOT-PPV was at 517 nm, with a shoulder peak at 549 nm. Also, *m*-SiPhPPV exhibited bimodal peaks at 525 and 562 nm, which corresponds to a bluish green color. The emission maximum of PDOT-PPV-*co*-*m*-SiPhPPV was located between the maxima for the homopolymers. We next evaluated the PLED performance of bilayer- and triple-layer cathode structures and the results are shown in Table 1.4. The turn-on voltages of the bilayer- and triple-layer cathode structures are between 5.5 and 9.0 V and devices containing PDOT-PPV-*co*-*m*-SiPhPPV (34:66 wt %) have the highest turn-on voltage. This is due to the higher energy barrier or band offset between the ITO and the HOMO state for polymers based on PDOT-PPV-*co*-*m*-SiPhPPV (34:66 wt %) than for those based on PDOT-PPV, which causes a drastic decrease in hole injection. The maximum luminescence of PDOT-PPV and PDOT-PPV-*co*-*m*-SiPhPPV devices with an LiF/Al cathode was 674 and 2879 cd/m<sup>2</sup>, respectively, which is much lower than that of *m*-SiPhPPV devices. However, by inserting an Alq<sub>3</sub> layer as an electron-transport layer between the emitting layer and the LiF layer, the maximum luminescence increased to 1693 and 5127 cd/m<sup>2</sup> for PDOT-PPV and PDOT-PPV-*co*-*m*-SiPhPPV devices, respectively, which is higher than that of *m*-SiPhPPV devices. The maximum luminance efficiency was found to be 3.75 cd/A with a triple-layer (Alq<sub>3</sub>/LiF/Al) cathode. The higher luminance efficiency of the

**TABLE 1.4**

PLED Performance of the Resulting Polymers in ITO/PEDOT/Polymer/Alq<sub>3</sub>/Cathode Device

Polymer	Cathode	Turn-On (V)	L <sup>a</sup> <sub>max</sub> (cd/m <sup>2</sup> , V)	LF <sup>b</sup> <sub>max</sub> (cd/A, V)
PDOT-PPV	Alq <sub>3</sub> /LiF/Al	6.0	1693 (17)	0.68 (9)
	LiF/Al	6.0	674 (18)	0.44 (9)
PDOT-PPV- <i>co</i> - <i>m</i> -SiPhPPV (73:27)	Alq <sub>3</sub> /LiF/Al	6.0	3897 (18)	2.70 (11)
	LiF/Al	6.0	958 (21)	1.14 (11)
PDOT-PPV- <i>co</i> - <i>m</i> -SiPhPPV (53:47)	Alq <sub>3</sub> /LiF/Al	6.0	5127 (18)	3.75 (9)
	LiF/Al	6.0	2879 (21)	2.81 (10)
PDOT-PPV- <i>co</i> - <i>m</i> -SiPhPPV (34:66)	Alq <sub>3</sub> /LiF/Al	8.0	1889 (26)	3.13 (16)
	LiF/Al	9.0	1028 (29)	2.46 (16)
<i>m</i> -SiPhPPV	Alq <sub>3</sub> /LiF/Al	6.0	2544 (19)	2.35 (16)
	LiF/Al	5.5	6370 (20)	3.27 (13)

Source: Reprinted from Jeon, H.-S. et al., *Macromolecules*, 40, 4794, 2007. With permission.

<sup>a</sup> Maximum luminescence.

<sup>b</sup> Maximum luminance efficiency.

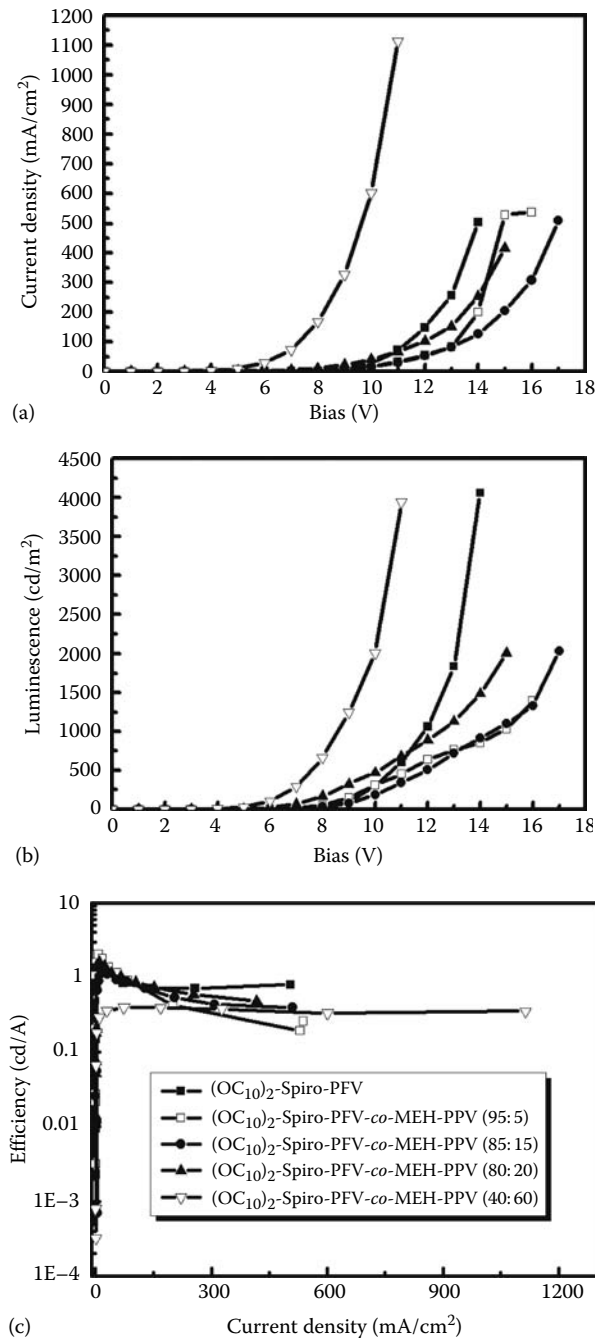
triple-layer cathode devices is attributed to their enhanced electron injection and transport, which results in efficient quenching of excitons into the EL polymer.

The absorption peak located at 409 nm in the  $(OC_{10})_2$ -Spiro-PFV spectrum was due to the  $\pi-\pi^*$  transitions of its conjugated polymer backbones and the shoulder peak at 377 nm is the characteristic peak of spirobifluorene units. As the MEH-PPV content increases in  $(OC_{10})_2$ -Spiro-PFV-*co*-MEH-PPV, absorption maximum shifts to lower energies.  $(OC_{10})_2$ -Spiro-PFV exhibits three characteristic emission peaks at 468, 500, and 533 nm, which are slightly blueshifted with respect to those of PFV.<sup>45</sup> These shifts are presumably due to the introduction of the bulky spirobifluorene unit into the polymer backbone, which reduces the effective conjugation length because of the resulting significant twisting of the polymer backbone. No emission peaks are observed due to the  $(OC_{10})_2$ -Spiro-PFV units in the spectra of the copolymers with an MEH-PPV content of more than 5 mol% and the maximum emission peak in the copolymers spectra gradually redshifts toward that of MEH-PPV, with the increase in MEH-PPV content. These results can be explained in terms of the efficient energy-transfer phenomena. To facilitate Förster-type energy transfer in blends or copolymer systems, the emission peak of the donor component with a wide band gap must overlap the absorption peak of the acceptor segment with a small band gap.<sup>47</sup> The PL spectrum of  $(OC_{10})_2$ -Spiro-PFV overlaps a major portion of the absorption spectrum of MEH-PPV. Thus, Förster-type intramolecular and/or intermolecular energy transfer from  $(OC_{10})_2$ -Spiro-PFV to MEH-PPV was expected to be efficient in copolymers composed of  $(OC_{10})_2$ -Spiro-PFV and MEH-PPV segments. To investigate the PLED performances of  $(OC_{10})_2$ -Spiro-PFV and  $(OC_{10})_2$ -Spiro-PFV-*co*-MEH-PPV copolymers, we fabricated PLEDs with ITO/PEDOT:PSS/polymer/Alq<sub>3</sub>/LiF/Al device. Figure 1.7 shows the *J-V-L* curves and luminance efficiency characteristics. The maximum brightness of the  $(OC_{10})_2$ -Spiro-PFV and  $(OC_{10})_2$ -Spiro-PFV-*co*-MEH-PPV (40:60) copolymer devices are 4062 cd/m<sup>2</sup> at 14 V and 3942 cd/m<sup>2</sup> at 11 V, respectively. The maximum luminance efficiency of the PLEDs was about 1.79 cd/A at 8 V with  $(OC_{10})_2$ -Spiro-PFV-*co*-MEH-PPV (95:5). The maximum emission peaks of  $(OC_{10})_2$ -Spiro-PFV and the  $(OC_{10})_2$ -spiro-PFV-*co*-MEH-PPV copolymers are at 469 and 587 nm, respectively, which corresponds to greenish blue and orange-red colors.

---

## 1.4 Summary and Conclusion

The main drawback of the PLED device with  $\pi$ -conjugated polymers is that there is an imbalance between the rate of electrons and hole injection near the interface between the polymer and the cathode. Many approaches have been proposed to improve the performance of the devices such as using

**FIGURE 1.7**

*J-V-L* characteristics and luminance efficiencies of (OC<sub>10</sub>)<sub>2</sub>-Spiro-PFV and (OC<sub>10</sub>)<sub>2</sub>-Spiro-PFV-*co*-MEH-PPV in Alq<sub>3</sub>/LiF/Al cathode. (Reproduced from Shin, W.S. et al., *J. Mater. Chem.*, 16, 4123, 2006. With permission.)

a triplet emitter, modifying the structure of the device by introducing an electron-transport layer, or a multiple quantum-well and blending or copolymer systems. However, it was observed that the devices still had a problem in achieving high EL efficiency. Since then, several research works have been extensively studied and reported with the  $\pi$ -conjugated polymers for PLED application. Among them, polymers with PPV and PF backbones have emerged as the leading candidate materials for the device applications. The advantage of using such a  $\pi$ -conjugated polymer with PPV and PFV backbones over organic fluorescent dyes for the OLED is the fact that more stable and resilient films can be easily processed onto the large area electrode surface by means of spin coating because of the solubility of the emitting polymers in common organic solvents. These highly efficient PPVs and PFVs with flexible side chain in their backbones interfere with the interaction between the polymer main chain, which results in amorphous morphology. Through the fine-tuning of their molecular architecture via the introduction of the bulky substituent into the PPV and PFV backbones with the Gilch polymerization method, these polymers have achieved ease of processability, high purity, and tuning of emission colors. Moreover these advanced light-emitting polymers exhibited high molecular weight, efficiency, brightness, and long-term operation in the PLEDs. On exploring our research achievements, the color-tunable EL phenoxy PPV backbone polymer with 3,7-dimethyloctyloxy side groups showed excellent fluorescent emission. The copolymer *p*-DMOP-PPV-*co*-MEH-PPV exhibited a sharp peak at about 600 nm with 40 nm of FWHM in solid state. The copolymers showed higher device performance as compared to the homopolymers and MEH-PPV. Similarly, the copolymers of *m*-SiPhPPV-*co*-MEH-PPV showed better optical and EL properties than those of homopolymers. The copolymers showed higher luminous efficiency compared to the *m*-SiPhPPV and MEH-PPV. From our research findings, it could be ascertained that the copolymer systems show better emission properties than their corresponding homopolymers. The 1,3,4-oxadiazole units incorporated between the phenoxy and alkoxyphenyl substituents improve the higher molecular weight with good solubility and ultimately ensure significant consequences for high quality optical thin films. The introduction of an electron-deficient 1,3,4-oxadiazole unit into the PPV backbone as the side chain enhances the electron affinity and increases the LUMO energy level, which facilitates the improvement of device performance. The improved device performance of Oxa-PPV over those of DMOP-PPV and Oxa-PPV-*co*-DMOP-PPV is due to better electron injection and efficient energy transfer from the modified 1,3,4-oxadiazole side group of the PPV main chain. The novel PPV-based homopolymer with PDOT moiety as a side chain, poly(PDOT-PV) and statistical copolymers poly(PDOT-PV-*co*-*m*-SiPhPV) had enough stability for the fabrication of the devices and they provide longevity to devices because they have high glass transition temperature ( $T_g$ ). The PLEDs containing poly(PDOT-PV) and poly(PDOT-PV-*co*-*m*-SiPhPV)

showed favorable performance when used in triple-layer cathode. The maximum luminous efficiency of 3.75 cd/A was found with triple-layer cathode structures.

On the study with copolymers composed of alternating 9,9-dialkyloxySpiro-bifluorene and vinylene-repeating units, the introduction of branched dialkyloxy pendant groups reduced the interchain interactions with an improvement in the polymer solubility and thermal stability. Owing to the introduction of bulky spirobifluorene units into  $(OC_{10})_2$ -Spiro-PFV, the PL quantum efficiency of  $(OC_{10})_2$ -Spiro-PFV is higher than that of  $(OC_{10})_2$ -Spiro-PFV-*co*-MEH-PPV copolymers and MEH-PPV. The PLED performance is significantly better with Alq<sub>3</sub> as an electron-transport layer and an LiF/Al cathode. It has been possible to ascertain from the results summarized above that the charge-injection properties of the conjugated polymers can be controlled by incorporating suitable substituents in the polymer backbone. By introducing suitable substituents in the polymer backbone, it can be dissolved in common organic solvents. The addition of the suitable substituents in the polymer backbone deviates the molecular structure, so that the tuning of color can be attained efficiently. Moreover, processability is an advantage, so that the device can be fabricated by casting the conjugated polymers from solution.

---

## Acknowledgments

This work was supported by the Korea Science and Engineering Foundation (KOSEF) grant funded by the Korean government (MOST) (No. M10600000157-06J0000-15710, R11-2008-088-01-003-0).

---

---

## References

1. MacDonald, W. A. 2004. Engineered films for display technologies. *J. Mater. Chem.* 14:4–10.
2. Cao, Y., Parker, I. D., Yu, G., Zhang, C., and Heeger, A. J. 1999. Improved quantum efficiency for electroluminescence in semiconducting polymers. *Nature* 397:414–417.
3. Kraft, A., Grimsdale, A. C., and Holmes, A. B. 1998. Electroluminescent conjugated polymers—Seeing polymers in a new light. *Angew. Chem. Int. Ed.* 37:402–428.
4. Lee, Y.-Z., Chen, X., Chen, S.-A., Wei, P.-K., and Fann, W.-S. 2001. Soluble electroluminescent poly(phenylene vinylene)s with balanced electron- and hole injections. *J. Am. Chem. Soc.* 123:2296–2307.

5. Garten, F., Hilberer, A., Cacialli, F., Esselink, E., Dam, Y. V., Schlatmann, B., Friend, R. H., Klapwijk, T. M., and Hadzioannou, G. 1997. Efficient blue LEDs from a partially Si-containing PPV copolymer in a double layer configuration. *Adv. Mater.* 9:127–131.
6. Tanase, C., Wildeman, J., and Blom, P. W. M. 2005. Luminescent poly(*p*-phenylenevinylene) hole transport layers with adjustable solubility. *Adv. Funct. Mater.* 15:2011–2015.
7. Greenham, N. C., Moratti, S. C., Bradley, D. D. C., Friend, R. H., and Holmes, A. B. 1993. Efficient light-emitting diodes based on polymers with high electron affinities. *Nature* 365:628–630.
8. Braun, D. and Heeger, A. J. 1992. Electroluminescence from light-emitting diodes fabricated from conducting polymers. *Thin Solid Films* 216:96–98.
9. Parker, I. D. 1994. Carrier tunneling and device characteristics in polymer light-emitting diodes. *J. Appl. Phys.* 75:1656–1666.
10. Bao, Z., Peng, Z., Galvin, M. E., and Chandross, E. A. 1998. Novel oxadiazole side chain conjugated polymers as single-layer light-emitting diodes with improved quantum efficiencies. *Chem. Mater.* 10:1201–1204.
11. Bruttig, W., Berleb, S., Egerer, G., Schwoerer, M., Wehrmann, R., and Elschner, A. 1997. Full color electroluminescence using dye-dispersed polymer blends. *Synth. Met.* 91:325–327.
12. Heischkel, Y. and Schmidt, H.-W. 1998. Synthesis of ABC-triblock copolymers for light emitting diodes. *Macromol. Chem. Phys.* 199:869–880.
13. Strukelj, M., Miller, T. M., Papadimitrakopoulos, F., and Son, S. 1995. Effects of polymeric electron transporters and the structure of poly(*p*-phenylenevinylene) on the performance of light-emitting diodes. *J. Am. Chem. Soc.* 117:11976–11983.
14. Halls, J. J. M., Walsh, C. A., Greenham, N. C., Marseglia, E. A., Friend, R. H., Moratti, S. C., and Holmes, A. B. 1995. Efficient photodiodes from interpenetrating polymer networks. *Nature* 376:498–500.
15. Xin, Y., Wen, G.-A., Zeng, W.-J., Zhao, L., Zhu, X.-R., Fan, Q.-L., Feng, J.-C., Wang, L.-H., Wei, W., Peng, B., Cao, Y., and Huang, W. 2005. Hyperbranched oxadiazole-containing polyfluorenes: Toward stable blue light PLEDs. *Macromolecules* 38:6755–6758.
16. Boyd, T. J., Geerts, Y., Lee, J.-K., Fogg, D. E., Lavoie, G. G., Schrock, R. R., and Rubner, M. F. 1997. Electroluminescence from new polynorbornenes that contain blue-light-emitting and charge-transport side chains. *Macromolecules* 30:3553–3559.
17. Becker, H., Spreitzer, H., Kreuder, W., Kluge, E., Schenk, H., Parker, I., and Cao, Y. 2000. Soluble PPVs with enhanced performance—A mechanistic approach. *Adv. Mater.* 12:42–48.
18. Chu, Q., Pang, Y., Ding, L., and Karasz, F. E. 2002. Synthesis, chain rigidity, and luminescent properties of poly[(1,3-phenyleneethynylene)-*alt*-tris(2,5-dialkoxy-1,4-phenyleneethynylene)]s. *Macromolecules* 35:7569–7574.
19. Lee, S. H., Jang, B.-B., and Tsutsui, T. 2002. Sterically hindered fluorenyl-substituted poly(*p*-phenylenevinylenes) for light-emitting diodes. *Macromolecules* 35:1356–1364.
20. Hsieh, B. R., Yu, Y., Forsythe, E. W., Schaaf, G. M., and Feld, W. A. 1998. A new family of highly emissive soluble poly(*p*-phenylene vinylene) derivatives. A step toward fully conjugated blue-emitting poly(*p*-phenylene vinylenes). *J. Am. Chem. Soc.* 120:231–232.

21. Yu, W.-L., Pei, J., Huang, W., and Heeger, A. J. 2000. Spiro-functionalized polyfluorene derivatives as blue light-emitting materials. *Adv. Mater.* 12:828–831.
22. Welsh, D. M., Kloepfner, L. J., Madrigal, L., Pinto, M. R., Thompson, B. C., Schanze, K. S., Abboud, K. A., Powell, D., and Reynolds, J. R. 2002. Regiosymmetric dibutyl-substituted poly(3,4-propylenedioxythiophene)s as highly electron-rich electroactive and luminescent polymers. *Macromolecules* 35:6517–6525.
23. Sokolik, I., Yang, Z., Karasz, F. E., and Morton, D. C. 1993. Blue-light electroluminescence from *p*-phenylene vinylene-based copolymers. *J. Appl. Phys.* 74:3584–3586.
24. Yang, Z., Karasz, E., and Geise, H. J. 1993. Intrinsically soluble copolymers with well-defined alternating substituted *p*-phenylenevinylene and ethylene oxide blocks. *Macromolecules* 26:6570–6575.
25. Pasco, S. T., Lahti, P. M., and Karasz, F. E. 1999. Synthesis of substituted poly(*p*-phenylenevinylene) copolymers by the Heck method for luminescence studies. *Macromolecules* 32:6933–6937.
26. Sims, M., Bradley, D. D. C., Ariu, M., Koeberg, M., Asimakis, A., Grell, M., and Lidzey, D. G. 2004. Understanding the origin of the 535 nm emission band in oxidized poly(9,9-dialkylfluorene): The essential role of inter-chain/intersegment interactions. *Adv. Funct. Mater.* 14:765–781.
27. Kulkarni, A. P., Kong, X., and Jenekhe, S. A. 2004. Fluorenone-containing polyfluorenes and oligofluorenes: Photophysics, origin of the green emission and efficient green electroluminescence. *J. Phys. Chem. B* 108:8689–8701.
28. Bliznyuk, V. N., Carter, S. A., Scott, J. C., Klärner, G., Miller, R. D., and Miller, D. C. 1999. Electrical and photoinduced degradation of polyfluorene based films and light-emitting devices. *Macromolecules* 32:361–369.
29. List, E. J. W., Guentner, R., Freitas, P. S. D., and Scherf, U. 2002. The effect of keto defect sites on the emission properties of polyfluorene-type materials. *Adv. Mater.* 14:374–378.
30. Silva, C., Russell, D. M., Dhoot, A. S., Herz, L. M., Greenham, N. C., Arias, A. C., Setayesh, S., Mullen, K., and Friend, R. H. 2002. Exciton and polaron dynamics in a step-ladder polymeric semiconductor: the influence of interchain order. *J. Phys.: Condens. Matter* 14:9803–9824.
31. Salbeck, J., Yu, N., Bauer, J., Weissortel, F., and Bestgen, H. 1997. Low molecular organic glasses for blue electroluminescence. *Synth. Met.* 91:209–215.
32. Johansson, N., Salbeck, J., Bauer, J., Weissortel, F., Broms, P., Andersson, A., and Salaneck, W. R. 1998. Solid-state amplified spontaneous emission in some spiro-type molecules: A new concept for the design of solid-state lasing molecules. *Adv. Mater.* 10:1136–1141.
33. Yang, Z., Hu, B., and Karasz, F. E. 1995. Polymer electroluminescence using ac or reverse dc biasing. *Macromolecules* 28:6151–6154.
34. Jung, S.-H., Kim, H.-K., Kim, S.-H., Kim, Y. H., Jeoung, S. C., and Kim, D., 2000. Palladium-catalyzed direct synthesis, photophysical properties, and tunable electroluminescence of novel silicon-based alternating copolymers. *Macromolecules* 33:9277–9288.
35. Miyaura, N. and Suzuki, N. 1995. Palladium-catalyzed cross-coupling reactions of organoboron compounds. *Chem. Rev.* 95:2457–2483.
36. Pei, Q. and Yang, Y. 1996. Efficient photoluminescence and electroluminescence from a soluble polyfluorene. *J. Am. Chem. Soc.* 118:7416–7417.

37. Gilch, H. G. and Wheelwright, W. L. 1966. Preparation of  $\alpha$ -halogenated *p*-xylenes with base. *J. Polym. Sci. Part A-1. Polym. Chem.* 4:1337–1349.
38. Jung, S. H., Cho, Y. R., Jin, S.-H., Kim, S.-C., Shin, W. S., Lee, J. W., and Gal, Y.-S. 2007. Synthesis and characterization of PPV-based light-emitting copolymer with alkylsilylphenyloxy pendant group for light-emitting diode applications. *Curr. Appl. Phys.* 7:375–379.
39. Jin, S.-H., Kang, S.-Y., Yeom, I.-S., Kim, J. Y., Park, S.-H., Lee, K., Gal, Y.-S., and Cho, H.-N. 2002. Color-tunable electroluminescent polymers by substitutents on the poly(*p*-phenylenevinylene) derivatives for light-emitting diodes. *Chem. Mater.* 14:5090–5097.
40. Jin, S.-H., Jang, M.-S., Suh, H.-S., Cho, H.-N., Lee, J.-H., and Gal, Y.-S. 2002. Synthesis and characterization of highly luminescent asymmetric poly(*p*-phenylenevinylene) derivatives for light-emitting diodes. *Chem. Mater.* 14:643–650.
41. Jin, S.-H., Kim, M.-Y., Kim, J. Y., Lee, K., and Gal, Y.-S. 2004. High-efficiency poly(*p*-phenylenevinylene)-based copolymers containing an oxadiazole pendant group for light-emitting diodes. *J. Am. Chem. Soc.* 126:2474–2480.
42. Jeon, H.-S., Lee, S. K., Lee, E.-J., Park, S.-M., Kim, S.-C., Jin, S.-H., Gal, Y.-S., Lee, J. W., and Im, C. 2007. Synthesis and electroluminescent properties of poly(*p*-phenylenevinylene)s with 3',3'-diheptyl-3,4-propylenedioxythiophene pendant group for light-emitting diode applications. *Macromolecules* 40:4794–4801.
43. Shin, W. S., Joo, M.-K., Kim, S. C., Park, S.-M., Jin, S.-H., Shim, J.-M., Lee, J. K., Lee, J. W., Gal, Y.-S., and Jenekhe, S. A. 2006. Synthesis and electro-optical properties of spiro-bifluorenylvinylene-based polymers for light-emitting diodes applications. *J. Mater. Chem.* 16:4123–4132.
44. Kim, S.-C., Park, S.-M., Park, J. S., Lee, S.-J., Jin, S.-H., Gal, Y.-S., and Lee, J. W. 2008. Synthesis and electro-optical properties of light-emitting polymers containing oxadiazole derivatives for light-emitting diodes applications. *J. Polym. Sci. Part A. Polym. Chem.* 46:1098–1110.
45. Jin, S.-H., Kang, S.-Y., Kim, M.-Y., Chan, Y. U., Kim, J. Y., Lee, K., and Gal, Y.-S. 2003. Synthesis and electroluminescence properties of poly(9,9-di-*n*-octyl-fluoren-2,7-vinylene) derivatives for light-emitting display. *Macromolecules* 36:3841–3847.
46. Jin, S.-H., Jung, H.-H., Hwang, C.-K., Koo, D.-S., Shin, W. S., Kim, Y.-N., Lee, J. W., and Gal, Y.-S. 2005. High electroluminescent properties of conjugated copolymers from poly[9,9-dioctylfluoren-2,7-vinylene]-co-(2-(3-dimethyl-dodecylphenyl)-1,4-phenylenevinylene)] for light emitting diode applications. *J. Polym. Sci. Part A. Polym. Chem.* 43:5062–5071.
47. Cleave, V., Yahioglu, G., Barny, P. L., Friend, R. H., and Tessler, N. 1999. Harvesting singlet and triplet energy in polymer LEDs. *Adv. Mater.* 11:285–288.

# 2

---

## *Organic Vapor-Phase Deposition\**

---

**Max Shtein**

### CONTENTS

2.1	Introduction .....	28
2.2	Evaporation and Vapor Pickup by the Carrier Gas .....	29
2.3	Vapor Transport.....	33
2.4	Film Deposition .....	36
2.5	Deposition in Confined Geometries, Application to Patterning .....	39
2.5.1	Introduction .....	39
2.5.2	Ballistic Transport in VTE and Use of Shadow Masks .....	39
2.5.3	Patterning and OVPD: Diffusive Transport through Shadow Masks.....	41
2.5.4	The Breakdown of the Continuous Medium Assumption for $Kn < 10$ .....	42
2.5.5	Modeling of Gas Transport in Confined Geometries .....	43
2.5.6	Monte-Carlo Simulation of OVPD through Apertures .....	44
2.5.6.1	Patterning of Alq <sub>3</sub> Films.....	45
2.5.6.2	Effects of Chamber Pressure on Deposit Shape.....	46
2.5.6.3	Effects of Mask Thickness and Separation .....	47
2.5.6.4	Optimizing Mask (Aperture) Shape.....	48
2.5.7	Experimental Validation of the Predictions .....	50
2.5.7.1	OVPD through Shadow Masks—Results and Discussion .....	53
2.5.7.2	Resolution Limits and Self-Aligned Contacts by Hybrid VTE-OVPD.....	54
2.6	Summary .....	55
	References.....	56

---

\* Portions of this chapter have previously appeared in the PhD dissertation of M. Shtein (Shtein 2004) and are being reproduced or modified here with permission, for the benefit of a broader readership and feedback.

## 2.1 Introduction

Conventionally, optoelectronic devices incorporating small molecular organic semiconductors are deposited using vacuum thermal evaporation (VTE). This traditional method preserves the purity of source material, the ability to deposit films with monolayer precision, and in some cases up to 50% materials utilization efficiency. At the same time, some characteristics inherent to VTE (e.g., strong dependence of evaporation rate on temperature or nonuniform heating of the source material) make commercial-scale deposition of organic electronics difficult. Organic vapor-phase deposition (OVPD) was developed in part to overcome the limitations of VTE. It decouples the evaporation and deposition events, using a carrier gas to mediate the transport of material from the source to the substrate, thereby achieving greater control of the deposition process.

The concept of OVPD is illustrated in Figure 2.1. The source material is heated to generate molecular vapor, which is picked up and transported by a hot inert carrier gas toward a cooled substrate, where the organic vapor selectively condenses. The parasitic condensation of the source material is avoided by cooling the substrate only, while actively heating the walls of the deposition system. To grow doped films, multiple component streams are mixed en route to the substrate. The process is carried out at reduced pressure, increasing gas diffusivity and thereby improving mass transfer rates (Bird et al., 1996; Wolf and Tauber, 1999). It is helpful to analyze OVPD as a succession of three steps: (1) evaporation and pickup, (2) vapor transport by convection, and (3) deposition (Shtein et al., 2001). The growth of polycrystalline thin films involves a simultaneous annealing of the growing film by molecular surface diffusion at elevated substrate temperature (Shtein et al., 2002).

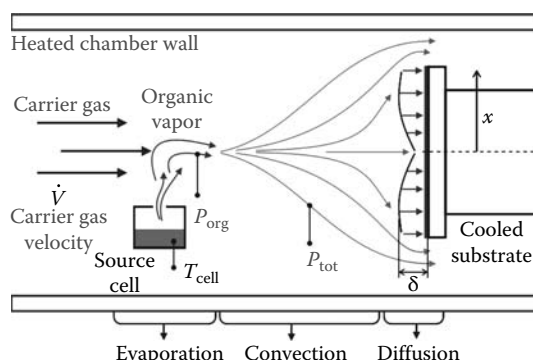


**FIGURE 2.1**

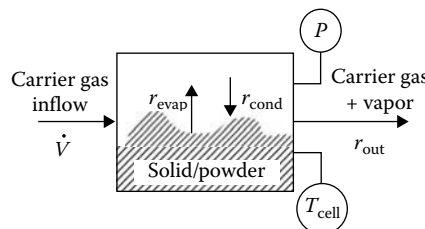
OVPD concept. A hot inert carrier gas (e.g.,  $N_2$ ) transports hot organic source vapor along a heated-wall reactor toward a cooled substrate, on which the organic molecules selectively physisorb. (From Shtein, M. et al., *J. Appl. Phys.*, 89, 1470, 2001. With permission.)

Since the late 1990s, OVPD has been used to deposit organic light-emitting devices (OLEDs) (Baldo et al., 1998; Shtein et al., 2001; Zhou et al., 2005), organic thin-film transistors (OTFTs) (Shtein et al., 2002), and organic photovoltaic (PV) cells (Yang et al., 2005a,b). OPVD-grown device performance matches or in some instances exceeds that of VTE-grown devices (Shtein et al., 2002; Yang et al., 2005a,b; Zhou et al., 2005), and commercial-scale OVPD instruments have been built (Shtein et al., 2002). Some of the characteristics of OVPD make it advantageous for scaled-up manufacturing of organic semiconductor-based devices (Shtein et al., 2002; Schwamberger et al., 2004). Due to length limitations, the scope of this chapter is confined to the growth and patterning of amorphous films (e.g., for OLED applications). That being said, this chapter discusses the *physical principles* of OVPD, with the focus on fundamental mass transport aspects of the deposition method and its theoretical underpinnings. The author hopes, therefore, that this work should provide a sound basis for understanding in greater depth the principles of growth of both amorphous and polycrystalline films by OVPD for device applications, including OLEDs, thin-film transistors, and solar cells. The reader is encouraged to consult other published work for specific examples of application of OVPD in device and film growth.

## 2.2 Evaporation and Vapor Pickup by the Carrier Gas

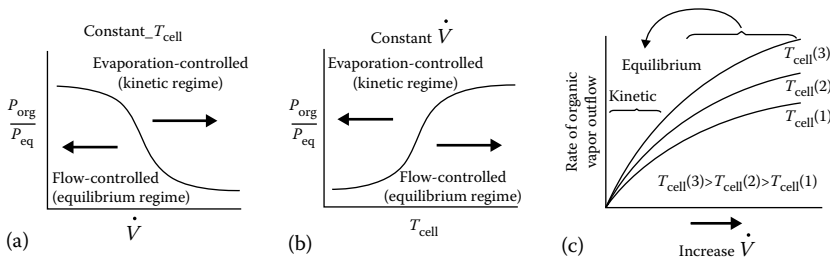
Film deposition rate can be evaporation limited, deposition limited, or it can proceed in the intermediate regime. To predict the operating regime, we first predict how the evaporation rate depends on processing conditions, such as temperature, pressure, carrier gas flow rate, and the surface area of the organic material.

The source cell is schematically shown in Figure 2.2. Organic source material, typically in the form of a crystalline powder, is heated inside of



**FIGURE 2.2**

Schematic of a source cell containing the organic source material, typically a crystalline powder, maintained at P and T<sub>cell</sub>. The carrier gas enters the cell picking up the organic vapor, carrying it out at a molar rate  $r_{out}$ , which is the balance between evaporation and recondensation rates,  $r_{evap}$  and  $r_{cond}$ , inside the cell.

**FIGURE 2.3**

(a,b) Qualitative depiction of the source cell operating regimes. (c) The resulting rate of organic vapor outflow vs. increasing carrier gas flow rate for a series of cell temperatures  $T_1$ ,  $T_2$ ,  $T_3$ .

a container, while a hot inert carrier gas flows over the organic surface. Qualitatively, for a fixed cell temperature, a very low carrier flow rate ( $\dot{V}$ ) will result in a vapor-saturated (i.e., vapor–solid equilibrated) cell environment. Here, carrier flow limits how much organic material escapes the cell, which is also said to be in the flow-limited operating regime. Increasing  $\dot{V}$  will cause organic molecules to be swept out of the source cell as soon as they evaporate, thereby decreasing the organic vapor pressure inside the cell and shifting it away from solid–gas equilibrium. Eventually, the source cell becomes evaporation-limited. These two regimes are depicted in Figure 2.3a. If the carrier flow rate is fixed, while the cell temperature,  $T_{\text{cell}}$ , is increased, the cell transitions from the evaporation-limited to the flow-limited regimes, as shown in Figure 2.3b. Note that although for higher  $\dot{V}$ , the organic vapor pressure inside the cell,  $P_{\text{org}}$ , drops, the molecules are still being swept out of the container. Thus, for a given  $T_{\text{cell}}$ , increasing  $\dot{V}$  will result in a monotonic increase in the rate of organic vapor outflow. This situation is depicted qualitatively in Figure 2.3c.

A quantitative analysis of the evaporation and vapor pickup begins with a mass balance on the organic species inside the evaporation cell:

$$r_{\text{evap}} - r_{\text{cond}} = r_{\text{out}} \quad (2.1)$$

where

$r_{\text{evap}}$  and  $r_{\text{cond}}$  are the evaporation and condensation rates, respectively  
 $r_{\text{out}}$  is the molar rate of organic vapor outflow from the evaporation cell

The rate at which the organic vapor condenses (redeposits) inside the source cell is given by the molecular collision rate with the surface and the molecular sticking probability,  $\alpha$ :

$$r_{\text{cond}} = P_{\text{org}} \times A_e \times \frac{1}{\sqrt{2\pi \times M_{\text{org}} \times k_B T}} \times \alpha \quad (2.2)$$

where

- $A_e$  is the effective surface area of the cell walls and of the organic material
- $M_{\text{org}}$  is its molecular mass
- $(2M_{\text{org}} \cdot k_B T)^{-1/2}$  is the surface collision frequency
- $k_B$  is the Boltzmann constant
- $T$  is the temperature

Similarly, the evaporation rate is

$$r_{\text{evap}} = P_{\text{eq}} \times A_e \times \frac{1}{\sqrt{2\pi \times M_{\text{org}} \times k_B T}} \quad (2.3)$$

At equilibrium  $P_{\text{org}} = P_{\text{eq}}$ , the evaporation and condensation rates balance, giving

$$\alpha P_{\text{org}} = P_{\text{eq}} \quad (2.4)$$

The net surface evaporation rate is thus given by

$$r_{\text{out}} = (P_{\text{eq}} - P_{\text{org}}) \cdot \alpha \cdot A_e \cdot \frac{1}{\sqrt{2\pi \times M_{\text{org}} \times k_B T}} \quad (2.5)$$

The Clausius–Clapeyron equation relates the equilibrium vapor pressure, the cell temperature, and the physical characteristics specific to the organic compound:

$$P_{\text{eq}} = P_0 \exp\left(\frac{-\Delta H^{\text{vap}}}{RT_{\text{cell}}}\right) \quad (2.6)$$

where

- $\Delta H^{\text{vap}}$  is the vaporization enthalpy of the organic material
- $P_0$  varies slowly with  $T_{\text{cell}}$ , and the ideal gas constant  $R = k_B \cdot 6.02 \times 10^{23} \text{ J} \cdot \text{K}^{-1} \cdot \text{mol}^{-1}$

If the vapor and the carrier gas mix perfectly inside the source cell, the molar outflow of organic material is

$$r_{\text{out}} = \dot{V} \times \frac{P_{\text{org}}}{RT_{\text{cell}}} \quad (2.7)$$

where  $\dot{V}$  is the volumetric flow rate of the carrier gas through the source cell.

Equations 2.1 through 2.7 combine to give

$$P_{\text{org}} = \frac{P_0 \exp\left(\frac{-\Delta H^{\text{vap}}}{RT_{\text{cell}}}\right)}{\frac{\dot{V}}{RT_{\text{cell}}} + \frac{\sqrt{2\pi \times M_{\text{org}} \times k_B T_{\text{cell}}}}{\alpha \times A_e}} \quad (2.8)$$

$$r_{\text{out}} = \frac{P_0 \exp\left(\frac{-\Delta H_i^{\text{vap}}}{RT_{\text{cell}}}\right)}{\frac{\sqrt{2\pi \times M_{\text{org}} \times k_B T_{\text{cell}}}}{\alpha \times A_e} + \frac{RT_{\text{cell}}}{\dot{V}}} \quad (2.9)$$

Since in practice the carrier gas flow in the deposition system is regulated by "mass flow" control devices, it will be more convenient to analyze data in terms of the mass flow rate units (e.g., standard cubic centimeters per minute, or sccm). The actual volumetric flow rate of the carrier gas,  $\dot{V}$ , can be expressed as

$$\dot{V} = \frac{T_{\text{cell}}}{T_{\text{std}}} \times \frac{P_{\text{std}}}{P_{\text{cell}}} \times \dot{V}_{\text{sccm}} \quad (2.10)$$

where

$\dot{V}_{\text{sccm}}$  is the measured flow rate in sccm

$T_{\text{std}}$  and  $P_{\text{std}}$  are the standard temperature and pressure, 298 K and 760 torr, respectively

Equation 2.9 becomes

$$r_{\text{out}} = \frac{P_0 \exp\left(\frac{-\Delta H^{\text{vap}}}{RT_{\text{cell}}}\right)}{\frac{\sqrt{2\pi \times M_i \times k_B T_{\text{cell}}}}{\alpha \times A_{\text{org}}} + \frac{RT_{\text{std}}}{\dot{V}_{\text{sccm}}} \times \frac{P_{\text{cell}}}{P_{\text{std}}}} \quad (2.11)$$

Figure 2.3c shows the same qualitative dependence of  $r_{\text{out}}$  on  $T_{\text{cell}}$  and  $\dot{V}_{\text{sccm}}$ , as predicted by Equation 2.11, assuming an idealized situation where the temperature, pressure, and gas flow rate do not influence  $\alpha$ . For constant  $\dot{V}_{\text{sccm}}$  and  $P_{\text{cell}}$ , raising  $T_{\text{cell}}$  will shift the source closer to the solid-vapor equilibrium (i.e., saturation regime), while at constant  $T_{\text{cell}}$  the source becomes depleted for higher  $\dot{V}_{\text{sccm}}$ . Equation 2.11 also predicts that lower source cell pressure helps maximize the rate of vapor supply. The cell loading and material specific variables, such as  $\Delta H^{\text{vap}}$ ,  $\alpha$ , and  $A_e$ , are typically obtained experimentally. In fact,  $\alpha$  and  $A_e$  are most likely to be lumped into a single coefficient obtained in the process of calibrating the evaporation cell.

## 2.3 Vapor Transport

Following evaporation, the organic compound is entrained in the stream of carrier gas en route to the substrate. During this time, the vapor from individual source cells may be further diluted and blended with the vapor from other sources. (Dilution may be necessary for several reasons, including the prevention of vapor supersaturation en route to the substrate, the need to achieve fully laminar or turbulent flow conditions, to regulate heat transfer in the transport lines, or to prevent cross-contamination between sources.) Assuming that the vapor streams become well-mixed en route to the substrate, the resulting molar vapor concentration,  $c$ , is given by

$$c = \frac{r_{\text{out}}}{V_{\text{tot}}} \quad (2.12)$$

where  $\dot{V}_{\text{tot}}$  is the total flow rate of the carrier gas which enters the deposition region. When two source materials, A and B, are blended,  $\dot{V}_{\text{tot}} = \dot{V}_A + \dot{V}_B + \dot{V}_{\text{dil}}$ , where  $\dot{V}_{\text{dil}}$  is the dilution flow rate. The resulting concentration of the source vapor of material  $i$  in the deposition chamber is

$$c_i = \frac{P_{0,i} \exp\left(\frac{-\Delta H_i^{\text{vap}}}{RT_{\text{cell}}}\right)}{\left[ \frac{\sqrt{2\pi \times M_i \times k_B T_{\text{cell},i}}}{\alpha_i \times A_{\text{org},i}} + \frac{RT_{\text{std}}}{\dot{V}_{i,\text{sccm}}} \times \frac{P_{\text{cell},i}}{P_{\text{std}}} \right] \times \left[ \sum \dot{V}_i + \dot{V}_{\text{dil}} \right]} \quad (2.13)$$

Equation 1.13 is important for determining the deposition rate, because in the majority of cases the film deposition rate is limited by diffusion across a boundary layer. Hence, the final concentration of component  $i$  in the film will scale with the vapor concentration given by Equation 2.13.

Both the boundary layer thickness and the mixing distance depend on the characteristics of the flow, including velocity, gas species, temperature, pressure, and whether the flow is laminar or turbulent. The transition between laminar and turbulent flow typically occurs when the Reynolds number ( $Re$ ) is  $\sim 2000$ ; Reynolds number is defined as

$$Re = \frac{U \times d_m \times \rho_f}{\mu_f} \quad (2.14)$$

where

$U$  is the linear flow velocity

$d_m$  is the diameter of the deposition chamber

$\rho_f$  and  $\mu_f$  are the density and viscosity of the fluid, respectively

Since the organic vapor is a minority species in the flow, it can be neglected in calculating  $Re$ . For  $N_2$  at 270°C and 1 torr, typical OVPD deposition conditions,  $\rho_f = 3.64 \times 10^{-2} \text{ kg/m}^3$  and  $\mu_f = 2.44 \times 10^{-5} \text{ kg/m}\cdot\text{s}$ . In the earliest versions, the OVPD apparatus consisted of an externally heated, 10 cm diameter glass tube, which utilized a maximum of 100 sccm volumetric flow rate. Converting to deposition temperature and pressure, this results in  $U = 0.32 \text{ m/s}$ , and  $Re = 48$ , well within the laminar regime. For typical deposition conditions,  $\dot{V}_{\text{tot}} < 30 \text{ sccm}$ , so the laminar flow assumption is valid.

Given the laminar nature of the flow, mixing of separate vapor streams is dominated by diffusion. The mixing will be complete and uniform, when the vapors diffuse radially to the point of filling the entire flow diameter, which occurs in characteristic time  $\tau_D$ :

$$\tau_D = \frac{d_m^2}{6D_i} \quad (2.15)$$

where  $D_i$  is the gas-phase diffusivity of organic vapor of material  $i$ . During this time, the gas molecules entering the main tube will travel a distance  $L_m$ :

$$L_m = U \times \tau_D = \frac{u \times d_m^2}{6D_i} \quad (2.16)$$

To first order,  $D_i$  is given by the gas kinetic theory:

$$D_i = \frac{1}{3} \times \bar{u} \times \lambda = \frac{1}{3} \times \sqrt{\frac{8 \times k_B T}{\pi \times M}} \times \frac{k_B T}{\sqrt{2} \times \pi \sigma^2 \times P_{\text{dep}}} \quad (2.17)$$

where

$M$  is the reduced molecular weight ( $M = M_A M_B / (M_A + M_B)$ , where A and B denote two different gas species)

$\bar{u}$  and  $\lambda$  are the molecular mean thermal velocity and mean free path, respectively

$\sigma$  is the average molecular diameter ( $(\sigma_A + \sigma_B)/2$ )

$P_{\text{dep}}$  is the total deposition chamber pressure

$T$  is the gas temperature

For Alq<sub>3</sub> diffusing in N<sub>2</sub>,  $M_A = 459 \text{ g/mol}$ , and  $M_B = 26.4 \text{ g/mol}$ , giving  $D_{\text{Alq}_3} \approx 57 \text{ cm}^2/\text{s}$ , and  $L_m = 9 \text{ cm}$ , or  $L_m \approx d_m$  in the experimental OVPD system. More accurate calculations of diffusivity can be obtained via group contribution methods that have been developed for petroleum processing, or estimated from correlations such as the Chapman–Enskog equation (Bird et al., 1996). Nevertheless, the simple Equation 2.17 provides a sufficient starting point for designing an OVPD apparatus specifically to take this mixing mechanism into account to achieve uniform deposition.

The carrier gas flow field can be visualized by numerically solving the complete Navier–Stokes equations for the deposition geometry. The momentum balance is given by

$$\rho_f \frac{\partial \vec{u}}{\partial t} + \rho_f (\vec{u} \cdot \nabla) \vec{u} = -\nabla p + \mu_f \nabla^2 \vec{u} + \rho_f \vec{g} \quad (2.18)$$

where  $\vec{g}$  is the gravitational acceleration, which can become important in accounting for buoyancy effects inside the chamber at very low flow rates. The continuity equation  $\nabla \cdot \vec{u} = 0$  is also included. To obtain the temperature profile of the system, the heat balance is included:

$$\rho_f \cdot C_{P_f} \cdot \frac{\partial T}{\partial t} + \nabla (-k \cdot \nabla T + \rho_f \cdot C_{P_f} \cdot T \cdot \vec{u}) = Q \quad (2.19)$$

where

$k$  is the thermal conductivity

$C_{P_f}$  is the isobaric heat capacity

$Q$  is the net heat flow to the cooled substrate holder

In Figure 2.4, a series of flow fields (white arrows) and a color-coded temperature map are shown for a simplified OVPD geometry. Nitrogen carrier gas enters the deposition chamber at room temperature through a single, axially positioned barrel and exits through the pump port positioned downstream. The walls of the main chamber are maintained at 500 K, while the substrate, situated downstream of the inlet, is maintained at 290 K. For very low flow rates ( $Re=0.05$ ), the carrier gas quickly thermally equilibrates with the chamber walls and cools rapidly upon contact with the substrate. Hydrodynamic and thermal boundary layers appear to form in front of the substrate. As the flow velocity (i.e., Reynolds number) increases, a greater distance is required to heat the carrier gas. At the same time, the boundary layer becomes more pronounced, while shrinking in thickness.

The organic species is introduced into the model via the mass balance:

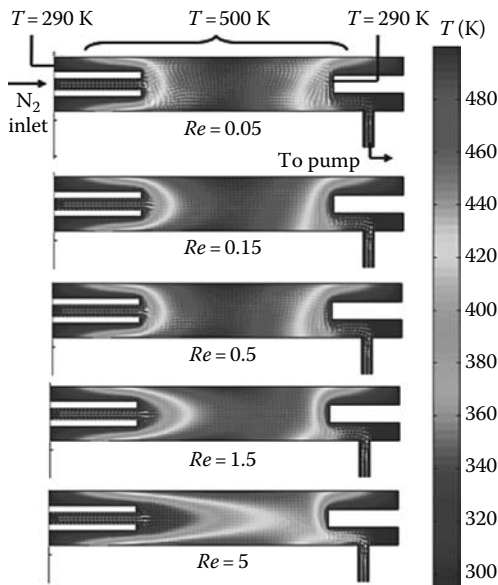
$$\frac{\partial c_i}{\partial t} + \nabla (-D_i \nabla c_i + c_i \cdot \vec{u}) = Q_D \quad (2.20)$$

where

$c_i$  is the organic species concentration

$Q_D$  is the net deposition rate

The numerical solutions to Equations 2.18 through 2.20, along with a set of realistic deposition conditions ( $T_{wall}=600$  K,  $T_{sub}=300$  K,  $Re=10$ ), are plotted

**FIGURE 2.4**

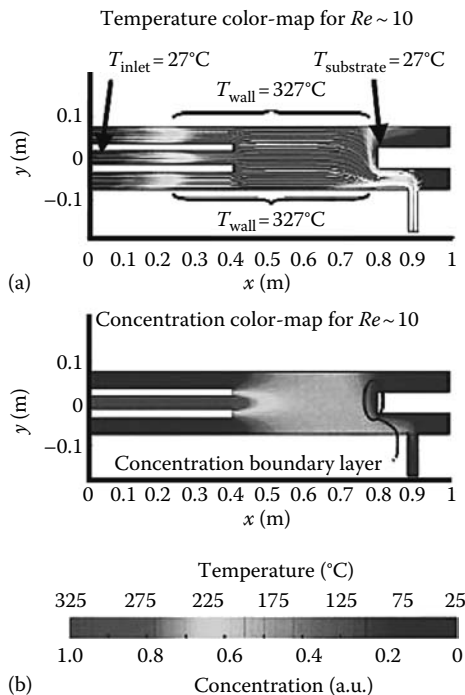
Modeling the flow field and temperature distribution in an OVPD system using numerical solutions to the Navier–Stokes equations. Unheated  $N_2$  is the carrier gas entering the deposition chamber requires longer distances from the inlet to thermally equilibrate for higher Reynolds numbers (i.e., flow velocity). As expected, the hydrodynamic boundary layer decreases in thickness for higher velocity flows. (From Shtein, M. et al., *J. Appl. Phys.*, 93, 4005, 2003. With permission.)

in Figure 2.5. The distribution of species follows the flow, establishing a concentration boundary layer near the substrate. Clearly then, the deposition of organic molecules on the substrate will proceed by diffusion across this boundary layer.

## 2.4 Film Deposition

As the vapor and carrier gas flow over the cold substrate, a stagnant boundary layer of thickness  $\delta$  develops above the surface (see Figures 2.1 and 2.5), across which the organic vapor must diffuse. Since  $P_{\text{org}}^{\text{eq}}$  depends exponentially on temperature, organic molecules condense on the cold substrate, giving rise to a concentration driving force across the boundary layer. The flux of organic molecules to the substrate,  $j_{\text{org}}$ , obeys Fick's law of diffusion:

$$j_{\text{org}} = D_{\text{org}} \cdot \nabla c_{\text{org}} = D_{\text{org}} \cdot \frac{\frac{P_{\text{org}}^{\text{gas}}}{RT} - \frac{P_{\text{org}}^{\text{surf}}}{RT_{\text{surf}}}}{\delta} \quad (2.21)$$

**FIGURE 2.5**

(a) Results of numerical solution of the Navier–Stokes equations for a simplified OVPD system geometry, where carrier gas is introduced into the barrel at a  $Re = 10$ ; the flow field is indicated by the streamlines, while the temperature distribution is shown by the color-map. The flow of the gas around the substrate creates a stagnant boundary layer evidenced by the flow field. (b) Concentration distribution color-map of the organic species carried by  $\text{N}_2$ . The concentration boundary layer near the substrate follows the hydrodynamic boundary layer from (a). (From Shtein, M. et al., *J. Appl. Phys.*, 93, 4005, 2003. With permission.)

where

$D_{\text{org}}$  is the gas-phase diffusivity of the organic species in the carrier gas  
 $P_{\text{org}}^{\text{gas}}$  and  $P_{\text{org}}^{\text{surf}}$  are the organic species' vapor pressures in the gas phase and at the substrate surface, respectively

$T$  and  $T_{\text{surf}}$  are evaluated at deposition chamber and surface temperatures, respectively

For low surface temperatures,  $P_{\text{org}}^{\text{surf}} \ll P_{\text{org}}^{\text{gas}}$ , Equation 2.21 thus becomes

$$j_{\text{org}} = D_{\text{org}} \times \frac{c_{\text{org}}}{\delta} \quad (2.22)$$

where  $c_{\text{org}}$  is the organic vapor concentration in the deposition chamber. Combining Equations 2.13 and 2.22 for the deposition of an organic compound  $i$ :

$$\frac{r_{\text{dep},i}}{A_{\text{sub}}} = j_i = \eta_{\text{dep}} \cdot \frac{D_i}{\delta} \left[ \frac{P_{0,i} \exp\left(\frac{-\Delta H_i^{\text{vap}}}{RT_{\text{cell}}}\right)}{\sqrt{2\pi \cdot mw_i \cdot RT_{\text{cell},i}} + \frac{RT_{\text{std}}}{\dot{V}_{i,\text{sccm}}} \times \frac{P_{\text{cell},i}}{P_{\text{std}}}} \right] \times \left[ \sum \dot{V}_i + \dot{V}_{\text{dil}} \right] \quad (2.23)$$

where

$r_{\text{dep},i}$  is the deposition rate

$A_{\text{sub}}$  is the substrate area

$\eta_{\text{dep}}$  is the deposition efficiency, which depends on the gas distributor design and the resulting flow pattern around the substrate

To predict the deposition rate for a given reactor geometry, the flow equations must be solved to provide information about  $\delta$ , while more precise values for  $D_i$  can be either obtained experimentally, or estimated from correlations such as the Chapman–Enskog equation (Bird et al., 1996).

Note that if  $U$ ,  $P_{\text{dep}}$ , and  $T$  remain constant,  $\delta$  does not change. However, since  $\delta$  typically varies as  $U^{-1/2}$  (Schlichting, 1968; Bird et al., 1996). Clearly then, if the vapor concentration is maintained, the decrease in  $\delta$  via larger flow rates can result in an increased deposition rate. If all flow conditions in the deposition chamber are kept constant,  $r_{\text{dep}}$  tracks  $r_{\text{evap}}$ . Figure 2.6 shows data from an experiment where  $\dot{V}_{\text{sccm}}$  was increased, while  $\dot{V}_{\text{tot}}$ ,  $P_{\text{cell}}$ , and  $T_{\text{cell}}$  were kept constant. The deposition rate behaves analogously to the evaporation rate, as depicted in Figure 2.3c. The plot of  $1/r_{\text{dep}}$

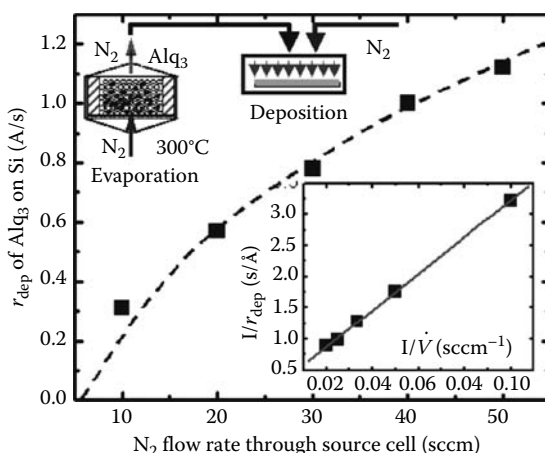


**FIGURE 2.6**

Experimentally determined deposition rate of Alq<sub>3</sub> on Si, matching the qualitative prediction in Figure 2.3c. Equation 2.23 is confirmed by plotting  $1/r_{\text{dep}}$  vs. the inverse of the carrier gas flow rate through the source ( $1/V$ ) cell, while keeping the total flow rate constant by means of the make-up N<sub>2</sub> flow.

vs.  $1/\dot{V}_{\text{scm}}$  is linear, as predicted by Equation 2.23, and can be used to estimate various parameters for each material source configuration, such as  $\alpha \cdot A_e$  and the equilibrium vapor pressure.

---

## 2.5 Deposition in Confined Geometries, Application to Patterning

### 2.5.1 Introduction

Many organic thin film-based devices require the active layers to be patterned in the substrate plane. For example, images on full color displays are composed of picture elements—pixels—each of which is in turn comprised of three subpixels, typically placed side by side. Each subpixel emits red, green, or blue light in predetermined proportions, such that any color can be perceived by the viewer in the far-field. Since the emission wavelength of OLEDs is dictated by the composition of the active organic layers, the latter must be patterned in the plane of the substrate. For layers comprised of small molecular compounds, this is typically accomplished by depositing through a “shadow mask.” This section considers this patterning approach in detail, comparing VTE and OVPD techniques in detail. A more recent, additive patterning method—organic vapor jet printing—can be learned through earlier publications (Shtein et al., 2004a,b; Sun et al. 2005); a more detailed account of OVJP is anticipated in a future publication.

### 2.5.2 Ballistic Transport in VTE and Use of Shadow Masks

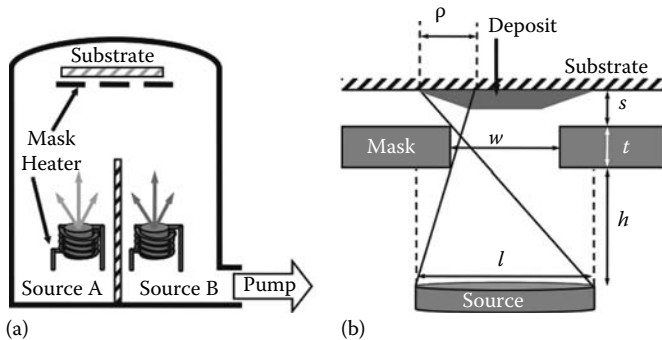
The chamber pressure during VTE is  $10^{-6}$  torr or lower, corresponding to a molecular mean free path,  $mfp$ , of 50 cm or greater, depending on the effective collision cross-section of the evaporant molecule. Placing the substrate within the  $mfp$  of the source results in a ballistic regime of transport from the source to the substrate. For patterned film deposition, a shadow mask is placed at a distance  $s$  in front of the substrate (Figure 2.7). Considering a scenario where the mask aperture has straight walls, thickness,  $t$ , and using a source of width  $l$  centered on the aperture axis, the shape of the deposit is approximately trapezoidal. The width of the edge taper is given by

$$\rho \approx \frac{(s + 2t)l}{2h} \quad (2.24)$$

where

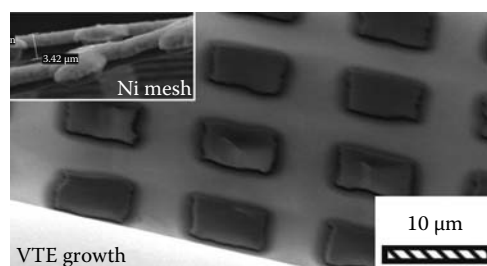
$w$  is the aperture width

$h$  is the source-to-mask separation, as defined in Figure 2.7

**FIGURE 2.7**

(a) Schematic of the VTE process. (b) Schematic of pattern formation in the case of ballistic transport occurring in VTE, with definition of the relevant geometrical parameters. (From Shtein, M. et al., *J. Appl. Phys.*, 93, 4005, 2003. With permission.)

The design guidelines suggested by Equation 2.24 are intuitive: the mask should be as thin as possible, while the separation,  $s$ , should be small to produce the sharpest edges. However, the mask also should not bow under its own weight, and it should withstand multiple mounting and cleaning cycles. Thus, the actual mask dimensions represent a compromise between the pattern resolution and hardware robustness requirements, with typical values for  $s$ ,  $t$ , and  $w$  about 10, 70, and 100  $\mu\text{m}$ , respectively. (Masks having comparable dimensions—also called aperture grills—are used to direct electron beams in CRT screens.) The typical source diameter,  $l \approx 1 \text{ cm}$ , and source-to-substrate distance  $h \approx 50 \text{ cm}$ , yielding  $p \approx 2 \mu\text{m}$ , adequate for full-color OLED display applications. For thinner masks and smaller mask-to-substrate gaps, sharper patterns can be achieved. Figure 2.8 shows a scanning electron micrograph (SEM) of an Alq<sub>3</sub> pattern deposited through a nickel mesh, with  $s < 0.5 \mu\text{m}$  and  $h = 50 \text{ cm}$ , resulting in  $p \approx 0.5 \mu\text{m}$ . Indeed, the limit of  $s=0$  is

**FIGURE 2.8**

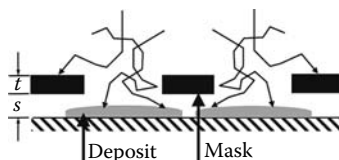
(a) SEM of an Alq<sub>3</sub> film deposited by VTE on Si through a mesh with an aperture width,  $w = 7.5 \mu\text{m}$  and mask-to-substrate separation,  $s \sim 0 \mu\text{m}$  at 10–6 torr. Inset: SEM of the nickel mesh used as a mask. (From Shtein, M. et al., *J. Appl. Phys.*, 93, 4005, 2003. With permission.)

obtained with conventional photoresist, but the vast majority of molecular compounds used in the active layers of high efficiency OLEDs are ill-suited for conventional photolithography.

### 2.5.3 Patterning and OVPD: Diffusive Transport through Shadow Masks

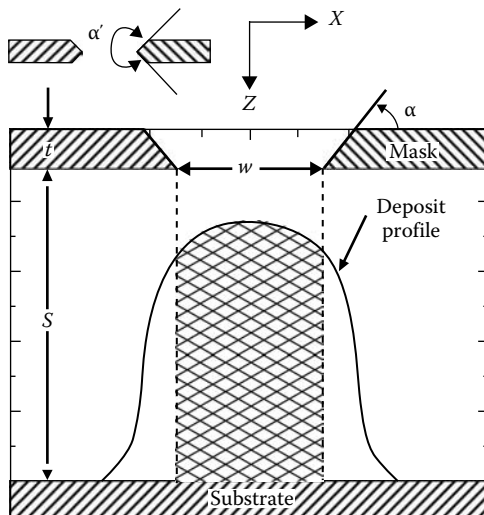
As discussed in Section 2.3, the carrier gas flow creates a hydrodynamic boundary layer at the substrate (typically  $1\text{ mm} < \delta < 5\text{ cm}$ ), across which the organic species diffuse prior to condensation. The organic vapor is a minority species (<1% molar concentration) and the organic molecules collide primarily with the carrier gas molecules en route to the substrate. The carrier gas background pressure far exceeds  $10^{-6}\text{ torr}$ , leading to the condition  $\lambda \ll \delta$ , where the molecular velocities are completely randomized near the substrate. This situation is depicted in Figure 2.9, equivalent to a source with  $l \gg w$  and with  $h \ll l$  (i.e., an infinitely wide source positioned very close to the aperture). This mode of transport is already dramatically different from VTE, where the molecular source-to-substrate distance,  $h$ , is large, transport is ballistic, and molecular trajectories are all nearly perpendicular to the substrate near the aperture. Furthermore, if  $\lambda < s$ , then the organic molecules undergo scattering collisions in the space between the mask and the substrate, with a potentially nontrivial dependence on the deposition conditions (i.e.,  $P_{\text{dep}}$ ,  $s$ , and  $t$ ). The resulting deposition pattern is likely to be bell-shaped, which is substantially different from the trapezoidal pattern typically obtained by VTE. The essential features of the masking geometry and the shape of the deposited pixel are depicted in Figure 2.10.

As a means for quantifying pattern shape, we define the shape factor,  $\eta$ , which is equal to the area bound by  $-w/2 < x < w/2$  (the cross-hatched region in Figure 2.10) divided by the total deposit cross-sectional area. Then  $\eta = 1$  for a rectangular deposit decreasing as the deposit becomes increasingly bell-shaped. For example, a deposit shaped as a Gaussian distribution, with half-width  $w/2$ , will have  $\eta \approx 0.67$ . In analyzing the effects of aperture geometry on the deposited feature shape, we also consider the fraction,  $f$ , of molecules lost by deposition on the side of the mask facing the substrate, and on the aperture walls. Then, the deposition efficiency is simply  $\Sigma = 1 - f$ .



**FIGURE 2.9**

Illustration of the diffusive mode of transport near the substrate resulting in randomized molecular trajectories in the vicinity of the mask, ultimately leading to more diffuse patterns than in the case of VTE. (From Shtein, M. et al., *J. Appl. Phys.*, 93, 4005, 2003. With permission.)

**FIGURE 2.10**

(a) Definition of relevant geometrical parameters for the mask aperture and the deposit formed during OVPD. The shaded region corresponds to the “useful” portion of the deposit, defined either by <90% decrease in the deposit height, or by the projected aperture width,  $w$ . (From Shtein, M. et al., *J. Appl. Phys.*, 93, 4005, 2003. With permission.)

#### 2.5.4 The Breakdown of the Continuous Medium Assumption for $Kn < 10$

The molecular mean free path is given by

$$\lambda = \frac{k_B \times T}{\sqrt{2} \times \pi d^2 \times P_{\text{dep}}} \quad (2.25)$$

where

$k_B$  is the Boltzmann constant

$T$  is the gas temperature

$\pi d^2$  is the effective collision area for two molecules, each having a diameter  $d$

At 25°C and a typical VTE chamber pressure of  $10^{-6}$  torr, the  $\lambda > 50$  cm for nitrogen ( $d=3.25$  Å), while in OVPD at  $P_{\text{dep}}=0.1-10$  torr,  $\lambda \sim 100-1 \mu\text{m}$ .

The Knudsen number,  $Kn$ , is frequently used to characterize different transport regimes in terms of the ratio of  $\lambda$  to the critical apparatus dimension,  $L$  ( $Kn=\lambda/L$ ) (Stechelmacher, 1986). The dimension  $L$  is typically chosen such that  $Kn$  represents the ratio of intermolecular to molecule-wall collision frequencies. For gas flow between the source and the substrate regions,  $L$  is the length of the transport chamber or the

run lines, so that  $Kn=1$ ; thus, continuum models can be used to understand flow dynamics and the deposition rate on the scale of centimeters or meters. However, when film patterning is considered, the apparatus dimension must account for the aperture geometry. In this case,  $L$  is  $1 - 100 \mu\text{m}$ , and  $0.1 < Kn < 10$  for much of the useful deposition pressure range. As it turns out to be the case, the discrete molecular nature of the gas flow cannot be ignored (Bird, 1994; Hirschfelder et al., 1965). This can be illustrated as follows.

For the geometry depicted in Figure 2.10, the mask of thickness  $t$  and aperture of width  $w$  is separated from the substrate by a distance  $s$ . For isotropic diffusion, the width of the deposit base will increase with  $s$ . That is, the longer it takes for a molecule to diffuse to the substrate, the longer it will take (by the same amount) for it to diffuse laterally. The mutual cancellation of these rates will result in identical patterns at different pressures, which, as will be discussed in the following sections, does not match the observed experimental trend. Moreover, in the continuum assumption, the pattern formation does not depend on the shape of the aperture above the edge closest to the substrate, which is again contrary to experiment. Due to the discrete nature of transport at very low pressure, some collimation of flux through the aperture must occur when the organic molecules condense on the aperture sidewall.

Thus, while the continuum analysis helps visualize transport on the scale of the chamber dimension, to predict the OVPD growth of *patterns* whose size and resolution are on the order of  $\lambda$ , the molecular nature of transport near the substrate must be considered.

### 2.5.5 Modeling of Gas Transport in Confined Geometries

Molecular flow through small channels has been previously studied using several techniques. For example, Guevremont and coworkers (Guevremont et al., 2000) experimentally analyzed the shape of molecular fluxes from collimated effusive beam sources and the nature of gas transport within small-diameter capillary arrays. The beam shape was obtained by translating the beam across a skimmer, behind which a mass spectrometer collected the molecular flux. Channel conductance was studied for a range of  $Kn$ . The sources consisted of arrays of capillaries, whose individual diameters were as small as  $10 \mu\text{m}$ . Although  $\lambda$  in their experiments ranged from 1 to  $10^4 \mu\text{m}$  thereby covering a wide range of  $Kn$ , the overall diameter of the source array, and hence the beam width, was  $>1 \text{ mm}$ . Furthermore, no substrate was present to affect the beam, leading to more collimated fluxes than are possible with the isotropic velocity distribution present in pure diffusion through apertures. Thus, although the beam profiles resemble the pattern shapes obtained by OVPD, those results are not strictly applicable.

In contrast to the case where collimated beams are employed, transport of species to the substrate is often diffusive during reactive ion etching

and physical vapor deposition. Semiconductor electronic device processing typically involves etching of, and deposition in holes and trenches of submicron dimensions (Wolf and Tauber, 1999). The processing pressure, however, is typically such that  $Kn \approx 1$ , similar to OVPD growth of patterned films. Studies reveal that Monte-Carlo type simulations can accurately predict deposition and etch rates when coupled with the proper surface reaction models (Akiyama and Imaishi, 1995; Griffiths and Nilson, 1998) suggesting their applicability to micropatterning of thin-film deposits by OVPD. Models of OVPD growth, however, are greatly simplified by the absence of gas phase and surface reactions, and re-evaporation of adsorbed species that must be considered for reactive deposition or etching (Wulu et al., 1991).

### **2.5.6 Monte-Carlo Simulation of OVPD through Apertures**

To avoid the shortcomings of the continuum approximation, the dynamic deposition process was studied using Monte-Carlo (MC) simulations. The objective of the simulations was to examine the trends in deposit shape as functions of process parameters such as the deposition pressure, temperature, molecular diffusivity, mask geometry, and mask-to-substrate spacing.

The MC model allows the variation of  $\lambda$  directly tracking the random path of a molecule as it diffuses through a background of carrier gas in the vicinity of the substrate. For simplicity, the molecular sticking probability on the substrate and mask surfaces is assumed to be unity, which is usually valid for typical multiring aromatic semiconductor molecules and substrate temperatures  $\leq 300\text{ K}$ . Generally, under OVPD growth at  $T=250^\circ\text{C}$ , the vapor pressure of the organics is in the  $10^{-3}$  torr range (Yase et al., 1995; Yase et al., 1996; Shtein et al., 2001), while the background carrier gas pressure is on the order of 0.01–10 torr allowing for a gradient in the organic vapor concentration at a relatively constant total pressure. In this case, organic–organic collisions are rare except at very high deposition rates where gas-phase nucleation can occur (Shtein et al., 2001). Hence the model is valid only for low-to-moderate ( $\leq 50\text{ \AA/s}$ ) film deposition rates.

The rate of molecular transport in gases due to a concentration gradient is characterized by the diffusivity,  $D$  (Hirschfelder et al., 1965):

$$D = \frac{1}{3} \bar{u} \times \lambda \quad (2.26)$$

where  $\bar{u}$  is the molecular mean thermal velocity. Since the organic vapors consist of molecules that have collision diameters greater than  $10\text{ \AA}$  and are geometrically and energetically more complex than the hard sphere atoms of kinetic theory, molecular dynamics simulations should be used for an accurate estimation of the  $\lambda$ . However, since this study is concerned with the dependence of *trends* in pattern evolution on process parameters, simple kinetic theory equations are sufficient for the analysis.

The Monte-Carlo simulation proceeds as follows. The computational space is divided into an  $x$ - $z$  grid extending infinitely in the  $y$ -direction (see Figure 2.10 for definition of the coordinate space). The purpose of the grid is to locate the substrate and mask surfaces, and track changes in the thickness of the deposits. A spherical “test organic molecule” is assigned a random initial location  $(x_0, y_0, z_0)$  inside the boundary layer and above the mask. A random initial direction is then chosen, and the molecule travels a distance  $r = [(x_1 - x_0)^2 + (y_1 - y_0)^2 + (z_1 - z_0)^2]^{1/2}$ , where  $(x_1, y_1, z_1)$  is its new location. Molecules escaping the boundary layer are reflected back toward the substrate. The distance  $r$  is the minimum of the grid size, or  $\lambda/10$ . The probability of collision,  $P_{\text{coll}}$ , with a carrier gas molecule is equal to  $r/\lambda$ , which is checked against a random number,  $r \cdot n$ , between 0 and 1. If  $P_{\text{coll}} < r \cdot n$ , the molecule is again allowed to proceed in the same direction for another step of distance  $r$ . If  $P_{\text{coll}} > r \cdot n$ , the particle is assumed to collide with a carrier gas molecule having a velocity chosen randomly from a Maxwell-Boltzmann distribution. The collision causes the molecule to be deflected with a velocity and an angle consistent with momentum and energy conservation in the elastic collision of two hard spheres. If the path of the particle crosses the substrate plane or the aperture wall, the particle is assumed to stick to the surface with unity efficiency. A single aperture is simulated, with periodic boundary conditions imposed in the  $x$ -direction. Effects of aperture geometry on deposited pattern formation are modeled by assigning different aperture sidewall angles,  $\alpha = 45^\circ, 90^\circ, 135^\circ$ , and  $\alpha' = 270^\circ$ .

### 2.5.6.1 Patterning of Alq<sub>3</sub> Films

Consider the growth of films of the archetype molecule, tris(8-hydroxyquinoline) (Alq<sub>3</sub>), having  $d \sim 10 \text{ \AA}$ . The mean free path is calculated using Equation 2.25, assuming that the collision diameter for a mixture of Alq<sub>3</sub> in a N<sub>2</sub> carrier gas is the average of the respective diameters of the two species in self-diffusion viz.:  $d = \frac{1}{2}(d_{\text{Alq}_3} + d_{\text{N}_2})$ .

Figure 2.11 top shows a grayscale map of the organic species concentration from a simulated deposition of  $10^5$  particles, with  $s = 7 \mu\text{m}$ ,  $t = 3 \mu\text{m}$ , and  $\alpha = 135^\circ$ , and  $\lambda = 100 \mu\text{m}$ , corresponding to a total deposition pressure of  $P_{\text{dep}} \sim 0.1 \text{ torr}$  at  $T = 500 \text{ K}$ . While the simulated particle diameter was  $10 \text{ \AA}$ , it was enlarged in the figure to better illustrate the deposited profile. The initial particle velocities were assigned from a random thermal distribution, and are superimposed onto a  $z$ -directed velocity vector with a magnitude of  $10 \text{ m/s}$ . The size of the individual particle has been enlarged to show the deposited film thickness profile. By decreasing the  $\lambda$  by a factor of 10, a more diffuse pattern is obtained as shown in Figure 2.11 bottom. Note that the films shown here are unrealistically thick and  $t$  is unrealistically thin for conventional OVPD conditions; a film thickness of  $\sim 1000 \text{ \AA}$  and  $t \geq 50 \mu\text{m}$  are more practical. The figure nevertheless illustrates the

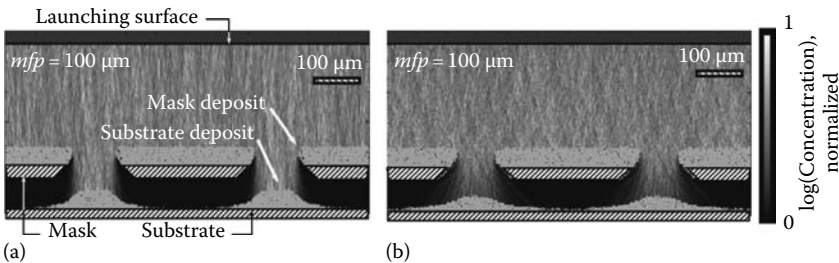


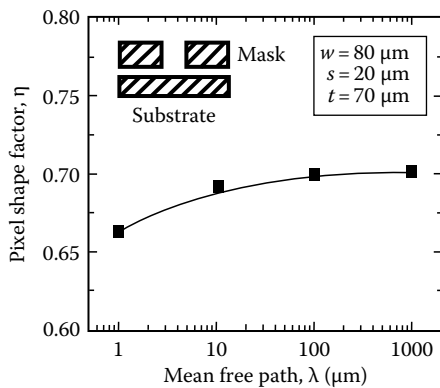
**FIGURE 2.11**

(a) Monte-Carlo simulation results plotted as a grayscale map of the organic species, both as a deposit and as gas-phase species using 105 particles, with  $s = 7 \mu\text{m}$ ,  $t = 3 \mu\text{m}$ , and  $\alpha = 135^\circ$ , and  $\lambda = 100 \mu\text{m}$ , corresponding to a total deposition pressure of  $P_{\text{dep}} \sim 0.1 \text{ torr}$  at  $T = 500 \text{ K}$ . While the simulated particle diameter was  $10 \text{ \AA}$ , it was enlarged in the figure to better illustrate the deposited profile. (b) Simulation conditions identical to (a), except  $\lambda = 10 \mu\text{m}$ , corresponding to a 10-fold increase in the deposition pressure leading to a broadened deposit. The time-averaged molecular trajectories are also visible showing the rapid dispersion of the species past the aperture edge. (From Shtein, M. et al., *J. Appl. Phys.*, 93, 4005, 2003. With permission.)

increased parasitic deposition on the mask and aperture walls when  $\lambda$  is reduced. For clarity, subsequent simulation results will provide only the thickness profile without the shadow mask shown. The total number of  $\text{Alq}_3$  molecules was also increased to  $10^6$  to obtain smoother, more accurate thickness profiles.

### 2.5.6.2 Effects of Chamber Pressure on Deposit Shape

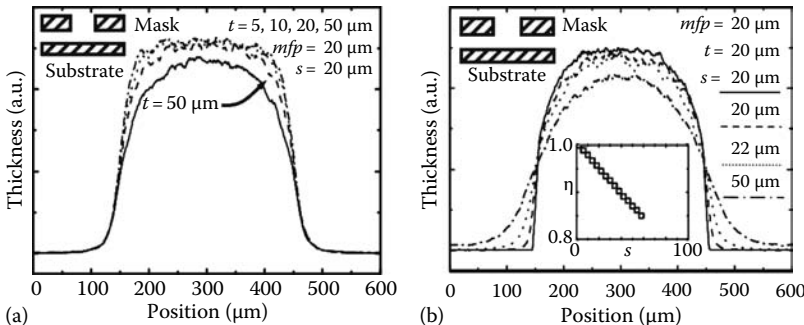
The effects of deposition pressure on pattern resolution were investigated by varying  $\lambda$ . Growth through an aperture with  $w = 80 \mu\text{m}$ ,  $t = 70 \mu\text{m}$ , and with the substrate separated from the lower mask edge by  $s = 20 \mu\text{m}$  was considered. The choices for  $s$  and  $t$  are consistent with deposition of high resolution display picture elements (pixels) by VTE, where the substrate-facing-downward evaporation geometry causes the mask to bow away from the substrate under gravity, leading to  $s \sim 20 \mu\text{m}$ . To stiffen the mask and minimize  $s$ , usually  $t > 70 \mu\text{m}$  is required for VTE. Considerably thinner masks (e.g.,  $t \leq 50 \mu\text{m}$ ) can be used with OVPD due to the possibility of top-down deposition. Figure 2.12 shows that the shape factor,  $\eta$ , increases only weakly as  $\lambda$  varies over four orders of magnitude ( $1 \mu\text{m} \leq \lambda \leq 1000 \mu\text{m}$ , corresponding approximately to  $10 \text{ torr} \geq P_{\text{dep}} \geq 0.01 \text{ torr}$ ), as would be expected for a system approaching the Knudsen transport regime. However,  $\eta$  does not reach unity (corresponding to a rectangular deposit profile) due to parasitic deposition on the sidewalls of the almost square aperture. As expected, the highest pattern edge resolution (and hence, highest  $\eta$ ) is achieved for the largest  $\lambda$ , i.e., the lowest  $P_{\text{dep}}$ . However, as discussed in the following text, the pattern profile exhibits a dome-like shape due to a relatively large  $t/w$ .

**FIGURE 2.12**

Variation in the pixel shape factor,  $\eta$ , with the mean free path,  $\lambda$ , obtained from the Monte-Carlo simulation. Depositing at lower pressure (or longer  $\lambda$ ) results in more sharply defined edges (i.e., larger  $\eta$ , as defined in the text). (From Shtein, M. et al., *J. Appl. Phys.*, 93, 4005, 2003. With permission.)

### 2.5.6.3 Effects of Mask Thickness and Separation

Increasing the aperture thickness can improve collimation of the molecular flux toward the substrate due to the condensation on the walls of the aperture. However, as Figure 2.13a shows, increasing  $t$  from 5 to 50  $\mu\text{m}$  for  $s = \lambda = 20 \mu\text{m}$  and  $w = 300 \mu\text{m}$  has no effect on the spreading of the lower edge of the deposit. However, as  $t/w$  increases, the deposited pattern becomes

**FIGURE 2.13**

(a) Deposit profile as a function of mask thickness,  $t$ , obtained from the Monte-Carlo simulation discussed in the text, using 106 Alq<sub>3</sub> molecules in N<sub>2</sub> background carrier gas with  $mfp = s = 20 \mu\text{m}$ . The aperture dimensions are listed in the plot. The pixel shape factor,  $\eta$ , decreases weakly with  $s$  for this set of parameters. (b) Simulated deposit profiles for a cylindrical aperture mask at various separation distances,  $s$ , with dimensions and details of the simulation listed in the plot. The pattern edge becomes more diffuse, while the deposition efficiency decreases with increasing  $t$  due to parasitic deposition on the aperture sidewall, as discussed in the text. Inset: The deposit shape factor decreases approximately linearly with  $s$ . (Legend:  $s = [—] 2, [--] 10, [\cdot\cdot\cdot] 22, [-\cdots] 50 \mu\text{m}$ ). (From Shtein, M. et al., *J. Appl. Phys.*, 93, 4005, 2003. With permission.)

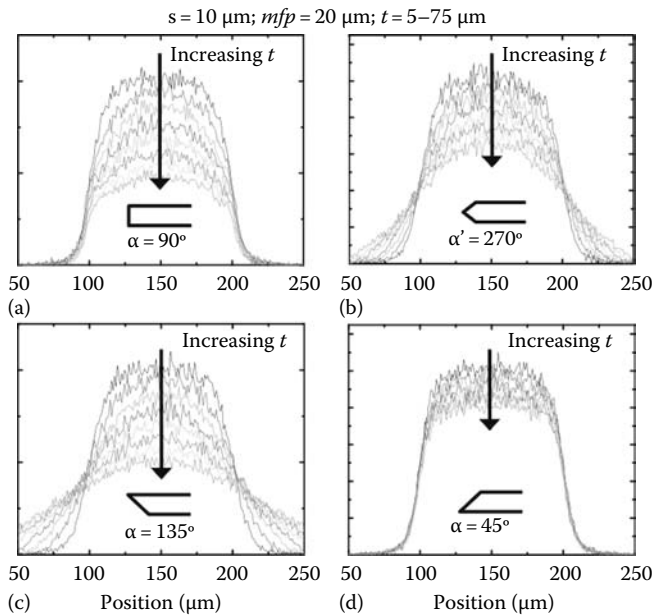
significantly more domed due to the scavenging of the organic molecules by the upper edges of the aperture. The shape factor decreases by less than 5% over the range  $1\text{ }\mu\text{m} < t < 100\text{ }\mu\text{m}$ .

The mask separation,  $s$ , can vary due to bowing under gravity (in VTE), or possibly heating during the deposition process. Figure 2.13b shows profiles for depositions where  $s = 2, 10, 22$ , and  $50\text{ }\mu\text{m}$ , and  $t = 20\text{ }\mu\text{m}$ ,  $w = 300\text{ }\mu\text{m}$ , and  $\lambda = 20\text{ }\mu\text{m}$ . Appreciable edge broadening arises due to collisions in the mask-substrate gap for  $s > \lambda$ . In addition, for large  $s$  the dome in the middle of the deposit is also pronounced and, in contrast to the case of large  $t/w$ , the profile is also broadened at the edges. The inset of Figure 2.13b shows a linear decrease in  $\eta$  with  $s$  for this series of depositions. Thus, an optimal pattern resolution leading to a rectangular deposit is achieved for the smallest values of  $s$  and  $t$ , as expected. Since OVPD can, in principle, be carried out with the mask positioned above the substrate, thin masks can be used while  $s$  is kept small, contrary to the case in VTE. By using thinner masks, the pattern deposition efficiency,  $\Sigma$ , is also increased because less material will be deposited on the aperture sidewall, as will be shown in the following. The drawback of thin masks is that they are more susceptible to thermally and mechanically induced stresses. Nevertheless, in a “top-down” configuration of OVPD, smaller values of  $s$  and  $t$  are possible, potentially leading to higher resolution patterns than is achievable using conventional VTE deposition.

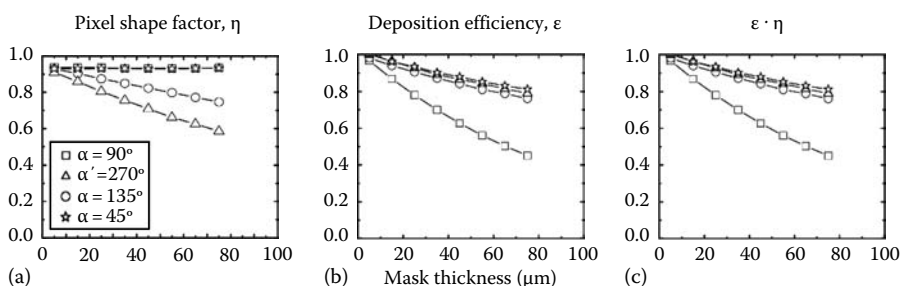
#### **2.5.6.4 Optimizing Mask (Aperture) Shape**

It is also possible to minimize  $t$  at the aperture edge while keeping the mask thick elsewhere. The variation in  $\eta$  with the aperture shape was investigated by varying the aperture sidewall angle,  $\alpha = 45^\circ, 90^\circ, 135^\circ$ , and  $\alpha' = 270^\circ$  (see Figure 2.10). The pattern profiles for these aperture shapes are shown in Figure 2.14. The aperture with  $\alpha = 135^\circ$  results in the most diffuse edge of the deposit (smallest  $\eta$ ) due to the lack of collimation of the approach angle of the molecules. This occurs to a lesser extent with the biconical aperture ( $\alpha' = 270^\circ$ ), but the sharpest patterns are achieved with  $\alpha = 90^\circ$  and  $\alpha = 45^\circ$ . The variation of the shape factor,  $\eta$  vs.  $t$  is plotted in Figure 2.15a for all four aperture geometries. While apertures with  $\alpha = 90^\circ$  and  $45^\circ$  show a minimal decrease in  $\eta$  with  $t$ , curves for  $\alpha' = 270^\circ$  and  $\alpha = 135^\circ$  drop significantly with  $t$ , consistent with the profiles in Figure 2.14.

In addition to allowing deposition of sharper patterns, it is desirable to maximize the material flux to the substrate. The pattern deposition efficiency,  $\varepsilon$ , normalized to that of the aperture with  $\alpha = 45^\circ$  and  $t = 2\text{ }\mu\text{m}$  is plotted vs.  $t$  in Figure 2.15b. For all four aperture shapes,  $\varepsilon$  decreases for larger  $t$ , the effect being most pronounced for  $\alpha = 90^\circ$ . By plotting the product  $\varepsilon \cdot \eta$  vs.  $t$ , the cumulative effect of aperture shape on the deposited pattern can be seen. While the aperture with  $\alpha = 90^\circ$  yields sharp deposit edges, the drop in  $\varepsilon$  with  $t$  for this shape makes it less desirable than the aperture with  $\alpha = 45^\circ$  for depositing well-defined patterns with the least amount of material wasted on coating the mask. However, since  $\varepsilon$  includes all material deposited on the

**FIGURE 2.14**

(a-d) Effects of aperture wall profile (and mask thickness,  $t$ ) on deposit cross-section. In each figure, the mask thickness increases from  $5\mu\text{m}$  (upper curve) to  $75\mu\text{m}$  (lower curve) in  $10\mu\text{m}$  increments. The mask-to-substrate separation,  $s$ , and  $mfp$  are held constant at  $10\mu\text{m}$  and  $20\mu\text{m}$ , respectively. (From Shtein, M. et al., *J. Appl. Phys.*, 93, 4005, 2003. With permission.)

**FIGURE 2.15**

(a) Deposit shape factor,  $\eta$ , as a function of the mask thickness,  $t$ , for the simulated depositions in Figure 2.14. (b) Plot of the deposition efficiency,  $\epsilon$  vs.  $t$  for various aperture shapes. The efficiency for  $\alpha = 90^\circ$  is lowest due to parasitic deposition on the aperture walls. (c) The figure of merit,  $\epsilon \cdot \eta$ , represents the combined effects of pattern sharpness and deposition efficiency using a particular aperture configuration. Apertures with  $\alpha = 45^\circ$  yield the highest  $\epsilon \cdot \eta$ . (From Shtein, M. et al., *J. Appl. Phys.*, 93, 4005, 2003. With permission.)

**TABLE 2.1**

Effects of Masking Geometry and Process Parameters on Pattern Shape

Parameter <sup>a</sup>	Pixel Shape Factor ( $\eta$ )	Deposition Efficiency ( $\epsilon$ )	Combined Figure of Merit ( $\eta \cdot \epsilon$ )
$S \uparrow$	↓	↓	↓
$a \uparrow$	↓	—	↓
$t \uparrow$	↓ <sup>b</sup>	↓	↓
$\lambda \uparrow$	↓	↓	↓

<sup>a</sup> Here ↑ indicates an increase in the parameter, ↓ a decrease.

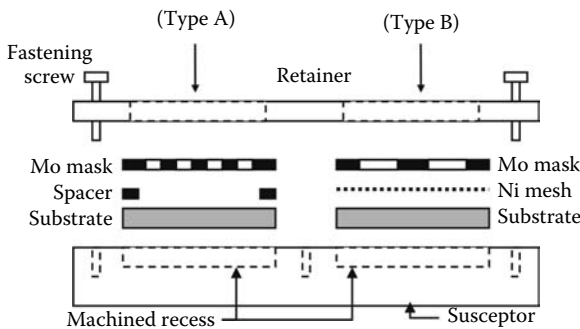
<sup>b</sup> For  $a \leq 90^\circ$ ,  $h$  was insensitive to  $t$ .

substrate,  $\epsilon \cdot \eta$  for  $\alpha = 135^\circ$  is greater than for  $\alpha' = 270^\circ$  and  $\alpha = 90^\circ$ , although the pattern edges are significantly more spread out. Table 2.1 contains a summary of the relative influences of changes in the deposition conditions and mask aperture geometry on the resulting pattern shape factor,  $\eta$ , pattern deposition efficiency,  $\epsilon$ , and the combined figure of merit. In the following sections, experimental results are shown confirming the models developed thus far. A novel method for depositing patterned organic films with self-aligned metal contacts is also demonstrated.

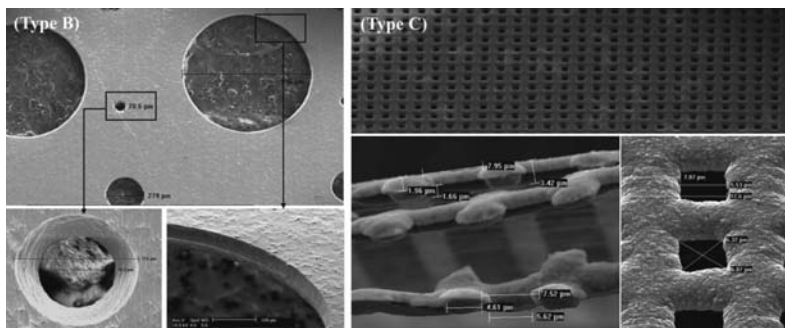
### 2.5.7 Experimental Validation of the Predictions

The deposition of thin films of Alq<sub>3</sub> was carried out using the horizontal reactor described in Section 2.1. The deposition profiles of organic thin films obtained using OVPD were compared with those prepared by VTE. The VTE source-to-substrate distance was approximately 30 cm and the deposition base pressure was maintained at  $10^{-6}$  torr. The mask and substrate configuration is shown in Figure 2.16.

The substrates were placed into recessed sections in a specially machined copper susceptor, the mask was layered on top of the substrate, and a retainer was clamped over the mask edges by means of several screws. The first mask (Type A) was a 60 μm thick, 1 cm × 1 cm Mo foil with circular openings having diameters of 1000, 300, and 100 μm. The aperture profile in this mask was cylindrical ( $\alpha = 90^\circ$ ). A second mask (Type B, Figure 2.17a) was a 75 μm thick Mo sheet with circular apertures having the same nominal diameters as in Type A. The openings in this mask had a double-beveled edge, forming a biconical aperture ( $\alpha' = 270^\circ$ ). The third mask (Mask C, Figure 2.17b) was a Ni mesh,  $3.5 \pm 0.5$  μm thick, with nominally 7.5 μm and 12.5 μm square openings separated by equally wide lines. The mask-to-substrate separation was controlled by shims of multiple layers of the Ni mesh placed between the Si substrate and the Mo mask bottom surface. In depositions through the Ni meshes, 1 cm × 1 cm mesh sheets were fixed to the substrate sandwiching

**FIGURE 2.16**

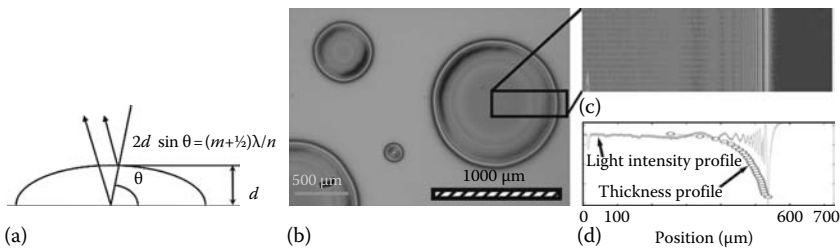
(a) Schematic of the substrate and mask assembly used for the micropatterning experiment. The substrate fits inside of a machined recess in the copper susceptor, while the Molybdenum mask is placed over it. The mask is separated from the substrate by a spacer (Type A) or by a Nickel mesh (Type B). The stack is compressed by a retainer which clamps the edges of the mask and substrate.

**FIGURE 2.17**

SEMs of the molybdenum mask (Type B) and the nickel mesh (Type C) used in the experiments. The Ni mesh was also used as a spacer of thickness  $\sim 4.5\mu\text{m}$  and flexible enough to be folded over several times for spacer thickness to be increased in small increments. Mask Type A (not shown) was identical to Type B, except the aperture that had a cylindrical profile with straight walls, and not the biconical ones of Type A.

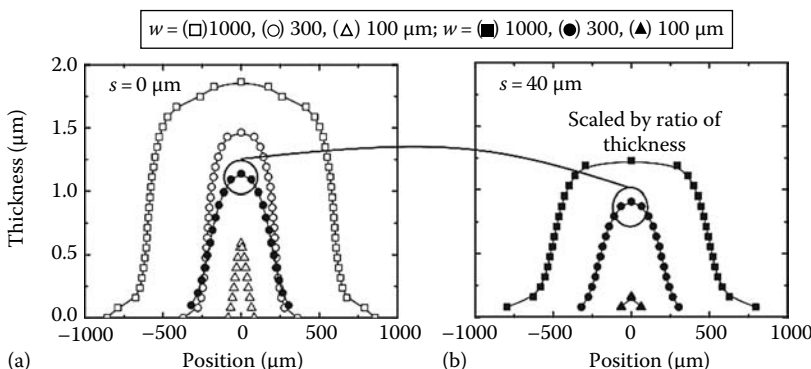
them between the substrate and the first or second type of mask, and then were clamped to the holder by the retainer. Due to the profile of the Ni mesh, the smallest effective separation was  $1.0 \pm 0.5\mu\text{m}$ .

An analysis of the deposited pattern profiles was performed using scanning electron microscopy (SEM) and atomic force microscopy (AFM) for the smallest pattern sizes, and interference microscopy (see Figure 2.18a) for the larger patterns. The latter method entailed illuminating the substrates with a monochromatic source [with wavelength  $\lambda = (540 \pm 10)\text{ nm}$ ] and observing the interference fringes formed at the sloping edge of the bell-shaped deposit (see, e.g., Figure 2.18b). The thickness profile was extracted from the

**FIGURE 2.18**

(a) Illustration of the interference microscopy method used to determine the thickness profile of the deposits. (b) Micrograph showing circular  $\text{Alq}_3$  patterns deposited on Si using OVPD. The interference fringes observed for each deposit indicate a variation in the thickness near its edge. Here, a cylindrical mask was used with  $t = 50\text{ }\mu\text{m}$ ;  $s = 0$ ; and  $w = 100, 300, \text{ and } 1000\text{ }\mu\text{m}$ . (c) Digitized image of a deposit showing the interference fringes near the edge of the deposit. (d) Plot of the light intensity along the radius of the deposit, and the corresponding thickness profile calculated from the interference pattern similar to the one shown in (b). (From Shtein, M. et al., *J. Appl. Phys.*, 93, 4005, 2003. With permission.)

digitized pattern image (Figure 2.19c) by counting the number of fringes from the edge (Figure 2.18d) and using  $H = m\lambda/2n$ , where  $H$  is the pattern thickness;  $m = 0, 1, 2, 3, \text{ etc.}$  is the fringe order; and  $n = 1.74$  is the refractive index of  $\text{Alq}_3$ .

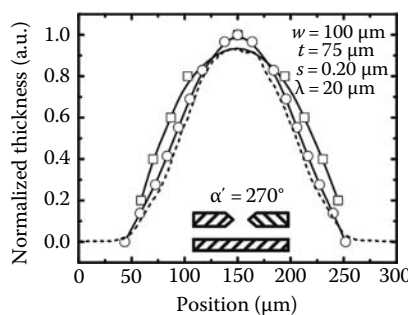
**FIGURE 2.19**

Experimental pixel profile for cases with a mask-to-substrate separation of (a)  $s = 0$  and (b)  $s = 40\text{ }\mu\text{m}$ , respectively. The nominal film thicknesses were (a)  $2\text{ }\mu\text{m}$  and (b)  $1.6\text{ }\mu\text{m}$ . The thickness profile was obtained for the larger diameter deposits by scanning from the center of the deposit outward and reflecting the resulting thickness profile about the origin. For smaller deposits, the entire deposit was scanned. Both (a) and (b) indicate that the pixel deposition efficiency decreases with the aperture aspect ratio,  $t/w$ , where  $t$  and  $w$  are the mask thickness and aperture width, respectively. The profiles from both runs for the  $w = 300\text{ }\mu\text{m}$  aperture are scaled by their thicknesses and compared in Figure 2.18a (open and solid circles). The experimental comparison shows that greater mask-to-substrate distance results in a more diffuse deposit and lower pattern deposition efficiency. (From Shtein, M. et al., *J. Appl. Phys.*, 93, 4005, 2003. With permission.)

### 2.5.7.1 OVPD through Shadow Masks—Results and Discussion

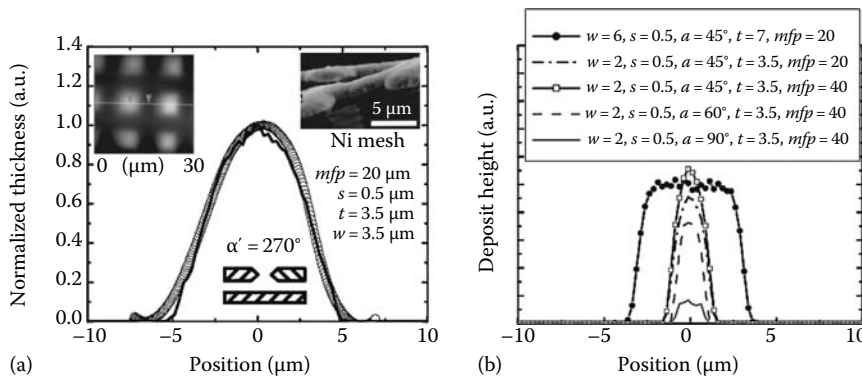
A micrograph with circular pixels deposited by OVPD through Mask A ( $\alpha = 90^\circ$ ) is shown in Figure 2.18b. In Figure 2.19a, the measured pattern profiles for  $s = 0 \mu\text{m}$  are plotted (open circles), while those for  $s = 40 \mu\text{m}$  are shown in Figure 2.19b. The open circles in Figure 2.19a correspond to films nominally  $2 \mu\text{m}$  thick, while those in Figure 2.19b were  $1.6 \mu\text{m}$  thick. Both plots indicate that the pattern deposition efficiency (inferred from the area under each profile) decreases with the aperture aspect ratio,  $t/w$ . The dome in the center of each pattern, which is particularly pronounced for large  $t$ , is similar to that obtained in the simulation. Also plotted in Figure 2.19a is the profile for  $w = 300 \mu\text{m}$  and  $s = 40 \mu\text{m}$  from Figure 2.19b (filled circles). It is evident that increasing  $s$  decreases the efficiency of pattern deposition (due to condensation on the mask) and edge sharpness. As discussed in Section 2.4, this result cannot be obtained using the simple continuum diffusion model.

Experimental deposition profiles for Mask B with  $\alpha' = 270^\circ$ ,  $w = 100 \mu\text{m}$ ,  $t = 75 \mu\text{m}$ , and  $s \approx 0 \mu\text{m}$  are compared to simulations in Figure 2.20. The simulation assumed  $\lambda = 20 \mu\text{m}$  and diffusive deposition (i.e., no bulk flow in the  $z$ -direction) at  $P_{\text{dep}} \approx 0.2$  torr, as used in the experiment. The simulated aperture geometry matches the experimental setup, but  $s$  was adjusted to  $20 \mu\text{m}$  to match the profile of the deposited pattern. The discrepancy is possibly due to the lack of control of mask-to-substrate separation used in the experiment. Using microscopic analysis, we find that the mask with  $t = 75 \mu\text{m}$  and  $\alpha' = 270^\circ$  has surface irregularities in the order of several microns in height such that  $s > 0$ , contrary to assumptions used in the simulations. Furthermore, uneven clamping of the mask to the substrate may lead to warping of the mask, and hence to a larger  $s$ .



**FIGURE 2.20**

Thickness profile of an  $\text{Alq}_3$  film grown by OVPD through a shadow mask with an aperture width  $w = 100 \mu\text{m}$  and mask thickness  $t = 75 \mu\text{m}$ . The simulation (dashed line) was performed with 106  $\text{Alq}_3$  molecules assuming  $s = 20 \mu\text{m}$  and  $mfp = 20 \mu\text{m}$  for  $\alpha' = 270^\circ$  mask. Experimental depositions employed the same type of mask, but without spacers, to obtain  $\text{Alq}_3$  patterns having  $0.9 \mu\text{m}$  (squares) and  $2.1 \mu\text{m}$  (circles) maximum thicknesses for  $w = 100 \mu\text{m}$ . The presence of pattern dispersion in both runs, and a close resemblance to the simulated result indicate inadequate control of the parameter  $s$  in the experiment. (From Shtein, M. et al., *J. Appl. Phys.*, 93, 4005, 2003. With permission.)

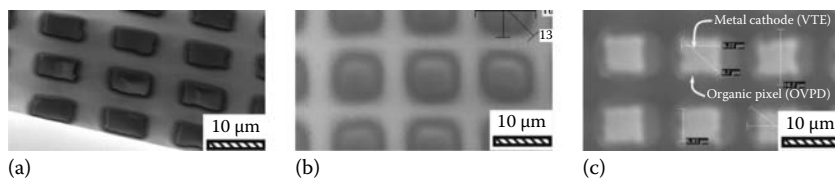
**FIGURE 2.21**

(a) Comparison of the experimental and simulated pattern profiles of a patterned  $\text{Alq}_3$  film, where the edge sharpness was approximately  $1\text{--}3 \mu\text{m}$ . Left inset: An AFM image of a patterned  $\text{Alq}_3$  film deposited by OVPD at 0.1 torr through a nickel mesh with an aperture width,  $w = 6 \mu\text{m}$  and mask thickness,  $t = 3.5 \mu\text{m}$ , with  $s < 1 \mu\text{m}$ . Right inset: SEM side view of the Ni mesh. (b) Simulation results for higher resolution patterns that are predicted for OVPD at the conditions listed in the figure. (From Shtein, M. et al., *J. Appl. Phys.*, 93, 4005, 2003. With permission.)

The highest resolution patterns achieved by OVPD used Mask C with the bottom of the Ni mesh in close contact with the substrate resulting in  $s \approx 1 \mu\text{m}$ , due to the profile of the mesh wires. A patterned  $\text{Alq}_3$  film deposited by OVPD at  $P_{\text{dep}} = 0.1$  torr was imaged using AFM as shown in Figure 2.21a. The edge sharpness is  $\sim 3 \mu\text{m}$  obtained from the thickness profile extracted from the image in the left inset of Figure 2.21a. Simulation of these deposition conditions is also shown as a solid line. The experimental deposit profile is fit assuming  $w = 6.0 \mu\text{m}$ ,  $t = 3.5 \mu\text{m}$ ,  $s = 0.5 \mu\text{m}$ ,  $\lambda = 20 \mu\text{m}$ , and  $\alpha' = 270^\circ$ . The simulated and experimental dimensions are nearly identical suggesting that the stochastic simulation accurately describes the patterned deposition mechanism. Similar patterns have been obtained for depositions at pressures from 0.1 to 2 torr, with the lower pressures increasing pattern definition, as expected. Figure 2.21b shows simulation results for several other deposition conditions. One curve (solid circles) is for an aperture with  $\alpha = 45^\circ$  and  $s = 0.5 \mu\text{m}$  showing improved pattern edge sharpness compared to that in Figure 2.21a. Rectangular patterns with  $\eta > 90\%$  can be achieved for  $w \leq 2 \mu\text{m}$  and  $\alpha = 90^\circ$ .

### 2.5.7.2 Resolution Limits and Self-Aligned Contacts by Hybrid VTE-OVPD

Two instances of micron-scale resolution patterning are illustrated by the SEMs in Figure 2.22: (a)  $\text{Alq}_3$  patterns deposited on Si by VTE through Ni meshes at  $P_{\text{dep}} = 10^{-6}$  torr and  $s \approx 1 \mu\text{m}$  without substrate rotation, and (b) analogous patterns deposited by OVPD at  $P_{\text{dep}} = 2$  torr. The vacuum-deposited patterns show the trapezoidal profile discussed in Section 2.5 where  $\rho < 1 \mu\text{m}$ , while OVPD patterns have edge dispersion in the order of  $1\text{--}3 \mu\text{m}$ . Simulations in

**FIGURE 2.22**

(a) SEM of an Alq<sub>3</sub> film deposited by VTE on Si through a mesh with an aperture width,  $w = 7.5\text{ }\mu\text{m}$  and mask-to-substrate separation,  $s \sim 0\text{ }\mu\text{m}$  at  $10^{-6}\text{ torr}$ . (b) SEM showing Alq<sub>3</sub> patterns deposited on Si using OVPD at  $0.1\text{ torr}$  through a nickel mesh with  $t = 3.5\text{ }\mu\text{m}$ ,  $w = 7.5\text{ }\mu\text{m}$ , and  $s < 1\text{ }\mu\text{m}$ . (c) SEM of hybrid OVPD-VTE deposition showing Alq<sub>3</sub> patterns deposited on Si by OVPD at  $1\text{ torr}$ , with Ag caps subsequently deposited by VTE at  $10^{-6}\text{ torr}$ , without shifting the shadow mask between depositions. (From Shtein, M. et al., *J. Appl. Phys.*, 93, 4005, 2003. With permission.)

Figure 2.21b indicate that if apertures with  $\alpha = 45^\circ$  and minimal  $s$  are used, submicron resolution is achievable using this growth technique.

Finally, the fabrication of OLED-based full-color displays entails the deposition of an array of pixels with one color emissive layer followed by the deposition of a second and third array of different color pixels forming the red–green–blue full-color triad (Tian et al., 1997; Tian et al., 1999). The deposition of organic layers is followed by metal deposition to form the cathode contacts to the OLEDs. To confine the metal cathode to coat only the organic films, and hence prevent the shorting of the cathode to the anode contacts, an “integrated” polymer shadow mask consisting of photoresist walls is prepattered onto the substrate (Tian et al., 1997). The integrated shadow mask can be eliminated by OVPD at moderate pressure through a conventional shadow mask yielding slightly broadened deposits. This is followed by the deposition of a well-defined metal contact in vacuum without moving the mask between the growth steps. The controlled dispersion of the organic coating, therefore, prevents electrical shorts around the edge of the organic film, since VTE of the electrode will automatically yield a smaller size “cap” over the organic pixel. An SEM image of the resulting confined electrode structure from such hybrid deposition is shown in Figure 2.22c. In the passive-matrix architecture, confined individual electrode squares are replaced by stripe electrodes. A second set of pixels may be deposited by simply translating the mask laterally (*possibly in situ*) avoiding the realignment of the mask to a previously deposited pattern.

## 2.6 Summary

Since the molecular mean free path of the organic molecules in OVPD is orders of magnitude smaller than in VTE, the mechanisms of film growth

and pattern formation using OVPD require a different theory to understand fully the film and device growth results obtained. In this chapter, we outlined the physical principles of OVPD concentrating on the fundamental transport aspects and discussing in depth the mechanism of pattern formation using the conventional method of depositing through a shadow mask. The aforementioned discussion should, therefore, provide a good basis for understanding other applications of OVPD, including the growth of specific OLEDs (Zhou et al., 2005), organic PV cells (Yang et al., 2005a,b), organic TFTs (Shtein et al., 2002), and other devices, as well as evolving the technique to other applications and fundamental studies of organic materials (Lunt 2008).

---

## References

- Akiyama, Y. and Imaishi, N., Applicability of one-dimensional diffusion-model for step coverage analysis—Comparison with a simple Monte-Carlo method. *Applied Physics Letters*, 1995. **67**(5): 620–622.
- Baldo, M.A., Deutsch, M., Burrows, P.E., Gossenberger, H.F., Gerstenberg, M., Ban, V.S., and Forrest, S.R., Organic vapor phase deposition. *Advanced Materials*, 1998. **10**(18): 1505.
- Bird, G.A., *Molecular Gas Dynamics and the Direct Simulation of Gas Flows*. 2nd edn. 1994, Oxford: Oxford University Press.
- Bird, R., Stewart, W., and Lightfoot, E., *Momentum, Heat and Mass Transfer*. 1996, New York: John Wiley & Sons.
- Griffiths, S.K. and Nilson, R.H., Optimum conditions for composites fiber coating by chemical vapor infiltration. *Journal of the Electrochemical Society*, 1998. **145**(4): 1263.
- Guevremont, J.M., Sheldon, S., and Zaera, F., Design and characterization of collimated effusive gas beam sources: Effect of source dimensions and backing pressure on total flow and beam profile. *Review of Scientific Instruments*, 2000. **71**(10): 3869.
- Hirschfelder, J.O., Curtiss, C.F., and Bird, R.B., *Molecular Theory of Gases and Liquids. Structure of Matter*, ed. Mayer, M.G. 1965, New York: John Wiley & Sons.
- Schwamberger, M., Gersdorff, M., Reinhold, M., Meyer, N., Strauch, G., Marheineke, B., Heukens, M., Zhou, T.X., Ngo, T., Brown, J.J., Shtein, M., and Forrest, S.R., *Asia Display/IMID'04 Digest*, Daegu, Korea, 2004, p. 824.
- Schllichting, H., *Boundary-Layer Theory*. 6th edn. 1968: New York: McGraw-Hill.
- Shtein, M., Gossenberger, H.F., Benziger, J.B., and Forrest, S.R., Material transport regimes and mechanisms for growth of molecular organic thin films using low-pressure organic vapor phase deposition. *Journal of Applied Physics*, 2001. **89**(2): 1470.
- Shtein, M., Mapel, J., Benziger, J.B., and Forrest, S.R., Effects of film morphology and gate dielectric surface preparation on the electrical characteristics of organic-vapor-phase-deposited pentacene thin-film transistors. *Applied Physics Letters*, 2002. **81**(2): 268.

- Shtein, M., Peumans, P., Benziger, J.B., and Forrest, S.R., Micropatterning of small molecular weight organic semiconductor thin films using organic vapor phase deposition. *Journal of Applied Physics*, 2003. **93**(7): 4005.
- Shtein, M., Peumans, P., Benziger, J.B., and Forrest, S.R., Direct mask- and solvent-free printing of molecular organic semiconductors. *Advanced Materials*, 2004a. **16**(18): 1615.
- Shtein, M., Peumans, P., Benziger, J.B., and Forrest, S.R., Direct mask-free patterning of molecular organic semiconductors using organic vapor jet printing. *Journal of Applied Physics*, 2004b. **96**(8): 4500.
- Stechelmacher, W., Knudsen flow 75 years on: The current state of the art for flow of rarefied gases in tubes and systems. *Reports on Progress in Physics*, 1986. **49**: 1083.
- Sun, Y., Shtein, M., and Forrest, S.R., Direct patterning of organic light-emitting devices by organic-vapor jet printing, *Applied Physics Letter*, 2005. **86**: 113504.
- Tian, P.F., Bulovic, V., Burrows, P.E., Gu, G., Forrest, S.R., and Zhou, T.X., Precise, scalable shadow mask patterning of vacuum-deposited organic light emitting devices. *Journal of Vacuum Science and Technology A—Vacuum Surfaces and Films*, 1999. **17**(5): 2975.
- Tian, P.F., Burrows, P.E., and Forrest, S.R., Photolithographic patterning of vacuum-deposited organic light emitting devices. *Applied Physics Letters*, 1997. **71**(22): 3197–3199.
- Wolf, S. and Tauber, R.N., *Silicon Processing for the VLSI Era: Process Technology*. 2nd edn. Vol. 1. 1999: Sunset Beach, CA: Lattice Press, p. 960.
- Wulu, H.C., Saraswat, K.C., and McVittie, J.P., Simulation of mass-transport for deposition in via holes and trenches. *Journal of the Electrochemical Society*, 1991. **138**(6): 1831–1840.
- Yang, F., Shtein, M., and Forrest, S.R., Controlled growth of a molecular bulk heterojunction photovoltaic cell. *Nature Materials*, 2005a. **4**: 37.
- Yang, F., Shtein, M., and Forrest, S.R., Morphology control and material mixing by high-temperature organic vapor-phase deposition and its application to thin-film solar cells. *Journal of Applied Physics*, 2005b. **98**: 014906.
- Yase, K., Takahashi, Y., Ara-Kato, N., and Kwazu, A., Vapor pressure of organics (CuPc, etc.). *Japanese Journal of Applied Physics Part 1-Regular Papers Short Notes & Review Papers*, 1995. **34**: 636.
- Yase, K., Yoshida, Y., Uno, T., and Okui, N., Vapor pressure of organics. *Journal of Crystal Growth*, 1996. **166**: 942.
- Zhou, T.X., Ngo, T., Brown, J.J., Shtein, M., and Forrest, S.R., Stable and efficient electrophosphorescent organic light-emitting devices grown by organic vapor phase deposition. *Applied Physics Letters*, 2005. **86**: 021107.



# **Part II**

# **Device Physics**



# 3

---

## *Charge Transport and Injection in Amorphous Organic Semiconductors*

---

S. C. Tse, C. H. Cheung, and S. K. So

### CONTENTS

3.1	Introduction .....	62
3.2	Basic Concepts in Amorphous Organic Electronic Solids .....	64
3.2.1	Fundamentals of Charge Transport Mechanism .....	65
3.2.2	Fundamentals of Charge Injection Mechanism .....	68
3.2.3	Experimental Techniques .....	71
3.2.3.1	Time-of-Flight Measurement.....	71
3.2.3.2	Organic Thin-Film Transistor .....	74
3.2.3.3	Current-Voltage ( <i>JV</i> ) Measurement .....	76
3.2.3.4	DISCLC Measurement.....	77
3.2.3.5	Admittance Spectroscopy Measurement .....	78
3.2.4	Phenylamine-Based Compounds .....	79
3.3	Bipolar Transport in Phenylamine-Based Compounds .....	82
3.3.1	Sample Preparations.....	82
3.3.2	Results and Discussion .....	83
3.3.2.1	Hole Mobilities by TOF and OTFT Measurements .....	83
3.3.2.2	Electron Mobilities in Two Phenylamine-Based Compounds.....	90
3.3.2.3	Microscopic Explanation.....	91
3.3.3	Conclusion .....	93
3.4	Nearly Ohmic Hole Injection in Phenylamine-Based Compounds .....	94
3.4.1	Sample Preparations.....	94
3.4.2	Results and Discussion .....	95
3.4.2.1	<i>JV</i> Characteristics for NPB with Different Anodes.....	95
3.4.2.2	Using PEDOT:PSS as Hole Injection Anode for Phenylamine-Based Compounds .....	96
3.4.2.3	DISCLC Measurement for Phenylamine-Based Compounds.....	96

3.4.2.4	Admittance Spectroscopy for Phenylamine-Based Compounds.....	97
3.4.2.5	Mechanism of Hole Injection Using PEDOT:PSS Anode.....	99
3.4.3	Conclusion .....	101
3.5	Devices Application.....	102
3.5.1	Single-Layer Organic Light-Emitting Diodes from NPB .....	102
3.5.2	Single-Layer OLEDs with Perylene Doping.....	104
3.5.3	Conclusion .....	106
	Acknowledgments .....	106
	References.....	106

---

### 3.1 Introduction

Organic electronic devices are receiving steady and increasing attention in optoelectronics in the past decade [1]. There are three broad classes of organic electronic devices that can be classified according to their functions. They include organic light-emitting diodes (OLEDs) [2], organic solar cells [3], and organic thin-film transistors (OTFTs) [4]. The technology has matured sufficiently, and commercial products are available, especially in the form of emissive flat panel displays. Irrespective of the functions of these devices, they generally have a sandwich structure of anode/organic material/cathode [5]. The entire device is, therefore, a stack of thin films. The total thickness is in the range of 50–200 nm. In the case of OLEDs, the device is commonly grown on a flat glass slide, which allows light viewing and provides mechanical support [2]. The active organic material in the middle is called an organic semiconductor. An organic semiconductor consists of aggregates of organic molecules bound by weak van der Waals forces. These molecules contain loosely bound  $\pi$ -electrons that are ultimately responsible for electrical conduction [1]. In applications of OLEDs and solar cells, the organic semiconductors involved have conductivities that resemble an insulator more than a conventional semiconductor (e.g., Si). In OTFT applications, the conductivity of the organic semiconductor is higher, but it is still much lower than a crystalline semiconductor [4].

Why are the emerging organic electronic devices so fascinating? Conventional inorganic electronic devices, e.g., light-emitting diodes (LEDs) or Si-based field-effect transistors (FETs), use “crystalline” inorganic semiconductors as the active electronic materials [6]. As a result, inorganic semiconductor devices are intrinsically inflexible. In contrast, organic devices employ organic semiconductors, which can be polycrystalline or amorphous. They have several advantages over inorganic devices. First, organic

semiconductors, especially those that are amorphous, are mechanically flexible. So, they can be grown on plastic substrates for the realization of flexible electronic devices, for instance, flexible and portable organic solar cells [7]. In addition, due to the weakly binding van der Waals forces, the processing temperatures of organic devices are usually much lower than their inorganic counterparts. So, they can be fabricated using high-throughput, low-temperature approaches that employ one of the several well-established printing techniques. Furthermore, due to versatility in organic synthesis, organic materials can be synthesized with a wide range of properties for device applications, including molecular weight, bandgap, molecular orbital energy levels, wetting properties, structural properties, and doping.

Many advances have been made in the applications of organic electronic devices [1]. However, key challenges remain for these devices to become truly practical and commercialized. One outstanding challenge is material stability. While van der Waals forces give rise to material flexibility in organic semiconductors, it also means these materials have low melting points, and glass transition temperatures ( $T_g$ ). Typical  $T_g$  in “practical” materials can be lower than 100°C. So, thin films of organic semiconductors are not heat durable. Once the film reaches its  $T_g$ , the organic film tends to crystallize, and delaminates from its adjacent contact electrodes or organic films. So there are abundant efforts for designing thermally durable organic semiconductors [8].

An equally important challenge is an understanding of the electrical processes inside an organic electronic device. An organic semiconductor often has an energy gap larger than 1.5 eV. So there are very few thermal-generated carriers at room temperature. However, proper operation requires the injection of free charge carriers from external electrode. (For organic solar cells, free charges are generated by the optical absorption of visible photons.) Once liberated in the organic semiconductors, how do these free charges move inside the semiconductors?

The scope of this chapter is to address the issues of transport and injection. There are existing reviews that describe these two issues [9–11]. We describe here charge transport and injection to phenylamine-based (PA) compounds, a very important class of amorphous hole-transporting materials (HTMs) that are universally used in OLED applications [10]. PA compounds are ideal for studies of materials physics because they are chemically and thermally stable. They form very smooth films on glass substrates. There are wide varieties of PA compounds with different physical or chemical properties. Table 3.1 shows the transport properties (mobilities) of three PA compounds in comparison to some traditional inorganic semiconductors [6,12,13]. It can be noted that organic semiconductors have carrier mobilities much lower than those of crystalline inorganic semiconductors. Below, we first give a brief overview of basic theories, including structures and electronic properties of organic semiconductors, charge transport and injection mechanism, current–voltage characteristics of organic

**TABLE 3.1**

Energy Gaps, Melting Points, and Mobilities of Some Common Inorganic and Organic Semiconductors [6,12,13]

	Material	Energy Gap (eV)	m.p. (°C)	Mobility (cm <sup>2</sup> /Vs)	
				Hole	Electron
Inorganic semiconductor	Si	1.11	1685	500	1900
	GaAs	1.35	1510	400	8800
	GaP	2.24	1750	150	300
	Ge	0.67	1231	1820	3800
Organic semiconductor	TPD	3.2	176	10 <sup>-3</sup>	10 <sup>-7</sup>
	$\alpha$ -NPB	3.0	280	10 <sup>-4</sup>	10 <sup>-4</sup>
	m-MTDATA	3.2	205	10 <sup>-5</sup>	—
	Alq <sub>3</sub>	2.7	>300	10 <sup>-8</sup> –10 <sup>-9</sup>	10 <sup>-6</sup>

The mobilities of organic semiconductors were recorded in the electric field strength of about 500 kV/cm by TOF technique.

solids, and the experimental details of the measuring systems. Next, we provide in-depth studies on the bipolar transport in PA compounds. Time-of-flight (TOF) and OTFT measurements are employed to obtain the hole and electron mobilities. Then, discussion is directed toward the experimental studies of hole injection into PA compounds. Current-voltage (*J*/*V*) measurement, dark-injection space-charge-limited current (DISCLC) transients, and admittance spectroscopy (AS) are used to examine the injection contact between PA compounds and different anode materials. We will also present the hole mobilities of PA compound derived from DISCLC and AS. Finally, the applications of PA compounds on single-layer OLEDs will be described.

### 3.2 Basic Concepts in Amorphous Organic Electronic Solids

Organic materials are aggregates of carbon-based small molecules or polymers. They have typical energy gaps ranging from about 1.5 to 3.5 eV. Generally, organic solids can be treated as insulators as they have few carriers at room temperature. The electronic states of organic molecules are derived from p-orbitals of carbon atoms through sp<sup>2</sup>-p hybridization. In a sp<sup>2</sup> hybridized orbital, there are three  $\sigma$ -bonds with large binding energies. The electrons in the  $\sigma$ -bond are called  $\sigma$ -electrons, which are localized. The remaining p-orbitals form relatively weak  $\pi$ -bonds with lower binding energies. The electrons in the  $\pi$ -bonds, namely,  $\pi$ -electrons, are loosely bound.

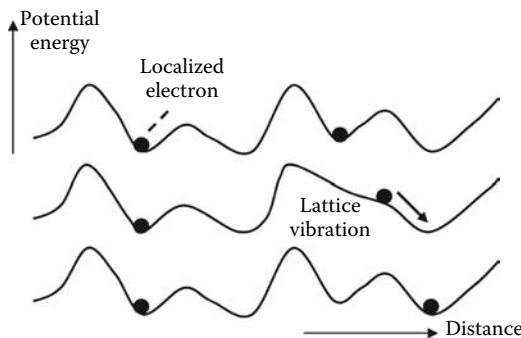
They are delocalized inside a molecule. The highest  $\pi$ -bonding orbital that is occupied by electrons is called the highest occupied molecular orbital (HOMO). The lowest  $\pi$ -antibonding orbital, which is unoccupied, is called the lowest unoccupied molecular orbital (LUMO) [14]. The HOMO and LUMO are, in some sense, analogous to the valence band and conduction band of an inorganic semiconductor.

The  $\sigma$ -bonds and  $\pi$ -bonds are the strong intramolecular covalent bonds that bind atoms to form a single organic molecule. When molecules are in the solid phase, they interact by weak van der Waals forces. If the interaction is sufficiently weak, the result is a disordered solid in which molecules have no long range order. The disorder is the result of variations of local environments of molecules, molecular geometries, and chemical defects. Furthermore, due to weak interactions, the intermolecular overlaps of wavefunction centered on neighboring molecules are very small. The electronic character of organic semiconductors, therefore, can be treated approximately by considering their molecular energy levels. These levels can be broadened in solid state [15].

### 3.2.1 Fundamentals of Charge Transport Mechanism

For charge conduction, we need to study the charge states of the molecule. However, adding or removing an electron from the molecule will lead to significant structural relaxations of the surrounding atomic and electronic environment, resulting in changes in bond lengths of neighboring bonds which implies changes in energetics as well. A structurally relaxed negatively charged state is called an electron polaron. When an electron is removed, a hole polaron is formed. For simplicity, these states are often called electron and hole. The fundamental mechanisms of electron and hole transport in amorphous organic solids, however, are not well understood. Generally, there are two approaches to describe the organic transport mechanisms. The first approach deals with transport process microscopically. The mechanism can be described by the hopping model that was proposed by L.D. Landau in 1933 [16]. As charge carriers move in an organic semiconductor, they can be localized by defects, disorder or potential well caused by the polarization. The charge conduction is an intermolecular process in which charges hop between two adjacent molecules due to the thermoactivated lattice vibrations (Figure 3.1). This hopping motion can be viewed as nonadiabatic electron-transfer reaction. The Marcus theory can be used to express the electron-transfer rate between neighboring molecules,  $k$ , in terms of the reorganization energy  $\lambda$  and the electronic charge-transfer integral  $V_{ab}$  between the hopping partners a and b. In the simplest case, where temperature is sufficiently high that vibrational modes can be treated classically, one obtains [17]:

$$k = \frac{4\pi^2}{h} \cdot V_{ab}^2 \cdot \frac{\exp(-\lambda/4k_B T)}{\sqrt{4\pi\lambda k_B T}} \quad (3.1)$$

**FIGURE 3.1**

Hopping transport mechanism—if the lattice is irregular, or if the carrier becomes localized on a defect site, then lattice vibrations are essential if the carrier is to move from one site to another. This is an activated process and the mobility increases with increasing temperature.

where

$k_B$  is the Boltzmann constant

$T$  is the absolute temperature

$h$  is the Planck's constant

For a fixed  $T$ , the charge hopping rate  $k$  depends on two material parameters, namely,  $V_{ab}$  and  $\lambda$ . The reorganization energy  $\lambda$  is usually defined as the change in free energy if the reactant state were to distort to the equilibrium configuration of the product state without the transfer of charge. It can be computed directly from techniques of quantum chemistry. On the other hand, the charge-transfer integral  $V_{ab}$  is the electronic coupling factor. It is much more difficult to estimate from first principle for amorphous materials because it depends on how the frontier orbitals overlap in the solid state. If indeed, both  $V_{ab}$  and  $\lambda$  are known, then the diffusion coefficient for charge carriers,  $D$ , can be computed from

$$D = a^2 \cdot k \quad (3.2)$$

where  $a$  is the average hopping distance. Knowing  $D$ , one can estimate the carrier mobility,  $\mu$ , from the Einstein relation:

$$\mu = \frac{qD}{k_B T} \quad (3.3)$$

where  $q$  is the charge of an electron. These sets of equations provide a framework for theoretical or computational evaluation of carrier mobilities in organic semiconductors [18–20]. However, it should be noted that in some amorphous organic semiconductors, the measured mobilities deviated substantially from the prediction of Equation 3.3 [11].

The second approach deals with charge transport macroscopically. An amorphous organic semiconductor can be treated as an ensemble of disordered hopping sites through which injected carriers drift under the influence of an external applied field. Historically, the Poole–Frenkel (PF) model was one of the first models to explain the electric field dependence of charge carrier drift mobilities [21,22]. The field-dependent mobility can be written as

$$\mu = \mu_0 \exp(\beta_{\text{PF}} \sqrt{F}) \quad (3.4)$$

$$\beta_{\text{PF}} = \left( \frac{q^3}{\pi \epsilon} \right)^{1/2} \quad (3.5)$$

where

$\mu_0$  is the zero-field mobility

$F$  is the electric field

$q$  is the unit of electronic charge

$\epsilon$  is the dielectric constant

$\beta_{\text{PF}}$  is the PF slope

It may be obtained experimentally from a plot of  $\log \mu$  vs  $F^{1/2}$  at a constant temperature. In many organic disordered systems, the hole and electron mobilities were reported and clearly follow the PF relation shown in Equation 3.4 [23–26]. The PF model, however, has a serious deficiency. According to Equation 3.5, it makes a definitive prediction on the value of  $\beta_{\text{PF}}$ . Yet, it turns out that most experimental results deviate significantly from the theoretical value of  $\beta_{\text{PF}}$ .

A more satisfactory charge transport model, known as the Gaussian disorder model (GDM), is now gaining increasing popularity. The GDM was first proposed by Bässler and is now widely used to describe the hopping motion of charges inside an amorphous organic solid [27]. The GDM is based on the concept of charge hopping in an amorphous solid whose transport site energies and separations are in Gaussian distribution. Within the ensemble, charge hopping is field assisted and thermally activated. So the carrier mobility is dependent on both electric field ( $F$ ) and temperature ( $T$ ). The GDM can be embodied in the following equations [27]:

$$\mu(F, T) = \mu_\infty \exp \left[ - \left( \frac{2\sigma}{3k_B T} \right)^2 \right] \cdot \exp(\beta \sqrt{F}) \quad (3.6)$$

$$\beta = C \left[ \left( \frac{\sigma}{k_B T} \right)^2 - \Sigma^2 \right] \quad (3.7)$$

In Equations 3.6 and 3.7,  $T$  is the absolute temperature,  $k_B$  is the Boltzmann constant,  $\mu_\infty$  is the high temperature limit of the mobility, and  $C$  is  $2.9 \times 10^{-4}$  (cm/Vs) $^{1/2}$ . The energetic disorder  $\sigma$  can be understood as the width of the Gaussian distribution of the density of energy states for the transport sites; the positional disorder  $\Sigma$  can be treated as the geometric randomness arising from structural or chemical defects [28,29]. In essence, only two material parameters, viz.,  $\sigma$  and  $\Sigma$ , are used to describe the randomness of the amorphous organic charge transporter. The PF slope,  $\beta_{PF}$ , is now replaced with  $\beta$  in Equation 3.7, and in the context of the GDM, it is related to the disorders of the material. From Equations 3.6 and 3.7,  $\sigma$  can be determined from the slope of the plot of  $\mu(0,T)$  vs  $1/T^2$ , while  $\Sigma$  can be determined from the  $x$ -intercept of a plot of  $\beta$  vs  $(\sigma/k_B T)^2$ .

### 3.2.2 Fundamentals of Charge Injection Mechanism

In general, there are three major theoretical approaches involved to describe the charge injection mechanism: (1) the field-assisted thermionic injection in which the carriers from the electrodes are thermally excited to overcome the potential barrier resulting from the superposition of the image charge potential and external field, (2) the Fowler–Nordheim (FN) tunneling injection model that the carriers tunnel through the potential barrier of the metal–organic (MO) contact under a high electric field, and (3) the thermoactivated hopping injection model, which is attributed to the hopping of carriers from the metal Fermi level into the localized states of the organic semiconductor [30–32].

In all of these approaches, the injection process is dominated by the charge injection barrier at the interfaces between the active layer and the metal electrodes, which is defined as the energy separation between Fermi-level  $E_F$  of the electrode and HOMO (or LUMO) of the organic layer. Thus, it is necessary to consider electronic properties and band alignment of the MO interfaces.

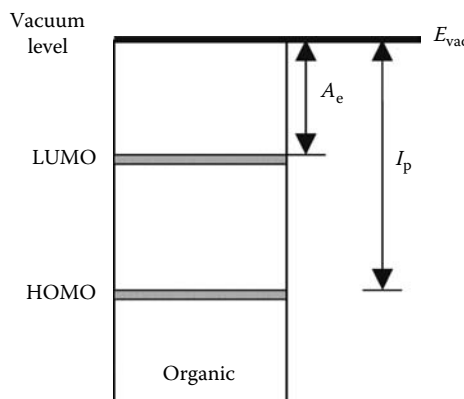


**FIGURE 3.2**

Energy diagram of an intrinsic molecular solid.  $I_p$  is the ionization potential and  $A_e$  is the electron affinity.

Figure 3.2 shows a schematic energy band diagram of a typical molecular solid. The upper most horizontal line is the vacuum level ( $E_{\text{vac}}$ ). It is defined as the minimum energy level for an electron to escape from the solid. The energy separation between the HOMO and  $E_{\text{vac}}$  is the ionization potential ( $I_p$ ). The separation between the LUMO and  $E_{\text{vac}}$  is the electron affinity ( $A_e$ ).

Next, we consider the energy level alignment when a metal and an organic solid are brought into contact. For organic semiconductors, the surface of molecular solid has no dangling bonds. Therefore, the molecular energy level alignment at MO interfaces ideally should obey the classic Mott–Schottky model, in which no interaction occurs at the MO interfaces [33]. So, vacuum

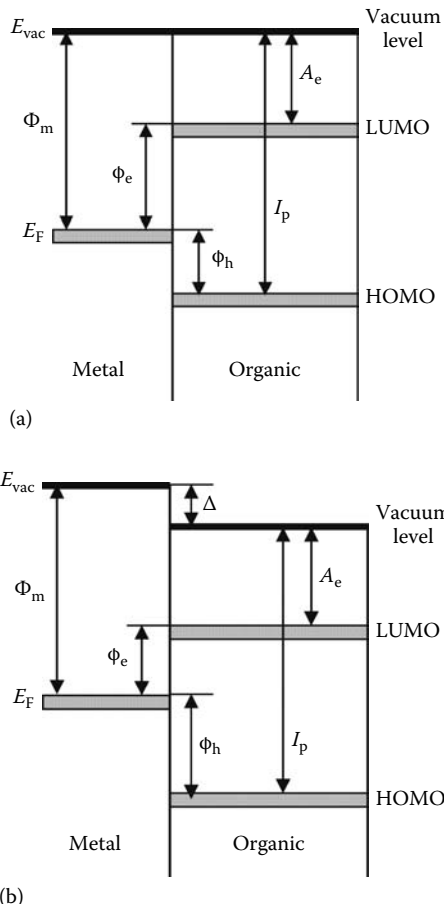


**FIGURE 3.3**

Schematic energy diagrams of an MO interface (a) assuming a common vacuum level and no interface dipole, and (b) with interface dipole.  $\Phi_m$  is the metal work function,  $I_p$  is the ionization potential,  $A_e$  is the electron affinity, and  $\Delta$  is the vacuum level shift due to the interface dipole. Band bending effects are ignored.

level alignment is used. Figure 3.3a illustrates the energy diagram according to the Mott–Schottky rule of a MO interface. The interface barrier heights for hole ( $\phi_h$ ) and electron ( $\phi_e$ ) can be expressed as

$$\phi_h = I_p - \Phi_m \quad (3.8)$$

$$\phi_e = \Phi_m - A_e \quad (3.9)$$

where

$\Phi_m$  is the metal work function

$I_p$  is the ionization potential

$A_e$  is the electron affinity

However, in the real MO interface, a common vacuum level is not achieved in most cases. An interface dipole layer can be formed between the metal and the organic. As a result, the vacuum level becomes discontinuous at the interface. So there will be an abrupt change ( $\Delta$ ) right across the interface, which was observed experimentally [34,35]. As shown in Figure 3.3b, the interface barriers have to be modified:

$$\phi_h = I_p - \Phi_m + \Delta \quad (3.10)$$

$$\phi_e = \Phi_m - A_e - \Delta \quad (3.11)$$

The origin of the interface dipole remains controversial. A variety of explanations has been put forward including (1) electron transfer between the metal and the organic layer, (2) image force effect or the modification of the metal surface that comes from the tailing of the electron cloud inside the metal, (3) chemical interaction that could lead to the arrangement or formation of new bonds, (4) existence of interfacial states, and (5) permanent dipole moment can lead to the large interface dipole formation [34]. Up to now, extensive experimental work has been done to study the formation of interface dipole in organic electronic devices. The most notable experimental technique is ultraviolet photoelectron spectroscopy (UPS). One measures a spectrum of photoelectrons emitted by the materials after a high energy monochromatic UV light irradiation [36–39]. It has been shown that tris(8-hydroxyquinoline) aluminum ( $\text{Alq}_3$ ), a common electron-transporting (ET) material in OLEDs, exhibits a large  $\Delta$  on Au up to  $-1.6\text{ eV}$  [40]. However, there is still no fundamental expression to rule out the interface as a universal function of the properties of two interface components, rather than analyzing them individually.

The injection barrier on the MO interface is ideally eliminated by using an appropriate electrode. In this case, carriers can freely inject into the organic solid without overcoming any barriers. The interface is viewed as an ohmic contact, that is, contact with a reservoir of free carriers sufficiently large

to supply the maximum charge capacity at the given applied voltage. As a result, the current–voltage characteristic of an organic solid exhibits a bulk-controlled behavior, namely space-charge-limited current (SCLC) [41].

### 3.2.3 Experimental Techniques

Several experimental techniques are used to investigate the carrier injection and transport in organic solids. TOF technique, current–voltage (*JV*) measurement, AS measurement, and DISCLC measurement are used and cross-compared. Table 3.2 shows a summary of these techniques.

#### 3.2.3.1 Time-of-Flight Measurement

TOF is, perhaps, the most widely used method of quantifying the conductivity of organic electronic materials [42]. The data interpretation of TOF is the simplest because ohmic contact is not required. A typical TOF configuration is shown in Table 3.2. A thick organic layer is sandwiched by two electrodes. Generally, a semitransparent metal is used as the cathode and a transparent indium-tin-oxide (ITO) is used as the anode. The thickness of the organic layer  $d$  is always chosen to have a thickness of several microns because the capacitance decreases and the transit time increases. So, the effect of  $RC$  decay time from the circuit can be minimized.

TOF experimental procedures involve applying the E-field, carrier generating, carrier transporting through the organic layer and photocurrent transient capturing. First, a high voltage dc power supply applies a reverse bias on the TOF sample in order to establish an external uniform E-field. For measuring electron mobility, a negative voltage is applied on the ITO side while the metal side was grounded. For measuring hole mobility, the semitransparent metal side is biased with a positive voltage and the ITO side is grounded. A pulsed laser is used to generate a sheet of free charges near one side of the sample. The incident laser intensity should be low enough so that a space-charge-free transient can occur. For measuring electron mobility, carriers are generated from the ITO side. Hole is generated from the metal side for hole mobility measurements. The injected carriers move through the sample under the external electric field and drift to the counterelectrode.

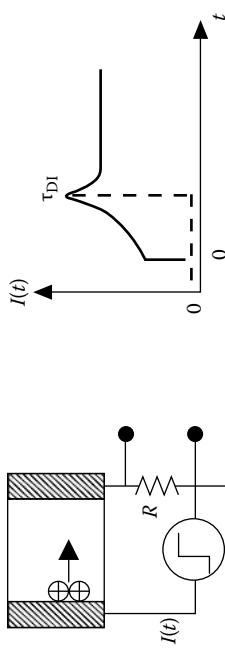
A current-sensing resistor  $R$  in series with the sample converts and magnifies the photocurrent into voltage. The value of  $R$  is adjusted between  $1\Omega$  and  $1\text{ M}\Omega$  so that the  $RC$  time constant should be at least 20 times less than the carrier transient time. The transient voltage across  $R$  can be captured by a digital oscilloscope. Figure 3.4 shows a typical TOF nondispersive transient signal. The general features of the TOF time transient include (1) a plateau region, (2) a clear turning point at time  $t = \tau$ , and (3) a dispersion tail region. In the plateau region, the photocurrent is induced by the movement of photogenerated carriers. While  $t = \tau$ , the photocurrent exhibits a discontinuous cusp. The time ( $\tau$ ) can be defined as the carrier transit time of the leading carriers across the organic layer. Following the turning point, the

**TABLE 3.2**  
Summary of Experimental Techniques

Technique	Sample Geometry	Typical Data	$\mu$	References
1. TOF			$\mu = \frac{d^2}{\tau V}$	[42]
2. OTFT			$\left. \frac{\partial I_D}{\partial V_G} \right _{V_D} = \frac{W}{L} C_V \mu_{FE,lin}$ $\left. \frac{\partial \sqrt{I_D}}{\partial V_G} \right _{V_D} = \sqrt{\frac{W}{2L}} C_V \mu_{FE,sat}$	[6]
3. $I/V$ (current-voltage characteristics)			$I_{SCL} = \frac{9}{8} \mu_0 \epsilon_0 \epsilon_r \exp \left( 0.89 \beta \sqrt{F} \right) \frac{F^2}{d}$	[41,46]

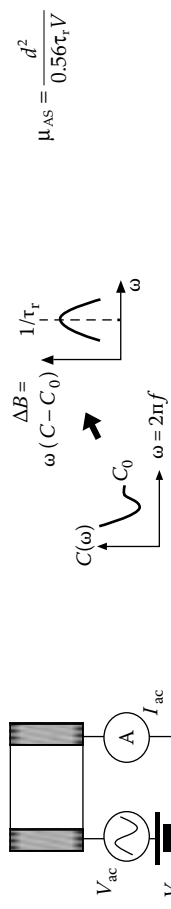
[41,51]

$$\mu_{DI} = \frac{0.786t^2}{\tau_{DI}V}$$



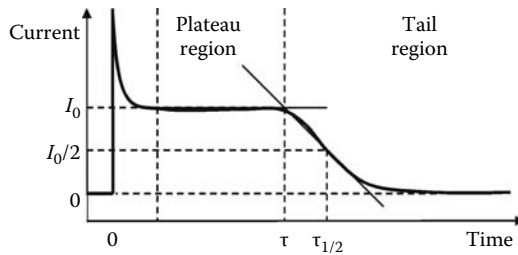
4. DISCLC

[53]



5. AS

TOF, time-of-flight; OTFT, organic thin film transistor; DISCLC, dark-injection space-charge-limited current; AS, admittance spectroscopy.

**FIGURE 3.4**

A typical nondispersive TOF transient signal.  $\tau$  is the transit time of the leading front carrier, and  $\tau_{1/2}$  is the average carrier transit time.

photocurrent drops rapidly in the dispersion tail region. The tail arises from the diffusion or from detrapping of carriers [43]. In the tail region, an “average” carrier transit time,  $\tau_{1/2}$ , can be defined at instant at which the TOF signal drops to 1/2 of the current in the plateau region. Knowing  $\tau$  and  $\tau_{1/2}$ , the leading front carrier mobility and the average carrier mobility can be determined from the relation Equations 3.12 and 3.13, respectively,

$$\mu = \frac{d}{\tau \cdot F} = \frac{d^2}{\tau \cdot V} \quad (3.12)$$

$$\mu_{ave} = \frac{d}{\tau_{1/2} \cdot F} = \frac{d^2}{\tau_{1/2} \cdot V} \quad (3.13)$$

where

$d$  is the organic thickness or flight distance

$F$  is the applied electric field

$V$  is the applied voltage

Traps in the organic layer are significant to the TOF transient signal. For materials with high density of traps, the transient signal becomes dispersive. The cusp disappears and the transit time is hard to be determined. Furthermore, because TOF samples usually have thicknesses of several micrometers, the material consumption is quite large. Moreover, the mobility values are always in low electric field regime in a PF plot, where  $F=0.1\text{--}0.8\text{ MV/cm}$ . This value is lower than the organic electronic device operation regime of  $\sim 1\text{ mV/cm}$ . Therefore, TOF measurements are most suitable for determining mobilities of trap-free organic material in the low field region.

### 3.2.3.2 Organic Thin-Film Transistor

As mentioned in Section 3.2.3.1, TOF is the most widely used method for quantifying the conductivity of organic electronic materials. However, it has

a distinct disadvantage. A thick film ( $\sim\mu\text{m}$ ) is generally required for TOF. In contrast, thin-film transistor (TFT) technique is less demanding in terms of material consumption since an organic layer with a thickness less than  $\sim 0.1\mu\text{m}$  is sufficient [44].

OTFT is a three-terminal device and usually has two configurations, bottom contact and top contact configurations [4]. The main difference between the two configurations is the sequence of film deposition. For bottom contact configuration, an overlayer of few hundred nanometers insulator (gate dielectric) is grown on a conducting substrate. The conducting substrate serves as the gate electrode of TFT. Another two electrodes, the source (S) and drain (D) electrodes, are then deposited on the predefined substrate. Finally, the active material is deposited on the electrodes. Conversely, in top contact configuration, the active material is deposited on the substrate first, followed by the S/D electrodes. There are two types of OTFTs in the charge transport point of view, namely, p-OTFTs and n-OTFTs [4]. For p-OTFTs, holes are the majority charge carriers, whereas for n-OTFTs, the majority charge carriers are electrons.

The procedures for extracting carrier mobility in OTFT are described as follows. A voltage (gate voltage,  $V_G$ ) is applied on the conducting substrate. Charges are then injected from the S electrode into the active material and accumulate at the layer adjacent to the gate dielectric to form a conducting channel under the influence of  $V_G$ . Under this situation, another voltage is applied at the drain electrode ( $V_D$ ). The charges would transport from S to D through the channel. The relation between the current flowing through the channel ( $I_D$ ) and the voltage at drain electrode ( $V_D$ ) can be recorded.

Typical output characteristics ( $I_D$  vs  $V_D$ ) with different  $V_G$  for OTFT are shown in Figure 3.5. Two regions can be resolved in the plot: linear and saturation regions. These two regions are described by the following equations [6]:

$$I_D = \frac{W}{L} \mu_{FE} C_i \left[ V_D (V_G - V_T) - \frac{V_D^2}{2} \right] \quad (\text{Linear}) \quad (3.14)$$

$$I_D = \frac{W}{2L} \mu_{FE} C_i (V_G - V_T)^2 \quad (\text{Saturation}) \quad (3.15)$$

where

$W$  and  $L$  are the channel width and length, respectively

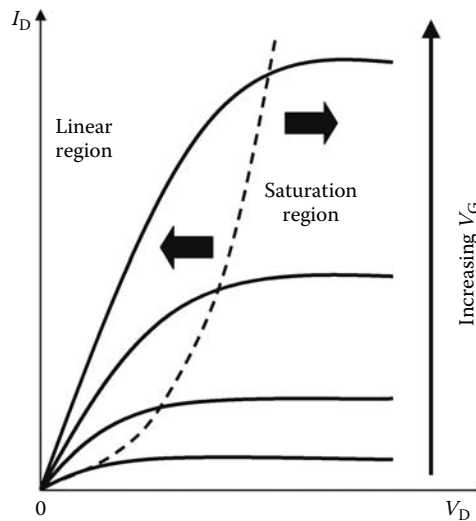
$C_i$  is the capacitance of gate dielectric per unit area

$V_T$  is the threshold voltage

$V_G$  and  $V_D$  are the voltages at gate and drain electrodes, respectively

$\mu_{FE}$  is the field effect (FE) mobility, which is the carrier mobility obtained from TFTs

In linear region at certain  $V_D$ , we can obtain the  $\mu_{FE}$  from the slope of the plot of  $I_D$  vs  $V_G$  according to Equation 3.14. On the other hand, in the saturation

**FIGURE 3.5**

A typical output characteristic of OTFTs with well-defined linear and saturation regions.

region, the  $\mu_{FE}$  can be obtained from the slope of the plot of  $\sqrt{I_D}$  vs  $V_G$  according to Equation 3.15. Summary of mobility extraction from OTFT can be found in Table 3.2.

### 3.2.3.3 Current–Voltage (JV) Measurement

JV measurement is the most straightforward technique in electrical measurement. It has been used to observe the injecting condition of MO interface [45]. As shown in Table 3.2, JV characteristics can be recorded by a computer-controlled source measure unit (SMU) as a steady-state voltage source and current measuring device. For organic transporter void of traps and with ohmic contact, the steady-state current density should obey the space-charge-limited current ( $J_{SCL}$ ). Following the work of Murgatroyd, the  $J_{SCL}$  of a trap-free material can be approximated by [46]

$$J_{SCL} = \frac{9}{8} \mu_0 \epsilon_0 \epsilon_r \exp(0.89\beta\sqrt{F}) \frac{F^2}{d} \quad (3.16)$$

where

$\mu_0$  is the zero-field mobility

$\beta$  is the PF slope

$\epsilon_0$  is the permittivity in vacuum

$\epsilon_r$  is the dielectric constant ( $\epsilon_r \sim 3$  for organic materials)

$F$  is the average electric field

$d$  is the sample thickness

Therefore, the  $J_{SCL}$  can be predicted if the field-dependent mobilities are known from an alternative method, such as TOF measurement.

However, experimental JV curves often deviate from the ideal  $J_{SCL}$ . In these cases, the measured current  $J_{INJ}$  is injection limited caused by a nonohmic contact or poor surface morphology. When the MO interface is nonohmic, carrier injection can be described by the Richardson–Schottky model of thermionic emission: the carriers are injected into organic solid only when they acquire sufficient thermal energy to overcome the Schottky barrier ( $\phi$ ), which is related to the organic ionization potential ( $I_p$ ), the electron affinity ( $A_e$ ), the metal work function ( $\Phi_M$ ), and the vacuum level shift ( $\Delta$ ) [34,35]. Thus, the carrier injection efficiency ( $\eta$ ) can be calculated by the following equation:  $\eta = J_{INJ}/J_{SCL}$ .

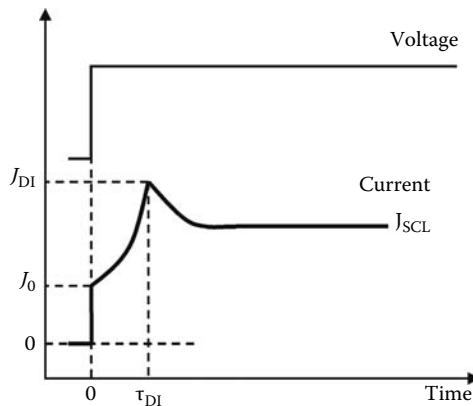
### 3.2.3.4 DISCLC Measurement

DISCLC is a well-known technique for measuring carrier mobility in organic materials [47–49]. Moreover, DISCLC is also used to examine the condition of the injection interface [50]. The DISCLC experimental setup is depicted in Table 3.2. The structure of the DISCLC sample is the same as TOF. An organic layer is sandwiched by two electrodes: metal as the cathode and transparent ITO as the anode. The thickness of the organic layer can vary between a few hundred nanometers to several microns. However, at lower thicknesses, the  $RC$  decay can dominate the current transient ( $C \propto 1/d$ ), making the determination of the transit time more difficult.

During DISCLC measurements, the sample is subject to a rectangular voltage pulse excitation by using a pulse generator. The material is assumed to be trap-free. One of the injecting contacts is taken to be ohmic. Then, the carriers are injected into the organic until the total number of injected carriers meets the space charge limit. A characteristic temporal evolution with a maximum is observed in the transient current. The time-varying current across the sample is sourced into a sensing resistor  $R$  from which the transient current signal can be displayed on a storage oscilloscope. Figure 3.6 outlines the ideal transient current response for a trap-free organic semiconductor. Three critical parameters can be extracted from the transient current density. First, the characteristic time  $\tau_{DI}$  is the arrival time of the leading front of the injected carrier at the noninjecting electrode.  $\tau_{DI}$  is related to the space-charge-free transient time  $\tau$  from TOF and the carrier mobility can be calculated as follows:

$$\tau_{DI} = 0.786\tau \quad (3.17)$$

$$\mu = \frac{0.786d}{\tau_{DI} \cdot F} = \frac{0.786d^2}{\tau_{DI} \cdot V} \quad (3.18)$$

**FIGURE 3.6**

An ideal DISCLC transient current.  $\tau_{DI}$  is the arrival time of the leading front carrier.  $J_0$ ,  $J_{DI}$ , and  $J_{SCL}$  are the instantaneous current, the current when  $t = \tau_{DI}$  and the space-charge-limited current, respectively. (From Tse, S.C. et al., *J. Appl. Phys.*, 100, 063708, 2006. With permission.)

where

$d$  is the thickness

$F$  is the applied electric field

$V$  is the applied voltage

Second, the ratio  $J_{DI}/J_0$  should be 2.72. However, in the real case, the transient current consists of a dark-injection current and a  $RC$  response of the circuit. The latter comes from the inevitable fact that the sample itself acts as a capacitor and its needs a finite time to charge up. Thus  $J_0$  is overestimated due to the effect of  $RC$  response, and therefore the ratio  $J_{DI}/J_0$  is always smaller than the ideal value. Third, another ratio  $J_{DI}/J_{SCL}$  should be 1.21 [41,51]. Departure from the ideal value of 1.21 may indicate that the injecting contact deviates from ohmic injection. Alternatively, if the charge injection remains ohmic, deviation of this ratio could also be a consequence of nonnegligible charge diffusion or field-dependent mobilities. A critical examination of this ratio under the condition of ohmic injection has been reported elsewhere [52].

### 3.2.3.5 Admittance Spectroscopy Measurement

AS has emerged as an interesting alternative for measuring carrier mobility in organic materials [53–55]. AS is known to be a very general and powerful technique for investigating charge transport kinetics and relaxation processes in solid state devices. Moreover, it is useful in examining the condition

of the injection interface [55]. In an AS experiment, the sample has a configuration of anode/organic/cathode. The cathode is designed to be electron blocking only if hole injection is examined. The sample is probed by a weak ac excitation voltage  $v_{ac}$  superimposed on a dc biased voltage. The response function, such as the ac current  $i_{ac}$ , is measured. In general,  $i_{ac}$  is not in phase with  $v_{ac}$  and the admittance  $Y$  is complex:

$$Y(\omega) = i_{ac}/v_{ac} = G + iB = G + i\omega C \quad (3.19)$$

where  $i^2 = -1$  and  $\omega = 2\pi f$ .  $G$ ,  $B$ , and  $C$  are the conductance, susceptance, and capacitance, respectively. The admittance  $Y$  can be determined experimentally by an impedance analyzer through which the frequency-dependent capacitance can be obtained. If the material is trap-free and with an ohmic injection contact, then a well-defined minimum can be observed from the plot of frequency-dependent capacitance, which is shown in Figure 3.7a.

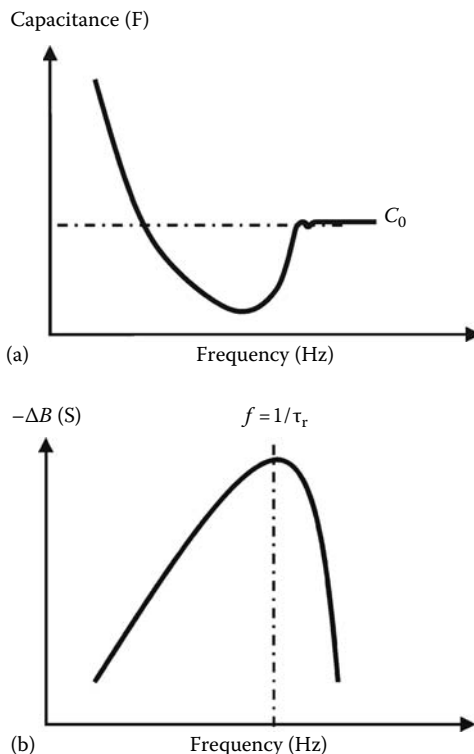
Additionally, AS can be used to delineate carrier mobilities in organic electronic materials. By solving the drift current equation and the Poisson equation for  $i_{ac}$ , one can show analytically that the admittance  $Y(\omega)$  depends on the carrier transit time. Furthermore, the differential susceptance,  $\Delta B \equiv \omega(C - C_0)$ , which is a measure of the differential capacitance, exhibits a peak in a plot of  $-\Delta B$  vs  $f$ . The characteristic time  $\tau_r \equiv 1/f_r$  (at  $f_r$ , the maximum in  $-\Delta B$  appears) is related to the average transit time  $\tau_{1/2}$  of the carriers via Equation 3.20. Hence, by measuring  $f_r$  in a  $-\Delta B$  vs  $f$  (Figure 3.7b), one can deduce  $\tau_{1/2}$  and the carrier mobility from the following relation:

$$\tau_{1/2} = 0.56\tau_r \quad (3.20)$$

$$\mu_{ave} = \frac{d}{\tau_{1/2} \cdot F} = \frac{d^2}{0.56\tau_r \cdot V} \quad (3.21)$$

### 3.2.4 Phenylamine-Based Compounds

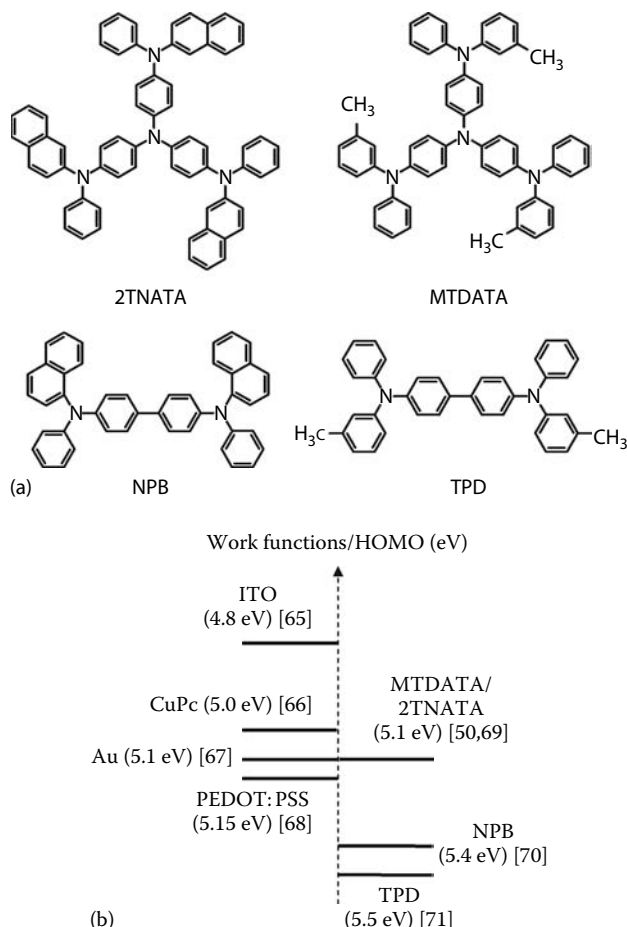
Four key PA-based compounds discussed in this chapter are shown in Figure 3.8a. Their full names are 4,4',4''-tris(*n*-(2-naphthyl)-*n*-phenylamino)-triphenylamine (2TNATA), 4,4',4''-tris(*N*-3-methylphenyl-*N*-phenylamino) triphenylamine (MTDATA), *N,N'*-diphenyl-*N,N'*-bis(1-naphthyl)(1,1'-biphenyl)-4,4'diamine (NPB), and *N,N'*-diphenyl-*N,N'*-bis(3-methylphenyl)(1,1'-biphenyl)-4,4'diamine (TPD). These four materials are widely used in the OLED industry or in the research community because they are very stable hole transporters. Generally, PA compounds possess at least an N-atom which is bound to three phenyl rings. The N-atom in a PA compound

**FIGURE 3.7**

(a) A typical plot of frequency-dependent capacitance for an organic material with ohmic injection contact. (b)  $-\Delta B$  vs  $f$  plots obtained from the plot of frequency-dependent capacitance.  $\tau_r$  is the characteristic time related to the average carrier transit time  $\tau_{1/2}$  via Equation 3.20.

acts as a site for oxidation, i.e., the location at which a hole can reside under the application of an external electric field [56]. The merits of PA compounds as HTMs are abundant. Usually, PA compounds form smooth and air-stable amorphous films by thermal evaporation [57]. Their hole-transporting (HT) capabilities are characterized by their hole mobilities ( $10^{-3}$ – $10^{-5}$  cm $^2$ /Vs) [55,58,59]. These values are at least one order of magnitude higher than the electron mobility of other common amorphous electron transporters, such as tris(8-hydroxyquinoline) aluminum ( $\text{Alq}_3$ ) and anthracene derivatives (e.g., ADN), which have electron mobilities in the range of  $10^{-7}$ – $10^{-5}$  cm $^2$ /Vs [60–62]. Although some ET materials are reported with satisfactory electron mobilities, they are often of limited use because of undesirable thermal stability or morphological properties [63,64].

Besides, hole injection capabilities of PA compounds are controlled by the positions of their HOMOs as indicated in Figure 3.8b [50,65–71]. PA

**FIGURE 3.8**

(a) Chemical structures of 2TNATA, MTDATA, NPB, and TPD. (b) Work functions and HOMO values of molecules. (From So, S.K. et al., *J. Display Technol.*, 3, 225, 2007. With permission.)

compounds with small HOMO values, e.g., MTDATA, facilitate hole injection whereas those with large HOMO values, e.g., TPD, may form hole-blocking contacts. Generally, PA compounds possess high ionization potentials that cause imperfect hole injection from ITO or metal anodes. Ideally, it is possible to use high work function metals (e.g., Pt). However, in reality, whenever high work function metals are in contact, it is very common to observe a higher hole injection barrier than expected [72]. The origin of the deviation is still controversial, but it is believed to be associated with charge redistribution in the MO interface.

For the PA compounds shown in Figure 3.8a, NPB and TPD are widely used HTMs for OLEDs [57]; 2TNATA and MTDATA are proven materials

for facilitating hole injection from ITO anode in OLEDs [50]. Several aspects of these materials are particularly noteworthy for physicists, materials scientists, and engineers. First, all PA compounds in Figure 3.8a possess desirable thermal stability and morphological properties in solid states. Second, they exhibit trap-free HT properties [55,58,59]. Third, they can be purchased in bulk quantities from multiple commercial suppliers and they can be used for measurements without additional purification. In view of these factors, we chose the PA compounds as candidates for studying fundamental mechanisms of charge transport and injection in amorphous organic solids.

---

### **3.3 Bipolar Transport in Phenylamine-Based Compounds**

In this section, we confine our discussion entirely to the charge transport in four PA-based compounds, commonly abbreviated as 2TNATA, MTDATA, NPB, and TPD. The most direct way of characterizing transport properties of an amorphous organic film is by measuring its carrier mobility. We use TOF technique and OTFT measurement to measure the carrier mobilities of the PA compounds. First, hole mobilities of the PA compounds were obtained and cross-compared by the TOF and OTFT measurements. Then, we present results of detailed studies of ET ability in two PA compounds, NPB and 2TNATA. Both of them possess surprisingly high electron mobilities as revealed by TOF measurements. We also examine the origin of the ET properties of NPB and 2TNATA in relation to the Marcus theory. A discussion of the good  $\mu_e$  in NPB and 2TNATA is presented using the concept of reorganization energy and orbital location of PA compounds.

#### **3.3.1 Sample Preparations**

For TOF measurements, the general structure was ITO/PA compounds/Al. ITO on glass was used as the substrate, which was first cleaned chemically using sequential baths of deconex, DI water, ethanol, and acetone, followed by exposure to UV-ozone for 10 min in order to remove the hydrocarbon contamination on the ITO surface [73,74]. Organic thin films were deposited inside a high vacuum evaporator. The coating rates were between 1 and 2 nm/s. The thicknesses  $d$  of the organic layers were measured *in situ* with a quartz crystal sensor. Sample thicknesses were further calibrated by a profilometer. The thicknesses were between 3 and 10  $\mu\text{m}$ . A semitransparent aluminum contact (15 nm) was coated on the top of the organic film. The sample active area was  $0.36\text{ cm}^2$ . After coating, the sample was immediately loaded inside a cryostat with a pressure less than  $10^{-3}$  torr for

temperature-dependent measurements. The temperature of the sample could be regulated between 200 and 400 K. Lower temperature resulted in delamination of the PA layer from the ITO substrate. An external resistor converted the time-dependent photocurrent into a voltage that was subsequently displayed by an oscilloscope.

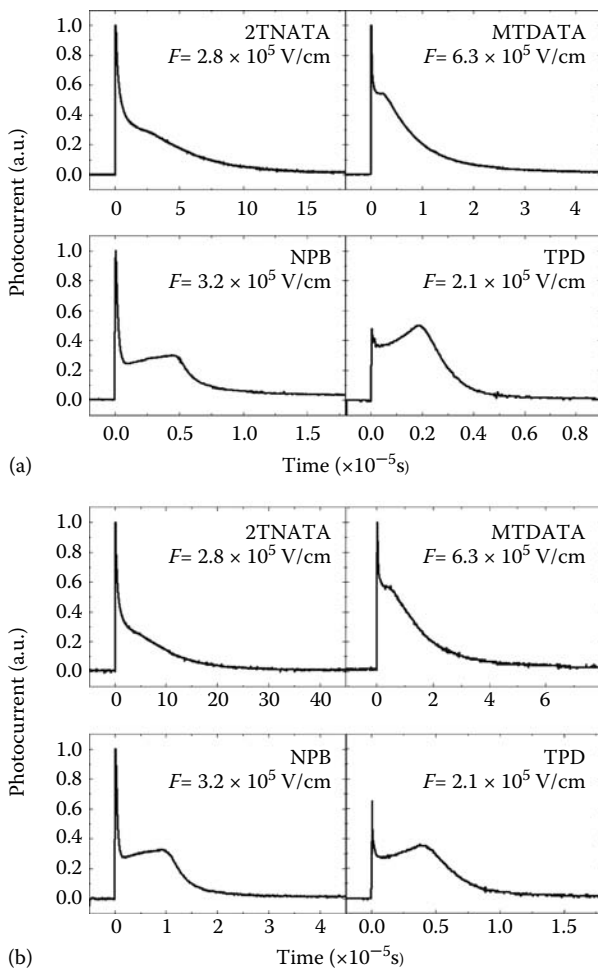
For OTFT measurement, a heavily doped p-Si wafer with an overlayer of SiO<sub>2</sub> (300 nm,  $C_i = 11 \text{ nF/cm}^2$ ) was used as the substrate. The substrate was cleaned sequentially using ethanol and acetone in ultrasonic bath, followed by an exposure to UV-ozone for 20 min [73]. During the organic film deposition, the substrate was kept at 60°C. The thickness of the organic layer was 100 nm. In the case of NPB, 20 nm of tungsten oxide ( $\text{WO}_x$ ,  $x \sim 2-3$ ) was thermally evaporated through a shadow mask on NPB before the deposition of S/D electrodes. A thin layer of transition metal oxide was demonstrated to reduce the contact resistance arising from the work function mismatch at the MO interface [75–77]. Gold was used as S/D electrodes with channel width ( $W$ ) of 9 mm and length ( $L$ ) of 50  $\mu\text{m}$ . After fabrication, the sample was immediately loaded inside a vacuum cryostat. The temperature of the sample could be regulated between 200 and 400 K. All measurements were performed in vacuum ( $< 10^{-3}$  torr).

### 3.3.2 Results and Discussion

#### 3.3.2.1 Hole Mobilities by TOF and OTFT Measurements

Figure 3.9 shows the representative TOF transients of the PA compounds at 290 and 258 K. With the exception of 2TNATA, the general features of the TOF time transients of PA films include (a) a plateau region, (b) a clear turning point at time  $t = \tau$ , and (c) a dispersion tail following  $\tau$ . Among the four PA, NPB has the most well-defined features (a)–(c). In the case of 2TNATA, the plateau region is absent, but the turning point  $\tau$  can be easily determined from a log–log plot of the TOF transient signal. Correspondingly, one can notice some deviations of the TOF transients from the ideal features. For example, in the case of TPD, feature (b) forms a cusp at room temperature (290 K), but the cusp becomes less pronounced at lower temperatures (e.g., 258 K).

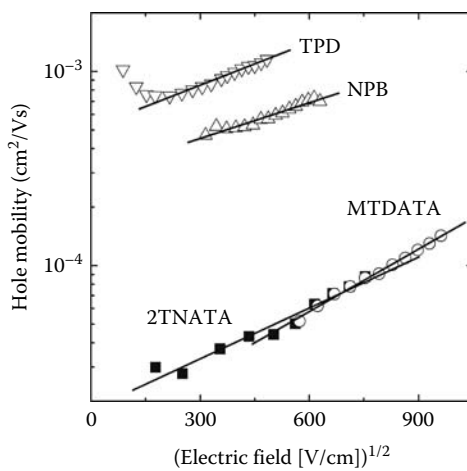
Strictly speaking,  $\tau$  measures the arrival time of the fastest carriers in TOF; it is related to  $\tau_{\text{DI}}$  by Equation 3.17. On the other hand,  $\tau_{1/2}$  can be understood as the “average” carrier transit time and is related to  $\tau_r$  by Equation 3.20. In principle, both  $\tau$  and  $\tau_{1/2}$  can be determined straightforwardly from the TOF signal. In reality, for many materials at room temperature, the determination of  $\tau_{1/2}$  is often obscured by poor signal-to-noise ratio. The PA hole transporters appear to be one of the few exceptions in which one can readily extract its  $\tau_{1/2}$  from TOF. The concurrence of two factors makes the PA to be the ideal choice for studying TOF transients. First, most PA compounds have strong optical absorption coefficient ( $\sim 10^{-5} \text{ cm}^{-1}$ ) in UV range [77]. So the optically

**FIGURE 3.9**

TOF transients for 2TNATA, MTDATA, NPB, and TPD at (a) 290 K and (b) 258 K. (From So, S.K. et al., *J. Display Technol.*, 3, 225, 2007. With permission.)

generated free carriers are abundant, resulting in large TOF signals. Second, all PA compounds are known to contain few traps [44,55,58,59]. So the plateau region, a signature of nondispersing carrier transport, is well-defined. Below, we use  $\tau$  to extract the hole mobilities of the PA compounds.

Figure 3.10 shows the hole mobilities ( $\mu_h$ ) of the PA vs the square root of the electric field ( $F$ ) at room temperature (290 K). Among the four materials, TPD has the largest  $\mu_h$  which is in the range of  $\sim 10^{-3} \text{ cm}^2/\text{Vs}$ . NPB has a slightly lower mobility in mid  $10^{-4} \text{ cm}^2/\text{Vs}$  whereas both two star-burst PA, i.e., 2TNATA and MTDATA, have almost the same but relatively low mobilities of  $10^{-5} \text{ cm}^2/\text{Vs}$ . For large  $F$ , the hole mobility  $\mu_h$  follows the PF form with  $\mu_h \sim \exp(\beta F^{1/2})$ . The PF factor  $\beta$  is a measure of the strength of the field

**FIGURE 3.10**

TOF-derived hole mobilities of 2TNATA, MTDATA, NPB, and TPD at room temperature. The solid lines are best line fits to the data points at regions at which they become linear. Note the hole mobilities of 2TNATA and MTDATA almost overlap. (From So, S.K. et al., *J. Display Technol.*, 3, 225, 2007. With permission.)

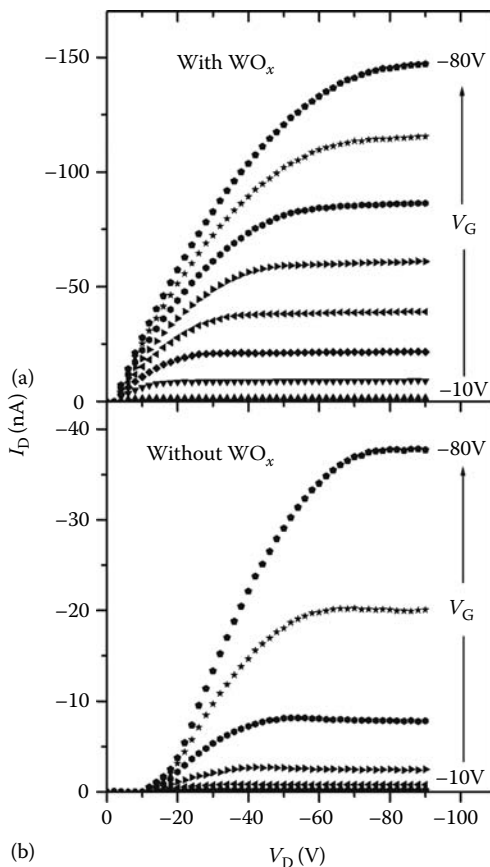
dependence of  $\mu_h$ . From Figure 3.10,  $\beta$  can be obtained by fitting a straight line to the data at the region of high electric field. Table 3.3 lists the room temperature transport parameters for the four compounds. The “zero-field mobility,”  $\mu_0$ , is obtained from the best line fit for each material (solid line) at  $F=0$  (Figure 3.10).

One of the PA compounds, NPB, is used below as an example for carrier mobility evaluation in TFT configuration. The output characteristics of NPB-based OTFTs are shown in Figure 3.11. Devices A and B are the OTFTs with and without  $\text{WO}_x$ , respectively. Both devices show typical p-type TFT characteristics. Device A shows well-defined linear and saturation regions whereas device B does not, especially when the  $V_G$  is small. From

**TABLE 3.3**

Hole-Transporting Properties of Phenylamine Compounds

Materials	Zero-Field Mobility, $\mu_0$ ( $\text{cm}^2/\text{Vs}$ )		PF Slope, $\beta$ [ $(\text{cm}/\text{V})^{1/2}$ ]	
	From $\tau$	From $\tau_{1/2}$	From $\tau$	From $\tau_{1/2}$
2TNATA	$1.6 \times 10^{-5}$	$8.7 \times 10^{-6}$	$2.2 \times 10^{-3}$	$2.9 \times 10^{-3}$
MTDATA	$1.3 \times 10^{-5}$	$1.3 \times 10^{-5}$	$2.5 \times 10^{-3}$	$2.1 \times 10^{-3}$
NPB	$3.1 \times 10^{-4}$	$2.7 \times 10^{-4}$	$1.2 \times 10^{-3}$	$1.3 \times 10^{-3}$
TPD	$4.9 \times 10^{-4}$	$4.0 \times 10^{-4}$	$1.8 \times 10^{-3}$	$1.5 \times 10^{-3}$

**FIGURE 3.11**

Typical output characteristics of a top contact OTFT with 100 nm of NPB at 290 K. The gate voltages varied in steps of  $-10\text{ V}$ , starting from  $-10\text{ V}$ . In (a), 20 nm of tungsten oxide was inserted between NPB and the top (source and drain) gold contacts. In (b), gold (source and drain) electrodes were directly in contact with NPB. The channel length ( $L$ ) and width ( $W$ ) are  $50\text{ }\mu\text{m}$  and  $9\text{ mm}$ , respectively. (From Cheung, C.H. et al., *Appl. Phys. Lett.*, 93, 083307, 2008. With permission.)

Equations 3.14 and 3.15, the FE mobilities for device A are found to be  $1.7 \times 10^{-5}$  and  $2.4 \times 10^{-5}\text{ cm}^2/\text{Vs}$  at linear and saturation regions, respectively. On the other hand, without a well-defined linear region, FE mobility for device B can only be extracted from the saturation region and is found to be  $2.7 \times 10^{-5}\text{ cm}^2/\text{Vs}$ . The threshold voltage ( $V_T$ ) for device A and B are  $-0.7$  and  $-40.7\text{ V}$ , respectively. The different shapes of output characteristics and the difference in threshold voltages suggest that the introduction of  $\text{WO}_x$  can effectively reduce the contact resistance at the Au/NPB interface.

**TABLE 3.4**

Transport Parameters of NPB and 2TNATA Evaluated by TFT and TOF Techniques

Material	Technique	Hole Mobility (cm <sup>2</sup> /Vs)	TFT Threshold Voltage (V)	Energetic Disorder (meV)	$\mu_\infty$ (cm <sup>2</sup> /Vs)
NPB	TFT with WO <sub>x</sub>	$2.4 \times 10^{-5}$ (saturation) $1.7 \times 10^{-5}$ (linear)	-0.7	84	$2.6 \times 10^{-3}$
NPB	TFT without WO <sub>x</sub>	$2.7 \times 10^{-5}$ (saturation)	-40.7	—	—
NPB	TOF	$3.0 \times 10^{-4}$	—	74	$1.4 \times 10^{-2}$
2TNATA	TFT <sup>a</sup>	$9.8 \times 10^{-7}$ (saturation)	25.2	79	$7.3 \times 10^{-5}$
2TNATA	TOF	$1.2 \times 10^{-5}$	—	70	$1.2 \times 10^{-3}$

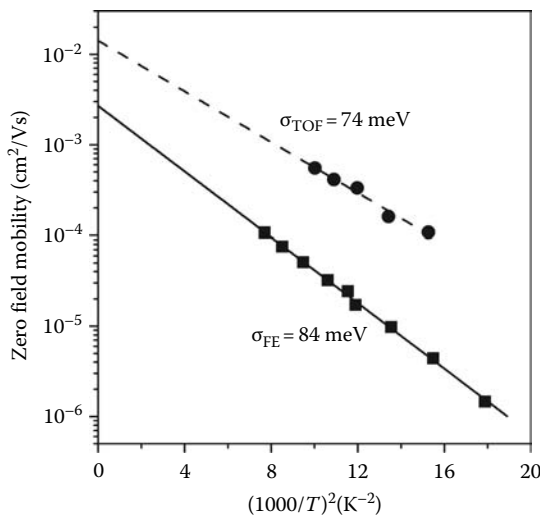
Source: Cheung, C.H. et al., *Appl. Phys. Lett.*, 93, 083307, 2008. With permission.

<sup>a</sup> Bottom contact configuration was used in 2TNATA OTFTs. Only FE mobility in saturation region can be extracted as the linear region was not well-defined.

The FE mobility is then compared with the TOF mobility. Since the FE mobility is extracted from the steady-state current, the TOF mobility derived from  $\tau_{1/2}$  is considered here. Table 3.4 shows the TOF mobility (obtained from  $\tau_{1/2}$ ) and the FE mobility of NPB. From Table 3.4, we can find that the FE mobility is about one order of magnitude smaller than the TOF mobility. Similar observations have been found from other amorphous organic materials recently [78,79].

As discussed earlier, the injected holes from the source (S) electrode are accumulated at the organic layer adjacent to the gate dielectric under the influence of  $V_G$ . The holes transport to the drain (D) electrode by hopping just above and parallel to the gate dielectric surface under the influence of  $V_D$ . Therefore, any changes in the organic layer caused by the presence of gate dielectric layer should affect the carrier mobility. The increase in the energetic disorder of an organic material in the neighborhood of a polar gate dielectric was observed by Veres et al. [79]. The polar groups in the dielectric are randomly oriented near the active interface, resulting in an additional fluctuation of local electrostatic field. This broadens the density of states (DOS) of the organic material, resulting in an increase in the energetic disorder and a decrease in the FE mobility.

In order to check if the energetic disorder is modified, we performed temperature-dependent measurements on the OTFT. The temperature-dependent FE mobilities were then analyzed by the GDM [27]. According to Equation 3.6, the second exponential term approaches 1 at low field ( $F \rightarrow 0$ ), and thus,  $\mu(0,T) \sim \exp[-4/9(\sigma/kT)^2]$ . Therefore, a semilog plot of low-field mobilities vs.  $1/T^2$  should yield a straight line. The slope of this line can be used to

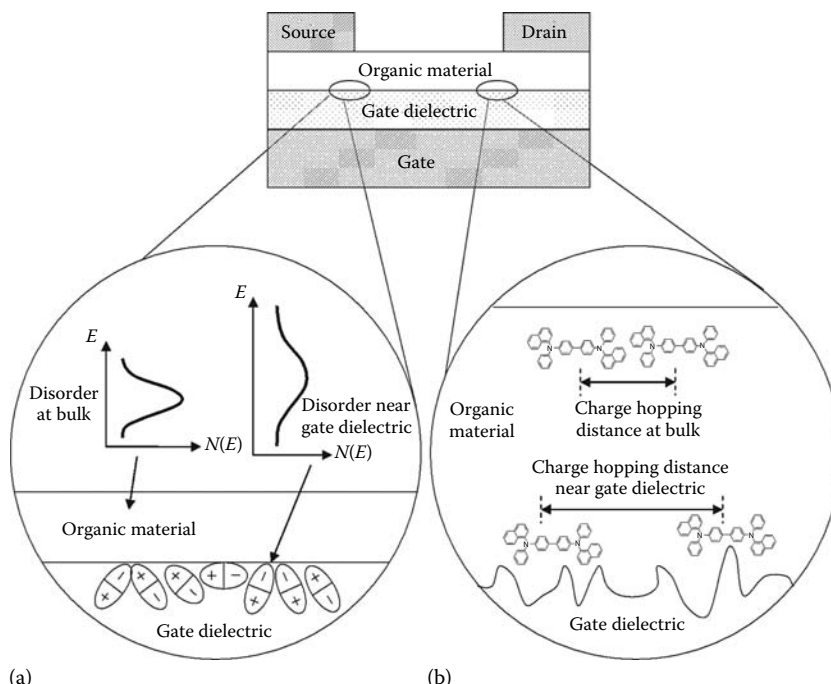
**FIGURE 3.12**

Low field FE mobilities from TFT, and zero-field mobilities (obtained from  $\tau_{1/2}$ ) from TOF against  $1/T^2$  for NPB. The solid and dashed lines are the best fits to TFT and TOF data, respectively. (From Cheung, C.H. et al., *Appl. Phys. Lett.*, 93, 083307, 2008. With permission.)

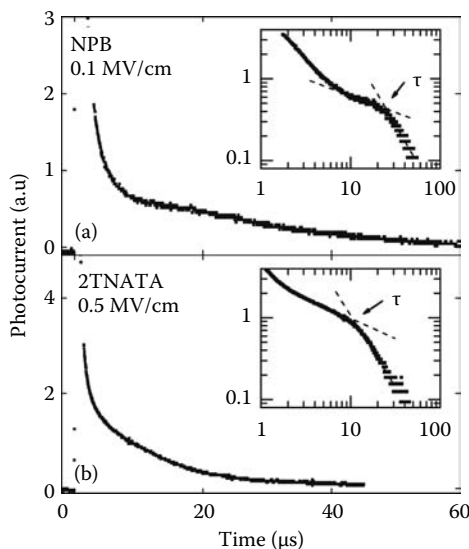
extract  $\sigma$ . With this concept, we extracted the FE mobilities extracted in low field region, i.e., the linear region in Figure 3.11a by using Equation 3.14 and plotted against  $1/T^2$ . The results are shown in Figure 3.12 as solid squares. The solid line is the best fit to the TFT data. The extracted  $\sigma$  for NPB in an OTFT is 84 meV. The energetic disorder of NPB from TOF technique can also be extracted by the same method. In this case, we extracted the zero-field mobilities from the plot of  $\mu_{\text{TOF}}$  vs.  $F^{1/2}$  at different temperatures. The zero-field mobilities were then plotted against  $1/T^2$ . The results are shown as solid circles in Figure 3.12. The dashed line is the best fit to the TOF data. From the slope of the dashed line, we deduce an energetic disorder parameter of 74 meV. The observation of higher energetic disorder from TFT is consistent with the work of Veres et al. [79]. They suggested that the polar dielectric can modify the energetic disorder of an organic material in a TFT configuration. Besides NPB, similar experiments were performed on another PA compound, 2TNATA. The results are summarized in Table 3.4 [44]. The extracted FE mobility of 2TNATA is  $9.8 \times 10^{-7} \text{ cm}^2/\text{Vs}$ , which is about one order of magnitude smaller than the TOF mobility ( $\mu_{\text{TOF}} \sim 1.2 \times 10^{-5} \text{ cm}^2/\text{Vs}$ ). In this case, the extracted energetic disorder from TFT is also larger than that from TOF, by about ~10 meV. The results from 2TNATA are consistent to those from NPB.

Apart from the energetic disorder, the temperature-dependent measurements can also be used to extract  $\mu_\infty$  (Equation 3.6). It is the high temperature

limit of mobility and can be regarded as the mobility of charge carriers in the absence of energetic disorder. The parameter can be found by obtaining the  $y$ -intercept of line of the best fit to the mobility data in Figure 3.12. The extracted  $\mu_{\infty}$  from TFT and TOF are shown in Table 3.4. Both NPB and 2TNATA show smaller  $\mu_{\infty}$  from TFT when compared with TOF. The mismatch of  $\mu_{\infty}$  suggests that the energetic disorder of the organic material was indeed modified by the presence of gate dielectric, but it is unlikely to be the only interface mechanism affecting the FE mobility. Morphological changes of active materials by the surface roughness of gate dielectric was reported to be a factor of lowering the FE mobility [80,81]. Gate dielectrics with rough surfaces would result in significant difference in the morphology of active material near the surface, when compared to that of bulk. This is likely another factor of the discrepancy between TOF and TFT, as TOF is measuring the carrier mobility at the bulk, while TFT measures the carrier mobility at the conducting channel forming at a thin layer of active material adjacent to the gate dielectric. Figure 3.13 shows a schematic diagram of the two possible factors causing the discrepancy between TFT and TOF mobilities.

**FIGURE 3.13**

Schematic diagram depicting the factors causing the discrepancy between TFT and TOF mobilities. In (a), DOS of the organic material is broadened by the polar insulator surface. In (b), the surface roughness of gate dielectric may affect charge hopping distances.

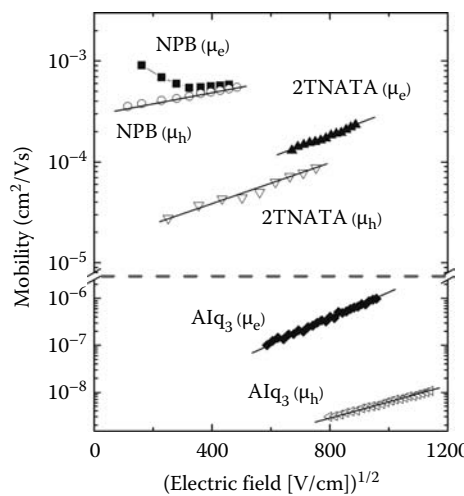
**FIGURE 3.14**

Electron TOF transients for (a) NPB and (b) 2TNATA under applied field strengths of 0.1 and 0.5 MV/cm, respectively. The samples have structures of Al (15 nm)/NPB (15.3  $\mu$ m)/ITO and Al (15 nm)/2TNATA (7.1  $\mu$ m)/ITO. The inset in each plot is a log–log plot from which the carrier arrival time ( $\tau$ ) is determined. (From Tse, S.C. et al., *Appl. Phys. Lett.*, 89, 262102, 2006. With permission.)

### 3.3.2.2 Electron Mobilities in Two Phenylamine-Based Compounds

Figure 3.14 shows an electron TOF signal of NPB and 2TNATA taken at room temperature under an external electric field  $F$ . For NPB samples, the photocurrents exhibit an initial spike, a plateau region, and then a gradual decay characteristic of classic nondispersive carrier transport commonly observed in amorphous organic charge transporters. The arrival time  $\tau$  can be determined directly from the TOF transient itself or a log–log plot as indicated in the inset of figures. For 2TNATA samples, the plateau region in the TOF transient is not as obvious as those of NPB. Yet, the carrier arrival time still can be determined from a log–log plot as shown in the insets of the figures. From  $\tau$ , the carrier mobilities can be determined by Equation 3.12.

Figure 3.15 summarizes the field dependence of the electron and hole mobilities of NPB and 2TNATA at room temperature. Except for the electron mobility of NPB, the hole mobility of NPB and the mobilities of 2TNATA follow the PF form,  $\mu = \mu_0 \exp(\beta\sqrt{F})$ , where  $\beta$  is the PF slope and  $\mu_0$  is the zero-field mobility. Generally, the values of the hole mobility of NPB are between  $3 \times 10^{-4}$  and  $6 \times 10^{-4}$  cm $^2$ /Vs, and in excellent agreement with previous reports [59]. On the other hand, the dependence of  $\mu_e$  exhibits a negative field dependence when  $F < 0.1$  MV/cm. In between a field strength of

**FIGURE 3.15**

Field-dependent mobilities of NPB, 2TNATA, and Alq<sub>3</sub> at 290K. The closed (■) and opened (□) symbols represent the electron and hole mobilities, respectively. The Alq<sub>3</sub> data was taken from Refs. [82,83]. (From Tse, S.C. et al., *Appl. Phys. Lett.*, 89, 262102, 2006. With permission.)

$0.1 < F < 0.25 \text{ MV/cm}$ ,  $\mu_e$  has a value between  $5 \times 10^{-4}$  and  $6 \times 10^{-4} \text{ cm}^2/\text{Vs}$ . Compared to NPB, 2TNATA exhibits lower electron and hole mobilities. For 2TNATA, the values of  $\mu_e$  are in the range  $1\text{--}3 \times 10^{-4} \text{ cm}^2/\text{Vs}$  for  $F$  between 0.4 and 0.8 MV/cm, and the values of  $\mu_h$  are in the range  $2\text{--}9 \times 10^{-5}$  for  $F$  between 0.04 and 0.6 MV/cm. For reference purpose, the electron and hole mobilities of a common electron transporter, Alq<sub>3</sub>, are also shown in Figure 3.15 [82,83]. Clearly, PA-based compounds are superior charge transporters in comparison to Alq<sub>3</sub>.

From Figure 3.15, it is interesting to note that  $\mu_e$  of NPB has a negative field dependence at low electric field. For hopping conduction, the carriers transport through the organic layer either in two classes of routes: a direct path that is along the electric field, and a longer indirect path that is against the electric field [27]. Under weak electric field, the carrier prefers to take the longer route which is faster due to the better wavefunction overlap between the hopping sites. Eventually, the electric field tends to eliminate such paths. This effect may lead to the decreasing electron mobility of NPB in low field region.

### 3.3.2.3 Microscopic Explanation

The electron transport capabilities in NPB and 2TNATA can be examined by the hopping model. Generally, transport of electrons and holes can

**TABLE 3.5**

Reorganization Energies  $\lambda_+$  and  $\lambda_-$  Calculated by the Density Functional Theory

Materials	Reorganization Energy for Hole $\lambda_+$ (eV)	Reorganization Energy for Electron $\lambda_-$ (eV)	$(k_+/k_-)^a$
NPB	0.29	0.19	0.31
TPD	0.28	0.56	21

Source: Lin, B.C. et al., *J. Phys. Chem., A* 107, 5241, 2003.

<sup>a</sup>  $(k_+/k_-)$  is the ratio hopping rate of hole to electron calculated for  $T = 300\text{ K}$ , neglecting differences in the charge-transfer integral  $V_{ab}$ .

be viewed as a hopping process, which occurs in the organic LUMO or HOMO, respectively. Thus, it is expected that the electron (hole) mobility should be dependent on the electron (hole) hopping rate in the LUMO (HOMO). So the electron to hole mobility ratio can be estimated if both carrier hopping rates can be computed. Marcus theory of electron transfer provides a semiempirical means of computing charge hopping rate in organic molecules [17]. In this approach, the charge hopping rate is controlled by two factors: the reorganization energy  $\lambda$  and the charge-transfer integral  $V_{ab}$ .

The hopping rates of holes and electrons in TPD and NPB have been estimated using the relevant reorganization energies as shown in Table 3.5 [20]. Results for TPD and NPB are quite different. For NPB, the ratio of hole to electron hopping rate is 0.31 at 300 K, suggesting that NPB should have stronger electron-conducting capability than hole. On the other hand, the ratio for TPD is 21, suggesting that TPD has much stronger hole-conducting capability than electron. The computational results are in good agreement with our experimental results in low field region (Figure 3.15).

Besides the reorganization energy factor, the charge-transfer integrals provide additional insights showing that NPB and 2TNATA have excellent electron conducting behaviors. Figure 3.16 shows a schematic diagram depicting the frontier orbitals of TPD and NPB. From density functional theory (DFT) calculations, the HOMO in both TPD and NPB are localized on the biphenyl moiety near the center of the molecule [20]. On the other hand, the LUMO in TPD are more concentrated on the center of the molecule and that increases the electron hopping distance. Thus, the absence of electron transport in TPD can be attributed to a smaller charge-transfer integral [84]. For NPB, however, the LUMO is associated with the naphthyl moiety located at both ends of the molecule. The intermolecular electron transfer between two adjacent NPB molecules would be easier when compared to those of TPD. The presence of the naphthyl groups is therefore responsible for the high electron mobility of NPB and 2TNATA. This explanation can be extended to all PA compounds.

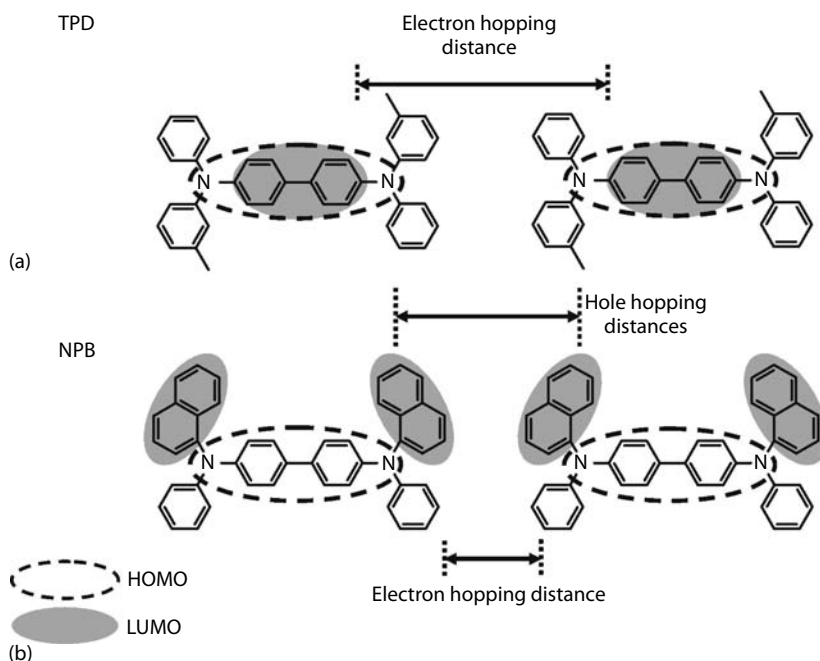


**FIGURE 3.16**  
Schematic diagram depicting the frontier orbitals of (a) TPD and (b) NPB.

### 3.3.3 Conclusion

The charge transport abilities of four PA-based compounds, 2TNATA, MTDATA, NPB, and TPD, are studied by TOF technique, OTFT measurement, and microscopic hopping model. To characterize the HT capabilities of the PA compounds, their hole mobilities were obtained and cross-compared by both TOF and OTFT measurements. We find that for both NPB and 2TNATA, the FE mobilities are one order of magnitude smaller than the TOF mobilities. Under the analysis with GDM, the energetic disorder and the  $\mu_{\infty}$  of these materials are modified by the presence of gate dielectric in TFT configuration. Besides, for the ET properties in PA compounds, we find that both NPB and 2TNATA possess significant electron mobilities of  $6\text{--}9 \times 10^{-4} \text{ cm}^2/\text{Vs}$  and  $1\text{--}3 \times 10^{-4} \text{ cm}^2/\text{Vs}$ , respectively, under an applied electric field of  $0.04\text{--}0.8 \text{ MV/cm}$ . The experimental results are consistent with the electron transport estimation in NPB by the reorganization energy and the LUMO location calculated from DFT. The LUMOs are localized on the naphthyl moieties at both ends of molecule. So the intermolecular electron transfer between two adjacent molecules would be easy, resulting in the high electron mobility of NPB and 2TNATA. This explanation can be extended to all naphthylamine-based compounds.

---

### 3.4 Nearly Ohmic Hole Injection in Phenylamine-Based Compounds

Following the discussion on charge transport in PA compounds, we extend our discussion to the problem of hole injection into PA compounds. Below, we use the zero-field mobilities and the PF slopes from TOF measurements to compute the theoretical space-charge-limited current ( $J_{SCL}$ ) of three PA compounds, MTDATA, NPB, and TPD. Then, we measure JV characteristics of NPB with different hole injection materials and compare them to the theoretical  $J_{SCL}$ . We find that poly(3,4-ethylenedioxythiophene)/polystrenesulfonic acid (PEDOT:PSS) can form nearly ohmic contact with NPB. Employing PEDOT:PSS as the anode, MTDATA and TPD also exhibit a bulk-limited hole current. It implies that PEDOT:PSS can behave effectively as quasiohmic contact. Analogous results are further discovered by DISCLC and AS measurements. Meanwhile, from DISCLC and AS, the hole mobilities of the PA compounds are measured and are in good agreement with those obtained independently from TOF. Finally, a discussion on the hole injection mechanism using PEDOT:PSS anode is presented. The hole injection efficiencies for three PA compounds and PEDOT:PSS are found and correlated with the energy barrier heights.

To study hole injection to PA compounds, we employ PEDOT:PSS as the hole injecting anode. PEDOT:PSS is a well-known hole-injecting material in polymer-based light-emitting diodes (PLEDs). With a high work function of about 5.15 eV (Figure 3.8b), PEDOT:PSS was shown to provide an ohmic contact to PFMO [85]. More recently, PEDOT:PSS was reported to form an efficient hole injection to NPB because of its special surface electronic structure [35]. The key factor may be related to the insulating PSS layer near the interface, which reduces the interaction between the doped PEDOT and NPB [86].

#### 3.4.1 Sample Preparations

A typical sample structure for JV, DISCLC, and AS measurements comprised of an organic thin film sandwiched between two electrodes. The bottom anode was a patterned layer of ITO on glass. The ITO substrates were first cleaned chemically using sequential baths of deconex, DI water, ethanol, and acetone, followed by exposure to UV-ozone for 10 min [73,74]. PEDOT:PSS solution, obtained from H.C. Starks GmbH (BAYRON PVP A1 4083; OLED grade), was filtered by 0.45 and 0.2  $\mu\text{m}$  PVDF filters. The solution was then spun onto a UV-treated ITO for 180 s at 1000 rpm. Afterwards, the film was annealed in air at 150°C for 30 min to drive out residual water. The resulting polymer film is ~50 nm thick. Subsequently, the organic film and a Ag cathode were thermally evaporated on the top of the PEDOT:PSS under a base pressure of 10<sup>-6</sup> torr. The coating rate was fixed at 1 nm/s. The general sample structure was ITO/PEDOT:PSS/PA compounds ( $d \mu\text{m}$ )/Ag (100 nm), where Ag behaves as the hole-collecting and electron-blocking cathode. The thicknesses  $d$  of

MTDATA, NPB, and TPD samples were 0.76, 4.11, and  $5.13\mu\text{m}$ , respectively. After coating, the samples were immediately loaded inside a vacuum cryostat with a pressure less than  $10^{-3}$  torr for JV, DISCLC, and AS measurements.

### 3.4.2 Results and Discussion

#### 3.4.2.1 JV Characteristics for NPB with Different Anodes

Knowing the zero-field mobility  $\mu_0$  and PF slope  $\beta$  of each PA compound shown in Table 3.3, one can predict the theoretical space-charge-limited current ( $J_{\text{SCL}}$ ) from Equation 3.16. Based on these theoretical  $J_{\text{SCL}}$ , we tried to study the effects of different hole injection materials into PA compounds. Among the hole transporters we are investigating, MTDATA has the highest-lying HOMO level and forms ohmic injection with ITO anode [55]. However, NPB is the most relevant in OLED technology and more thermally stable material. So, it was used as a reference hole transporter to examine how hole-injecting materials affect the JV characteristic. The hole-injecting materials adopted are ITO, CuPc, Au, and PEDOT:PSS. The four contacts are of general importance because they represent conducting oxide, organic buffer layers, noble metals and conducting polymeric electrodes, all of which are used in device applications. Their nominal work functions are shown in Figure 3.8b. Figure 3.17 shows the JV data for devices having the structure ITO/HIL/NPB/Ag, where HIL=hole injection layer can be ITO, CuPc, Au, or PEDOT:PSS. The solid line, which acts as an upper bound for the experimental current density, is the computed  $J_{\text{SCL}}$  of NPB using Equation 3.16. Clearly, with the exception when HIL=PEDOT:PSS at high voltages, all devices operate well below the solid line, i.e., the condition of SCLC under the condition of ohmic contact. As NPB is

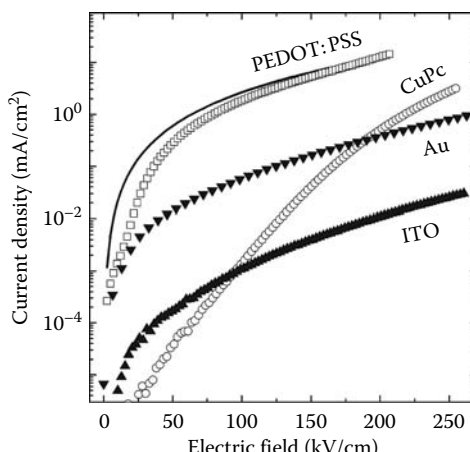


**FIGURE 3.17**

Current-voltage characteristics of ITO/HIL/NPB/Ag devices using different HIL materials. The HIL are ITO, Au, CuPc, and PEDOT:PSS. The solid line is the theoretical trap-free SCLC of NPB. (From Tse, S.C. et al., *J. Appl. Phys.*, 100, 063708, 2006. With permission.)

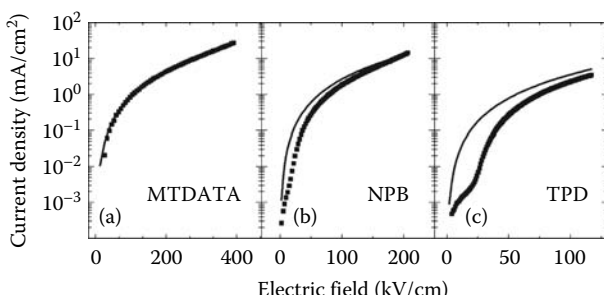
trap-free for hole transports, the results indicate that among the HI materials, only PEDOT:PSS can form nearly ohmic contact with NPB.

### **3.4.2.2 Using PEDOT:PSS as Hole Injection Anode for Phenylamine-Based Compounds**

Apart from NPB, we attempted to use PEDOT:PSS to act as the hole injection layer for MTDATA and TPD. Figure 3.18 summarizes the corresponding theoretical  $J_{SCL}$  for MTDATA, NPB, and TPD. The symbols in each panel were the measured JV characteristics, using PEDOT:PSS as the hole-injecting anode and Ag as an electron-blocking cathode. For MTDATA, the fit almost overlaps with the measured JV data in the entire range of applied voltage, indicating that PEDOT:PSS indeed forms an ohmic contact to MTDATA, and that hole conduction in MTDATA is trap-free. For NPB, the theoretical fit and the experimental data agree very well for about  $F > 100 \text{ kV/cm}$ . Beyond this field, conduction is trap-free and nearly space-charge-limited, and is dominated by bulk conduction of holes. In the case of TPD, the experimental data deviates substantially from the theoretical fit at the low field region. It appears that a more substantial hole injection barrier (Figure 3.8b) is present between PEDOT:PSS and the HOMO of TPD. The barrier limits the injection of holes from the polymeric anode into TPD and results in a current well below the theoretical JV curve.

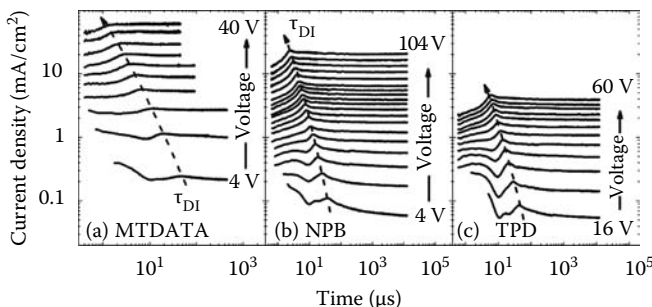
### **3.4.2.3 DISCLC Measurement for Phenylamine-Based Compounds**

To demonstrate that PEDOT:PSS can behave effectively as a quasiohmic contact, analogous DISCLC measurements were carried out for same samples in JV measurements. Figure 3.19 shows log-log plots of sequences of DI transients for MTDATA, NPB, and TPD at progressively higher bias voltages in room temperature. Due to the quasiohmic injection from PEDOT:PSS, all DI transient signals generally exhibit ideal behaviors as characterized in Figure 3.6.

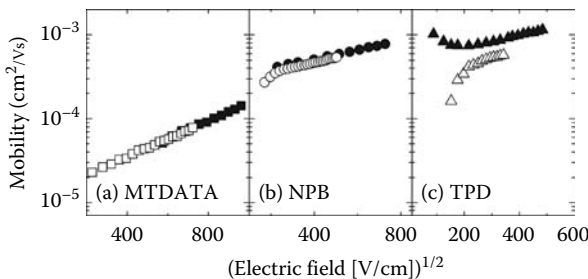


**FIGURE 3.18**

Current-voltage characteristics of ITO/PEDOT:PSS/PA compound/Ag devices, where PA compound is (a) MTDATA, (b) NPB, or (c) TPD. Solid lines are fits to the experimental JV using SCLC theory. (From Tse, S.C. et al., *J. Appl. Phys.*, 100, 063708, 2006. With permission.)

**FIGURE 3.19**

A sequence of DI signals of (a) MTDATA, (b) NPB, and (c) TPD derived from a sample structure of PEDOT:PSS/phenylamine/Ag under different applied voltages. The applied voltage varied in steps of 4V. The film thicknesses for MTDATA, NPB, and TPD were 0.76, 4.11, and 5.13  $\mu\text{m}$ , respectively. (From Tse, S.C. et al., *Proc. SPIE*, 6333, 63331P, 2006. With permission.)

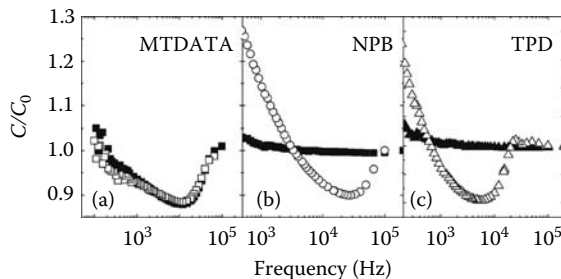
**FIGURE 3.20**

Field-dependent hole mobilities of (a) MTDATA, (b) NPB, or (c) TPD at 290 K. The closed (■) and open (□) symbols represent the data obtained by TOF and DISCLC, respectively. (From Tse, S.C. et al., *J. Appl. Phys.*, 100, 063708, 2006. With permission.)

In each case, the DI signal reaches a peak at a well-defined time,  $\tau_{\text{DI}}$ , and settles down to a steady-state value after a long time. The DI transients grow progressively as the applied voltage increases. Simultaneously, a gradual reduction in  $\tau_{\text{DI}}$  was also observed for all PA transporters. From Figure 3.19 and Equation 3.18, one can extract the hole transit time and hence the hole mobilities alone. The results are shown as open symbols in Figure 3.20. For MTDATA and NPB, hole mobilities derived from DI experiments are in excellent agreement with those deduced independently from TOF (solid symbols). However, for TPD, there are substantial differences between the hole mobilities derived from DI and from TOF, especially when the applied field is small. Clearly, for TPD, the DI-derived hole mobility underestimates the true mobility.

#### 3.4.2.4 Admittance Spectroscopy for Phenylamine-Based Compounds

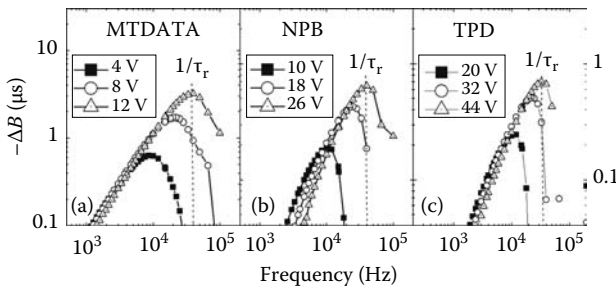
Besides JV and DISCLC, AS measurement can also be used to probe the contact conditions between PDEDOT:PSS and PA compounds. Figure 3.21

**FIGURE 3.21**

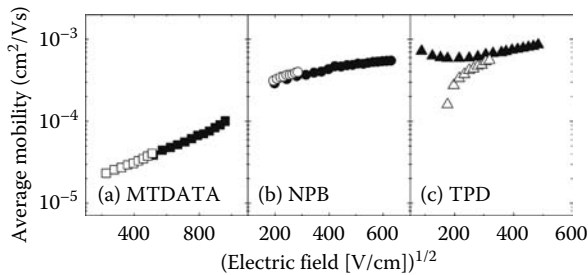
Experimentally determined frequency-dependent capacitances of (a) MTDATA, (b) NPB, and (c) TPD from a sample structure of ITO/HIL/phenylamine/Ag. The HIL are ITO and PEDOT:PSS, represented in closed (■) and open (□) symbols, respectively. The applied field strengths  $F$  were (a) 0.14, (b) 0.07, and (c) 0.04 MV/cm, respectively.

shows the frequency-dependent capacitances of the same samples in JV and DI measurements. In order to give a fair comparison, the same voltage bias  $V_{dc}$  is used and the measured capacitance  $C$  is normalized by the geometrical capacitance  $C_0 = \epsilon A/d$  of each device. In the case of *m*-MTDATA devices, the general frequency-dependent capacitances (Figure 3.21a) are almost identical for both the ITO anode and the PEDOT:PSS anode. The normalized capacitances  $C/C_0$  go through a minimum at an intermediate frequency; at high frequencies, the capacitances reach their geometrical values. On the other hand, for NPB and TPD, there are drastic differences between the samples with PEDOT:PSS anode and the one with ITO anode. A well-defined minimum can be observed in the capacitance only when PEDOT:PSS is used as the anode. This feature cannot be found in the device with an ITO anode. In the latter case, the capacitance is practically bias independent for  $f > 10^4$  Hz. The appearance of the well-defined minimum indicates that PEDOT:PSS achieve nearly ohmic hole injection contacts to PA compounds.

From AS measurements, the average hole mobilities  $\mu_{ave}$  of MTDATA, NPB, and TPD were also extracted by plotting  $-\Delta B$  vs.  $f$  and from  $\Delta B \equiv \omega(C - C_0)$ . Figure 3.22 shows the  $-\Delta B$  vs.  $f$  plots of MTDATA, NPB, and TPD. For each applied voltage ( $V$ ), there exists a maximum at a well-defined frequency  $f_r$ . This maximum shifts to higher frequency as  $V$  increases. Therefore, the location of the relaxation peak  $\tau_r^{-1} \equiv f_r$  for each  $V$  can be clearly resolved. From Figure 3.22 and Equation 3.21, one can extract the characteristic time  $\tau_r$  and hence the hole mobilities alone. The results are summarized as open symbols in Figure 3.23. The solid symbols are average hole mobilities derived by TOF at  $\tau_{1/2}$ , the time that the current has dropped to half of its value in the plateau region. In both Figure 3.23a and b, the mobilities of MTDATA and NPB extracted by AS are in excellent agreement with those obtained independently from TOF. However, in the case of TPD, there are substantial

**FIGURE 3.22**

Negative differential susceptances  $-\Delta B$  of (a) MTDATA, (b) NPB, and (c) TPD derived from measured frequency-dependent capacitance data at different voltage biases.

**FIGURE 3.23**

Field-dependent average hole mobilities of (a) MTDATA, (b) NPB, and (c) TPD at 290K. The closed (■) and open (□) symbols represent the data obtained by TOF and AS, respectively.

differences between the hole mobilities derived from AS and from TOF at the low field region. For TPD, similar to the result in DI-experiment, the AS-derived hole mobility underestimates the true mobility.

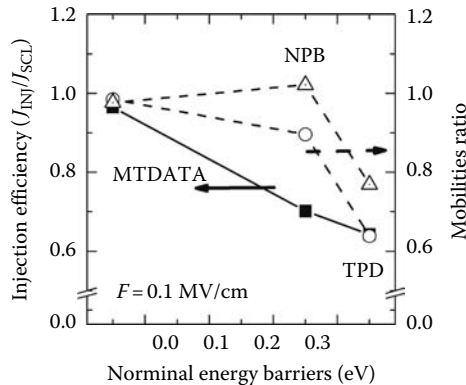
### 3.4.2.5 Mechanism of Hole Injection Using PEDOT:PSS Anode

The above experimental observations can be interpreted from numerical studies that dealt with the problem of charge injection from metal into organic charge transporters [87,88]. When the injection barrier height is lower than  $\sim 0.3$  eV, the MO interface can maintain ohmic contact as the contact is capable of supplying the bulk of organic layer with  $J_{\text{SCL}}$ . However, when the barrier height increases after the crossover value of 0.3 eV, the steady-state current of the organic layer decreases dramatically from  $J_{\text{SCL}}$ . Meanwhile, the shape of DISCLC transient deviates from the ideal case and the AS signal deviates from the ideal feature. As a result, the characteristic time  $\tau_{\text{DI}}$  and  $\tau_r$  shift to longer time and the mobility is underestimated.

According to the energy diagram in Figure 3.8b, the work function ( $\Phi_m$ ) of ITO is about 4.8 eV. So, when the ITO anode is in contact with NPB, the hole injection barrier is, to a reasonable approximation, given by the energy difference between the HOMO level of NPB and the work function of ITO. Viewed in this manner, one expects that the hole injection barrier of the ITO/NPB interface is at least 0.6 eV. So, the contact of ITO/NPB is clearly Schottky in nature and the JV curve is injection-limited. For Au and CuPc, if the Mott–Gurney rule of simple vacuum level alignment were correct, the hole injection barrier should be similar and have values of about 0.3 eV [35]. According to Ref. [87], they should also form quasiohmic contacts to NPB and hence sustain a  $J_{SCL}$ . However, both Au and CuPc contacts clearly operate below  $J_{SCL}$ . CuPc is the worst, especially at the low field region. For the contact of Au, the JV curve is an order of magnitude below the computed  $J_{SCL}$ . This deviation can be attributed to the dipole layer at the Au/NPB interface. The existence of such a dipole layer was demonstrated unambiguously by UPS [70]. The net result is an enlarged hole injection barrier of 1.4 eV. Using this as a reference value, the hole injection barrier of ITO and CuPc to NPB could be even larger.

The same concept can be applied to the PEDOT:PSS anode with PA compounds. However, in these cases, recent spectroscopic studies showed that the interface dipole does not have a significant effect on the contact of PEDOT:PSS and PA compounds [89,90]. Therefore, with  $\Phi_m=5.15$  eV (Figure 3.8b), PEDOT:PSS should obviously form an ohmic contact with MTDATA, and Schottky contacts with NPB and TPD with hole injection barrier of about 0.25 and 0.35 eV, respectively. Viewed in this manner, our JV, DISCLC, and AS experimental results are entirely consistent with the reported numerical simulations. If the crossover value is ~0.3 eV, then the NPB interface with PEDOT:PSS can be treated as ohmic although technically a finite energy barrier does exist between PEDOT:PSS and NPB. On the other hand, the hole injection barrier height  $\phi_h$  at the PEDOT:PSS/TPD interface is about 0.35 eV, which is 0.1 eV higher than the case of NPB. And this hole injection barrier height 0.35 eV is just in the neighborhood of the crossover value of 0.3 eV required for sustaining  $J_{SCL}$ . From Ref. [87], the steady-state current is deduced to around 70% of  $J_{SCL}$  for  $\phi_h=0.35$  eV. So, we observe deviations of the JV characteristics from the ideal  $J_{SCL}$  (Figure 3.18c). Furthermore, for TPD, the nominal hole mobilities extracted from DI and AS results are lower than those extracted from TOF (Figures 3.20c and 3.23c). The deviations from ohmic behaviors are reduced as the applied voltage increases because the barrier height is lowered simultaneously.

Detailed comments are deserved for the JV characteristics of different contact combinations. When the contacts are nonohmic, we note that the JV curves depart from the ideal  $J_{SCL}$ . The experimentally determined hole current is injection-limited. At a particular electric field, the measured peak current density can be denoted by  $J_{INJ}$  whereas the corresponding

**FIGURE 3.24**

Hole injection efficiencies ( $J_{\text{INJ}}/J_{\text{SCL}}$ ) and mobilities ratios in different energy barriers between phenylamine and PEDOT:PSS. The open circles (O) and triangles ( $\Delta$ ) represent the ratios of mobility values from DISCLC ( $\mu_{\text{DI}}/\mu$ ) and AS ( $\mu_{\text{AS}}/\mu_{\text{ave}}$ ), respectively.

space-charge-limited current is  $J_{\text{SCL}}$ . So, one natural way of evaluating the hole injection efficiency,  $\eta$ , is to compute the ratio [71]:

$$\eta = J_{\text{INJ}}/J_{\text{SCL}} \quad (3.22)$$

Hence,  $\eta$  is equal to 1 if the hole injection efficiency is 100%, and the contact can be viewed as truly ohmic. On the other hand,  $\eta$  should be less than 1 if the contact is Schottky. Figure 3.24 shows  $\eta$  (solid squares) vs the nominal hole injection barrier at a field strength  $F=0.1 \text{ MV/cm}$ . The open circles are the ratios of mobilities derived from DI experiments  $\mu_{\text{DI}}$  to the TOF-derived hole mobilities  $\mu$ . Moreover, the open triangles are ratios of AS-derived mobilities  $\mu_{\text{AS}}$  to the average hole mobilities derived from TOF  $\mu_{\text{ave}}$ . For the ohmic contact of PEDOT:PSS/MTDATA,  $\eta \approx 1$  and the hole injection approaches an efficiency of nearly 100%. Meanwhile, the injection efficiency for NPB is lowered to about 70%, but the nominal hole mobilities derived from DI and AS reach 90% and 100% of the TOF-derived mobility value respectively. For the contact of TPD, the injection efficiency and the nominal hole mobilities are less than 80%. Therefore, PEDOT:PSS forms the worst contact with TPD among those PA compounds.

### 3.4.3 Conclusion

The hole injection properties of PA-based compounds were investigated and cross-compared by JV, DISCLC, and AS measurements. We demonstrate that PEDOT:PSS can act as an excellent hole injection material for PA compounds

that possess high ionization potentials. Using PEDOT:PSS as the hole-injecting anode, the *JV* characteristics exhibited ohmic behavior for MTDATA, and quasiohmic behavior for NPB and TPD. Those quasiohmic injections were accounted for the formation of PSS layer on the PEDOT surface.

Applications of PEDOT:PSS anode in DI experiments reveal current transients with a cusp in all PA compounds. Meanwhile, a well-defined minimum can be observed from the plot of frequency-dependent capacitance in AS measurement. Thus, the results from DISCLC and AS are entirely consistent with the *JV* results, which by themselves indicate that the contact between PEDOT:PSS and PA compounds is very close to ohmic. The hole mobilities of MTDATA, NPB, and TPD could also be determined from DISCLC and AS techniques. Those mobilities are in good agreement with the TOF measurement. In addition, both injection efficiency ( $\eta$ ) and mobilities ratio are reduced due to the injection barrier increase, and indicate that the hole current of TPD still exhibits the injection-limited behavior.

---

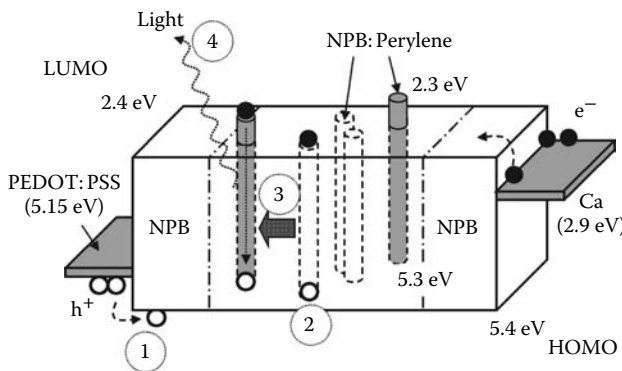
### 3.5 Devices Application

In principle, an organic electronic molecule can be designed in a way that it can encompass all essential attributes for the optimization of OLED performance. These attributes are ET, HT, and light-emitting capabilities. In this way, the multifunctional compound can be used to fabricate a single-layer OLEDs with simple device architecture. Such simplified configuration is industrially favorable because the production steps can be reduced. Thus, there are many attempts to fabricate a single-layer device, in which the active organic material is capable of acting simultaneously as the HT, ET, and light-emitting units [91–95].

To achieve efficient and long-lived single-layer devices, the active materials should satisfy a few additional requirements: (1) desirable thermal stability and morphological properties in solid state, (2) satisfactory mobilities of both electrons and holes, and (3) appropriate energy levels for the HOMO and the LUMO. Below, we demonstrate that a single-layer OLED can be fabricated from NPB, a well-recognized PA hole transporter with good film forming and thermal stability. In the forgoing session, NPB was shown to exhibit an ambipolar-transporting ability by TOF measurements. In addition, NPB has the appropriate HOMO and LUMO of about 5.4 and 2.4 eV, respectively. Thus, it is expected that NPB can form appreciable charge injection contacts with some common electrodes, such as PEDOT:PSS, Ca, and Mg:Ag.

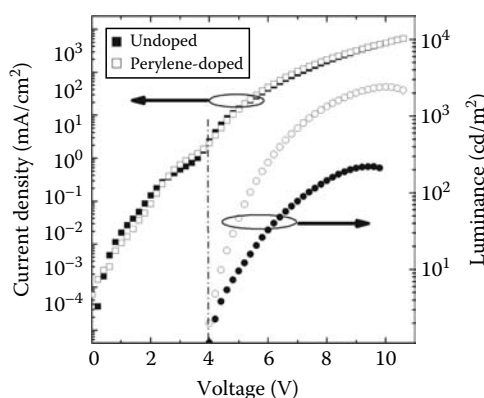
#### 3.5.1 Single-Layer Organic Light-Emitting Diodes from NPB

A single-layer OLED was fabricated with a configuration of ITO/PEDOT:PSS (50 nm)/NPB (120 nm)/Ca/Ag. Figure 3.25 shows an energy diagram depicting

**FIGURE 3.25**

Schematic energy diagram of the NPB single-layer devices, and energy transfer mechanism of perylene-doped device includes: 1, carrier injection; 2, charge transport in pristine NPB; 3, electrons and holes are trapped and recombine; and 4, light emission.

the relevant energy levels for the device [96]. PEDOT:PSS acted as the hole-injecting anode. Ca cathode was used to provide an efficient electron injection and was protected by a top layer of Ag. Figure 3.26 (filled symbols) shows the current–voltage–luminance (JVL) characteristics of the undoped NPB single-layer device. The turn-on voltage is about 4 V and the maximum luminance achieved is  $220 \text{ cd/m}^2$ . At a current density of  $80 \text{ mA/cm}^2$ , the luminance and the current efficiency were  $66 \text{ cd/m}^2$  and  $0.1 \text{ cd/A}$ , respectively. These results clearly show that NPB has the potential of acting as the active material in single-layer OLEDs. However, this single-layer device structure brings out several problems.

**FIGURE 3.26**

Current–voltage (JV) characteristics and luminance–current (LJ) characteristics of NPB devices. The filled (■) and opened (□) symbols represent the undoped and perylene-doped devices, respectively. (From Tse, S.C. et al., *Appl. Phys. Lett.*, 90, 213502, 2007. With permission.)

The first problem is the existence of electron injection barriers. In our work, NPB was discovered to form a quasiohmic contact with PEDOT:PSS by JV, DISCLC, and AS measurements. Thus, with this understanding, we can attribute the conduction of NPB device in low-voltage regime (<4 V) primarily to the hole-dominated and bulk-limited current in Figure 3.26. For applied voltage >4 V, the JV curve of NPB device acquires a distinctly different shape due to the electron injection from the Ca cathode. The turning point of the JV curve is at about 4 V and coincides with the starting voltage of LV characteristics, at which the detectable light emission can be observed from the device. Viewed in this manner, for the undoped NPB device, the turning point of the JV curve (vertical line in Figure 3.26) corresponds to the onset of electron injection from the Ca cathode.

The second problem is the undefined recombination zone in single-layer device. In bilayer structure OLEDs, the recombination zone is easily defined at the hole-transporting layer (HTL) and electron-transporting layer (ETL) interface. Holes and electrons accumulate at interface and then recombine [97]. For single-layer devices, however, electrons and holes cannot accumulate for the recombination due to the lack of heterointerface. These uncombined electrons and holes become the dark current of the single-layer device. Furthermore, if the electron–hole pair recombines near the metal cathode, exciton quenching occurs at the cathode and is responsible for lowering the device performance [98]. In order to create an efficient site for the recombination, an intentional doping was applied in the middle of NPB layer.

### 3.5.2 Single-Layer OLEDs with Perylene Doping

A doped device structure was fabricated with a configuration of ITO/PEDOT:PSS/NPB (40 nm)/NPB:perylene (40 nm)/NPB (40 nm)/Ca/Al, where perylene was doped at 10% concentration by volume. The JVL characteristics of the perylene-doped NPB device are shown as the open symbols in Figure 3.26. Detailed performances of the undoped and perylene-doped NPB devices are summarized in Table 3.6. Compared to the undoped device, the current efficiency of perylene-doped device was enhanced seven times to about 0.7 cd/A at 80 mA/cm<sup>2</sup>, and the maximum luminance also increased to

**TABLE 3.6**

EL Performances of Undoped and Perylene-Doped NPB Single-Layer Devices at 80 mA/cm<sup>2</sup>

Devices	Maximum Luminance (cd/m <sup>2</sup> )	Luminance (cd/m <sup>2</sup> )	Current Efficiency (cd/A)	CIE	
				X	Y
Undoped	220 (376 mA/cm <sup>2</sup> )	66	0.1	0.16	0.11
Perylene-doped	2400 (490 mA/cm <sup>2</sup> )	536	0.7	0.19	0.27

Source: Tse, S.C. et al., *Appl. Phys. Lett.*, 90, 213502, 2007. With permission.

2400 cd/m<sup>2</sup>. Thus, after doping with perylene, the NPB single-layer devices have a notable improvement in the electroluminescence (EL) performance such as the current efficiency and the luminance. With a view to optimizing device performance, 5% and 20% perylene-doped NPB devices were also constructed. However, both the current efficiency and the EL spectrum were not sensitive to changes in the doping concentration.

The working principle of perylene-doped NPB single-layer device can be described by two mechanisms. The first mechanism is associated with Förster energy transfer, which is often used to explain the energy transfer phenomenon in doped system [77,99]. Förster energy transfer is a long range, nonradiative, dipole–dipole coupling of donor (D) and acceptor (A) molecules, which requires allowed transitions from ground to the excited states for both D and A species. Figure 3.27 shows the EL spectra of the single-layer devices and the absorption spectrum of perylene. Based on the overlap between the EL spectrum of undoped device (solid line) and the perylene absorption spectrum (dotted line), Förster energy transfer can be employed to describe the excitation mechanisms of the perylene-doped NPB device. In principle, NPB and perylene can be viewed as donor and acceptor, respectively. In Figure 3.25, holes and electrons are injected under an external electric field and form excitons in NPB molecules. Förster energy transfer occurs from excited NPB to perylene. Then light will be emitted when the exciton recombines in perylene molecules. The EL spectrum of perylene-doped NPB device is shown as the dashed line in Figure 3.27.

Charge trapping is an alternative mechanism responsible for the observed light emission in perylene-doped NPB devices. In this approach, dopants

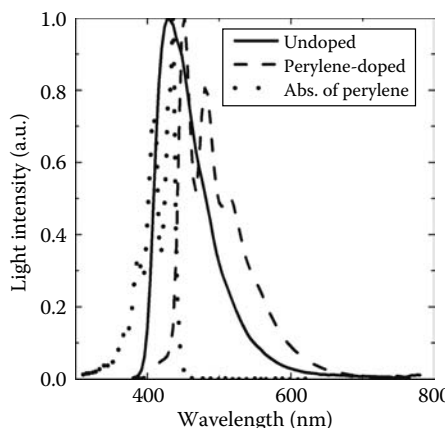


**FIGURE 3.27**

EL spectra of undoped NPB devices (in solid line) and perylene-doped NPB devices (in dashed line). The dotted line is the absorption spectrum of perylene. (From Tse, S.C. et al., *Appl. Phys. Lett.*, 90, 213502, 2007. With permission.)

are depicted as traps that provide recombination sites in the doped layer. Thus the injected electron and hole are trapped and recombine at the dopant molecule. From Figure 3.26, however, the *JV* curves of the undoped and perylene-doped NPB devices are essentially identical. It suggests that the trapping effect does not occur in the perylene-doped device. Hence, for the NPB single-layer devices, the significant improvement by intentional doping can be accounted for the Förster energy transfer between NPB and perylene. As evident from the doped device structure, the recombination zone is confined to the middle of the device.

### 3.5.3 Conclusion

We demonstrate that NPB, a common PA-based hole transporter, can be employed as the host material in single-layer OLEDs. With the ambipolar transporting ability of NPB, the single-layer device attains an appreciable performance. From current–voltage–luminance (*JVL*) measurement, NPB device exhibited a bulk-limited hole current in low-voltage region. Electron injection was clearly observed at about 4 V, which coincides with the onset of light emission. Moreover, perylene was doped into the single-layer device in order to confine the recombination zone. Upon doping, the device performance has a notable improvement and the current efficiencies increase seven times to about 0.7 cd/A. While the number is by no means impressive, this example clearly suggests that the ambipolar material and intentional doping can be applied to simplify OLED architecture.

---

### Acknowledgments

Support of this research by the Research Grant Council of Hong Kong under Grant No. HKBU/2110/06E and HKBU/2111/07E is gratefully acknowledged.

---

### References

1. G.G. Malliaras and R.H. Friend, *Phys. Today* **58**, 53 (2005).
2. C.W. Tang, S.A. Van Slyke, and C.H. Chen, *J. Appl. Phys.* **65**, 3610 (1989).
3. C. Brabec, N. Sariciftci, and J. Hummelen, *Adv. Funct. Mater.* **11**, 15 (2001).
4. G. Horowitz, *J. Mater. Res.* **19**, 1946 (2004).
5. N. Koch, *Chem. Phys. Chem.* **8**, 1438 (2007).
6. S.M. Sze and K.K. Ng, *Semiconductor Devices*, 3rd edn., Wiley, New York, 2006.
7. S.R. Forrest, *Nature* **428**, 911 (2004).

8. T.P.I. Saragi, T. Spehr, A. Siebert, T. Fuhrmann-Lieker, and J. Salbeck, *Chem. Rev.* **107**, 1011 (2007).
9. Y. Shirota and H. Kageyama, *Chem. Rev.* **107**, 953 (2007).
10. P.W.M. Blom and M.C.J.M. Vissenberg, *Mater. Sci. Eng.* **27**, 53 (2000).
11. S.D. Baranovskii and O. Rubel, *Charge Transport in Disordered Solids with Applications in Electronics*, Chapter 6, Wiley, Chichester, 2006.
12. H.H. Fong, PhD thesis, Hong Kong Baptist University, Hong Kong, 2004.
13. S.C. Tse, PhD thesis, Hong Kong Baptist University, Hong Kong, 2007.
14. M. Pope and C.E. Swenberg, *Electronic Processes in Organic Crystals and Polymers*, 2nd edn., Oxford Science Publications, Oxford, 1999.
15. I.G. Hill, A. Kahn, J. Cornil, D.A. dos Santos, and J.L. Brédas, *Chem. Phys. Lett.* **317**, 444 (2000).
16. E.A. Slinsh and V. Capek, *Organic Molecular Crystals: Interaction, Localization, and Transport Phenomena*, AIP, New York, 1982.
17. R.A. Marcus, *Rev. Mod. Phys.* **65**, 3 (1993).
18. See, e.g., C. Risko, G.P. Kushto, Z.H. Kafafi, and J.L. Bredas, *J. Chem. Phys.* **121**, 9031 (2004).
19. B.C. Lin, C.P. Cheng, Z.Q. You, and C.P. Hsu, *J. Am. Chem. Soc.* **127**, 66 (2005).
20. B.C. Lin, C.P. Cheng, and Z.P.M. Lao, *J. Phys. Chem. A* **107**, 5241 (2003).
21. J. Frenkel, *Phys. Rev.* **54**, 647 (1938).
22. J.G. Simmons, *Phys. Rev.* **155**, 657 (1967).
23. M. Redecker, D.D.C. Bradley, M. Inbasekaran, W.W. Wu, and E.P. Woo, *Adv. Mater.* **11**, 241 (1999).
24. H. Ohishi, M. Tanaka, H. Kageyama, and Y. Shirota, *Chem. Lett.* **33**, 1266 (2004).
25. D. Poplavakyy and J. Nelson, *J. Appl. Phys.* **93**, 341 (2003).
26. D. Poplavakyy, W. Su, and F. So, *J. Appl. Phys.* **98**, 014501 (2005).
27. H. Bässler, *Phys. Stat. Sol. B* **175**, 15 (1993).
28. A.J. Campbell, D.D.C. Bradley, and D.G. Lidzey, *J. Appl. Phys.* **82**, 6326 (2007).
29. T. Nagase and H. Naito, *J. Appl. Phys.* **88**, 252 (2000).
30. P.R. Emtage and J.J. O'Dwyer, *Phys. Rev. Lett.* **16**, 356 (1966).
31. I.D. Parker, *J. Appl. Phys.* **75**, 1656 (1994).
32. M. Abkowitz, H.A. Mizes, and J.S. Facci, *Appl. Phys. Lett.* **66**, 1288 (1995).
33. W.R. Salaneck, K. Seki, A. Kahn, and J.J. Pireaux, *Conjugated Polymer and Molecular Interface: Science and Technology for Photonic and Optoelectronic Applications*, Marcel Dekker Inc., New York, 2002.
34. H. Ishii, K. Sugiyama, E. Ito, and K. Seki, *Adv. Mater.* **11**, 605 (1999).
35. A. Kahn, N. Koch, and W. Gao, *J. Polymer Sci., Part B, Polymer Phys.* **41**, 2529 (2003).
36. Th. Kugler, W.R. Salaneck, H. Post, and A.B. Holmes, *Chem. Phys. Lett.* **310**, 391 (1999).
37. I.G. Hill, A.J. Makinen, and Z.H. Kafafi, *J. Appl. Phys.* **88**, 889 (2000).
38. L. Yan, N.J. Watkins, S. Zorba, and Y. Gao, *Appl. Phys. Lett.* **81**, 2752 (2002).
39. H. Peisert, M. Knupfer, T. Schwieger, J.M. Auerhammer, M.S. Golden, and J. Fink, *J. Appl. Phys.* **91**, 4872 (2002).
40. H. Peisert, M. Knupfer, and J. Fink, *Appl. Phys. Lett.* **81**, 2400 (2002).
41. M.A. Lampert, and P. Mark, *Current Injection in Solids*, Academic Press, New York, 1970.
42. P.M. Borsenberger and D.S. Weiss, *Organic Photoreceptors for Imaging Systems*, Chapter 9, Marcel Dekker, New York, 1993.

43. W. Warta, R. Stehel, and N. Karl, *Appl. Phys. A* **36**, 163 (1985).
44. C.H. Cheung, K.K. Tsung, K.C. Kwok, and S.K. So, *Appl. Phys. Lett.* **93**, 083307 (2008).
45. P.S. Davids, I.H. Campbell, and D.L. Smith, *J. Appl. Phys.* **82**, 6319 (1997).
46. P.N. Murgatroyd, *J. Phys. D: Appl. Phys.* **3**, 151 (1970).
47. M. Abkowitz, J.S. Facci, and M. Stolka, *Appl. Phys. Lett.* **63**, 1892 (1993).
48. A.J. Campbell, D.D.C. Bradley, H. Antoniadis, M. Inbasekaran, W.W. Wu, and E.P. Woo, *Appl. Phys. Lett.* **76**, 1734 (2000).
49. I.H. Campbell, D.L. Smith, C.J. Neef, and J.P. Ferraris, *Appl. Phys. Lett.* **74**, 2809 (1999).
50. C. Giebel, H. Antoniadis, D.D.C. Bradley, and Y. Shirota, *Appl. Phys. Lett.* **72**, 2448 (1998).
51. K.C. Kao and W. Hwang, *Electrical Transport in Solids*, Pergamon, Oxford, 1981.
52. D.M. Goldie, *J. Phys. D* **32**, 3058 (1999).
53. H.C.F. Martens, H.B. Brom, and P.W.M. Blom, *Phys. Rev. B* **60**, R8489 (1999).
54. H.H.P. Gommans, M. Kemerink, G.G. Andersson, and R.M.T. Pijper, *Phys. Rev. B* **69**, 155216 (2004).
55. S.W. Tsang, S.K. So, and J.B. Xu, *J. Appl. Phys.* **99**, 013706 (2006).
56. M. Stolka, J.F. Yanus, and D.M. Pai, *J. Phys. Chem.* **88**, 4707 (1984).
57. S.A. Van Slyke, C.H. Chen, and C.W. Tang, *Appl. Phys. Lett.* **69**, 2160 (1996).
58. H.H. Fong, K.C. Lun, and S.K. So, *Chem. Phys. Lett.* **353**, 407 (2002).
59. E.W. Forsythe, M.A. Abkowitz, and Y. Gao, *J. Phys. Chem. B* **104**, 3948 (2000).
60. S.C. Tse, H.H. Fong, and S.K. So, *J. Appl. Phys.* **94**, 2033 (2003).
61. G.G. Malliaras, Y. Shen, D.H. Dunlap, H. Murata, and Z.H. Kafafi, *Appl. Phys. Lett.* **79**, 2582 (2001).
62. S.C. Tse, S.K. So, M.Y. Yeung, C.F. Lo, S.W. Wen, and C.H. Chen, *Jpn. J. Appl. Phys.* **45**, 555 (2006).
63. S. Naka, H. Okada, H. Onnagawa, and T. Tsutsui, *Appl. Phys. Lett.* **76**, 197 (2000).
64. C.C. Wu, T.L. Liu, W.Y. Hung, Y.T. Lin, K.T. Wong, R.T. Chen, Y.M. Chen, and Y.Y. Chien, *J. Am. Chem. Soc.* **125**, 3710 (2003).
65. F. Nuesch, L.J. Rothberg, E.W. Forsythe, Q.T. Le, and Y. Gao, *Appl. Phys. Lett.* **74**, 880 (1999).
66. I.G. Hill and A. Kahn, *J. Appl. Phys.* **84**, 5583 (1998).
67. D.R. Lide, *Handbook of Chemistry and Physics*, 76th edn., CRC Press, Boca Raton, FL, pp. 12–122, 1995.
68. J. Hwang and A. Kahn, *J. Appl. Phys.* **97**, 103705 (2005).
69. Y. Hamada, N. Matsusue, H. Kanno, H. Fujii, T. Tsujioka, and H. Takahashi, *Jpn. J. Appl. Phys.* **40**, L753 (2001).
70. A. Wan, J. Hwang, F. Amy, and A. Kahn, *Org. Electron.* **6**, 47 (2005).
71. M. Abkowitz, J.S. Facci, and J. Rehm, *J. Appl. Phys.* **83**, 2670 (1998).
72. D. Cahen, A. Kahn, and E. Umbach, *Mater. Today*, **8** (August issue), 32 (2005).
73. S.K. So, W.K. Choi, C.H. Cheung, L.M. Leung, and C.F. Kwong, *Appl. Phys. A* **68**, 447 (1999).
74. W. Song, S.K. So, and L. Cao, *Appl. Phys. A* **72**, (2001).
75. C.W. Chu, S.H. Li, C.W. Chen, V. Shrotriya, and Y. Yang, *Appl. Phys. Lett.* **87**, 193508 (2005).
76. T. Matsushima, Y. Kinoshita, and H. Murata, *Appl. Phys. Lett.* **91**, 253504 (2007).

77. H. Mattoussi, H. Murata, C.D. Merritt, Y. Iizumi, J. Kido, and Z.H. Kafafi, *J. Appl. Phys.* **86**, 2642 (1999).
78. T.P.I. Saragi, T.F. Lieker, and J. Salbeck, *Adv. Funct. Mater.* **16**, 966 (2006).
79. J. Veres, S.D. Ogier, S.W. Leeming, and D.C. Cupertino, *Adv. Funct. Mater.* **13**, 199 (2003).
80. Y. Jung, R.J. Kline, D.A. Fischer, E.K. Lin, M. Heeney, I. McCulloch, and D.M. DeLongchamp, *Adv. Funct. Mater.* **18**, 742 (2008).
81. M.L. Chabinyc, R. Lujan, F. Endicott, M.F. Toney, I. McCulloch, and M. Heeney, *Appl. Phys. Lett.* **90**, 233508 (2007).
82. H.H. Fong and S.K. So, *J. Appl. Phys.* **98**, 023711 (2005).
83. H.H. Fong and S.K. So, *J. Appl. Phys.* **100**, 094502 (2006).
84. S.C. Tse, S.K. So, M.Y. Yeung, C.F. Lo, S.W. Wen, and C.H. Chen, *Chem. Phys. Lett.* **422**, 354 (2006).
85. D. Poplavskyy, T. Kreouzis, A.J. Campbell, J. Nelson, and D.D.C. Bradley, *Mat. Res. Soc. Symp. Proc.* **725**, 67 (2002).
86. J. Hwang, F. Amy, and A. Kahn, *Org. Electron.* **7**, 387 (2006).
87. B. Ruhstaller, S.A. Carter, S. Barth, H. Reil, W. Riess, and J.C. Scott, *J. Appl. Phys.* **89**, 4575 (2001).
88. G.G. Malliaras, and J.C. Scott, *J. Appl. Phys.* **85**, 7426 (1999).
89. N. Koch, A. Kahn, J. Ghijssen, J.J. Pireaux, J. Schwartz, R.L. Johnson, and A. Elschner, *Appl. Phys. Lett.* **82**, 70 (2003).
90. A. Kahn, W. Zhao, W. Gao, H. Vázquez, and F. Flores, *Chem. Phys.* **325**, 129 (2006).
91. W. Hu and M. Matsumura, *Appl. Phys. Lett.* **81**, 806 (2002).
92. Q. Huang, J. Cui, H. Yan, J.G.C. Veinot, and T.J. Marks, *Appl. Phys. Lett.* **81**, 3528 (2002).
93. Y. Gao, L. Wang, D. Zhang, L. Duan, G. Dong, and Y. Qiu, *Appl. Phys. Lett.* **82**, 155 (2003).
94. H.F. Wang, L.D. Wang, Z.X. Wu, D.Q. Zhang, J. Qiao, Y. Qui, and X.G. Wang, *Appl. Phys. Lett.* **88**, 131113 (2006).
95. P.A. Lane, G.P. Kushto, and Z.H. Kafafi, *Appl. Phys. Lett.* **90**, 023511 (2007).
96. Y. Hamada, H. Kanno, T. Tsujioka, H. Takahashi, and T. Usuki, *Appl. Phys. Lett.* **75**, 1682 (1999).
97. C.W. Tang and S.A. VanSlyke, *Appl. Phys. Lett.*, **51**, 913 (1987).
98. A.L. Burin and M.A. Ratner, *J. Phys. Chem. A* **104**, 4704 (2000).
99. V. Bulović, A. Shoustikov, M.A. Baldo, E. Bose, V.G. Kozlov, M.E. Thompson, and S.R. Forrest, *Chem. Phys. Lett.* **287**, 455 (1998).



# 4

---

## *Magnetic Field Effects in Organic Semiconducting Materials and Devices*

---

Bin Hu and Liang Yan

### CONTENTS

4.1	Introduction .....	111
4.1.1	Electron and Hole Capture toward Formation of Excited States.....	112
4.1.2	Intersystem Crossing in Intermolecular and Intramolecular Excited States.....	113
4.2	Magnetic Field Effects on Photoluminescence .....	115
4.2.1	Intramolecular Excited States in MFPL .....	116
4.2.2	Intermolecular Excited States in MFPL .....	118
4.3	Magnetic Field Effects on Photocurrent .....	121
4.4	Magnetic Field Effects on Electroluminescence .....	126
4.4.1	Electrofluorescence-Based MFEL .....	127
4.4.2	Electrophosphorescence-Based MFEL.....	129
4.5	Magnetic Field Effects on Injection Current: Magnetoresistance.....	132
4.5.1	Excited States-Based Magnetoresistance.....	133
4.5.2	Charge Transport-Based Magnetoresistance.....	135
4.6	Conclusion .....	136
	References.....	138

---

### 4.1 Introduction

Magnetic field effects (MFEs) are defined as a change caused by an applied magnetic field in electroluminescence, photoluminescence, photocurrent, and electrical injection current in organic semiconducting materials. The amplitude of MFEs is given by the relative change in percent:  $MFE = ((S_B - S_0)/S_0) \times 100\%$ , where  $S_B$  and  $S_0$  are the signal strengths with and without applied magnetic

field. In general, MFEs can be attributed to two spin-dependent excited processes: (1) electron and hole pairing during the formation of excited states and (2) postelectronic developments of excited states. As a result, the excited states are a critical issue in the determination of MFEs. An excited state is defined as an electron–hole (e–h) pair in organic semiconductors. In essence, electron and hole capture determines the formation of e–h pairs through inter-charge electrical and magnetic interactions. It is noted that the electron and hole capture depends on the Coulombic capture radius ( $R_C = e^2/\epsilon KT$ ) and the physical contact time, where  $R_C$  is the Coulombic capture radius,  $\epsilon$  is the dielectric permittivity,  $K$  is the Boltzmann constant, and  $T$  is the temperature. When electrons and holes are moving in an organic semiconducting material, the Coulombic capture radius is determined by the electrical screening resulting from the dielectric field background. The electron and hole contact time is dependent on charge mobility. As a result, internal dielectric field and charge mobility can affect the formation of excited states and the resultant MFEs. Furthermore, due to electron spin multiplicities the electron and hole can have antiparallel or parallel spin orientation and form singlet or triplet excited state. As a consequence, the singlet and triplet excited states have zero and nonzero angular spin momentums, respectively. There exist two internal interactions, namely long-range Coulombic attraction ( $\propto (1/r)$ ) and short-range spin–exchange interaction ( $\propto \exp(-r)$ ) between electron and hole in an excited state, where  $r$  is the e–h separation distance. The Coulombic attraction accounts for the binding energy between the electron and hole in an excited state while the spin–exchange interaction generates an energy difference between the singlet and triplet states. An external magnetic field may influence the spin-dependent formation and postelectronic processes in excited states and consequently change electroluminescence, photoluminescence, photocurrent, and electrical current in organic semiconducting materials.

#### **4.1.1 Electron and Hole Capture toward Formation of Excited States**

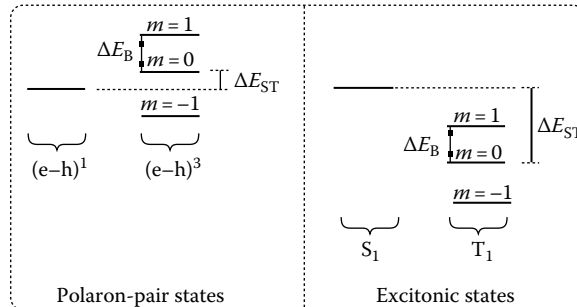
We note that the spin correlation between electron and hole is the magnetic interaction that determines whether the formation of excited states is spin dependent [1–4]. An external magnetic field can perturb the electron–hole spin correlation and thus change the singlet and triplet formation ratios. Equivalently, the spin correlation functions as a bridge for an external magnetic field to change the singlet and triplet formation ratios in excited states. Since the spin correlation largely increases with decreasing the electron–hole separation distance, it can be assumed that an external magnetic field can have a larger influence on the singlet and triplet formation ratios when randomly spin-orientated electron and hole are captured at a short distance in forming an electron–hole pair. In contrast, the magnetic

field dependence of the singlet and triplet formation ratios would become weaker when randomly spin-orientated electron and hole are captured at relatively long distance.

After randomly orientated electrons and holes are captured to generate excited states, internal magnetic field resulting from hyperfine interaction (HYI) or spin-orbital coupling (SOC) forms a mechanism to flip electron spin orientation based on magnetic scattering, and causes an intersystem crossing (ISC) between singlet and triplet excited states. On the other hand, the internal magnetic field can split three degenerate triplet energy levels with spin angular momentums of  $m = 0$ ,  $m = +1$ , and  $m = -1$ , leading to internal Zeeman splitting and consequently changing the energy difference between singlet and subtriplet levels. Clearly, the internal magnetic field has two opposite effects: increasing and decreasing ISC through spin flip and internal Zeeman splitting, respectively. The observed ISC is essentially determined by the competition between these two opposite effects. When an applied external magnetic field is comparable to internal magnetic field in strength, an external magnetic field can weaken the electron flip mechanism induced by internal magnetic scattering and increase the triplet splitting (namely external Zeeman effect). These two effects can cause a perturbation in the singlet-triplet ISC and consequently modify the singlet and triplet ratios after excited states are formed. In principle, magnetic field-dependent singlet and triplet ratios can consist of two contributions from spin-dependent formation of excited states and from the magnetically sensitive ISC. This leads to formation and ISC-based MFEs, respectively, in organic semiconducting materials.

#### 4.1.2 Intersystem Crossing in Intermolecular and Intramolecular Excited States

When an electron is captured with a hole within their Coulombic radius, both the intermolecular and intramolecular e-h pairs can be formed in organic semiconducting materials. The intermolecular e-h pairs are also named as polaron pairs when the electron and the hole are bound to different molecules with the electron-hole separation distance normally larger than 1 nm. The intramolecular electron-hole pairs have been defined as Frenkel excitons when the electron and hole are bound to a singlet molecule with the electron-hole separation distance smaller than 1 nm. It is further noted that the electron-hole separation distances have a broad distribution in polaron pairs. However, the electron-hole separation distances in excitons are well defined with a narrow distribution. There are two major differences between polaron pairs and excitons due to their difference in electron-hole separation distance. First, the polaron pairs have largely smaller binding energies as compared to excitons. Second, the singlet-triplet energy difference  $\Delta E_{ST}$  caused by spin-exchange interaction is much smaller in polaron-pair states than that in excitonic states. The  $\Delta E_{ST}$  can become negligible with

**FIGURE 4.1**

The energy levels for polaron (e–h) pair and excitonic states in an external magnetic field.  $\Delta E_{ST}$  and  $\Delta E_B$  are the singlet–triplet energy difference and magnetic splitting energy, respectively.

increasing the electron–hole separation distance in polaron-pair states. In excitonic states the  $\Delta E_{ST}$  can be significantly large when the electron and hole are closely located in a single molecule where the Pauli exclusion minimizes the kinetic energy to avoid “electron collision” (see Figure 4.1). In general, the internal magnetic field leads to an ISC in both polaron-pair and excitonic states with the rates of  $K_{ISCP}$  and  $K_{ISCE}$ , respectively.

Because singlets and triplets have different contributions to light emission, dissociation, and charge reaction in excited states due to their different spin configurations, binding energies, and lifetimes, the MFEs can be observed when an external magnetic field can change the singlet and triplet ratios through either formation or ISC in excited states. Due to the nature of short-range spin correlation between electron and hole, the magnetic field may affect the singlet and triplet formation ratios by perturbing the electron–hole spin correlation only when randomly orientated electrons and holes are captured at short distance. At long electron–hole capture distance, the spin correlation becomes negligible and consequently MFEs on the singlet and triplet formation ratios through spin correlation can be removed. It is noted that injected electrons and holes are captured at various distances to form excited states. Therefore, whether or not the formation-based MFEs can be observed depends on electron–hole capture distance.

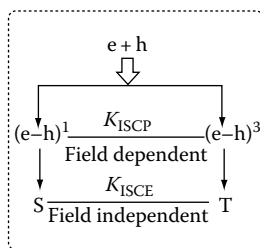
There are two necessary conditions, namely, magnetic requirements, for ISC to be magnetic-field dependent (Scheme 4.1). First, external Zeeman splitting  $\Delta E_{EZ}$  must be larger than internal Zeeman splitting  $\Delta E_{IZ}$ . Second, the external Zeeman splitting  $\Delta E_{EZ}$  should be comparable to the singlet–triplet energy difference  $\Delta E_{ST}$  caused by electron–hole separation distance-dependent spin-exchange interaction.

Based on these magnetic requirements, it is obvious that an external magnetic field can change the ISC rate

$$\begin{aligned}\Delta E_{EZ} &> \Delta E_{IZ} \\ \Delta E_{EZ} &> \Delta E_{ST}\end{aligned}$$

**SCHEME 4.1**

Magnetic requirements to realize MFEs.

**FIGURE 4.2**

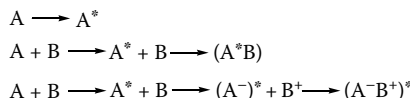
Intermolecular excited states (polaron pairs) and intramolecular excited states (excitons) with magnetic field-dependent and independent ISC rates  $K_{ISCP}$  and  $K_{ISCE}$ , respectively.  $(e-h)^1$  and  $(e-h)^3$  represent singlet and triplet polaron pairs. S and T are singlet and triplet excitons.

$(K_{ISCP})$  in polaron-pair states but has little influence on the ISC rate ( $K_{ISCE}$ ) in excitonic states. Therefore, the  $K_{ISCP}$  and  $K_{ISCE}$  can be named as field-dependent and field-independent parameters, respectively. Clearly, the field-dependent  $K_{ISCP}$  can lead to magnetic field-dependent singlet and triplet ratios in polaron-pair states. We should note that the field-dependent  $K_{ISCP}$  can also result in magnetic field-dependent singlet and triplet exciton ratios when the polaron pairs evolve into excitons under electrical excitation (Figure 4.2). However, an external magnetic field is difficult to change the singlet and triplet exciton ratios through ISC in excitonic states when polaron-pair states are absent under photo-excitation. As a result, adjusting the electron–hole separation distance in excited states can change the magnetic field dependence of ISC and consequently determines whether ISC-based MFEs can be observed in organic semiconducting materials.

## 4.2 Magnetic Field Effects on Photoluminescence

Photoluminescence results from the radiative emission of photon absorption-generated excited states. In principle, both intramolecular and intermolecular excited states can be generated with singlet and triplet configurations by photon absorption in organic semiconducting materials (Scheme 4.2).

The intramolecular excited states are essentially Frenkel excitons. However, the intermolecular excited states consist of exciplexes and charge-transfer complexes. The exciplex is generated when an excited molecule  $A^*$  is coupled with an unexcited molecule B to form an intermolecular excited state: an excited “complex molecule ( $A^*B$ ).” If A and B are the same type of molecules, this intermolecular excited state is called an excimer. The charge-transfer complex is formed when charge transfer occurs within an exciplex. The formation of a

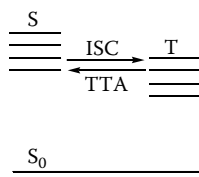
**SCHMENE 4.2**

Schematic formation for intramolecular exciton ( $A^*$ ), intermolecular exciplex ( $A^*B$ ), and intermolecular charge-transfer complex ( $(A^-B^+)^*$ ). A and B are two different molecules. The superscript \* represents excited state. The  $A^+$  and  $B^-$  are positive and negative molecules.

charge-transfer complex includes two steps: (1) charge transfer between excited molecule  $A^*$  and unexcited molecule  $B$  to generate  $(A^+)^*$  and  $B^-$  and (2) coupling between  $(A^+)^*$  and  $B^-$  to form an excited complex  $(A^+B^-)^*$ .

Due to the spin selection rule, photon absorption can only generate singlet excitons. However, the ISC induced by internal magnetic interaction (from hyperfine coupling or SOC) can convert singlets into triplets in excitonic states (Scheme 4.3).

On the other hand, two triplet excitons can interact through electrical dipole–dipole interaction and consequently annihilate into one singlet excited state [5–7]. This process is called triplet–triplet annihilation (TTA) that can be described by bimolecular reaction dynamics [8]. Particularly, the TTA rate is quadratically proportional to the triplet density. The light emission from the singlet excitons generated from TTA is named as delayed fluorescence [9–11]. In addition, the TTA must satisfy both spin momentum and energy conservations. This implies that the internal magnetic interaction must flip electron spin polarization to complete the conversion from triplets to singlets during the TTA process. Nevertheless, the ISC and TTA can redistribute the singlet and triplet exciton ratios in organic semiconducting materials. If an external magnetic field can change the singlet and triplet ratios in excited states through ISC or TTA, magnetic field effects on photoluminescence (MFPL) can then be observed.



**SCHEME 4.3**

ISC and TTA.  $S_0$  is ground state.  $S$  and  $T$  are singlet and triplet excitonic states.

#### 4.2.1 Intramolecular Excited States in MFPL

Intramolecular excitons are generated by exciting an electron from highest occupied molecular orbital (HOMO) to lowest unoccupied molecular orbital (LUMO) in a single molecule based on photon absorption. There are three major channels for excitons to release their energies: radiative emission, nonradiative multiphonon emission, and dissociation. The radiative excitonic emission gives rise to prompt photoluminescence that can be either fluorescence if singlets emit or phosphorescence if triplets emit. The nonradiative multiphonon emission transfers excitonic energies to chemical bond vibrations to produce heat. The dissociation of excitons is the responsible process to generate free electrons and holes through intermolecular interactions. It is noted that the dissociation can go through either Poole-Frenkel process [12] due to thermal activation or Onsager process [13] due to diffusion and Coulombic interaction in organic materials. However, the dissociated electrons and holes can recombine to form intermolecular electron–hole pairs followed by the relaxation into intramolecular Frenkel excitons due to Coulombic attraction. The light emission from the recombination of dissociated electrons and holes is defined as charge recombination photoluminescence. As a result, the photoluminescence (PL) ( $I_{PL}$ ) can consist of

prompt excitonic ( $I_{\text{Exciton}}$ ) and charge recombination ( $I_{\text{Charge}}$ ) components [14], given by

$$I_{\text{PL}} = I_{\text{Exciton}} + I_{\text{Charge}} \quad (4.1)$$

An external magnetic field may change  $I_{\text{Exciton}}$  or  $I_{\text{Charge}}$  component, leading to MFPL in organic semiconducting materials. In the prompt excitonic photoluminescence ( $I_{\text{Exciton}}$ ), an external magnetic field may decrease the ISC in excitonic states if the external Zeeman splitting is greater than the internal Zeeman splitting, yielding an increase and a decrease in the singlet and triplet exciton densities, respectively. This ISC dependence of magnetic field would generate positive (negative) MFE in fluorescence (phosphorescence). Furthermore, an applied magnetic field can compete with internal magnetic interaction and weaken the spin flip mechanism in TTA. This can be explained by MFEs on singlet character of triplet states during TTA (Merrifield theory [15,16]). As a result, the magnetic field-induced modification of TTA would yield a negative (positive) MFE in fluorescence (phosphorescence). In charge recombination photoluminescence, the capture of dissociated electrons and holes forms both singlet and triplet intermolecular electron–hole pairs with ISC. Certain electron–hole separation distance can satisfy the magnetic requirements (Scheme 4.1), leading to MFEs based on charge recombination photoluminescence. Specifically, an external magnetic field can reduce the ISC between singlet and triplet exciplex states, giving a positive magnetic field dependence of photoluminescence.

In the prompt photoluminescence from intramolecular Frenkel excitons, an applied magnetic field may reduce the ISC and TTA, and consequently modify the singlet and triplet ratios if two magnetic requirements (Scheme 4.1) are satisfied. We note that the singlet–triplet energy difference  $\Delta E_{\text{ST}}$  in excitonic states is normally between 0.5 and 1.5 eV in organic materials [17,18]. This spin–exchange interaction-induced  $\Delta E_{\text{ST}}$  is much larger than the external Zeeman splitting  $\Delta E_{\text{EZ}}$ , dissatisfying the two magnetic requirements (Scheme 4.1) to activate MFEs. As a consequence, an external magnetic field cannot influence the prompt photoluminescence component from Frenkel excitons through ISC. This leaves TTA and charge recombination as two possible channels to generate MFEs based on intramolecular excited states under photoexcitation. The time-resolved photoluminescence has shown that the lifetime of TTA-generated delayed fluorescence increases with magnetic field [19]. The intensity measurements have shown in anthracene crystal that the delayed fluorescence can considerably decrease with increasing applied magnetic field [15,16,20,21]. These experimental results clearly indicate that an external magnetic field can reduce the TTA, leading to a negative MFPL in organic materials. However, we have measured the steady-state photoluminescence from organic semiconducting molecules and polymers with weak, intermediate, and strong SOC strengths at different temperatures as a function of magnetic field [22–25]. The steady-state photoluminescence shows

independence of magnetic field up to 1 T. It can be experimentally suggested that (1) an external magnetic field cannot change the ISC in excitonic states, (2) the TTA-generated delayed fluorescence is not an appreciable component in overall steady-state photoluminescence, and (3) charge recombination does not generate a considerable photoluminescence component in common organic semiconducting materials.

#### **4.2.2 Intermolecular Excited States in MFPL**

Intermolecular excited states including excimers, exciplexes, and charge-transfer complexes can be, in principle, formed in solid or liquid state in organic materials. In principle, the formation of intermolecular excited states is determined by background electrical polarization field and intermolecular electrical dipole–dipole interaction. In solid state the formation of intermolecular excited states involves energy transfer and migration of excited states between different molecules. However, in liquid state the molecular motion mainly accounts for the formation of intermolecular excited states. The intermolecular excited states can offer significant tuning properties in light emission color and intensity through material selection and mixing for solid-state lighting and sensing applications. Particularly, the relatively large electron–hole separation distance can lead to a situation in which the two magnetic requirements (Scheme 4.1) can be satisfied to activate MFEs in intermolecular excited states.

Intermolecular excited states can be essentially treated as ion pairs in spin physics. Therefore, intermolecular excited states can be formed with the singlet and triplet configurations. There are two important interactions occurring within an intermolecular excited state: long-range Coulombic attraction from intermolecular electrical dipole–dipole interaction and short-range internal magnetic interaction from HYI and SOC. The long-range Coulombic attraction is responsible for the binding energies in intermolecular excited states. The intermolecular electrical polarization field can significantly influence the formation of excimers, exciplexes, and charge-transfer exciplexes. The short-range magnetic interaction forms a mechanism to flip electron spins and causes internal Zeeman splitting of triplet intermolecular excited states, consequently generating ISC between singlets and triplets in intermolecular excited states. Because SOC requires large penetration of  $\pi$  electrons into the magnetic field generated by molecular orbital current, HYI is mainly accountable for the internal magnetic interaction and ISC in intermolecular excited states when heavy-metal complex structures are absent. Intermolecular excited states can also experience radiative emission, nonradiative multiphonon emission, and charge dissociation to release their energies. When an external magnetic field changes the singlet and triplet ratios in intermolecular excited states, MFEs can then be observed in excimers [26–28], exciplexes, and charge-transfer complexes [29–33] based on the fact that singlets and triplets have different contributions to radiative emission

and charge dissociation due to their different spin configurations involved in electronic transitions and ionic natures involved in the interaction with intermolecular electrical polarization.

Magnetic field-dependent singlet and triplet ratios in intermolecular excited states can be, in general, realized through two different channels: spin-dependent formation and magnetic field-sensitive ISC based on ion-pair model. First, spin-dependent formation can yield negative MFPL if an external magnetic field can influence spin polarizations between the electron in excited molecule and the hole in unexcited molecule toward triplet formation with parallel spin configuration. Second, an external magnetic field can cause an external Zeeman splitting on triplet intermolecular excited states and thus change the ISC if the external Zeeman splitting is greater than the internal Zeeman splitting. The sufficient external Zeeman splitting can generate two possible outcomes for ISC in intermolecular excited states (Figure 4.3). For the intermolecular excited states with relatively small electron–hole separation distance, the large singlet–triplet energy difference caused by spin–exchange interaction can be much larger than the Zeeman splitting. Applying magnetic field can reduce the energy gap between singlet and triplet ( $m = -1$ ) (Figure 4.3a). When the ISC is considered as phonon-assisted transition from  $T_{m=-1}$  to S, reducing the energy gap facilitates the

ISC and increases singlet ratio. As a result, magnetic field-dependent ISC can yield an increase in photoluminescence, leading to positive MFE in the intermolecular excited states with relatively short electron–hole separation distance. When the electron–hole separation distance is relatively large, continuously increasing the external Zeeman splitting can cause an intersect point between singlet and triplet ( $m = -1$ ) levels, forming a level-crossing point. As a consequence, the ISC would show a non-monotonic change: first increase and then decrease with increasing magnetic field before and after the level-crossing point, respectively. This implies that magnetic field-dependent ISC gives rise to positive and then negative MFEs in the intermolecular excited states with relatively large electron–hole separation distance. Nevertheless, the combination of spin-dependent formation and magnetic field-sensitive ISC effects can, in general, yield four possibilities: positive, negative, positive and then negative, and negative and then positive MFPL in the intermolecular excited states. The type of MFPL that can be observed depends on the internal magnetic interaction resulting from HYI and SOC, and the singlet–triplet energy difference resulting from

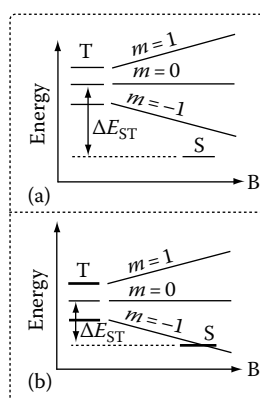


**FIGURE 4.3**

External Zeeman splitting effects on ISC in intermolecular polaron-pair states. (a) Polaron-pair states with large singlet–triplet energy difference  $\Delta E_{ST}$  due to short electron–hole separation distance. (b) Polaron-pair states with small singlet–triplet energy difference  $\Delta E_{ST}$  due to long electron–hole separation distance.

the spin–exchange interaction determined by electron–hole separation distance. On the other hand, the MFPL can be used as an experimental tool to investigate the spin-dependent formation, charge dissociation, and magnetic field-dependent ISC for intermolecular excited states.

It is particularly noted that adjusting the electron–hole separation distance through material mixing can conveniently modify the MFEs in intermolecular excited states. As the electron–hole separation distance increases, the singlet–triplet energy difference  $\Delta E_{ST}$  due to spin–exchange interaction decreases. On the other hand, changing electron–hole separation distance does not affect the internal magnetic interaction and the resultant internal Zeeman splitting because the intermolecular magnetic interaction mainly comes from HYI in intermolecular excited states. As a consequence, the magnetic field dependence of ISC can increase with increasing the e–h separation distance. This provides a mechanism to tune MFEs in intermolecular excited states. It has been found that 2,5-bis(5-*tert*-butyl-2-benzoxazolyl)-thiophene (BBOT) and *N,N'*-bis(3-methylphenyl)-*N,N'*-diphenylbenzidine (TPD) can form strong intermolecular excited states: exciplex [34,35]. Figure 4.4a shows the broad photoluminescence spectrum peaked at 525 nm from the intermolecular exciplex. The photoluminescence from BBOT and TPD is located at 440 and 400 nm, respectively. We can clearly see in Figure 4.4b that the photoluminescence from the intermolecular exciplex shows appreciable positive MFE while the intramolecular excited states from TPD and BBOT exhibit independence of magnetic field in photoluminescence. Furthermore, decreasing the density of intermolecular exciplex by adjusting chromophore (BBOT + TPD with 1:1 molar ratio) concentration in poly(methyl methacrylate) (PMMA) leads to an increase

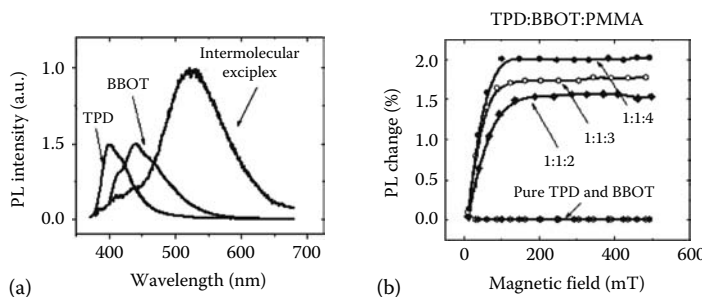


**FIGURE 4.4**

Photoluminescence spectra and photoluminescence dependence of magnetic field for intramolecular excitons and intermolecular exciplex. (a) Photoluminescence spectra for intramolecular exciton emission from pure TPD and BBOT and for the intermolecular exciplex formed between TPD and BBOT in PMMA matrix at the excitation wavelength of 360 nm. (b) Photoluminescence dependence of magnetic field dependence for intramolecular excited states in TPD and BBOT and for intermolecular exciplex formed between TPD and BBOT dispersed in PMMA matrix (with molar ratios indicated). (From Hu, B., *Adv. Mater.*, 21, 1, 2009. With permission.)

in the MFPL. Although magnetic field-dependent ISC was questioned [36], this concentration-dependent MFPL confirms that adjusting the electron–hole separation distance through material mixing forms a convenient methodology to tune the MFPL in intermolecular excited states (Table 4.1).

---

### 4.3 Magnetic Field Effects on Photocurrent

It was experimentally found in anthracene crystal that a low magnetic field can change the photocurrent [37,38]. This phenomenon can be named as magnetic field effects of photocurrent (MFPC). The MFPC can be readily observed in organic semiconducting materials [39–42] and also in organic material complex systems [29,43,44] with the amplitude of about 5%. It can be envisioned that the MFPC can elucidate not only photoexcited processes but also photovoltaic channels in organic semiconducting materials. Especially, MFPC can be used as an “inside-out” experimental approach to reveal detailed singlet and triplet photovoltaic processes in organic solar cells [22,45,46]. It is noted that photocurrent generation consists of four necessary processes: light absorption, formation of excited states, generation of charge carriers from photoexcited states, and transport of charge carriers in organic semiconducting materials. Particularly, generation of charge carriers from photoexcited states is sensitive to magnetic field and consequently accounts for MFPC in organic semiconducting materials.

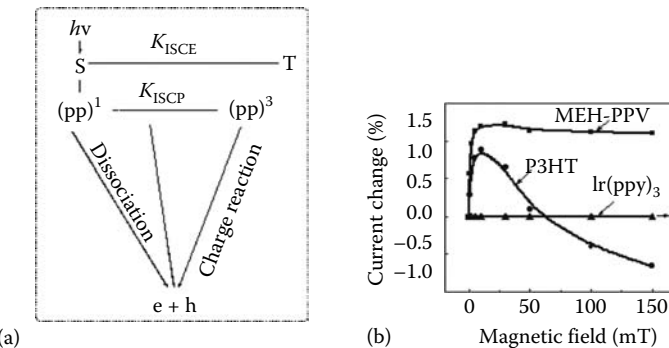
There are two photovoltaic channels for excited states to generate photocurrent: dissociation and charge reaction in organic semiconducting materials [45]. The dissociation is driven by intermolecular electrical dipole–dipole interaction. The charge reaction is essentially Coulombic scattering between an excited state and a charge carrier. This charge reaction can provide strong electrical force to break strongly bound electron–hole pairs in excited states for the generation of charge carriers. The excited states, which have lower binding energies, can, however, dominate the dissociation channel during the generation of photocurrent. The excited states, which have larger binding energies, have to experience charge reaction to generate photocurrent. We note that the major outcome of light absorption is the generation of intramolecular excited states: Frenkel excitons. Because of spin selection rule, photoexcitation only generates singlet excitons. However, singlet excitons can be partially converted into triplet excitons through ISC caused by internal magnetic interaction from hyperfine or SOC. Therefore, both singlet and triplet excitons can exist in organic semiconducting materials under photoexcitation. In addition, the singlet excitons can dissociate into intermolecular excited states: singlet polaron pairs due to their low binding energies toward the generation of photocurrent. The singlet polaron pairs can partially convert into triplet polaron pairs through ISC. As a result, photon absorption

**TABLE 4.1**  
Emission Characteristics and Modulation Speed of Four Kinds of Materials with Molecular Structure

Material	$\alpha$ -NPD	Alq <sub>3</sub>	Rubrene	TPP
Molecular structure				
Wavelength	430 nm	520 nm	560 nm	655 nm, 720 nm
Modulation speed	>100 MHz	60 MHz	>100 MHz	>100 MHz

generates both excitons and polaron pairs with singlet and triplet configurations toward the generation of photocurrent. In principle, both exciton and polaron pairs in singlet and triplet states can be involved in dissociation and charge reaction to generate photocurrent. However, the singlets and triplets in the excitonic and polaron-pair states have largely different contributions to these two photovoltaic channels of dissociation and charge reaction due to their different binding energies, ionic natures, and lifetimes. For the dissociation occurring in excitonic states, the singlets can have dominant contribution due to the lower binding energies as compared to triplet excitons. For the charge reaction in excitonic states, triplets can be, however, largely involved due to the sufficient physical contacts with charge carriers based on their long lifetimes. For the dissociation in polaron-pair states, both singlets and triplets can have very significant contributions because of their lower binding energies. However, the singlets have a larger dissociation rate relative to triplets [42,47]. This is because the wavefunction of singlets has more ionic characteristic that can effectively interact with intermolecular electrical interaction for dissociation. The remaining singlet and triplet polaron pairs may also experience charge reaction with similar reaction rates due to their similar lifetimes. As a result, the major channels for the generation of photocurrent can be described by the dissociation dominated by singlets and the charge reaction dominated by triplets (Figure 4.5a).

An external magnetic field can change the photocurrent through the singlet-dominated dissociation and triplet-dominated charge reaction, leading to MFPC in organic semiconducting materials. Specifically, applying magnetic field can increase the singlet polaron pairs through magnetic field-dependent ISC  $K_{ISCP}$  due to the satisfaction of two magnetic requirements

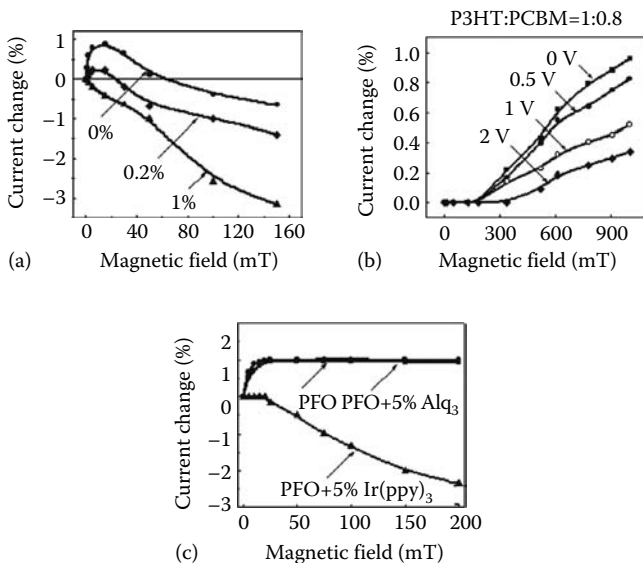


**FIGURE 4.5**

Photovoltaic channels and magnetic field dependence of photocurrent. (a) Two photovoltaic channels: dissociation dominated by polaron pairs and exciton-charge reaction dominated by triplet excitons. (b) Magnetic field dependence of photocurrent for MEHPPV, P3HT, and  $\text{Ir}(\text{ppy})_3$ . (From Hu, B., *Adv. Mater.*, 21, 1, 2009. With permission.)

(Scheme 4.1), leading to a positive component in the MFPC [40,41]. Second, the triplet–charge reaction can decrease with magnetic field and yield a negative component in the MFPC. Since an applied magnetic field has little influence on singlet and triplet exciton ratios due to the field-independent ISC  $K_{ISC}$  in excitonic states, the magnetic field-dependent triplet–charge reaction can be attributed to the reaction-rate constant. Figure 4.5b shows the MFPC for three typical organic semiconducting materials: poly[2-methoxy-5-(2'-ethylhexyloxy)-1,4-phenylenevinylene] (MEHPPV), poly[3-methylthiophene] (P3HT), and *fac* tris (2-phenylpyridine) iridium Ir(ppy)<sub>3</sub>. It is noted that the triplet exciton densities are about 1.0% in MEHPPV [48], 70% in P3HT [49], and 100% in Ir(ppy)<sub>3</sub> [50]. It can be seen in Figure 4.5b that the MEHPPV shows only positive component due to nearly 100% singlet exciton fraction while the P3HT contains both positive and negative components due to significant triplet exciton fraction in the MFPC. It is obvious that the negative component in the MFPC can be attributed to triplet exciton–charge reaction [39]. It is particularly noted that the triplet Ir(ppy)<sub>3</sub> does not show any MFPC. This suggests that the MFEs on triplet–charge reaction-rate constant depend on SOC. This is because, when the SOC is not too strong, a low magnetic field can weaken the ionic characteristic of triplet excitons and consequently decrease the triplet–charge reaction governed by electrical dipole–dipole interaction [19]. Nevertheless, it can be assumed that the triplet exciton–charge reaction-rate constant is responsible for negative MFPC in organic semiconducting materials.

We note that there are two important issues related to the positive and negative components in the MFPC in organic semiconducting materials. First, the direct experimental proof has been absent to support the proposed polaron pair model [39–41] in which the positive MFPC is due to the dissociation of polaron pairs based on magnetic field-dependent singlet and triplet ratios in polaron-pair states. Second, there are two proposed mechanisms for negative MFPC: triplet exciton–charge reaction, named as charge reaction model [39–41], or intersection between singlet and triplet ( $T_{m=-1}$ ) levels, named as level-crossing model [29,42,43]. It has been experimentally unclear which proposed model accounts for the negative MFPC in organic semiconducting materials. We recently examined the positive MFPC before and after the polaron-pair states were removed upon introducing donor–acceptor interaction from doping. We found that removing polaron-pair states have led to significant reduction in positive MFPC. Specifically, we used the photovoltaic system: P3HT doped with surface-functionalized fullerene 1-[3-(methoxycarbonyl)propyl]-1-phenyl-[6.6]C<sub>61</sub> (PCBM). The donor–acceptor interaction can be effectively formed between P3HT chain and PCBM molecule interfaces [51,52]. Especially, the donor–acceptor interaction strength can be adjusted by changing the PCBM concentration in the P3HT. It can be seen in Figure 4.6a that the positive MFPC gradually decreases with increasing PCBM doping concentration. The weak donor–acceptor interaction from 1% PCBM doping can completely remove the positive component but leaves

**FIGURE 4.6**

MFPC versus doping, voltage, and triplet density. (a) MFPC versus PCBM doping ( $x\%$  = PCBM weight concentration). (b) High-field MFPC versus applied reverse bias in solar cell of ITO/PEDOT/P3HT:PCBM(1:0.8)/Al. (c) MFPC for pure PFO, Alq<sub>3</sub> doped PFO, and Ir(ppy)<sub>3</sub> doped PFO. (From Zu, Z. and Hu, B., *Adv. Func. Mater.*, 18, 2611, 2008. With permission.)

the negative component unchanged in the MFPC. We know that the weak donor–acceptor interaction can sufficiently dissociate polaron pairs while the exciton dissociation requires much stronger donor–acceptor interaction due to the difference in binding energy between polaron pairs and excitons [45]. As a result, this observation provides a direct experimental evidence that polaron-pair states are responsible for the positive MFPC. In addition, we found that the charge-transfer complexes, equivalent to intermolecular electron–hole pairs, formed from the recombination of dissociated electrons and holes between P3HT chain and PCBM molecule interfaces give rise to positive MFPC at high field (Figure 4.6b). This is because (1) the ISC between singlet and triplet charge-transfer complex states is sensitive to magnetic field due to large electron–hole separation distance and (2) singlet and triplet charge-transfer complexes can redisassociate into free charge carriers with high and low rates [45]. It is further noted that this high-field positive MFPC can be reduced by applying an electrical field due to electrical field-assisted dissociation of charge-transfer complex. As a result, our doping-related MFPC results have provided direct experimental evidence to confirm that positive MFPC comes from polaron-pair states in organic semiconducting materials. For the comparison between triplet–charge reaction and level-crossing models proposed for negative MFPC, we recently found that increasing triplet exciton density can significantly lead to negative MFPC at low magnetic

field. Specifically, we uniformly dispersed fluorescent  $\text{Alq}_3$  and phosphorescent  $\text{Ir}(\text{ppy})_3$  molecules into poly(9,9-dioctylfluorenyl-2,7-diyl) (PFO) matrix to form singlet and triplet systems, respectively, under photoexcitation. The dispersed  $\text{Ir}(\text{ppy})_3$  molecules can significantly increase the triplet exciton ratio in the PFO matrix under photoexcitation [53,54] while the dispersed  $\text{Alq}_3$  molecules have unappreciable influence on the triplet exciton ratio. Figure 4.6c clearly shows that increasing triplet exciton density can significantly induce negative MFPC upon  $\text{Ir}(\text{ppy})_3$  dispersion. However, the MFPC remains unchanged when the triplet exciton density is not appreciably varied upon  $\text{Alq}_3$  dispersion. This experimental result suggests that the triplet–charge reaction accounts for the negative MFPC and level-crossing mechanism cannot be activated in low magnetic field in organic semiconducting materials.

---

#### 4.4 Magnetic Field Effects on Electroluminescence

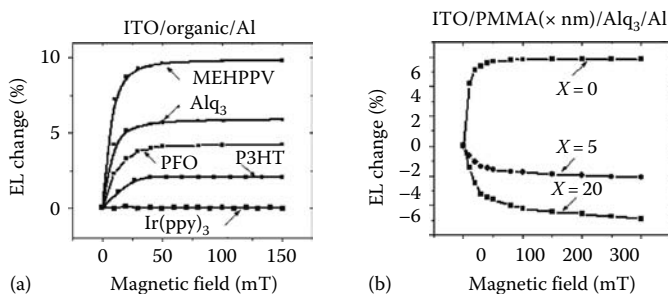
An external magnetic field can change steady-state electroluminescence (EL), leading to magnetic field effects of electroluminescence (MFEL) at constant injection current in nonmagnetic common organic semiconducting materials [24,55–58]. This phenomenon indicates that nonmagnetic organic semiconductors have potential applications in spintronic devices where electronic, optical, and magnetic properties can mutually control. On the other hand, the studies of MFEL can enhance the critical understanding of intrinsic useful and nonuseful excited processes in respective optoelectronic devices. It was reported in 1975 that an applied magnetic field of 900 mT can significantly reduce the delayed electrofluorescence, leading to negative MFEL in anthracene crystal based on time-resolved measurement. This experimental result indicates that a high magnetic field can reduce the TTA under electrical excitation [55], which has been observed under photoexcitation [15,19,59,60]. Positive MFEL has been also observed in  $\text{Alq}_3$ -based light-emitting diode [61]. The EL from the radiative singlet excitons in  $\text{Alq}_3$  rapidly increases with magnetic field by about 5% and then becomes saturated at around 300 mT. The authors proposed that an external magnetic field, when stronger than internal HYI, can decrease the ISC from singlets to triplets in polaron-pair (intermolecular electron–hole pair) states based on Zeeman splitting effect and therefore leads to an increase in the density of light-emitting singlet excitons after polaron pairs are evolved into excitons. At high magnetic field ( $\sim 2\text{ T}$ ), nonmonotonic MFEL was also observed in the  $\text{Alq}_3$ -based light-emitting diodes that the EL first increases from 0 to about 50 mT (estimated from their published data) and then slowly decreases up to 1.9 T at steady-state measurement [62]. The observed negative MFEL was attributed to both TTA and triplet–charge reaction. While the TTA contributes to the negative MFEL, the authors assumed that an external magnetic field can align the spin orientations of electrons

and holes generated from triplet exciton-charge reaction and lead to the formation of triplet excitons at the expense of light-emitting singlet excitons. Therefore, triplet-charge reaction can also contribute to the negative MFEL. However, the contribution from TTA was found to be not significant in the negative MFEL at low magnetic field (<80 mT) based on the studies of magnetic field dependence of EL at low electrical excitation where TTA is unimportant [63]. This experimental result further suggests that the low-field EL enhancement is due to magnetic field-induced modification of singlet and triplet ratios in polaron-pair states. Taking all possibilities into account, it can be suggested, based on published results, that positive low-field MFEL originates from magnetic field-dependent singlet and triplet ratios in polaron-pair states while the negative MFEL may contain the contributions from TTA and triplet-charge reaction in excitonic states.

There are three important issues that require further discussion in understanding the MFEL from nonmagnetic organic semiconducting materials. First, it needs to be further determined whether the magnetic field-induced modification of the singlet and triplet ratios comes from ISC or from spin-dependent formation in polaron-pair states. Second, further understanding on how the TTA and triplet-charge reaction generate negative MFEL in steady state is required. Third, it is unclear whether intermolecular SOC should be considered in the MFEL. We know that random electron and hole capture generates four polaron-pair states with 25% fraction for each state: one singlet  $[(e-h)^1]$  and three triplet  $[(e-h)_{m=1}^1, (e-h)_{m=0}^3, (e-h)_{m=-1}^3]$  based on spin statistics, if spin correlation is absent. The polaron pairs, regarded as intermolecular excited states, can evolve into intramolecular excited states: Frenkel excitons as the electron-hole separation decreases due to Coulombic attraction. Spin selection rule allows only singlet emission, leading to electrofluorescence. However, electrophosphorescence resulting in triplet emission can be observed when strong SOC exists to flip electron spins. Clearly, we should carefully examine electrofluorescence- and electrophosphorescence-based MFEL in order to further discuss these three fundamental issues.

#### 4.4.1 Electrofluorescence-Based MFEL

Electrofluorescence-based MFEL can be readily observed in common organic semiconducting materials (Figure 4.7a). The light-emitting singlet exciton ratio can be changed by an external magnetic field either through spin-dependent electron-hole pairing during the formation of excited states or the postelectronic processes after the formation of excited states. If electron-hole pairing is spin-dependent in the formation of polaron pairs, negative MFEL can be observed because an applied magnetic field, when stronger than internal magnetic interaction, tends to align electron and hole with parallel spin orientation for triplet formation. It should be particularly noted that the formation of polaron pairs can result from injected

**FIGURE 4.7**

MFEL and MFEL tuning. (a) MFEL for various organic semiconducting materials. (b) Tuning MFEL from positive to negative value by adjusting bipolar charge injection toward unbalanced state through using thin insulating PMMA layer. (From Hu, B., *Adv. Mater.*, 21, 1, 2009. With permission.)

electrons and holes, namely primary charge carriers, or regenerated electrons and holes from dissociation and charge reaction in excited states, namely, secondary charge carriers. Therefore, the polaron pairs can be divided into primary and secondary types. Published results have shown that negative MFEL can be observed when two unbalanced electrodes are used for electron and hole injection [62]. This experimental result implies that unbalanced bipolar electron and hole injection leads to negative MFEL at low magnetic field. We found that the electrofluorescence-based MFEL clearly changes from positive to negative value when the bipolar electron and hole injection is adjusted toward unbalanced state by reducing the hole injection through increasing the insulating PMMA layer thickness in  $\text{Alq}_3$ -based light-emitting diode (Figure 4.7b). It is noted that unbalanced bipolar charge injection reduces the electron–hole pairing product for the formation of polaron pairs and excitons, and therefore increases the triplet exciton–charge reaction in organic light-emitting diodes [64]. The relevant outcome of triplet exciton–charge reaction is the generation of secondary electrons and holes by destroying the bound electron–hole pairs in excitonic states. The secondary electrons and holes can recapture to form polaron pairs with singlet and triplet configurations due to Coulombic attraction, generating secondary polaron pairs. It should be particularly noted that the secondary electrons and holes are captured at much short distances after the exciton–charge reaction as compared to the charge capture from primary electrons and holes injected from electrodes. In the first-order approximation, it can be assumed that the primary and secondary polaron pairs are formed from long- and short-distance charge captures, respectively. As a result, the EL can consist of two contributions from primary and secondary charge captures. The MFEL can then be divided into primary and secondary components, as shown in Equation 4.2:

$$\text{MFEL} = \text{MFEL}_{\text{Primary}} + \text{MFEL}_{\text{Secondary}} \quad (4.2)$$

It can be assumed that the secondary electrons and holes can experience spin correlation in the short-distance charge capture as compared to the primary electrons and holes in long-distance charge capture. An external magnetic field can interfere with the spin correlation and consequently change the singlet and triplet formation ratios in secondary polaron-pair states. This can lead to formation-based negative MFEL due to secondary charge capture. On the other hand, the singlet-triplet ISC in secondary polaron-pair states can be insensitive to applied magnetic field because of the large energy difference between singlet and triplet levels caused by spin-exchange interaction at short electron-hole separation distance. The ISC-based MFEL should be then negligible in the EL generated from the short-distance charge capture of secondary electrons and holes. As a result, the overall  $\text{MFEL}_{\text{Secondary}}$  should be negative. In contrast, the long-distance charge capture of primary electrons and holes experience negligible spin interaction during the formation of polaron pairs. The absence of spin interaction implies that an external magnetic field has little influence on the singlet and triplet formation ratios in primary polaron-pair states. This leads to unappreciable formation-based MFEL due to primary charge capture. However, the long electron-hole capture distance allows the singlet-triplet ISC in primary polaron-pair states to be magnetic field sensitive, generating ISC-based positive MFEL. Therefore, the overall  $\text{MFEL}_{\text{Primary}}$  should be positive. The observed MFEL combining  $\text{MFEL}_{\text{Primary}}$  and  $\text{MFEL}_{\text{Secondary}}$  can yield the positive and negative components. Changing the balancing degree of bipolar electron and hole injection can modify the relative ratio between  $\text{MFEL}_{\text{Primary}}$  and  $\text{MFEL}_{\text{Secondary}}$  and consequently lead to a tuning in MFEL between positive and negative values, as shown in Figure 4.7b.

In addition, the photoluminescence study has found that TTA can lead to a negative MFPL based on time-resolved measurement of delayed fluorescence. However, in steady state the PL independence of magnetic field [65,66] has suggested that TTA should have unappreciable contribution to MFEL. Furthermore, if the TTA is the governing mechanism for the negative MFEL, adjusting bipolar injection toward unbalanced state would generate a positive MFEL because an unbalanced bipolar injection can largely consume triplet excitons by having charge reaction and therefore reduce the TTA probability. This is inconsistent with experimental results where unbalanced bipolar injection corresponds to a negative MFEL. Therefore, the experimental result of bipolar injection-dependent MFEL does not suggest that the TTA has significant contribution to negative MFEL at low field in steady state.

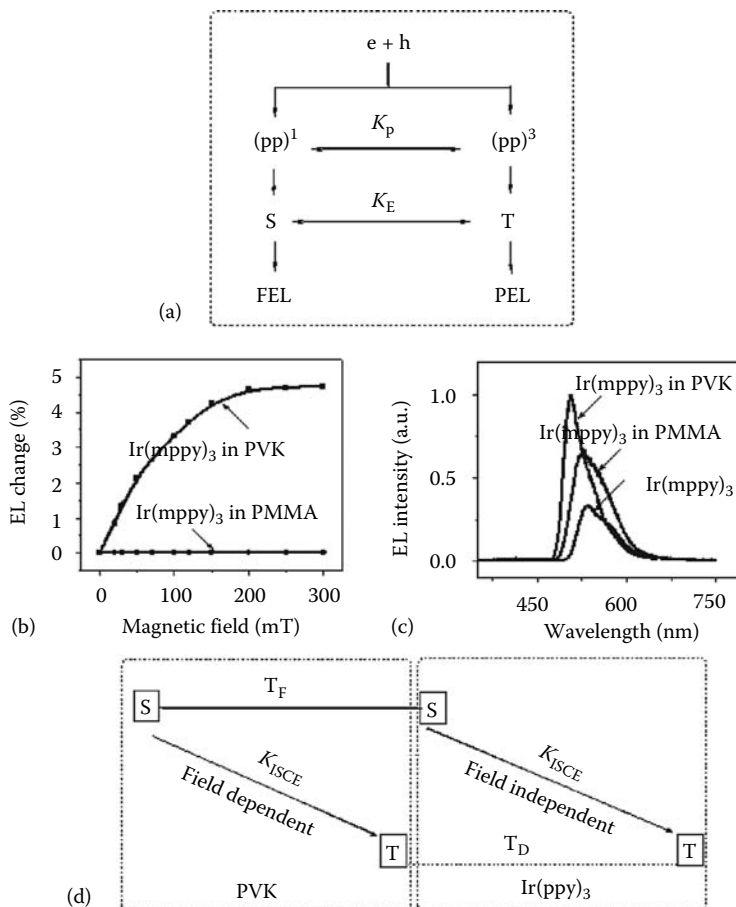
#### 4.4.2 Electrophosphorescence-Based MFEL

Electrophosphorescence results from triplet emission in excitonic states activated by strong SOC. The strong SOC requires heavy-metal complex structures to increase the internal magnetic interaction between electron spins and orbital magnetic field. It is noted that the use of heavy-metal complex

increases not only intramolecular SOC but also intermolecular SOC in phosphorescent materials. In contrast, fluorescent materials such as most organic semiconducting materials have very weak intermolecular magnetic interaction mainly resulting from hyperfine coupling. A low magnetic field can compete with the weak internal magnetic interaction and modify the singlet and triplet ratios in polaron-pair states, leading to positive MFEL based on electrofluorescence. However, it is difficult to generate MFEL based on electrophosphorescence when intermolecular SOC is strong [24].

We note that increasing the intermolecular distance in dilute solid solution can significantly decrease the intermolecular SOC but leaves the intramolecular SOC unchanged in phosphorescent heavy-metal complex molecules. When the intermolecular SOC is sufficiently weakened at certain intermolecular distance, the ISC in polaron-pair states can become sensitive to a low magnetic field by satisfying the two magnetic requirements (Scheme 4.1). As a consequence, an external magnetic field can increase the singlet polaron pairs at the expense of triplet polaron pairs. The change in the singlet and triplet polaron-pair ratios can be reflected as an increase and decrease in singlet and triplet exciton densities, respectively, after polaron pairs evolve into excitons (Figure 4.8a). However, the near 100% ISC in excitonic states, which is magnetic field independent, always convert singlet excitons into triplet excitons. This leads to a negligible change in triplet exciton ratio; even an external magnetic field can change the singlet and triplet polaron-pair ratios after the intermolecular SOC is sufficiently weakened by increasing the intermolecular distance. As a result, it is difficult to generate electrophosphorescence-based MFEL by using molecular dispersion if the excitonic ISC is near 100% in phosphorescent molecules with strong SOC such as iridium complex molecules. It can be seen in Figure 4.8b that dispersing Ir(mppy)<sub>3</sub> molecules into PMMA matrix does not lead to appreciable MFEL based on phosphorescence. In addition, adjusting the balancing degree of bipolar injection at different current densities does not yield phosphorescence-based MFEL in iridium dyes in both pure PMMA blend forms. This means that the TTA and triplet-charge reaction cannot generate any MFEL in strong-spin-orbital-coupling phosphorescent materials. It can be thus suggested that the strong SOC disables phosphorescence-based MFEL when the excitonic ISC is near 100%. However, magnetic field-sensitive ISC in polaron-pair states should yield phosphorescence-based MFEL if the excitonic ISC is not 100% in organic semiconducting materials with intermediate SOC. This scenario can be supported by the phosphorescence-based MFEL observed from the Alq<sub>3</sub> that has considerable SOC strength [63].

It has been experimentally found that electrophosphorescence-based MFEL can be observed when phosphorescent iridium complex molecules are dispersed in an active organic material matrix [24,56]. Figure 4.8b clearly shows that the phosphorescence becomes magnetic-field dependent when the phosphorescent heavy-metal complex iridium (III) tris(2-(4-totyl)pyridinato-N,C2) molecules, named as Ir(mppy)<sub>3</sub>, are dispersed in poly(*N*-vinylcarbazole)

**FIGURE 4.8**

Electroluminescence (EL) processes, MFEL, and energy transfer effects on singlet and triplet excitonic ratios. (a) Electrofluorescence and electrophosphorescence processes. (b) MFEL for 1 wt%  $\text{Ir(mppy)}_3$  dispersed in PVK and PMMA matrices, respectively. (c) EL spectra for pure  $\text{Ir(mppy)}_3$ , 1%  $\text{Ir(mppy)}_3$  dispersed in PMMA, 1%  $\text{Ir(mppy)}_3$  dispersed in PVK. (d) Förster ( $T_F$ ) and Dexter ( $T_D$ ) energy transfer in excitonic states from PVK matrix to  $\text{Ir(mppy)}_3$  dopant together with field-dependent and field-independent excitonic ISCs. (From Hu, B., *Adv. Mater.*, 21, 1, 2009. With permission.)

(PVK) matrix. The respective EL spectra are shown in Figure 4.8c. We know that the singlet and triplet exciton ratios are sensitive to magnetic field through the ISC in polaron-pair states in the PVK matrix under electrical excitation due to the weak SOC. However, an external magnetic field cannot change the singlet and triplet exciton ratios in the  $\text{Ir(mppy)}_3$  molecules due to the strong intraspin-orbital coupling and near 100% excitonic ISC. Furthermore, we note that the energy transfer can occur from PVK matrix to the dispersed  $\text{Ir(mppy)}_3$  molecules through the Förster and Dexter channels

for singlet and triplet excitons, respectively [24]. Because the Förster and Dexter are long and short range processes, the Förster process can dominate the energy transfer from the PVK matrix to the Ir(mppy)<sub>3</sub>. Due to efficient Förster transfer and inefficient Dexter transfer, magnetic field-induced increase of singlet excitons in the PVK matrix can be reflected as an increase of triplet excitons in the dispersed Ir(mpp)<sub>3</sub> molecules in the PVK + Ir(mppy)<sub>3</sub> blend when the ISC in excitonic states is near 100% in the Ir(mppy)<sub>3</sub> molecules (Figure 4.8d). As a consequence, this internal energy transfer can cause phosphorescence-based MFEL when phosphorescent heavy-metal complex molecules are dispersed into active polymer matrix. In essence, this energy transfer-induced MFEL presents a new mechanism to induce MFEs based on electrophosphorescence.

---

## 4.5 Magnetic Field Effects on Injection Current: Magnetoresistance

The EL studies have shown that a low external magnetic field can increase the electrical injection current in nonmagnetic organic Alq<sub>3</sub>-based light-emitting diode [61]. It was reported that the injection current gradually increases up to about 2% with applied magnetic field and becomes saturated at around 300 mT. The MFEs of electrical injection current were also observed by using different electrode materials in Alq<sub>3</sub> [62]. This phenomenon was then named as organic magnetoresistance (OMA) [67,68]. These experimental findings have clearly indicated that nonmagnetic organic semiconducting materials can have significant magnetic response in electrical injection current. Scientifically, understanding of OMA can reveal intrinsic magnetic field-sensitive charge generation and transport processes in nonmagnetic organic semiconducting materials. Technically, the magnetoresistance presents unique possibilities to use common nonmagnetic organic semiconducting materials for magnetic electronic devices.

We know that the electrical injection current is determined by both potential-barrier height and thicknesses at respective electrode interfaces in organic light-emitting diodes based on tunneling theory [69]. A specific potential barrier is determined by the energy difference between the responsible charge-injecting electronic levels of organic semiconducting material and selected electrode material. With given cathode and anode materials the potential thickness is inversely proportional to applied electrical voltage. When both electrode materials and applied electrical voltage are fixed, the bulk electrical injection current is determined by charge carrier densities and mobilities based on Drude model, given by

$$J = e \cdot n \cdot \mu \quad (4.3)$$

where

$J$  is the bulk injection current

$e$  is the charge of an electron

$n$  and  $\mu$  are charge density and charge mobility, respectively

Because both electrodes and organic semiconducting materials are nonmagnetic, the magnetoresistance (MR) requires that charge density or charge transport must be sensitive to the applied magnetic field in bulk organic semiconducting materials. This reasoning suggests that magnetoresistance phenomenon can be developed through two different channels based on the charge density or charge transport, respectively, as described by Equation 4.4.

$$\text{MR} = \text{MR}(n) + \text{MR}(\mu) \quad (4.4)$$

In general, the bulk charge density can be sensitive to applied magnetic field when the secondary charge carriers generated from magnetic field-sensitive singlet and triplet excited states are counted. On the other hand, the charge transport can be magnetic field sensitive if (1) different types of charge carriers exist, (2) different types of charge carriers have low and high mobilities, and (3) interconversions between different types of charge carriers are magnetic field sensitive. In principle, organic semiconducting materials can exhibit excited states-based magnetoresistance and charge transport-based magnetoresistance.

#### 4.5.1 Excited States-Based Magnetoresistance

The experimental results have shown that the magnetoresistance dramatically increases when the electrical injection current is approaching the bipolar injection threshold to realize excited states [70–78]. This provides direct evidence to show that excited states are largely involved in magnetoresistance to change the total charge density by generating secondary charge carriers in organic semiconducting materials under the influence of applied magnetic field. It is noted that the secondary charge carriers can be generated through two different magnetic field-sensitive channels: dissociation [42,63,79–81] and charge reaction [19,39,82–85] in excited states. It has been experimentally shown that the dissociation and charge reaction form two major channels to generate photocurrent in organic materials under photoexcitation [45]. Because of different binding energies and lifetimes, singlet and triplet excited states can have different contributions to the dissociation and charge reaction in the generation of secondary charge carriers. As a consequence, magnetic field-dependent singlet and triplet ratios can lead to negative and positive magnetoresistance based on dissociation and charge reaction in organic semiconducting materials [25,71,72,86,87]. Specifically, the secondary charge generation consists of dissociation dominated by polaron pairs due to their low binding energies and exciton-charge reaction dominated by triplet excitons due to long triplet lifetimes for sufficient physical contact with charge

carriers. In the dissociation channel, the singlet polaron pairs have relatively larger dissociation rates as compared to triplet polaron pairs because singlet polaron pairs can more effectively interact with localized electrical polarization field for dissociation due to their ionic characteristics [42,47]. As a consequence, an external magnetic field can increase the dissociation in polaron-pair states by increasing the singlet polaron-pair ratio through field-dependent ISC  $K_{ISCP}$  in the generation of secondary charge carriers, leading to negative magnetoresistance ( $-MR_S$ ) (Figure 4.9a). On the other hand, an external magnetic field can decrease the triplet-charge reaction by reducing triplet exciton density or charge reaction-rate constant [88]. Therefore, an external magnetic field can decrease the secondary charge generation through triplet-charge reaction channel, yielding positive magnetoresistance ( $+MR_T$ ) (Figure 4.9a). The observed overall magnetoresistance should reflect the combination of dissociation-induced negative magnetoresistance ( $-MR_S$ ) and charge reaction-related positive magnetoresistance ( $+MR_T$ ).

The proposed magnetoresistance theory involving dissociation and charge reaction indicates that adjusting the relative ratio between negative  $-MR_S$  and positive  $+MR_T$  can lead to a substantial tuning of overall magnetoresistance between positive and negative values. Essentially, tuning magnetoresistance requires the modification on the contributions of dissociation and charge reaction to the generation of secondary charge carriers. There are two ways to relatively change the dissociation and charge reaction in organic light-emitting diodes: adjusting the balancing degree of bipolar

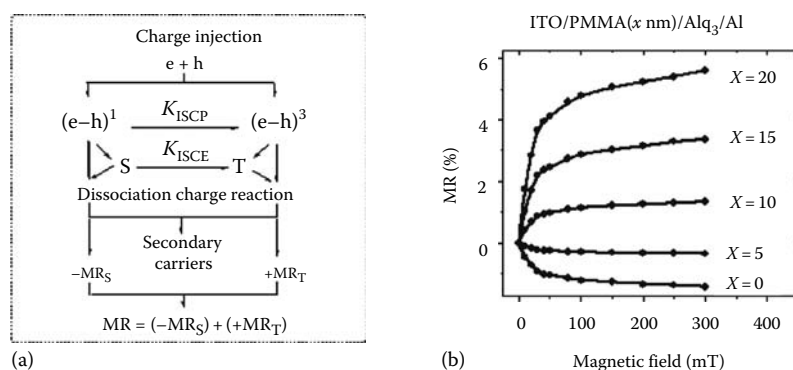


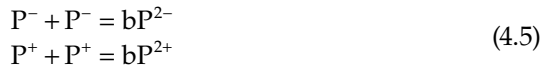
**FIGURE 4.9**

Magnetoresistance generation and tuning. (a) Schematic diagram for positive and negative magnetoresistance components  $-MR_S$  from the dissociation dominated by singlet excited states and  $+MR_T$  from the charge reaction dominated by triplet excited states.  $(e-h)^1$  and  $(e-h)^3$  are singlet and triplet intermolecular e-h pairs. S and T represent singlet and triplet excitons.  $K_{ISP}$  and  $K_{ISC}$  are ISC in e-h pair and excitonic states, respectively. (b) Tuning magnetoresistance from negative to positive value by adjusting bipolar injection toward unbalanced state through using hole-blocking PMMA layer in the double-layer Alq<sub>3</sub>-based light-emitting diode of ITO/PMMA( $x$  nm)/Alq<sub>3</sub>(80 nm)/Al. (From Hu, B. and Wu, Y., *Nat. Mater.*, 6, 985, 2007. With permission.)

charge injection or changing the applied electrical field. First, changing the balancing degree of bipolar injection can modify the electron–hole pairing product toward the formation of excited states and cause the excessive charge carriers to alter the exciton-charge reaction. Specifically, the dissociation in polaron-pair states can become a dominated process at balanced bipolar injection while the exciton-charge reaction is enhanced at unbalanced bipolar injection in the generation of secondary charge carriers. As a consequence, changing bipolar charge injection can lead to magnetoresistance tuning between positive and negative values [25]. In addition, varying the applied electrical field can change the electrical force for the dissociation in polaron-pair states and the physical contact probabilities between long-lifetime triplet excitons and charge carriers for triplet-charge reaction. Therefore, tuning magnetoresistance with positive and negative signs can be expected by adjusting applied electrical field in organic light-emitting diodes [72]. Figure 4.9b shows that the magnetoresistance clearly changes from negative to positive values when the bipolar charge injection is adjusted toward unbalanced state by increasing the hole injection-blocking PMMA layer thickness in the double-layer Alq<sub>3</sub>-based organic light-emitting diode of ITO/PMMA( $x$  nm)/Alq<sub>3</sub>(80 nm)/Al. As a result, using magnetic field-dependent excited processes in polaron-pair dissociation and exciton-charge reaction presents a unique pathway to obtain excited states-based magnetoresistance from nonmagnetic organic semiconductor devices.

#### 4.5.2 Charge Transport-Based Magnetoresistance

It has been experimentally reported that OMA can be observed in organic light-emitting diodes when only single-carrier charge injection is realized by using different electrode materials [89,90]. These experimental findings indicate that magnetic field-dependent charge transport can be developed in nonmagnetic organic semiconductor devices. Based on the fact that single-carrier charge injection does not generate excited states in organic semiconducting materials, the single carrier-generated magnetoresistance can be named as charge transport-based magnetoresistance. It is further noted that an external magnetic field cannot change charge mobilities in nonmagnetic materials. As a result, one can reasonably assume that (1) singlet charge injection forms different types of charge carriers with magnetic field-dependent intertype conversions and (2) the different types of charge carriers have low and high mobilities in organic semiconducting materials. We know that injected charge carriers strongly interact with lattice vibrations, forming charged polarons in organic materials [91]. Particularly, optical absorption has shown that both polarons and bipolarons can exist under electrical excitation [92]. The relevant interconversions are given in Equation 4.5, where P<sup>-</sup> and P<sup>+</sup> are negative and positive polarons, and bP<sup>2-</sup> and bP<sup>2+</sup> represent negative and positive bipolarons. It can be assumed that charge polarons and bipolarons have high and low mobilities due to their different lattice distortions, respectively.



Based on spin-dependent interconversion between polarons and bipolarons, it was proposed that an external magnetic field can change the bipolaron density and consequently affect the overall charge transport in nonmagnetic semiconducting materials [93]. Specifically, bipolarons can be formed with both singlet and triplet configurations. An external magnetic field can compete with internal magnetic interaction from hyperfine or SOC and then reduce the electron spin flip. As a consequence, the total bipolaron density becomes a function of applied magnetic field. Because polarons and bipolarons have different mobilities, magnetically changing the polaron and bipolaron densities essentially lead to positive and negative magnetoresistance in organic semiconducting materials. This proposed bipolaron mechanism can also apply to excited states-based magnetoresistance under bipolar charge injection. Nevertheless, it can be suggested that the single carrier-based magnetoresistance is determined by (1) the coexistence of different types of charge carriers, (2) magnetic field-dependent intertype conversions, and (3) low and high mobilities of different types of charge carriers.

It is clear that the recently discovered magnetic field-dependent injection current demonstrates a novel phenomenon: magnetoresistance from non-magnetic organic semiconductor devices. The understanding of both bipolar and unipolar injection-based magnetoresistance can reveal the fundamental mechanisms of magnetic field-dependent excited states and charge transport. On the other hand, the magnetoresistance presents as a powerful tool to experimentally visualize charge capture, charge generation, and charge transport in the intermolecular and intramolecular excited states in light-emitting and photovoltaic devices.

## 4.6 Conclusion

It has been experimentally found that nonmagnetic organic semiconducting materials can have significant responses to a low magnetic field in electroluminescence, photoluminescence, photocurrent, and electrical injection current. The current studies have indicated that the intrinsic excited states and related charge transport are sensitive to magnetic field due to electron spin multiplicities. Specifically, an external magnetic field can change singlet and triplet ratios in excited states through two possible processes: (1) spin-dependent electron–hole pairing toward the formation of excited states and (2) interconversions between singlet and triplet excited states. Because singlets and triplets have different contributions to excited state-excited state interaction,

dissociation of excited states, and excited state–charge reaction, an external magnetic field can influence electroluminescence, photoluminescence, photocurrent, and electrical injection current, leading to MFEs in nonmagnetic organic semiconducting materials. Essentially, whether singlet and triplet ratios in excited states can be changed by applied magnetic field determines whether MFEs can be observed. The photoluminescence dependence of magnetic field from intermolecular excited states together with the photoluminescence independence of magnetic field from intramolecular excited states in steady state clearly suggests that the electron–hole separation distance and its related spin–exchange interaction in excited states are the main factors that determine MFEs. At long electron–hole separation and weak exchange interaction, ISC becomes magnetic field sensitive in intermolecular excited states, which is accountable for primary MFEs. At short electron–hole separation distance and strong exchange interaction, secondary MFEs may be observed by involving intramolecular exitonic processes: TTA and triplet–charge reaction. The magnetic field dependence of photocurrent indicates that the intermolecular excited states (polaron pairs) correspond to positive MFE based on dissociation. The intramolecular excitons give rise to negative MFE based on exciton–charge reaction. The magnetic field dependence of electroluminescence shows that the electron–hole separation distance at charge capture for the formation of excited states determines whether an external magnetic field can change singlet and triplet ratios in excited states through electron–hole pairing and ISC. At long-distance electron–hole capture, the ISC is the dominant mechanism responsible for positive MFE. However, at short-distance electron–hole capture the spin-dependent electron–hole pairing plays an important role in the determination of negative MFE. Magnetic field-dependent injection current (magnetoresistance) confirms that the intermolecular excited states with long electron–hole separation distance and the intramolecular excited states with short electron–hole separation distance have positive and negative contributions to the generation of charge carriers through dissociation and charge reaction, respectively. As a result, the MFEs can be attributed to both electron–hole separation distance-dependent spin interaction and ISC in organic semiconducting materials.

Although spin-dependent electron–hole pairing, magnetic field-dependent ISC, and related excited processes demand further experimental and theoretical investigations, it is clear that magnetic field-dependent excited processes form a unique mechanism to obtain magnetic responses in electroluminescence, photoluminescence, photocurrent, and electrical injection current from nonmagnetic organic semiconducting materials. We can envision that these interesting MFEs can lead to new potential applications to use nonmagnetic organic semiconducting materials for magnetic electronic and optical devices. It is also clear that the studies of MFEs can increase the critical understanding of how internal electrical and magnetic interactions affect the formation and postelectronic processes in intermolecular and intramolecular excited states occurring in organic electronic and optical devices.

---

## References

1. J. S. Wilson, A. S. Dhoot, A. J. A. B. Seeley, M. S. Khan, A. Köhler, and R. H. Friend, *Nature* 2001, **413**, 828.
2. M. Wohlgemant, X. M. Jiang, Z. V. Vardeny, and R. A. J. Janssen, *Phys. Rev. Lett.* 2002, **88**, 197402.
3. K. Tandon, S. Ramasesha, and S. Mazumdar, *Phys. Rev. B* 2003, **67**, 045109.
4. S. Karabunarlie and E. R. Bittner, *Phys. Rev. Lett.* 2003, **90**, 057402.
5. U. E. Steiner and T. Ulrich, *Chem. Rev.* 1989, **89**, 51.
6. S. Reineke, K. Walzer, and K. Leo, *Phys. Rev. B* 2007, **75**, 125328.
7. W. Staroske, M. Pfeiffer, K. Leo, and M. Hoffmann, *Phys. Rev. Lett.* 2007, **98**, 197402.
8. A. Mozumder and S. M. Pimblott, *Chem. Phys. Lett.* 1990, **167**, 542.
9. R. G. Kepler, J. C. Caris, P. Avakian, and E. Abramson, *Phys. Rev. Lett.* 1963, **10**, 400.
10. S. Jockusch, H. J. Timpe, W. Schnabel, and N. J. Turro, *J. Phys. Chem. A* 1997, **101**, 440.
11. G. Grabner, K. Rechthaler, B. Mayer, and G. Kohler, *J. Phys. Chem. A* 2000, **104**, 1367.
12. J. Frenkel, *Phys. Rev.* 1938, **54**, 647.
13. L. Onsager, *Phys. Rev.* 1938, **54**, 554.
14. E. L. Frankevich, G. E. Zorinians, A. N. Chaban, M. M. Triebel, S. Blumstengel, and V. M. Kobryanskii, *Chem. Phys. Lett.* 1996, **261**, 545.
15. R. E. Merrifield, *J. Chem. Phys.* 1968, **48**, 4318.
16. R. P. Groff, R. E. Merrifield, A. Suna, and P. Avakian, *Phys. Rev. Lett.* 1972, **29**, 429.
17. A. Köhler and D. Beljonne, *Adv. Funct. Mater.* 2004, **14**, 11.
18. D. Beljonne, J. Cornil, R. H. Frend, R. A. J. Janssen, and J. L. Brédas, *J. Am. Chem. Soc.* 1996, **118**, 6453.
19. V. Ern and R. E. Merrifield, *Phys. Rev. Lett.* 1968, **21**, 609.
20. G. Hüttmann and H. Staerk, *J. Phys. Chem.* 1991, **95**, 4951.
21. R. P. Groff, A. Suna, P. Avakian, and R. E. Merrifield, *Phys. Rev. B* 1974, **9**, 2655.
22. Z. Xu, Y. Wu, and B. Hu, *Appl. Phys. Lett.* 2006, **89**, 131116.
23. Y. Wu, A. Li, J. Howe, J. Shen, and B. Hu, *Phys. Rev. B* 2007, **75**, 075213.
24. Y. Wu, B. Hu, and J. Howe, *Phys. Rev. B* 2007, **75**, 035214.
25. B. Hu and Y. Wu, *Nat. Mater.* 2007, **6**, 985.
26. N. K. Petrov, A. I. Shushin, and E. L. Frankevich, *Chem. Phys. Lett.* 1981, **82**, 339.
27. H. Cao, Y. Fujiwara, T. Haino, Y. Fukazawa, C. H. Tung, and Y. Tanimoto, *Bull. Chem. Soc. Jpn.* 1996, **69**, 2801.
28. H. Cao, K. Miyata, T. Tamura, Y. Fujiwara, A. Katsuki, C. H. Tung, and Y. Tanimoto, *J. Phys. Chem. A* 1997, **101**, 407.
29. F. Ito, T. Ikoma, K. Akiyama, A. Watanabe, and S. Tero-Kubota, *J. Phys. Chem. B* 2005, **109**, 8707.
30. K. Awasthi, M. Mizoguchi, T. Iimori, T. Nakabayashi, and N. Ohta, *J. Phys. Chem. A* 2008, **112**, 4432.
31. M. Mizoguchi and N. Ohta, *Chem. Phys. Lett.* 2003, **372**, 66.
32. E. S. Medvedev, M. Mizoguchi, and N. Ohta, *J. Phys. Chem. B* 2006, **110**, 3938.
33. T. Yoshizawa, M. Mizoguchi, T. Iimori, T. Nakabayashi, and N. Ohta, *Chem. Phys.* 2006, **324**, 26.

34. J. S. Kim, B. W. Seo, and H. B. Gu, *Synth. Met.* 2003, **132**, 285.
35. J. Yang and K. C. Gordon, *Chem. Phys. Lett.* 2003, **375**, 649.
36. M. Reufer, M. J. Walter, P. G. Lagoudakis, A. B. Hummel, J. S. Kolb, H. G. Roskos, U. Scherf, and J. M. Lupton, *Nat. Mater.* 2005, **4**, 340.
37. E. L. Frankevich and E. I. Balabanov, *JETP Lett.* 1965, **1**, 169.
38. E. L. Frankevich and I. A. Sokolik, *Solid State Commun.* 1970, **8**, 251.
39. I. V. Tolstove, A. V. Belov, M. G. Kaplunov, I. K. Yakuschenko, N. G. Spitsina, M. M. Triebel, and E. L. Frankevich, *J. Lumin.* 2005, **112**, 368.
40. E. L. Frankevich, A. A. Lymarev, I. Sokolik, F. E. Karasz, S. Blumstengel, R. H. Baughman, and H. H. Horhold, *Phys. Rev. B* 1992, **46**, 9320.
41. E. Frankevich, A. Zakhidov, K. Yoshino, Y. Maruyama, and K. Yakushi, *Phys. Rev. B* 1996, **53**, 4498.
42. J. Kalinowski, J. Szmytkowski, and W. Stapor, *Chem. Phys. Lett.* 2003, **378**, 380.
43. F. Ito, T. Ikoma, K. Akiyama, Y. Kobori, and S. Tero-Kubota, *J. Am. Chem. Soc.* 2003, **125**, 4722.
44. T. Ikoma, F. Ito, T. Ogiwara, K. Akiyama, and S. Tero-Kubota, *Chem. Lett.* 2005, **34**, 1424.
45. Z. Xu and B. Hu, *Adv. Func. Mater.* 2008, **18**, 2611.
46. Z. Xu, B. Hu, and J. Howe, *J. Appl. Phys.* 2008, **103**, 043909.
47. M. Wohlgemuth and Z. V. Vardeny, *J. Phys.: Condens. Mater.* 2003, **15**, R83.
48. H. D. Burrows, J. Seixas de Melo, C. Serpa, L. G. Arnaut, A. P. Monkman, I. Hamblett, and Navaratnam, *J. Chem. Phys.* 2001, **115**, 9601.
49. H. D. Burrows, M. Fernandes, J. S. Melo, A. P. Monkman, and S. Navaratnam, *J. Am. Chem. Soc.* 2003, **125**, 15310.
50. W. Holzer, A. Penzkofer, and T. Tsuibo, *Chem. Phys.* 2005, **308**, 93.
51. G. Yu, J. Gao, J. C. Hummelen, F. Wudl, and A. J. Heeger, *Science* 1995, **270**, 1789.
52. B. Kraabel, J. C. Hummelen, D. Vacar, D. Moses, N. S. Sariciftci, A. J. Heeger, And F. Wudl, *J. Chem. Phys.* 1996, **104**, 4267.
53. M. Sudhakar, P. I. Djurovich, T. E. Hogen-Esch, and M. E. Thompson, *J. Am. Chem. Soc.* 2003, **125**, 7796.
54. N. Corcoran, A. C. Arias, J. S. Kim, J. D. Mackenzie, and R. H. Friend, *Appl. Phys. Lett.* 2003, **82**, 299.
55. M. Wittmer and I. Zschokke-Grannaher, *J. Chem. Phys.* 1975, **63**, 15.
56. J. Kalinowski, M. Cocchi, D. Virgili, V. Fattori, and P. Di Macro, *Phys. Rev. B* 2004, **70**, 205303.
57. Y. Iwasaki, T. Osasa, M. Asahi, and M. Matsumura, *Phys. Rev. B* 2006, **74**, 195209.
58. H. Odama, Y. Okimoto, T. Yamada, M. Kawasaki, and Y. Tokura, *Appl. Phys. Lett.* 2006, **88**, 123501.
59. R. C. Johnson and R. E. Merrifield, *Phys. Rev. B* 1970, **1**, 896.
60. A. Suna, *Phys. Rev. B* 1970, **1**, 1716.
61. J. Kalinowski, M. Cocchi, D. Virgili, P. Di Macro, and V. Fattori, *Chem. Phys. Lett.* 2003, **373**, 380.
62. A. H. Davis and K. Bussmann, *J. Vac. Sci. Technol. A* 2004, **22**, 1885.
63. J. Wilkinson, A. H. Davis, K. Bussmann, and J. P. Long, *Appl. Phys. Lett.* 2005, **86**, 111109.
64. C. Ganzorig and M. Fujihira, *Appl. Phys. Lett.* 2002, **81**, 3137.
65. B. Hu, Y. Wu, Z. Zhang, S. Dai, and J. Shen, *Appl. Phys. Lett.* 2006, **88**, 022114.
66. Y. Wu, B. Hu, J. Howe, A. Li, and J. Shen, *Phys. Rev. B* 2007, **75**, 075413.

67. T. L. Francis, Ö. Mermér, G. Veeraraghavan, and M. Wohlgenannt, *New J. Phys.* 2004, **6**, 185.
68. Y. Sheng, T. D. Nguyen, G. Veeraraghavan, Ö. Mermér, M. Wohlgenannt, S. Qiu, and U. Scherf, *Phys. Rev. B* 2006, **74**, 045213.
69. I. D. Parker, *J. Appl. Phys.* 1994, **75**, 1656.
70. Y. Wu and B. Hu, *Appl. Phys. Lett.* 2006, **89**, 203510.
71. P. Desai, P. Shakya, T. Kreouzis, W. P. Gillin, N. A. Morley, and M. R. J. Gibbs, *Phys. Rev. B* 2007, **75**, 094423.
72. J. D. Bergeson, V. N. Prigodin, D. M. Lincoln, and A. J. Epstein, *Phys. Rev. Lett.* 2008, **100**, 067201.
73. J. H. Wei, S. J. Xie, L. M. Mei, J. Berkdar, and Y. J. Yan, *Org. Electron.* 2007, **8**, 487.
74. T. H. Lee, T. F. Guo, J. C. A. Huang, and T. C. Wen, *Appl. Phys. Lett.* 2008, **92**, 153303.
75. P. Desai, P. Shakya, T. Kreouzis, and W. P. Gillin, *Phys. Rev. B* 2007, **76**, 235202.
76. P. Shakya, P. Desai, M. Somerton, G. Gannaway, T. Kreouzis, and W. P. Gillin, *J. Appl. Phys.* 2008, **103**, 103715.
77. C. Gärditz, A. G. Mückl, and M. Cölle, *J. Appl. Phys.* 2005, **98**, 104507-1.
78. P. Shakya, P. Desai, T. Kreouzis, and W. P. Gillin, *J. Appl. Phys.* 2008, **103**, 043706.
79. A. Köhler, D. A. dos Santos, D. Beljonne, Z. Shuai, J. L. Bredas, R. H. Friend, S. C. Moratti, and A. B. Holmes, *Synth. Met.* 1997, **84**, 675.
80. J. G. Muller, J. M. Lupton, J. Feldmann, U. Lemmer, M. C. Scharber, N. S. Sariciftci, C. J. Brabec, and U. Scherf, *Phys. Rev. B* 2005, **72**, 195208.
81. J. Szmytkowski, W. Stąpor, J. Kalinowski, and Z. H. Kafafi, *Appl. Phys. Lett.* 2002, **80**, 1465.
82. J. Kalinowski, W. Stąpor, J. Szmytkowski, D. Virgili, M. Cocchi, V. Fattori, and C. Sabatini, *Phys. Rev. B* 2006, **74**, 085316.
83. M. Pope and C. E. Swenberg, *Electronic Processes in Organic Crystals*, 2nd edn., Oxford University Press, Oxford, 1999.
84. M. Wittmer and I. Zschokke-Gränacher, *J. Chem. Phys.* 1975, **63**, 4187.
85. M. S. Meruvia, J. A. Freire, I. A. Hümmelgen, J. Gruber, and C. F. O. Graeff, *Org. Electron.* 2007, **8**, 695.
86. P. Desai, P. Shakya, T. Kreouzis, and W. P. Gillin, *J. Appl. Phys.* 2007, **102**, 073710.
87. F. L. Bloom, W. Wagemans, M. Kemerink, and B. Koopmans, *Phys. Rev. Lett.* 2007, **99**, 257201.
88. C. Doubleday Jr., N. J. Turro, and J. F. Wang, *Acc. Chem. Res.* 1989, **22**, 199.
89. T. D. Nguyen, Y. Sheng, J. Rybicki, and M. Wohlgenannt, *Phys. Rev. B* 2008, **77**, 235209.
90. T. D. Nguyen, Y. Sheng, J. Rybicki, G. Veeraraghavan, and M. Wohlgenannt, *J. Mater. Chem.* 2007, **17**, 1995.
91. W. Graupner, J. Partee, J. Shinar, G. Leising, and U. Scherf, *Phys. Rev. Lett.* 1996, **77**, 2033.
92. K. F. Voss, C. M. Foster, L. Smilowitz, D. Mihailovic, S. Askaris, G. Srđanov, Z. Ni, S. Shi, A. J. Heeger, and F. Wudl, *Phys. Rev. B* 1991, **43**, 5109.
93. P. A. Bobbert, T. D. Nguyen, F. W. A. van Oost, B. Koopmans, and M. Wohlgenannt, *Phys. Rev. Lett.* 2007, **99**, 216801.

# 5

---

## *Interface in Organic Semiconductor Devices: Dipole, Doping, Band Bending, and Growth*

---

**Yongli Gao**

### CONTENTS

5.1	Introduction .....	141
5.2	Experimental Techniques .....	142
5.3	Modeling Metal/Organic Interface Dipole .....	147
5.4	Alkali Doping and Modeling.....	150
5.5	Reversal of Doping-Induced Energy-Level Shift.....	158
5.6	LiF Insertion Layer .....	161
5.7	Organic/Organic Interface Band Bending and Debye Screening .....	167
5.8	Interface Growth Mode and Modeling.....	171
5.9	Summary.....	175
	Acknowledgments .....	177
	References.....	177

---

### 5.1 Introduction

As proven in over five decades of research, the understanding of interfaces has a tremendous impact on semiconductor device technology. In organic semiconductor (OSC) devices, the thickness of the active organic layer is typically only a few hundred angstroms, which further blurs the distinction between the bulk and the interface. At this point, an important distinction must be made between inorganic semiconductors and OSCs. Inorganic semiconductors have occupied and unoccupied energy levels, valence and conduction bands, respectively, that can extend over many unit cells. The semiconductor can be appropriately doped n-type or p-type. The interaction between charge carriers and the lattice is generally weak, and the transport of the charge carriers can be adequately described as delocalized Bloch

waves in the bands. In OSCs, the occupied and unoccupied energy levels for OSCs are formed from planar structures of  $sp^2$  bonds as well as  $\pi$ -bonds, and the  $\pi$ -bonds between carbon atoms in organic molecules usually form the highest occupied molecular orbital (HOMO) and lowest unoccupied molecule orbital (LUMO) in most OSCs. The interactions between the molecules are van der Waals in nature and the electron wave function overlap between the molecules is small. The charge carriers are localized and surrounded by significant nuclear relaxation, and are better described together with the surrounding nuclear deformation as polarons instead of electrons or holes. As a result, the transport from one molecule to another is typically described by the hopping of polarons.

Understanding the interface processes in organic devices is critical for their further advance in performance. The surface and interface analytical studies have generated critical insight of the fundamental processes at interfaces involving OSCs.<sup>1-4</sup> For example, it has now been established from surface analytical studies that the interface energy-level alignment is not from a common vacuum level as previously believed. Instead, it depends on the detailed interface interactions including wave function hyperdization, charge transfer, chemical reaction, and intermixing. Understanding issues regarding metal/organic interfaces, such as the formation of the interface dipole, the injection barrier, the diffusiveness of the interface, and the origin of ionized species, is beginning to take shape. This chapter is intended to introduce the readers to the field by providing some insights on aspects of interfaces in OSCs obtained by using popular interface analytical techniques. These aspects include experimental techniques, modeling the formation of interface dipole, doping and interface electronic structure modification, inserting of thin layers to improve charge injection, band bending, and thin organic film growth.

---

## 5.2 Experimental Techniques

The electronic structure at interfaces with semiconductors is generally described by charting the energy levels, such as the vacuum level, the valence band, and the conduction band, as a function of distance from the interface. There are indirect electrical measurements capable of determining this profile but they generally rely on a theoretical model of the system to determine the general features of the interface with the electrical measurements merely determining the bounds of the energy and spatial values of the profile of the system. The technological success of devices whose performance is dictated by the interface characteristics has driven the development of increasingly sophisticated instrumentation designed to better probe the surface properties. Currently, there exist a large number of surface and interface

analytical tools capable of providing complementary information. The usefulness of these analytic instruments has been proven by their successful application in the study of inorganic semiconductor devices where the interfaces were found to dictate the performance of the device. Many tools have been successfully applied to study organic/metal interfaces, including photoemission spectroscopy (PES), scanning probe microscopy (SPM) and spectroscopy, secondary ion mass spectroscopy (SIMS), near edge x-ray absorption fine structure (NEXAFS), Kelvin probe, internal photoemission, Penning spectroscopy, reflection infrared spectroscopy (RIRS), high-resolution electron energy loss spectroscopy (HREELS), low-energy electron microscopy (LEEM), low-energy electron diffraction (LEED), and temperature-programmed desorption (TPD). In the following sections, we will briefly discuss some of those more frequently used tools for the study of OSCs, including ultraviolet photoemission spectroscopy (UPS), x-ray photoemission spectroscopy (XPS), inverse photoemission spectroscopy (IPES), scanning tunneling microscopy (STM), and atomic force microscopy (AFM).

Photoelectron spectroscopy is based on the photoelectric effect explained by Einstein in 1905; it relies on the creation of photoelectrons via interaction between the irradiating photons and the sample. Since the total energy must be conserved in this process, the kinetic energy,  $E_k$ , imparted to an electron satisfies<sup>5</sup>

$$E_k = h\nu - E_B - \phi \quad (5.1)$$

where

$\phi$  is the work function of the sample

$E_B$  is the binding energy (BE) of the initial state of the electron with respect to the Fermi level

Figure 5.1a schematically summarizes these phenomena. As indicated in Figure 5.1a, photoelectrons originate from energy levels occupied by electrons, including the valence band in inorganic semiconductors or HOMO energy levels for OSCs as well as from core-level states, which correspond to closed atomic shells. PES techniques are customarily named according to the type of photon source used. Most commonly in-house ones are XPS and UPS. In addition to XPS and UPS, synchrotron radiation, which requires expensive central synchrotron facilities, covers photon energies from infrared up to hard x-ray. UPS has been extensively used for studying OSC surface and interfaces. These photons are generated by a He gas discharge lamp, with an energy of 21.2 eV (He I) or 40.8 eV (He II). These low-energy photons are restricted to probing the valence structure of samples. The line width of the UV lamp is small, only about 20 meV, and this allows higher resolution spectra to be measured for the valence levels. Another benefit is that the interactions between these photons and the valence electrons

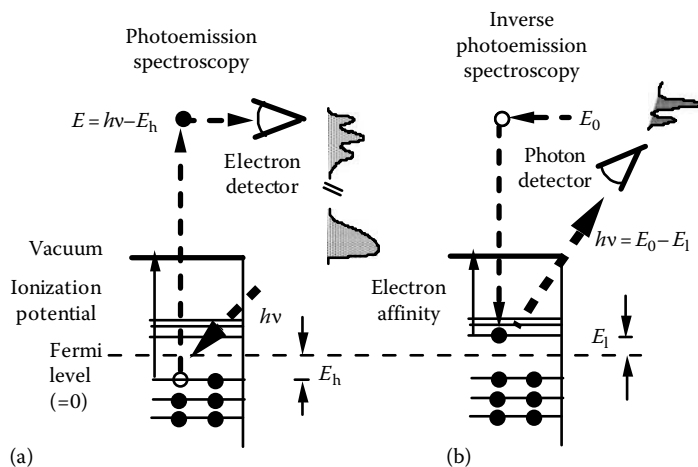


**FIGURE 5.1**  
A schematic representation of (a) PES and (b) IPES.

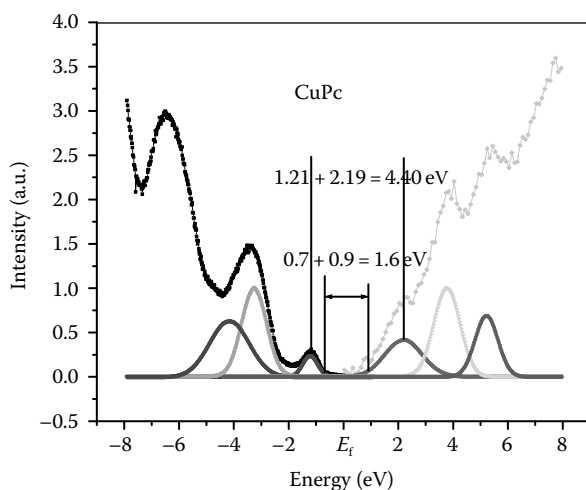
have a higher cross section than with x-rays, allowing improved statistics for these measurements and thereby faster measurements. Finally, UPS is typically less damaging to the sample than XPS, a feature especially valuable to OSCs that are usually vulnerable to photo-induced damages and chemistry.

IPES is time-reversed PES. The schematics of IPES are shown in Figure 5.1b. The surface under investigation is bombarded with electrons of a known kinetic energy, between 0 and 20eV. These incident electrons radiatively decay into unoccupied energy levels. The ejected photons are then measured thus providing a direct measure of the unoccupied energy levels of the surface. There are two methods of performing this experiment. The first is to bombard the surface with electrons of a single kinetic energy and directly measure the spectrum of emitted photons using a spectrometer. The second approach is to vary the kinetic energy of the electrons and measure single photon energy. Given the energies of the incident electrons this technique has approximately the same surface sensitivity as UPS.

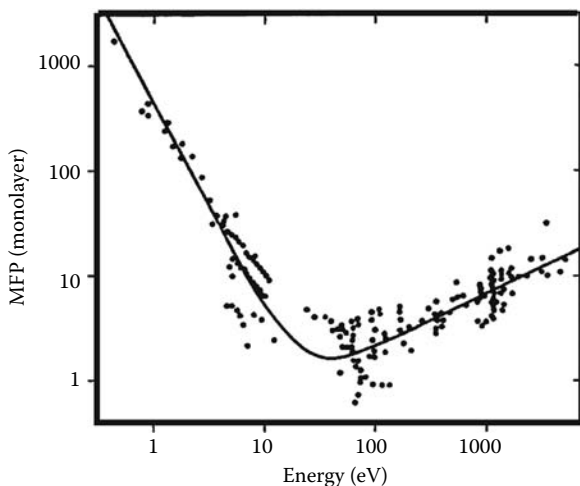
The observed UPS spectrum is the representation of the filled states of a molecular cation resulting from the photoelectric process modified by the relaxation (polarization). The width of the peaks is presumably due to inhomogeneity of the film since the organic film is normally amorphous with random disorder. Therefore, the center of the HOMO peak corresponds to the HOMO energy of the most populous molecular cation, with the emitted photoelectron at infinity (beyond vacuum level). Conceptually, a similar analysis applies to the IPES spectrum. Induced by the injected electron, the relaxation (polarization) of the surrounding medium makes the IPES spectrum the representation of the relaxed anion instead of the neutral state of the

molecule. Thus the energy separation of the HOMO–LUMO peaks obtained by UPS and IPES is the energy difference of relaxed positive and negative polarons separated at infinity, sometimes referred to as polaron energy gap ( $E_p$ ) of the organic material. However, the charge injection into solid does not necessarily occur at the most populous or average species. Rather, when the injection is contact limited [usually the case in organic light-emitting diode (OLED) devices], the charge injects to the molecules with the lowest energy difference to the Fermi level. The onset is defined as the extrapolation of the leading edge (closer to the Fermi level) in spectrum. Similarly, the barrier for the electron injection will be from the Fermi level to the onset of LUMO. In most organic molecular devices, the cathode and the anode are separated far enough so that the injection of hole and electron occurs at different molecules and beyond the size of the polarons. It is a general practice to define the onset of HOMO peak as the HOMO position of the copper phthalocyanine (CuPc) film, at  $-0.7\text{ eV}$ , as shown in Figure 5.2. A similar term is used for the LUMO position, at about  $0.9\text{ eV}$ , for the pristine CuPc film. The result is an injection energy gap ( $E_g$ ) of about  $1.6\text{ eV}$ , interestingly very close to the CuPc optical band gap  $E_{\text{opt}}$  ( $\sim 1.7\text{ eV}$ ).

The surface sensitivity of PES comes from the strong interaction of the photoexcited electron with the rest of the solid, resulting in a relatively short distance, or a mean-free path (MFP), so that it can travel before suffering an inelastic scattering. The MFP depends strongly on the kinetic energy of the photoelectron.<sup>6</sup> The dependence on different materials is relatively minor. The MFP dependence on the kinetic energy has been summarized as the universal curve as shown in Figure 5.3.



**FIGURE 5.2**  
UPS and IPES spectrum of CuPc.

**FIGURE 5.3**

Universal curve of electron MFP in solids. (From Seah, M.P. and Dench, W.A., *Surf. Interface Anal.*, 1, 2, 1979. With permission.)

SPM has transformed into an indispensable tool in the area of science and technology for the study of a whole range of materials properties in the nanoscale regime with very high spatial resolution. SPM with its ever-expanding family enables us to characterize and correlate the materials properties such as topographical, mechanical, optical, electrical, and thermal properties.<sup>7</sup> The basic idea behind SPM techniques is straightforward. There is an interaction parameter (such as the tunneling current in STM; and van der Waals, electrostatic, and capillary forces in AFM) established between the microscope tip and the surface under investigation. The dependence of the interaction parameter on the distance between the probe and the sample is exploited in order to elicit information about the sample, and sometimes the tip. This is done by establishing a feedback mechanism based on the interaction parameter. The ability of STM to achieve atomic resolution is owing to the fact that the tunneling current dependence on the height of the gap (the distance between the tip and the sample) is exponential.

$$I = C \exp(-2\kappa d); \quad \kappa = (2m\phi)^{1/2} \quad (5.2)$$

where

$I$  is the tunneling current

$\kappa$  is the wave function decay constant

$d$  is the separation between the tip and the sample

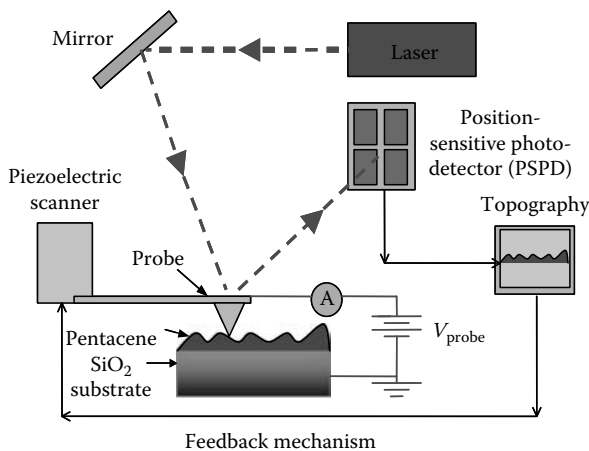


**FIGURE 5.4**  
Schematic diagram of AFM with conducting-probe AFM option.

$m$  is the electron mass

$\phi$  is the work function of the metal substrate (since STM relies on the tunneling current as its interaction mechanism, a sample must be conductive if it is to be operated on by STM)

Today's AFMs mostly use optical detection mechanism. Figure 5.4 shows a schematic drawing of a typical AFM (with conducting-probe option) that is commonplace in laboratories today. A laser beam is reflected off of the back of a cantilever, which has a very small protruding tip facing the surface whose radius of curvature is about  $100\text{ \AA}$ , that is attached to a piezoelectric ceramic scanner. As the cantilever is scanned over a surface, it is deflected up and down due to the local structure of the surface. This bending of the cantilever is detected through the movement of the laser that is reflected from the cantilever and hit the four-quadrant position-sensitive photo detector (PSPD). The level of the deflection is compared, by a computer, to a predetermined set point value. Unlike STM, AFM can be used to measure the topography of insulators and semiconductors, as well as conducting materials. The most dominant force contributing to the deflection of the AFM cantilever is due to the interatomic van der Waals forces.

### 5.3 Modeling Metal/Organic Interface Dipole

Metal/organic interface is a focus of both device engineering and basic science, since it is a key factor in nearly all important aspects of device performances,

including operation voltages, degradation, and efficiency. The complexity of metal/organic interfaces is also intriguing in basic organic condense matter physics. The energy-level alignment and charge injection at the interface are among the most concerned fundamental issues.

The energy-level alignment at the interface involves a number of physical and chemistry processes. In these processes, the most important ones related to the device performances include possible chemical reaction, interface dipole, diffusion, charge transfer, and possible band bending. The vacuum-level alignment (VLA) model is the earliest proposed model.<sup>1</sup> In this model, the vacuum level of metal cathode and indium-tin-oxide (ITO) anode is aligned with that of the organic layer. As a result, the LUMO and HOMO shift inside the organic layer accordingly. Although used widely in the early days of metal/organic studies with mixed results, this simple model has been disapproved by many studies, most persuasively by UPS studies. The most important difference between the interface dipole model and the VLA model is that the interface dipole model states that a dipole layer exists at the metal/organic interfaces. The interface dipole causes an abrupt shift of potentials across the dipole layer, which in turn determines the LUMO and HOMO energy-level alignment with respect to the Fermi level of the metal electrodes. This model has gained support through various UPS and Kelvin probe works.<sup>8</sup>

Several possible mechanisms may contribute to the interface dipole. In their review article,<sup>8</sup> Ishii et al. listed six possible causes, including (a) charge transfer across the interface, (b) image potential-induced polarization of the organic material, (c) pushing back of the electron cloud tail out of the metal surface by the organic material, (d) chemical reactions, (e) formation of interface state, and (f) alignment of the permanent dipole of the organic material. Among these factors, (a)–(c) are more general in metal/organic interfaces, while (d)–(f) are specific to the individual metal/organic pair. These factors provide a plausible foundation to explain qualitatively the interface dipole formation. XPS analysis of the core-level evolution indicates that (b) is unlikely to be a major factor contributing to the interface dipole formation.<sup>9</sup> Should the polarization inside the organic molecule be significant, one would expect that core-level peaks, especially that of the most common carbon atoms, would be broadened due to the intramolecular polarization. This is not generally observed for organic/metal interfaces. In fact, the lack of peak width change indicates that the dipole is predominantly confined to the interface between the metal surface and organic molecules.

Extra care should be taken in calculating the dipole for the case of metal deposited on organic. For organic not undergoing destructive chemical reactions, all the energy levels of the organic should shift the same amount to the first order of approximation, corresponding to the change of the Fermi level in the organic. As a result, the interface dipole is not the vacuum-level shift observed in UPS alone, but the difference between the vacuum-level and the core-level shifts.

Further quantitative understanding of the interface dipole formation can be obtained by realizing that the metal and organic material must reach thermodynamic equilibrium when in contact. Tung devised a model of inorganic semiconductor/metal interface based on charge transfer and thermodynamic equilibrium between the metal and the semiconductor.<sup>10</sup> According to his model, the interface dipole is given by

$$V_{\text{dipole}} = \frac{-ed_{\text{MS}}N_{\text{B}}}{\epsilon_{\text{it}}} \cdot \frac{\Phi_{\text{M}} - (IP - E_g/2)}{E_g + \kappa} \quad (5.3)$$

where

$d_{\text{MS}}$  is the distance between the metal and semiconductor atoms at the interface

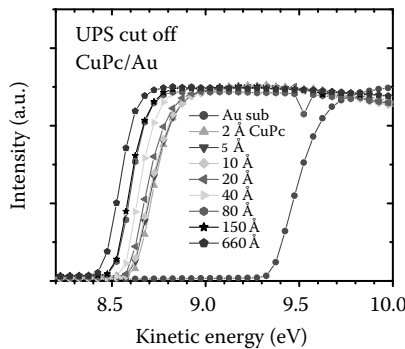
$N_{\text{B}}$  is the density of bonds through which charge transfer takes place

$\epsilon_{\text{it}}$  is the dielectric constant in the interface region

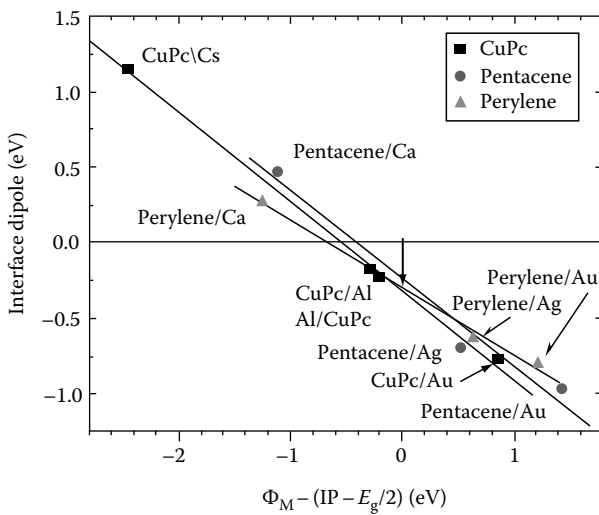
$\kappa$  is the sum of all the Coulombic interactions for charges at different sites

The model suggests that charge transfer is a primary mechanism of Schottky barrier formation, and a good agreement with the experimental results is found for polycrystalline inorganic semiconductors. It should be emphasized that the model is based on the thermodynamic equilibrium of electrons across the interface between the metal and the semiconductor, and is facilitated by the interface bonds. Therefore, it does not depend on the details of the interface reactions, so long as the physical properties of the semiconductor, such as  $IP$  and  $E_g$ , remain intact at the interface. The model does not apply to interfaces where strong chemical reactions result in the domination of the interface by new reacted species.

As an example of organic/metal interface, the cutoff evolution of the UPS spectra of CuPc on Au is shown in Figure 5.5. The cutoff corresponds to the vacuum level of the surface. It is clear that most of the change of the vacuum level (0.8 eV) occurs at the very first layer of 2 Å CuPc. Smaller changes continue when more CuPc is deposited. Most of the additional shift may be attributed to the polarization effect or extended charge diffusion, and is unlikely to be a result of the interface dipole. From Figure 5.5, it can therefore be estimated that the interface dipole is about 0.8 eV at CuPc/Au. Figure 5.6 summarizes the experimental results of the interface dipole measurements of metals with CuPc, pentacene, and perylene.<sup>11</sup> The positive dipole is defined as pointing away from the metal surface. The dipole is plotted as a function of the difference of the metal work function,  $\Phi_{\text{M}}$ , and the energy at the mid-gap of the organic,  $IP - E_g/2$ , where  $IP$  and  $E_g$  are the ionization energy and band gap of the organic, respectively. Despite different  $IP$  and  $E_g$ , all dipoles seem to fall into straight lines with different slopes from -0.6 for CuPc to -0.4 for perylene. Several groups have observed a similar linear dependence on metal work function.<sup>9,11,12</sup>

**FIGURE 5.5**

Determination of interface dipole at CuPc/Au interface from the vacuum-level cutoff of UPS spectra. (From Yan, L. et al., *Appl. Phys. Lett.*, 81, 2752, 2002. With permission.)

**FIGURE 5.6**

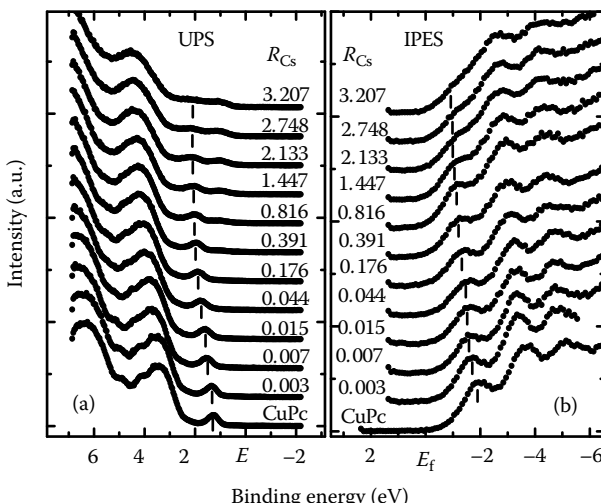
Linear relation between interface dipole and the metal work function. The difference of metal work function  $\Phi_M$  and the mid-gap ( $IP - E_g/2$ ) vs. the interface dipole. (From Yan, L. et al., *Appl. Phys. Lett.*, 81, 2752, 2002. With permission.)

## 5.4 Alkali Doping and Modeling

Doping is used to improve OSC devices, analogous to that in inorganic semiconductors. Doping in OLEDs is a widely used method to convert the emission wavelength and to improve the efficiency. For alkali metal/organic

interface, doping of organic materials often causes significant energy-level shift in these materials and it is of both fundamental and practical interest. Kido and Matsumoto reported that doping of tris (8-hydroxyquinoline) aluminum ( $\text{Alq}$ ) with Li near the cathode interface significantly improved the device performance, and the highest luminescence was observed with the ratio  $\text{Li}/\text{Alq} = 1$  (atom/molecule).<sup>13</sup> Lous et al. and Heller et al. observed that doping of C<sub>60</sub> can result in the Schottky barrier formation.<sup>14,15</sup> Yang and Heeger<sup>16</sup> and Antoniadis and coworkers<sup>17</sup> successfully used doped polyaniline as a buffer layer between the anode and a hole transport layer, which results in efficient suppression of leakage currents. Alkali metals, which can be easily used as electron donors, are good candidates for prototypical studies due to their simple electronic structures and low electron affinity. Several groups have investigated alkali metal doping in commonly used OSCs, such as CuPc,<sup>18,19</sup> Alq,<sup>20,21</sup> and perylene-3,4,9,10-tetracarboxylic-dianhydride (PTCDA).<sup>22,23</sup> The experimental results suggest that doping of alkali metals in OSCs induces energy-level shift due to electron donation from the outmost s orbital.

CuPc is one of the most widely used molecules in both fundamental researches and technological applications.<sup>19,24,25</sup> It has an optical gap of 1.6 eV,<sup>19</sup> which is of great interest for visible absorption, and a transport gap of 2.3 eV,<sup>26</sup> which is very useful in electronic devices. The evolution of the electronic structure of Cs:CuPc for both the HOMO region and the LUMO region is plotted in Figure 5.7 as a function of Cs doping ratio  $R_{\text{Cs}}$ , the Cs atom to CuPc molecule ratio, which is obtained from the XPS core-level intensities.<sup>27</sup> For

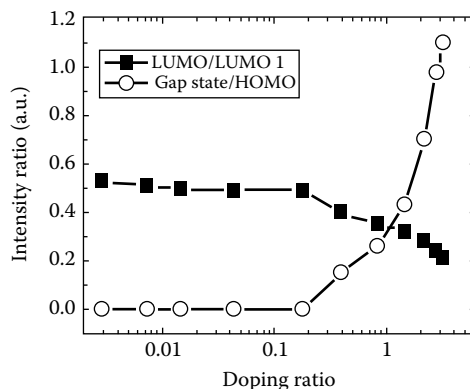


**FIGURE 5.7**

Evolution of the HOMO (a) and the LUMO (b) region in the UPS and IPES spectra of Cs:CuPc, as a function of Cs doping ratio  $R_{\text{Cs}}$ , derived from XPS core-level intensities. (From Ding, H. and Gao, Y., *Appl. Phys. Lett.*, 92, 053309, 2008. With permission.)

$R_{\text{Cs}} < 0.8$ , a monotonic shift toward high BE can be observed for all the features in the UPS spectra, which is in good agreement with our previous studies of alkali metal doping in OSCs.<sup>19</sup> It is interesting that the IPES spectra show a similar shift for the low doping ratios. The amount of the shift for the LUMO at  $R_{\text{Cs}} = 0.8$  is identical to that of the HOMO, which confirms the previous assumption of rigid shift.<sup>21</sup> It suggests that the electronic structure of a CuPc molecule is well preserved under low doping ratios, and that the energy-level shift at this stage is mainly due to the Fermi-level shift within the energy gap. Another issue worth mentioning is that, due to the downward shift and the doping-induced broadening, the position of the LUMO onset in the IPES spectrum is very close to the Fermi level at this doping level. For more Cs doping, the shift of all energy levels becomes saturated. The saturation of the energy-level shift provides direct evidence for the Fermi-level pinning in heavily doped system, as has been proposed earlier.<sup>19</sup> Although the energy-level shift has saturated, the shape of both the UPS and IPES spectra are significantly modified at higher doping ratios. A new state emerges from the former energy gap in the UPS spectrum, and its intensity increases monotonically as  $R_{\text{Cs}}$  increases. The peak separation between the HOMO and the gap state is about 1.0 eV, which remains the same for all doping ratios. At the same time, the intensity of the CuPc LUMO in the IPES spectra starts to decrease as  $R_{\text{Cs}}$  increases. The increase of the intensity of the gap state, at the expense of that of the LUMO, further confirms the previous assumption that the gap state induced by n-type doping is originated from the filling of the former LUMO in the CuPc molecules.<sup>28</sup> For high doping ratios, the spectral broadening becomes more and more pronounced in both the UPS and IPES. For  $R_{\text{Cs}} = 3.2$ , the HOMO and the gap state are so broad that they almost merge together. Similar broadening can be found in the IPES spectra, where the LUMO becomes too weak to be visually distinguishable. Finally, it should also be noted that no Fermi edge could be observed in the UPS spectra for doping ratios as high as 3.2, indicating a nonmetallic surface.

The intensity evolution of the frontier orbital is shown in Figure 5.8. In this plot, the intensity of the LUMO is calibrated by that of the LUMO + 1 of the same IPES spectrum to remove the uncertainty of the electron flux from measurement to measurement.<sup>27</sup> Similar calibrations have been employed for the intensity ratio between the gap state and the HOMO in UPS. The assumption is that the intensities of the LUMO + 1 and the HOMO remain relatively unchanged since Cs doping involves mainly the modification of the LUMO and the gap state. There is hardly any change in the LUMO intensity at low doping ratios, and it starts to decrease as the gap state rises. At  $R_{\text{Cs}} = 3.2$ , the LUMO intensity has been reduced by 60%. Assuming that the first main feature in the IPES spectra consists of only the LUMO with double degeneracy,<sup>29</sup> it can be deduced that 2.4 electrons have been transferred into a single CuPc molecule. This doping ratio estimated from the LUMO intensity is substantially lower than  $R_{\text{Cs}}$  from the XPS core-level intensities. This discrepancy can partly be attributed to the attenuation of the C 1s core-level intensity

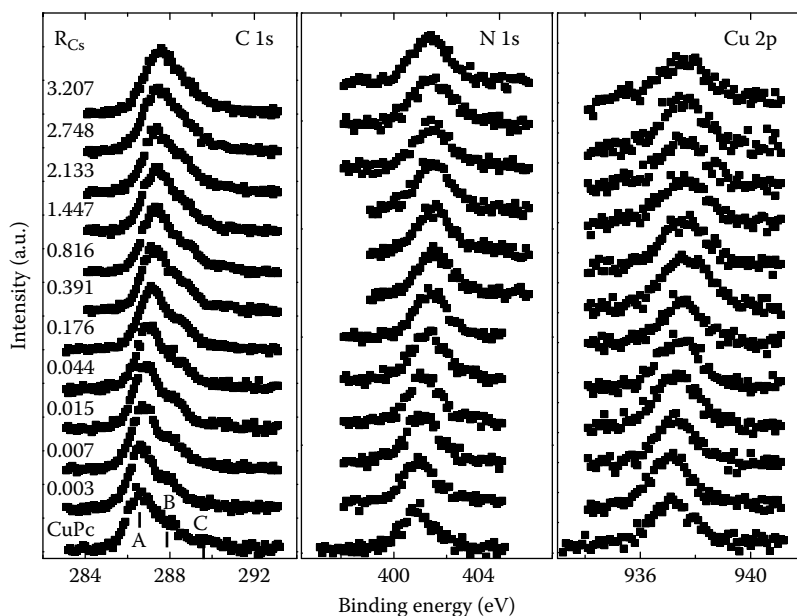
**FIGURE 5.8**

The evolution of the LUMO/LUMO + 1 and the gap state/HOMO intensity ratio of Cs:CuPc as a function of  $R_{Cs}$ . (From Ding, H. and Gao, Y., *Appl. Phys. Lett.*, 92, 053309, 2008. With permission.)

in the XPS spectra at high ratios, as well as possible incomplete ionization of the Cs atoms. The charge transfer amount per molecule can also be estimated from the gap\_state/HOMO intensity ratio. According to the Gaussian fitting, the gap\_state/HOMO intensity ratio at  $R_{Cs} = 3.2$  is derived to be about 1.1. The doping ratio can then be estimated to be 2.2, if one assumes that the HOMO consists of only one orbital. On the basis of these ratios, we suggest that multiple charged CuPc species exist in the heavily doped film. The multiple charged CuPc species must have been stabilized by the nearby  $Cs^+$  counterions, as multiple charging is energetically unfavorable for isolated CuPc molecules.<sup>25</sup>

In Figure 5.9, the XPS spectra of the C 1s, N 1s, and Cu 2p<sub>3/2</sub> core level of Cs:CuPc are presented as a function of  $R_{Cs}$ . The C 1s core level consists of three visible peaks: the first (C 1s(A) as marked in Figure 5.9) can be associated with the aromatic rings of CuPc; the second (C 1s(B)) is due to the pyrrole carbon being in contact with N, with some contribution from the C 1s(A) satellite; and the third (C 1s(C)) is a  $\pi-\pi^*$  satellite feature from the pyrrole carbon.<sup>30</sup> What is immediately evident is that all the three core levels shift toward higher BE as  $R_{Cs}$  increases. However, the shift of Cu 2p<sub>3/2</sub> and N 1s saturate or even reverse slightly as  $R_{Cs}$  increases beyond 0.8, whereas the shift of C 1s does not show any signs of reversion. Another important feature is that while the shapes of the Cu and N core levels remain more or less the same, the three components of C 1s at higher Cs doping ( $R_{Cs} \geq 2.7$ ) merge into one broad and asymmetric peak. The different behaviors of the core levels at higher doping levels indicate that the electronic structure of CuPc is significantly modified at this stage.

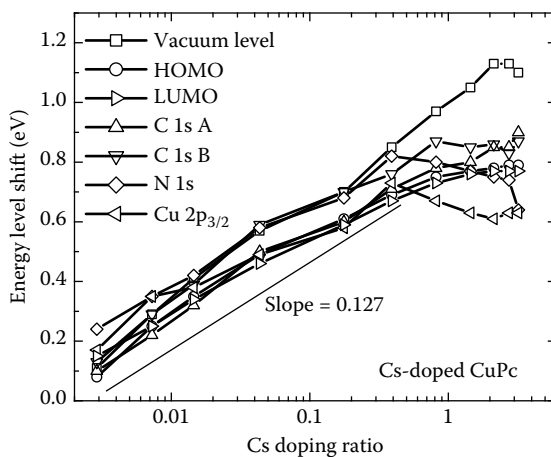
The evolution of the core levels in alkali metal-doped CuPc turns out to be a general behavior, as similar results can be found in Na-doped CuPc.

**FIGURE 5.9**

XPS spectra of C 1s, N 1s, and Cu 2p<sub>3/2</sub> core level as a function of the doping concentration  $R_{Cs}$ , the Cs atom to CuPc molecular ratio, calculated from the XPS core-level intensities. The three components of C 1s for pristine CuPc is noted by short bars.

However, more significant modifications are found in the core levels of Cu 2p<sub>3/2</sub> when the CuPc film is intensively doped by Na.<sup>31</sup> For  $R_{Na} > 4$ , a new component appears at lower BE of Cu 2p<sub>3/2</sub>, and its intensity increases with further increases in  $R_{Na}$ . The energy separation between these two peaks is about 2.0 eV, which is consistent with the energy separation between Cu<sup>2+</sup> and Cu<sup>+</sup>. This indicates that at high Na doping ratios, strong chemical interactions take place due to the addition of the excess electrons into the CuPc molecular orbits, resulting in a reduction from Cu<sup>2+</sup> to Cu<sup>+</sup> by charge transfer and a multiply charged CuPc anion.

For Cs-doped CuPc, the energy-level shifts can be summarized as shown in Figure 5.10. The vacuum-level cutoff was obtained at the maximum of the differential curve of the UPS spectrum. The HOMO and the LUMO were determined by the extrapolation of the leading edge in the UPS and IPES spectra, respectively. The core-level shifts were deduced by fitting the spectra with Gaussian curves for C 1s, N 1s, and Cu 2p<sub>3/2</sub>. The C 1s core level consists of two main components: the leading peak C 1s A, which can be associated with the aromatic carbon of the benzene rings, and the second peak C 1s B, which is due to the pyrrole carbon in contact with N.<sup>30</sup> Note that  $R_{Cs}$  is in logarithmic scale to emphasize the initial shift. The energy-level shift induced by Cs doping can be seen in two stages. At the first stage

**FIGURE 5.10**

The energy-level shift of Cs-doped CuPc as a function of  $R_{\text{Cs}}$ . Note that  $R_{\text{Cs}}$  is in logarithmic scale to emphasize the initial shift.

when the Cs doping ratio is below 0.8, all energy levels shift simultaneously and linearly in the semi-log plot. By linear fitting, the slope of the energy-level shift can be estimated to be 0.127 eV, which is more than four times  $k_{\text{B}}T$  (0.026 eV), a value that is dictated by the classical theory for inorganic semiconductors.<sup>32</sup> One should also note that at this stage, the amounts of the shift for all the energy levels are very close, especially for that of the HOMO and the LUMO. This suggests that the rigid shift assumption is still valid under low doping ratios. As the doping ratio increases, the modification of the CuPc electronic structure moves into a second stage, which is characterized by diverse behaviors for different energy levels. For the frontier orbital, the HOMO and the LUMO shift simultaneously, while the vacuum level shifts much further toward high BE. For the core levels, a reversal of the energy-level shift is observed for N 1s, Cu 2p<sub>3/2</sub>, and C 1s B, which can be attributed to the correlation effect as the donated electrons start to alter the electronic structure of CuPc. The reversal shift for the core levels coincidentally occurs with the appearance of the gap state in the occupied region and the reduction of the LUMO in the unoccupied region, which further corroborates the explanation provided earlier.

Such a two-stage doping process can also be found in other alkali metal-doped OSCs. The slope of the line drawn from the first several data points is 0.28 eV for Cs-doped Alq, which is even larger than that of the Cs-doped CuPc. The slope of Na-doped Alq deduced from cutoff data is 0.22 eV, which is noticeably smaller than the case of Cs doping. Both samples show a saturation of the energy-level shift, as well as a reverse shift for some of the core levels. At the same time, the electronic structure of Alq has been significantly modified, which is evident by the appearance of the gap state and the splitting of the N 1s core level.

The difference between Na and Cs doping in Alq may arise from the fact that the electron affinity of Na (0.55 eV) is larger than that of Cs (0.47 eV).<sup>33</sup> As a result, the ionization of Na is less complete than that of Cs, resulting in some neutral Na capable of further chemical reaction with the O in Alq. Such delayed reaction after the initial charge transfer has also been observed previously in Ca/Alq.<sup>34</sup> Incomplete ionization may also have contributed to the smaller slope in comparison with Cs-doped Alq.

The energy-level dependence on the doping density in OSC is fundamental for understanding the interaction between the dopant and the host system. In an inorganic semiconductor, the electron concentration is given by<sup>32</sup>

$$n = \int d\epsilon D(\epsilon) f_{FD}(\epsilon) \quad (5.4)$$

where

$D(\epsilon)$  is the electron density of states

$f_{FD}(\epsilon)$  is the Fermi–Dirac distribution

For most crystalline inorganic semiconductors,  $D(\epsilon)$  is broad and smooth in comparison with  $k_B T$ , and in the nondegenerate limit Equation 5.4 leads to

$$n = N_C \exp\left[\frac{-(\epsilon_C - \epsilon_F)}{k_B T}\right] \quad (5.5)$$

where

$\epsilon_F$  is the Fermi level

$\epsilon_C$  is the conduction band minimum

$N_C$  is the quantum concentration of the given material

If the doping density,  $N_D$ , is much larger than the intrinsic carrier concentration and if one assumes full ionization, the Fermi-level position can be deduced as

$$\epsilon_F = \epsilon_C - k_B T \ln\left(\frac{N_C}{N_D}\right) \quad (5.6)$$

Therefore, a linear dependence with a slope of about  $k_B T$  is generally expected for nondegenerate inorganic semiconductors. However, in the case of alkali metal-doped OSCs, the slope is much larger than  $k_B T$ . This is a clear indication that the classical result for crystalline inorganic semiconductors does not apply to OSCs.

The fundamental difference between an organic and an inorganic semiconductor is in their bonding. The covalent bonding that prevails in inorganic semiconductors results in a large electronic wave function overlap, which is the basis for forming the Bloch waves and the band structure. In OSCs,

however, the bonding is predominantly van der Waals and the electronic structure remains largely molecular and localized. The localized nature of the electronic structure causes large correlation effects—either electron–electron or electron–phonon. If the molecular orbital were fully isolated from the doping metal atom, one would expect the same energy-level dependence on the doping density as in Equation 5.6, that is, logarithmic with slope of  $k_B T$  in the semi-log plot. However, a broad Lorentzian distribution of the LUMO, caused by metal/organic interaction, may result in a linear behavior in the semi-log plot as can be seen from Equation 5.7. The slope is then given by the Lorentzian width  $\Gamma$ , which can be much larger than  $k_B T^{18}$ :

$$n \equiv N_0 \exp\left[\frac{-(\varepsilon_0 - \varepsilon_F)}{\Gamma}\right] \quad (5.7)$$

Another surprise from the alkali metal-doping experiments is that the slope cannot be explained by a Gaussian broadening of the LUMO. If the energy distribution is a broad Gaussian, with  $\sigma \gg k_B T$ , the electron concentration will be dominated by the Gaussian and the charge density will be given by

$$n \equiv N_0 \left\{ 1 - \operatorname{erf} \left[ \frac{\varepsilon_0 - \varepsilon_F}{\sigma} \right] \right\} \quad (5.8)$$

where  $\operatorname{erf}(x)$  is the error function. Experimentally, both UPS and IPES peaks appear to be Gaussian. It has also been attempted to fit the data in Figure 5.10 with Equation 5.8 to see if the energy-level shift can be explained by Gaussian broadening. However, the curve from Equation 5.8 bends opposite to that of the experimental data, indicating that Equation 5.8 cannot be applied in this case.

The linear shift stage at low doping ratios can be understood as the Fermi level shifts within the energy gap, in order to reach an equilibrium with the low work function metal dopant. It should also be noted that Equation 5.6 is derived for the nondegenerate case, where the doping density is low and the overlap of wave functions between the dopants themselves is small. This aspect may diminish the applicability of Equation 5.6 to the doping density dependence in our measurements, and we observed the saturation of the energy-level shift as the Fermi level is aligned with the LUMO. The second doping stage is usually manifested by the gap state, the LUMO reduction, and the different shift behavior of the valence and core features. At this stage, the doped electrons become more localized near the organic molecules, leading to a strong correlation effect, which explains the reverse shift for some of the core levels. In the case of CuPc, the XPS results suggest that the doped electrons are mainly located near the central part of the CuPc molecules, which results in a reversed shift for C 1s(B), N 1s, and Cu 2p<sub>3/2</sub>. A recent theoretical calculation<sup>25</sup> pointed out that although the 3d-like orbital from the center Cu atom is half occupied and locates in the gap between the Pc HOMO and the

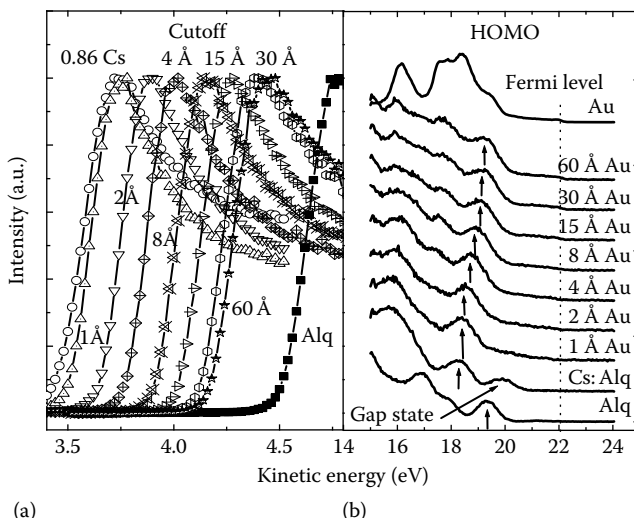
LUMO, reduction steps correspond to the deposition of electrons into the  $\text{Pc}$  LUMO, bypassing the lower orbital from Cu. It turns out that the  $\text{Pc}$  macrocycle plays the role of an electron buffer in the metal oxidation and reduction. However, as the doping ratio increases, the energy difference of adding electrons into  $\text{Pc}$  LUMO and Cu 3d for  $[\text{CuPc}]^{x-}$  reduces dramatically. It is then expected that by intensive charge transfer, the center Cu atom can be finally affected and strong chemical reactions take place. In fact, the split of Cu 2p<sub>3/2</sub> core level at high doping ratios supports the above predictions very well. For alkali metal doping in Alq, the appearance of the gap state in the HOMO region and the splitting of N 1s core levels at higher doping concentrations indicate that as charge transfer progresses, correlation interaction becomes significant. The excess electron is localized on the pyridyl side of one of the three quinolate rings,<sup>20</sup> forming an Alq<sup>-</sup> radical anion.

---

## 5.5 Reversal of Doping-Induced Energy-Level Shift

The earlier results indicate that the electronic structures of the OSCs can be modified by alkali metal doping, and the electron-injection barrier can be minimized to achieve a lower driving voltage and higher efficiency. However, fundamental issues still remain, such as whether the electronic structure modification is due simply to charge transfer, or whether more profound molecular structure modifications and chemical reactions are responsible for this. At the same time, the environment for the doped organic thin films can be complicated in the real device applications. Therefore, it is interesting to study the energy-level modification of doped OSCs under the presence of the opposite dopant, such as Au and oxygen.

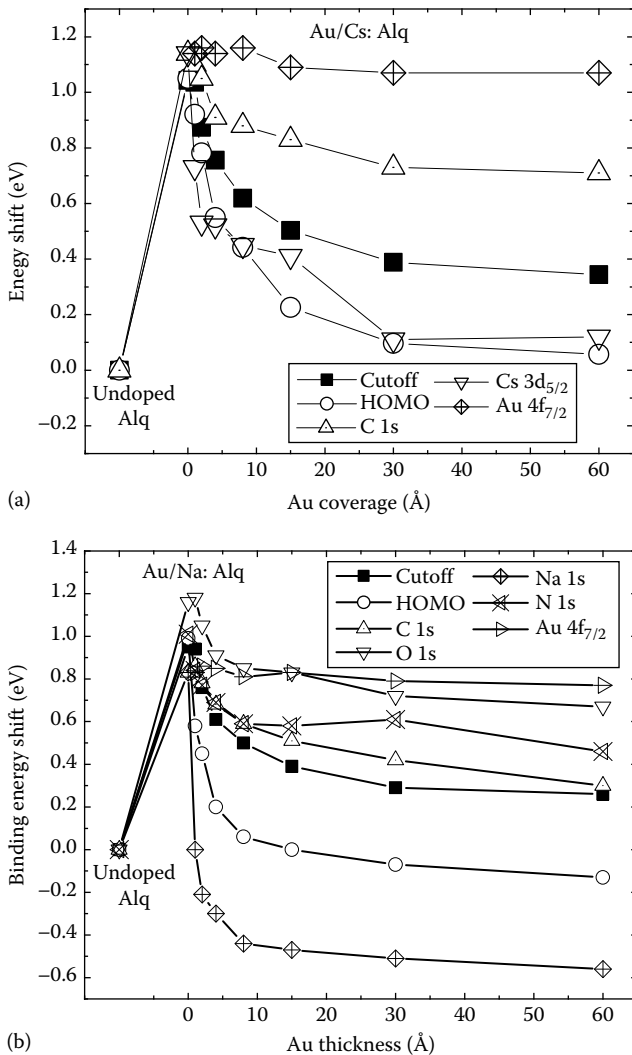
Figure 5.11 depicts the UPS spectra of both the low-energy secondary cut-off and the HOMO region for Au deposition on Cs-doped Alq film.<sup>35</sup> The Fermi level derived from the Au substrate is indicated by the dashed line. Determined from the XPS core-level intensities, 0.86 (atom to molecule ratio) Cs was doped into the Alq film before Au evaporation. According to a previous study,<sup>21</sup> the energy-level shifts are fully saturated at this doping density. It can be seen that after doping the cutoff shifts toward high BE by about 1.0 eV, and a significant gap state of 1.6 eV is introduced above the HOMO. It is very interesting that the initial deposition of 1 Å Au completely quenches the gap state while it does not induce much shift in the cutoff and the HOMO. As the Au coverage increases, the cutoff shifts backward to low BE until it saturates after 30 Å of Au deposition. The total reverse shift is about 0.7 eV, and the final work function of 3.4 eV is substantially lower than that of pure Au (5.4 eV). A similar reversal of the Cs-induced shift can also be observed in the HOMO region. The Alq peaks broaden and shift monotonically toward the Fermi level as the Au coverage increases. However, an important difference

**FIGURE 5.11**

The UPS spectra evolution as a function of Au thickness deposited onto the Cs-doped Alq film: (a) cutoff and (b) the HOMO region. (From Ding, H. and Gao, Y., *Appl. Phys. Lett.*, 87, 051918, 2005. With permission.)

from the cutoff shift is that the HOMO shifts faster and the saturation position actually turns out to be that of the pristine Alq film. Another interesting observation is that after the annihilation of the gap state, the shape of the Alq HOMO peak does not change much by further Au depositions. The persistence of Alq HOMO feature even up to 60 Å of Au indicates that no significant chemical reaction has taken place. Finally, it should be noticed that the Fermi level, which can be seen beyond 15 Å Au coverage, is the same as that of the Au substrate. Therefore, the charging effect during the measurement was insignificant at this stage.

The simplest explanation of the reversal of the energy-level shift is the compensation of the n-doping Cs by the p-doping Au as frequently observed in crystalline inorganic semiconductors. However, more detailed analysis shows that the situation in an OSC can be more complicated. The energy-level shifts of Au on Cs- and Na-doped Alq are summarized in Figure 5.12a and b, respectively. The core-level shifts were deduced by fitting the spectra with Gaussian curves for C 1s, Cs 3d<sub>5/2</sub>, and Au 4f<sub>7/2</sub>. The vacuum-level cutoff was obtained at the maximum of the differential curve of the UPS spectra. The cutoff and the HOMO positions of the pristine Alq film are also presented as the very first points to compare with the doped cases. It is clear that 86% Cs doping causes a Fermi-level shift as large as 1.0 eV, which agrees with our previous data of Cs-doped Alq.<sup>21</sup> The deposition of Au causes a significant reversal of both the frontier orbital and the core levels. There is a dramatic shift of 0.6 eV for Cs 3d<sub>5/2</sub> at low Au coverage (1–2 Å), while the shift for C 1s,

**FIGURE 5.12**

The summarization curves of energy-level shifts for Au on Cs-doped Alq (a) and Na-doped Alq (b) film. The energy-level positions for pristine Alq are drawn as the first points.

during the same time period, is less than 0.1 eV. The abrupt shift of Cs 3d<sub>5/2</sub> may stem from the removal of the donated electron from the N of Alq<sup>-</sup>. This explanation is supported by the quenching of the gap state in the HOMO region, which is observed to be affiliated to the formation of Alq<sup>-</sup>. Another important observation is that while the HOMO shifts completely back to that of the undoped Alq, the C 1s peak does not. It saturates after shifting about 0.4 eV, which is only halfway toward that of the pristine Alq film. Apparently,

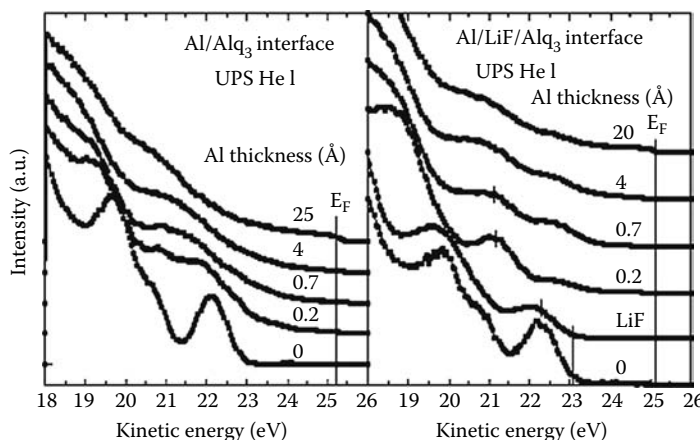
the modification of the Alq electron energy-level shift by Cs doping cannot be fully compensated by simply removing the electrons from the host.

---

## 5.6 LiF Insertion Layer

Having a thin LiF layer between the electron-transporting organic layer and the metal cathode has been widely practiced in organic optoelectronic devices to enhance the transport of electrons from the organic layer to the cathode. Alq is one of the most widely used light-emitting materials for OLEDs.<sup>36,37</sup> It also acts as an electron-transport-layer material and efficient electron injection into Alq is critical to improve the performance of the OLED. Among the early approaches, Mg–Ag alloy has been widely used as cathodes for OLEDs. However, the reactive nature of Mg is one of the factors that limits the lifetime of the OLED, and it is preferable for a more stable material to be used as the cathode. More recent approaches to forming efficient and stable cathodes introduce a thin layer of an ionic insulator such as LiF,<sup>38–41</sup> MgO,<sup>38</sup> or MgF<sub>2</sub><sup>42</sup> at the Al/organic interface, or dope the organic layer (or the cathode) with LiF<sup>40</sup> (or Li<sup>13</sup>), which significantly enhance the electron injection and prolong the lifetime of the device. An early suggestion by Hung et al.<sup>38</sup> was that the LiF layer reduced the electron-injection barrier height, but it is also found that it depends strongly on the metal deposited on top of the LiF.<sup>43</sup> Schlaf et al. measured the electronic structure of LiF on Al and Pt, and attributed the improvement in injection to band bending in LiF caused by charged defect.<sup>44</sup> Wang et al. attributed the improvement to energy-level realignment by interface dipole.<sup>45</sup> More recently, Zhao et al. suggested that tunneling in LiF and thus induced energy-level realignment are responsible for the improvement in electron injection.<sup>46</sup>

In Figure 5.13, the UPS spectra are presented for Al depositions onto clean Alq and Alq with the 5 Å LiF buffer layer.<sup>47</sup> The spectra for clean Alq are comprised of several well-defined peaks and are consistent with those found in the literature.<sup>48,49</sup> The peak at the highest kinetic energy is referred to as the HOMO and is attributed to the  $\pi$ -orbital located on the phenoxide side of the quinolate ligand.<sup>48</sup> The position of the HOMO is found at 2.1 eV below the Fermi level, which is in good agreement with the values reported for Alq/Au.<sup>50,51</sup> Deposition of an Al layer as thin as 0.2 Å represents a significant change in the valence spectrum of Alq and induces the formation of new states that extend into the energy gap. The fingerprint of the Alq structure has virtually vanished after deposition of 0.7 Å Al, indicating the relatively strong reaction between the Al atoms and the Alq molecules. The appearance of the Al Fermi level for  $\Theta_{Al} = 4 \text{ \AA}$  is in good agreement with the XPS results, for which the Al metallic peak begins to grow after deposition of the same Al thickness. The spectra observed with Al deposition is consistent

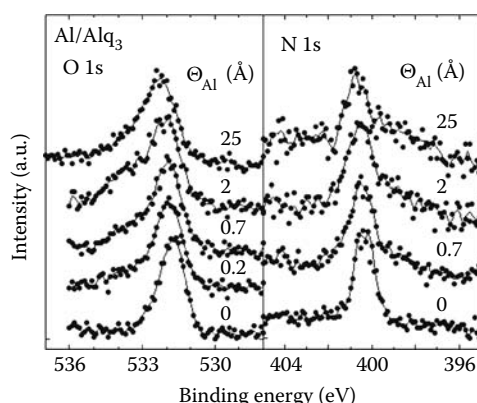
**FIGURE 5.13**

Evolution of the UPS spectra as a function of Al thickness for Al/Alq and Al/LiF/Alq interfaces. (From Le, Q.T. et al., *J. Appl. Phys.*, 87, 375, 2000. With permission.)

with an extensive chemical reaction forming a product significantly different from Alq, as predicted by the density-functional theory (DFT) calculations. The new states observed in the energy gap are a reflection of the molecular orbital structure of this reaction product.

As shown in Figure 5.13, the presence of a thin LiF layer on the Alq surface does not substantially modify the HOMO position of Alq, although it does induce significant broadening as in the XPS spectra.<sup>47</sup> The deposition of aluminum induces new states above the HOMO in the energy gap, and results in a shift of the position of the HOMO to higher BE. These states are fundamentally different from those formed in the absence of LiF. The molecular orbital structure of Alq is preserved with LiF present. States are shifted to higher BE and the gap state that is formed is well defined. In the absence of LiF, the molecular orbital structure of Alq is broadened beyond recognition even at very low coverages of Al. The states that are formed in the gap appear to result from an extreme line broadening as a result of the Alq decomposition process. The presence of the LiF layer not only decreases the extent of the reaction with Al, but also decreases the thickness of the reacted layer. The Alq valence band is still identifiable at  $\Theta_{\text{Al}} \approx 4 \text{ \AA}$ , and the Fermi level is observed at an Al coverage as low as  $\approx 2 \text{ \AA}$ .

The evolution of the XPS O 1s, N 1s, Al 2p, and C 1s spectra at representative Al coverages on Alq is shown in Figure 5.14.<sup>47</sup> The XPS spectra were normalized to constant intensity for them to be compared. The bottom curve in each set represents pristine Alq, and can be fit very well by a single component, Gaussian line shape. All core levels showed significant broadening and shifting to higher BE with increasing aluminum. However, the more detailed behaviors are very element specific. The C 1s exhibits only the above-mentioned broadening and shifting as does the Al 2p up to a coverage of

**FIGURE 5.14**

Evolution of XPS O 1s, N 1s, Al 2p, and C 1s spectra as a function of Al coverage observed at the Al/Alq interface. (From Le, Q.T. et al., *J. Appl. Phys.*, 87, 375, 2000. With permission.)

$\Theta_{\text{Al}} \approx 4 \text{ \AA}$  where a low BE component begins to emerge. The O 1s develops a distinct asymmetry to the high BE side while in the N 1s spectrum, a broad feature appears to evolve on the low BE side of the principal peak. This variety of element-specific responses to the Al deposition is clear evidence that something much more complicated than simple band bending<sup>44,52</sup> is occurring and implies that significant chemical interactions are taking place. In contrast to Ca/Alq,<sup>34</sup> where the nitrogen spectrum is singularly influenced by the metal interaction, it is the oxygen emission that is most significantly affected in the Al/Alq. To further our qualitative understanding of the possible chemistry at this interface, we have performed quantum chemical calculations for the interaction of Al with Alq using DFT.<sup>53</sup> These calculations predict that the incoming Al will bond directly to oxygen atoms on two of the three quinolate rings in the Alq molecule. The resulting inequivalent oxygen atoms are consistent with the observed asymmetry and increased width of the O 1s line. Above  $\Theta_{\text{Al}} \approx 4 \text{ \AA}$ , the intensity of the reacted O 1s component remains essentially constant. The coverage dependence of the N 1s spectra can also be understood in terms of the theoretical model. Mulliken population analysis of the atomic charges shows that two of the quinolate nitrogen atoms are very similar, while the third has a significantly higher electron density. Photoemission from the more highly charged nitrogen should occur at lower BE, as is observed in the measured spectra. The broadening of the Al and C spectra is due to the greater diversity in chemical states and environments of the atoms. While both the original Alq aluminum and the deposited aluminum are bonded to oxygen, both the coordination and charges are different and at least a modest increase in line width is to be expected. The C 1s line width is quite large, even for the pristine material. This results from the variations in bonding within the quinolate ring<sup>48</sup> and the lack of symmetry in the Alq molecule that combine to make each carbon atom chemically unique.

This effect is amplified by the reaction with deposited Al that produces an even less symmetric molecular structure. The low BE peak that first appears in the Al 2p spectra at  $\Theta_{\text{Al}} \approx 4 \text{ \AA}$  is simply due to unreacted, metallic Al. The intensity of this peak increases with coverage while that of all the other elements decreases as a true metallic film is formed. A clear demarcation is seen in the core-level spectra for coverages above and below  $\Theta_{\text{Al}} \approx 4 \text{ \AA}$ . For  $\Theta_{\text{Al}} \geq 4 \text{ \AA}$ , the binding energies and line widths are virtually independent of coverage and all of the added Al is found in the metallic state. This clearly indicates that the reaction is limited within the first  $\approx 4 \text{ \AA}$  of deposited aluminum. While a  $4 \text{ \AA}$  layer of Al would be extremely thin, the modified layer, which would result from a reaction between the deposited Al and the Alq, would be much thicker. Due to the extreme difference in molecular/atomic sizes,  $\approx 0.2 \text{ \AA}$  of Al corresponds to approximately one metal atom for every surface Alq molecule. If each deposited Al atom reacts with one Alq molecule and can freely diffuse into and react with the bulk Alq, then a  $\approx 4 \text{ \AA}$  deposition would produce a reacted layer of  $>150 \text{ \AA}$ . This also explains why such dramatic spectral changes occur when only  $\approx 0.2 \text{ \AA}$  of metal are deposited.

Figure 5.15 depicts the O 1s, N 1s, Al 2p, and C 1s spectra with  $5 \text{ \AA}$  LiF insertion layer and with increasing Al coverage.<sup>47</sup> An unfortunate result of the LiF deposition is a significant increase in the observed line widths. This probably results from the incomplete coverage of the surface that causes it to be very inhomogeneous. With the exception of the C 1s peak, all core levels showed significant broadening with LiF and subsequent Al deposition. The increased full width at half maximum (FWHM) with overlayer deposition makes it difficult to resolve multicomponent lines. This effect is most relevant in the O 1s spectrum. Although this appears to remain a single-component peak for all  $\Theta_{\text{Al}}$  and shows none of the asymmetry characteristics of the Al/Alq interface, some asymmetry may be hidden by the increased

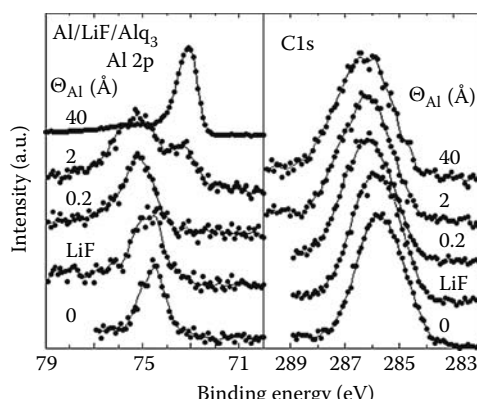


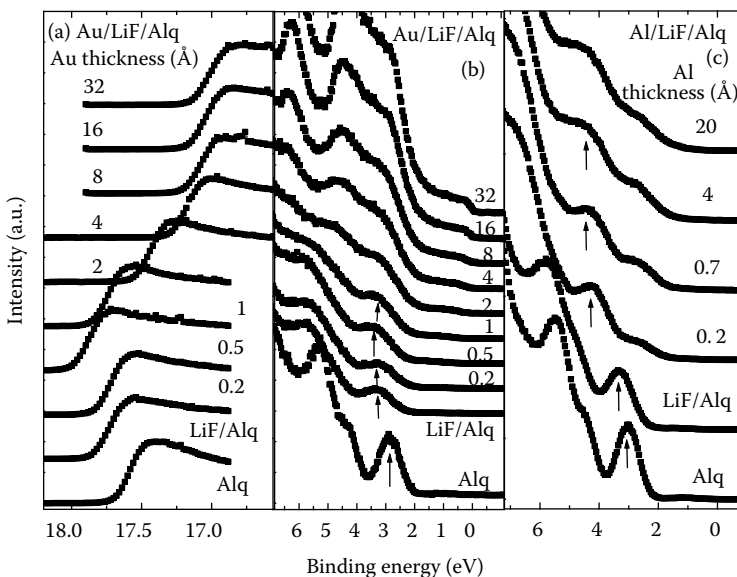
**FIGURE 5.15**

Evolution of XPS O 1s, N 1s, Al 2p, and C 1s spectra as a function of Al coverage observed at the Al/LiF/Alq<sub>3</sub> interface. (From Le, Q.T. et al., *J. Appl. Phys.*, 87, 375, 2000. With permission.)

line width. The FWHM does increase from 1.17 to 1.45 eV with the deposition of LiF and to 1.89 eV for  $\Theta_{\text{Al}} = 20 \text{ \AA}$ . Even though no splitting is observed, such a significant increase in line width suggests a substantial alteration of the oxygen environment. In contrast to the O 1s spectrum, a new component in the N 1s spectrum is observable at  $\approx 1.6 \text{ eV}$  to lower BE, even at the lowest coverage of Al. The intensity of this reacted component is higher than in the case of Al on Alq in the absence of the LiF layer. The pyridyl species appears to be significantly modified by even a small amount of deposited Al. The evolution of the Al 2p signals is similar to that of the Al/Alq interface but the magnitude of the shift is significantly greater. Furthermore, the metallic component appears at a significantly lower coverage suggesting that that LiF, at least, partially protects the Alq surface from reaction with the deposited Al. In the absence of LiF, the metallic signal is first noticeable at a coverage of  $\Theta_{\text{Al}} \approx 4 \text{ \AA}$ , whereas a similar relative contribution of the metal is observed at  $\Theta_{\text{Al}} \approx 2 \text{ \AA}$  when the LiF layer is present.

The XPS and UPS spectra of Al on Alq appear to be understandable simply in terms of a “destructive” chemical reaction between the organic and the reactive metal. To understand the role of LiF in modifying this interface, we consider the results of previous work involving alkali and alkali earth metals deposited on Alq. The metals Ca,<sup>29</sup> Mg,<sup>20,51</sup> Na,<sup>20</sup> K,<sup>54</sup> or Li<sup>54</sup> on Alq have been studied by XPS and UPS and show remarkably similar characteristics. In all cases, the core levels shift to higher BE. The N 1s peak splits with a separation between 1.6 and 1.8 eV, and the O 1s broadens significantly but symmetrically. In the UPS spectra, the HOMO shifts to higher BE and a new state is formed in the previously existing energy gap and is separated from the original HOMO by 1.6 eV. All of these characteristics are observed in the case of aluminum deposited on the Alq with the thin layer of LiF. The previous work on Ca<sup>34</sup> claimed and the more recent work on Li and K<sup>54</sup> essentially proved that the modifications to the spectra are due the formation of the Alq radical anion. It can be concluded that when Al, LiF, and Alq are all present, Li is liberated and reacts with Alq to form the radical anion.<sup>20,47</sup> The beneficial effects on reactive metal deposition can be achieved without actually employing the metals themselves.

In Figure 5.16a and b, the UPS spectra are presented for different thickness Au deposited onto Alq with a 5 Å LiF buffer layer.<sup>55</sup> The presence of the thin LiF layer on the Alq surface preserves most of the valence features, although it does induce a 0.14 eV shift toward higher BE and some broadening. The deposition of Au initially produces a slight shift of the HOMO position to higher BE reaching a maximum of 0.26 eV at gold coverage  $\Theta_{\text{Au}} = 0.5 \text{ \AA}$ . Further Au deposition gradually reverses the shift toward lower BE. The final Alq HOMO position, however, cannot be observed from the valence spectra since the Au features dominate after  $\Theta_{\text{Au}} = 4 \text{ \AA}$ . Figure 5.16a depicts the low-energy secondary cutoff region of the UPS spectra. The vacuum level shifts 0.15 eV toward lower energy, as reflected in the cutoff spectra, when LiF is deposited. The existence of an interface dipole can be ruled out since the HOMO in Figure 5.16b

**FIGURE 5.16**

Evolution of the cutoff (a) and the HOMO region (b) of the UPS spectra as a function of Au thickness for the Au/LiF/Alq interfaces. (c) Evolution of the HOMO region of the UPS spectra as a function of Al thickness for the Al/LiF/Alq interfaces. (From Ding, H. and Gao, Y., *Appl. Phys. Lett.*, 91, 172107, 2007. With permission.)

show the same shift at this stage, reflecting VLA. For the initial Au deposition ( $\Theta_{\text{Au}} \leq 0.5 \text{ \AA}$ ), the vacuum-level shift is consistent with that of the valence features in Figure 5.16b indicating the nature of rigid shift for the lower coverages. As the Au overlayer grows thicker, the vacuum level shifts upward toward that of pure Au, but saturates at  $\Theta_{\text{Au}} = 8 \text{ \AA}$  at a position of 1.1 eV below that of pure Au, whose work function is 5.3 eV. This phenomenon has been observed in other Au depositions on organic systems and can be attributed to Au intermixing with and clustering in the substrate material.<sup>51</sup>

It is intriguing to compare the valence energy-level evolution of the Au/LiF/Alq interface with that of Al/LiF/Alq depicted in Figure 5.16c.<sup>47</sup> For both interfaces, the molecular orbital structure of Alq is preserved when LiF is present. It is less of a surprise for the Au case than for Al, since the latter would induce significant chemical reaction with Alq if LiF were not present.<sup>47</sup> As shown in Figure 5.16a and b, Au induces little energy-level shift, and leaves a “flat-band” in Alq in the interface region. As a result, the electron-injection barrier is unaltered compared to that of pristine Alq. The situation is dramatically different in the case of Al/LiF/Alq, as can be seen in Figure 5.16c, where the deposition of Al on 5 Å LiF/Alq shifts the Alq HOMO to the higher BE by as much as 1.0 eV. Within the rigid shift assumption, the LUMO is also lowered by the same amount, resulting in a significant reduction of the electron-injection barrier that can lead to substantial improvement

in electron injection as observed in devices.<sup>38</sup> Such improvement can be attributed to doping by Li released through the interface reaction by Al deposition.<sup>20,47</sup> The assessment of doping is also supported by the gap state and new N 1s component. More direct evidence of the existence of Li<sup>+</sup> in such a system has been demonstrated by Wu et al. with synchrotron radiation PES, where the high photon flux allows direct observation of Li 1s.<sup>56</sup> For the case of Au/LiF/Alq, neither the gap state nor the extra N 1s component could be observed.

## 5.7 Organic/Organic Interface Band Bending and Debye Screening

In contrast to metal/OSC interfaces where an interface dipole  $D$  of about 0.5–1 eV is usually observed,<sup>8</sup> most OSCs heterojunctions are characterized by VLA where  $D$  is less than 0.1 eV.<sup>57</sup> This is because of the relatively weak van der Waals interactions between organic materials. Band bending and space charge in organic heterojunction have also been observed.<sup>58–60</sup> It remains to be explored how band bending in the organic heterojunction would affect device performances.

In Figure 5.17, the UPS spectra of the cutoff region (a) and the valence region (b) are shown as F<sub>16</sub>CuPc is deposited onto a 20 nm BP2T film.<sup>61</sup> The HOMO

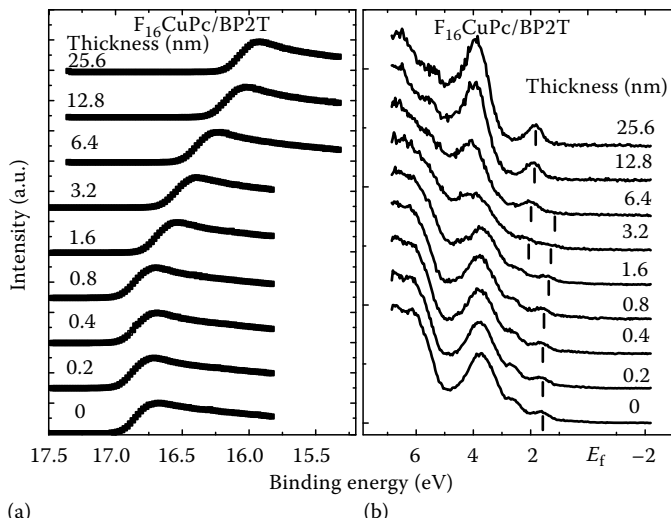


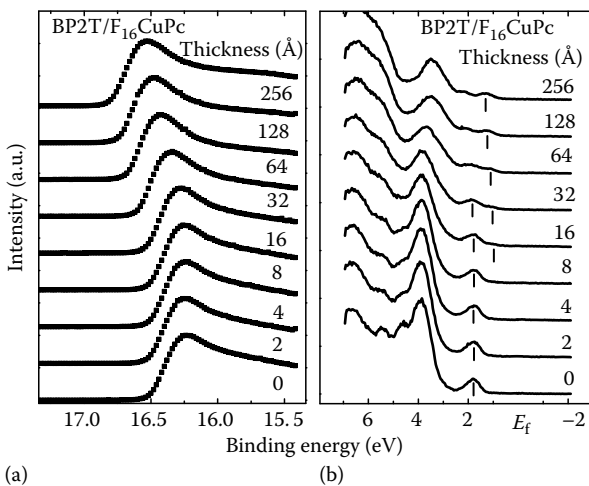
**FIGURE 5.17**

Evolution of the cutoff (a) and the HOMO region (b) of the UPS spectra as F<sub>16</sub>CuPc is deposited on BP2T. (From Gao, Y. et al., *Appl. Phys. Lett.*, 91, 142112, 2007. With permission.)

peak positions are marked by short bars. It can be seen that at low  $F_{16}\text{CuPc}$  coverages ( $\Theta_F \leq 0.8\text{ nm}$ ), there is hardly any change in the spectrum, indicating negligible interface reaction and dipole formation. Spectral changes start to appear for higher  $F_{16}\text{CuPc}$  coverages. Most significantly, the HOMO peak positions of both  $F_{16}\text{CuPc}$  and BP2T can be seen to shift to lower BE as  $\Theta_F$  increases, which clearly demonstrates band bending in the heterojunction in both materials. The BP2T HOMO can be observed up to  $\Theta_F = 3.2\text{ nm}$ , above which it is hardly visible because of the attenuation by the  $F_{16}\text{CuPc}$  overlayer. The shift of the BP2T HOMO is measured to be  $0.36\text{ eV}$  at this stage. At the same stage, the overlayer  $F_{16}\text{CuPc}$  features become discernible, and dominate for higher  $F_{16}\text{CuPc}$  coverages. The total shift of the  $F_{16}\text{CuPc}$  HOMO can be deduced to be  $0.30\text{ eV}$ . At the final coverage  $\Theta_F = 25.6\text{ nm}$ , the valence spectrum becomes completely that of  $F_{16}\text{CuPc}$  as previously reported,<sup>13</sup> and similar to that of CuPc with a rigid shift of  $0.6\text{ eV}$  to higher BE.<sup>14</sup> The cutoff shift shown in Figure 5.17a, which reflects the vacuum-level change of the surface, gives a trend very close to that in the valence region, and the total shift of  $0.78\text{ eV}$  is slightly larger than the sum of the observed band bending in BP2T and  $F_{16}\text{CuPc}$ . The small difference occurs mainly as the  $F_{16}\text{CuPc}$  HOMO peak position is saturated, and is therefore likely due to a change in the morphology at the surface that in turn modifies the ionization potential of the  $F_{16}\text{CuPc}$ .

The data presented in Figure 5.17 clearly demonstrate that in the  $F_{16}\text{CuPc}/\text{BP2T}$  heterojunction formed by  $F_{16}\text{CuPc}$  deposition on BP2T is characterized by no interface dipole and reaction, and by band bending in both materials. Given that the  $F_{16}\text{CuPc}$  shift is mostly saturated at  $\Theta_F = 12.8\text{ nm}$ , it can be deduced that the Debye length, an important parameter that characterizes the distance over which an electric field can be effectively screened by the semiconductor,<sup>15</sup> is about  $3\text{ nm}$  in  $F_{16}\text{CuPc}$ . To learn the band-bending region and obtain the Debye length in BP2T, we reversed the deposition order and measured the interface electronic structure as BP2T is deposited onto a  $20\text{ nm}$   $F_{16}\text{CuPc}$  film.

The measured UPS spectra of the cutoff and the valence region from the BP2T/ $F_{16}\text{CuPc}$  heterojunction are shown in Figure 5.18a and b, respectively, and the HOMO peak positions are marked.<sup>61</sup> At initial BP2T coverages ( $\Theta_B \leq 1.6\text{ nm}$ ), the UPS spectra of BP2T/ $F_{16}\text{CuPc}$  show little change, which is similar to  $F_{16}\text{CuPc}/\text{BP2T}$  and confirms that between the two materials there is neither interface reaction nor dipole formation. Interestingly, as the BP2T coverage increases from  $\Theta_B = 1.6\text{ nm}$ , the vacuum level starts to move, while the HOMO peak of  $F_{16}\text{CuPc}$  remains stationary as long as it can still be distinguished at  $\Theta_B = 6.4\text{ nm}$ . In contrast, the HOMO peak of BP2T, first discernable at  $\Theta_B = 3.2\text{ nm}$ , continuously shifts to the lower BE till its saturation at about  $0.83\text{ eV}$  below the Fermi level at  $\Theta_B = 25.6\text{ nm}$ . The shift of BP2T HOMO in the BP2T/ $F_{16}\text{CuPc}$  interface is consistent with that in the  $F_{16}\text{CuPc}/\text{BP2T}$  interface, i.e., bending upward from the bulk BP2T to the interface. The total band

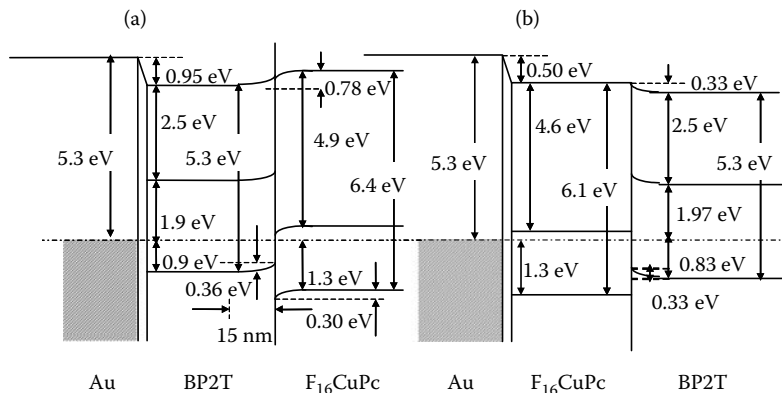
**FIGURE 5.18**

Evolution of the cutoff (a) and the HOMO region (b) of the UPS spectra as BP2T is deposited on  $F_{16}\text{CuPc}$ . (From Gao, Y. et al., *Appl. Phys. Lett.*, 91, 142112, 2007. With permission.)

bending of BP2T, as judged by the vacuum level and the HOMO peak shift, is 0.33 eV, which is quite consistent to the BP2T portion in the  $F_{16}\text{CuPc}/\text{BP2T}$  interface. The band-bending region in BP2T is about 15 nm, indicating that the Debye length in BP2T is similar to that in  $F_{16}\text{CuPc}$ .

It can be seen that for  $F_{16}\text{CuPc}$  on BP2T, there is band bending in both materials resulting in hole accumulation in the BP2T side and electron accumulation in the  $F_{16}\text{CuPc}$  side. For BP2T on  $F_{16}\text{CuPc}$ , the band bending only occurs in BP2T. The dissimilarity between the two interfaces can be understood from the fact that in bulk  $F_{16}\text{CuPc}$ , the replacement of H by F substantially increases the ionization potential and pins the Fermi level at the edge of the LUMO. As a result of the Fermi-level pinning, the energy levels in  $F_{16}\text{CuPc}$  remain stationary as BP2T is deposited onto it. Such pinning does not occur for the initial depositions of  $F_{16}\text{CuPc}$  on BP2T, since the vacuum level has to be aligned and the amount of  $F_{16}\text{CuPc}$  is small.

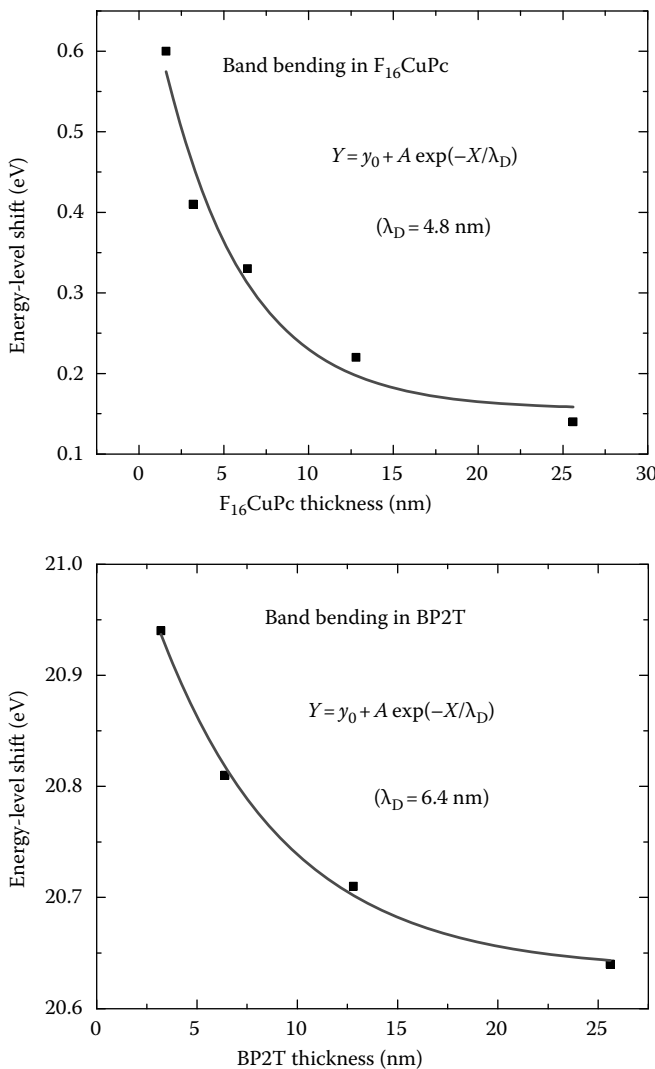
The schematics of the interface electronic structure of  $F_{16}\text{CuPc}/\text{BP2T}$  and  $\text{BP2T}/F_{16}\text{CuPc}$  are shown in Figure 5.19,<sup>61</sup> where the sequence of deposition is from the left to right. The vacuum level is determined from the maximum of the cutoff derivative. The HOMO and LUMO positions are obtained from the linear extrapolation of the leading edge of UPS and IPES. The most remarkable feature of the  $F_{16}\text{CuPc}/\text{BP2T}$  heterojunction, as shown in Figure 5.19a, is that the band bending occurs in both materials, 0.36 and 0.30 eV in BP2T and  $F_{16}\text{CuPc}$ , respectively. Incorporating the band bending, the discontinuity of the HOMO levels at the interface can be deduced to be 1.03 eV. There is also

**FIGURE 5.19**

Energy diagram of (a)  $F_{16}\text{CuPc}$  deposited on  $\text{BP}2\text{T}$  and (b)  $\text{BP}2\text{T}$  deposited on  $F_{16}\text{CuPc}$ . (From Gao, Y. et al., *Appl. Phys. Lett.*, 91, 142112, 2007. With permission.)

an interface dipole potential of 0.95 eV between the  $\text{BP}2\text{T}$  and the  $\text{Au}$  substrate. For  $\text{BP}2\text{T}/F_{16}\text{CuPc}$  (Figure 5.18b), the band bending of 0.33 eV is mainly confined in  $\text{BP}2\text{T}$ , as the Fermi level in bulk  $F_{16}\text{CuPc}$  is pinned near the edge of its LUMO. The interface dipole between the  $F_{16}\text{CuPc}$  and the  $\text{Au}$  substrate is measured to be 0.50 eV. It can be noticed that the ionization potential for  $F_{16}\text{CuPc}$  in the two interfaces have some variations, which remain unexplained to this day.

The Debye length of  $\text{BP}2\text{T}$  and  $F_{16}\text{CuPc}$  in the interface region can be deduced from the observed band bending, if the latter can be attributed completely to the screening effect of the accumulated charge carriers. The Debye length thus deduced is conventionally referred to as extrinsic, in contrast to the intrinsic one from the ionized dopants in the depletion region. Here it should be emphasized that strong accumulation in inorganic semiconductor heterojunctions is rare because the Fermi level is close to the band edges as there is little defect states tailing into the band gap. In OSCs, there can still be n- or p-type, although the organic materials are not intentionally doped. Furthermore, OSCs are typically polycrystalline or amorphous, resulting in a relatively large number of defect states in the band gap in comparison to crystalline inorganic semiconductors. As a result, for n- or p-type OSCs, the Fermi level can be 0.5 eV or more from the band edges, and the band bending in the accumulation region can be substantial. In the cases of  $\text{BP}2\text{T}$  and  $F_{16}\text{CuPc}$ , it reaches several tenths of an electron volt as observed with UPS (see Figures 5.17 through 5.19). The fitting of the band bending by Debye exponential decay is shown in Figure 5.20. It is deduced that the Debye lengths in  $F_{16}\text{CuPc}$  and  $\text{BP}2\text{T}$  are 4.8 and 6.4 nm, respectively.

**FIGURE 5.20**

Fitting of the band-bending data and deduction of the Debye lengths in  $F_{16}\text{CuPc}$  and BP2T.

## 5.8 Interface Growth Mode and Modeling

Organic molecules, when deposited onto an inorganic substrate, can result in three different growth modes depending on the relative strengths of the adsorbate–adsorbate, and adsorbate–substrate interactions.<sup>62</sup> First, if the

substrate is chemically inert, the adsorbate–substrate interaction will be very small having almost no influence on the growth of the organic film. This will enable the organic molecules to move freely on the surface and form large, separated islands of crystals after adsorption. This type of growth is known as Volmer–Weber or 3D-island growth. Second, if the substrate has highly reactive bonds, the adsorbate–substrate interaction will be very large, and as soon as the organic molecules hit the surface they will be bound strongly to the substrate. This will prevent self-ordering mechanism of the organic molecules, which is crucial for ordered growth, and hence will result in disorder. This mode of growth is known as Frank-van der Merwe or layer-by-layer growth. The third type of growth is a moderate combination of the first two scenarios, that is, the adsorbate–substrate interaction is neither too strong, nor too weak. It is such that the substrate has a strong-enough influence on the deposited particles to impose its crystallinity to the grown organic film, and the deposited particles have enough mobilities to self-order themselves. This type of growth is known as the Stranski–Krastanov mode or layer + island growth.

In order to study the growth kinetics of a surface one can use the  $q$ th-order height–height correlation function, which can be defined as<sup>63</sup>

$$C_q(r, t) = \left( (1/N) \sum_{i=1}^N |h(r_i, t) - h(r_i + r, t)|^q \right)^{1/q} \quad (5.9)$$

where  $N$  is the number of sites with single-valued heights  $h(r_i, t)$ . By definition, the  $q = 2$  case refers to the height–height correlation function, which is the rms fluctuation in the height difference between two surface points separated by a lateral distance  $r$ . It scales as follows according to the scaling hypothesis<sup>63–65</sup>:

$$C_2(r, t) \sim t^\beta g\left(\frac{r}{\xi(t)}\right) \quad (5.10)$$

where

$r$  is the lateral separation

$t$  is the time

$\beta$  is the scaling exponent

$g$  is the scaling function that depends on  $r$  and  $\xi$ , where  $\xi$  is the correlation length

The correlation length is the critical distance over which two heights are correlated.  $C_2(r, t)$  takes the following asymptotic behavior:

$$C_2(r, t) \sim t^\beta \quad (5.11)$$

Namely, for distances much larger than the correlation length,  $C_2(r, t)$  increases as a power of time.  $\beta$  in the above equation is called the growth

exponent. It characterizes the time-dependent dynamics of the growth. For distances much less than the correlation length  $\xi$ ,  $C_2(r, t)$  is independent of time for surfaces that obey the normal scaling law. It reads as

$$C_2(r, t) \sim \rho r^H \quad (5.12)$$

where

$\rho$  is the local slope of the interface

$H$  is a second scaling exponent called the Hurst exponent

The Hurst exponent  $H$  characterizes the roughness of the saturated interface. As for the local slope  $\rho$ , it is literally the approximate average slope of the local structure. Its value is related to the intersection of  $C_2(r, t)$  with the vertical axis. For normal scaling, it does not depend on time.<sup>66,67</sup> If  $\rho$  does depend on time, the scaling becomes anomalous. As one can see, to be able to characterize a growing interface, one needs the height-height correlation function  $C_2(r, t)$ , and more specifically, the critical exponents  $H$  and  $\beta$ .

The top panel of Figure 5.21 depicts some tapping mode AFM images of pentacene thin films evaporated on  $\text{SiO}_2$  substrate.<sup>68</sup> It can be observed for the initial stages of the growth that the number and size of the mounds increase with growth time. This increase stops once the individual islands become large enough to touch each other. However, new monolayers start

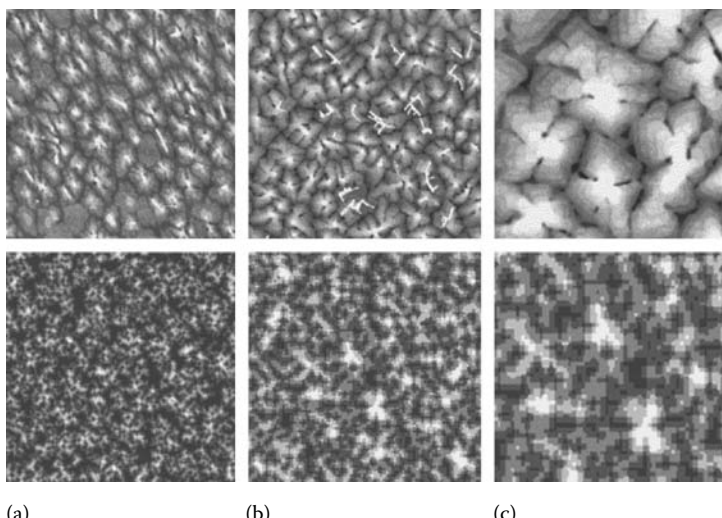


**FIGURE 5.21**

*Top panel:* Some representative surface morphologies of pentacene scanned by tapping mode AFM. (a) 20 Å pentacene—three monolayers can be seen—and  $5 \times 5 \mu\text{m}^2$  field of view. (b) 50 Å pentacene—five monolayers can be seen—and  $5 \times 5 \mu\text{m}^2$  field of view. (c) Area zoomed in (b). *Bottom panel:* Computer simulation results where one can identify (a) three monolayers and (b) five monolayers. (c) Area zoomed in (b). The size of the lattice is  $200 \times 200$  and the total number of particles deposited in (c) is about 90,000. (From Zorba, S. et al., *Phys. Rev. B*, 74, 245410, 2006. With permission.)

nucleating a good deal without waiting for the underlying monolayer(s) to form fully. This can be seen in the top panel of Figure 5.21. A closer look at the AFM images of the pentacene film in Figure 5.21 reveals that the ordered growth of pentacene is really a very peculiar one that incorporates a number of different growth mechanisms, not just fractal growth as caused by diffusion-limited aggregation (DLA) mechanism. As can be seen from the top panel of Figure 5.21, the pentacene forms a mixture of both regular- and irregular-sized mounds on  $\text{SiO}_2$  surface. In addition, one can readily observe the monolayer structures forming pyramid-like mounds. In fact, the average step size of the monolayers was found to be  $15.8\text{\AA}$ , which matches the length of a pentacene molecule closely.<sup>69</sup> Moreover, these terraced mounds are in a shape that bespeaks fat-DLA growth. DLA forms via diffusion of molecules through pure random walk and their sticking to a cluster to create irregularly branched and chaotic patterns. Fat DLA forms when the particles are allowed to diffuse on the boundary of the cluster to increase the number of nearest neighbors.<sup>70</sup> Indeed, our fractal dimension analysis revealed a dimension of about 1.6, which agrees very closely with that of a DLA surface.<sup>62</sup> In addition, the Fourier transform of the surface revealed a ringlike behavior, which is a sign of mound growth.<sup>67</sup> As a result, what one has as the dominant growth mechanisms behind pentacene's growth seems to be an interplay between the DLA-type growth and the mound growth. To our knowledge, such coexistence of both effects has not been observed in any other system.

There have been a number of epitaxial growth experiments recently, which have shown pyramid-like mound morphology in inorganic systems.<sup>71,72</sup> This phenomenon is mainly attributed to a growth instability caused by the step (or Schwoebel) barrier that creates a bias in the upward and downward diffusions in favor of the former. In the presence of a step-edge barrier on a terrace, the newly landing molecules are prevented from hopping down the edge, which in turn spawns an uphill current.<sup>62,73</sup> This results in the formation of regular pyramid-like mounds. The power spectrum of such a surface will be ringlike, indicating a length selection in real space.

The bottom panel in Figure 5.21 shows Monte Carlo simulation results.<sup>68</sup> To the naked eye, the real morphology data and the simulation morphology data resemble each other closely. In fact, one can easily distinguish the DLA-type formation in the initial coverages (lower panel Figure 5.21c). With more particles landing, newer DLA-type monolayers formed on top of existing ones much more quickly due to the uphill diffusion bias driven by the Schwoebel barrier effect. As a result, a novel morphology that closely resembles that of pentacene was generated, as shown in the simulation figures. In both sets of data individual monolayer terraces can easily be identified. DLA with dendritic patterns can also be seen.

In order to make the comparison quantitative and more tangible, we have also calculated the scaling exponents of both systems. The scaling approach<sup>62,65</sup> was introduced primarily to study self-affine surfaces. In such

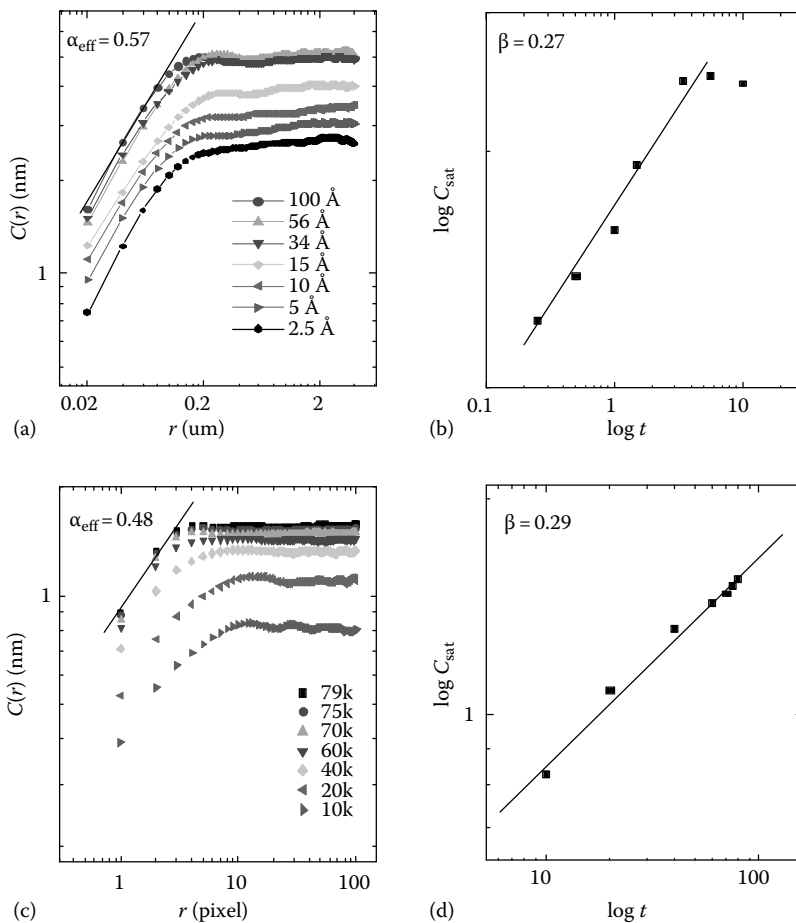
surfaces, height–height correlation function,  $C(r, t)$ , is used to characterize the growth. The height–height correlation function is the rms fluctuations in the height difference between two points separated by a distance  $r$  at time  $t$ . It behaves as  $C(r, t) \sim pr^\alpha$  for distances less than the correlation length  $\xi(t)$ , where  $\alpha$  is the roughness exponent. For  $r > \xi(t)$ , it saturates to the value of the roughness that increases with time as  $t^\beta$ , where  $\beta$  is the growth exponent. These exponents are also used to describe mound growth. In these cases,  $\beta$ , sometimes replaced by  $n$  when related to mounds, describes the mound height growth and is larger than 0.25.<sup>62,71</sup>  $\xi(t)$  is then the lateral size of the mounds. The roughness exponent is trivially  $\alpha = 1$  if a single slope is selected, which is almost always the case for regular (circular) mounds. If the mounds are not circular, the slope is not uniform and  $\alpha$  is then an “effective” roughness exponent smaller than one (since the smaller slopes become more important at large distances). The height–height correlation function  $C(r)$  is plotted in Figure 5.22a and c as a function of distance  $r$ , and the saturated  $C_{\text{sat}}(r)$  as a function of time in Figure 5.22b and d for both the real (a,b) and simulation (c,d) data. For small distances,  $C(r)$  changes linearly with  $r$ , and saturates beyond the characteristic length  $\xi(t)$ . The characteristic length is about the size of individual islands. The fact that the former is not larger than the latter suggests that the surface is not self-affine in the usual sense. It has a different self-affinity: mound growth rescaling in the vertical direction and DLA-type rescaling in the lateral direction.<sup>68</sup>

The calculated  $\alpha_{\text{eff}}$  and  $\beta$  values for the real data are  $0.57 \pm 0.03$  and  $0.27 \pm 0.03$ , respectively. The simulation values for  $\alpha_{\text{eff}}$  and  $\beta$  are  $0.48 \pm 0.07$  and  $0.29 \pm 0.01$ , respectively. The close agreement of these two sets of numbers with each other further corroborates quantitatively our earlier assessment that the morphology of the pentacene on  $\text{SiO}_2$  is dominated by two different growth mechanisms, diffusion and step-edge barrier effect. The interplay of these mechanisms results in a novel and interesting morphology that is known as “fractal-mound” growth, in contrast to the typical mound growth.<sup>71,73</sup>

---

## 5.9 Summary

There is a strong dependence of the device performance on interfaces in OSC devices. The surface and interface analytical investigations of the interfaces in organic devices have generated critical insight into the fundamental processes at these interfaces. There has been some progress in modeling the formation of interface dipole, but more work needs to be done to be general and quantitative. Doping alkali metals in organic materials reduces the electron–injection barrier, and the n-doping is reversible in the sense that counter p-doping can erase the effect. There is clear evidence that the gap

**FIGURE 5.22**

(a) Height-height correlation functions of real pentacene surface calculated for different thicknesses and plotted in log-log scale. (b) Evolution of the saturated height-height correlation function in time, also plotted in log-log scale. The slope of this plot gives the growth exponent  $\beta$ . (c,d) The corresponding graphs as obtained from the simulation results to render comparison with the real data results in (a,b). (From Zorba, S. et al., *Phys. Rev. B*, 74, 245410, 2006. With permission.)

state created by n-doping is at the expense of the LUMO state. The effect of inserting LiF thin layers depends on the metal overlayer, and Al deposition results in strong n-doping of the organic. Band bending is observed in organic/organic interface, and the bending can be strongly accumulative. The growth of thin organic films reveals a combination of DLA and mound growth, a phenomenon not observed before in inorganic films. These studies have shown that the design and control of surfaces and interfaces are important for delivering stable organic devices.

---

## Acknowledgments

The author gratefully acknowledges contributions of the following scientists with whom he has had the pleasure to work with on the topics presented in this chapter: H. Ding, S. Zorba, L. Yan, N.J. Watkins, C.W. Tang, M.G. Mason, and Q.T. Le. The work was supported in part by the National Science Foundation under Grant No. DMR-0602870.

---

## References

1. W.R. Salaneck, S. Stafstrom, and J.L. Bredas, *Conjugated Polymer Surfaces and Interfaces* (Cambridge University Press, Cambridge, U.K. 1996).
2. Y. Gao, Surface analytical studies of interface formation in organic light emitting devices, *Acc. Chem. Res.* **32**, 247 (1999).
3. E.W. Forsythe and Y. Gao, in *Handbook of Surfaces and Interfaces of Materials*, H.S. Nalwa, Ed., p. 286 (Academic Press, New York, 2001).
4. S. Zorba and Y. Gao, in *Encyclopedia of Nanoscience and Nanotechnology*, H.S. Nalwa, Ed., vol. 8, p. 271 (American Scientific Publishers, Los Angeles, CA, 2004).
5. S. Hufner, *Photoelectron Spectroscopy: Principles and Applications* (Springer-Verlag, Berlin, Germany, 1995).
6. M.P. Seah and W.A. Dench, *Surf. Interface Anal.* **1**, 2 (1979).
7. R. Wiesendanger, *Scanning Probe Microscopy and Spectroscopy: Methods and Applications* (Cambridge University Press, Cambridge, U.K. 1995).
8. H. Ishii, K. Sugiyama, E. Ito, and K. Seki, *Adv. Mater.* **11**, 605 (1999).
9. L. Yan and Y. Gao, *Thin Solid Films* **417**, 101 (2002).
10. R.T. Tung, *Phys. Rev. Lett.* **84**, 6078 (2000).
11. Li Yan, N.J. Watkins, S. Zorba, Y. Gao, and C.W. Tang, *Appl. Phys. Lett.* **81**, 2752 (2002).
12. I.G. Hill, A. Rajagopal, and A. Kahn, *J. Appl. Phys.* **84**, 3236 (1998).
13. J. Kido and T. Matsumoto, *Appl. Phys. Lett.* **73**, 2866 (1998).
14. E.J. Lous, P.W.M. Blom, L.W. Molenkamp, and D.M. de Leeuw, *Phys. Rev. B* **51**, 17251 (1995).
15. C.M. Heller, I.H. Campbell, D.L. Smith, N.N. Barashkov, and J.P. Ferraris, *J. Appl. Phys.* **81**, 3227 (1997).
16. Y. Yang and A.J. Heeger, *Nature* **372**, 344 (1994).
17. J.R. Sheats, H. Antoniadis, M.R. Hueschen, W. Leonard, J. Miller, R. Moon, D. Roitman, and A. Stocking, *Science* **273**, 884 (1996).
18. Y. Gao and L. Yan, *Chem. Phys. Lett.* **380**, 451 (2003).
19. L. Yan, N.J. Watkins, S. Zorba, Y. Gao, and C.W. Tang, *Appl. Phys. Lett.* **79**, 4148 (2001).
20. M.G. Mason, C.W. Tang, L.S. Hung, P. Raychaudhuri, J. Madathil, D.J. Giesen, L. Yan, et al., *J. Appl. Phys.* **89**, 2756 (2001).
21. H. Ding and Y. Gao, *Appl. Phys. Lett.* **86**, 213508 (2005).

22. J. Wusten, S. Berger, K. Heimer, S. Lach, and Ch. Ziegler, *J. Appl. Phys.* **98**, 013705 (2005).
23. J. Wusten, K. Heimer, S. Lach, and Ch. Ziegler, *J. Appl. Phys.* **102**, 023708 (2007).
24. Y. Harima, K. Yamashita, H. Ishii, and K. Seki, *Thin Solid Films* **366**, 237 (2000).
25. M.S. Liao and S.J. Scheiner, *Chem. Phys.* **114**, 9780 (2001).
26. A. Yakimov and S.R. Forrest, *Appl. Phys. Lett.* **80**, 1667 (2002).
27. H. Ding and Y. Gao, *Appl. Phys. Lett.* **92**, 053309 (2008).
28. H. Ding and Y. Gao, *J. Appl. Phys.* **102**, 043703 (2007).
29. A. Rosa and E.J. Baerends, *Inorg. Chem.* **31**, 4717 (1992).
30. T. Schwieger, H. Peisert, M.S. Golden, M. Knupfer, and J. Fink, *Phys. Rev. B* **66**, 155207 (2002).
31. H. Ding, K.W. Park, K. Green, and Y. Gao, *Chem. Phys. Lett.* **454**, 229 (2008).
32. S.M. Sze, *Physics of Semiconductor Devices* (John Wiley, New York, 1981).
33. R.C. Weast, M.J. Astle, and W.H. Beyer, *CRC Handbook of Chemistry and Physics* (CRC Press, Boca Raton, FL, 1985).
34. V.E. Choong, M.G. Mason, C.W. Tang, and Y. Gao, *Appl. Phys. Lett.* **72**, 2689 (1998).
35. H. Ding and Y. Gao, *Appl. Phys. Lett.* **87**, 051918 (2005).
36. C.W. Tang and S.A. VanSlyke, *Appl. Phys. Lett.* **51**, 913 (1987).
37. S.A. VanSlyke, C.H. Chen, and C.W. Tang, *Appl. Phys. Lett.* **69**, 2160 (1996).
38. L.S. Hung, C.W. Tang, and M.G. Mason, *Appl. Phys. Lett.* **70**, 152 (1997).
39. G.E. Jabbour, B. Kippelen, N.R. Armstrong, and N. Peyghambarian, *Appl. Phys. Lett.* **73**, 1185 (1998).
40. G.E. Jabbour, Y. Kawabe, S.E. Shaheen, J.F. Wang, M.M. Morrell, B. Kippelen, and N. Peyghambarian, *Appl. Phys. Lett.* **71**, 1762 (1997).
41. S.E. Shaheen, G.E. Jabbour, M.M. Morrell, Y. Kawabe, B. Kippelen, N. Peyghambarian, M.-F. Nabor, R. Schlaf, E.A. Mash, and N.R. Armstrong, *J. Appl. Phys.* **84**, 2324 (1998).
42. C.H. Lee, *Synth. Met.* **91**, 125 (1997).
43. X. Yang, Y. Mo, W. Yang, G. Yu, and Y. Cao, *Appl. Phys. Lett.* **79**, 563 (2001).
44. R. Schlaf, B.A. Parkinson, P.A. Lee, K.W. Nebesny, and N.R. Armstrong, *Appl. Phys. Lett.* **73**, 1026 (1998).
45. K.L. Wang, B. Lai, M. Lu, X. Zhou, L.S. Liao, X.M. Cing, X.Y. Hou, and S.T. Lee, *Thin Solid Films* **363**, 25 (2000).
46. J.J. Zhao, S.T. Zhang, X.J. Wang, Y.Q. Zhan, X.Z. Wang, G.Y. Zhong, Z.J. Wang, X.M. Ding, W. Huang, and X.Y. Hou, *Appl. Phys. Lett.* **84**, 2913 (2004).
47. Q.T. Le, Li Yan, Y. Gao, M.G. Mason, D.J. Giesen, and C.W. Tang, *J. Appl. Phys.* **87**, 375 (2000).
48. A. Curioni, W. Andreoni, R. Treusch, F.J. Himpel, E. Haskal, P. Seidler, C. Heske, S. Kakar, T. van Buuren, and L.J. Terminello, *Appl. Phys. Lett.* **72**, 1575 (1998).
49. S.T. Lee, X.Y. Hou, M.G. Mason, and C.W. Tang, *Appl. Phys. Lett.* **72**, 1593 (1998).
50. H. Ishii and K. Seki, *IEEE Trans. Electron Dev.* **44**, 1295 (1997).
51. A. Rajagopal and A. Kahn, *J. Appl. Phys.* **84**, 355 (1998).
52. K. Horn, *Appl. Phys. A: Solids Surf. A* **51**, 289 (1990).
53. M.J. Frisch et al., *Geometry and Charges were Calculated with Gaussian98, Revision A.7Gaussian* (Gaussian, Inc., Pittsburgh, PA, 1998).
54. N. Johanson, T. Osada, S. Stafström, W.R. Salaneck, V. Parente, D.A. dos Santos, X. Crispin, and J.L. Brédas, *J. Chem. Phys.* **111**, 2157 (1999).

55. H. Ding and Y. Gao, *Appl. Phys. Lett.* **91**, 172107 (2007).
56. C.I. Wu, C.R. Lee, and T.W. Pi, *Appl. Phys. Lett.* **87**, 212108 (2005).
57. H. Namatame, M. Tamura, M. Nakatake, H. Sto, Y. Ueda, M. Taniguchi, and M. Fujisawa, *J. Elec. Spectrosc. Relat. Phenom.* **80**, 393 (1996).
58. E.W. Forsythe, V.-E. Choong, C.W. Tang, and Y. Gao, *J. Vac. Sci. Technol. A* **17**, 3429 (1999).
59. J.X. Tang, K.M. Lau, C.S. Lee, and S.T. Lee, *Appl. Phys. Lett.* **88**, 232103 (2006).
60. K.M. Lau, J.X. Tang, H.Y. Sun, C.S. Lee, S.T. Lee, and D.H. Yan, *Appl. Phys. Lett.* **88**, 173513 (2006).
61. Y. Gao, H. Ding, H. Wang, and D. Yan, *Appl. Phys. Lett.* **91**, 142112 (2007).
62. A.-L. Barabási and H.E. Stanley, *Fractal Concepts in Surface Growth* (Cambridge University Press, Cambridge, U.K. 1995).
63. A.-L. Barabási and T. Vicsek, *Phys. Rev. A* **44**, 2730 (1991).
64. F. Family and T. Vicsek, *J. Phys. A* **18**, L75 (1985).
65. P. Meakin, *Fractals, Scaling and Growth Far from Equilibrium* (Cambridge University Press, Cambridge, U.K. 1998).
66. T.-M. Lu, H.-N. Yang, and G.-C. Wang, *Mater. Res. Soc. Symp. Proc.* **367**, 283 (1995).
67. Y. Zhao, G.-C. Wang, and T.-M. Lu, *Characterization of Amorphous and Crystalline Rough Surface: Principles and Applications* (Academic Press, New York, 2001).
68. S. Zorba, Y. Shapir, and Y. Gao, *Phys. Rev. B* **74**, 245410 (2006).
69. D.J. Gundlach, Y.Y. Lin, T.N. Jackson, S.F. Nelson, and D.G. Schlom, *IEEE Electron Dev. Lett.* **18** (3), 87 (1997).
70. T. Vicsek, *Phys. Rev. Lett.* **53**, 2281 (1984).
71. J.-K. Zuo and J.F. Wendelken, *Phys. Rev. Lett.* **78**, 2791 (1997), and references 1–6 therein.
72. P.P. Chatraphorn, Z. Toroczkai, and S. Das Sarma, *Phys. Rev. B* **64**, 205407 (2001).
73. M.D. Johnson, C. Orme, A.W. Hunt, D. Graff, J. Sudijono, L.M. Sander, and B.G. Orr, *Phys. Rev. Lett.* **72**, 116 (1994).



# 6

---

## *Interfaces in Organic Electronic Devices— New Insights to Traditional Concepts*

---

Man-Keung Fung, Chun-Sing Lee, and Shuit-Tong Lee

### CONTENTS

6.1	Introduction .....	181
6.2	Electronic Structures of Organic Semiconductors .....	182
6.3	Traditional Concepts to Elucidate Metal/Organic and Organic/ Organic Interfaces .....	185
6.4	Experimental Techniques .....	187
6.5	Electronegativity Model for Barrier Formation at Metal/Organic Interfaces .....	189
6.5.1	Work Function versus Electronegativity .....	189
6.5.2	Extension of the Electronegativity Concept .....	194
6.6	O/O Heterojunctions .....	195
6.6.1	Substrate Effect on Alq <sub>3</sub> /CuPc Interface .....	196
6.6.2	Energy-Level Alignment at Different O/O Heterojunctions .....	199
6.7	Implications .....	203
6.7.1	Ambipolar Organic Field-Effect Transistor .....	203
6.7.2	Stacked Organic Light-Emitting Diode .....	204
6.8	Conclusions .....	207
	Acknowledgment .....	208
	References .....	208

---

### 6.1 Introduction

An epoch of using organic materials for electrical, electronic, and opto-electronic applications has been going on since 1977, when Chiang et al. [1] discovered a tremendous increase of 11 orders of magnitude in electrical conductivity of polymer when halogen was introduced into polyacetylene. A new nomenclature of “organic semiconductors” was therefore coined

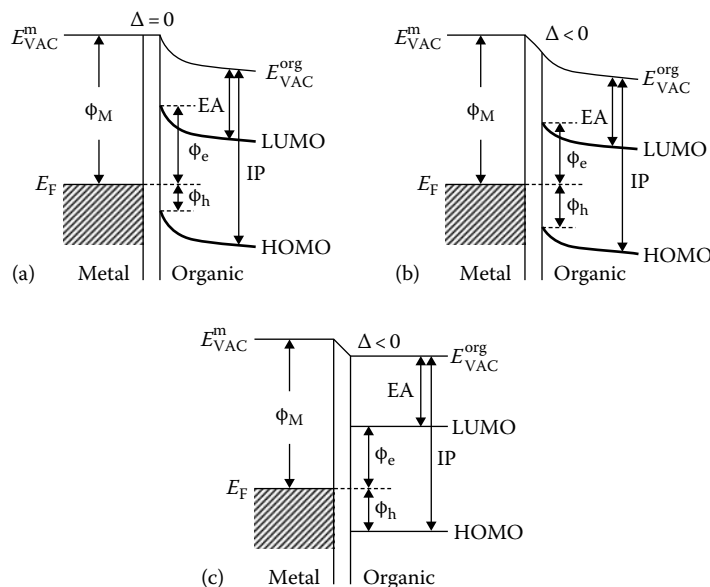
specifically for this new class of conducting materials. In the last 20 years, organic semiconductors have graduated rapidly from a topic of research interest to a material with a wide range of applications, which include polymer light-emitting diodes (PLEDs) [2,3], small-molecule-based organic light-emitting diodes (OLEDs) [4–7], organic lasers [8,9], organic transistors [10–12], solar cells [13–15], organic memory [16,17], etc.

The charge–carrier injection process at the metal/organic and organic/organic junctions is well known to have paramount influences on the performance of those organic electronic and optoelectronic devices. To use OLED as an example, its threshold voltage is mostly determined by the injection barrier (the barrier height at the contacting electrode/organic interface) of the majority carriers. Optimization of device efficiency requires a balanced injection of holes and electrons which are controlled by proper matching of electronic energy levels at various interfaces. The chemistry at the organic/electrode and organic/organic interfaces is also a critical factor affecting the operation stability and luminous efficiency. In other words, understanding the electronic structures and chemical properties of the metal/organic and the organic/organic interfaces is of crucial importance for improving the performance of OLEDs and other organic semiconductor devices.

---

## 6.2 Electronic Structures of Organic Semiconductors

As seen in Figure 6.1, surface electronic properties of metals and organic materials, such as work function ( $\phi$ ), ionization potential (IP), electron affinity (EA), and band gap ( $E_g$ ), are determined by the vacuum level ( $E_{VAC}$ ), highest occupied molecular orbital (HOMO), and lowest unoccupied molecular orbital (LUMO).  $E_{VAC}$  is the energy of an electron at a point sufficiently far away from the surface to be free from the influence of the surface.  $\phi$  is defined as the minimum energy required to remove an electron from the interior of the solid to a point just outside the solid, which corresponds to the energy difference between the Fermi level ( $E_F$ ) and  $E_{VAC}$ . HOMO and LUMO are the terminologies used to describe the energy levels in an organic semiconductor, and are actually analogous to valence and conduction band edges, respectively, in inorganic semiconductors. IP is the minimum energy required to bring an electron from the HOMO in a neutral molecule to the vacuum to form a positive ion, while EA is the minimum energy required to form a negative ion.  $\phi$  and IP can be measured by ultraviolet photoemission spectroscopy (UPS), and EA is typically estimated by the subtraction of band gap from the IP. The band gap determined by absorption spectroscopy is considered as the optical band gap ( $E_{opt}$ ) of a material in an ionized state. However, for a realistic electron injection process in organic electronic devices, the LUMO level corresponds to the electron energy of an additional electron occupying the LUMO of the singly negative-charged ground-state

**FIGURE 6.1**

Schematic energy diagrams of an organic/metal interface (a) with band bending and no interface dipole  $\Delta$ ; (b) with band bending and interface dipole; and (c) with an interface dipole and flat molecular levels.

molecule and the HOMO level is the energy level of an electron removed from the HOMO of the singly positive-charged ground-state molecule. Hence, the energy separation of the HOMO and the LUMO levels involved in the electron injection process is called charge-transport gap ( $E_{CT}$ ). These two energy levels can be obtained via the combination of UPS and inverse photoemission spectroscopy (IPES). Thus,  $E_{CT}$  rather than  $E_{opt}$  is more appropriate for the estimation of the carrier injection barrier heights.

It should be noted that the molecular-level alignment at metal/organic interfaces in early days was believed to obey the classical Schottky–Mott limit, which assumes that no interaction occurs at interfaces and the  $E_{VAC}$  between the metal and organic layer is aligned [18,19]. Figure 6.1a illustrates the energy diagram according to the Schottky–Mott model of a metal/organic interface. In this case, the interface barrier heights for hole and electron are simply given by

$$\phi_h = IP - \phi_M \quad (6.1)$$

and

$$\phi_e = \phi_M - EA \quad (6.2)$$

Equations 6.1 and 6.2 imply a linear relationship between the barrier heights and metal work function. Their dependencies are characterized by an interface parameter,  $S$ , which is defined as the derivative of  $\phi_e$  or  $\phi_h$  with respect to  $\phi_M$  (i.e.,  $S \equiv \partial\phi_e/\partial\phi_M$  or  $S \equiv \partial\phi_h/\partial\phi_M$ ). Under the Schottky–Mott model,  $S$  would be equal to one as suggested by Equations 6.1 and 6.2. In general, Schottky–Mott limit assumes that when the metal and semiconductor come into contact, a thermodynamic equilibrium is accomplished with the formation of band bending on the semiconductor side (Figure 6.1a). Band bending in organic solids is defined as a gradient of molecular levels of the molecules in a solid. In fact, the Schottky barrier height is much less dependent on the metal work function, i.e.,  $S < 1$ . This is usually attributed to the presence of interface states in the band gap of the semiconductor, leading to a discontinuity of the vacuum level at the interface and hence the formation of interface dipole ( $\Delta$ ) (Figure 6.1b). Various sources of gap states have been proposed, including surface states [20], metal-induced gap states (MIGSs) [21,22], defect-related states [23], and disorder-induced gap states [24]. As such, the interface barriers have to be modified as

$$\phi_h = IP - \phi_M - \Delta \quad (6.3)$$

and

$$\phi_e = \phi_M - EA + \Delta \quad (6.4)$$

Note that the sign of  $\Delta$  is negative in Figure 6.1b. The equations obviously depict that the interface barrier heights for holes and electrons would be underestimated or overestimated if the  $\Delta$  is not considered. However, it is difficult to quantitatively predict the magnitude of the  $\Delta$  and thereby the interface barrier heights from the well-known bulk values.

The redistribution of the space charges  $N$  and the built-in potential  $V_{bi}$  with a depletion region are governed by the Poisson equation. Analogous to inorganic semiconductor, the depletion layer width  $W$  is expressed as

$$W = \sqrt{2\epsilon_o\epsilon_s V_{bi}/qN} \quad (6.5)$$

where  $\epsilon_s$  is the dielectric constant of the organic layer. However, the band bending as shown in Figure 6.1b requires sufficient number of mobile charge carriers either in a rather thick organic layer or in an organic layer with a good semiconductor character. The photoemission spectroscopic measurements of organic layers with a thickness of up to 100 nm typically show a flat energy level. This controversial point could be explained with two scenarios. (1) For well-purified organic materials, the density of free carriers is low. Analogous to inorganic semiconductors, molecular-level bending could be observed only when the organic semiconductor is doped [25]. (2) No intrinsic Fermi level exists in organic layer, even though the organic

layer is thick enough. As the molecular-level bending is negligible in films of typical experimental thickness, the picture of flat molecular levels is used in the energy diagram as shown in Figure 6.1c.

### 6.3 Traditional Concepts to Elucidate Metal/Organic and Organic/Organic Interfaces

So far surface scientists have substantiated vacuum-level discontinuity at metal/organic interfaces and thus the invalidity of the Schottky–Mott model [26–30]. However, for some specific systems the sign of the interface dipole is apparently inconsistent with the direction of the charge transfer determined by both the experimental measurements and theoretical calculations [28,29]. For example, the trend of the interface dipole observed in *tris*(8-hydroxyquinoline) aluminum ( $\text{Alq}_3$ ) on Au, Ag, Al, and Mg, which indicates electron transfer from the organic into the metals [26], is apparently inconsistent with the photoemission studies that showed that Mg and Al donate their valence electrons to  $\text{Alq}_3$  [31]. Figure 6.2 shows an example of  $\text{Alq}_3$ -on-Mg interface unveiled by UPS and x-ray photoelectron spectroscopy (XPS) N 1s core-level spectra. The vacuum-level shift in Figure 6.2a is commonly explained as the formation of interface dipole, suggesting that electrons are transferred from the organic semiconductor to the metal. This trend contradicts the evidence provided by XPS (Figure 6.2b) that Mg atoms

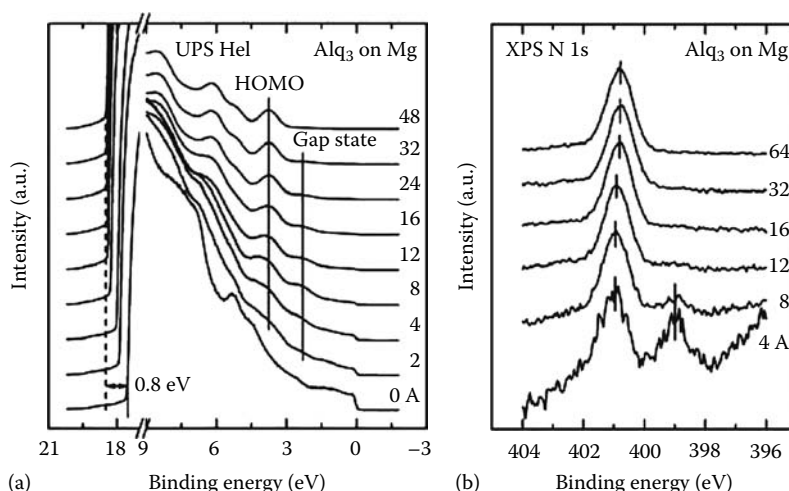


**FIGURE 6.2**

(a) UPS and (b) XPS N 1s core-level spectra of  $\text{Alq}_3$ -on-Mg interface.

donate their valence electrons to  $\text{Alq}_3$ . Therefore, it raises the question whether the experimental vacuum-level discontinuity is indeed associated with a real interface dipole resulting from charge transfer across the interface.

This seemingly conflicting phenomenon originates from a confusion caused by taking work function of metal as a bulk material property. In reality, the measured  $\phi_M$  comprises two parts: the bulk contribution to the work function or the internal work function,  $\phi_{mb}$ , and a surface electric dipole  $\Delta_0$  associated with the tail of the electron wave function spilling out of metal surface into vacuum, as depicted in Figure 6.3. Thus, the work function of metal is in fact a parameter characterized by the metal/vacuum interface. When the metal comes in contact with an organic semiconductor, naturally the dipole barrier certainly would not be the same as that when the metal faces the vacuum. In actuality, the wave functions of electrons on both sides of the metal/organic interface will interact and induce charge density redistribution so as to achieve thermodynamic equilibrium and hence alignment of Fermi levels across the interface. This leads to the formation of a new electric dipole,  $\Delta_1$ , caused by charge redistribution upon replacing the vacuum with an organic film. The resulting shift of the vacuum level across a metal/organic contact or  $\Delta$  is then the difference of  $\Delta_0$  and  $\Delta_1$ , i.e.,  $=-(\Delta_0 - \Delta_1)$  (as shown in Figure 6.4). As a result, it is generally not reliable to estimate the direction of the interfacial charge transfer from  $\Delta$ . If one accepts the notion that the experimentally observed vacuum-level discontinuity at the interface is not a real interface dipole, it would naturally follow that  $\phi_M$  would not be an ideal parameter to describe the variation of interfacial barrier heights

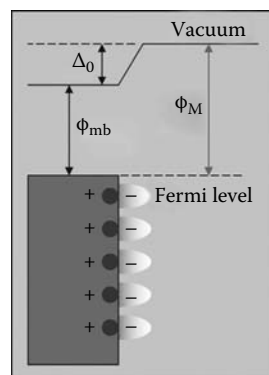


**FIGURE 6.3**

Schematic representation of metal/vacuum interface showing various relevant energies.

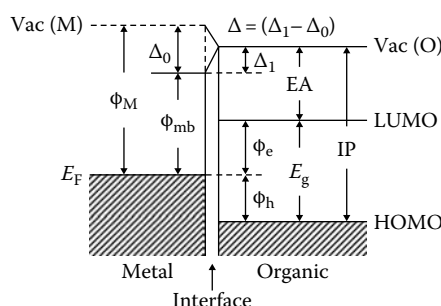


**FIGURE 6.4**

Schematic energy diagram of metal/organic interface. Vac (M) and Vac (O) represent the vacuum level of the metal and the organic layer, respectively.

and hence there exists no quantitative, predictive theory applicable for the estimation of the charge-injection barrier.

The same problem exists in metal/inorganic semiconductor interfaces and has been extensively investigated in the past couple of decades. Metal electronegativity,  $X_M$ , has been successfully used as a key parameter to characterize the trend of carrier-injection barrier heights at the interfaces between metals and inorganic semiconductors [32,33]. For an accurate description and prediction of charge-injection properties, it is necessary to draw a complete picture of these interfacial electronic structures. In this chapter, we discuss the validity of the electronegativity model for metal/organic semiconductor interfaces and extend the investigation for compound electrodes to provide support for the wide generality of the model.

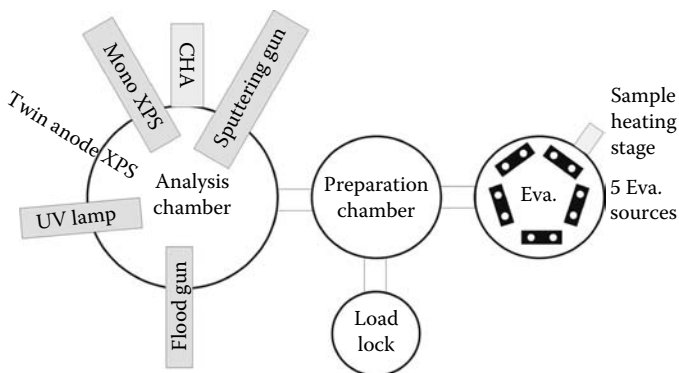
Though the Schottky–Mott model does not give an accurate account of the electronic structures of metal/organic interfaces, it seems to be valid in predicting the energy-level offsets for prevalent undoped organic/organic (O/O) heterojunctions [34–38]. In other words, when two organic semiconductors are brought into contact with one another, vacuum level is aligned with flat energy levels across the heterojunction. It is generally believed that there is a very little charge transfer between any two organic layers and therefore neither dipole nor band bending occurs at the interface. Although there is no strong theoretical support, vacuum-level alignment at the junction is traditionally attributed to the weak intermolecular van der Waals interactions across the heterojunction interface.

In fact, there are still some uncertainties about the applicability of Schottky–Mott model to O/O heterojunctions. For example, it is not clear whether the energy-level alignment is controlled only by the constituents of the heterojunction and is independent of the substrates and the formation sequence of the junction. In this chapter, we also discuss the electronic structures of some representative O/O heterojunctions and investigate the substrate effects on the energy-level alignment. In Section 6.7, we address the implications of the aforementioned for the design of ambipolar OFETs and stacked OLEDs.

---

## 6.4 Experimental Techniques

Photoemission spectroscopy (PES) is by far the most widely used and powerful spectroscopic technique for interface research. XPS and UPS are complementary techniques that utilize different light sources, e.g., x-ray and ultraviolet, to excite electrons in solids via photoelectric effect and then collect the escaped photoelectrons with an energy analyzer. In general, photoemission experiments for interface formation studies are performed in the following way. The study begins with the photoemission analysis of a clean surface of the material that will eventually form one side of the

**FIGURE 6.5**

Schematic drawing of the VG ESCALAB 220i-XL surface analysis system, which consists of an analysis chamber, a multiport carousel chamber, an evaporation chamber, and a sample load lock chamber.

interface, commonly prepared under ultrahigh vacuum (UHV) to prevent contamination. Then, an interface is formed step-by-step by subsequent depositions of another material, which produce an overlayer of gradually increasing thickness. Following this process, the surface-sensitive analysis is repeated after each deposition step.

All photoemission studies reported here were performed in a VG ESCALAB 220i-XL PES system with a monochromatic aluminum K $\alpha$  source (1486.6 eV) for XPS analysis and an unfiltered He I (21.2 eV) and He II (40.8 eV) gas-discharge lamps for UPS analysis. The photoelectrons are collected by a concentric hemispherical analyzer (CHA) equipped with six channeltrons. Shown in Figure 6.5 is a schematic drawing of the surface analysis system. This system consists of an analysis chamber, a multiport carousel chamber, an evaporation chamber with substrate heating elements, and a sample load lock chamber. The base pressures in the analysis chamber, the multiport carousel chamber, the evaporation chamber, and the load lock chamber were  $3 \times 10^{-10}$ ,  $9 \times 10^{-10}$ ,  $5 \times 10^{-10}$ , and  $2 \times 10^{-7}$  mbar, respectively. The absolute energy resolution of the analyzer was 0.018 eV for the UPS and 0.36 eV for the XPS measurements, thus obtaining a spectral resolution of approximately 0.1 eV as estimated from the Fermi edge of Au and a full width at half maximum (FWHM) of 0.7 eV from Au 4f<sub>7/2</sub>. UPS spectra were recorded with a sample bias of -4.0 V to allow observation of the inelastic electron cut-off, so that sharp cut-off edges were observed in all the He I UPS spectra. All the thin films of various materials for surface analyses, including organic small molecular compounds and metals, were in situ deposited by thermal evaporation under UHV conditions. A quartz crystal oscillator is equipped close to the substrate to monitor the thickness and the deposition rate of the films via changes in resonant frequency due to the additional mass of deposited materials.

---

## 6.5 Electronegativity Model for Barrier Formation at Metal/Organic Interfaces

Though Schottky–Mott model has been shown to be invalid at many metal/organic interfaces and can even lead to significant errors on the estimation of injection barriers, it is still extensively used because of the lack of a better alternative solution. After all, there is no quantitative and predictive theory to account for the measured injection barriers. In this section, we discuss the energy-level alignments at interfaces between metal and certain representative organic semiconductors. We present a good linear dependence of the carrier-injection barriers against metal electronegativities, which is rationalized in terms of charge transfer associated with the electronegativity differences of metals and organic semiconductors.

### 6.5.1 Work Function versus Electronegativity

As pointed out earlier, vacuum-level discontinuity across an interface is commonly attributed to the formation of an electric dipole,  $\Delta$ . As a result, barrier heights should be  $\phi_h = IP - \phi_M + \Delta$  and  $\phi_e = \phi_M - EA - \Delta$ . Based on a static dipole model developed by Cowley and Sze, a dipole is established mainly due to electron transfer between the metal and the MIGSs at the interface [39]. A detailed energy band diagram of a metal/n-type semiconductor contact taken from Ref. [39] is replotted in Figure 6.6. The MIGS is essentially determined by the interface Fermi level position and the charge neutrality level (CNL) of the gap states. Assuming a constant density of MIGS ( $D_s$ , number of states per area per electron volt), the interface dipole in thermodynamic equilibrium can be expressed as

$$\Delta = e^2 D_s \Delta \phi \delta / \epsilon_0 \quad (6.6)$$

where

$\epsilon_0$  is the vacuum permittivity

$\Delta\phi$  the energy difference between Fermi level and CNL

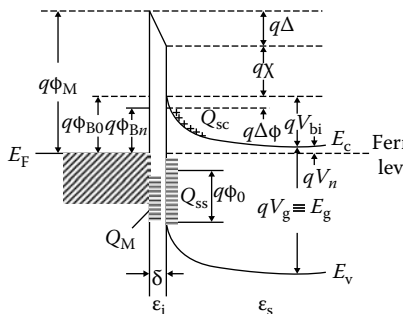
$\delta$  the effective thickness of the interfacial layer

The barrier heights for hole and electron injection are, respectively, given by

$$\phi_h = -S_M \phi_M + \phi_0 \quad (6.7)$$

and

$$\phi_e = E_g - \phi_h = S_M \phi_M + E_g - \phi_0 \quad (6.8)$$



$\Phi_M$  = Work function of metal

$\Phi_{Bn}$  = Barrier height of metal/semiconductor barrier

$\Phi_{B0}$  = Asymptotic value of  $\Phi_{Bn}$  at zero electric field

$\phi_0$  = Energy level at surface

$\Delta\phi$  = Image force barrier lowering

$\Delta$  = Potential across interfacial layer

$\chi$  = Electron affinity of semiconductor

$V_{bi}$  = Built-in potential

$\epsilon_s$  = Permittivity of semiconductor

$\epsilon_i$  = Permittivity of interfacial layer

$\delta$  = Thickness of interfacial layer

$Q_{sc}$  = Space charge density in semiconductor

$Q_{ss}$  = Surface-state density on semiconductor

$Q_M$  = Surface-charge density on metal

**FIGURE 6.6**

Schematic energy band diagram of the metal/n-type semiconductor interface according to interface gap state models. (From Cowley, A.M. and Sze, S.M., *J. Appl. Phys.*, 36, 3212, 1965. With permission.)

Here

$S_M$  is the interface parameter representing the extent of Fermi level stabilization for a given organic semiconductor

$\phi_o$  is a material property

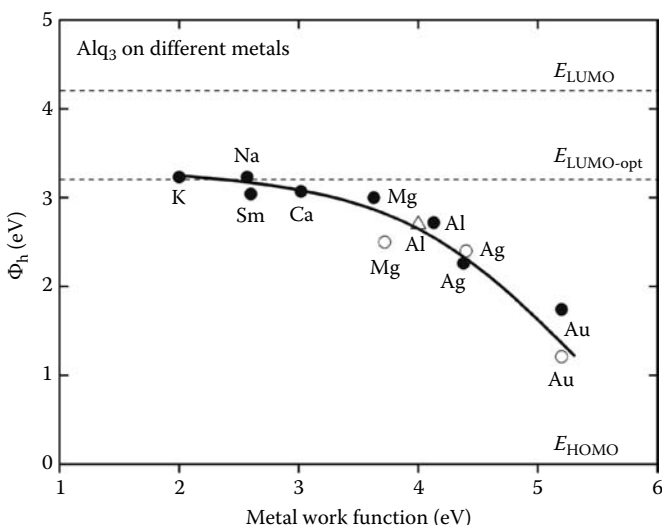
$E_g$  is the energy gap of the organic semiconductor

Interface parameter  $S_M$  is formulated by

$$S_M = \frac{1}{1 + e^2 D_s \delta / \epsilon_o} \quad (6.9)$$

According to Equations 6.7 and 6.8, it can be seen that the injection barriers are a linear function of the metal work function.

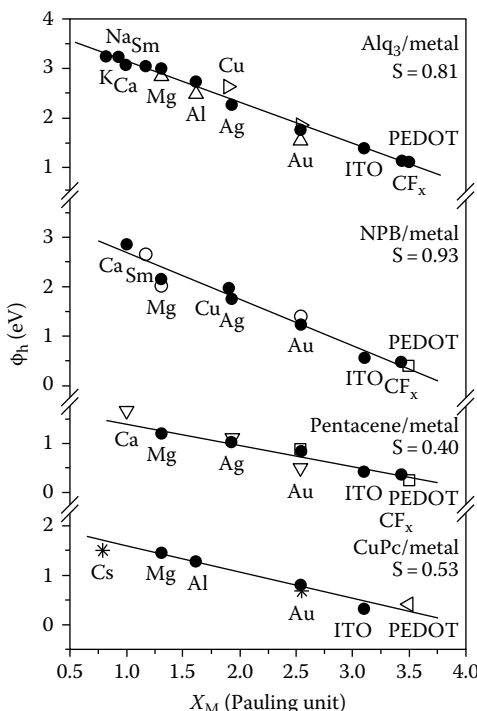
Figure 6.7 shows the variation of  $\phi_h$  versus  $\Phi_M$  for  $\text{Alq}_3$ /metal interfaces. All the  $\phi_h$  were determined from UPS spectra, and the HOMO edge of  $\text{Alq}_3$  ( $E_{HOMO}$ ) is arbitrarily aligned at  $\phi_h = 0$  eV. The open circles and triangle symbols correspond to data taken, respectively, from Refs. [26] and [40] for comparison. It can be seen that  $\phi_h$  deviates from a linear function of  $\Phi_M$ . This phenomenon has been attributed to Fermi level pinning at the onset of the

**FIGURE 6.7**

Hole-injection barrier as a function of metal work function  $\phi_M$ . Filled circles identify results in this work. The remaining results are taken from Refs. [26,40]. (From Tang, J.X. et al., *Chem. Phys. Lett.*, 396, 92, 2004. With permission.)

LUMO of  $\text{Alq}_3$  [30,41]. However, for an actual electron injection process in organic electronic devices, as stated in Section 6.2,  $E_{\text{CT}}$  rather than  $E_{\text{opt}}$  is more appropriate for the estimation of the electron-injection barrier. In Figure 6.7, the two LUMO positions ( $E_{\text{LUMO-opt}}$  and  $E_{\text{LUMO}}$ ) of  $\text{Alq}_3$  are shown with dashed lines for comparison, in which the  $E_{\text{LUMO}}$  was extracted from Ref. [42]. Obviously, the  $E_{\text{LUMO}}$  locates around 1 eV above  $E_F$ , which is too high to account for the Fermi level pinning.

The same problem exists in other metal/inorganic semiconductor interfaces. As explained in Figure 6.3,  $\phi_M$  should only be considered as an interfacial parameter of the metal/vacuum interface rather than a bulk quantity of the metal. It is more reasonable to use  $\phi_{\text{mb}}$  to replace  $\phi_M$  in Equations 6.7 and 6.8 to account for the trend of barrier heights at the interfaces. However,  $\phi_{\text{mb}}$  is not a measurable property and thus cannot be used directly for the estimation of the barrier heights. Instead, metal electronegativity,  $X_M$ , can be used to characterize the trend of carrier injection barrier heights at the interfaces between metals and organic semiconductors. The  $X_M$  is defined as the power of an atom in a molecule to attract electrons to itself. Using UPS, we measured the energy-level alignment at interfaces between metals and representative organic materials that are commonly used in OLEDs, organic transistors, and photovoltaic cells, including  $\text{Alq}_3$ ,  $N,N'$ -bis-(1-naphthyl)- $N,N'$ -diphenyl-4,4'-diamine (NPB), Copper phthalocyanine (CuPc), and Pentacene. Upon the use of Pauling electronegativity scale, our UPS experimental results of  $\phi_h$  versus  $X_M$  for organic materials in contact with metals are plotted in

**FIGURE 6.8**

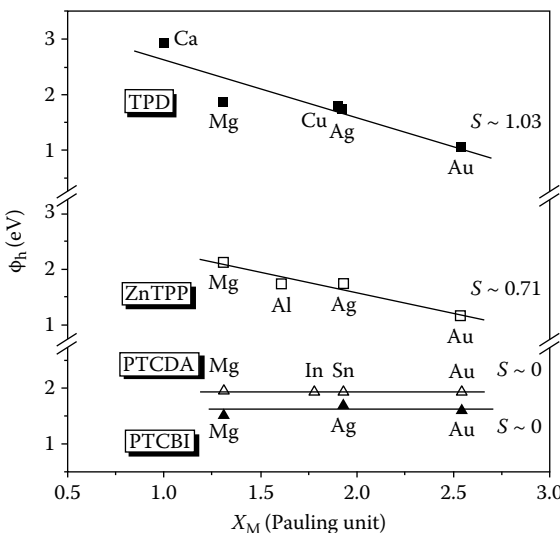
Barrier heights  $\Phi_h$  for interfaces between metals and  $\text{Alq}_3$ , NPB, Pentacene, and CuPc as a function of metal electronegativity  $X_M$ . The  $S$  values are obtained by using a linear least-square fit. The open triangles, squares, and circles correspond to data taken from Refs. [43–45].

Figure 6.8. The open triangles, square, and circles correspond to data taken, respectively, from Refs. [28], [43], and [44] for comparison. It can be seen that all results show a remarkable linear relationship between  $\Phi_h$  and  $X_M$ .

Similarly, when replotted other previously reported data (Figure 6.9), good linear relationships also exist between  $\Phi_h$  and  $X_M$  for other organic semiconductors, such as *N,N'*-bis(3-methylphenyl)-*N,N'*-diphenyl-[1,1'-bisphenyl]-4,4'-diamine (TPD), Zn tetraphenylporphyrin (ZnTPP), 3,4,9,10-perylenetetracarboxylic dianhydride (PTCDA), and 3,4,9,10-perylene-tetracarboxylic bisimidazole (PTCBI) [28,45,46]. The linear relationship of  $\Phi_h$  versus  $X_M$  can be expressed by

$$\Phi_h = -SX_M + \phi'_o \quad (6.10)$$

Least-square straight line fit to the barrier heights data as a function of metal electronegativity yields slopes ( $S = \partial\Phi_h/\partial X_M$ ) from 0 to 1.03 for different organic materials. The results shown here suggest that metal electronegativity is a more appropriate property for describing the barrier heights of metal/organic semiconductor interfaces.

**FIGURE 6.9**

Plots of barrier heights against metal electronegativity for interfaces of TPD, ZnTPP, PTCDA, and PTCBI deposited on metals. The  $\Phi_h$  data are taken from Refs. [28,45,46]. (From Tang, J.X. et al., *Appl. Phys. Lett.*, 87, 252110, 2005. With permission.)

While the theoretical basis for the validity of the electronegativity model needs further investigation, it is nevertheless straightforward to understand why the work function model is not appropriate. Work function is defined as the minimum energy to bring an electron from the surface to a point in vacuum immediately outside the surface, and represents the ability of a material to exchange electrons with vacuum. When a metal comes in contact with an organic material, the metal/vacuum interface no longer exists, and is replaced by a metal/organic interface. The injection barrier is now associated with the ability of the material to exchange electrons with another in contact. This ability is by definition what is measured by electronegativity, as it represents the affinity of a material to attract electrons. According to definition, the electronegativity should predict the direction of charge transfer between the electropositive and the electronegative layer. The local interface dipole, or  $\Delta_1$  as discussed earlier, is established due to the transferred charge between the metal and organic semiconductor as a result of the electronegativity difference.

From a viewpoint of chemistry, charge transfer can associate with chemical interaction between the metal and the organic semiconductor. The electronegativity difference of two materials determines the strength of the chemical bonding and thus the barrier height. According to the derivation proposed by Louie et al. [22], the interface parameter  $S$  can be expressed as

$$S_M = \frac{2.7}{1 + e^2 D_s \delta / \epsilon_0} \quad (6.11)$$

The effective thickness of interfacial layer  $\delta$  is estimated to be  $\delta = d_M/\epsilon_M + d_s/\epsilon_s$ , where  $d_M/\epsilon_M$  in the metal is determined approximately by the Thomas-Fermi screening length ( $\sim 0.5 \text{ \AA}$ ), and the screening length  $d_s/\epsilon_s$  in the organic semiconductor is determined by the organic dielectric constant  $\epsilon_s$  and the distance  $d_s$  between the metal surface and the molecular core of the first monolayer. For PTCDA,  $\epsilon_s$  is estimated to be about 1.9 [47]. Due to the lack of experimental data for  $\epsilon_s$ , the values of other organic dielectric constants are approximated to be about 2. For planar molecules such as PTCDA, Pentacene, and CuPc, the distance  $d_s$  is estimated by assuming all the molecules in the first layer to be lying flat on the metal surface, and is about  $3 \text{ \AA}$  [48]. We may assume that each molecule at the interface region undergoes interaction with metal atoms contributing only one gap state, while each PTCDA molecule contributes four gap states [49]. Here,  $D_s$  is assumed to be uniform in the energy gap and approximated by  $(E_g \cdot A_s)^{-1}$ , where  $A_s$  is the molecular area. The values of organic charge transport gaps are used in this work [28].  $A_s$  of Alq<sub>3</sub> is found to be  $\sim 64 \text{ \AA}^2$  [50]. Areas of PTCDA, CuPc, and Pentacene are estimated to be the values of a unit cell of crystalline films (see Table 6.1) [51–53]. Table 6.1 compares the experimental and calculated values of the interface parameter  $S$ . In most of our studies, good agreement was found between the calculated and experimental values, indicating the validity of Equation 6.11. However, there is relatively large discrepancy for planar molecules including CuPc, Pentacene, and PTCDA. This might be due to the underestimation of the magnitude of  $D_s$ .

### 6.5.2 Extension of the Electronegativity Concept

The electronegativity model has been used successfully on metal/organic semiconductor interfaces, and shown to give a satisfactory description of the interface barrier formation. As electronegativity is defined only for elements it is of interest to investigate if the electronegativity model can be extended to compound electrodes such as indium tin oxide (ITO), which

**TABLE 6.1**

Experimental ( $S_{\text{expt}}$ ) and Calculated ( $S_{\text{cal}}$ ) Values of the Interface Parameter  $S$  at Metal/Organic Interfaces

Material	Alq <sub>3</sub>	NPB	TPD	Pentacene	CuPc	PTCDA
$A (\text{\AA}^2)$	64	200	200	120	190	130
$d_s (\text{\AA})$	4	5	5	3	3	3
$D_s$	0.42	0.25	0.25	0.38	0.39	1.30
$E_g (\text{eV})$	3.70	4.00	4.00	2.20	1.70	2.20
$\epsilon$	2	2	2	2	2	2
$S_{\text{expt}}$	0.81	0.93	1.03	0.44	0.53	0
$S_{\text{cal}}$	0.8	1.0	1.0	0.9	0.9	0.4

Note:  $D_s$  is in the units of  $10^{14} \text{ eV}^{-1} \text{ cm}^{-2}$ .

is widely used in organic optoelectronics. We then check the feasibility of defining an equivalent electronegativity for each compound electrode.

The barrier height,  $\phi_h$ , between  $\text{Alq}_3$  and UV-ozone-treated ITO was experimentally determined to be 1.39 eV by UPS (not shown here). Assuming the electronegativity model to be valid for ITO, this barrier height should also fall on the  $\text{Alq}_3$ /metal straight line in Figure 6.8 and an effective electronegativity of 3.10 for ITO is thus deduced. Similar procedure was repeated, also shown in Figure 6.8, for the interfaces between  $\text{Alq}_3$  and plasma-polymerized fluorocarbon (CFx) and between  $\text{Alq}_3$  and poly(3,4-ethylenedioxy thiophene)/poly(styrenesulfonate) (PEDOT:PSS), giving effective electronegativities of 3.43 for CFx and 3.50 for PEDOT:PSS. Simultaneously, the barrier heights  $\phi_h$  at interfaces between three organic semiconductors (i.e., NPB, Pentacene, and CuPc) and three compound electrodes (i.e., ITO, CFx, and PEDOT:PSS) were measured via UPS [44,45]. It is found that the experimental  $\phi_h$  data points fit very well on the extrapolated straight lines of NPB/metal, Pentacene/metal, and CuPc/metal, suggesting the self-consistence of the electronegativity values and model. While the theoretical base for the extension of the electronegativity model for compounds and alloys has not yet been established, the results are remarkable and warrant further exploration.

The electronegativity model provides a simpler and more realistic method than the “work function approach” to estimate the carrier-injection barriers in contacts between organic semiconductors and electrodes. However, it should be pointed out that other factors, especially the influence of morphological structures of organic semiconductors also play a secondary role in determining the barrier height formation at the metal/organic interfaces. Generally, the metal/organic interfaces are formed between organic films with amorphous geometry and polycrystalline metals, but the electronic structures of crystalline organic semiconductors deposited onto single-crystal metals with different crystalline orientation and surface reconstructions are unknown. Consequently, more systematic experimental work and theoretical refinements are clearly needed.

---

## 6.6 O/O Heterojunctions

The interfaces of undoped O/O heterojunctions generally have a near vacuum-level alignment, which is attributed to the weak intermolecular Van der Waals interaction between organic materials. The  $\phi_h$  and  $\phi_e$  are commonly estimated by the difference of IP and EA, respectively, between the two organic layers. The energy offsets across organic heterojunctions are therefore considered to be independent of substrates and the formation sequence.

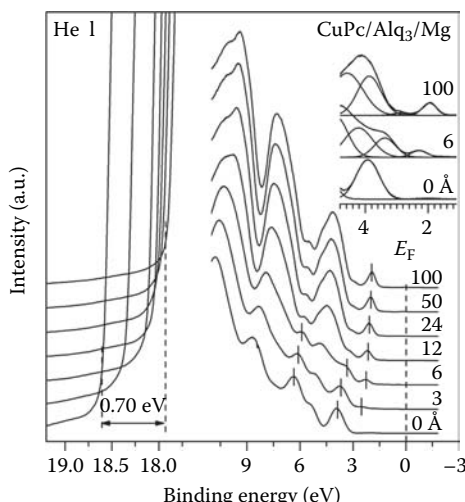
Nevertheless, the mechanisms of the variation of the  $E_F$  position in the organic layers and “band bending” in the energy-level alignment at the organic heterojunctions are yet unclear. In particular, when the Fermi level

is close to the HOMO or LUMO, the validity of the vacuum-level alignment concept remains to be examined. In the following section, we perform a direct measurement of the electronic structure at the interface between CuPc and Alq<sub>3</sub> on Mg and ITO substrates using UPS and XPS. Possible effects of the substrate-induced  $E_F$  variation in the organic energy gap on the energy-level alignment are explored.

### 6.6.1 Substrate Effect on Alq<sub>3</sub>/CuPc Interface

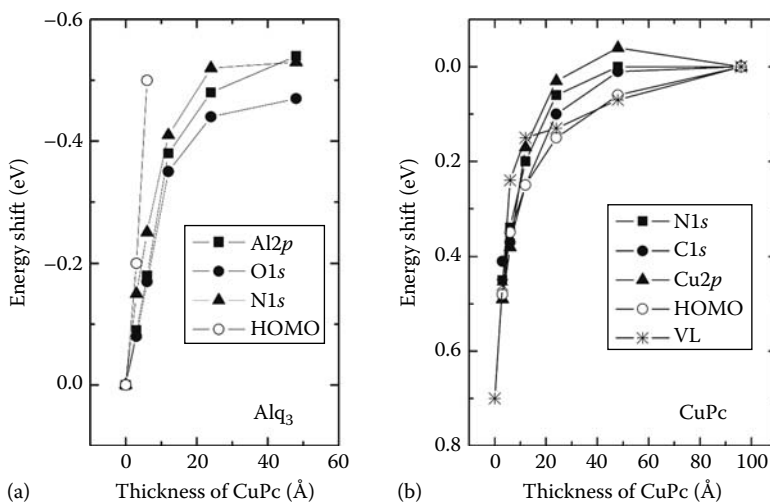
Figure 6.10 shows the UPS spectra of the CuPc/Alq<sub>3</sub> interface on Mg substrate as a function of CuPc thickness. The bottom spectrum was measured from a 100 Å thick Alq<sub>3</sub> layer deposited on Mg substrate. Upon increasing CuPc coverage, characteristic emission features of CuPc and Alq<sub>3</sub> show progressive shifts toward the lower binding energy (BE) region. This is accompanied by a 0.7 eV increase in the vacuum level. When the nominal thickness of CuPc is larger than 12 Å, all the valence features of the underlying Alq<sub>3</sub> layer are fully attenuated. The IP values obtained are 5.8 eV for Alq<sub>3</sub> and 4.8 eV for CuPc.

The HOMO peak offset at the interface is estimated by spectral decomposition using a Gaussian function after background subtraction (see the inset of Figure 6.10). The HOMO peak of Alq<sub>3</sub> is located at 3.92 eV with a full width at half maximum (FWHM) of about 0.85 eV. The HOMO edge of Alq<sub>3</sub> ( $E_{HOMO}$ ) is thus estimated to be 3.20 eV by linear extrapolation at low BE of  $FWHM/\sqrt{2\ln 2}$  from the peak maximum. The  $E_{HOMO}$  of a 100 Å-thick CuPc film is at 1.50 eV with an FWHM of 0.53 eV.



**FIGURE 6.10**

UPS He I spectra as a function of incremental CuPc deposition on Alq<sub>3</sub> on Mg substrate. The inset shows the decomposition of the HOMO levels at the CuPc/Alq<sub>3</sub> interface after background subtraction. (From Tang, J.X. et al., *Appl. Phys. Lett.*, 88, 232103, 2006. With permission.)

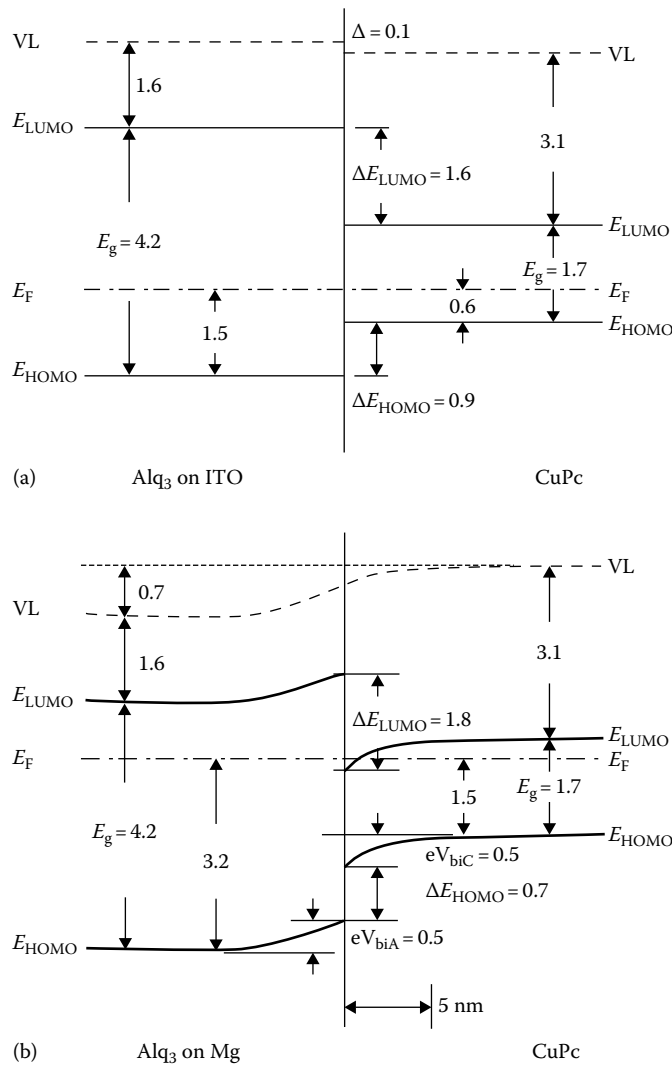
**FIGURE 6.11**

Shift of binding energy related to the features of (a)  $\text{Alq}_3$  and (b) CuPc as a function of CuPc coverage. (From Tang, J.X. et al., *Appl. Phys. Lett.*, 88, 232103, 2006. With permission.)

Figure 6.11 shows the shifts of HOMO, vacuum level (VL) and XPS core levels of (a)  $\text{Alq}_3$  and (b) CuPc as functions of CuPc coverage for the CuPc/ $\text{Alq}_3$  junction on Mg. Due to the superposition of C1s core-level spectra, it is somewhat difficult to determine the exact amount of C1s core-level shift in the  $\text{Alq}_3$  layer. As shown in Figure 6.11, similar shifts are found for both the valence band features and the core levels, which are associated with the energy-level bending at the interface. With increasing CuPc coverage, electronic features of  $\text{Alq}_3$  at the interface show a  $\sim 0.5\text{ eV}$  shift toward the lower BE region (Figure 6.11a). These rule out the contribution from charging in  $\text{Alq}_3$  and reflect the energy-level bending in organic semiconductors at the interface. Spectral features of CuPc show a rigid downward shift of about  $0.5\text{ eV}$  toward the interface.

The same UPS and XPS experiments were repeated by depositing the CuPc/ $\text{Alq}_3$  junction onto a UV-ozone-treated ITO instead of Mg substrate (individual spectrum is not shown here). In this case, except for the intensity of the  $\text{Alq}_3$  features attenuated by the CuPc overlayer, all the molecular-level positions remain constant with a negligible vacuum-level shift at the interface, indicating the absence of band bending in either layer.

Combining the results from the UPS and XPS measurements, energy diagrams of the CuPc/ $\text{Alq}_3$  heterojunction on ITO and Mg substrate are depicted in Figure 6.12. The Fermi levels in two materials are aligned in a thermodynamic equilibrium state. In the schematic energy diagram, the LUMO edge ( $E_{\text{LUMO}}$ ) is derived via the charge transport gaps of  $4.2$  and  $1.7\text{ eV}$  for  $\text{Alq}_3$  and CuPc, respectively [54]. ITO and Mg substrates shift the  $E_F$  position in  $\text{Alq}_3$  film from  $1.5$  to  $3.2\text{ eV}$  above the HOMO edge. The energy-level

**FIGURE 6.12**

Schematic energy-level diagrams of the CuPc/Alq<sub>3</sub> junction on (a) ITO and (b) Mg substrates. All the values shown are in units of eV. Work functions of UV-ozone-treated ITO and Mg substrates are 4.90 and 3.75 eV, respectively. (From Tang, J.X. et al., *Appl. Phys. Lett.*, 88, 232103, 2006. With permission.)

lineup at the CuPc/Alq<sub>3</sub> interface on ITO is consistent with the traditional concept of vacuum-level alignment. However, the same heterojunction formed on Mg substrate shows remarkably different electronic structures. The HOMO offset in the bulks of the two organics on the Mg substrate is estimated to be 1.7 eV, which is different from the value of 0.9 eV in the same

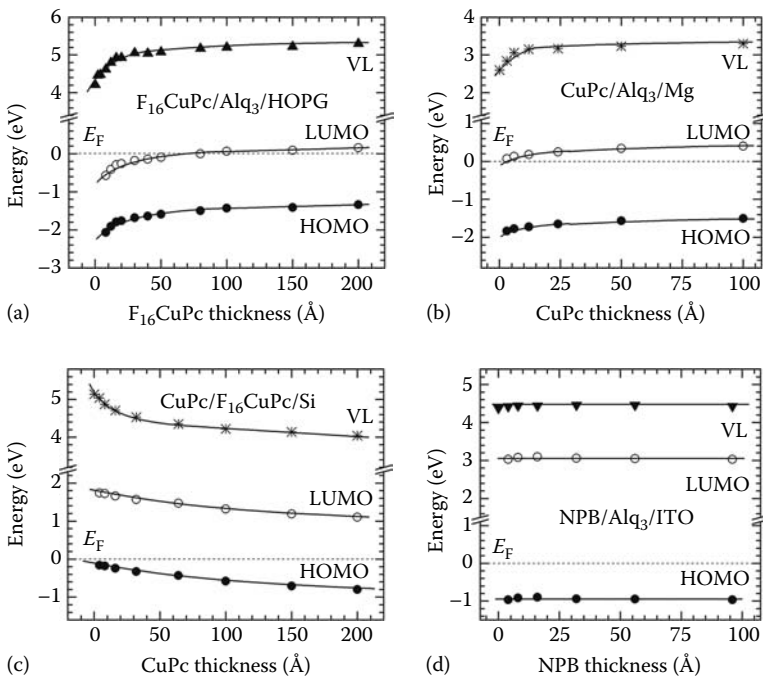
junction formed on ITO. As shown in Figure 6.11b, the built-in potential barriers in Alq<sub>3</sub> and CuPc ( $eV_{biA}$  and  $eV_{biC}$ ) represent the energy-level bending in the space charge regions. Taking into account the total energy-level bending, the HOMO offset directly at the interface ( $\Delta E_{HOMO}$ ) for CuPc/Alq<sub>3</sub> on Mg is, however, reduced to 0.7 eV, while the LUMO offset ( $\Delta E_{LUMO}$ ) is increased to 1.8 eV.

The results observed here indicate that the energy-level alignment at organic heterojunction is affected by the  $E_F$  position in the energy gap, and the applicability of traditional concept of vacuum-level alignment at organic heterojunction is obviously limited to some specific conditions. For example, the energy offsets at the NPB/bathocuproine (BCP) interface remain unchanged with respect to the modification of the  $E_F$  position by changing the metal substrates [42]. It is believed that the Fermi level is located near the middle of the energy gap with few excess densities of states, and therefore the energy levels remain flat corresponding to the vacuum-level alignment as shown in Figure 6.12a.

### 6.6.2 Energy-Level Alignment at Different O/O Heterojunctions

We further present photoemission spectroscopic studies on other O/O heterojunctions, i.e., copper hexadecafluorophthalocyanine (F<sub>16</sub>CuPc)/Alq<sub>3</sub>, CuPc/F<sub>16</sub>CuPc, and NPB/Alq<sub>3</sub> on different substrates. Figure 6.13 depicts the electronic structures of F<sub>16</sub>CuPc/Alq<sub>3</sub>, CuPc/Alq<sub>3</sub>, CuPc/F<sub>16</sub>CuPc, and NPB/Alq<sub>3</sub> heterojunctions as derived from the UPS spectra. Note that the above heterojunctions were deposited onto HOPG, Mg, Si, and ITO, respectively, and the  $E_{LUMO}$  is deduced from the charge transport gaps. Phenomena similar to those in the CuPc/Alq<sub>3</sub> heterojunction as shown in the previous section (the experiment was redone and its result is shown in Figure 6.13b) were also observed in the F<sub>16</sub>CuPc/Alq<sub>3</sub> and CuPc/F<sub>16</sub>CuPc heterojunctions (Figure 6.13a and c), indicating energy-level shifts at the interface. Analogous to the conventional semiconductor heterojunction, the energy-level bending occurring at the O/O heterojunction is associated with the formation of space charge layers. An accumulation layer of negative space charges adjacent to the interface is formed in the F<sub>16</sub>CuPc layer of the F<sub>16</sub>CuPc/Alq<sub>3</sub> heterojunction (Figure 6.13a) and in the CuPc layer of the CuPc/Alq<sub>3</sub> heterojunction (Figure 6.13b). Meanwhile, Fermi level pinning to the  $E_{LUMO}$  or  $E_{HOMO}$  occurs at the heterojunction interface. In contrast, the NPB/Alq<sub>3</sub> heterojunction on ITO is formed in a different manner (Figure 6.13d); here the energy-level alignment at the NPB/Alq<sub>3</sub> interface is in agreement with the classical vacuum-level alignment rule. In this case, the energy positions of all the molecular orbitals remain fixed with a negligible VL shift at the interface, indicating the absence of energy-level bending in either layer.

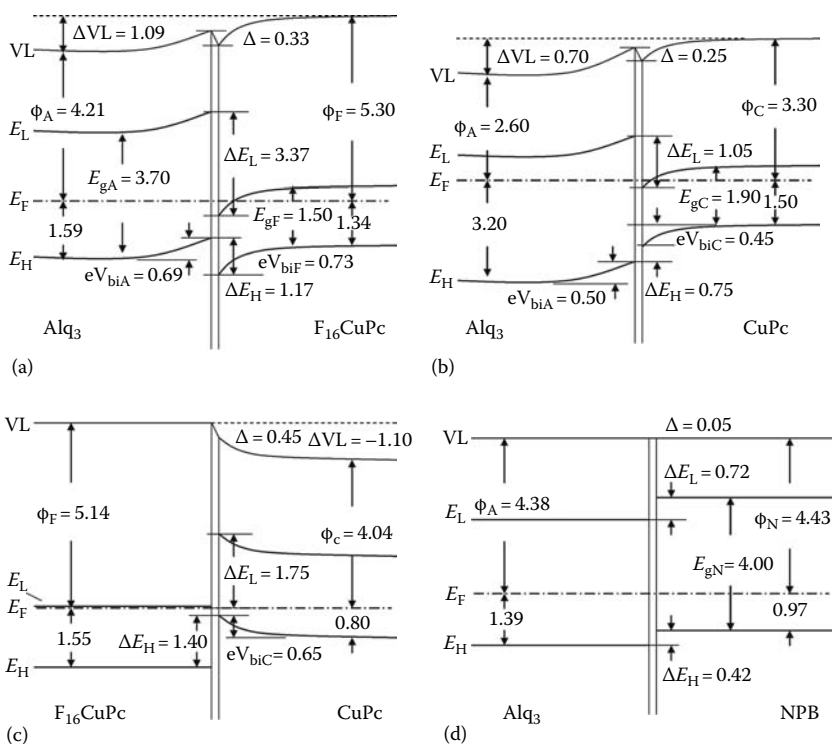
Figure 6.14 shows the schematic energy diagrams of the four heterojunctions using data from Figure 6.13. Fermi levels in two semiconductors are aligned in a thermodynamic equilibrium. The built-in potential barrier,  $eV_{bi}$ ,

**FIGURE 6.13**

Energy shifts of the HOMO, LUMO, and VL of (a)  $F_{16}\text{CuPc}$  in  $F_{16}\text{CuPc}/\text{Alq}_3$ , (b) CuPc in CuPc/ $\text{Alq}_3$ , (c) CuPc in  $\text{CuPc}/F_{16}\text{CuPc}$ , and (d) NPB in NPB/ $\text{Alq}_3$ , deduced from UPS measurements. The zero of the energy scale corresponds to the Fermi level. (From Tang, J.X. et al., *J. Appl. Phys.*, 101, 064504, 2007. With permission.)

represents the energy-level bending at the interface. The interface dipole effect occurring directly at the interface can be distinguished by taking into account the total energy-level bending. In Figure 6.14a through c, the energy-level alignment of O/O heterojunctions clearly deviates from the vacuum-level alignment rule. The observed  $\Delta E_H$  in the bulks of two organic semiconductors are remarkably different from the predicted values under the vacuum-level alignment rule: 0.25 eV versus 0.84 eV for  $F_{16}\text{CuPc}/\text{Alq}_3$ , 1.70 eV versus 1 eV for CuPc/ $\text{Alq}_3$ , and 0.75 eV versus 1.89 eV for CuPc/ $F_{16}\text{CuPc}$ . The experimental findings here suggest that energy-level alignment in O/O heterojunctions does not always obey the vacuum-level alignment rule. On the other hand, these results also hint that the position of the Fermi level with respect to the energy gaps of the organic semiconductors might be an important factor that influences energy-level alignment.

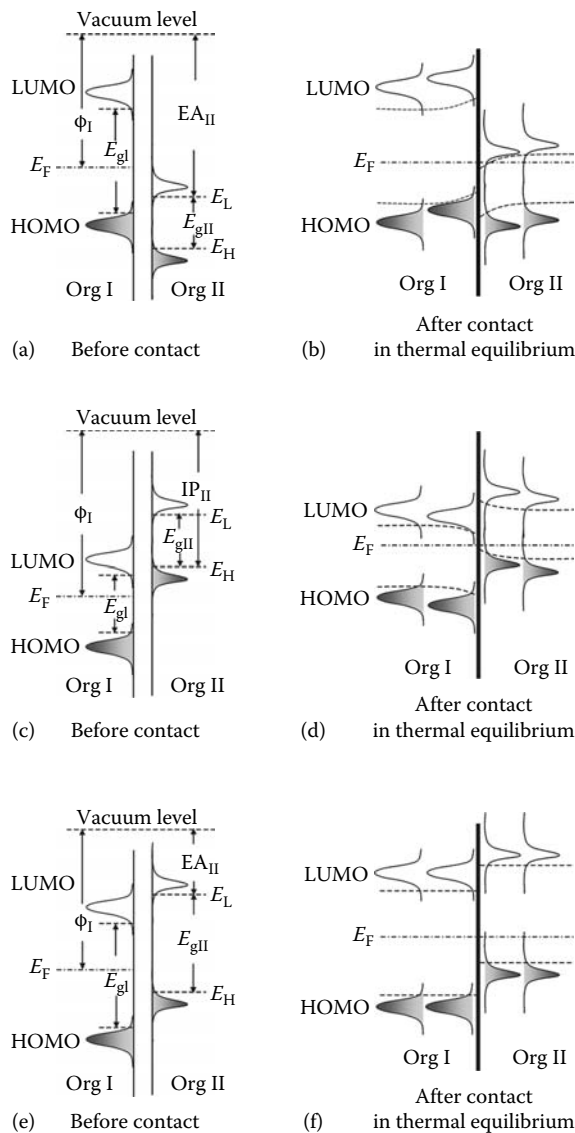
Here we propose a mechanism to describe the formation of O/O heterojunctions. The position of the Fermi level in organic semiconductors (e.g.,  $\text{Alq}_3$  and TPD) is observed to depend strongly on metal substrates, rather than on the thickness of the organic films [55]. Besides an abrupt VL shift at the interface with a thickness lower than 10 Å, the Fermi level position

**FIGURE 6.14**

Schematic energy-level diagrams of (a) F<sub>16</sub>CuPc/Alq<sub>3</sub> heterojunction on HOPG, (b) CuPc/Alq<sub>3</sub> heterojunction on Mg, (c) CuPc/F<sub>16</sub>CuPc heterojunction on Si, and (d) NPB/Alq<sub>3</sub> heterojunction on ITO. All the values shown are in the units of eV. The work function of the HOPG, Mg, Si, and ITO substrates are estimated to be 4.43, 3.75, 3.95, and 4.95 eV, respectively. (From Tang, J.X. et al., *J. Appl. Phys.*, 101, 064504, 2007. With permission.)

remains constant in the energy gap at thicker region up to 6000 Å for Alq<sub>3</sub> and 1100 Å for TPD [56]. Therefore, for film thickness (<300 Å) used here and in typical organic devices (films of about 500–1000 Å are used), the Fermi level in the underlying organic semiconductor (Org I) is a quasi-quantity controlled by the substrates instead of the intrinsic bulk value.

Consider the situation shown in Figure 6.15a (or Figure 6.15c), the work function of the underlying organic semiconductor (Org I) is initially smaller (or larger) than the EA (or IP) of the top layer (Org II) when two semiconductors are separated. Upon the formation of the O/O heterojunction, the Fermi level in Org I is expected to exceed the LUMO (or HOMO) edge of Org II, resulting in the spontaneous charge redistribution at the interface and therefore the formation of space charge layers. The negative space charge in the accumulation layer in Org II is balanced by the positive space charge in the depletion layer of Org I. After matching up the Fermi levels

**FIGURE 6.15**

Schematic diagrams showing possible formation of O/O heterojunctions. Simplified energy-level schemes of two organic semiconductors I and II ( $\phi_I < EA_{II}$ ) (a) before and (b) after contact with thermal equilibrium is established. Energy-level schemes of two organic semiconductors I and II ( $\phi_I > IP_{II}$ ) before (c) and after (d) contact. Energy-level schemes of two organic semiconductors I and II ( $\phi_I > EA_{II}$ ) before (e) and after (f) contact. (From Tang, J.X. et al., *J. Appl. Phys.*, 101, 064504, 2007. With permission.)

in thermal equilibrium, the Fermi level is pinned at the LUMO (or HOMO) edge of Org II as shown in Figure 6.15b (or Figure 6.15d). The energy-level offsets are consequently changed. Considering the localization nature of

carrier wave functions in molecules and the absence of chemical interaction at the interface, the pinning phenomenon cannot be presumably attributed to the presence of a continuum of surface- or interface-induced gap states [56]. The space charges may be stored by states of sufficient density generated by the extension of occupied and unoccupied orbitals or by trapping states exponentially distributed in the energy gap.

On the other hand, for the situation shown in Figure 6.15e, the Fermi level of Org I is initially far from the HOMO or LUMO edge of Org II. Since the process of aligning Fermi level at O/O heterojunction interface involves negligible densities of states in the energy gap, charge redistribution is expected not to take place at the interface. The O/O heterojunction formation therefore follows the vacuum-level alignment rule (Figure 6.15f). This is the reason why it is commonly observed that wide-energy gap O/O heterojunctions, such as NPB/Alq<sub>3</sub> (Figure 6.14d) follows the vacuum alignment rule, even though the Fermi level position is manipulated by changing the substrates [35–37,54].

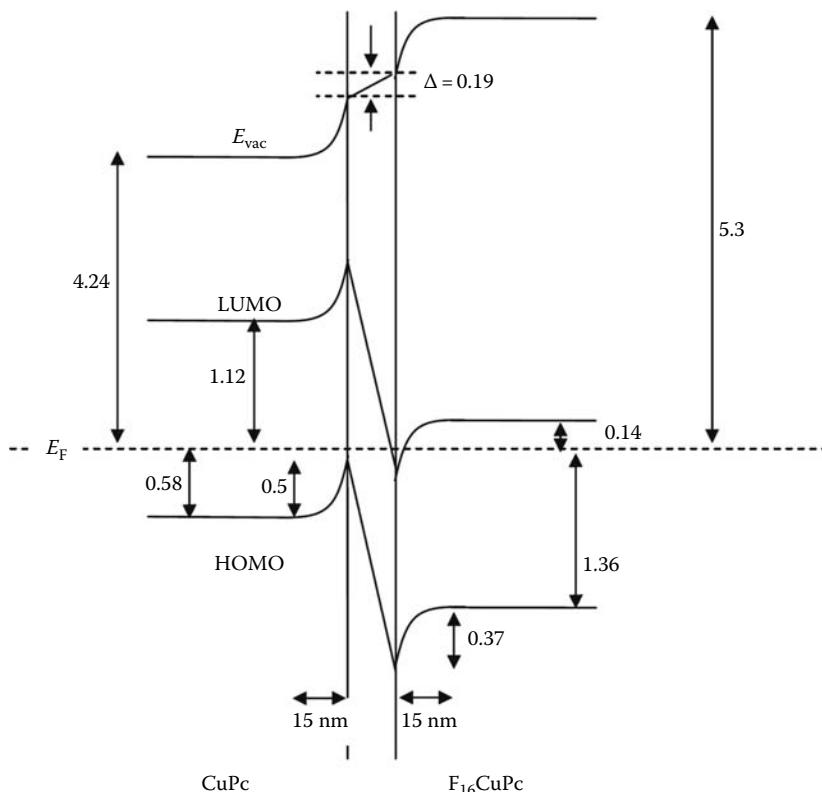
---

## 6.7 Implications

### 6.7.1 Ambipolar Organic Field-Effect Transistor

Recently, a number of ambipolar OFETs have been developed to make complementary logic circuit based on organic heterojunctions between p- and n-type conductors [57–62], e.g., organic heterojunctions of  $\alpha$ -sexithiopene ( $\alpha$ -6T)/fullerene (C<sub>60</sub>) [58], pentacene/C<sub>60</sub> [60], and F<sub>16</sub>CuPc/CuPc [57,62]. As what we found in Section 6.6, we realize that the O/O interfaces do not necessarily follow the vacuum-level alignment rule. Therefore, we will discuss how the organic heterojunction derived from the discontinuities in the energy levels at the interfaces influences the operating characteristics of ambipolar OFETs.

Figure 6.16 shows the electronic structures of F<sub>16</sub>CuPc-on-CuPc junction as revealed by UPS. First and foremost, it can also be seen that the molecular levels of the two materials exhibit a progressive shift upon the deposition and become nearly constant, reflecting the band bending of energy levels of organic semiconductors at the interface. The bending widths for both CuPc and F<sub>16</sub>CuPc are about 15 nm. Using Poisson's equation and assuming a dielectric constant of 5 for both CuPc and F<sub>16</sub>CuPc [63], we estimate the charge carrier density to be about  $10^{18} \text{ cm}^{-3}$ , which is six orders of magnitude larger than the upper limit of the intrinsic carrier concentration for pure organic films ( $\sim 10^{12} \text{ cm}^{-3}$ ) [64]. The excessive carrier density is attributed to extrinsic carriers transferred from the adjacent organic material. When CuPc and F<sub>16</sub>CuPc come into contact, CuPc serves as a donor while F<sub>16</sub>CuPc becomes an acceptor. Electrons would move from CuPc to F<sub>16</sub>CuPc across the interface and holes would be created in CuPc. Consequently, the accumulation

**FIGURE 6.16**

A schematic energy-level diagram of the  $\text{F}_{16}\text{CuPc}/\text{CuPc}$  heterojunction. (From Lau, K.M. et al., *Appl. Phys. Lett.*, 88, 173513, 2006. With permission.)

of holes and electrons at the interface leads to substantial band bending in both the CuPc and  $\text{F}_{16}\text{CuPc}$  layers. In a CuPc- $\text{F}_{16}\text{CuPc}$  OFET, the free holes and electrons in, respectively, the CuPc and the  $\text{F}_{16}\text{CuPc}$  sides can be easily driven along the interface by an electric field applied across the drain and the source electrodes. Hence, the  $\text{F}_{16}\text{CuPc}/\text{CuPc}$  heterojunction exhibits ambipolar characteristics [57,62]. Furthermore, the electronic structure at the  $\text{F}_{16}\text{CuPc}/\text{CuPc}$  interface would facilitate the carrier transfer across the interface, which is potentially applicable as a connection unit in stacked OLEDs.

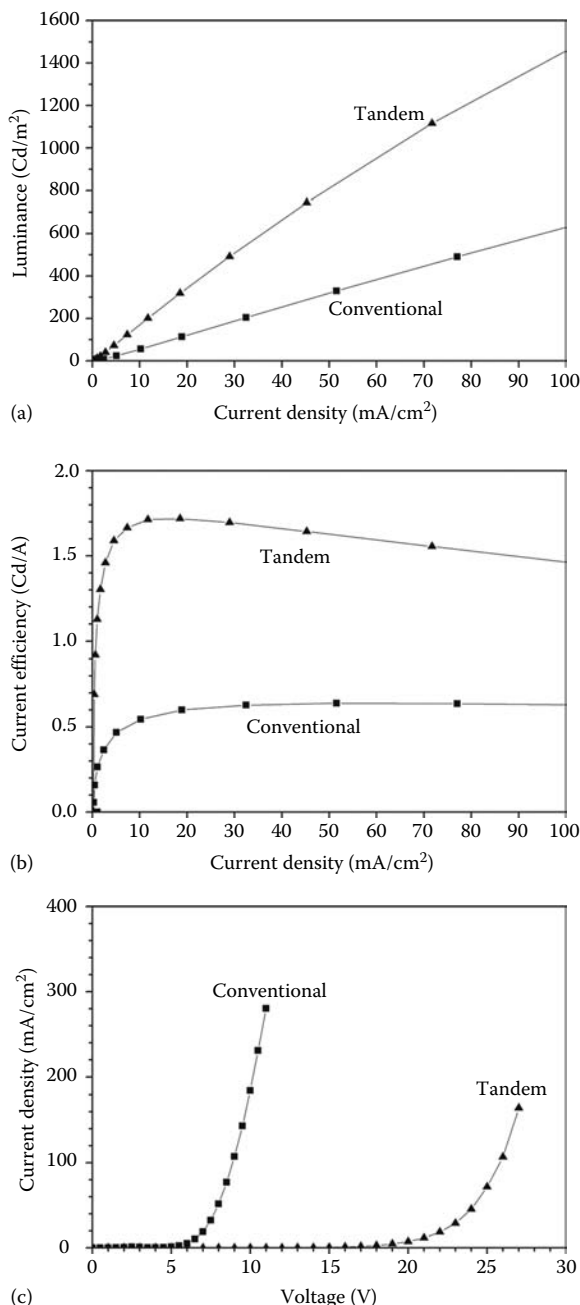
### 6.7.2 Stacked Organic Light-Emitting Diode

To date, a variety of connecting units have been introduced for stacked OLEDs, which include Cs:BCP/ITO [65], Cs:BCP, Li:BCP/ $\text{V}_2\text{O}_5$  [66,67], Li:Alq<sub>3</sub>, Li:1,3,5-tris(*N*-phenylbenzimidazol-2-yl) benzene (TPBI)/FeCl<sub>3</sub>:NPB [68], Mg:Alq<sub>3</sub>:WO<sub>3</sub>, V<sub>2</sub>O<sub>5</sub>, 2,3,5,6-tetrafluoro-7,7,8,8-tetracyanoquinodimethane

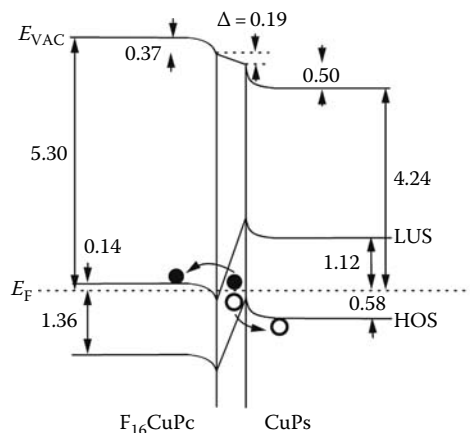
(F<sub>4</sub>-TCNQ):4,4'4''-tris(3-methylphenylphenylamino) triphenylamine (m-MTDATA) [69–72], Li:BPhen, Cs<sub>2</sub>CO<sub>3</sub>:Alq<sub>3</sub>/MoO<sub>3</sub> [73,74], and Cs:BPhen/F<sub>4</sub>-TCNQ:NPB [75]. The fabrication of these connecting units typically requires sputtering or coevaporation processes. Since these units all consist of reactive metals or toxic metal oxides, their fabrication therefore either requires high-temperature deposition and/or delicate handling care, which inevitably increases manufacturing cost. Another potential problem in these doped organic systems is that some metals (e.g., Li) and organic dopants (e.g., F<sub>4</sub>-TCNQ) are known to have high diffusivity in organic layers, in which the diffusion length of Li in Alq<sub>3</sub> can be up to 30 nm [76–78]. The diffusion of dopants significantly alters the electrical conductivity of organic layers, and thus readily causes undesirable changes in the device characteristics under continuous operation. It is thus of interest to investigate the feasibility of using undoped and pure organic-based connecting units. As we have successfully explained the binary system of F<sub>16</sub>CuPc-on-CuPc in OFETs, in this section we will investigate CuPc-on-F<sub>16</sub>CuPc as a connecting unit to join two deep-blue-emitting stacked OLEDs.

Emitting units were fabricated with a hole-transporting NPB, blue light-emitting 2-methyl-9,10-di(2-naphthyl) anthracene (MADN), and electron-transporting BPhen layer; while the CuPc/F<sub>16</sub>CuPc connecting unit was used for joining two emitting units. Ag/Yb was used as a light-reflective cathode. Figure 6.17a and b depicts the luminance and current efficiency as a function of current density for the conventional and the tandem OLEDs. Clearly, the device performance is significantly improved for the tandem OLED. For instance, at a luminance of 100 cd/m<sup>2</sup> (typical brightness for display application), the current density required is only 6.2 mA/cm<sup>2</sup> for the tandem OLED, much lower than that is required for the conventional single-emitting-unit device (17.1 mA/cm<sup>2</sup>). Similarly, at a current density of 100 mA/cm<sup>2</sup>, the current efficiency of the conventional OLED is 0.63 cd/A, while that of the tandem OLED remarkably increases to 1.47 cd/A. These values clearly demonstrate the effectiveness of the two-emitting-unit tandem architecture on improving the current efficiency. However, the notable weakness of the tandem devices is their high driving voltages. As shown in Figure 6.17c, the driving voltage of the tandem OLED is higher than that of the conventional device, which is attributed to the larger series resistance of the thicker organic layers in the former. It should be mentioned that the device efficiency may depend on the purity of chemicals used and the fabrication conditions (e.g., sheet resistance and surface treatment of ITO substrates), so it is quite difficult to compare the device performance of similar structures prepared by different laboratories. Nevertheless, our tandem device exhibits a doubling in current efficiency as compared to the single-unit device.

Undoubtedly, the device performance of tandem OLEDs depends critically on the effectiveness of the connecting units. The simple stacking of individual emitting units together would generally lead to poor performance [68,73]; thus an understanding of the underlying working mechanism

**FIGURE 6.17**

(a) Luminance and (b) current efficiency as a function of current density, and (c) current density–voltage characteristics of conventional and tandem OLEDs. (From Lai, S.L. et al., *J. Appl. Phys.*, 101, 014509, 2007. With permission.)

**FIGURE 6.18**

A schematic energy-level diagram of the CuPc/F<sub>16</sub>CuPc interface on ITO ( $\Delta$  denotes the interfacial dipole). • represents electron and ◦ hole. (From Lai, S.L. et al., *J. Appl. Phys.*, 101, 014509, 2007. With permission.)

is essential to achieve optimal device performance. Figure 6.18 depicts the schematic energy-level diagram of the interface of the connecting unit as revealed from UPS measurement. Interfacial dipole and band bending on both sides of CuPc-on-F<sub>16</sub>CuPc-on-ITO (analogous to CuPc-on-F<sub>16</sub>CuPc-on-Si in Figure 6.14c) can be clearly observed, which are attributed to the formation of an accumulation layer in F<sub>16</sub>CuPc (acceptor) and a depletion layer in CuPc (donor). Upon the formation of the contact, electrons would move from CuPc to F<sub>16</sub>CuPc across the junction and thus holes would be created in the CuPc layer. Upon the application of a positive bias voltage, mobile electrons in F<sub>16</sub>CuPc can be injected into the adjacent BPhen layer of the first emitting unit; while holes in CuPc can be injected into the adjacent NPB layer of the second emitting unit. The simultaneous injection of electrons and holes from the F<sub>16</sub>CuPc/CuPc connecting unit, respectively, into the two emitting units completes the electric circuits of the two stacked devices and results in enhanced current efficiency. The importance of the present findings suggests that it is possible to construct an effective connecting unit for tandem OLEDs using undoped pure organic materials. With no highly diffusive metals and organic dopants, tandem OLEDs made with the organic connecting unit are expected to have more consistent long-term performance.

## 6.8 Conclusions

In this chapter, we review our recent photoemission spectroscopic studies on metal/organic interfaces and organic/organic heterojunctions and provide

new insights into certain traditional concepts. In Section 6.5, we propose a new characteristic coordinate—electronegativity to characterize the barrier heights at the metal/organic semiconductor interfaces. Good linear relationship is obtained between the interface barrier heights of several prototypical organic semiconductors and metal electronegativity. The present work suggests that the charge-injection barrier at organic/metal interfaces can be better described in term of metal electronegativity rather than metal work function. The results in Section 6.5.2 illustrate the use of effective electronegativity for compounds and alloys, and are found to be consistent with elemental electronegativity and the electronegativity model. The electronegativity model provides a simple and reliable approach to estimate carrier-injection barriers between organic semiconductor and electrodes. In Section 6.6, we report the electronic structures of the CuPc/Alq<sub>3</sub> junction on Mg and ITO substrates. Although the CuPc/Alq<sub>3</sub> junction on ITO can be described by vacuum-level alignment, the same junction formed on Mg substrate shows a significant energy-level bending through the formation of space charge regions at the interface. We have also explored different O/O heterojunctions. The results suggest that the energy-level alignment at the O/O heterojunction is dependent on the position of the Fermi level in the organic energy gap. Fermi level pinning to the HOMO or LUMO edge is observed, in accordance with charge redistribution at the interface and the formation of interface dipole and space charge layers. Our present findings substantiate that the vacuum-level alignment rule is valid only for specific O/O heterojunctions (mostly formed between wide energy gap materials) rather than a general rule. Finally, we have elucidated the importance of band bending on a specific O/O heterojunction for ambipolar OFET and stacked OLED applications.

---

## Acknowledgment

This work is supported by the Research Grants Council of Hong Kong (grant no. CityU 115605).

---

---

## References

1. Chiang, C.K., Fincher, C.R., Park, Y.W. et al. 1977. *Phys. Rev. Lett.* 39:1098.
2. Burroughes, J.H., Bradley, D.D.C., Brown, A.R. et al. 1990. *Nature* 347:539.
3. Friend, R.H., Gymer, R.W., Holmes, A.B. et al. 1999. *Nature* 397:121.
4. Tang, C.W. and Van Slyke, S.A. 1987. *Appl. Phys. Lett.* 51:913.
5. Shen, Z., Burrows, P.E., Bulović, V. et al. 1997. *Science* 276:2009.
6. Baldo, M.A., Thompson, M.E., and Forrest, S.R. 2000. *Nature* 403:750.

7. Baldo, M.A., O'Brien, D.F., You, Y. et al. 1998. *Nature* 395:151.
8. Kozlov, V.G., Bulović, V., Burrows, P.E. et al. 1997. *Nature* 389:362.
9. Tessler, N., Denton, G.J., and Friend, R.H. 1996. *Nature* 382:695.
10. Brown, A.R., Pomp, A., Hart, C.M. et al. 1995. *Science* 270:972.
11. Yang, Y. and Heeger, A.J. 1994. *Nature* 372:344.
12. Garnier, F., Hajlaoui, R., Yassar, A. et al. 1994. *Science* 265:1684.
13. Yu, G., Gao, J., Hummelen, J.C. et al. 1995. *Science* 270:1789.
14. Tang, C.W. 1986. *Appl. Phys. Lett.* 48:183.
15. Granström, M., Petritsch, K., Arias, A.C. et al. 1998. *Nature* 395:257.
16. Ma, L.P., Liu, J., and Yang, Y. 2002. *Appl. Phys. Lett.* 80:2997.
17. Bozano, L.D., Kean, B.W., Deline V.R. et al. 2004. *Appl. Phys. Lett.* 84:607.
18. Schottky, W., Stormer, R., and Waibel, F. 1931. *Z. Hochfrequenztechnik* 37:162.
19. Salaneck, W.R., Stafström, S., and Brédas J.L. 1996. *Conjugated Polymer Surfaces and Interfaces: Electronic and Chemical Structure of Interfaces for Polymer Light Emitting Devices*. Cambridge, U.K.: Cambridge University Press.
20. Bardeen, J. 1947. *Phys. Rev.* 71:717.
21. Heine, V. 1965. *Phys. Rev.* 138:A1689.
22. Louie, S.G., Chelikowsky, J.R., and Cohen, M.L. 1977. *Phys. Rev. B* 15:2154.
23. Spicer, W.E., Chye, P.W., Skeath, P.R. et al. 1979. *J. Vac. Sci. Technol.* 16:1422.
24. Hasegawa, H. and Ohno, H. 1986. *J. Vac. Sci. Technol. B* 4:1068.
25. Gao, W. and Kahn, A. 2003. *J. Phys.: Condens. Mater* 15:S2757.
26. Ishii, H., Sugiyama, K., Ito, E. et al. 1999. *Adv. Mater.* 11:605.
27. Lee, S.T., Hou, X.Y., Mason, M.G. et al. 1998. *Appl. Phys. Lett.* 72:1593.
28. Kahn, A., Koch, N., and Gao, W. 2003. *J. Polym. Sci. Pol. Phys.* 41:2529.
29. Crispin, X., Geskin, V., Crispin, A. et al. 2002. *J. Am. Chem. Soc.* 124:8131.
30. Li, Y., Watkins, N.J., Zorba, S. et al. 2002. *Appl. Phys. Lett.* 81:2752.
31. Shen, C., Kahn, A., and Schwartz, J. 2001. *J. Appl. Phys.* 89:449.
32. Kurtin, S., McGill, T.C., and Mead, C.A. 1969. *Phys. Rev. Lett.* 22:1433.
33. Möch, W. 1999. *J. Vac. Sci. Technol. B* 17:1867.
34. Shen, C., Kahn, A., and Hill, I. 2002. Organic molecular interfaces: Investigations of electronic structure, chemistry, and carrier injection properties. In *Conjugated Polymers and Molecular Interfaces: Science and Technology for Photonic and Optoelectronic Applications*, eds. W.R. Salaneck, K. Seki, A. Kahn, and J.-J. Pireaux, p. 351. New York: Marcel Dekker.
35. Lee, S.T., Wang, Y.M., Hou, X.Y. et al. 1999. *Appl. Phys. Lett.* 74:670.
36. Schlaf, R., Parkinson, B.A., Lee, P.A. et al. 1998. *Appl. Phys. Lett.* 73:1026.
37. Hill, I. and Kahn, A. 1999. *J. Appl. Phys.* 86:4515.
38. Hill, I. and Kahn, A. 1999. *J. Appl. Phys.* 86:2116.
39. Cowley, A.M. and Sze, S.M. 1965. *J. Appl. Phys.* 36:3212.
40. Hill, I., Rajagopal, A., Kahn, A. et al. 1998. *Appl. Phys. Lett.* 73:662.
41. Schwieger, T., Peisert, H., Knupfer, M. et al. 2001. *Phys. Rev. B* 63:165104.
42. Hill, I.G., Kahn, A., Soos, Z.G. et al. 2000. *Chem. Phys. Lett.* 327:181.
43. Koch, N., Kahn, A., Ghijssen, J. et al. 2003. *Appl. Phys. Lett.* 82:70.
44. Peisert, H., Knupfer, M., Zhang, F. et al. 2003. *Appl. Phys. Lett.* 83:3930.
45. Ishii, H., Oji, H., Ito, E. et al. 2000. *J. Lumin.* 87–89:61.
46. Narioka, S., Ishii, H., Yoshimura, D. et al. 1995. *Appl. Phys. Lett.* 67:1899.
47. Shen, Z. and Forrest, S.R. 1997. *Phys. Rev. B* 55:10578.
48. Krause, B., Dürr, A.C., Schreiber, F. et al. 2003. *J. Chem. Phys.* 119:3429.
49. Hirose, Y., Kahn, A., Aristov, V. et al. 1996. *Appl. Phys. Lett.* 68:217.

50. Martin, R.L., Kress, J.D., Campbell, I.H. et al. 2000. *Phys. Rev. B* 61:15804.
51. Baldacchini, C., Betti, M.G., Corradini, V. et al. 2004. *Surf. Sci.* 566–568:613.
52. Glöckler, K., Seidel, C., Soukopp, A. et al. 1998. *Surf. Sci.* 405:1.
53. Takajo, D., Nemoto, T., Ozaki, H. et al. 2004. *Appl. Surf. Sci.* 238:282.
54. Gao, W. and Kahn, A. 2003. *Appl. Phys. Lett.* 82:4815.
55. Ishii, H., Hayashi, N., Ito, E. et al. 2004. *Phys. Stat. Sol. (a)* 201:1075.
56. Vazquez, H., Gao, W., Flores, F. et al. 2005. *Phys. Rev. B* 71:041306.
57. Wang, J., Wang, H., Yan, X. et al. 2005. *Chem. Phys. Lett.* 407:87.
58. Dodabalapur, A., Katz, H.E., Torsi, L. et al. 1995. *Science* 269:1560.
59. Anthopoulos, T.D., de Leeuw, D.M., Cantatore, E. et al. 2004. *Appl. Phys. Lett.* 85:4205.
60. Kang, S.J., Yi, Y., Kim, C.Y. et al. 2005. *Appl. Phys. Lett.* 87:233502.
61. Rost, C., Gundlach, D.J., Karg, S. et al. 2004. *J. Appl. Phys.* 95:5782.
62. Wang, J., Wang, H., Yan, X. et al. 2005. *Appl. Phys. Lett.* 87:093507.
63. Gorgoi, M. and Zahn, D.R.T. 2005. *Org. Electron.* 6:168.
64. Hill, I.G., Mäkinen, A.J., and Kafafi, Z.H. 2000. *J. Appl. Phys.* 88:889.
65. Kido, J., Nakada, T., Endo, J. et al. 2002. *Proceedings of the 11th International Workshop on Inorganic and Organic Electroluminescence and 2002 International Conference on the Science and Technology of Emissive Displays and Lighting*, 539. Gent, Belgium: Universiteit Gent Press.
66. Matsumoto, T., Nakada, T., Endo, J. et al. 2003. *SID Int. Symp. Digest Tech. Papers* 34:979.
67. Guo, F. and Ma, D. 2005. *Appl. Phys. Lett.* 87:173510.
68. Liao, L.S., Klubek, K.P., and Tang, C.W. 2004. *Appl. Phys. Lett.* 84:167.
69. Chang, C.C., Chen, J.F., Hwang, S.W. et al. 2005. *Appl. Phys. Lett.* 87:253501.
70. Tsutsui, T. and Terai, M. 2004. *Appl. Phys. Lett.* 84:440.
71. Law, C.W., Lau, K.W., Fung, M.K. et al. 2006. *Appl. Phys. Lett.* 89:133511.
72. Chan, M.Y., Lai, S.L., Lau, K.M. et al. 2007. *Adv. Funct. Mater.* 17:2509.
73. Kanno, H., Holmes, R.J., Sun, Y. et al. 2006. *Adv. Mater.* 18:339.
74. Chen, C.W., Lu, Y.J., Wu, C.C. et al. 2005. *Appl. Phys. Lett.* 87:241121.
75. Cho, T.Y., Lin, C.L., and Wu, C.C. 2004. *Appl. Phys. Lett.* 88:111106.
76. Gao, W. and Kahn, A. 2002. *Org. Electron.* 3:53.
77. Gao, W. and Kahn, A. 2001. *Appl. Phys. Lett.* 79:4040.
78. Parthasarathy, G., Shen, C., Kahn, A. et al. 2001. *J. Appl. Phys.* 89:4986.
80. Tang, J.X., Lee, C.S., Lee, S.T. et al. 2004. *Chem. Phys. Lett.* 396:92.
81. Tang, J.X., Lee, C.S., and Lee, S.T. 2005. *Appl. Phys. Lett.* 87:252110.
82. Tang, J.X., Lau, K.M., Lee, C.S. et al. 2006. *Appl. Phys. Lett.* 88:232103-1.
83. Tang, J.X., Lee, C.S., and Lee, S.T. 2007. *Appl. Phys. Lett.* 101:064504.
84. Lau, K.M., Tang, J.X., Sun, H.Y. et al. 2006. *Appl. Phys. Lett.* 88:173513.
85. Lai, S.L., Chan, M.Y., Fung, M.K. et al. 2007. *J. Appl. Phys.* 88:014509.

# 7

---

## *The Role of Homolytic Reactions in the Intrinsic Degradation of OLEDs*

---

Denis Y. Kondakov

### CONTENTS

7.1	Introduction .....	211
7.2	Physical Studies of the Intrinsic Degradation of OLED Devices .....	217
7.2.1	Voltammetry.....	217
7.2.2	Electric Field Profiling.....	226
7.2.3	Photoluminescence.....	229
7.3	Chemical Analysis of Degrading OLED Devices.....	233
7.4	Mechanistic Conclusions .....	237
	References.....	240

---

### 7.1 Introduction

In the more than 20 years since the invention of organic light-emitting diodes (OLEDs) by Tang and Van Slyke [1], durability remains one of the most serious issues hindering wide commercial acceptance of OLED technology [2]. In general, durability is meaningful only in the context of a specific application. For example, a tolerable decrease in the brightness of an OLED device designed for lighting may be completely unacceptable in a display application because of pixel-to-pixel differences and static image burn-in. On the other hand, a complete catastrophic failure of a single pixel may be hardly noticeable in a display, yet it is likely to render a lighting device unusable.

A gradual decrease in efficiency and catastrophic failure represent two polar cases of instability commonly observed in OLEDs. Such classification is not particularly useful from a mechanistic point of view because it does not reflect the multitude of processes responsible for the instabilities of OLED devices. It also does not reflect the distinction between intrinsic and extrinsic causes of instability. Here we define the intrinsic degradation processes as inherent and qualitatively unavoidable for a certain type of OLED device. By

way of illustration, the presence of excited states of organic molecules during operation is obviously inescapable. Although the concentration and localization of excited states can be readily manipulated to some degree, the fundamental limit of the radiative rate constant of organic emitters ( $\sim 10^9 \text{ s}^{-1}$  [3]) results in the existence of a lower bound for the number of excited molecules present in OLED devices operating at a given brightness level. Hence, we would consider OLED degradation processes caused by excited states of emitter molecules to be intrinsic.

In contrast, extrinsic degradation causes are not inherent and, at least in principle, can be eliminated by modifying the composition of a device or its external environment [4–8]. The reduction of an emissive area due to the formation of dark spots and the expansion of edges is a classic example of an extrinsic degradation process caused by the diffusion of oxygen and water vapor through the device pinholes and edges. Subsequent chemical reactions with an electropositive metal render parts of a cathode incapable of injecting electrons and the respective part of the device nonemissive. The remaining active area shrinks, which results in a shift of the current–voltage characteristic of the device and a respective decrease in power efficiency. The extrinsic nature of this degradation process is readily recognizable because of several *additional* attributes—spatial nonuniformities and the external character of its driving force. The former attribute can be readily established by visual inspection and the latter one by controlling the partial pressures of water vapor and oxygen in the OLED device environment.

It is noteworthy that in some cases, extrinsic nature degradation may be more difficult to recognize. For example, it is well known (even if not well documented) that, in OLED device fabrication, even the minute presence of certain contaminants in organic layers or on the electrode surfaces may result in substantial decreases in operational stability [9]. Faster degradation caused by such contaminants would normally be spatially uniform and without any detectable contributions from the operating environment, hence it is readily mistaken for an intrinsic process. It is noteworthy that extrinsic causes, such as contamination, are probably responsible for much of the stability differences observed for the nominally identical devices between different laboratories and even between different fabrication equipment in the same laboratory. Unfortunately, low-level contaminants are notoriously difficult to detect in extremely thin OLED devices, particularly without the knowledge of their chemical structures. Therefore, using brute force methods such as chemical analysis of OLED devices may or may not be effective in order to rule out contamination as the cause of degradation. As this example demonstrates, scientists studying OLED degradation phenomena are often faced with the daunting question of whether their subjects are affected by intrinsic or extrinsic degradation processes. Although there is no general way to answer such a question, the following sections will focus on the cases where intrinsic degradation is most probable.

Phenomenologically, intrinsic degradation normally manifests in the form of a gradual, monotonic decrease in device efficiency during operation. Both current–external quantum efficiency (EQE, measured as the percentage of injected electrons that result in emitted photons) and current–voltage characteristics are degraded, so the OLED devices are typically operated at a constant current to decouple these effects and thus make brightness loss less pronounced [1]. In many cases, electroluminescence spectra are also affected by OLED degradation, which makes two commonly used measures of efficiency—luminance efficiency (measured in cd/A) and EQE—result in somewhat different assessments of the relative luminance loss during operational degradation. However, they are usually sufficiently close and we will use them interchangeably for the remainder of this chapter in order to gauge the extent of OLED degradation.

Considering the practical importance of the durability of OLED devices, it is not surprising that degradation processes received considerable scientific attention for over two decades since the invention of OLEDs. Many mechanistic studies were performed resulting in significant advances in the understanding of the physical and chemical processes associated with OLED degradation [2]. However, the overall coverage remains quite fragmentary, with a typical mechanistic study limited to a specific structure of OLED devices. Therefore, before reviewing the accumulated mechanistic knowledge, it is instructive to consider several of the most general characteristics of intrinsic degradation:

- Coulombic, which means that the luminance decay rate is approximately proportional to injection current density or, in integral form, the extent of luminance loss is approximately proportional to the total charge driven through the OLED device [10]
- Thermally activated, faster degradation at higher temperature [11–16]
- Irreversible, for the major part [10,17–19]
- Absence of the common form of efficiency vs. time curve, which varies between linear and exponential or power law

These characteristics suggest that the mechanism of intrinsic degradations of OLED devices is quite complex. Furthermore, it is entirely possible that there is no general mechanism applicable to all common types of OLED devices. Although activated and irreversible characteristics of degradation are suggestive of chemical reactions, some purely physical processes, e.g., diffusion of ions and changes in morphology, may exhibit similar behavior.

However, a common observation of the coulombic character of degradation suggests that at least some generality in OLED degradation mechanisms exists. Such a generality may stem from an involvement of excited states in the rate-determining step of OLED degradation. As the light output and,

therefore, the concentration of excited states are approximately proportional to the current flowing through a device, the coulombic nature of intrinsic degradation follows naturally from the assumption that the degradation processes are initiated by excited states.

In this context, charge carriers as sole initiators appear less likely because, in general, their concentration in any given layer may not be expected to scale linearly with current density. For instance, in the case of a space-charge-limited current, the average concentration of charge carriers is proportional to the square root of current density. In another common situation—*injection-limited* current—the concentration of charge carriers is also expected to be a sublinear function of current density due to the changes in carrier drift velocity caused by changes in the electric field and mobility. However, considering that degradation is only approximately coulombic and, in some special cases, concentration of charge carriers may be an approximately linear function of current density, an involvement of charge carriers as initiators of OLED degradation cannot be ruled out.

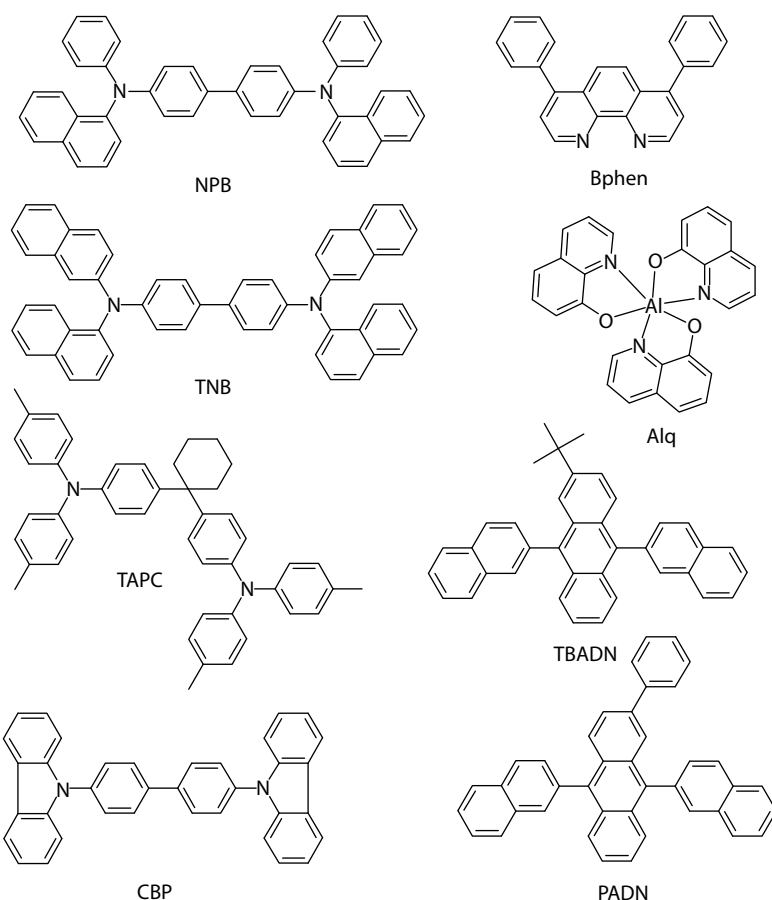
On the other hand, the coulombic character of intrinsic degradation suggests that various purely physical processes are unlikely as primary drivers for OLED degradation. For example, the reorientation of molecular dipoles [18,19], morphological changes [20–22], and migrations of metal ions [23,24] cannot be expected to exhibit coulombic behavior. In this context, mechanisms involving chemical transformations of molecules in operating devices are more likely to be responsible for OLED degradation. From a chemist's perspective, an operating OLED device is an unusual reaction vessel having a truly negligible presence of otherwise ubiquitous contaminants such as oxygen and water. Furthermore, the reaction medium in such a reaction vessel is typically a rigid solid, which makes long-range molecular movement practically nonexistent under normal storage or operating conditions. Many notions of chemical reactivity need to be rethought in this context. We expect that various ionic and radical species, which are generally short lived, may persist inside an OLED device. For example, a benzyl radical, despite significant stabilization by spin-density delocalization, would normally be considered as a highly reactive, short-lived species. The rate of its reaction with oxygen approaches the diffusion limit in solution [25]. Even in the absence of oxygen, the dimerization of two benzyl radicals to yield 1,2-diphenylethane is also very effective. Low-temperature matrices are typically employed to obtain long-lived benzyl radical samples by restricting both diffusion and chemical reactivity [26]. However, the benzyl radical is likely to be unreactive in an OLED-like matrix even at room temperature provided that the matrix consists of OLED material with negligible reactivity toward benzyl radicals, such as a fully aromatic hydrocarbon.

Another aspect of uniqueness of the OLED matrix is that a typical operating OLED device has remarkably high concentrations of short-lived, operation-related species such as excited states and ion-radicals. For example, the concentration of singlet excited states in an archetypal NPB|Alq

OLED device can be as high as 0.01 mM assuming a 15 ns lifetime [27] and uniform distribution across a 75 nm layer of Alq. In actuality, excited states and ion-radicals are typically distributed very unevenly within a device, which results in the formation of regions with even higher concentrations of chemically reactive species (e.g., recombination zones) and regions that are nearly devoid of them (e.g., the bulk of the transport layers). As a result, even the processes involving two highly reactive molecules such as excited states or ion-radicals are believed to be quite common in operating OLED devices. Many examples of physical processes of this kind are well documented in the literature, e.g., triplet-triplet annihilation [28–33] and excited singlet state quenching by ion-radicals [34]. Although in-device chemical reactions of such a kind, i.e., involving two highly reactive molecules such as excited states or ion-radicals, have not been reported thus far, it is clear that they are likely to take place in an operating OLED device.

Overall, we can expect that the chemical processes taking place in operating OLED devices are quite diverse and considerably different from textbook liquid- or gas-phase chemistries. Actual mechanisms would obviously depend on the chemical materials comprising an OLED device as well as on the device physics, particularly charge transport and recombination processes. It is plausible that such tentative chemistries are responsible for much of the intrinsic degradation processes in operating OLED devices. Unraveling their mechanisms is clearly beneficial for the development of durable devices.

As mentioned earlier, although many mechanistic studies of OLED degradation were reported, the coverage remains very fragmentary, with a typical mechanistic study limited to a specific structure of an OLED device. Furthermore, much of the reported mechanistic work was performed on Alq-based devices, which may or may not serve as a good model of the current generation of efficient and long-lived OLEDs. The fundamental energetic factor precludes Alq from being used as the main component of emissive layers in efficient blue and white devices. Instead, materials with completely different and often proprietary chemical structures are being used in modern OLEDs. Some examples that illustrate the chemical diversity of OLED materials are shown in Figure 7.1. Unfortunately, mechanistic studies of degradation processes in such devices are as yet almost nonexistent in the open literature. Therefore, for the purpose of reviewing available mechanistic knowledge in this chapter, we decided to avoid classification by the chemical structures of OLED materials. Similarly, classification by proposed types of degradation mechanisms was rejected because of a limited conceptual space. In essence, there are only two hypotheses, which link degradations to (1) long-range migrations of device components, such as ions and molecules, and (2) instabilities and changes of materials in certain device regions. As argued above, the former hypothesis cannot serve as a general explanation of OLED instability because of inconsistency with the coulombic nature of intrinsic degradation.

**FIGURE 7.1**

Molecular structures of some common OLED materials.

Thus, in order to provide an instructive overview of the mechanistic aspects of OLED degradations in the remainder of this chapter, we chose to employ a classification that is based on research methodology rather than subject matter (i.e., device type and composition) or mechanistic hypotheses. There are two key types of research methods as applied to OLED degradation studies—physical and chemical. Former methods (see Section 7.2) provide important insights into the physics of the degradation process, but offer almost no information about the underlying chemical changes. This shortcoming of physical methods is addressed in Section 7.3, which examines the degradation process from the perspective of chemical analysis. Section 7.4 summarizes physical and chemical studies in a framework of a hypothetical general mechanism of the intrinsic degradation of OLED devices.

---

## 7.2 Physical Studies of the Intrinsic Degradation of OLED Devices

As discussed in Section 7.1, the intrinsic degradation of OLED devices is likely to be caused by the transformations of materials in certain regions of operating devices, particularly in the region where the processes of recombination of charge carriers and emission of light take place. The loss of electroluminescence can also be caused by changes at substantial distances away from a recombination zone such as, for example, injecting interface deterioration. It is therefore not surprising that the physical methods capable of probing the dynamics and distributions of excited states and charge carriers are informative with respect to the intrinsic degradation of OLED devices.

### 7.2.1 Voltammetry

Popovic et al. proposed the formation of charge traps that act as nonradiative recombination centers in the emissive material as one possible explanation for the relative differences in the electroluminescence and photoluminescence losses in operating OLEDs [27]. Despite the absence of direct evidence of the formation of such traps or their ability to act as nonradiative recombination centers, the proposal was quite plausible, particularly in view of a complementary notion that, in some cases, recombination on highly emissive charge traps is responsible for the predominant emission by the dopants [35,36]. The rise in voltage required to drive a constant current through a device has been cited as possible evidence of the formation of traps, but the voltage rise could be, in fact, attributed to mechanistically unrelated phenomena, such as electrode deterioration.

Clearly, to assess the involvement of nonradiative recombination centers in the intrinsic degradation of OLEDs, it is necessary (1) to demonstrate their accumulation in the recombination zone of degrading devices, and (2) to establish a quantitative connection between their concentration and the extent of electroluminescence loss. Therefore, a method to measure and locate charge traps inside OLED devices is required. Voltammetry, which is a general name for several large amplitude time-domain  $I$ - $V$  (current-voltage) techniques [37], proved to be useful to probe charge densities and injection/transport characteristics of separate layers in aging OLED devices. The details of this OLED technique [38] and the related physical model [39] are described elsewhere and the brief discussion is provided in the following.

In a typical voltammetric experiment, the applied voltage ( $V$ ) is ramped at a constant rate,  $dV/dt$ , and the resulting transient current response is acquired. In general, the measured current has two components: a conductive component that persists with a constant bias, and a capacitive component that is proportional to the sweep rate ( $dV/dt$ ) and the capacitance ( $C$ ). The conductive component is normally negligible below the turn-on voltage of an OLED

device. By varying the direction of the voltammetric sweep (sign of  $dV/dt$ ), the processes of charging and discharging can be studied separately. By convention,  $dV/dt$  is positive in a forward voltammetric sweep and negative in a reverse voltammetric sweep.

Remarkably, for some OLEDs, the capacitive component is not constant below turn-on voltage, but rather, indicates the existence of two or three distinct capacitances depending on the voltage range [38,40,41]. The first observation of variable capacitance in OLED devices below the turn-on voltage was reported by Brütting et al. using a complementary technique of capacitance–voltage measurements by AC impedance [39]. The physical model introduced by Brütting et al. to explain the variation in capacitance at low applied voltages is illustrated in Figure 7.2. Two organic layers, a hole-transport layer (HTL) and an electron-transport layer (ETL), are sandwiched between an anode and a cathode. For each electrode, it is assumed that injection begins as the field at the contact becomes positive, i.e., as the contact becomes forward biased. Figure 7.2a through c illustrates the behavior of an OLED containing no fixed (trapped or otherwise immobile) charge or macroscopic dipoles. Under reverse bias, or small forward bias (Figure 7.2a), the internal electric

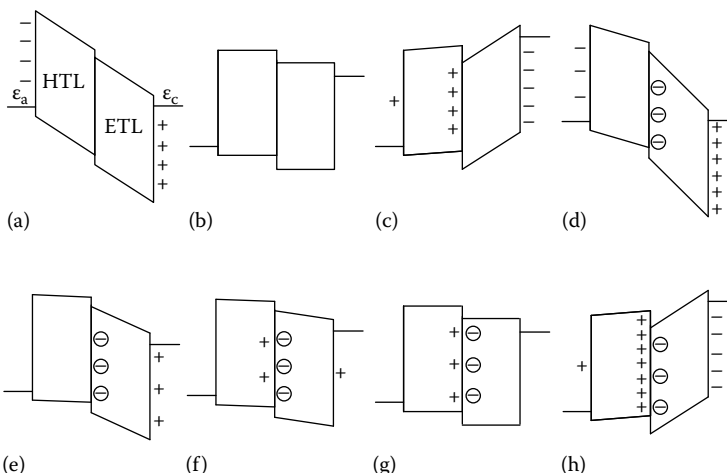


**FIGURE 7.2**

Structure, charge distributions, and electric fields of a bilayer OLED containing HTL, ETL, an anode ( $\epsilon_a$ ), and a cathode ( $\epsilon_c$ ). Energies of the HOMO and LUMO of the two layers are shown schematically, along with the Fermi levels of the cathode and anode. The slopes represent the internal electric field dependent on the applied voltage (equal to the difference between  $\epsilon_a$  and  $\epsilon_c$ ) and the density of the internal fixed charge shown schematically as circled “minus” signs. Mobile charge densities are shown schematically as “plus” and “minus” signs. (a)–(c) Internal electric fields and charges at anode, cathode, and HTL|ETL interface without internal fixed charge below  $V_{bi}$  (a), at  $V_{bi}$  (b), and above  $V_{bi}$  (c). (d)–(h) Internal electric fields and charges at anode, cathode, and HTL|ETL interface with negative internal fixed charge below  $V_0$  (d), at  $V_0$  (e), above  $V_0$ , and below  $V_{bi}$  (f), at  $V_{bi}$  (g), and above  $V_{bi}$  (h).

field is negative (directed toward the anode), a negative charge is stored on the anode, an equal positive charge is stored on the cathode, and there are no charge carriers in the organic layers. As the applied voltage is increased, the magnitudes of the field and the stored charge change accordingly, and the device behaves as a simple capacitor with geometric capacitance corresponding to the total thickness of the ETL and the HTL. When the applied voltage reaches the built-in voltage ( $V_{bi}$ ), which is defined as the difference in work function between the two contacts and approximately equal to the turn-on voltage, the field and the stored charge vanish (Figure 7.2b). At larger forward bias, the electric field becomes positive in both layers, and both contacts begin to inject carriers (Figure 7.2c). Generally, the conduction regime results in the capacitance of an OLED device becoming ill defined because of the absence of a simple equivalent circuit.

Figure 7.2d through h illustrate an OLED containing a negative fixed charge at the ETL|HTL interface. At a sufficiently large negative bias, that is the only charge inside the cell and, according to Poisson's equation, the electric fields in the ETL and the HTL are different by  $\sigma/\epsilon\epsilon_0$ , where  $\sigma$  is the charge density at the HTL|ETL interface (Figure 7.2d),  $\epsilon$  is the relative dielectric constant of the ETL and HTL, and  $\epsilon_0$  is the permittivity of free space. The device again behaves like a simple capacitor with geometric capacitance corresponding to the total thickness of the ETL and HTL. As the applied voltage is increased, the charge stored on the electrodes increases proportionately, but the charge at the HTL|ETL interface does not change and neither does the difference in electric field across the interface. In that regime, the presence of a fixed charge has no effect on capacitance. At a certain applied voltage, termed the transition voltage ( $V_0$ ), the field in the HTL vanishes, while the field in the ETL remains negative (Figure 7.2e). Thus, once the applied voltage exceeds the transition voltage, holes are injected but the cathode cannot yet inject electrons. As long as the applied voltage remains below built-in, the injected holes are blocked from injecting into the ETL by the negative electric field. Because there are no electrons at the HTL|ETL interface, holes remain at the HTL|ETL interface and no conduction occurs. As illustrated by Figure 7.2f, the equilibrium concentration of holes at the HTL|ETL interface is determined by the condition of the near-zero field in the HTL. Essentially, the HTL acts as a conductor while the ETL remains insulating. The capacitance of the OLED device in that regime corresponds to geometric capacitance of the ETL. As the applied voltage is increased, holes continue to accumulate at the HTL|ETL interface until the fixed negative charge is fully compensated at  $V_{bi}$  (Figure 7.2g) and electric fields in both HTL and ETL are vanishingly small. At that point, the device goes into conduction mode (Figure 7.2h) and the negative fixed charge affects only the density of holes at the HTL|ETL interface (cf. Figure 7.2c).

The key prediction of this model is that, in the presence of the internal fixed charge, an OLED device can exhibit transition between two capacitances at a certain applied voltage below the  $V_{bi}$ . The effect of the fixed negative charge

is to shift the transition voltage to smaller values than  $V_{bi}$ . Therefore, the internal fixed charge density ( $\sigma$ ) can be calculated from the transition voltage and the thickness of the ETL ( $d_{ETL}$ ):

$$\sigma = (V_0 - V_{bi})\epsilon\epsilon_0/d_{ETL} \quad (7.1)$$

It should be emphasized that the transition voltage evaluations do not require measuring capacitance–voltage characteristics of OLED devices. In fact, transition voltages and, respectively, internal fixed charge densities, can be measured even in some devices that do not show well-defined transitions between capacitances. Recall that the definition of transition voltage requires that the field in one transport layer (HTL in Figure 7.2) vanishes while the other transport layer remains nonconductive. If the charge injection is reversible below  $V_{bi}$ , the capacitance–voltage characteristic of an OLED device is well defined and nearly independent of the choice of technique—voltammetry or AC impedance. The forward and reverse voltammetric sweeps, which correspond, respectively, to charge injection and retraction, are mostly symmetrical and carry essentially the same information. Conversely, if the charge injection is irreversible or occurs at a very different timescale compared to charge retraction, the capacitance becomes ill defined because of a strong asymmetry in the charging and discharging of a putative capacitor. In actual devices, the asymmetry between charge injection and retraction processes can be caused by various reasons, e.g., hole trapping at the HTL|ETL interface or an injection barrier at the anode|ETL interface. Nonetheless, it can still be possible to measure transition voltage by detecting the onset of charge injection or the end of charge retraction in separate forward and reverse voltammetric sweeps.

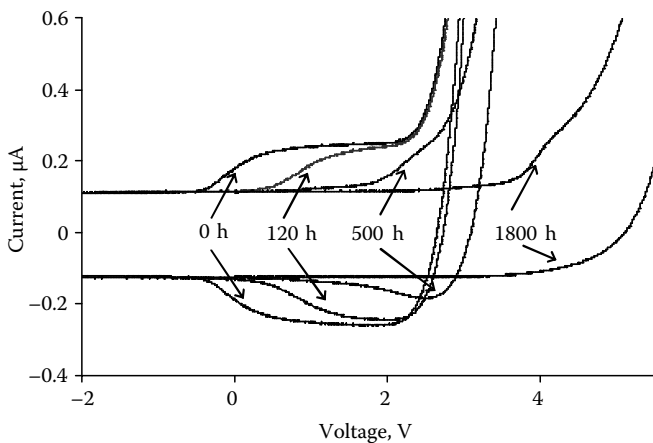
Further complications occur when the fixed charge density at the HTL|ETL interface is positive. The model discussed earlier is symmetrical, and the positive sign of the internal fixed charge should result in electron injection taking place below  $V_{bi}$  and the appearance of a corresponding transition in a voltammogram. Although such behavior was observed in some devices, it is fairly exceptional [41]. The reason must be that the electron injection from the cathode typically requires substantial field, so that the ETL behaves like an insulator that does not become conductive on the timescale of voltammetric experiments. Therefore, even in the devices with a positive internal fixed charge, only the voltammetric transition that corresponds to the injection of holes might still be observed. Because this transition occurs when applied voltage is above the  $V_{bi}$  and the ETL is forward biased, the holes can irreversibly inject into the ETL and drift toward the cathode resulting in a strong asymmetry between the hole injection and retraction processes. In practice, the actual OLED devices with a positive fixed charge density at the HTL|ETL interface show a strongly suppressed and distorted response in hole retraction. Nonetheless, the transition voltage corresponding to hole injection can still be measured in a forward sweep as long as the positive

fixed charge is sufficiently low to keep the electron injection at a negligible level during sweep.

The nature of a negative fixed charge in unaged OLED devices of various structures is unclear. No plausible explanation of its microscopic origin was provided by Brütting et al., who discovered this remarkable phenomenon [39]. However, several years later, Ito et al. reported that films of Alq deposited on an Au substrate electrode demonstrate high and persistent positive surface potential [42]. They convincingly argued that, because the potential was a linear function of film thickness, there was no net charge inside the film, and the surface potential was due to the formation of a macroscopic dipole by partly orientated Alq molecules. Although the *positive* surface potential reported by Ito et al. may seem to be a contrary phenomenon compared with the “negative” charge at the Alq|NPB interface reported by Brütting et al., it is easy to show that both cases are actually equivalent with respect to the direction of the respective macroscopic dipoles toward the supporting substrate. Despite the drastic differences in the experimental systems, there is also a close agreement in the strengths of the putative dipoles: 0.35 MV/cm [39] vs. 28 V/560 nm = 0.5 MV/cm [42]. In view of these results, we surmise that it is plausible that the interfacial negative charges observed in some OLED structures are actually manifestations of the macroscopic dipoles formed by partly orientated polar molecules, such as Alq. Nonetheless, the alternative explanation involving the presence of nondischargeable anions of an unknown nature at the NPB|Alq interface cannot be ruled out. It is noteworthy that, despite having no discernable influence on the durability of OLEDs, the fortuitous existence of such a macroscopic dipole makes it possible to detect and measure substantial concentrations of fixed charge of both signs accumulated during operation. In less favorable circumstances, when such dipoles were not present, only limited accumulations of positive fixed charge would be measurable.

We applied the voltammetric technique to a diverse set of OLED devices to examine the possible connection between the operational degradation and the formation of nonradiative recombination centers. A representative case of the degradation of the NPB|Alq device is illustrated in Figure 7.3. In forward sweeps, the transition voltage monotonically shifts to more positive values as the device degrades, whereas the shape of the transition remains nearly unchanged. Even several volts above the  $V_{bi}$ , the transition remains discernable. Conversely, the transition almost disappears in reverse sweeps as it shifts above the  $V_{bi}$ , which, in good agreement with the discussion earlier, suggests the asymmetry in injection and retraction processes that is due to hole trapping and injection into the Alq. More importantly, the gradual shift of transition voltage to more positive values points to the accumulation of positive charge density somewhere away from the electrodes.

Here we assume that the macroscopic dipole, which manifests as the negative charge density at the NPB|Alq interface in unaged devices, remains unchanged during operation. This is a plausible assumption in view of the

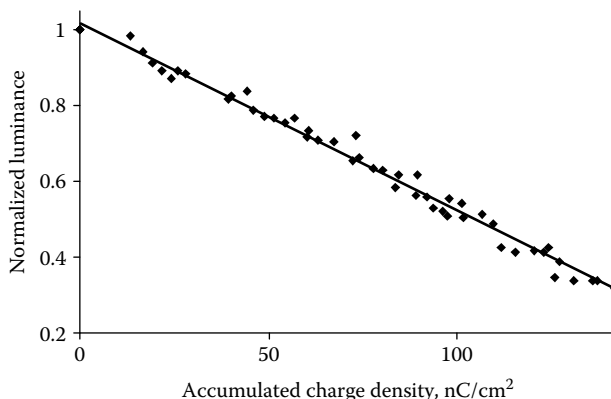
**FIGURE 7.3**

Voltammery of aging NPB|Alq device. Aging times identified by labels. Top curves correspond to forward sweeps ( $dV/dt = 50 \text{ V/s}$ ) and bottom curves correspond to reverse sweeps ( $dV/dt = -50 \text{ V/s}$ ).

complementary experiments that show that the apparent negative charge density remains mostly unchanged when NPB|Alq devices are kept for over a year at the applied voltages in the +2 V to -10 V range. In terms of absolute magnitude, this range of applied voltages encompasses the electric fields found in operating devices. Still, as the devices remain below turn-on voltage, there are negligible currents and, respectively, no changes in luminance efficiencies. There are also no significant changes in transition voltages, which confirm that, at least at room temperature, the electric fields present in operating NPB|Alq devices cannot effect the reorientation of Alq molecules and, accordingly, the strength of the macroscopic dipole.

An alternative explanation of the shift of transition voltage to more positive values during operation involves discharging hypothetical anions at the NPB|Alq interface. However, the disappearance of negatively charged species is insufficient to explain the transition voltage shift above the  $V_{bi}$  during operation. Hence, the accumulation of positive charge density somewhere away from the electrodes must be invoked to explain the experimental results.

The location of positive charge density can be approximately determined from transition voltages of degraded devices with varying layer thickness. For NPB|Alq devices, a detailed study showed that the operation-generated positive charge is in the vicinity of the NPB|Alq interface, i.e., in or near the recombination zone [38]. Knowing the location of charge density, it is possible to calculate its magnitude from transition voltage with Equation 7.1. The magnitude of the accumulated charge density can be obtained as the difference between the degraded and nondegraded devices. Figure 7.4 shows

**FIGURE 7.4**

Dependence of luminance of NPB (110 nm)–Alq (30–180 nm) devices on accumulated charge density during aging (0, 4, 24, 48, 96, 144, 192, 312, 456 h at 40 mA/cm<sup>2</sup> and 70°C).

the relationship between normalized luminance and accumulated charge density in NPB|Alq devices aged to various degrees. Remarkably, despite the systematic and substantial changes in layer thicknesses as well as random device-to-device variability, there is a general correlation between luminance losses and the amounts of the positive charge accumulated at the NPB|Alq interfaces. Although each of these quantities evolves in a nontrivial manner during device operation, the correlation between them is linear and strong ( $R^2 = 0.99$ ). It is therefore highly likely that the decreasing luminance is a consequence of the increasing positive fixed charge.

Having established that the operation of NPB|Alq devices leads to the accumulation of positive charge, which appears to be directly linked to luminance loss, it is natural to ask about its microscopic nature. Interestingly, when the transition voltage is below  $V_{bi}$ , as in moderately degraded NPB|Alq devices, the voltammograms are fairly independent of the conditions prior to the measurement. For example, the transition voltage remains unchanged whether a moderately degraded device is kept at -18 V or at 0 V applied voltage for several days immediately before voltammetric measurement. This indicates that the positive charge created during degradation cannot be discharged even by a relatively strong electric field. In view of these observations, electric field-induced migration of ions or the reorientation of Alq molecules appear implausible to explain the positive charge accumulation during operation. We surmise that the deep hole traps are formed during the operation of the NPB|Alq device. Such hole traps are sufficiently deep, so they do not discharge under the reverse bias during or before voltammetric measurement, and appear as fixed charge density. In view of the substantial trap depth and the associated small band gap, it is also plausible that the recombinations of such filled traps with mobile electrons are mostly nonradiative.

Further support for the notion that the hole traps are formed during operation can be found in voltammetry of strongly aged OLEDs. Although the reverse sweep of NPB|Alq devices with a transition voltage exceeding  $V_{bi}$  does not show well-defined transitions, a broad and delayed peak corresponding to the partial retraction of holes can be detected [38]. Therefore, in addition to the deep hole traps, present as fixed charge density, OLED operation also yields shallower hole traps.

Although the experiments discussed earlier do not show any evidence of the formation of electron traps in operating OLED devices, their presence cannot be ruled out based solely on the positive sign of accumulating charge densities. It is possible that the electron traps are generated in smaller concentrations so that the total charge density is composed of a negative contribution from charged electron traps and a larger positive contribution from charged hole traps. Furthermore, because the injection of holes is substantially more facile relative to the injection of electrons in a typical NPB|Alq device, most of the mobile charges in the vicinity of the NPB|Alq interface are holes. It is therefore likely that, even in a hypothetical case of equal concentrations of the hole and electron traps, hole traps would have higher occupancy and the overall sign of charge density would be positive. Even though a voltammetric measurement is incapable of measuring tentative positive and negative components of the total charge density, this technique can still be used to demonstrate the presence of the charged electron traps in the degraded NPB|Alq devices [43]. Using photogeneration of charges, a strongly degraded NPB|Alq device can be placed into a state with total internal charge that has a negligible magnitude. When the device is in such a state, the first forward voltammetric sweep results in the emission of a brief pulse of light, associated with the voltammetric transition near  $V_{bi}$ . This phenomenon is illustrated in Figure 7.5.

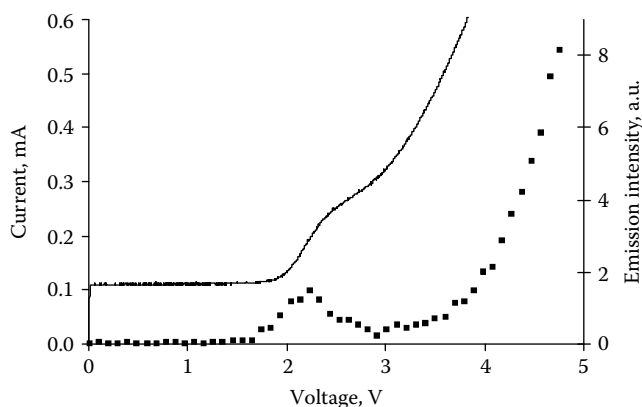


**FIGURE 7.5**

Voltammetric response (solid curve, left axis) and light emission (squares, right axis) in forward sweep (50 V/s) of strongly aged NPB|Alq device that was briefly exposed to white light prior to voltammetric measurement.

The initial emission of light is clearly discontinuous and occurs at applied voltage  $\sim 2$  V, whereas regular continuous emission requires  $> 3.5$  V to reach the same intensity. The subsequent sweeps do not show additional pulses of light indicating that the species responsible for the discontinuous emission are completely consumed and can only be regenerated by the photogeneration of charges. In additional experiments, we showed that the pulse of light is a product of recombination of mobile holes and trapped electrons in the immediate vicinity of the NPB|Alq interface. Similarly to the trapped holes discussed earlier, the trapped electrons reside in deep traps and cannot be released by electric fields of comparable strengths. Interestingly, detection of light associated with the injected hole current allowed us to confirm that such recombination centers are essentially nonradiative, with quantum efficiency being at least two orders of magnitude smaller than the efficiency of Alq.

The present results indicate that the operation of NPB|Alq OLEDs generates deep traps near the HTL|ETL interface. Although both hole and electron traps are formed, the overall sign of accumulated fixed charge density is positive. The strong linear correlation between the accumulated fixed charge densities and the luminance losses strongly suggests that the deep traps formed during device operation act as nonradiative recombination centers and thereby cause the decreasing luminance.

As discussed in Section 7.1, NPB|Alq devices may not be representative of many different OLED device structures. It is therefore natural to ask whether the role deep traps play in operational degradation is unique for the NPB|Alq devices. To answer this question, we examined a diverse set of fluorescent and phosphorescent OLED devices spanning more than two orders of magnitude difference in stability. The results are summarized in Table 7.1 and the following is noteworthy. Despite the structural and functional dissimilarities in the experimental set, the operation-induced accumulation of fixed positive charge densities and correlation with luminance loss were invariably observed. Although we observed some nonlinearity in luminance–charge

**TABLE 7.1**

Accumulated Charge Densities and Half-Lives of OLED Devices Operated at  $40 \text{ mA/cm}^2$

OLED Structure	Average Half-Life, h	Accumulated Charge Densities at Half-Life, $\text{nC/cm}^2$	Ref.
NPB Alq	1200	128	[38]
NPB Alq ( $70^\circ\text{C}$ )	200	104	[38]
NPB TBADN Alq ( $70^\circ\text{C}$ )	170	125	[38]
NPB TBADN	24	16	[38]
NPB CBP+Ir(ppy) <sub>3</sub>  BAIq Alq	63	70	[64]
TAPC Alq	30	274 (extrapolated)	[50]
NPB rubrene+Alq+DCJTB Alq	7400	51	—

density correlations in a few cases, the generality of operation-related formation of nonradiative recombination centers is clearly evident.

### 7.2.2 Electric Field Profiling

As discussed in Section 7.2.1, decreasing luminance efficiency in operating OLED devices appears to be linked to the accumulation of charge traps. Although deep traps of both signs are readily detectable in degraded devices, the quantitative relationships between luminance efficiencies and trapped charge densities are only observed for deep (nondischargeable) hole traps.

In principle, this may be a limitation of the experimental technique—voltammetry, which is strongly tuned to detecting fixed positive charge densities in typical OLED devices employing materials favoring the injection of holes. Furthermore, voltammetric measurements are normally conducted on formally nonoperating OLED devices (below turn-on voltage or on such a timescale that the device is essentially monopolar). While the densities of deeply trapped charge can be expected to remain unchanged in an operating device, the distribution of filled shallow traps is likely to be substantially different. For example, shallow traps might be mostly unfilled in a nonoperating device and, therefore, undetectable in a voltammetric measurement. In contrast, such species are considerably more likely to be filled in operating devices, thereby acting as nonradiative recombination centers and resulting in the development of transient (i.e., undetectable in the off-state) charge density. Depending on their spatial distribution, both luminance efficiency and operating voltage might be adversely affected.

Despite the potential significance of shallow traps in the operational degradation of OLED devices, there are no established general techniques for their effective detection and measurement in such an environment. The application of methods, such as electron spin resonance [43], electrically detected magnetic resonance [44], and charge modulation spectroscopy [45,46], is hindered by their limited sensitivities and selectivities in operationally degraded OLED devices.

Electric field profiling provides an alternative method of evaluation of charge densities in operating OLED devices. The Poisson equation relates charge density and the change in electric field strengths. For example, in a simple bilayer OLED device, such as ETL|HTL, the charge density  $\sigma$  at the ETL|HTL interface can be obtained from the difference in electric field strengths in ETL ( $E_{\text{ETL}}$ ) and HTL ( $E_{\text{HTL}}$ ):

$$\sigma = (E_{\text{ETL}} - E_{\text{HTL}})\epsilon\epsilon_0 \quad (7.2)$$

Although in some cases the layer-by-layer electric field strengths can be measured spectroscopically [47] in a single OLED device, it is often more practical to obtain electric fields from operating voltage evaluations in a series of devices with variations in specific layer thickness. Within a layer with

negligible space charge, the electric field is approximately constant and independent of layer thickness. The voltage drop across such a layer is simply a product of electric field strength and layer thickness, which allows the evaluation of the electric field as a slope of linear dependences of operating voltage on layer thickness. After applying this technique to two adjacent layers, the overall charge density in the immediate vicinity of the interface can be calculated using Equation 7.2.

The presence of a significant space charge within a layer can be identified from nonlinear dependencies of operating voltage on layer thickness. Although quantitative interpretation in terms of charge densities becomes rather speculative in that case, even a qualitative detection of a degradation-related space charge in a certain layer is informative.

The electric field profiling also provides an important insight into injecting electrode deterioration during operation. Because currents in OLED devices are commonly injection-limited, the electrode deterioration results in increasing electric fields in adjacent layers. The total operating voltages and, consequently, power efficiencies, are adversely affected.

The aging experiments [38] on a series of devices ITO|NPB|Alq|Mg:Ag with the Alq thickness varying from 30 to 180 nm in 30 nm steps can serve as a good illustration of the electric field profiling technique. Figure 7.6 shows operating voltages as functions of Alq layer thickness before and after 192 h of operation at 70°C and 40 mA/cm<sup>2</sup> (approximately half-life). Both plots are sufficiently linear to conclude that the space charge contribution is minor and roughly independent of operational degradation. Thus, the Alq layer electric fields in unaged and aged devices at 20 mA/cm<sup>2</sup> are 0.81 MV/cm and 1.01 MV/cm, respectively. The electric field in the NPB layer obtained in a complementary experiment is approximately constant ~0.05 MV/cm during operational degradation. With Equation 7.2, it can be estimated that the unaged devices have ~235 nC/cm<sup>2</sup> total charge density at the NPB|Alq

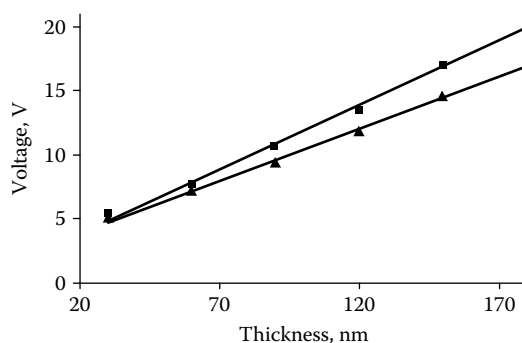


**FIGURE 7.6**

Operating voltages as functions of Alq layer thickness in NPB|Alq devices before (lower line) and after (upper line) 192 h of operation at 70°C and 40 mA/cm<sup>2</sup>.

interface when operated at  $20\text{ mA/cm}^2$  current density, which includes a polarization-related negative component ( $\sim -87\text{ nC/cm}^2$  [38]). A similar estimate for the aged-to-half-life devices gives  $\sim 297\text{ nC/cm}^2$  total charge density. Thus, the operational degradation results in  $\sim 62\text{ nC/cm}^2$  increase in total charge density at the NPB|Alq interface. Interestingly, the voltammetrically measured increase in deeply trapped positive charge is significantly higher:  $\sim 98\text{ nC/cm}^2$ , even neglecting the quadratic term. We conclude that, whereas deeply trapped positive charge at the NPB|Alq interface increases during operational degradation, mobile (which includes shallow trapped) charge density decreases.

It is noteworthy that the decreasing mobile charge density in this case is not a fundamental characteristic of the operational degradation process, but rather a product of the interaction between two apparently independent processes taking place in the operating OLED device: accumulation of trapped positive charge and cathode deterioration. Although it is possible to construct holes-only Alq devices, electron current is predominant in the Alq layer in the devices discussed earlier. Considering the absence of significant space charge in the Alq layer (as indicated by nearly linear plots in Figure 7.6), the electric field at the electron-injecting interface determines the current density. The higher electric field in the Alq layer of operationally degraded devices is therefore indicative of cathode deterioration during device operation. Unlike the accumulation of a deeply trapped charge, which demonstrates approximately coulombic character, the deterioration of the electron-injecting interface appears to be strongly affected by the average electric field during operation. For example, NPB|Alq devices exhibit similar rates of luminance loss and accumulation of deeply trapped positive charge when operated at the same average current densities in ac and dc modes [38]. In contrast, the increase of electric field in the Alq layer is strongly enhanced ( $\sim 0.5\text{ MV/cm}$  in dc vs.  $\sim 0.2\text{ MV/cm}$  in ac at half-life) by dc operation. In agreement with Yahiro et al., who originally reported the recoverable degradation phenomenon in Alq-based OLED devices [19], we note that, although the major part of the electric field increase observed in dc operation is reversible after applying reverse bias for several hundred hours, only a minor ( $\sim 10\%$ ) fraction of the initial luminance is recovered.

Clearly, in addition to the degradation processes in the vicinity of the recombination zone, which are immediately reflected in decreased luminance efficiencies and accumulated deeply trapped charge, there is also spatially and mechanistically separate cathode deterioration, detectable by electric field profiling. Operating voltage, power efficiency, and mobile charge density at the NPB|Alq interface are directly affected by cathode deterioration. The secondary effect on the luminance efficiency might also be expected because of quenching emissive excited states by mobile charge carriers [48].

As mentioned earlier, the presence of a significant space charge within a layer can be determined from nonlinear dependencies of operating voltage on layer thickness. For example, despite comparable hole mobilities

and HOMO energy levels, the replacement of NPB in the HTL with TAPC typically results in remarkably short-lived devices showing disproportionately high increases in operating voltage [1,49]. Analysis of voltage rise as a function of HTL layer thickness shows strongly superlinear dependency, which rules out the deterioration of the anode hole injection interface as the main reason for the rapid voltage rise in TAPC-based devices [50]. Instead, the thickness dependence suggests that the TAPC layer undergoes degradation that results in the formation of hole traps in the bulk of the layer.

### 7.2.3 Photoluminescence

Quenching of luminescence is one of the frequently cited processes responsible for electroluminescence efficiency loss in operating OLED devices. In 1996, Papadimitrakopoulos et al. showed that solid-state photoluminescence of the common OLED host and emitter material Alq is strongly quenched by products of its hydrolysis and oxidation [51]. In the same year, Scott et al. proposed that one of the processes responsible for the degradation of polymer-based OLED devices is the accumulation of oxidation product—aromatic aldehyde that quenches the fluorescence [52]. Although these studies reported what appear to be essentially extrinsic processes (aside from localized regions of edges and dark spots, a typical OLED device has a negligible presence of oxygen and water between two impermeable electrodes), pointing out the importance of luminescence quenchers was undoubtedly a major conceptual advance in the understanding of intrinsic degradation of OLED devices.

Broadly defined in the context of OLEDs, luminescence quenching is a process of radiationless energy transfer between the emissive excited state and the quencher, which is the nonemissive molecule with a comparable or lower energy excited state. There are several elementary mechanisms of radiationless energy transfer: The long-range dipole–dipole mechanism, which is also called Förster energy transfer, is effective in transferring singlet excited states and, therefore, is commonly utilized in fluorescent OLED devices that use dopant to emit light [53]. Even though typical dopant concentration is only a small percent, long-range energy transfer results in a predominant emission from dopant molecules. The dipole–dipole mechanism is almost completely ineffective for energy transfer between triplet excited states. Instead, the short-range electron exchange mechanism dominates triplet–triplet energy transfer. Although this type of energy transfer is particularly important for transferring triplet excitation to an emitting dopant in the operation of phosphorescent OLED devices [36], it also makes it possible for triplet–triplet annihilation to contribute significantly to the electroluminescence of fluorescent OLED devices [33,54]. Both energy transfer mechanisms might result in an excited state moving tens of nanometers from the electron–hole recombination site before deactivating. By analogy, it is therefore clear that the presence of even low concentrations of a quencher, which acts as a

nonemissive energy trap, can result in substantially decreased luminescence in fluorescent and phosphorescent OLED devices.

Because excited states generated by charge carrier recombinations or by photoexcitation undergo quenching regardless of their origin, photoluminescence measurements may be used to detect the contribution of quenching processes to the overall loss of electroluminescence efficiency. However, the quantitative interpretation of photoluminescence measurements in terms of the quenching contribution to the overall loss of electroluminescence efficiency is hindered by the generally unavoidable differences in spatial distributions of quenchers and excited states in the electroluminescence and photoluminescence experiments: Whereas electroluminescence is typically tied to some interface and distributed unevenly within an emissive layer, photoluminescence results from the mostly uniform excitation of an emissive layer. Considering that the distribution of quenchers is likely to be nonuniform (see, for example, [55]), it follows that the quantitative relationship between the extents of photoluminescence and electroluminescence quenching processes is generally not known.

The photoluminescence experiments can also be used to make order-of-magnitude estimates of quencher concentrations. With respect to the kinetics of quenching, there are several theoretical treatments of static fluorescence quenching in solids. The quenching sphere model introduced by Perrin [56] is mostly of historic interest since the development of theories of energy transfer by Förster [57] and Dexter [58]. Using Förster's expression for a static quenching, the relationship between the concentration of quencher and device luminance ( $L$ ) can be written as follows:

$$L/L_0 = 1 - \pi^{0.5} Q/Q_0 \exp((Q/Q_0)^2) (1 - \text{erf}(Q/Q_0)) \quad (7.3)$$

where

$L_0$  is the luminance in the absence of quencher

$Q_0$  is the Förster's critical concentration, which is dependent on the properties of quencher and quenchee molecules

In the context of OLED operational degradation, the structure and properties of putative quencher molecules are generally not known, which precludes using Equation 7.3 to obtain quencher concentration from luminance efficiency. Furthermore, Equation 7.3 has another important shortcoming: Although Förster's derivation of the bulk quenching has proven useful in many experimental systems, it only considers direct energy transfer from emitter to quencher. Energy transfers between emissive molecules such as OLED host molecules are not considered by Förster's theory. Yet such a degenerate energy transfer process might be expected to play an important role in OLED devices with significant exciton diffusion lengths. Our numerical simulations of the systems where exciton diffusion is significant showed that Förster's derivation might indeed be inaccurate. Depending on

the length of exciton diffusion, Stern–Volmer’s kinetics [59] can provide an alternative description for the relationship between luminance and quencher concentration.

$$L_0/L = 1 + k_{sv} Q \quad (7.4)$$

Here,  $k_{sv}$  is the characteristic constant, which, in the case of classical Stern–Volmer treatment is the product of the bimolecular quenching rate constant and lifetime of the quenchee. Considering that Stern–Volmer kinetics is a textbook case of a quenching in fluid (low viscosity) solutions, it is somewhat surprising to find that it is also applicable to quenching in a rigid solid. A simple explanation of this behavior is that, although the molecules in OLED-like systems are stationary, excitons can diffuse to a significant length resulting in fluid-solution-like kinetics.

In principle, Equations 7.3 and 7.4, which emphasize long- and short-range energy transfer processes, respectively, can be used to describe corresponding limiting cases. It is noteworthy that, neglecting spatial nonuniformities, a theoretical model of photoluminescence change during OLED operation can be constructed based on (1) a function describing the relationship between the concentration of a quencher and the emission intensity, i.e., Equations 7.3 and 7.4, and (2) a function describing the kinetics of quencher formation. Here we consider four models constructed as follows:

Model (I): The rate of quencher formation is proportional to the luminance ( $dQ/dt = k_1 L$ , where  $k_1$  is first-order rate constant and  $t$  is time) and the quenching follows Förster kinetics. Although the resultant differential equation has no obvious analytical solution, it can be readily solved numerically.

Model (II): The rate of quencher formation is proportional to the luminance and the quenching follows Stern–Volmer kinetics. The resultant differential equation can be solved to yield this simple equation describing the kinetics of luminance loss:

$$L_0/L = (2k_1 k_{sv} L_0 t + 1)^{0.5} \quad (7.5)$$

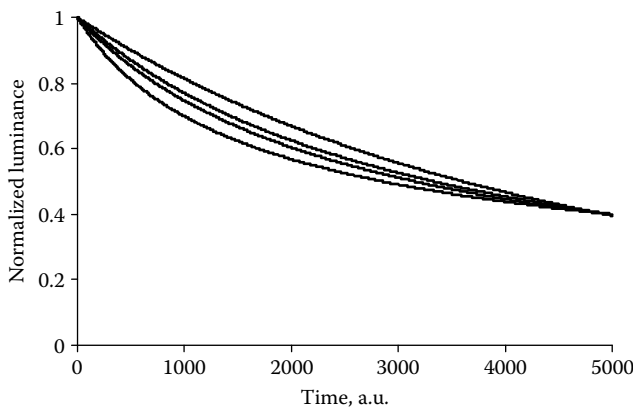
Model (III): The rate of quencher formation is constant ( $dQ/dt = k_2$ ) and the quenching follows Förster kinetics:

$$L/L_0 = 1 - \pi^{0.5} k_2 t / Q_0 \exp((k_2 t / Q_0)^2) (1 - \text{erf}(k_2 t / Q_0)) \quad (7.6)$$

Model (IV): The rate of quencher formation is constant and the quenching follows Stern–Volmer kinetics:

$$L_0/L = 1 - k_{3v} k_2 t \quad (7.7)$$

Figure 7.7 shows the predictions of four models scaled to fit on a similar timescale. Despite the very dissimilar analytic forms, all models result

**FIGURE 7.7**

Luminance decay profiles as predicted by models III, IV, I, and II, top to bottom curves, respectively.

in luminance vs. time curves that resemble experimental dependencies observed in the operational degradation of OLEDs. Although such nondistinctive behavior makes it difficult to extract mechanistic information from the shapes of experimental luminance vs. time curves, it may be viewed as consistent with the notion that luminescence quenching contributes significantly to the overall loss of electroluminescence efficiency in operating OLED devices. However, satisfactory fits to photo- and electroluminescence decays were also obtained with fundamentally different models of luminance efficiency loss, such as a trapping mechanism [60] and a trivial loss of emitting centers [61]. Considering the multitude of experimentally unsupported assumptions about distribution and dynamics of charge carriers and excited states required for such models, it is doubtful that reliable mechanistic conclusions can be reached based on fitting operational characteristics to some models.

Despite the complexity (discussed earlier) in the quantitative interpretation of photoluminescence measurements, they proved to be very effective in mechanistic studies of OLED degradation. A seminal work by Aziz, Popovic, and coworkers demonstrated that Alq cation-radicals are unstable in a solid-state, OLED-like environment [62]. They designed mostly monopolar devices to study the separate effects of charge carriers on the stability of Alq.

The monopolar devices with predominantly hole current were constructed by placing a thin Alq layer between NPB layers, which act as hole-transport and electron-blocking layers. The nearly monopolar characteristic of such devices was confirmed by observing only weak electroluminescence, which also precluded using it to evaluate the extent of operational degradation. On the other hand, the differences in absorption spectra of Alq and NPB permitted the separate photoexcitation of the thin Alq layer with 442 nm Hg line. *In situ* measurements revealed continuously decreasing photoluminescence

of Alq during device operation. After 50 h of operation at  $50\text{ mA/cm}^2$ , a nearly  $2\times$  decrease in photoluminescence efficiency was observed, which is comparable to the decrease in electroluminescence efficiency during the operation of standard bilayer NPB|Alq devices reported in the same study (half-life of  $\sim 20\text{ h}$  at  $25\text{ mA/cm}^2$ ). An even faster decrease in photoluminescence efficiency was observed in monopolar devices with pure Ag cathodes, which further suppress the injection of electrons. These experiments strongly supported the notion of instability of the cation-radicals of Alq.

In contrast, the initial experiments on monopolar devices with Alq exposed to only electrons did not show any decrease in photoluminescence efficiency under similar operating conditions [62]. However, in a more recent work, it was reported that Alq also shows instability when exposed to a much stronger electron current [63].

In bipolar Alq-based devices, the photoluminescence experiments clearly showed that quenching was one of the major contributors to the total loss of electroluminescence efficiency. Simultaneous monitoring of electro- and photoluminescence intensities of Alq emission in bipolar devices (utilizing thin Alq layers to minimize depth profile differences between electric- and photoexcitation) showed comparable changes in both signals during device operation. Even stronger evidence of the quenching process was obtained in a time-resolved experiment, which showed a significantly increased decay rate of Alq fluorescence in the degraded device [27].

Based on the comparisons of (1) photoluminescence quenching in bipolar and holes-only devices and (2) photo- and electroluminescence loss in bipolar devices, the plausible hypothesis was put forward that the instability of Alq cation-radicals plays a key role in bipolar devices as well as in holes-only devices [62]. However, considering that the concentrations of Alq cation-radicals could be substantially less in operating bipolar devices relative to holes-only devices, the alternative degradation mechanisms, involving, for example, unimolecular reactions of excited states or bimolecular reactions of charge carriers and excited states, cannot be rigorously ruled out.

The demonstration of the usefulness of photoluminescence measurements to probe mechanisms of Alq-based OLED degradation paved the way for their routine use in the studies of various OLED devices, including those based on phosphorescent emitters. For example, quenching was demonstrated to play a significant role in the degradation of phosphorescent OLEDs with CBP as the emissive layer host [55,64].

---

### 7.3 Chemical Analysis of Degrading OLED Devices

Although the physical methods discussed earlier provide important information about the degradation processes in operating OLED devices, the quantitative evaluations of neither concentrations of degradation products

and intermediates nor their distributions within device layers are typically possible. Even more problematic is the qualitative structural identification of these putative species. Yet these pieces of information are clearly essential for understanding the mechanisms of the operational degradation of OLED devices. Thus, chemical analysis of degraded OLED devices appears to be unavoidable in order to gain further mechanistic insight. Surprisingly, only few such studies were reported in OLED devices [50,55,64,65] and in a related field of light-emitting electrochemical cells [66]. It is likely that the technical difficulties caused by extremely small quantities of materials inside experimental OLED devices prevent the common use of chemical analysis in operational degradation studies.

Perhaps one of the most important pieces of information that can potentially be obtained in chemical analysis is the unambiguous confirmation of the hypothesis that *significant quantities* of organic materials in operating OLED devices undergo chemical transformations. Unfortunately, there are no reasons to believe that the OLED degradation of any given device involves only a single sequence of selective chemical reactions. Instead, it is likely that a multitude of chemical reactions occurs during device operation. Some of these supposed reactions can belong to chemically independent mechanisms and have orders-of-magnitude different rates. A detected (but not quantified) chemical product might not be representative of the OLED operational degradation process at all, but, rather, correspond to a sequence of chemical reactions that is quantitatively minor and, therefore, has an insignificant effect on device performance. In that regard, quantitative information is clearly one of the required elements for formulating a mechanistic hypothesis. Even measuring operation-related chemical conversion, i.e., the loss of organic materials initially comprising OLED devices provides important indications of the chemical initiation step in the operational degradation mechanism. Because OLED devices normally include many chemical materials and layers, measurements of the losses of specific components can also be used to determine the location of the operational degradation process or to rule out an involvement of a particular layer or material.

Research OLED devices (0.01–1 cm<sup>2</sup> active area) typically contain microgram levels of combined quantities of organic materials. Individual materials such as dopants can be present in quantities of less than a nanogram. Although very small by synthetic chemistry standards, these quantities are actually sufficient for many common chemical analysis techniques. For the purpose of measuring losses of known components in complex mixtures such as are found in OLED devices, it is not particularly important to use analytical techniques capable of structural identification of unknown chemical materials. Instead it is preferable to have sufficiently high selectivity to quantify individual components in complex mixtures. In that respect, chromatographic methods that are inexpensive and commonly used in chemical laboratories, such as reverse-phase HPLC with UV-detection, can be effective in the analysis of OLED devices [50,55,64].

For example, the chemical conversion of device components was studied in exemplary phosphorescent OLED devices with the general structure NPB|CBP + 8%Ir(ppy)<sub>3</sub>|BAIq|Alq [55, 64]. The HPLC technique was applied to measure the relative quantities of NPB, CBP, and Ir(ppy)<sub>3</sub>. Other materials present in the device—Alq and BAlq—were not quantifiable because of their hydrolytic instability, which illustrates some limitations of the reverse phase HPLC method as applied to OLED device analysis. Substantial aging-time-dependent decreases in CBP and Ir(ppy)<sub>3</sub> quantities relative to NPB were detected. This indicated that both components of the light emissive layer—CBP and Ir(ppy)<sub>3</sub>—undergo chemical reactions. Similar experiments on OLEDs incorporating an additional layer of TNB between NPB and ITO showed that the NPB/TNB ratio did not change appreciably during aging suggesting that the quantity of NPB was not changing during operational degradation, and absolute losses of CBP and Ir(ppy)<sub>3</sub> could be calculated using NPB as an internal standard. Overall, after 4000 h of operation at 40 mA/cm<sup>2</sup>, 21% of CBP and 25% of Ir(ppy)<sub>3</sub> were chemically transformed. Observing such degrees of conversion supports the hypothesis that chemical reactions play an important role in the operational degradation of OLED devices.

Although in the devices discussed earlier, the detected losses were almost entirely localized within the emissive layer, other devices show that the operation-related chemical reactions may also occur mostly in transport layers [50]. For example, in OLED devices with TAPC-based HTLs, the chemical loss occurred primarily within a TAPC layer adjacent to the recombination zone. Even though most of the TAPC is not in immediate contact with the recombination zone, the chemical reactions of TAPC extended in the bulk of the HTL. The aggregate extent of the chemical conversion of TAPC was remarkably high: For example, after 1176 h of operation at 5 mA/cm<sup>2</sup>, the TAPC losses were 62% (6.2 nm), 43% (33 nm), and 38% (57 nm) in devices with TAPC layer thicknesses of 10, 75, and 150 nm, respectively. Evidently, the TAPC degradation process extends at least 60 nm away from the emissive layer, yet the distribution is nonuniform with the region in close proximity to the main recombination interface degraded significantly more. Interestingly, the nonuniformity of TAPC layer degradation is even stronger at the earlier stages of operation. For example, after 270 h of operation at 5 mA/cm<sup>2</sup>, the absolute extent of TAPC loss was nearly identical at ~3 nm in all three devices.

As the study of chemical conversion of TAPC shows, it is possible to determine the location of chemical reaction analyzing devices with appropriate variations of layer thicknesses. However, in some cases the chemical reactions are strongly confined within a few monolayers from an interface. For example, in OLED devices with NPB HTL, the chemical degradation of NPB is mostly confined within the first 2 nm on early stages of degradation, which requires an extremely thin NPB layer for accurate measurements of material losses [50]. Yet it is important to keep the overall

thickness of the HTL at a reasonable level to prevent electrical shorts as well as potential complications that are due to the proximity to ITO. A bilayer structure with two chemically distinct yet functionally similar materials provides a useful solution in such a case. Using this approach it was established that the chemical degradation of NPB gradually extends, but remains confined to 5–10 nm adjacent to the emissive layer even after prolonged operation.

Having established that substantial quantities of various OLED materials undergo chemical transformations during device operation, it is imperative to ask about the products of such reactions. However, without any preceding knowledge of their chemical structures and properties, the detection and quantification of operation-related chemical degradation products are considerably more difficult relative to the quantification of OLED materials initially present in a device. Unfortunately, in all cases studied thus far, operational degradation results in the complex mixtures of products. The low chemical yields of individual components further complicate their detection, quantification, and structural identification. Nonetheless, knowing the products of operational degradation is clearly very valuable from a mechanistic point of view.

Because of limited quantities of degradation products, their chemical structures are frequently inferred solely from mass spectrometry, either in combination with the HPLC analysis (HPLC/MS) of extracted OLED devices [50,64] or by the direct laser excitation (LDI-TOF) of the complete OLED device [65]. Unfortunately, mass spectrometry provides only limited structural information so that the proposed chemical structures are often tentative. In particular, chemical isomers with different substitution patterns are difficult to distinguish with mass spectrometric techniques. In some cases, more structurally informative methods such as one- and two-dimensional NMR can be used [55]. Additional data, such as chromatographic (GPC and HPLC) retention times and UV absorption spectra, are also very useful to support proposed chemical structures, particularly when an independently synthesized sample of a tentative degradation product is available.

Despite the aforementioned difficulties, many degradation products have been identified so far in different OLED device types. Based on the available quantitative information, most prominent degradation products were lower molecular weight materials, which corresponded to the products of carbon–carbon and carbon–nitrogen bond dissociation processes of OLED materials. Even though no quantitative information was available, interesting products resulting from ligand dissociation in organometallic materials were detected in phosphorescent OLED devices [65]. Some higher molecular weight products, corresponding to addition and dimerization reactions, were also identified [50,55]. Although the higher molecular weight products were typically present in smaller amounts, their concentrations were still sufficient to assume that the structures of these molecules were likely to shed light on chemical mechanisms associated with OLED operational

degradation. Furthermore, the products of additional reactions appeared to be structurally linked to the lower molecular weight products. It is therefore plausible that both types of degradation products belong to a single chemical mechanism or, in other words, have common intermediates and reactive species.

Although the identified products are formed in more than trace amounts, the chemical yields are generally low. For example, the combined chemical yield of all detected degradation products in CBP-based devices was <50%, based on the amount of consumed CBP. Even more deficient material balances were observed for chemical degradation processes involving NPB and TAPC materials. Evidently, major amounts of the materials consumed during OLED operation are converted into degradation products that are not readily detected. It is plausible that the “missing” degradation products are insoluble or irreversibly retained by the HPLC system because of their polymeric nature. Some support for the latter explanation was obtained in the GPC analysis of degraded devices, which showed the presence of high-molecular-weight components ( $1,000 < \text{MW} < 100,000$ , based on calibration with a set of polystyrene standards) [50,55]. Although the chemical yields of such products cannot be accurately determined from the available experimental data, we estimate that their amounts are comparable to the amounts of consumed materials on the assumption of similar absorption spectra and extinction coefficients of high-molecular-weight products and initial materials.

---

## 7.4 Mechanistic Conclusions

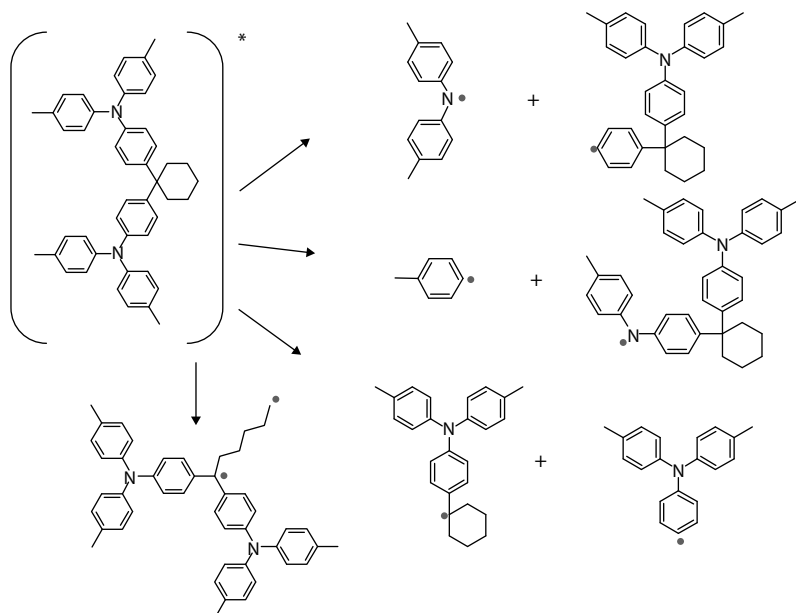
The preceding sections provided a noncomprehensive overview of OLED operational degradation studies with a strong focus on identification of chemical and physical changes in organic layers. Qualitatively, the physical changes in operating OLED devices appear to be nearly device-structure-independent processes of the accumulation of charge traps and fluorescence quenchers. On the other hand, the degradation processes taking place in operating OLED devices are evidently quite diverse from a chemical changes point of view. Whereas the large multitude of degradation products have been identified already, they are likely to represent only a subset of chemistries associated with operational degradation. Despite the fragmentary coverage of chemical classes—for example, in-device chemical reactions of the even ubiquitous OLED material Alq remain unknown—some preliminary mechanistic generalizations can be made based on the combined results of physical and chemical studies of OLED operational degradation.

It is noteworthy that there is a significant divergence between the results of physical and chemical studies with regard to detected species. Specifically, none of the structurally identified degradation products can be expected to

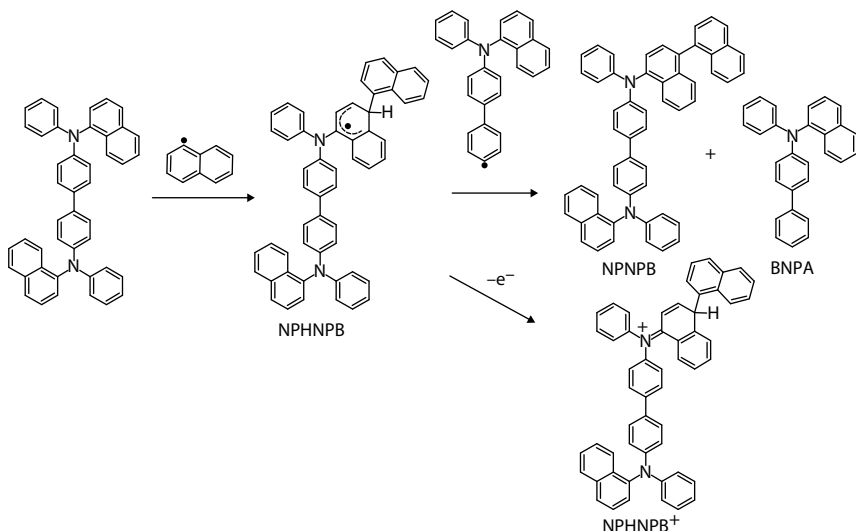
act as an effective fluorescence quencher or a nondischargeable charge carrier trap. However, considering that, generally, the combined yields of the identified degradation products are substantially <100%, the results of physical and chemical studies can be readily reconciled by theorizing that quenchers and traps are among the unidentified degradation products. In addition to being consistent with quantitative data, this hypothesis is also plausible from chemical reactivity of the degradation products. For example, unfilled deep traps can be expected to undergo redox reactions immediately upon exposure to ambient atmosphere, which is likely to render them undetectable in a typical extraction-followed-by-HPLC analysis.

Despite the absence of direct structural information, the chemical structures of some reactive degradation products can be tentatively inferred from the available data. From a chemist's point of view, it is obvious that any identified degradation product that formally corresponds to carbon–nitrogen or carbon–carbon bond breaking cannot be formed in a single-step chemical reaction. Instead, homo- or heterolytic bond breaking must occur as the first step followed by the transfer of the hydrogen atom or ion in a distinct chemical reaction. As argued in [50,55,64], photochemical experiments in solid state and solution as well as quantum chemical calculations suggest that the bond-breaking reactions occur as homolytic dissociations of relatively weak bonds of OLED materials in a singlet excited state. The resultant carbon- and nitrogen-centered free radicals are highly reactive species capable of the addition of the solid matrix to aromatic  $\pi$ -systems of neighboring molecules to generate delocalized  $\pi$ -radicals. Such  $\pi$ -radicals are likely to be relatively unreactive and can probably exist in a solid matrix as long as there are no neighboring radicals or ion-radicals. On the other hand, such radical species would generally have a singly occupied molecular orbital (SOMO) level within the HOMO–LUMO (lowest unoccupied molecular orbital) gap of the matrix molecules, and, therefore, are expected to be readily oxidized or reduced by charge carriers—cation-radicals and anion-radicals of the matrix molecules. In other words, these radicals may act as deep charge traps potentially manifesting as internal fixed charge when filled. Furthermore, these radical species may also provide nonradiative recombination centers and luminescence quenching sites. Quantum chemical calculations generally predict the presence of low-lying excited states with low values of oscillator strengths, which suggests almost nonemissive character. Clearly, charge recombination on these centers would be virtually nonradiative. Similarly, short- or long-range energy transfer from normally emissive matrix excited states to these neutral radicals would amount to quenching of the OLED emitters. Both processes, nonradiative recombination and quenching, would result in a decrease of electroluminescence efficiency. In general, the presence of low energy, low oscillator strength transitions in these species is linked to the presence of the SOMO level, and, therefore, may be fairly common among radical products and intermediates in the operational degradation of OLED devices.

The  $\pi$ -radicals resulting from the addition of matrix materials to aromatic  $\pi$ -systems are also mechanistically significant to explain the formation of various identified products of operational degradation. Acting as donors of hydrogen atoms, they undergo energetically favorable disproportionation reactions with the initially formed reactive radicals resulting in the formation of stable, closed-shell molecules such as the identified degradation products. In principle, this chain of chemical reactions—homolytic dissociation, addition, and disproportionation—is sufficient to explain the phenomenon of operational degradation of OLED devices. Examples of dissociation reactions are depicted in Figure 7.8 using TAPC as a representative molecule with several different types of relatively weak bonds. A small subset of possible addition and disproportionation reactions following NPB excitation is shown in Figure 7.9 to yield stabilized  $\pi$ -radical NPHNPB and neutral, closed-shell degradation products NPNPB and BNPA. Interestingly, a special case of radical attack on the *para*- or *ortho*-position of arylamine may serve to explain the formation of fixed (nondischargeable) positive charge during OLED degradation. It is clear that the nitrogen lone pair allows the classical electronic structure to be drawn for the cationic form of NPHNPB (denoted as NPHNPB<sup>+</sup> in Figure 7.9), which suggests a very substantial depth of hole trap. This expectation is also supported by high-accuracy *ab initio* calculations of ionization potentials of model molecules [50].

**FIGURE 7.8**

Examples of the proposed homolytic dissociation reactions of singlet excited state of TAPC.

**FIGURE 7.9**

Radical addition and disproportionation reactions involving NPB and radicals derived from NPB. NPHNPB exemplifies the structures of suggested  $\pi$ -radicals that accumulate during device operation and cause the deterioration of performance characteristics. The structures of BNPA and NPNPB correspond to stable, detectable degradation products, which are operationally inert. NPHNPB<sup>+</sup> is an example of a putative stable, closed-shell cation formed by hole trapping on NPHNPB to act as fixed (nondischargeable) positive charge associated with OLED operation.

Many other radical or ionic reactions, e.g., hydrogen atom abstractions, radical recombinations, and electrophilic additions, can also be expected to involve radicals as well as corresponding ions—oxidized or reduced radicals. As a result, a very complex mixture of degradation products is formed. Although molecular diffusion is unlikely in a rigid matrix of the OLED device layer, a radical center (unpaired electron) can still migrate via a chain of chemical reactions resulting in spatially, long-lived separated radicals. Overall, operational degradation results in the formation of a complex mixture of products including some fraction of stabilized, long-lived free radicals in neutral forms as well as oxidized or reduced forms, which act as nonradiative recombination centers and fluorescence quenchers.

## References

1. Tang, C. W. and S. A. Van Slyke. 1987. *Appl. Phys. Lett.* 51:913.
2. For a recent review, see Aziz, H. and Z. D. Popovic. 2004. *Chem. Mater.* 16:4522.
3. Turro, N. J. 1991. *Modern Molecular Photochemistry*. Sausalito, CA: University Science Books, p. 110.

4. Burrows, P. E., V. Bulovic, S. R. Forrest, L. S. Sapochak, D. M. McCarty, and M. E. Thompson. 1994. *Appl. Phys. Lett.* 65:2922.
5. Do, L.-M., E.-M. Han, Y. Niidome, M. Fujihira, T. Kanno, S. Yoshida, A. Maeda, and A. J. Ikushima. 1994. *J. Appl. Phys.* 76:5118.
6. Fujihira, M., L.-M. Do, A. Koike, and E.-M. Han. 1996. *Appl. Phys. Lett.* 68:1787.
7. McElvain, J., H. Antoniadis, M. R. Hueschen, J. N. Miller, D. M. Roitman, J. R. Sheets, and R. L. Moon. 1996. *J. Appl. Phys.* 80:6002.
8. Liu, Y., H. Aziz, N. Hu, H. Chan, G. Xu, and Z. Popovic. 2000. *Appl. Phys. Lett.* 77:2650.
9. Boroson, M. L., A. Pleton, S. A. Van Slyke, and T. R. O'Toole. 2006. *PCT Int. Appl. WO 2006127411A1.*
10. Van Slyke, S. A., C. H. Chen, and C. W. Tang. 1996. *Appl. Phys. Lett.* 69:2160.
11. Sheats, J. R., H. Antoniadis, M. Hueschen, W. Leonard, J. Miller, R. Moon, D. Roitman, and A. Stocking. 1996. *Science* 273:884.
12. Parker, I. D., Y. Cao, and C. Y. Yang. 1999. *J. Appl. Phys.* 85:2441.
13. Choong, V.-E., J. Shen, J. Curless, S. Shi, J. Yang, and F. So. 2000. *J. Phys. D: Appl. Phys.* 33:760.
14. Ishii, M. and Y. Taga. 2002. *Appl. Phys. Lett.* 80:3430.
15. Aziz, H., Z. D. Popovic, and N. X. Hu. 2002. *Appl. Phys. Lett.* 81:370.
16. Vamvouris, G., H. Aziz, N.-X. Hu, and Z. D. Popovic. 2004. *Synth. Met.* 143:69.
17. Zou, D., M. Yahiro, and T. Tsutsui. 1997. *Synth. Met.* 91:191.
18. Yamada, T., D. Zou, H. Jeong, Y. Akaki, and T. Tsutsui. 2000. *Synth. Met.* 111–112:237.
19. Yahiro, M., D. Zou, and T. Tsutsui. 2000. *Synth. Met.* 111–112:245.
20. Adachi, C., T. Tsutsui, and S. Saito. 1990. *Appl. Phys. Lett.* 56:799.
21. Tokito, S., H. Tanaka, A. Okada, and Y. Taga. 1996. *Appl. Phys. Lett.* 69:878.
22. Shirota, Y., K. Okumoto, and H. Inada. 2000. *Synth. Met.* 111–112:387.
23. Lee, S. T., Z. Q. Gao, and L. S. Hung. 1999. *Appl. Phys. Lett.* 75:1404.
24. Luo, Y., H. Aziz, Z. D. Popovic, and G. Xu. 2007. *J. Appl. Phys.* 101:034510.
25. Maillard, B., K. U. Ingold, and J. C. Scaiano. 1983. *J. Am. Chem. Soc.* 105:5095.
26. Ripoche, J. 1967. *Spectrochim. Acta A* 23:1003.
27. Popovic, Z. D., H. Aziz, A. Ioannidis, and P. N. M. Anjos. 2001. *J. Appl. Phys.* 89:4673.
28. Ganzorig, C. and M. Fujihira. 2002. *Appl. Phys. Lett.* 81:3137.
29. Sinha, S. and A. P. Monkman. 2003. *Appl. Phys. Lett.* 82:4651.
30. Wilkinson, J., A. H. Davis, K. Bussmann, and J. P. Long. 2005. *Appl. Phys. Lett.* 86:111109.
31. Popovic, Z. D. and H. Aziz. 2005. *J. Appl. Phys.* 98:013510.
32. Odaka, H., Y. Okimoto, T. Yamada, H. Okamoto, M. Kawasaki, and Y. Tokura. 2006. *Appl. Phys. Lett.* 88:123501.
33. Kondakov, D. Y. 2007. *J. Appl. Phys.* 102:114504.
34. Young, R. H., C. W. Tang, and A. P. Marchetti. 2002. *Appl. Phys. Lett.* 80:874.
35. Adachi, C., M.A. Baldo, and S. R. Forrest. 2000. *J. Appl. Phys.* 87:8049.
36. H. Yersin. 2004. *Proc. SPIE* 5214:124.
37. Heineman, W. R. and P. T. Kissinger. 1996. *Laboratory Techniques in Electroanalytical Chemistry*. New York: Marcel Dekker, Chap. 3.
38. Kondakov, D. Y., J. R. Sandifer, C. W. Tang, and R. H. Young. 2003. *J. Appl. Phys.* 93:1108.
39. Berleb, S., W. Brütting, and G. Paasch. 2000. *Org. Electron.* 1:41.

40. Brown, C. T. and D. Kondakov. 2004. *J. Soc. Inf. Display* 12:323.
41. Kondakov, D. Y. 2006. *J. Appl. Phys.* 99:024901.
42. Ito, E., N. Hayashi, H. Ishii, N. Matsuie, K. Tsuboi, Y. Ouchi, Y. Harima, K. Yamashita, and K. Seki. 2002. *J. Appl. Phys.* 92:7306.
43. Kwong, C. Y., A. B. Djurisic, W. C. H. Choy, D. Li, M. H. Xie, W. K. Chan, K. W. Cheah, P. T. Lai, and P. C. Chui. 2004. *Mater. Sci. Eng. B* B116:75.
44. Li, G., C. H. Kim, P. A. Lane, and J. Shinar. 2004. *Phys. Rev. B* 69:165311.
45. Haskins, T., A. Chowdhury, R. H. Young, J. R. Lenhard, A. P. Marchetti, and L. J. Rothberg. 2004. *Chem. Mater.* 16:4675.
46. Sims, M., S. W. Venter, and I. D. Parker. 2008. *Soc. Inf. Display Digest* XXXIX:227.
47. Rohlfing, F., T. Yamada, and T. Tsutsui. 1999. *J. Appl. Phys.* 86:4978.
48. Young, R. H., J. R. Lenhard, D. Y. Kondakov, and T. K. Hatwar. 2008. *Soc. Inf. Display Digest* 39:705.
49. Shirota, Y., Y. Kuwabara, H. Inada, T. Wakimoto, H. Nakada, Y. Yonemoto, S. Kawami, and K. Imai. 1994. *Appl. Phys. Lett.* 65:807.
50. Kondakov, D. Y. *J. Appl. Phys.* 104:084520.
51. Papadimitrakopoulos, F., X.-M. Zhang, D. L. Thomsen, and K. A. Higginson. 1996. *Chem. Mater.* 8:1363.
52. Scott, J. C., J. H. Kaufman, P. J. Brock, R. Dipietro, J. Salem, and J. A. Goitia. 1996. *J. Appl. Phys.* 79:2745.
53. Tang, C. W., S. A. Van Slyke, and C. H. Chen. 1989. *J. Appl. Phys.* 65:3610.
54. Kondakov, D. Y. 2008. *Soc. Inf. Display Digest* XXXIX:617.
55. Kondakov, D. Y., T. D. Pawlik, W. F. Nichols, and W. C. Lenhart. 2008. *J. Soc. Inf. Display* 16:37.
56. Perrin, J. 1927. *Comp. Rend. Acad. Sci. Paris* 184:1097.
57. Förster, T. 1951. *Fluorenzenz Organische Verbindungen*. Göttingen: Vandenhoech and Rupprech.
58. Dexter, D. L. 1953. *J. Chem. Phys.* 21:836.
59. Stern, O. and M. Volmer. 1919. *Physik Z* 20:183.
60. Giebink, N. C., B. W. D'Andrade, M. S. Weaver, P. B. Mackenzie, J. J. Brown, M. E. Thompson, and S. R. Forrest. 2008. *J. Appl. Phys.* 103:044509.
61. Féry, C., B. Racine, D. Vaufrey, H. Doyeux, and S. Cinà. 2005. *Appl. Phys. Lett.* 87:213502.
62. Aziz, H., Z. D. Popovic, N.-X. Hu, A.-M. Hor, and G. Xu. 1999. *Science* 283:1900.
63. Luo, Y., H. Aziz, G. Xu, and Z. D. Popovic. 2007. *Chem. Mater.* 19:2079.
64. Kondakov, D. Y., W. F. Nichols, and W. C. Lenhart. 2007. *J. Appl. Phys.* 101:024512.
65. Meerheim, R., S. Scholz, S. Olthof, G. Schwartz, S. Reineke, K. Walzer, and K. Leo. 2008. *J. Appl. Phys.* 104:014510.
66. Soltzberg, L. J., J. D. Slinker, S. Flores-Torres, D. A. Bernards, G. G. Malliaras, H. D. Abruna, J.-S. Kim, R. H. Friend, M. D. Kaplan, and V. J. Goldberg. 2006. *J. Am. Chem. Soc.* 128:7761.

# 8

---

## *Materials and Interface Engineering in Organic Light-Emitting Diodes*

---

Fei Huang and Alex K.-Y. Jen

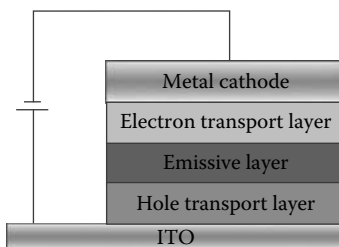
### CONTENTS

8.1	Introduction .....	243
8.1.1	Interface Engineering between Emission Layer and Cathode .....	244
8.1.2	Interface Engineering between Emission Layer and Anode ...	249
8.1.2.1	Perfluorocyclobutane-Based Cross-Linkable HTMs as HTLs in OLEDs .....	251
8.1.2.2	Styrene-Based Cross-Linkable HTMs as HTLs in OLEDs.....	254
8.1.2.3	Quantum Dot Light-Emitting Diodes.....	257
8.2	Summary.....	258
	Acknowledgments .....	258
	References.....	258

---

### 8.1 Introduction

Among the various fields of research on organic electronics, one of the most successful areas is related to organic light-emitting diodes (OLEDs) where significant improvements, such as good efficiency, high brightness, and low drive voltage, have been achieved. These improvements have led to the realization of high-efficiency full-color and white-color OLEDs.<sup>1,2</sup> It is now well known that efficient electron and hole injection/transport from cathodes and anodes is essential for high-efficiency OLED devices. That requires the electroluminescent (EL) materials to have a good luminescence property as well as good electron- and hole-transporting abilities, which is hard to be met by almost any of the current EL materials. One of the alternative approaches to overcome this problem is to fabricate multi-layer OLEDs by using a hole-transport layer (HTL) or an electron-transport

**FIGURE 8.1**

Schematic drawing of typical multilayer OLED device structure.

layer (ETL) in device fabrication.<sup>3–5</sup> As a consequence, the commonly used OLED devices normally adopt a multilayer device structure including the transparent conducting indium tin oxide (ITO) anode, HTL, emissive layer (EML), ETL, and metallic electrode cathode (Figure 8.1). And it has been found that carrier transport in most OLED heterostructures is largely injection limited.<sup>6</sup> Thus, interfacial phenomena have been an important subject of OLED science and technology and many interfacial modification efforts have been applied to cathode/organic, anode/organic, and organic/organic interfaces resulting in improved device response.<sup>3</sup> In this chapter, we review our recent progress on the development of materials and their applications on interface engineering between organic layer and electrodes to optimize charge-injection, -transport, and -recombination in OLEDs.

### 8.1.1 Interface Engineering between Emission Layer and Cathode

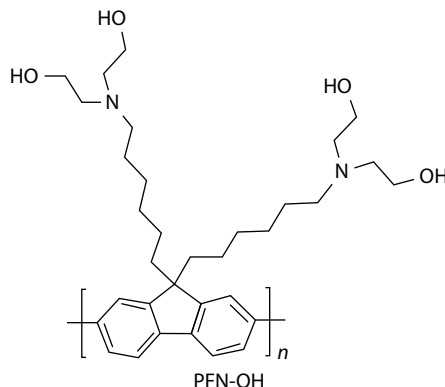
Most approaches to cathode/organic interface modification involve vapor-phase deposition. To ensure efficient electron injection in the bilayer device structure, low work-function metals, such as calcium (Ca) and barium (Ba), are commonly used as the cathode.<sup>7,8</sup> However, low work-function metals are very sensitive to moisture and oxygen that often cause the formation of detrimental quenching sites at areas near the interface between the EL layer and the cathode. In addition, metal ions formed at the interface tend to migrate into the EL layer thus affecting the long-term stability of devices.<sup>9</sup> To circumvent these problems, it is desirable to use high work-function metals (such as Al, Ag, or Au) as cathode because of their better environmental stability and simplicity involved for device fabrication. As a result, most of cathode/organic interface modification efforts have attempted to improve electron injection from high work-function metals into the emitting layer. For example, a layer of ultra thin “insulating” compound, such as lithium fluoride (LiF) or cesium fluoride (CsF), has been used as a buffer layer between EML and a high work-function Al electrode.<sup>10,11</sup> The devices fabricated using this approach show very encouraging results with efficiency and brightness equaling or exceeding those using Ca as the cathode. A possible explanation

for this improvement is the dissociation of the alkaline metal fluoride. The alkaline metal ions migrate into the EML, dope the material and lower the electron injection barrier. This creates the same problem encountered when using active metals as cathode due to the diffusion of the metal ions. Recently, dramatically enhanced electron injection from Al cathode has been reported by using either soluble ion-containing polymers or surfactants.<sup>12–16</sup> Those ion-containing polymers or surfactants can be processed on top of EML as ETL via spin-coating. However, the mobile counterions of these organic surfactants tend to migrate into the EL layer and affect the long-term stability of devices. In addition, the electron injection ability of these polymer electrolytes is also strongly influenced by the nature of their counterions.<sup>16</sup> Recent study showed that the similar enhanced electron injection from Al cathode also can be achieved by blending a neutral surfactant, poly(ethylene glycol) (PEG) into the EL polymer.<sup>17</sup> Thus, the ionic-free neutral surfactants could be potential candidates for interface modifying the high work-function metal cathode to enhance the electron injection in OLEDs.

Our approach to improve the electron injection from Al cathode is to introduce a layer of nonionic PEG-based neutral surfactants between the EML and the Al cathode. As a result, highly efficient polymer light-emitting diodes (PLEDs) can be obtained.<sup>18,19</sup> For example, when poly[2-methoxy-5-(2'-ethyl-hexyloxy)-1,4-phenylene vinylene] (MEH-PPV) is used as the EL polymer and the combination of surfactant, e.g., polyoxyethylene(12) tridecyl ether ( $P_{12}TE$ ), and Al is used as the cathode ( $P_{12}TE/Al$ ), the luminous efficiency (LE) of the OLED device reaches 3.59 cd/A, which is nearly twice that of the control device using Ca as cathode (1.89 cd/A). Several factors contribute to the device performance enhancement. First is the increase of the built-in field. The open-circuit voltage ( $V_{oc}$ ) of this LED device obtained from the photocurrent study is 1.56 V, almost the same as the  $V_{oc}$  of the device with Ca/Al as the cathode (1.52 V), and much larger than that of the LED with the Al cathode (1.26 V). This suggests a reduced electron injection barrier from the  $P_{12}TE/Al$  cathode. The elimination of the metal quenching sites also plays a key role in increasing the device performance. During metal evaporation, due to the impact and implantation of metal ion, many quenching sites are formed in the recombination/emission zone near the cathode side. The quenching effect is more severe for Ca, which is more reactive than Al. By inserting a buffer layer such as  $P_{12}TE$ , this kind of problem can be avoided and the emission quenching by cathode metal can be significantly reduced. Furthermore, atomic force microscopy (AFM) topographic images reveal that some spikes formed after spin-coating the layer of  $P_{12}TE$  on the relatively smooth surface of MEH-PPV. The local electric field intensity is enhanced at the spike positions, resulting in efficient electron injection. In addition, due to the ohmic contact between the MEH-PPV and the poly(3,4-ethylenediox thiophene):poly(styrenesulfonic acid) (PEDOT:PSS) layer, holes pile up at the MEH-PPV/ $P_{12}TE$  interface, leading to an increase in the local electrical field and the electron tunneling efficiency. Our investigation demonstrates

a significant difference between the efficiency of devices with and without a PEDOT:PSS anode buffer layer. For PLEDs using either Al or Ca/Al as cathode, the lack of a hole-injecting layer causes a difference of only a factor of two in performance. However, when the PEDOT:PSS layer is excluded, the device using  $P_{12}TE/Al$  performs much worse than the one that uses Al alone. These results indicate that the increased local electric field in a device with  $P_{12}TE/Al$  as cathode lowers the electron-injection barrier to a level almost similar to that using low work-function Ca as cathode. We also discovered that using surfactants with high enough molecular weight to form a solid film and with a general chemical formula of  $C_mH_{2m+1}(OC_kH_{2k})_nOH$ , can yield similar performance enhancements.<sup>19</sup>

Besides the use of nonconjugated neutral surfactants, conjugated neutral surfactant poly[9,9-bis(6'-diethanolamino)hexyl]-fluorene] (PFN-OH) was also developed as an electron-injection material for PLED applications (Figure 8.2).<sup>20</sup> Compared to previously reported nonconjugated neutral surfactants, there are several advantages of using PFN-OH as an electron injection layer (EIL) material for PLEDs, such as the following: (1) The conjugated poly-fluorene backbone endows it with good conductivity; (2) The surfactant-like side chain imparts the material with good solubility in alcohol-based solvents and with efficient electron injection from high work-function metals; (3) The amino groups on the side chain also significantly improve the electron injection from Al and higher work-function metal Ag or Au. Based on all these unique advantages, the PLEDs based on PFN-OH show excellent device performances even with a high work-function metal as cathode. For example, using a polymer blend of PF3B:PHF(1:5) as the EL layer, the PLED with a configuration of ITO/PEDOT:PSS/PF3B:PHF(1:5)/Al shows a very poor device performance with a maximum LE around 0.127 cd/A, due to the poor electron injection from the Al cathode. When PFN-OH is used as the EIL, the device ITO/PEDOT:PSS/PF3B:PHF(1:5)/PFN-OH/Al shows a

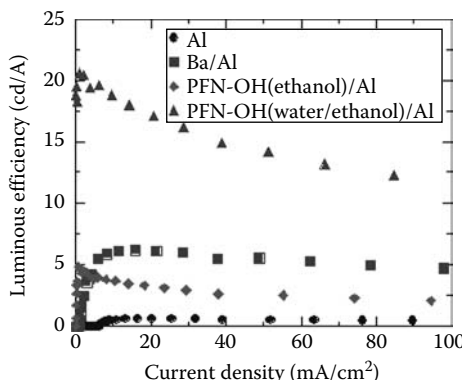


**FIGURE 8.2**

The chemical structure of PFN-OH.

much improved device performance with a maximum LE around 10.4 cd/A, which is even better than that of the device with Ca cathode. The maximum brightness of PFN-OH/Al device reaches 34,900 cd/m<sup>2</sup>, which is much higher than that obtained from the device using Ca/Ag as cathode (<4000 cd/m<sup>2</sup>). This is probably due to the prevention of cathode quenching. There are two possible mechanisms that contribute to the device performance enhancement when PFN-OH is used as the EIL in the Al cathode device. First, the oxygen atoms on the hydroxyl groups of PFN-OH can coordinate with Al atoms and cause n-type doping to the EL polymer near the surfactant.<sup>17-19</sup> Second, the amino groups on PFN-OH can form a positive interface dipole between the EL polymer and the high work-function metal cathode, producing a negative dipole potential for electrons.<sup>15,21</sup> Both these actions could reduce the barrier height for electron injection at the interfaces and lead to better electron injection. Results from photovoltaic measurements showed that the open circuit voltage moves from approximately 0.2 V for a plain Al device to around 1.6 V for the device with an additional PFN-OH layer, indicating that the effective barrier height for electron injection is substantially lowered by inserting a PFN-OH layer between Al cathode and emission layer. This leads to a more balanced population of electrons and holes for efficient recombination. Unlike traditional neutral surfactants, PFN-OH can also be applied to other high work-function metals such as Ag ( $\varphi=4.4\text{ eV}$ ) or Au ( $\varphi=5.2\text{ eV}$ ) because its amino groups interact strongly with Ag and Au metal surfaces, which can generate positive interface dipole, thereby enhancing the electron injection from Au cathode in PLEDs.<sup>20</sup> When PFN-OH was used as EIL, the performance of the devices could be improved greatly, the device with PFN-OH/Ag as cathode shows an LE of 4.01 cd/A and a brightness of 1405 cd/m<sup>2</sup> at a current density of 35 mA/cm<sup>2</sup> and drive voltage of 6.1 V, compared with the LE of 0.04 cd/A at the same current density for device with plain Ag as cathode. Similarly, with PFN-OH/Au as cathode, the device showed an LE of 2.74 cd/A at a current density of 35 mA/cm<sup>2</sup>, whereas with the device with neat Au as cathode there was hardly any light that could be detected. Considering the environmental stability and good thermal conductivity of these high work-function metals, the combination of excellent electron injection properties of PFN-OH with these metals can potentially improve the lifetime of PLED-based flat panel displays.

The general applicability of PFN-OH as EIL has also been examined in a series of electrophosphorescent LEDs. High-efficiency blue, green as well as the white emission phosphorescent PLEDs (with a LE of 43.0 cd/A for green-, 14.2 cd/A for blue-, and 20.7 cd/A for white-light emission) were also realized by using PFN-OH/Al cathode. However, it was found that those phosphorescent PLEDs' device performances depended highly on the processing condition of the PFN-OH layer.<sup>22</sup> For example, when using white phosphorescent PLEDs with the device configuration of ITO/PEDOT:PSS/FIrpic (5 wt%):Os-R (0.15 wt%):PVK:OXD-7(30 wt%)/PFN-OH/Al, where PEDOT:PSS is used as the HTL, greenish-blue phosphorescent iridium complex bis[4,6-di-fluorophenyl]-pyridinato-N, C<sup>2</sup>] (picolinate) Ir(III) (FIrpic)

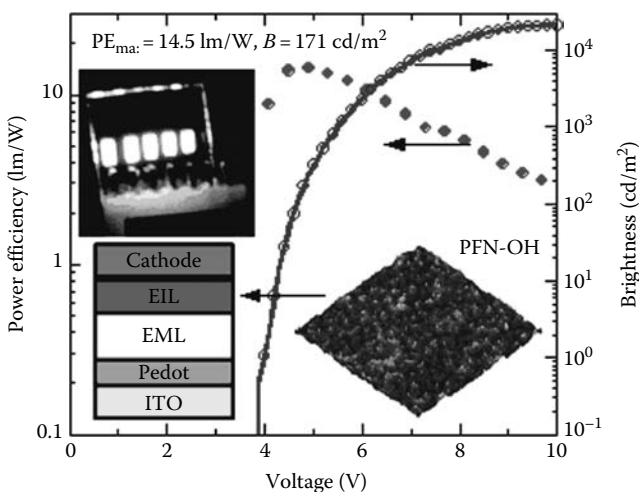
**FIGURE 8.3**

LE versus current density characteristics of the white PLEDs with Al, Ba/Al, PFN-OH(ethanol)/Al, and PFN-OH(water/ethanol)/Al cathodes, where PFN-OH(ethanol) stands for PFN-OH film spin-cast from ethanol solution and PFN-OH(water/ethanol) stands for PFN-OH film spin-cast from water/ethanol (1/4 v/v) solution. (From Zhang, Y. et al., *Adv. Mater.*, 20, 1565, 2008. With permission.)

and orange phosphorescent osmium complex (Os-R) are codoped into poly (*N*-vinylcarbazole) (PVK) host as the EML to achieve white light emission, it was found that the device with PFN-OH spin-coated from water/ethanol (1/4 v/v) solution exhibited a much better performance than the device with PFN-OH spin-coated from ethanol solution. The maximum luminescence efficiency of the devices with different cathodes follow the trend Al (0.62 cd/A) < PFN-OH (ethanol)/Al (4.83 cd/A) < Ba/Al (6.18 cd/A) < PFN-OH (water/ethanol)/Al (20.7 cd/A) (Figure 8.3). This dramatic solvent effect originated from two possible reasons. First, it was found that the OXD-7 can be washed out by alcohol solvents and this kind of erosion can be greatly suppressed by adding small amount of water to the alcohol. At the same time, it was found that the PFN-OH will form more aggregates by adding water to their ethanol solution, leading to rougher surface of the prepared ETL films. The hole/electron dominated device results indicate that the PFN-OH ETL processed from ethanol and water/ethanol solvent possessed different electronic properties, leading to different injection and transport properties of ETLs, which may also contribute to the dramatic changes in device performance.<sup>23</sup>

The device' performance can be further improved by inserting active metal Ba between the aggregated PFN-OH layer and the Al cathode. The turn-on voltage (defined as the voltage required to give a brightness of 1cd/m<sup>2</sup>) of the device decreases from 4.5V for the system using PFN-OH(water/ethanol)/Al to 3.9 V when PFN-OH(water/ethanol)/Ba/Al is used. The highest power efficiency (PE) was improved to 14.5lm/W at a brightness of 171 cd/m<sup>2</sup> (Figure 8.4), which is comparable to the PE of incandescent light bulbs.

Most interestingly, the unique solubility and excellent injection ability of these neutral surfactants offer the possibility to improve electron injection and

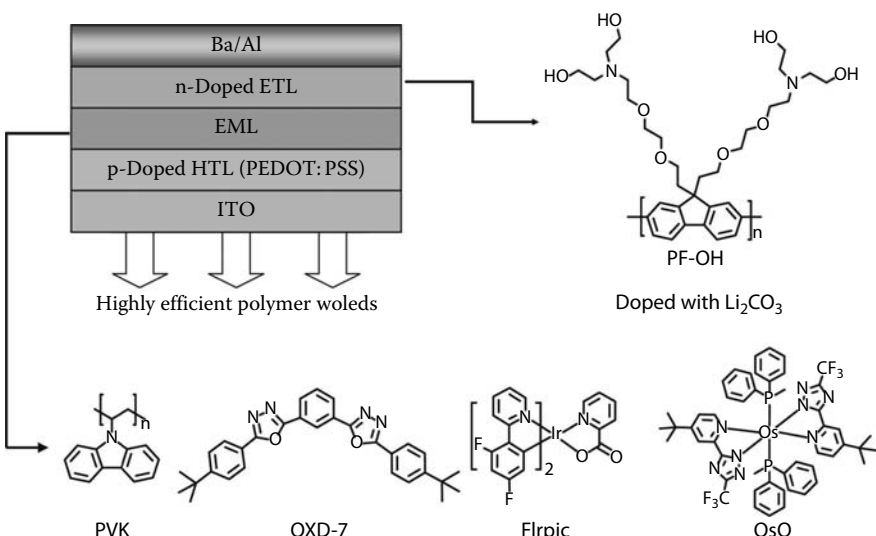
**FIGURE 8.4**

PE and brightness versus voltage characteristics of the white PLED. (Device configuration: ITO/PEDOT:PSS/FIrpic (5 wt%):Os-R (0.15 wt%):PVK:OXD-7(30 wt%)/PFN-OH(water/ethanol)/Ba/Al.

conduction by doping them with water soluble alkali or alkaline earth metal salts, which have been successfully used as n-dopants in OLEDs. Moreover, these neutral surfactants are ideal hosts for n-doping because they do not involve the complexity of the counterions in conjugated polyelectrolytes. By using another neutral water/alcohol soluble neutral conjugated polymer poly[9,9-bis(2-(2-(2-diethanolamino ethoxy)ethoxy)ethyl) fluorene] (PF-OH) as ETL host and Li<sub>2</sub>CO<sub>3</sub> as the dopant, the performance of neutral surfactant ETL based WPLEDs can further improved (Figure 8.5).<sup>24</sup> It was found that the electron transporting ability of PF-OH ETL can be dramatically improved upon doping with Li<sub>2</sub>CO<sub>3</sub> salt. Consequently, a very high-efficiency polymer white-emitting OLED (WOLED) with a maximum forward viewing LE of 36.1 cd/A and PE of 23.4 lm/W was achieved, which is comparable to those reported from the state-of-the-art vacuum deposited small molecule WOLEDs.<sup>24</sup>

### 8.1.2 Interface Engineering between Emission Layer and Anode

ITO has been widely used as the anode in OLEDs because of its transparency, good conductivity, and high work function. Therefore, most of anode–organic interface modifications were focused on improving the hole injection from ITO to the organic layer. It has been shown that the surface properties of ITO can be improved by various methods, including wet treatment, O<sub>2</sub> plasma treatment, UV ozone treatment, and coating treatment using self-assembly monolayers.<sup>25–27</sup> At present, the most effective method is plasma treatment. The work function of O<sub>2</sub> plasma-treated ITO can be improved

**FIGURE 8.5**

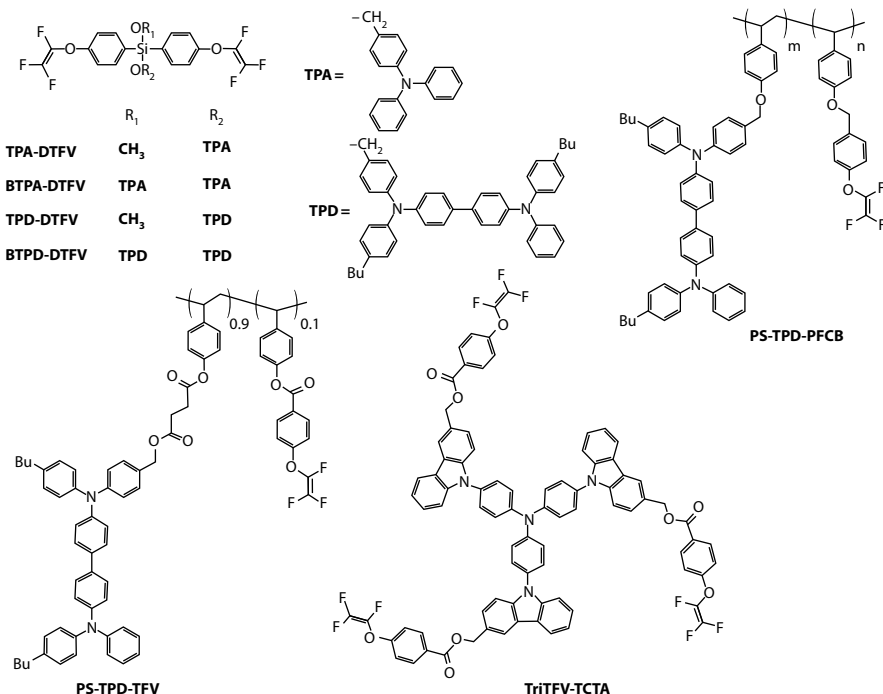
Schematic of the device structure based on doped ETL and chemical structure of relevant materials. (From Huang, F. et al., *Adv. Mater.*, 21, 361, 2009. With permission.)

to around 4.8 eV. However, most of emission materials, especially for blue-emitting materials, generally have a much lower highest occupied molecular orbital (HOMO) level than this. Hence, the hole transport/injection materials such as *N,N'*-3-methyl-phenyl)-1,1'-biphenyl-4,4'-diamine (TPD), 4,4'-bis[N-(1-naphthyl)-N-phenyl-amino]-biphenyl (NPD), tri(*N*-carbazolyl) triphenylamine (TCTA), etc. have been well developed as HTL materials in OLEDs to minimize the hole injection barrier between the ITO anode and the EML. Those HTL materials can facilitate hole-injection from the ITO anode and block the electron overflow from the EML to maximize charge recombination. Moreover, they can also confine the exciton within EML to avoid exciton quenching at the electrode.<sup>28,29</sup> All these factors will result in a greatly improved device performance. However, as the underneath layer of EML, the HTL needs to have good mechanical properties to avoid solvent-induced erosion, especially in PLEDs which are usually fabricated by a spin-coating technique.<sup>2</sup> To overcome this, many efforts have been exhibited. One of the useful approaches is to develop water/alcohol soluble hole-transporting materials (HTMs) with totally different solubility property from the traditional emission materials. A typical example is the water soluble PEDOT:PSS, which has been widely used in OLEDs as HTL.<sup>30</sup> However, PEDOT:PSS as HTL also have serious drawbacks such as corrosion of the ITO anode, poor hole injection for most of blue and green emitting materials due to their high HOMO level and induced exciton quenching at the interface of the PEDOT:PSS and the emissive materials.<sup>31,32</sup> Furthermore, the question still remains as to whether PEDOT:PSS has the magnitude of

electron-blocking capacity. Thus multilayer HTLs are needed to improve hole injection and reduce exciton quenching in these devices. However, this makes it difficult to choose the suitable second layer HTMs with solubility different from the underneath HTL and the subsequent EML. An alternative approach is to develop cross-linkable HTMs, which can form perfect solvent-resistant HTLs after thermo- or photo-crosslinking. In this way, it is easy to fabricate multilayer HTLs in OLEDs to improve the devices' performance, which actually offer a foundation stone for high-efficiency multilayer solution-processed LEDs. To meet all the desired requirements and challenges, we have developed a series of *in situ* thermally cross-linkable HTMs. Based on this unique advantage of these cross-linkable HTMs, high-efficiency RGB, white-emitting OLEDs and even inorganic quantum dots (QDs) LEDs have been realized.

### 8.1.2.1 Perfluorocyclobutane-Based Cross-Linkable HTMs as HTLs in OLEDs

By attaching trifluorovinyl groups to the traditional HTMs, a series PFCB-based cross-linkable HTMs were developed (Figure 8.6). It is well-documented that trifluorovinyl aromatic ether can undergo thermal



PFCB-based cross-linkable HTMs.

cyclopolymerization to form high molecular weight polymers with perfluorocyclobutane (PFCB) aromatic ether linkage.<sup>33</sup> This type of polymers exhibited high glass transition temperature, high thermal stability, high optical transparency, and low dielectric constants. In addition, the thermally induced reaction does not require catalysts or initiators and does not generate any by-products. Due to these desirable mechanical and thermal properties of PFCB type polymers, trifluorovinyl aromatic ether has been applied to HTMs to serve as an efficient thermally cross-linkable functionality. All these PFCB-based HTMs (Figure 8.6) can form an insoluble PFCB polymer film by *in situ* polymerization at 225°C for 1 h under nitrogen.<sup>34,35</sup> The cyclic voltammetry (CV) measurements on these polymer films showed that all of them have a very good electrochemical reversibility, similar to that of the triarylamine-based small molecule analogues, either TPA or TPD. The HOMO level of TPA-PFCB, BTPA-PFCB, TPD-PFCB, and BTPD-PFCB are found to be -5.17, -5.18, -5.31, and -5.32 eV, respectively, which are very close to the work function of ITO. The results indicate that all these HTMs can be used to reduce the hole-injection barrier and thus facilitate the injection of hole from ITO to EML. UV-visible absorption, photoluminescence (PL), and electroluminescence (EL) spectral studies indicate that aggregates are also formed during thermal polymerization. The enhanced  $\pi$ -orbital overlap in the aggregates may create a very efficient hopping pathway that facilitates hole transport. The study of hole-only devices shows that BTPD-PFCB, which has the highest density of the triarylamine functional group, possesses the best hole-injecting/transporting ability. After polymerization, the resulting BTPD-PFCB film is colorless and transparent. The transmission spectra show that over the entire visible spectrum, the transmittance of BTPD-PFCB film is higher than 93%; essentially, no light from the emitting layer is absorbed. For PEDOT:PSS, ~10%–17% of the emitted light is absorbed. A surface morphology study conducted by tapping mode AFM shows that the root-mean-square (rms) of the BTPD-PFCB film on ITO is around 0.86 nm, while the bare ITO substrate has a rms roughness of 3.2 nm, indicating that BTPD-PFCB HTL can also effectively planarize the ITO anode surface. Consequently, this film will prevent local shorting currents, thus improving device performance and uniformity of performance. Indeed, low currents are observed from BTPD-PFCB-containing devices at voltages below threshold, implying low leakage and the absence of “microshorts.” Using BTPD-PFCB as the HTL, highly efficient blue-, green-, and red-emitting polymer LEDs have been fabricated, demonstrating the superior performance of the PFCB and triarylamine-based polymers as HTMs.<sup>34–37</sup> For example, using fluorene-based green emission polymer poly[9,9-dihexyl-fluorene]-*co*-(benzothiadiazole)-*co*-(2,5-diptyoxy)phenylene] as the emitting layer and calcium as the cathode, the device showed a maximum LE of 18 cd/A. On the other hand, when PEDOT:PSS was used as the HTL, the maximum LE is only 4.7 cd/A. The improved performance was attributed to BTPD-PFCB’s good hole injection

and electron-blocking ability.<sup>34</sup> In addition, using BTPD-PFCB as HTL and thermal depositing 2,2',2''-(1,3,5-benzenetriyl)tris[1-phenyl-1H-benzimidazole] (TPBI) as electron-transporting/hole-blocking layer, the maximum external quantum efficiency (EQE) of 7.9 ph/el % was obtained based on the red emission Ir complex doped into a bipolar conjugated polymer (PFO-TPD-OXD) as the EML.<sup>37</sup>

Besides the small molecule cross-linkable materials, two TPD-based cross-linkable polymers PS-TPD-PFV and PS-TPD-PFCB were also developed by simply incorporating trifluorovinyl phenyl ether groups and TPD units into a commercially available poly(4-vinylphenol) backbone using a one-pot, sequential post-functionalization reaction.<sup>38–40</sup> By this way, the active TPD content can be easily controlled by changing the feed ratio of the monomers and the HOMO energy level of PS-TPD-PFV and PS-TPD-PFCB were around  $-5.32\text{ eV}$ , which is very similar to that of TPD. And robust highly cross-linking hole-transporting network with good film quality based on PS-TPD-PFV and PS-TPD-PFCB can be achieved by thermal treatment at  $230^\circ\text{C}$  for 30 min under nitrogen. Using PS-TPD-PFV as HTL and thermal depositing TPBI as electron-transporting/hole-blocking layer, a neutral Os complex doped into a bipolar conjugated polymer as the EML and an EQE of 12.8 ph/el % were realized with CIE coordinated at  $x=0.67$  and  $y=0.33$ .<sup>38</sup> CV reveals that the cross-linked polymer, PS-TPD-PFCB, possesses the same HOMO energy level ( $-5.32\text{ eV}$ ) as BTPD-PFCB; therefore, the hole injection barriers from ITO anode to these two HTLs are the same. However, the device using PS-TPD-PFCB as the HTL and a blue-emitting polymer, PF-TPA-OXD, as the EML exhibits slightly higher device performance compared to a BTPD-PFCB-based device. The maximum EQE is 0.58%, the maximum brightness ( $B_{\max}$ ) is  $7630\text{ cd/m}^2$ , and the maximum LE is  $0.91\text{ cd/A}$ . The device based on BTPD-PFCB as the HTL exhibits a maximum EQE of 0.51%, a maximum brightness of  $6350\text{ cd/m}^2$ , and a maximum LE of  $0.89\text{ cd/A}$ . Both devices can be turned on around  $4.0\text{ V}$ . Such subtle performance enhancement is attributed to the enhanced hole transport in the PS-TPD-PFCB layer. This thermally cross-linked HTM, PS-TPD-PFCB was also evaluated in a green-emitting PLED device with the configuration of ITO/HTL/PF9B/Ca/Ag to compare its device performance with the device using a conventional PEDOT:PSS. Both devices can be turned on at  $4.0\text{ V}$ ; however, a luminance of about  $20,600\text{ cd/m}^2$  is reached for the device using PS-TPD-PFCB as the HTL, which is 60% higher than that of the PEDOT:PSS-based device. The device using PS-TPD-PFCB as the HTL also has lower current density. As a result, the EL efficiency nearly doubles (from  $2.13\text{ cd/A}$  for PEDOT-PSS to  $3.82\text{ cd/A}$  for PS-TPD-PFCB).

The same structural design was also applied to TCTA which is a good HTM with HOMO level at  $-5.7\text{ eV}$ .<sup>39</sup> Three trifluorovinyl phenyl ethers were connected to TriTFV-TCTA by ester linkages. Since TriTFV-TCTA has a suitable HOMO ( $-5.7\text{ eV}$ ) and lowest unoccupied molecular orbital (LUMO) ( $-2.3\text{ eV}$ ) level, it can be used on top of the other cross-linkable HTL to form

a bilayer HTL configuration with gradient energy level for the more effective cascade hole-injection/transport and electron-blocking/exciton confinement in the devices. That is especially useful for the blue-emitting device where the emitting or host materials' HOMO level is usually lower than  $-6.0\text{ eV}$ . For example, TriTFV-TCTA was used in a blue-emitting phosphorescent OLED with an emission layer based on a blue triplet emitter bis(4',6'-difluorophenylpyridinato)-tetrakis(1-pyrazolyl)borate (FIr6) doped into a poly(*N*-vinylcarbazole) (PVK) host. Using PS-TPD-PFV as the first HTL and TriTFV-TCTA as the second HTL in the blue-emitting device with the configuration of ITO/PS-TPD-PFV/TriTFV-TCTA/10% FIr6 in PVK/TPBI/CsF/Al, a maximum EQE of 3.00 ph/el % and LE of 6.09 cd/A were achieved based on FIr6 doped into PVK as the blue emissive materials.<sup>39</sup> However, maximum EQE and LE from using PS-TPD-PFV as the single HTL were only 1.24 ph/el % and 2.39 cd/A, respectively.

### **8.1.2.2 Styrene-Based Cross-Linkable HTMs as HTLs in OLEDs**

Although light-emitting devices made from these PFBCB-based HTMs have been shown to have very good device performance, the required curing temperature of  $>225^\circ\text{C}$  for 1–2 h to complete the reaction is very harsh, which often imposes limitations on other device components that can be used. PEDOT:PSS is widely used as an efficient hole-injection layer due to its good electrical and mechanical properties.<sup>30</sup> By forming a HTL on PEDOT:PSS, it provides an ideal path for cascade hole injection to improve device performance.<sup>41</sup> It also leads to reduced turn-on voltage and improved device lifetime.<sup>42</sup> Moreover, the insertion of a HTM interlayer between PEDOT:PSS and the EML prevents the quenching of excitons at the adjacent PEDOT:PSS interface and provides effective electron blocking for confining excitons. However, the prolonged high temperature curing for the upper HTM layer tends to degrade PEDOT:PSS because of the decomposition of sulfonic acids in PSS or etching of the ITO. Therefore, it is desirable to find an alternative to reduce the curing temperature and time for the top layer HTM. It was reported that styrene can undergo rapid polymerization to form polystyrene simply by heating generated radicals without using any initiators.<sup>43</sup> Small molecules based on TPD, NPD, and TCTA (Figure 8.7) functionalized with two styryl groups were hence designed and synthesized.<sup>44–46</sup> 2-TPD and 2-NPD consisting of two connecting diamine molecules with two styryl groups were designed to improve the content of active hole-transporter (75.3 wt% and 77.6 wt%) over 1-TPD and 1-NPD (63.6 wt% and 66.6 wt%) that contain two styryl groups but with only one diamine molecule. The general cross-linking temperature can be decreased to  $150^\circ\text{C}$ – $180^\circ\text{C}$  to obtain polymer network with complete resistance towards common organic solvents. Because the naphthyl group lowers the electron density at the nitrogen due to better electron delocalization, the HOMO of 1-NPD and 2-NPD (ca.  $-5.4\text{ eV}$ ) is generally higher than

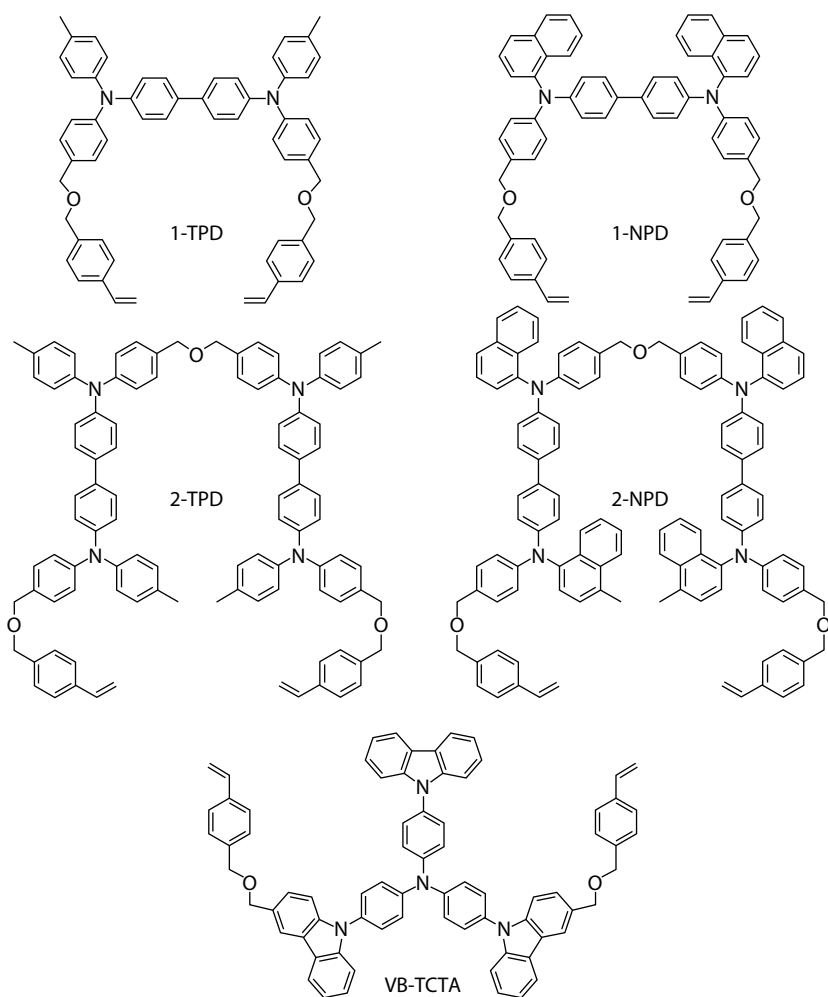


**FIGURE 8.7**  
Styrene-based cross-linkable HTMs.

that of 1-TPD and 2-TPD (ca.  $-5.3$  eV). LED devices based on a green emitting polymer poly[2,7-(9,9'-dihexylfluorene)-co-4,7-(2,1,3-benzothiadiazole)] (PFBT5) with the configuration of ITO/HTL/PFBT5/CsF/Al were fabricated for evaluating the hole-transporting properties of these new materials. The HTMs based on an ether linkage connected triarylamine dimers 2-TPD and 2-NPD exhibited better hole-transporting ability compared to their corresponding triarylamine monomers 1-TPD and 1-NPD due to higher active content as well as closer distance of the hole-transporting units. By taking advantage of the lower curing temperature offered by the styrene cross-linkable functionality in these new HTMs, PEDOT:PSS was used as

the bottom hole-injection layer in the configuration of ITO/PEDOT:PSS/HTL/PFBT5/CsF/Al to fabricate the optimal devices. The second HTLs were then spin-coated and cross-linked at 180°C on top of the PEDOT:PSS layer for 30 min. Again, devices using 2-TPD and 2-NPD showed better results than their corresponding counterparts 1-TPD and 1-NPD. 2-NPD exhibited the best device performance with the turn-on voltage decreased to 3.3 V, maximum EQE of 3.2%, LE of 10.8 cd/A and maximum brightness of 21,500 cd/m<sup>2</sup>.

The styrene-based cross-linkable HTM VB-TCTA (Figure 8.7) was also developed and the HOMO of VB-TCTA is located at -5.7 eV.<sup>44</sup> It has been proved that the formed cross-linked HTL VB-TCTA with the optimized thickness could also function as a spacer to prevent the PEDOT:PSS chain and other mobile constituents from penetrating into the EML and quenching the emission, which would potentially increase the devices' long-term stability.<sup>44</sup> Using PEDOT:PSS/VB-TCTA as the cascade HTL and thermal depositing TPBI as ETL, a maximum PE of ~5.6 lm/W at a forward brightness of 800 cd/m<sup>2</sup> has been achieved for white emission OLEDs with RGB phosphorescent dyes (bis[4,6-difluorophenyl]-pyridinato-N, C<sup>2</sup>](picolinato) Ir<sup>III</sup> (FIrpic), tris(2-(4-tolyl)phenylpyridine)iridium (Ir(mppy)<sub>3</sub>), and Os complex) doped into PVK as the EML. A possible surface-mixing structure formed at the interface between the PEDOT and VB-TCTA facilitated cascade hole injection and lowered the driving voltage.

#### **8.1.2.3 Quantum Dot Light-Emitting Diodes**

Besides the successful application in OLEDs, cross-linkable HTMs also show great application potential in inorganic quantum dots (QDs) LEDs.<sup>40,45</sup> Colloidal nanocrystal QDs are solution-processable chromophores with size-tunable band-gaps, high PL quantum efficiency (QE), excellent photo-stability, narrow emission line widths (<30 nm), and large spin-orbit coupling. These factors make them good candidates for use in next-generation thin-film optoelectronic devices such as LEDs<sup>47</sup> and solar cells,<sup>48</sup> which often adopt hybrid structures that incorporate both QDs and conjugated polymers or small-molecule organic semiconductors. Despite the potential advantages of using QDs as emitters, early QD light-emitting diodes (QD-LEDs) exhibited low efficiencies, and often produced broad voltage-dependent emission with spectral contributions from both the QDs and the organic host materials. Following lessons from OLEDs, a group from MIT reported a multilayer LED structure incorporating a monolayer of CdSe/ZnS core/shell QDs sandwiched between small molecule hole and ETLs, which exhibited a much improved device performance compared to the early QD-LEDs.<sup>49</sup> Their results indicate that the monolayer QDs help mitigate the impact of the low QD carrier mobilities<sup>50</sup> while the sandwich structure helps balance carrier injection. However, this multilayer device structure also brings big

challenges of controlling deposition of thin, uniform QD layers as well as controlling the interface between the organic transporting layer and eliminating EL from organic device layers.

Nevertheless, all these challenges can be overcome by using cross-linkable HTMs in QDs-LEDs. Jen and Ginger et al. reported a new approach for QD-LED fabrication that allows for the independent control of the QD and HTL thicknesses by spin-coating the QD layer onto a thermally cross-linked HTL (Device configuration: ITO/PS-TPD-PFCB/QDs/TPBI/Ca/Ag).<sup>40</sup> First, a thin layer of cross-linkable hole-transporting TPD polymer PS-TPD-PFCB was spin-coated on top of ITO HTL. After cross-linking, the solvent-resistant HTL can be easily formed. Then the CdSe/CdS core/shell QD emission layer can be solution processed on top of the HTL without any interface mixing. It was found that high-quality, easily varied QD films can be formed by this method. The coverage of the QD layer can be varied from submonolayer with a rms surface roughness of 1.62 nm to a more complete monolayer with rms roughness near 0.68 nm and the one monolayer of QDs is very smooth with a roughness of 0.62 nm. Due to the good film quality of the QD emission layer, the device shows a good device performance. It was found that the EL spectrum of the device is almost the same as the PL spectrum of the QDs and that there is no emission observed from the organic layers. The device showed an EQE of 0.4% at 100 cd/m<sup>2</sup>. The device's performance can be further improved by using bilayer HTL configuration. By adding the second cross-linkable VB-TCTA as the injection layer, the hole injection barrier between the HTL and the QD emission layer can be effectively decreased. As a result, the device performance was greatly improved. The QD-LEDs based on this bilayer HTL (Device configuration: ITO/PS-TPD-PFCB/VB-TCTA/QDs/TPBI/Ca/Ag) exhibit EQE of 0.8% at 100 cd/m<sup>2</sup> and a maximum luminescence more than 1000 cd/m<sup>2</sup>.

Very recently, it was shown that this kind of QD-LED performance can be substantially improved both by using an improved HIL/HTL structure and by performing a thermal annealing of the QD layer prior to the final deposition of the organic electron-transport layer.<sup>30</sup> A cross-linkable HTM 1-TPD was used as the HTL and two kinds of QDs (CdSe/CdS or CdSe/CdZnS/ZnS core/shell nanocrystals) were used as the emission layer in the devices with configuration: ITO/PEDOT:PSS/1-TPD/QDs/TPBI/CsF/Al. After being spin-coated on top of the cross-linked HTL, the QD emission layer was annealed for 15 min at different temperatures. It was found that the devices' performances were greatly improved by this thermal annealing treatment. Without the thermal annealing, the CdSe/CdS device exhibited a very poor performance with an LE of 0.232 cd/A at the luminescence of 100 cd/m<sup>2</sup>. However, after thermal annealing at 140°C for 15 min, the device's LE was improved to 1.70 cd/A at the luminescence of 100 cd/m<sup>2</sup>. Besides the improved efficiency, the devices with thermal annealing treatment also show a much better color purity than

that of the device without thermal annealing. The CdSe/CdZnS/ZnS also show the improved spectral purity and enhanced efficiency after thermal annealing. Without thermal annealing, the device based on CdSe/CdZnS/ZnS has a LE of 1.37 cd/A at the luminescence of 100 cd/m<sup>2</sup>, whereas this value can be improved to 4.24 cd/A after thermal annealing at 180°C. It was found that the thermal annealing treatment significantly improved the morphology of the QD film resulting in closer packed, more ordered QD layers on top of HTL films. Thus, the improved device performance was attributed to a combination of improved film morphology and improved charge transport and injection into the QD layer.

---

## 8.2 Summary

Water/alcohol soluble neutral surfactants and cross-linkable HTMs have been developed and used for multilayer engineering of PLEDs. All the cross-linkable HTMs can form perfect solvent-resistant HTLs after thermo or photocross-linking, which is beneficial for solution processing the subsequent emitting layer, whereas the water/alcohol soluble neutral surfactants can be spin-coated on top of the emitting layer as good electron injection materials. By taking advantage of all these novel materials, high-efficiency QD LEDs as well as white- and RGB-emitting OLEDs have been realized through materials and interface engineering to control charge injection, transport, and recombination.

---

## Acknowledgments

The authors thank the National Science Foundation (NSF-STC program under DMR-0120967) and the University of Washington through the Technology Gap Innovation Fund for financial support.

---

## References

1. Tang, C. W. and VanSlyke, S. A. 1987. Organic electroluminescent diodes. *Appl. Phys. Lett.* 51:913–915.
2. Burroughes, J. H.; Bradley, D. D. C.; Brown, A. R.; Marks, R. N.; Mackay, K.; Friend, R. H.; Burn, P. L.; and Holmes, A. B. 1990. Light-emitting diodes based on conjugated polymers. *Nature* 347:539–541.

3. Veinot, J. G. C. and Marks, T. J. 2005. Toward the ideal organic light-emitting diode. The versatility and utility of interfacial tailoring by cross-linked siloxane interlayers. *Acc. Chem. Res.* 38:632–643.
4. Hughes, G. and Bryce, M. R. 2005. Electron-transporting materials for organic electroluminescent and electrophosphorescent devices. *J. Mater. Chem.* 15:94–107.
5. Kulkarni, A. P.; Tonzola, C. J.; Babel, A.; and Jenekhe, S. A. 2004. Electron transport materials for organic light-emitting diodes. *Chem. Mater.* 16:4556–4573.
6. Baldo, M. A. and Forrest, S. R. 2001. Interface-limited injection in amorphous organic semiconductors. *Phys. Rev. B* 64:85201.
7. Braun, D. and Heeger, A. J. 1991. Visible light emission from semiconducting polymer diodes. *Appl. Phys. Lett.* 58:1982–1984.
8. Cao, Y.; Yu, G.; Parker, I. D.; and Heeger, A. J. 2000. Ultrathin layer alkaline earth metals as stable electron-injecting electrodes for polymer light emitting diodes. *J. Appl. Phys.* 88:3618–3623.
9. Parker, I. D.; Cao, Y.; and Yang, C. Y. 1999. Lifetime and degradation effects in polymer light-emitting diodes. *J. Appl. Phys.* 85:2441–2447.
10. Hung, L. S.; Tang, C. W.; and Mason, M. G. 1997. Enhanced electron injection in organic electroluminescence devices using an Al/LiF electrode. *Appl. Phys. Lett.* 70:152–154.
11. Piromerium, P.; Oh, H.; Shen, Y.; Malliaras, G. G.; Scott, J. C.; and Brock, P. J. 2000. Role of CsF on electron injection into a conjugated polymer. *Appl. Phys. Lett.* 77:2403–2405.
12. Xu, Q.; Ouyang, J.; Yang, Y.; Ito, T.; and Kido, J. 2003. Ultrahigh efficiency green polymer light-emitting diodes by nanoscale interface modification. *Appl. Phys. Lett.* 83:4695–4697.
13. Lee, T.-W.; Park, O. O.; Do, L.-M.; Zyung, T.; Ahn, T.; and Shim, H.-K. 2001. Polymer light-emitting devices using ionomers as an electron injecting and hole blocking layer. *J. Appl. Phys.* 90:2128–2134.
14. Cao, Y.; Yu, G.; and Heeger, A. J. 1998. Efficient, low operating voltage polymer light-emitting diodes with aluminum as the cathode material. *Adv. Mater.* 10:917–920.
15. Huang, F.; Wu, H. B.; Peng, J. B.; Yang, W.; and Cao, Y. 2007. Polyfluorene polyelectrolytes and their precursors processable from environment-friendly solvents (alcohol or water) for PLED applications. *Curr. Org. Chem.* 11:1207–1219.
16. Yang, R. Q.; Wu, H. B.; Cao, Y.; and Bazan, G. C. 2006. Control of cationic conjugated polymer performance in light emitting diodes by choice of counterion. *J. Am. Chem. Soc.* 128:14422–14423.
17. Deng, X. Y.; Lau, W. M.; Wong, K. Y.; Low, K. H.; Chow, H. F.; and Cao, Y. 2004. High efficiency low operating voltage polymer light-emitting diodes with aluminum cathode. *Appl. Phys. Lett.* 84:3522–3524.
18. Niu, Y. H.; Ma, H.; Xu, Q. M.; and Jen, A. K.-Y. 2005. High-efficiency light-emitting diodes using neutral surfactants and aluminum cathode. *Appl. Phys. Lett.* 86:0835041–0835043.
19. Niu, Y. H.; Jen, A. K.-Y.; and Shu, C. F. 2006. High-efficiency polymer light-emitting diodes using neutral surfactant modified aluminum cathode. *J. Phys. Chem. B* 110:6010–6014.

20. Huang, F.; Niu, Y. H.; Zhang, Y.; Ka, J. W.; Liu, M. S.; and Jen, A. K.-Y. 2007. A conjugated, neutral surfactant as electron-injection material for high-efficiency polymer light-emitting diodes. *Adv. Mater.* 19:2010–2014.
21. Wu, H. B.; Huang, F.; Mo, Y. Q.; Yang, W.; Wang, D. L.; Peng, J. B.; and Cao, Y. 2004. Efficient electron injection from a bilayer cathode consisting of aluminum and alcohol-/water-soluble conjugated polymers. *Adv. Mater.* 16:1826–1830.
22. Zhang, Y.; Huang, F.; Chi, Y.; and Jen, A. K.-Y. 2008. Highly efficient white polymer light-emitting diodes based on nanoscale control of the electron injection layer morphology through solvent processing. *Adv. Mater.* 20:1565–1570.
23. Huang, F.; Zhang, Y.; Liu, M. S.; and Jen, A. K.-Y. 2009. Electron-rich alcohol-soluble neutral conjugated polymers as highly efficient electron-injecting materials for polymer light-emitting diodes. *Adv. Funct. Mater.* 19:2457–2466.
24. Huang, F.; Shih P.-I.; Shu, C.-F.; Chi, Y.; and Jen, A. K.-Y. 2009. Highly efficient white polymer light-emitting diodes based on lithium salts doped electron transporting layer. *Adv. Mater.* 21:361–365.
25. Li, F.; Tang, H.; Shinar, J.; Resto, O.; and Weisz, S. Z. 1997. Effects of aqua-regia treatment of indium-tin-oxide substrates on the behavior of double layered organic light-emitting diodes. *Appl. Phys. Lett.* 70:2741–2743.
26. Kim, J. S.; Friend, R. H.; and Cacialli, F. 1999. Improved operational stability of polyfluorene-based organic light-emitting diodes with plasma-treated indium-tin-oxide anodes. *Appl. Phys. Lett.* 74:3084–3086.
27. Appleyard, S. F. J. and Willis, M. R. 1998. Electroluminescence: Enhanced injection using ITO electrodes coated with a self assembled monolayer. *Opt. Mater.* 9:120–124.
28. Parker, I. D. 1994. Carrier tunneling and device characteristics in polymer light-emitting diodes. *J. Appl. Phys.* 75:1656–1666.
29. Yan, H.; Lee, P.; Armstrong, N. R.; Graham, A.; Evmenenko, G. A.; Dutta, P.; and Marks, T. J. 2005. High-performance hole-transport layers for polymer light-emitting diodes. Implementation of organosiloxane cross-linking chemistry in polymeric electroluminescent devices. *J. Am. Chem. Soc.* 127:3172–3183.
30. Groenendaal, L.; Jonas, F.; Freitag, D.; Pielartzik, H.; and Reynolds, J. R. 2000. Poly(3,4-ethylenedioxothiophene) and its derivatives: Past, present, and future. *Adv. Mater.* 12:481–494.
31. de Jong, M. P.; van IJzendoorn, L. J.; and de Voigt, M. J. A. 2000. Stability of the interface between indium-tin-oxide and poly(3,4-ethylenedioxothiophene)/poly(styrenesulfonate) in polymer light-emitting diodes. *Appl. Phys. Lett.* 77:2255–2257.
32. Kim, J. S.; Friend, R. H.; Grizzi, I.; and Burroughes, J. H. 2005. Spin-cast thin semiconducting polymer interlayer for improving device efficiency of polymer light-emitting diodes. *Appl. Phys. Lett.* 87:023506.
33. Ji, J.; Narayan-Sarathy, S.; Neilson, R. H.; Oxley, J. D.; Babb, D. A.; Rondon N. G.; and Smith, D. W. Jr. 1998. [p-(Trifluorovinyl)oxy]phenyllithium: Formation, synthetic utility, and theoretical support for a versatile new reagent in fluoropolymer chemistry. *Organometallic* 17:783–785.
34. Jiang, X. Z.; Liu, S.; Liu, M. S.; Herguth, P.; Jen, A. K.-Y.; Fong, H.; and Sarikaya, M. 2002. Perfluorocyclobutane-based arylamine hole-transporting materials for organic and polymer light-emitting diodes. *Adv. Funct. Mater.* 12:745–751.

35. Liu, S.; Jiang, X. Z.; Ma, H.; Liu, M. S.; and Jen, A. K.-Y. 2000. Triarylamine-containing poly(perfluorocyclobutane) as hole-transporting material for polymer light-emitting diodes. *Macromolecules* 33:3514–3517.
36. Gong, X.; Moses, D.; Heeger, A. J.; Liu, S.; and Jen, A. K.-Y. 2003. High-performance polymer light-emitting diodes fabricated with a polymer hole injection layer. *Appl. Phys. Lett.* 83:183–185.
37. Niu, Y. H.; Chen, B. Q.; Liu, S.; Yip, H.; Bardecker, J.; Jen, A. K.-Y.; Kavitha, J.; Chi, Y.; Shu, C. F.; Tsemg, Y. H.; and Chien, C. H. 2004. Highly efficient red electrophosphorescent devices based on an iridium complex with trifluoromethyl-substituted pyrimidine ligand. *Appl. Phys. Lett.* 85:1619–1621.
38. Niu, Y. H.; Tung, Y. L.; Chi, Y.; Shu, C. F.; Kim, J. H.; Chen, B. Q.; Luo, J. D.; Carty, A. J.; and Jen, A. K.-Y. 2005. Highly efficient electrophosphorescent devices with saturated red emission from a neutral osmium complex. *Chem. Mater.* 17:3532–3536.
39. Niu, Y. H.; Liu, M. S.; Ka, J. W.; and Jen, A. K.-Y. 2006. Thermally crosslinked hole-transporting layers for cascade hole-injection and effective electron-blocking/exciton-confinement in phosphorescent polymer light-emitting diodes. *Appl. Phys. Lett.* 88:093505.
40. Zhao, J.; Bardecker, J. A.; Munro, A. M.; Liu, M. S.; Niu, Y. H.; Ding, I. K.; Luo, J.; Chen, B.; Jen, A. K.-Y.; and Ginger, D. S. 2006. Efficient CdSe/CdS quantum dot light-emitting diodes using a thermally polymerized hole transport layer. *Nano. Lett.* 6:463–467.
41. Choulis, S. A.; Choong, V.-E.; Mathai, M. K.; and So, F. 2005. The effect of interfacial layer on the performance of organic light-emitting diodes. *Appl. Phys. Lett.* 87:113503.
42. Brown, T. M.; Kim, J. S.; Friend, R. H.; Cacialli, F.; Daik, R.; and Feast, W. J. 1999. Built-in field electroabsorption spectroscopy of polymer light-emitting diodes incorporating a doped poly(3,4-ethylene dioxythiophene) hole injection layer. *Appl. Phys. Lett.* 75:1679–1681.
43. Mayo, F. 1968. The dimerization of styrene. *J. Am. Chem. Soc.* 90:1289–1295.
44. Niu, Y.-H.; Liu, M. S.; Ka, J.-W.; Bardeker, J.; Zin, M. T.; Schofiled, R.; Chi, Y.; and Jen, A. K.-Y. 2007. Crosslinkable hole-transport layer on conducting polymer for high-efficiency white polymer light-emitting diodes. *Adv. Mater.* 19:300–304.
45. Niu, Y.-H.; Munro, A. M.; Cheng, Y.-J.; Tian, Y.; Zhao, J.; Bardecker, J. A.; Plante, J.-L.; Ginger, D. S.; and Jen, A. K.-Y. 2007. Improved performance light-emitting diodes quantum dot layer. *Adv. Mater.* 19:3371–3376.
46. Cheng, Y.-J.; Liu, M. S.; Zhang, Y.; Niu, Y.-H.; Huang, F.; Ka, J.-W.; Yip, H.-L.; and Jen, A. K.-Y. 2008. Thermally cross-linkable hole-transporting materials on conducting polymer: Synthesis, characterization, and applications for polymer light-emitting devices. *Chem. Mater.* 20:413–422.
47. Colvin, V. L.; Schlamp, M. C.; and Alivisatos, A. P. 1994. Light-emitting diodes made from cadmium selenide nanocrystals and a semiconducting polymer. *Nature* 370:354–357.
48. Nozik, A. J. 2002. Quantum dot solar cells. *Physica E* 14:115–120.
49. Coe, S.; Woo, W.-K.; Bawendi, M.; and Bulović, V. 2002. Electroluminescence from single monolayers of nanocrystals in molecular organic devices. *Nature* 420:800–803.
50. Ginger, D. S. and Greenham, N. C. 2000. Charge injection and transport in films of CdSe nanocrystals. *J. Appl. Phys.* 87:1361–1368.



## **Part III**

# **Organic Electronic Devices**



# 9

---

## *Microcavity Effects in Organic Light-Emitting Devices*

---

Chung-Chih Wu and Hao-Wu Lin

### CONTENTS

9.1	Background Introduction .....	265
9.2	Theories .....	267
9.2.1	Fabry–Perot Formulation .....	267
9.2.2	Rigorous Electromagnetic Modeling .....	270
9.3	Microcavity/Interference Effects in Weak Microcavity OLEDs .....	272
9.4	Microcavity OLEDs .....	276
9.4.1	Microcavity OLEDs Having Two Metal Mirrors.....	276
9.4.2	Influences of Resonant Wavelengths on Microcavity OLEDs.....	279
9.5	Microcavity OLEDs Integrated with Microlens .....	284
9.6	Summary .....	289
	References.....	289

---

### 9.1 Background Introduction

Since the first report of efficient and practical organic light-emitting devices (OLEDs) in 1987 by Tang and VanSlyke [1], OLEDs have been the subject of intensive studies for flat-panel displays and lighting applications due to several advantages such as high efficiency, wide viewing angle, fast response, and potential low cost. In addition, their low processing temperatures and thereby versatility in substrates make them suitable for some novel applications such as flexible displays and lighting. Over the last two decades, OLED technology has made rapid progress, and several types of OLED displays have been manufactured and commercialized. With the continuous improvements in the efficiencies of OLEDs and white-emitting OLEDs, the application of OLEDs in lighting is also becoming realistic.

The basic structure of OLEDs consists of multi-layers of organic materials sandwiched between two electrodes (Figure 9.1). The total thickness of organic materials is usually of the order of 100 nm and is comparable to the emission wavelength. Therefore, emission properties of devices depend not only on intrinsic properties of emitting materials but are also often significantly modified by the optical structures of OLEDs. For instance, a typical OLED, which usually has one reflective metal cathode and one transparent indium tin oxide (ITO) anode on glass substrates (Figure 9.1), behaves like a weak microcavity. The device exhibits wide-angle interference between directly emitting radiation and reflected radiation, as shown in Figure 9.2a [2,3]. On the other hand, in some advanced OLED structures, such as microcavity OLEDs and top-emitting OLEDs, two electrodes of strong reflection are implemented in the devices, and one of them obtains a strong one-dimensional microcavity [2,3]. The optical characteristics of such strong microcavity structures are usually significantly tailored not only by wide-angle interference but also by multiple-beam interference, as illustrated in Figure 9.2b [2,3]. The optical microcavity effects inherent within OLEDs can spatially and spectrally redistribute the emission of devices, having a strong influence on the performance of OLEDs (efficiency, color, and viewing characteristic), and must therefore be carefully considered in any type of OLEDs.

This chapter provides the general theories and discussions of optical structures and characteristics of OLEDs. To start with, it presents a simple and analytical formulation of microcavity effects in OLEDs based on the concepts of the Fabry–Perot cavity; this provides a clearer physical insight but is more limited in its description of the effects of microcavity. Subsequently, this chapter provides a brief description of rigorous electromagnetic modeling of optical characteristics of OLEDs. These notions are then used as the

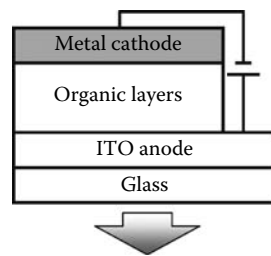


**FIGURE 9.1**

The device structure of a conventional bottom-emitting OLED. (From Wu, C.-C. et al., *J. Display Technol.*, 1, 248, 2005. With permission.)

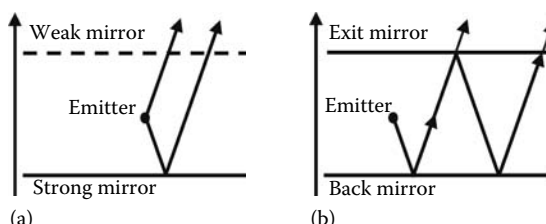


**FIGURE 9.2**

Illustration of optical phenomena in OLEDs: (a) wide-angle interference in noncavity (weak microcavity) OLED; (b) wide-angle and multiple-beam interference in strong microcavity OLEDs. (From Wu, C.-C. et al., *J. Display Technol.*, 1, 248, 2005. With permission.)

basis for discussing optical characteristics of various OLED structures such as typical bottom-emitting OLEDs and microcavity OLEDs.

## 9.2 Theories

### 9.2.1 Fabry–Perot Formulation

Optically, an OLED may be considered as a Fabry–Perot cavity (either strong or weak cavity) embedded with a source, as shown in Figure 9.3, in which  $E_0$  represents the free-space electric-field intensity of the source,  $E_2$  is the electric-field intensity of the wave outcoupled through the mirror  $M_2$ ,  $\sqrt{R_1}e^{j\phi_1}$  is the complex reflection coefficient of the mirror  $M_1$  (with a reflectance  $R_1$ ),  $\sqrt{R_2}e^{j\phi_2}$  is the complex reflection coefficient of the mirror  $M_2$  (with a reflectance, a transmittance, and an absorptance of  $R_2$ ,  $T_2$ , and  $A_2$ , respectively),  $L_1$  is the source-to- $M_1$  distance,  $L_2$  is the source-to- $M_2$  distance, and  $L$  is the total cavity length ( $L=L_1+L_2$ ). In such a configuration,  $M_1$  and  $M_2$  are effective mirrors on two sides of the devices representing optical properties of interfaces and layer stacks beyond giving dominant reflection properties, while the total cavity length represents all other layers sandwiched between these two interfaces. Considering both the field redistribution due to cavity and the influence of cavity on the transition rate of molecular excited states, one obtains the enhancement factor  $G_{\text{cav}}(\lambda)$  for emission through  $M_2$  (in the forward direction) relative to free-space emission at a wavelength  $\lambda$  [4–10]:

$$G_{\text{cav}}(\lambda) = \frac{|E_2|^2}{|E_0|^2} \times \frac{\tau_{\text{cav}}}{\tau_0} = \left[ 1 - \frac{4\sqrt{R_1} \sin^2\left(\frac{\phi_1 - 2kL_1}{2}\right)}{(1 + \sqrt{R_1})^2} \right] \times \left[ \frac{T_2(1 + \sqrt{R_1})^2}{(1 - \sqrt{R_1R_2})^2 + 4\sqrt{R_1R_2} \sin^2\left(\frac{\phi_1 + \phi_2 - 2kL}{2}\right)} \right] \frac{\tau_{\text{cav}}}{\tau_0} \quad (9.1)$$

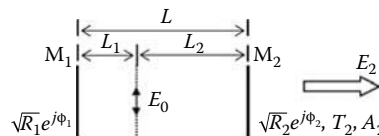


**FIGURE 9.3**

Schematic diagram showing the general optical structure and characteristics of an OLED device. (From Lin, C.-L. et al., *Appl. Phys. Lett.*, 87, 021101-1, 2005. With permission.)

where

$k$  is the wavevector in the organic layer

$\tau_{\text{cav}}$  and  $\tau_0$  are lifetimes of the molecular excited state in the cavity and in the free space, respectively

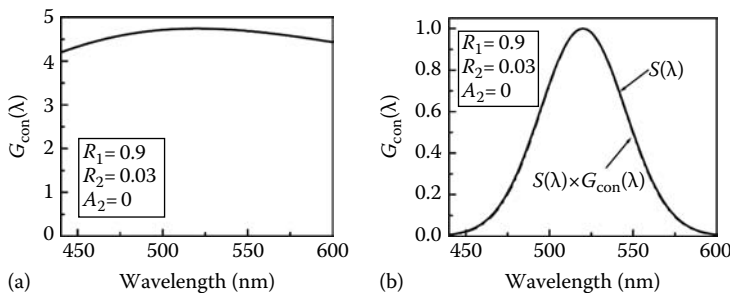
One can also derive a similar equation to Equation 9.1 for emission through the mirror  $M_1$  if it also permits optical transmission (e.g., in transparent OLEDs and double-side-emitting OLEDs).

Consider an organic emitter with an intrinsic emission spectrum  $S(\lambda)$ , which, for convenience of the following discussions, is assumed Gaussian with a peak wavelength  $\lambda_{\text{em}}$  and a full width at half maximum (FWHM)  $\Delta\lambda_{\text{em}}$ . According to Equation 9.1, to maximize luminance through the mirror  $M_2$  of a cavity, the resonance needs to be set ( $\phi_1 + \phi_2 - 2kL = 2m\pi$ ,  $m$ : an integer representing the cavity mode) near  $\lambda_{\text{em}}$  by adjusting the cavity length  $L$  and the emitter needs to be placed near the antinode of  $M_1$  ( $\phi_1 - 2kL_1 = 2l\pi$ ,  $l$ : integer).  $G_{\text{cav}}(\lambda)$  in Equation 9.1 describes the single-wavelength enhancement (in the forward direction) relative to free-space emission. Since organic emitters, in general, have rather broad emission spectra, of more practical interest is the spectrally integrated enhancement  $G_{\text{int}}$  for emission through one mirror of a particular OLED structure, as defined in Equation 9.2, relative to emission from a conventional noncavity (weak microcavity) bottom-emitting OLED (Figure 9.1), which has an ITO as the transparent bottom electrode and a high-reflectivity top metal electrode:

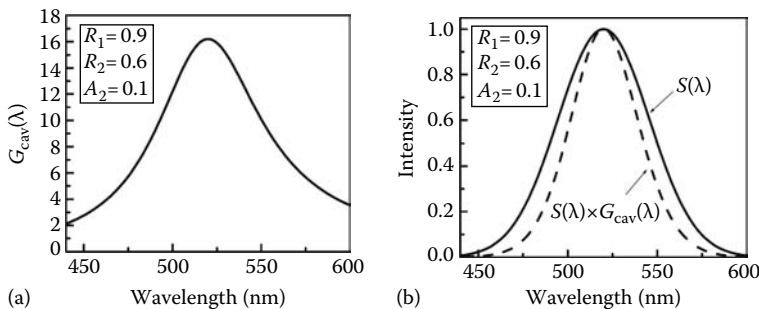
$$G_{\text{int}} = \frac{\int S(\lambda)G_{\text{cav}}(\lambda)d\lambda}{\int S(\lambda)G_{\text{con}}(\lambda)d\lambda} \quad (9.2)$$

where  $G_{\text{con}}(\lambda)$  is the emission enhancement of an optimized conventional bottom-emitting OLED (i.e., satisfy antinode and resonance conditions) relative to free-space emission as described in Equation 9.1. For such conventional bottom-emitting OLEDs, one mirror typically has a strong reflectance of ~90% (from highly reflective Al or Ag electrodes) while the other has a weak reflectance of ~3% (from the ITO/glass interface) and an absorptance of ~0%.

Consider an organic emitter with an intrinsic emission spectrum  $S(\lambda)$  with  $\lambda_{\text{em}}$  of 520 nm and  $\Delta\lambda_{\text{em}}$  of 60 nm. Figure 9.4a shows  $G_{\text{con}}(\lambda)$  of the optimized conventional bottom-emitting OLED for such an emitter, which is rather broad and remains rather constant over the spectral range of  $S(\lambda)$ . As a result, the emission spectrum from such a device (calculated by  $S(\lambda) \times G_{\text{con}}(\lambda)$ ) remains identical to  $S(\lambda)$  (Figure 9.4b). On the other hand, Figure 9.5a shows  $G_{\text{cav}}(\lambda)$  (for emission through  $M_2$ ) of an optimized strong-microcavity OLED with  $R_1 = 0.9$ ,  $R_2 = 0.6$ , and  $A_2 = 0.1$  for the same emitter, which now has a much

**FIGURE 9.4**

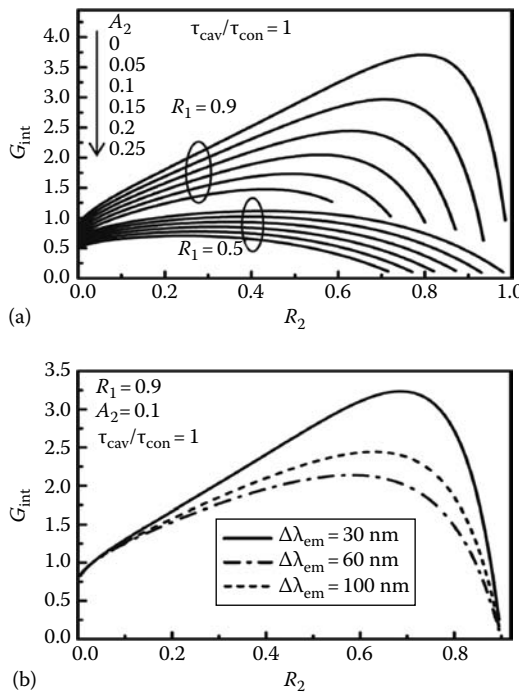
(a) The forward enhancement factor for a conventional noncavity bottom-emitting OLED and (b) its effect on the device-emission spectrum. (From Wu, C.-C. et al., *J. Display Technol.*, 1, 248, 2005. With permission.)

**FIGURE 9.5**

(a) The forward enhancement factor for a microcavity OLED and (b) its effect on the device-emission spectrum. (From Wu, C.-C. et al., *J. Display Technol.*, 1, 248, 2005. With permission.)

narrower shape and a much larger peak value than  $G_{\text{con}}(\lambda)$ . As a result, the strong-microcavity device shows narrowed emission (and thus better color purity) in comparison with the original intrinsic emission (Figure 9.5b).

In general, for emission through one mirror (e.g.,  $M_2$ ),  $G_{\text{int}}$  is a function of  $R_1$ ,  $R_2$ ,  $A_2$  ( $T_2 = 1 - R_2 - A_2$ ), and  $\Delta\lambda_{\text{em}}$  according to Equations 9.1 and 9.2. Since  $\tau_{\text{con}}$ , the molecular excited-state lifetime in the conventional noncavity device differs, in general, from  $\tau_{\text{cav}}$ ,  $G_{\text{int}}$  also depends on the ratio  $\tau_{\text{cav}}/\tau_{\text{con}}$ . Experimentally measured  $\tau_{\text{cav}}/\tau_{\text{con}}$ , however, is usually close to 1 (mostly 0.8–1) [6–10]. Thus, for all practical purposes, it is good enough to set  $\tau_{\text{cav}}/\tau_{\text{con}}$  to 1 for examining the major influences of other device parameters. For instance, Figure 9.6a shows calculated  $G_{\text{int}}$  for the lowest cavity mode ( $m=0$ ,  $l=0$ ) as a function of  $R_2$  with  $\Delta\lambda_{\text{em}}=60\text{ nm}$  (and  $\lambda_{\text{em}}=520\text{ nm}$  for a typical OLED green emitter),  $R_1=0.9–0.5$ , and  $A_2=0–0.25$ . The results in Figure 9.6a indicate that to obtain decent luminance (e.g.,  $G_{\text{int}}>1$ ) from one side of a particular device structure (e.g., through  $M_2$  in this case), it is critical to keep  $R_1$  large enough and  $A_2$  small enough, and have  $M_2$  ( $R_2$ ) designed carefully. The

**FIGURE 9.6**

Calculated  $G_{\text{int}}$  as a function of  $R_2$  ( $\lambda_{\text{em}}=520 \text{ nm}$ ): (a)  $\Delta\lambda_{\text{em}}=60 \text{ nm}$ ; (b)  $\Delta\lambda_{\text{em}}$  varied. (From Lin, C.-L. et al, *Appl. Phys. Lett.*, 87, 021101-1, 2005. With permission.)

maximal enhancement obtained drops rapidly with the decrease of  $R_1$  and the increase of  $A_2$ . Roughly, with  $R_1 < 0.5$  or  $A_2 > 0.25$ , there is no enhancement observed (i.e.,  $G_{\text{int}} < 1$ ). In the ideal (lossless) case of  $A_2=0$ ,  $G_{\text{int}}$  as high as  $\sim 4$  may be obtained.

Figure 9.6b shows calculated  $G_{\text{int}}$  as a function of  $R_2$  with  $R_1=0.9$ ,  $A_2=0.10$ , and  $\Delta\lambda_{\text{em}}=30-100 \text{ nm}$ . Narrower molecular emission spectra match the peak region of the cavity mode better (Figure 9.5a), and thus give substantially larger enhancement with the same cavity structure. In Figure 9.6, the value of  $R_2$  for achieving maximal  $G_{\text{int}}$  in each curve is of particular interest. This can quickly be estimated with  $R_2=R_1(1-A_2)^2$ , which maximizes  $G_{\text{cav}}(\lambda_{\text{em}})/G_{\text{con}}(\lambda_{\text{em}})$  and is obtained by solving  $d[G_{\text{cav}}(\lambda_{\text{em}})/G_{\text{con}}(\lambda_{\text{em}})]/d\sqrt{R_2} \approx d[(1-R_2-A_2)/(1-\sqrt{R_1}\sqrt{R_2})^2]/d\sqrt{R_2}=0$ . True optimal  $R_2$  is slightly lower than this value, so that FWHM of  $G_{\text{cav}}(\lambda)$  expands slightly to better match  $\Delta\lambda_{\text{em}}$  (meanwhile the peak value of  $G_{\text{cav}}(\lambda)$  also reduces).

### 9.2.2 Rigorous Electromagnetic Modeling

The Fabry–Perot formulation like Equation 9.1 treats only the optical characteristics along the forward direction of an OLED, in which there is no difference for *s* or *p* polarizations. However, when considering detailed emission

characteristics along different viewing angles of an OLED, the dependence on both wavelength and polarization must be considered. Furthermore, in the more accurate treatment of optical characteristics of OLEDs, the influence of cavity on the transition rate of molecular excited states must be included. All these can be considered by adopting the rigorous and full-vectorial electromagnetic modeling of OLEDs.

Such a rigorous electromagnetic model adopts a classical approach based on the equivalence between the emission of a photon due to an electrical dipole transition and the radiation from a classical electrical dipole antenna, which can take into account losses due to electrodes and absorption [2,11–14]. The formulations are quite complicated and therefore only a brief outline of the treatment has been provided in the following text. First, consider the radiation field from a single dipole of particular position, orientation, and frequency embedded in a general layered structure, as illustrated in Figure 9.7. With plane-wave expansion of the dipole field, the full-vectorial electromagnetic fields generated by a radiation dipole embedded in a layered structure is calculated, from which are obtained the distribution of the radiation power into different plane-wave modes and the far-field radiation related to emission characteristics of an OLED [2,11–14]. In the plane-wave expansion, each plane-wave mode can be characterized by an in-plane wavevector,  $k_t$ , where  $k_t$  is the component of the wavevector parallel to the layer surface. To model emission characteristics of a real OLED, one treats the emitting layer as an ensemble of mutually incoherent dipole radiators with distributions in dipole orientations, locations, and frequencies (using the photoluminescence [PL] spectrum of the emitter as the intrinsic spectral distribution of the dipole radiators) [14]. The total emission intensity  $I$  from the OLED as a function of the wavelength  $\lambda$

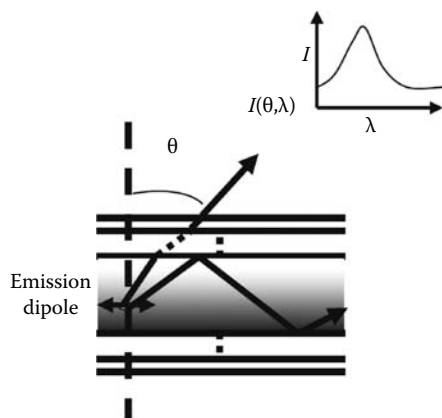


**FIGURE 9.7**

Illustration of radiation from an oscillating dipole of a particular position, orientation, and frequency embedded in a general, layered structure. (From Wu, C.-C. et al., *J. Display Technol.*, 1, 248, 2005. With permission.)

and the viewing angle  $\theta$  (i.e.,  $I(\theta,\lambda)$ , with  $\theta$  measured relative to the surface normal, Figure 9.7) is then obtained by averaging contributions over these distributions. Color coordinates of emission at various angles can then be calculated from  $I(\theta,\lambda)$ .

---

### 9.3 Microcavity/Interference Effects in Weak Microcavity OLEDs

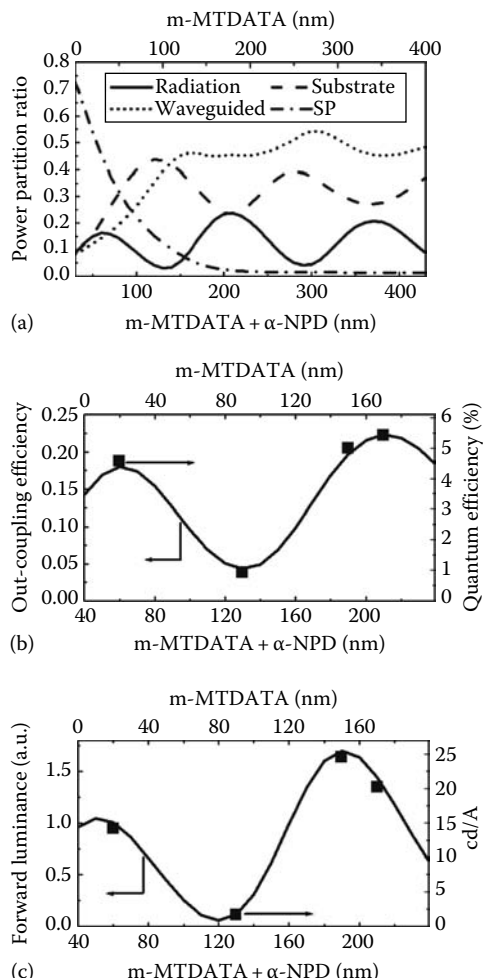
In a typical bottom-emitting OLED structure, as shown in Figure 9.1, directly outgoing beams of the emission interfere with the beams reflected from the metal electrode due to the strong reflection of the metal electrode, influencing outcoupled emission intensity [10,15]. To obtain constructive interference and to optimize light extraction from the device, it roughly requires that the locations of emitters to the metal electrode be consistent with the antinode condition of major emission wavelengths (i.e., the emitter-to-metal round-trip phase change equals multiple integers of  $2\pi$ ) [10,15]. Due to generally low conductivity and low carrier mobilities of organic materials, OLEDs are typically optimized by locating emitters around the first antinode of the metal electrode to minimize the layer thickness and device voltage. Furthermore, placing emitters at a further antinode by using a thicker carrier-transport layer may significantly disturb and complicate the scenario of carrier recombination (e.g., the location and distribution). Recent advances in conductive doping of organic semiconductors and high-mobility materials [16–19] may, however, remove such constraints. By utilizing device structures containing conductive doping, it is interesting to see theoretically and experimentally the influences of the location of emitters relative to the metal electrode on OLED emission.

Consider an inverted OLED structure: glass/ITO (120 nm)/Bphen:Cs (5 wt%, 20 nm)/Bphen (20 nm)/Alq<sub>3</sub>:C545T (1 wt%, 20 nm)/ $\alpha$ -NPD (40 nm)/m-MTADATA:F4-TCNQ (1.5 wt%,  $x$  nm)/Ag (100 nm), which adopts the inverted structure with conductive doping in carrier-transport layers for current conduction and carrier injection [20]. ITO and Ag serve as the bottom cathode and the top anode, respectively. Other layers in sequence consist of 4,7-diphenyl-1,10-phenanthroline (Bphen) doped with 5 wt% Cs as the n-doped electron-injection layer [17], undoped Bphen as the electron-transport layer, tris-(8-hydroxyquinoline) aluminum (Alq<sub>3</sub>) doped with the fluorescent dye C545T as the emitting layer [1,10],  $\alpha$ -naphthylphenylbiphenyl diamine ( $\alpha$ -NPD) as the hole-transport layer [21], and 4,4',4''-tris(3-methylphenylphenylamino)triphenylamine (m-MTADATA) doped with 1.5 wt% of tetrafluorotetracyano-quinodimethane (F4-TCNQ) as the p-doped hole-injection layer [16]. The thickness of m-MTADATA:F4-TCNQ is varied to adjust the distance between emitters and the metal electrode.

The rigorous electromagnetic model described in Section 9.2 is used to perform the analysis, which can take into account loss due to electrodes. To model emission characteristics of an OLED, it is assumed that the emitting layer contains an ensemble of mutually incoherent dipole radiators with distributions in dipole orientations (a random isotropic distribution), locations (a decaying exponential distribution from the  $\alpha$ -NPD/Alq<sub>3</sub> interface into Alq<sub>3</sub> with an exciton diffusion length of 15 nm) [22], and frequencies (using the PL spectrum of Alq<sub>3</sub>:C545T as the intrinsic spectral distribution of the dipole radiators). Radiation characteristics of OLEDs are then obtained by averaging contributions over these distributions.

In general, radiation in OLEDs is coupled into four different modes [23]: radiation modes that are outcoupled as useful emission, substrate modes that are trapped and waveguided in the substrate, waveguided modes that are trapped and waveguided in the high-index organic/ITO layers, and surface-plasmon (SP) modes that are guided along the organic/metal interface. The partition of OLED radiation into these modes is strongly dependent on the location of emitters relative to the metal electrode [20]. For instance, Figure 9.8a shows the fractions of radiation from single-frequency (520 nm, corresponding to the peak wavelength of C545T emission) and single-position-emitting (the  $\alpha$ -NPD/Alq<sub>3</sub> interface) dipoles coupled into different modes as a function of its distance to the Ag electrode (by varying m-MT-DATA thickness). With emitting dipoles getting close to the metal (and thus smaller thickness of the overall structure), ratios of substrate modes and waveguided modes are low, yet most of the radiation is coupled into SP modes and OLED emission is significantly quenched. By increasing the distance of emitting dipoles to the reflective metal, coupling into SP modes drops rapidly and those into other modes first rises and then becomes somewhat periodic with the increasing distance. The maximum and minimum that occur in outcoupling (i.e., fraction of radiation modes) roughly correspond to the antinodes and nodes of the metal electrode, respectively. Interestingly, the second antinode gives the highest outcoupling efficiency among all antinodes, particularly the first antinode condition that is typically implemented in optimized OLEDs. It can be seen that the highest efficiency is achieved around the second antinode because the coupling into SP modes has dropped to an almost negligible level and both substrate and waveguided modes happen to be around their local minima.

Taking into consideration the complete distributions of dipole frequencies and locations, Figure 9.8b and c shows the calculated outcoupling efficiency and the forward luminance, respectively, as a function of the distance to Ag (by varying m-MTADATA thickness). In Figure 9.8c, the forward luminance is normalized to that of a conventional OLED optimized around the first antinode, i.e., the device with the structure of glass/ITO (120 nm)/Bphen:Cs (5 wt%, 20 nm)/Bphen (20 nm)/Alq<sub>3</sub>:C545T (1 wt%, 20 nm)/ $\alpha$ -NPD (40 nm)/m-MTADATA:F4-TCNQ (1.5 wt%, 20 nm)/Ag (100 nm) (device A). In Figure 9.8b and c, it can be seen that locating emitters around the first node

**FIGURE 9.8**

Efficiency characteristics of the device of glass/ITO (120 nm)/Bphen:Cs (5 wt%, 20 nm)/Bphen (20 nm)/Alq<sub>3</sub>:C545T (1 wt%, 20 nm)/α-NPD (40 nm)/ m-MTDATA:F4-TCNQ (1.5 wt%,  $x$  nm)/Ag (100 nm): (a) calculated fractions of radiation coupled into different modes, (b) calculated (line) and measured (symbol) outcoupling efficiency, and (c) calculated (line) and measured (symbol) forward luminance (normalized to the  $x=20$  nm case), as a function of the distance between emitters and reflective Ag electrode (by varying m-MTDATA thickness). Results of (a) are calculated with single-frequency (520 nm) and single-position ( $\alpha$ -NPD/Alq<sub>3</sub> interface) emitting dipoles, while those of (b) and (c) are calculated with the complete dipole distributions. (From Lin, C.-L. et al., *Appl. Phys. Lett.*, 88, 081114-1, 2006. With permission.)

(m-MTDADA = 90 nm, device B) give the least outcoupling, while locating emitters around the second antinode enhance both outcoupling and forward luminance. The conditions for obtaining maximal outcoupling and maximal forward luminance are slightly different. The maximal forward luminance (~1.6 times larger than that of device A) occurs around m-MTDADA = 150 nm (device C), at which the antinode condition is exactly satisfied by a wavelength

of 520 nm. The maximal outcoupling (~1.2 times larger than that of device A) occurs around m-MTDATA = 170 nm (device D), at which the antinode condition is exactly satisfied by a wavelength (560 nm) larger than the peak wavelength of C545T.

Experiments were conducted on devices A–D to compare with analyses [20]. Electrical properties of these devices are almost identical despite very large variations in the thickness of the hole-injection layer (m-MTDATA:F4-TCNQ), indicating the effectiveness of the conductive doping in enhancing conductivity. In Figure 9.8b and c, measured efficiencies of devices A–D (symbols) are compared with calculated efficiencies (lines). A reasonably good agreement is obtained between calculated and experimental values.

The angular dependence of electroluminescence (EL) characteristics is also an important concern in applications. Along with PL of Alq<sub>3</sub>:C545T, Figure 9.9a through c shows measured (symbols) and simulated (lines) EL spectra with relative intensities at viewing angles of 0° and 60° off the surface normal for devices A, C, and D, respectively, in which a reasonably good agreement is again obtained [20]. Figure 9.9d compares angular distributions of the measured EL intensity (normalized to 0° intensity) for the same three devices. Because the antinode condition is set for a larger wavelength, EL of device D at small angles is broader than PL of C545T. Other than that, devices C and D do not exhibit any obvious color shift with viewing angles. Device C (with highest forward luminance) exhibits more directed emission (Figure 9.9d), as often observed in strong-microcavity

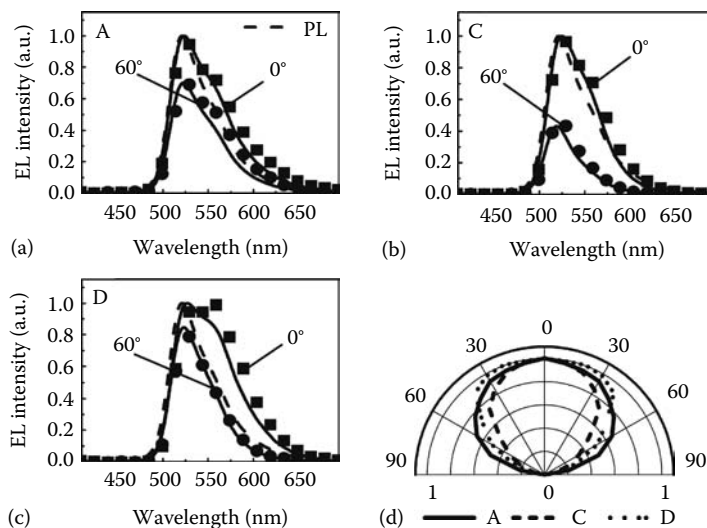


**FIGURE 9.9**

Measured (symbols) and calculated (lines) EL spectra with relative intensities at viewing angles of 0° and 60° for (a) device A, (b) device C, and (c) device D. (d) Polar plots of measured EL intensities (normalized to the 0° intensity) for devices A, C, and D. In (a)–(c), PL of Alq<sub>3</sub>:C545T is also shown for comparison. (From Lin, C.-L. et al., *Appl. Phys. Lett.*, 88, 081114-1, 2006. With permission.)

devices, due to enhanced forward luminance without exhibiting color shift with viewing angles [10,14]. Such characteristics may be useful in display applications, since advantages similar to those of microcavity OLEDs can be obtained by simply increasing layer thickness without having to involve more complicated fabrication and tuning of microcavity OLED structures.

These results also have certain implications on tandem OLEDs, which have multiple OLED units stacked vertically in series [24–26]. In the simplest viewpoint, a proportional increase in the luminance efficiency could be expected (i.e., cd/A) with the number of emitting units. However, the results here suggest that the enhancement in cd/A efficiency could significantly exceed such proportional increase (extra efficiency gain from the tandem structure), since the emitting unit further away from the reflective metal electrode could contribute a larger cd/A efficiency or total outcoupling.

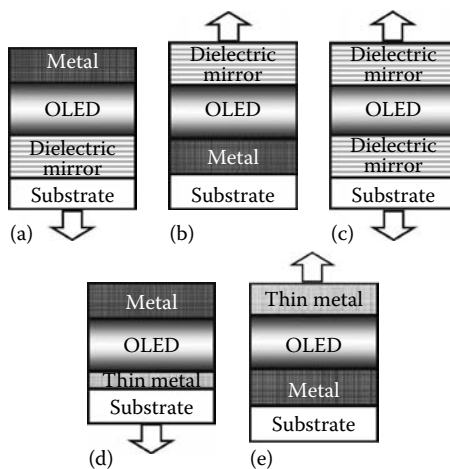
---

## 9.4 Microcavity OLEDs

### 9.4.1 Microcavity OLEDs Having Two Metal Mirrors

As discussed earlier, microcavity effects are inherent in any OLED structures. Microcavity OLEDs discussed in this section are, however, strong microcavity devices having electrode mirrors of strong reflection. As discussed earlier, the incorporation of strong microcavity structures in OLEDs can narrow emission spectra of devices and thus improve color purity for display applications. With appropriate microcavity designs, microcavity OLEDs may also give enhanced luminance and cd/A efficiency at least along the forward direction. Thus, microcavity OLEDs are becoming more attractive for high-performance AMOLEDs.

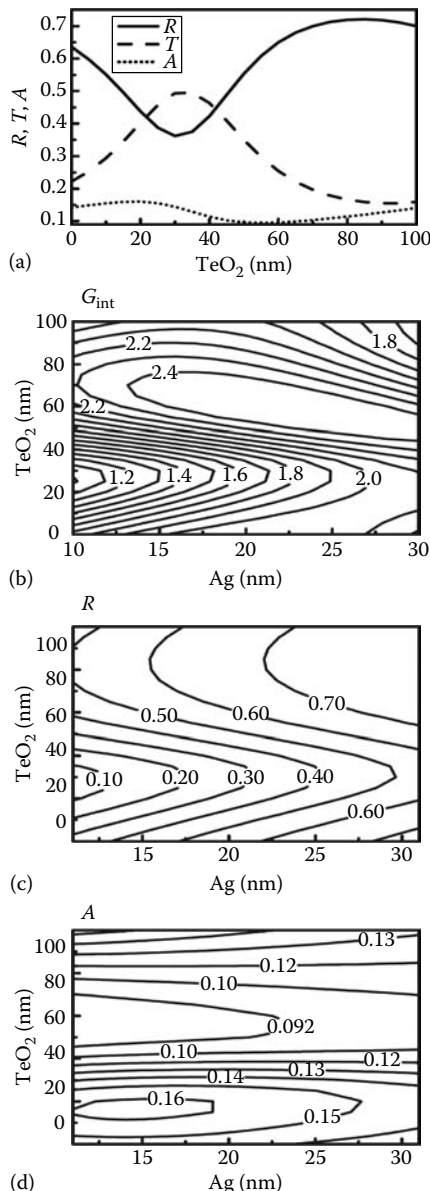
The mirrors for microcavity devices may be implemented with dielectric mirrors (distributed Bragg reflectors [DBR] composed of alternating high/low-index layers) or reflective metals. Various possible structures of microcavity OLEDs employing different combinations of mirrors are shown in Figure 9.10 [3,6,7,10,14,27–33]. In the early development of microcavity OLEDs, Nakayama et al. and Dodabalapur et al. demonstrated microcavity bottom-emitting OLEDs with the reflective top metal electrode and the dielectric mirrors of  $\text{TiO}_2/\text{SiO}_2$  or  $\text{Si}_x\text{N}_y/\text{SiO}_2$  below the bottom ITO anode (i.e., the structure of Figure 9.10a) [6,7,30–31]. Narrowed EL emission spectra were observed when compared with intrinsic PL spectra of emitting materials. Tsutsui et al. observed directed emission in microcavity bottom-emitting OLEDs with the structure of Figure 9.10a [32]. In 1996, Jordan et al. were the first to show that by using one metal mirror and one lossless dielectric mirror (i.e., the structure of Figure 9.10a), microcavity OLEDs could give substantially enhanced luminance in comparison with noncavity (weak microcavity) OLEDs [7].

**FIGURE 9.10**

Various structures of microcavity OLEDs employing different combinations of mirrors: using one metal mirror and one dielectric mirror (a and b), using two dielectric mirrors (c), and using two metal mirrors (d and e). (From Wu, C.-C. et al., *J. Display Technol.*, 1, 248, 2005. With permission.)

The general complexity in the fabrication of dielectric mirrors and their strong wavelength-dependent reflection properties makes it very difficult for them to be implemented in real OLED displays. In view of these, microcavity OLEDs using metal mirrors (one reflective and one semi-transparent/reflective, Figure 9.10d and e) are more practical for display applications [3,10,27–29,33]. However, due to absorption (loss) in metals, it is not clear whether one can still obtain luminance enhancement as in microcavity OLEDs using lossless dielectric mirrors, and it is also not clear to what degree and under what conditions one obtains most luminance enhancement.

As discussed previously, to obtain maximal luminance enhancement (in the forward direction) in any microcavity OLED relative to conventional noncavity bottom-emitting devices, a back mirror with the highest possible reflectance and an exit mirror with a high reflectance matching that of the back electrode and a lowest possible loss are essential. Yet for an exit mirror using a semitransparent metal electrode, at the thickness of large enough reflectance, the absorptance may, however, become too large and degrade luminance enhancement. The exit mirror combining a thin metal and a transparent high-index dielectric layer may overcome such a dilemma [3,10,28,29]. For instance, Figure 9.11a shows the calculated optical characteristics (reflectance [R], transmittance [T], absorptance [A] at 520 nm) viewed from a typical organic material for a thin Ag electrode (24 nm) with  $\text{TeO}_2$  of varied thickness [10]. Ag is considered as it has a relatively larger reflection, smaller absorption, and higher conductivity among metals. Reflectance of Ag/ $\text{TeO}_2$  is largely modulated

**FIGURE 9.11**

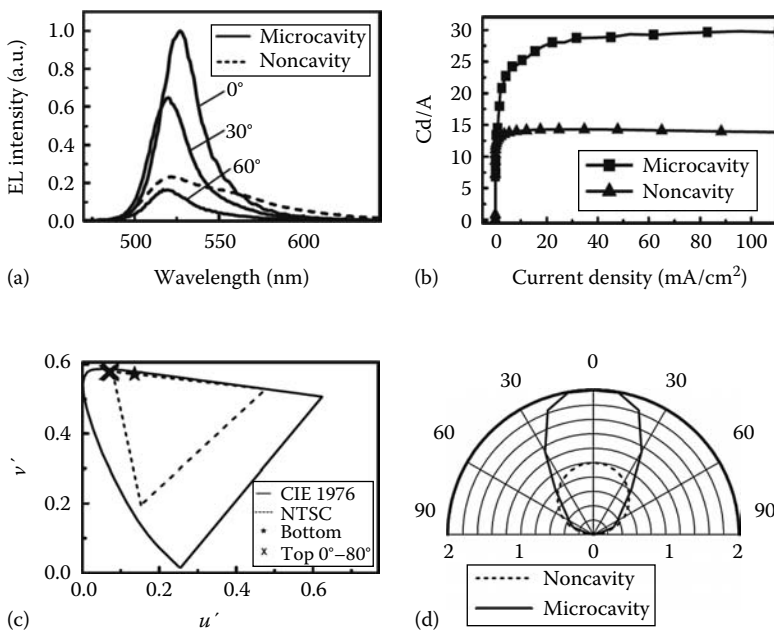
(a) Calculated  $R$ ,  $T$ ,  $A$  (at 520 nm) of the composite mirror of thin Ag (24 nm) and  $\text{TeO}_2$ . (b) Contour plot of calculated  $G_{\text{int}}$  vs. Ag and  $\text{TeO}_2$  thicknesses for the optimized microcavity OLED having a back mirror with a reflectance of 0.9, and having an emitter with  $\lambda_{\text{em}} = 520 \text{ nm}$ ,  $\Delta\lambda_{\text{em}} = 60 \text{ nm}$ ,  $\tau_{\text{cav}}/\tau_{\text{con}} = 1$ . ((a) and (b) From Lin, C.-L. et al., *Appl. Phys. Lett.*, 87, 021101-1, 2005. With permission.) (c) Contour plot of  $R$  (at 520 nm) of the composite mirror of thin Ag (24 nm) and  $\text{TeO}_2$ . (d) Contour plot of  $A$  (at 520 nm) of the composite mirror of thin Ag (24 nm) and  $\text{TeO}_2$ . ((c) and (d) From Wu, C.-C. et al., *J. Display Technol.*, 1, 248, 2005. With permission.)

with the  $\text{TeO}_2$  thickness, and for a certain range of thickness, reflectance is enhanced and absorptance is reduced down to ~9% (vs. 15% with no  $\text{TeO}_2$ ). In this case, to search for combinations of Ag/ $\text{TeO}_2$  giving optimal luminance enhancement from a microcavity device, it is useful to construct a contour plot of  $G_{\text{int}}$  vs. Ag and  $\text{TeO}_2$  thicknesses (Figure 9.11b). For a certain range of Ag/ $\text{TeO}_2$  combinations, one obtains maximal  $G_{\text{int}}$  of ~2.4–2.6. Detailed analyses (comparing Figure 9.11b through d) reveal that these conditions are roughly coincident with those giving high reflection and low absorption.

Comparisons can be made between the above analytical results and experiments on microcavity top-emitting OLEDs with a nearly optimized structure of [10]: glass/Ag (80 nm)/m-MTDATA:F4-TCNQ (2 wt%, 20 nm)/ $\alpha$ -NPD (25 nm)/Alq<sub>3</sub>:C545T (1 wt%, 20 nm)/Alq<sub>3</sub> (35 nm)/LiF (0.5 nm)/Al (1 nm)/Ag (24 nm)/ $\text{TeO}_2$  (55 nm), in which Ag and Ag/ $\text{TeO}_2$  serve as the bottom anode and the top cathode, respectively. Undoped Alq<sub>3</sub> is the electron-transport layer, and thin LiF/Al is the electron-injection layer. For comparison, an optimized noncavity (weak microcavity) bottom-emitting device was also fabricated with the structure of: glass/ITO (120 nm)/m-MTDATA:F4-TCNQ (2 wt%, 20 nm)/ $\alpha$ -NPD (20 nm)/Alq<sub>3</sub>:C545T (1 wt%, 20 nm)/Alq<sub>3</sub> (40 nm)/LiF (0.5 nm)/Al (1 nm)/Ag (150 nm). In both devices, layer thicknesses had been determined based on the antinode and resonance conditions near  $\lambda_{\text{em}}$  of C545T (520 nm). Figure 9.12a shows the measured EL spectra with relative intensities at viewing angles of 0°, 30°, and 60° off the surface normal of the microcavity device, and at 0° of the noncavity device. The microcavity device shows a forward  $G_{\text{int}}$  of ~2.0 (and an enhancement of ~4.3 at the 0° resonance wavelength). Correspondingly, the microcavity device gives a ~2.0 times larger cd/A efficiency than the noncavity device (30 cd/A vs. 14.2 cd/A, Figure 9.12b). Figure 9.12c shows the CIE coordinates (1976 uniform color space) of 0°–80° EL of the microcavity device and that of the noncavity device. The microcavity device shows more saturated colors than the NTSC green standard and negligible color shift with viewing angles, both the desired characteristics for displays. Figure 9.12d compares the angular distributions of EL intensity (normalized to the 0° intensity of the noncavity device) for both devices. The microcavity device shows more directed emission and enhanced luminance for 0°–45°. Such characteristics can be an advantage for small- or medium-sized OLED displays, which are mainly viewed from the forward direction. The external EL quantum efficiency for the cavity device is slightly higher than that of the noncavity device (4.1% vs. 3.8%), indicating the forward-direction enhancement results mainly from the redistribution of emission directions.

#### 9.4.2 Influences of Resonant Wavelengths on Microcavity OLEDs

When designing microcavity devices, the three most important considerations are the following: mirror properties, the length of the cavity

**FIGURE 9.12**

Comparison of optical characteristics of a microcavity device and a noncavity device. (a) Measured EL spectra with relative intensities at 0°, 30°, and 60° off the surface normal of the microcavity device, and at 0° of the noncavity device. (b) cd/A efficiencies for both devices. (c) 1976 CIE coordinates of 0°–80° EL of the microcavity device and 0° EL of the noncavity device. (d) Polar plots of measured EL intensities (normalized to the 0° intensity of the noncavity device) for both devices.

(determined by the cavity-resonant wavelength desired), and the location of emitters in the cavity [6,10,30]. Once the mirror structures are determined, the other cavity geometries are mainly determined by the cavity-resonant wavelength. For devices containing narrow-band emitters, to obtain optimal light output it is intuitive to set the resonant wavelength of the microcavity at the peak wavelength of the intrinsic emission and subsequently to locate the emitters around a common antinode of both mirror electrodes (i.e., the emitter-to-mirror round-trip phase change equal to the integral multiples of  $2\pi$ ) [6,10,30]. Yet in most cases of OLEDs, the intrinsic emission spectra of emitters are so broad (typically  $> 50$  nm) that it becomes less obvious where the resonant wavelength should be set in the broad spectra for performance optimization. In this section, influences of the resonant wavelength on characteristics (efficiencies and viewing characteristics) of microcavity OLEDs having two metal mirrors are discussed.

Again, consider the device structure of: glass/Ag (80 nm)/m-MTDATA:  
F<sub>4</sub>-TCNQ(2 wt%,  $x$  nm)/ $\alpha$ -NPD(20 nm)/Alq<sub>3</sub>:C545T(1 wt%, 20 nm)/Alq<sub>3</sub>( $y$  nm)/  
LiF (0.5 nm)/Al (1 nm)/Ag (22 nm)/Alq<sub>3</sub> (70 nm), which adopts the top-emitting

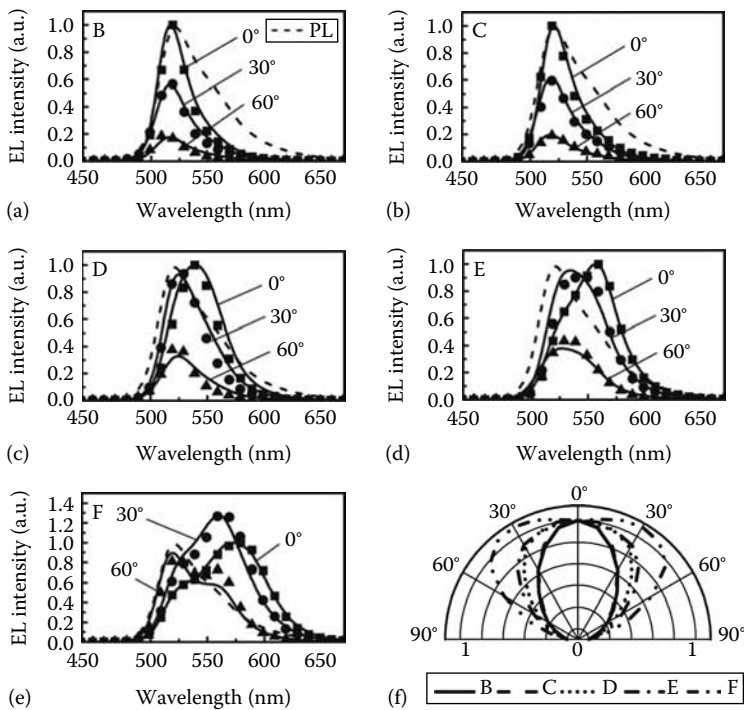
microcavity configuration with the high-reflectivity Ag (80 nm) as the bottom anode and the semitransparent Ag (22 nm) as the top cathode. According to what has been discussed previously, for maximizing optical output of cavity OLEDs, the thin Ag is further capped with a 70-nm high-index organic layer ( $\text{Alq}_3$ ,  $n \sim 1.7\text{--}1.8$ ) to achieve both high reflection (~55%, seen from the inside of the device) and low absorption (~8%) for major emission wavelengths of C545T.

In this device configuration, the thicknesses of m-MTDATA:F<sub>4</sub>-TCNQ and  $\text{Alq}_3$  are varied to adjust the resonant wavelength (at the lowest resonance mode) and the emitter location (according to the antinode condition of the resonant wavelength). Microcavity OLEDs with five different normal-direction resonant wavelengths  $\lambda_R(0^\circ)$  of 500 (device B), 515 (device C), 545 (device D), 560 (device E), and 590 nm (device F) were fabricated and characterized using the (MTDATA:F<sub>4</sub>-TCNQ,  $\text{Alq}_3$ ) thicknesses = (25, 29), (27, 31), (32, 35), (35, 37), and (40, 41) nm, respectively. For purposes of comparison, a nearly optimized conventional bottom-emitting OLED (device A) was also tested.

The rigorous electromagnetic model is used for performing the analysis. The influence of the device (microcavity) structure on the molecular transition rates (the exciton lifetimes) had been included in the electromagnetic modeling. The total emission intensity  $I$  from the OLED as a function of the wavelength  $\lambda$  and the viewing angle  $\theta$  (i.e.,  $I(\theta, \lambda)$ , with  $\theta$  measured relative to the surface normal) is then obtained by averaging contributions over these distributions. Color coordinates of emissions at various angles, ( $u'(\theta)$ ,  $v'(\theta)$ ), can then be calculated from  $I(\theta, \lambda)$ . To better quantify differences in colors, the 1976  $u'v'$  uniform color space (UCS) is used [34].

To better quantify influences of resonant wavelengths on emission characteristics, four parameters are defined: the outcoupling efficiency, which is the ratio of the outcoupled emission to internally generated emission; the forward enhancement ratio, which is the ratio between the normal-direction luminescence of a cavity device to that of an optimized conventional bottom-emitting OLED; the color shift, which is defined as [variance of  $u'(\theta)$  + variance of  $v'(\theta)$ ] and measures variation of colors over angles; and the Lambertian offset, which is defined as  $\Sigma |I(\theta)/I(0^\circ) - \cos \theta|$  and measures the difference between the emission pattern of a device and the ideal Lambertian distribution (where  $I(\theta)$  is spectrally integrated  $I(\theta, \lambda)$ ). Values of these parameters are obtained using both the simulated data and the measured EL characteristics.

Apart from PL of  $\text{Alq}_3:\text{C545T}$ , Figure 9.13a through e shows measured (symbols) and simulated (lines) EL spectra with relative intensities at viewing angles of 0°, 30°, and 60° off the surface normal for devices B–F, respectively. A reasonably good agreement is obtained between the measured data and the simulated data, indicating that the simulation is accurate. In these devices, the 0° EL peak does shift consistently with the set  $\lambda_R(0^\circ)$ . For each device, the EL spectra tend to blue-shift with viewing angles according to the angular dependence of the resonant wavelength [35]:

**FIGURE 9.13**

Measured (symbols) and calculated (lines) EL spectra with relative intensities at viewing angles of 0°, 30°, and 60° for: (a) device B, (b) device C, (c) device D, (d) device E, and (e) device F. (f) Polar plots of measured EL intensities (normalized to the 0° intensity) for devices B–F. In (a)–(e), PL of Alq<sub>3</sub>:C545T is also shown for comparison. (From Lin, C.-L. et al., *Appl. Phys. Lett.*, 90, 071111-1, 2007. With permission.)

$$\lambda_R(\theta) = \frac{4\pi L \cos \theta}{\phi(\theta) - 2\pi m} \quad (9.3)$$

where

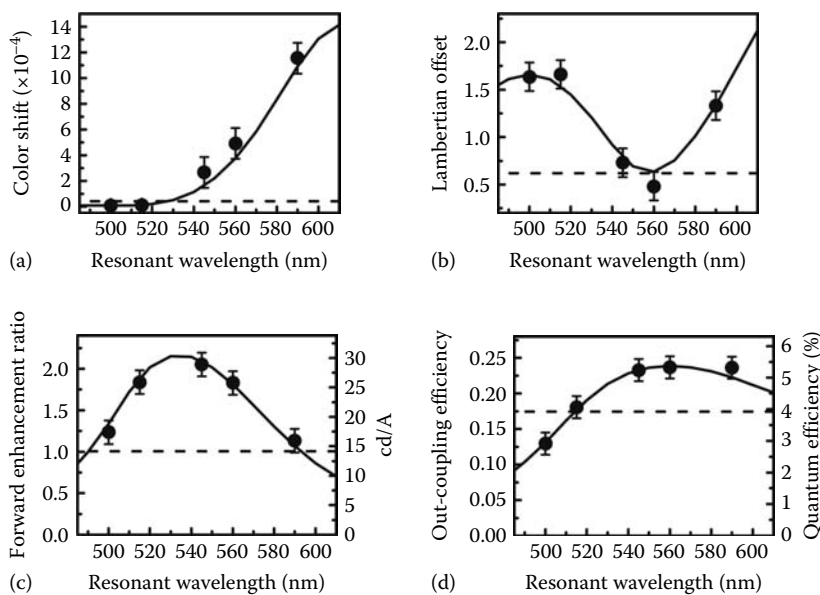
$L$  is the cavity length

$\phi(\theta)$  is the total phase shift caused by reflections at two mirrors

$n$  is the refractive index of the organic material

$m$  is the cavity mode number ( $m=0$  in the present case)

The color shift with viewing angles is particularly significant for devices having  $\lambda_R(0^\circ)$  set at longer wavelengths. Yet, devices having  $\lambda_R(0^\circ)$  set around or smaller than  $\lambda_{PL}$  of C545T (e.g., devices B and C) hardly exhibit detectable color shift. This is mainly because the tendency of blue-shift with viewing angles is largely suppressed by a rapid fall-off of the intrinsic emission intensity at shorter wavelengths. Figure 9.14a shows the measured color shift

**FIGURE 9.14**

Calculated values (lines) of (a) color shift, (b) Lambertian offset, (c) forward enhancement ratio, and (d) outcoupling efficiency as a function of the normal-direction resonant wavelength. The calculated results are compared with experimentally obtained values (symbols) of color shift, Lambertian offset, cd/A efficiency, and external quantum efficiency in (a)–(d), respectively. The horizontal dashed lines in (a)–(d) represent experimental values of the conventional bottom-emitting device A. (From Lin, C.-L. et al., *Appl. Phys. Lett.*, 90, 071111-1, 2007. With permission.)

(symbols) as a function of  $\lambda_R(0^\circ)$ , which is consistent with the trend predicted by the simulation (line). For devices having  $\lambda_R(0^\circ)$  set around or smaller than  $\lambda_{PL}$ , the values of color shift are comparable to that of the conventional device A ( $\sim 4 \times 10^{-5}$ , the horizontal dashed line).

Figure 9.13f compares angular distributions of the measured EL intensity (spectrally integrated and normalized to  $0^\circ$  intensity) for devices B–F, in which one sees the strong dependence of emission patterns on  $\lambda_R(0^\circ)$ . Devices having  $\lambda_R(0^\circ)$  around or smaller than  $\lambda_{PL}$  (e.g., B and C, which also have small color shifts) show strongly directed emission toward the surface normal. Devices having  $\lambda_R(0^\circ)$  20–40 nm longer than  $\lambda_{PL}$  (e.g., D and E) show emission patterns close to the Lambertian distribution. For the device having  $\lambda_R(0^\circ)$  substantially longer than  $\lambda_{PL}$  (e.g., F), the emission pattern not only deviates substantially from the Lambertian distribution but also shows the highest intensity at an off-axis angle. Since  $\lambda_R(\theta)$  in general blue-shifts with viewing angles, the emission pattern is controlled not only by the microcavity modification but also by the spectral shape of the intrinsic PL. As such, the directionality of microcavity emission is enhanced when setting  $\lambda_R(0^\circ)$  at the short-wavelength falling edge of the PL spectrum; setting  $\lambda_R(0^\circ)$

at the long-wavelength falling edge makes the strongest emission occur at some off-axis angles; setting  $\lambda_R(0^\circ)$  somewhere in between may give nearly Lambertian distributions. Figure 9.14b shows the measured Lambertian offset (symbols) as a function of  $\lambda_R(0^\circ)$ , which is consistent with the trend predicted by the simulation (line). For devices having  $\lambda_R(0^\circ)$  set 20–40 nm longer than  $\lambda_{PL}$  (e.g., devices D and E), the Lambertian offset achieves a lowest value similar to that of the conventional device A (0.6, the horizontal dashed line).

Both cd/A and quantum efficiencies vary substantially among devices. As shown in Figure 9.14c and d, the measured cd/A efficiencies and quantum efficiencies (symbols) as a function of  $\lambda_R(0^\circ)$  follow closely the calculated forward enhancement ratio (Figure 9.14c) and the calculated outcoupling efficiency (Figure 9.14d), respectively. As expected, setting  $\lambda_R(0^\circ)$  near  $\lambda_{PL}$  (e.g., 515 nm for C, 545 nm for device D) gives the highest forward enhancement ratio of ~2 (26.3 cd/A of device C and 29.6 cd/A of device D vs. 14.6 cd/A of the conventional device A). On the other hand, by setting  $\lambda_R(0^\circ)$  20–40 nm longer than  $\lambda_{PL}$  (e.g., 545 nm for device D, 560 nm for device E), the highest outcoupling and quantum efficiency are achieved (~1.4 times higher than the conventional bottom-emitting device; e.g., 5.4% of device D and 5.6% of device E vs. 4% of device A).

In summary, the emission characteristics (color, efficiency, emission pattern) of microcavity OLEDs show strong dependence on the resonant wavelength. In addition, there are trade-offs between different characteristics in choosing the resonant wavelength, as clearly manifested in Figure 9.14. For instance, by setting  $\lambda_R(0^\circ)$  around  $\lambda_{PL}$ , one obtains the optimal enhancement in the cd/A efficiency/brightness and the slightest color shift with viewing angles, but accompanied by highly directed emission, large Lambertian offset, and lower external quantum efficiency. On the other hand, by setting  $\lambda_R(0^\circ)$  20–40 nm larger than  $\lambda_{PL}$ , one obtains enhanced external quantum efficiency and nearly Lambertian distribution, but with trade-offs of more significant color shift and lower cd/A efficiency. Thus, the exact design of the microcavity device would depend on actual applications. For display applications that desire small color shifts over viewing angles and highest brightness along the normal viewing direction,  $\lambda_R(0^\circ)$  can be set near  $\lambda_{PL}$ . For applications (like lighting) in which the highest possible external quantum efficiencies and more uniform intensity distributions are highly desired while the color shift may be more tolerable,  $\lambda_R(0^\circ)$  may be moved 20–40 nm away from  $\lambda_{PL}$ .

---

## 9.5 Microcavity OLEDs Integrated with Microlens

Incorporation of the microcavity structure into OLEDs is demonstrated to narrow emission spectra (and thus improve color saturation for display

applications), to enhance the luminance, and to enhance the quantum efficiency in some cases. However, all these characteristics do not normally occur simultaneously for a same microcavity OLED design. Earlier discussions have shown that these inconsistent results are associated mainly with settings of microcavity-resonant wavelengths. By setting the normal-direction resonant wavelength around the peak wavelength of the intrinsic emission (i.e., PL) of OLED emitters, one obtains the highest luminance enhancement along the normal direction and negligible color shift with viewing angles, but accompanied by lower external quantum efficiencies. On the other hand, the highest enhancement in external quantum efficiencies can be obtained by setting the normal-direction resonant wavelength 20–40 nm longer than the peak wavelength of the intrinsic emission, but exhibiting significant color shift over viewing angles. These trade-offs between different emission characteristics (in choosing the resonant wavelength) complicate the design of microcavity devices for different applications. Nevertheless, by integrating top-emitting microcavity OLEDs with microlenses, all the enhancements in external quantum efficiency, cd/A efficiency, and color performances (color saturation, small color shift with viewing angles) can be achieved simultaneously [36]. In addition, the blurred image that normally accompanies the employment of microlens arrays to OLEDs is also largely reduced by a combination of microcavity OLEDs and microlenses [36]. These characteristics may render it universal device architecture for various applications.

Consider a top-emitting microcavity OLEDs without microlenses shown in Figure 9.15a [36]: glass/Ag (100 nm)/m-MTADATA:F<sub>4</sub>-TCNQ (2 wt%, 30 nm)/ $\alpha$ -NPD (20 nm)/Alq<sub>3</sub>:C545T (1 wt%, 20 nm)/Alq<sub>3</sub> (40 nm)/LiF (0.5 nm)/Al (1 nm)/Ag (20 nm)/ZnSe (45 nm)/polymer (1  $\mu$ m). For maximizing optical output of cavity OLEDs, the thin Ag cathode is further capped with a 45-nm high-index layer of thermally evaporated ZnSe ( $n \sim 2.4$ –2.5) to form a low-absorption high-reflection composite mirror for major emission

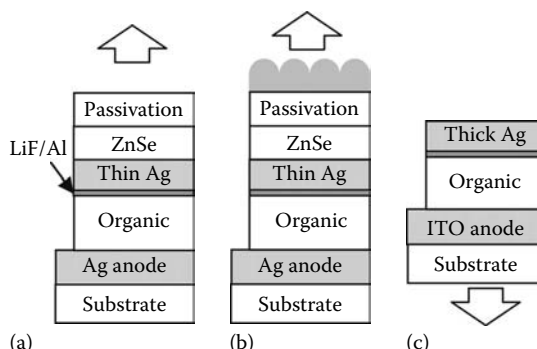
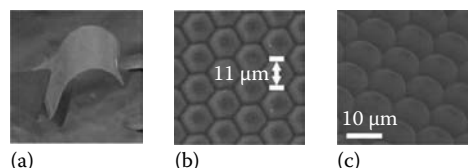


**FIGURE 9.15**

Device structures of (a) top-emitting microcavity OLED without microlenses; (b) top-emitting microcavity OLED with microlenses; and (c) conventional bottom-emitting OLED. (From Yang, C.-J. et al., *Appl. Phys. Lett.*, 91, 253508-1, 2006. With permission.)

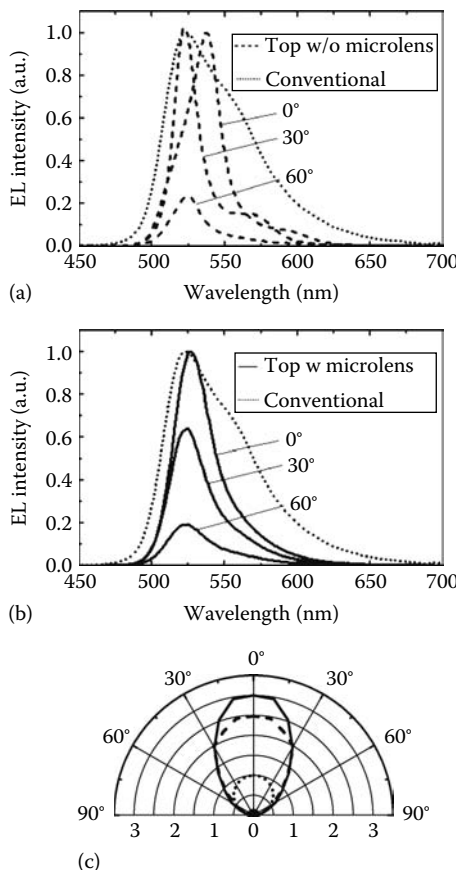
wavelengths of C545T. The micrometer-thick parylene layer is then coated by the room-temperature vapor phase deposition on top of the device as the passivation layer [37]. The thicknesses of organic layers and the ZnSe layer had been adjusted to set the normal-direction resonant wavelengths around 540 nm and to locate emitters around the antinode of the cavity. The resonant wavelength is set ~20 nm longer than the PL peak wavelength of C545T to achieve the highest outcoupling and quantum efficiency from the microcavity OLED, according to the discussions provided earlier. For the top-emitting OLED with microlenses (Figure 9.15b), all the layer structures are the same except for a thin sheet of polydimethylsiloxane (PDMS, ~50  $\mu\text{m}$ ) with the microlens array further laminated on top of the parylene. For purposes of comparison, a roughly optimized conventional bottom-emitting OLED (Figure 9.15c) was also tested. The microlens array on PDMS was fabricated by the micromolding technique using the Si master mold [38]. The fabricated thin PDMS sheets (~50  $\mu\text{m}$  thick) with microlens arrays (Figure 9.16a) were examined with the scanning electron microscopy (SEM). The top-view SEM micrograph (Figure 9.16b) shows the hexagonal arrangement of the microlens array, while the oblique-view SEM micrograph in Figure 9.16c indicates the near hemispherical shape (with the diameter of ~10  $\mu\text{m}$ ) of the microlenses [36].

Figure 9.17a and b shows the measured EL spectra with relative intensities for the top-emitting OLED without and with microlenses, respectively, at viewing angles of 0°, 30°, and 60° off the surface normal, compared to the (normalized) 0° EL spectrum of the conventional bottom-emitting device [36]. Figure 9.17c shows the polar plots of the emission intensities (normalized to the 0° intensity of the conventional device) for the three devices [36]. Compared to the conventional bottom-emitting device, both top-emitting microcavity devices show narrowed EL spectra and enhanced forward emission intensities. The enhancement of the 0° intensity is up to 2.5 $\times$  and 3 $\times$  for top-emitting devices without or with microlenses, respectively. For the top-emitting OLED without microlenses (Figure 9.17a), the EL shows a sharp emission peak at 538 nm at 0° (as expected), and a significant shift to shorter wavelengths with the viewing angles due to strong microcavity effects. Interestingly, with microlens lamination (Figure 9.17b, the 0° emission peak slightly blue-shifts to 527 nm and the shift of EL spectra with viewing angles is eliminated. It is



**FIGURE 9.16**

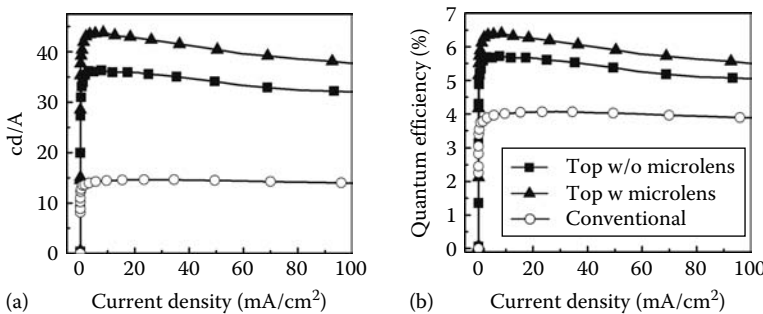
(a) Photo of the PDMS sheet with microlens arrays; (b) top-view SEM image of the microlenses; (c) oblique-view SEM image of the microlenses. (From Yang, C.-J. et al., *Appl. Phys. Lett.*, 91, 253508-1, 2006. With permission.)

**FIGURE 9.17**

EL spectra with relative intensities at viewing angles of 0°, 30°, and 60° for top-emitting device (a) without and (b) with microlenses. In (a) and (b), the EL spectrum of the conventional bottom-emitting OLED is also shown for comparison. (c) Polar plots of emission intensities of the three devices (normalized to the 0° intensity of the conventional bottom-emitting device). (From Yang, C.-J. et al., *Appl. Phys. Lett.*, 91, 253508-1, 2006. With permission.)

also noted that the spectral shapes are modified with microlens lamination. By considering results of Figure 9.17a through c, it may be concluded that the lamination of microlenses has led to mixing/averaging EL of different angles and redirecting more light into the forward direction, consequently giving stable/saturated colors over angles and slightly more directed emission (as compared to microcavity OLEDs without microlenses).

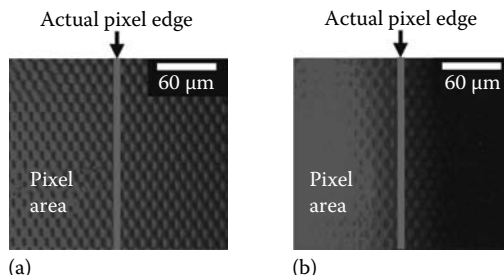
Figure 9.18a and b shows the cd/A efficiencies and the external quantum efficiencies, respectively, of the three devices [36]. The conventional bottom-emitting device, the microcavity device without microlenses, and the microcavity device with microlenses show efficiencies up to (14.5 cd/A,

**FIGURE 9.18**

(a) cd/A efficiencies and (b) quantum efficiencies of the three devices. (From Yang, C.-J. et al., *Appl. Phys. Lett.*, 91, 253508-1, 2006. With permission.)

4%), (36.3 cd/A, 5.7%), and (43.8 cd/A, 6.4%), respectively. As expected, with the resonant wavelength set at 538 nm (~20 nm longer the PL peak of C545T), the top-emitting microcavity device shows not only enhanced cd/A efficiency (2.5×) but also substantially enhanced external quantum efficiency (1.42×), as compared to the conventional bottom-emitting device. With microlens lamination, the top-emitting microcavity OLED shows even larger enhancement in both quantum efficiency (1.6×) and cd/A efficiency (3.0×).

Microlens arrays have been used to enhance the outcoupling efficiencies of conventional bottom-emitting OLEDs [39]. However, as illustrated in Figure 9.19a, serious image blurring occurs and pixels become hardly distinguishable when the conventional bottom-emitting OLEDs are laminated with microlenses. In contrast, the blurring of pixel emission is substantially reduced for the case of top-emitting OLEDs laminated with microlenses. As illustrated in Figure 9.19b, with microlens lamination, the top-emitting

**FIGURE 9.19**

Images of (a) the conventional bottom-emitting device laminated with microlenses and (b) the top-emitting device laminated with microlenses, both taken near the edges of turned-on pixels. (From Yang, C.-J. et al., *Appl. Phys. Lett.*, 91, 253508-1, 2006. With permission.)

OLED still exhibits a distinguishable pixel edge and clear-enough pixel definition for display applications [36].

Microcavity OLEDs have been useful for enhancing the brightness and color saturation of OLEDs. A long-standing issue in microcavity OLEDs is the difficulty to simultaneously achieve enhanced cd/A efficiency, enhanced external quantum efficiency, enhanced color saturation, and stable colors with viewing angles in a same device design. Here, it is seen that microcavity top-emitting OLEDs integrated with microlenses may provide a universal approach for simultaneously achieving all these desired characteristics. Furthermore, the pixel blurring that often occurs in employment of microlenses in conventional bottom-emitting OLEDs is significantly suppressed by a combination of top-emitting microcavity OLEDs and microlenses. Since the microlenses can be fabricated separately and then laminated on microcavity OLEDs, the approach reported here is simple, effective, and highly compatible.

---

## 9.6 Summary

General discussions of the optical structures and optical characteristics of OLEDs based on analytical Fabry–Perot formulations and rigorous electromagnetic modeling are provided and then used as the basis in discussions of optical characteristics of advanced OLED structures. In general, an OLED can optically be considered as a microcavity, either weak or strong. To optimize optical performances of devices, such as efficiencies and colors, different resonance conditions must be appropriately set. When designed and considered carefully, incorporation of microcavity effects and structures in any type of OLED could be used to enhance color performances, brightness, and efficiency for various applications. The combination of microcavity structures and micro-optic elements/structures may also bring about some useful new characteristics in OLED devices.

---

## References

1. C. W. Tang and S. A. Vanslyke, *Appl. Phys. Lett.*, 51, 913–915, 1987.
2. K. A. Neyts, *J. Opt. Soc. Am. A*, 15, 962–971, 1998.
3. H. Riel, S. Karg, T. Beierlein, W. Ries, and K. Neyts, *J. Appl. Phys.*, 94, 5290–5296, 2003.
4. Z. Huang, C. Lei, D. G. Deppe, C. C. Lin, C. J. Pinzone, and R. D. Dupuis, *Appl. Phys. Lett.*, 61, 2961–2963, 1992.

5. E. F. Schubert, N. E. J. Hunt, M. Micovic, R. J. Malik, D. L. Sivco, A. Y. Cho, and G. J. Zydzik, *Science*, 265, 943–945, 1994.
6. A. Dodabalapur, L. J. Rothberg, R. H. Jordan, T. M. Miller, R. E. Slusher, and J. M. Phillips, *J. Appl. Phys.*, 80, 6954–6964, 1996.
7. R. H. Jordan, L. J. Rothberg, A. Dodabalapur, and R. E. Slusher, *Appl. Phys. Lett.*, 69, 1997–1999, 1996.
8. G. R. Hayes, F. Cacialli, and T. R. Phillips, *Phys. Rev. B*, 56, 4798, 1997.
9. U. Lemmer, R. Hennig, W. Guss, A. Ochse, J. Pommerehne, R. Sander, A. Greiner, R. F. Mahrt, H. Bässler, J. Feldmann, and E. O. Göbel, *Appl. Phys. Lett.*, 66, 1301, 1995.
10. C.-L. Lin, H.-W. Lin, and C.-C. Wu, *Appl. Phys. Lett.*, 87, 021101, 2005.
11. W. Lukosz and R. E. Kunz, *J. Opt. Soc. Am.*, 67, 1607–1615, 1977.
12. J. E. Sipe, *Surf. Sci.*, 105, 489–504, 1981.
13. J. A. E. Wasey and W. L. Barnes, *J. Mod. Opt.*, 47, 725–741, 2000.
14. C.-C. Wu, C.-L. Lin, P.-Y. Hsieh, and H.-H. Chiang, *Appl. Phys. Lett.*, 84, 3966–3968, 2004.
15. S. K. So, W. K. Choi, L. M. Leung, and K. Neyts, *Appl. Phys. Lett.*, 74, 1939–1941, 1999.
16. X. Zhou, M. Pfeiffer, J. Blochwitz, A. Werner, A. Nollau, T. Fritz, and K. Leo, *Appl. Phys. Lett.*, 78, 410–412, 2001.
17. G. He, O. Schneider, D. Qin, X. Zhou, M. Pfeiffer, and K. Leo, *Appl. Phys. Lett.*, 95, 5773–5775, 2004.
18. C.-C. Wu, T.-L. Liu, W.-Y. Hung, Y.-T. Lin, K.-T. Wong, R.-T. Chen, Y.-M. Chen, and Y.-Y. Chien, *J. Am. Chem. Soc.*, 125, 3710, 2003.
19. L.-Y. Chen, W.-Y. Hung, Y.-T. Lin, C.-C. Wu, T.-C. Chao, T.-H. Hung, and K.-T. Wong, *Appl. Phys. Lett.*, 87, 112103, 2005.
20. C.-L. Lin, T.-Y. Cho, C.-H. Chang, and C.-C. Wu, *Appl. Phys. Lett.*, 88, 081114, 2006.
21. L. S. Hung, C. W. Tang, M. G. Mason, P. Raychaudhuri, and J. Madathil, *Appl. Phys. Lett.*, 78, 544, 2001.
22. C. W. Tang, S. A. Vanslyke, and C. H. Chen, *J. Appl. Phys.*, 65, 3610–3616, 1989.
23. M. H. Lu and J. C. Sturm, *J. Appl. Phys.*, 91, 595, 2002.
24. T. Matsumoto, T. Nakada, J. Endo, K. Mori, N. Kavamura, A. Yokoi, and J. Kido, 2003 Society for Information Display (SID) International Symposium, *Digest of Technical Papers* (Baltimore, MD, 2003), p. 979.
25. L. S. Liao, K. P. Klubek, and C. W. Tang, *Appl. Phys. Lett.*, 84, 167 (2004).
26. C. C. Chang, S. W. Hwang, C. H. Chen, and J. F. Chen, *Jpn. J. Appl. Phys.*, 43, 6418, 2004.
27. M.-H. Lu, M. S. Weaver, T. X. Zhou, M. Rothman, R. C. Kwong, M. Hack, and J. J. Brown, *Appl. Phys. Lett.*, 81, 3921–3923, 2002.
28. H. Riel, S. Karg, T. Beierlein, B. Ruhstaller, and W. Rieß, *Appl. Phys. Lett.*, 82, 466–468, 2003.
29. C.-W. Chen, P.-Y. Hsieh, H.-H. Chiang, C.-L. Lin, H.-M. Wu, and C.-C. Wu, *Appl. Phys. Lett.*, 83, 5127–5129, 2003.
30. T. Nakayama, Y. Itoh, and A. Kakuta, *Appl. Phys. Lett.*, 63, 594–595, 1993.
31. A. Dodabalapur, L. J. Rothberg, and T. M. Miller, *Appl. Phys. Lett.*, 65, 2308–2310, 1994.
32. T. Tsutsui, N. Takada, S. Saito, and E. Ogino, *Appl. Phys. Lett.*, 65, 1868–1870, 1994.

33. N. Takada, T. Tsutsui, and S. Saito, *Appl. Phys. Lett.*, **63**, 2032–2034, 1993.
34. H. Widdel and D. L. Post (Eds.), *Color in Electronic Displays*, 39, Plenum Press, New York, 1992.
35. M. Born and E. Wolf, *Principles of Optics*, 7th ed., Cambridge University Press, Cambridge, 1999.
36. C.-J. Yang, S.-H. Liu, H.-H. Hsieh, C.-C. Liu, T.-Y. Cho, and C.-C. Wu, *Appl. Phys. Lett.*, **91**, 253508, 2007.
37. K. Yamashita, T. Mori, and T. Mizutani, *J. Phys. D: Appl. Phys.*, **34**, 740, 2001.
38. Y. Xia and G. M. Whitesides, *Angew. Chem. Int. Ed.*, **37**, 550, 1998.
39. S. Moller and S. R. Forrest, *J. Appl. Phys.*, **91**, 3324, 2002.



# 10

---

## *Vertical-Type Organic Transistors*

---

**Yasuyuki Watanabe, Masakazu Nakamura, and Kazuhiro Kudo**

### CONTENTS

10.1	Introduction .....	293
10.2	Organic Transistors .....	295
10.3	Vertical-Type Organic Transistors .....	297
10.4	Organic Static Induction Transistors.....	298
10.4.1	Fabrication Process for Organic Static Induction Transistors .....	298
10.4.1.1	Shadow Evaporation Technique.....	299
10.4.1.2	Colloidal Lithography .....	300
10.4.2	Operational Mechanism of OSITs .....	302
10.4.3	Static and Dynamic Characteristics of OSITs and OFETs .....	303
10.4.4	Improvement in Device Performance .....	306
10.4.4.1	Control of Interfaces Related to Carrier Injection .....	306
10.4.4.2	Fabrication of a Gate Electrode with a Nanogap.....	308
10.5	Application to Flexible Sheet Displays .....	309
10.5.1	Flexible Organic Transistor Based on OSITs .....	309
10.5.2	Organic Logic Devices Based on OSITs .....	311
10.5.3	Organic Light-Emitting Transistors .....	312
10.6	Summary.....	314
	Acknowledgments .....	315
	References.....	315

---

### **10.1 Introduction**

In the 1980s, research into organic field-effect transistors (OFETs) was initiated to investigate the characteristics of organic semiconductors, such as field-effect mobility [1]. In recent years, OFETs have been developed for novel

electronic devices such as flexible displays based on organic light-emitting diodes (OLEDs), electronic papers, radio frequency identity (RF-ID) tags, and biosensors [2–6]. In the intervening quarter-century, field-effect mobility has been increased from  $1 \times 10^{-5}$  [cm<sup>2</sup>/Vs] to 40 [cm<sup>2</sup>/Vs] [7–8]. However, conventional OFETs have remaining issues, such as higher operational voltage compared with inorganic transistors, which have prevented the fabrication of practical mobile electronic devices. The low performance of such devices is mainly due to the low-mobility and high-resistivity of organic semiconductors. Many different approaches have been made in an attempt to improve the performance of OFETs, as shown in Figure 10.1.

For practical applications of OFETs, it is necessary to improve not only the electrical properties of the organic semiconductors but also the device structures. It should be noted that commercialized organic devices, such as organic photoconductors (OPC) and OLEDs, are comprised of a vertical structure, which can also be applied to organic transistors. Therefore, we have focused on the device structure and proposed “vertical-type organic transistors.” In addition, the channel length is shortened in vertical-type organic transistors, which can lead to a decrease in the operational voltage.

In conventional OFETs with channel lengths in the order of several tens of micrometers, the current flows along the channel formed at the organic semiconductor/gate insulator interface in the lateral direction, which results in a high operational voltage in the order of several tens of volts. On the other hand, in the vertical type organic transistors with channel lengths of several hundreds of nanometers, the current flows in the vertical direction

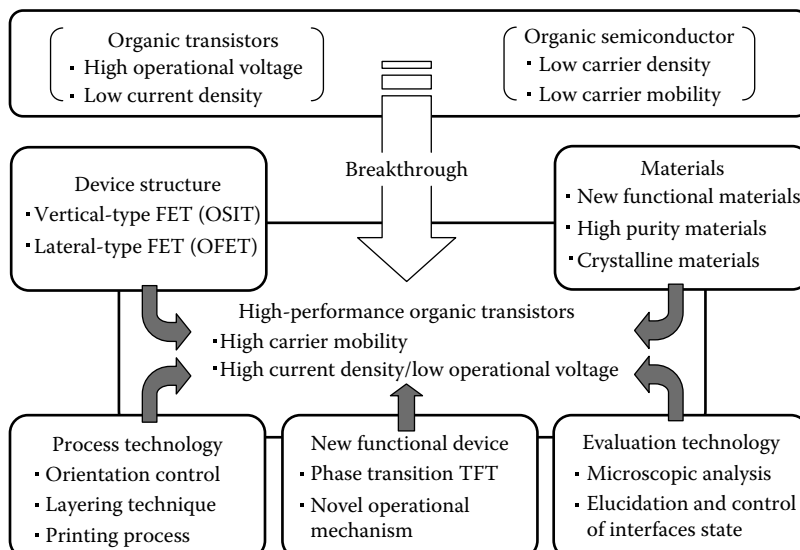


**FIGURE 10.1**

Approaches for the achievement of high-performance organic transistors.

through the thin film, which results in a low operational voltage of only a few volts.

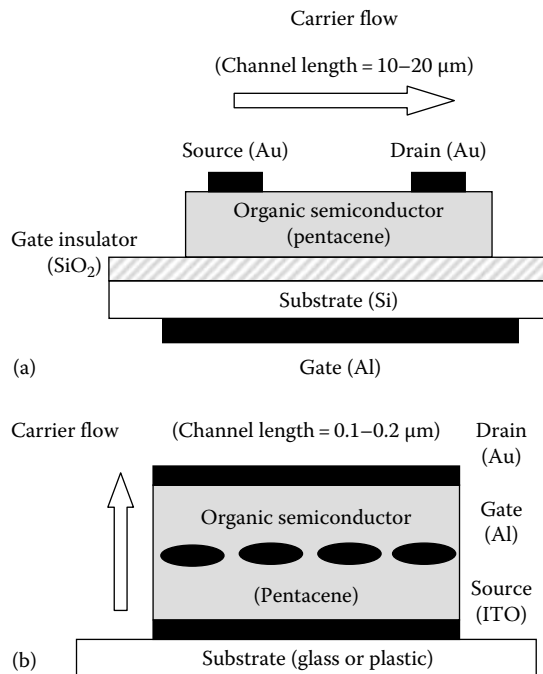
Many types of vertical-type transistors [9–11] have been proposed in the field of transistors based on inorganic semiconductors, and these are detailed in Section 10.3. Among these transistors, we have focused on the static induction transistors (SITs), as proposed by Nishizawa et al. [10], which are also known as vertical-type field-effect transistors. It is known that SITs are promising devices because of their high-speed and high-power operation [10]. High-speed and high-power SITs have already been proposed and some inorganic power switching devices with similar structures have been realized. However, in the fabrication of inorganic SITs, perfect crystal technology is necessary because defects in the semiconductor layer around the gate region result in the degradation of the device characteristics. Most organic materials form molecular crystals or amorphous films, and their physical properties are related to the conditions used for the growth of the organic films. Crystal imperfections sometimes have little effect on the electrical properties compared with inorganic semiconductors [12–14]. The device structure of the SIT was applied to organic transistors, which is referred to as an organic SIT (OSIT). Our recent efforts to improve the performance of OSITs by optimizing the device structure and organic materials are reported. In addition, OSITs were fabricated on plastic substrates, and the characteristics of the flexible OSITs were investigated. OSITs are proposed for application in flexible displays, logic devices, and organic light-emitting transistors (OLETs).

---

## 10.2 Organic Transistors

Based on the device structure, organic transistors can be classified into two groups: lateral-type organic transistors and vertical-type organic transistors. Figure 10.2 shows cross-sectional schematic illustrations of a lateral-type OFET and vertical-type OSIT. The advantages of OSITs over OFETs are the realization of low voltage operation and the ease of fabrication on flexible substrates. In lateral-type OFETs (Figure 10.2a), the current flows along the channel formed in the lateral direction. In general, the channel length between the source and drain electrodes is limited by the size of the evaporation mask (10–20  $\mu\text{m}$ ). On the other hand, the current flows in the vertical direction through the thin film in a vertical-type OSIT (Figure 10.2b). The channel length corresponds to the thickness of the organic semiconductors (0.1–0.2  $\mu\text{m}$ ). Therefore, the channel length of the OSIT is shorter than that of the OFET, which leads to lower operational voltage.

Furthermore, the effect of surface roughness on the characteristics of OFETs may be significant because the channel is formed along the interface

**FIGURE 10.2**

Device structure of (a) lateral-type OTFTs (OFETs) and (b) vertical-type OTFTs (OSITs).

of the gate insulator and the semiconductor film. In contrast, the characteristics of OSITs may be less affected by surface roughness because the channel is formed in the vertical direction through the thin film.

The lateral-type OFET was proposed as a prototype for the thin film transistor (TFT), where a highly doped silicon (Si) substrate functions as the gate electrode [1]. However, in order to fabricate flexible OFETs, not only should nonflexible Si wafers be replaced with flexible substrates such as plastic, but the nonflexible  $\text{SiO}_2$  gate insulator should also be replaced with a flexible material. In contrast, vertical-type OSITs consist of organic semiconductors and metal electrodes. It should be noted that no gate insulator is required for the fabrication of the OSITs; therefore, only the nonflexible glass substrate requires replacement by a flexible substrate. This means that OSITs can be fabricated on a flexible substrate in the same manner as those on glass substrates. Considering this, a simple method such as a vacuum evaporation technique could be applied to the fabrication of OSITs on either glass or flexible plastic substrates.

To confirm the advantages of vertical-type FETs, OSITs using pentacene or CuPc evaporated films were fabricated on glass substrates and the basic characteristics were evaluated [15,16], as detailed in Section 10.4.3. Furthermore, OSITs based on pentacene evaporated film were fabricated

on flexible substrates [17] and the electrical characteristics under bending were measured [18], as outlined in Section 10.5.1. These results show that OSITs have potential for use as flexible organic transistors with low operational voltage.

In application, optoelectronic elements using organic materials show promise for low-cost, large-area, light-weight, and flexible devices. In particular, liquid crystals and OLEDs are expected to be used as display components of mobile electronic devices, and OLEDs have been developed with excellent stability and high efficiency [19,20]. On the other hand, organic transistors have been greatly improved in recent years, and all-organic displays are expected to be developed using organic transistors [21–24]. However, for practicality, it is necessary to operate with a drive voltage as low as a few volts and with sufficient reliability. The vertical transistors, particularly OSITs, are suitable for flexible displays and the basic characteristics of OSITs as driving elements for organic display devices have already been reported [25]. In addition, OLETs combined with OSITs and OLEDs [26], and organic logic devices using OSITs have also been reported [16].

### 10.3 Vertical-Type Organic Transistors

In the research field of TFT based on inorganic transistors, many kinds of vertical-type transistors such as metal-base transistor (MBT) [9], SIT [10], and permeable-base transistor (PBT) [11] have been proposed. In the research of organic TFTs, polymer grid triode (PGT) [27], OSITs [28], vertical organic field-effect transistor (VOFET) [29], and metal-base organic transistor (MBOT) [30] have also been reported as vertical-type organic transistors. Figure 10.3a through c show the device structures of PGT, VOFET, and MBOT. Here, we have focused on the vertical-type organic transistors that operate as a SIT, that is, the OSITs (Figure 10.2b).

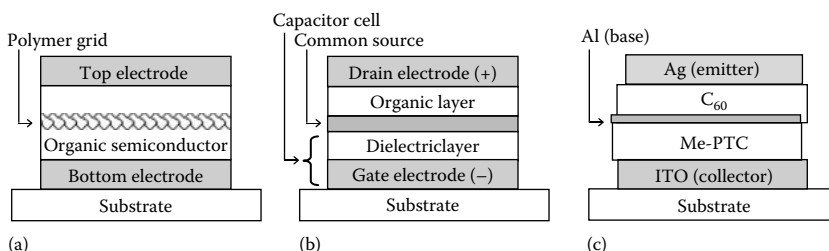


**FIGURE 10.3**

Various structures of vertical-type organic transistors. (a) PGT, polymer grid triode; (b) VOFET, vertical organic field effect transistor; and (c) MBOT, metal-base organic transistor.

## 10.4 Organic Static Induction Transistors

### 10.4.1 Fabrication Process for Organic Static Induction Transistors

OSITs have a buried grid-type Al gate electrode, as shown in Figure 10.2b. For the fabrication of the OSITs, it is important to fabricate the Al gate electrode with a narrow gap equivalent to the width of the depletion layer formed around the Al electrode. The thicker Al part of the grid gate controls the current flow from the source to the drain electrode due to the formation of double Schottky barriers; therefore, the wider gap region of the gate electrode does not effectively control the current flow.

Two fabrication processes for OSITs are proposed, and the resulting OSITs are schematically shown in Figure 10.4. One process is the shadow evaporation technique [16–18,25,26,28], and the other is colloidal lithography [31].

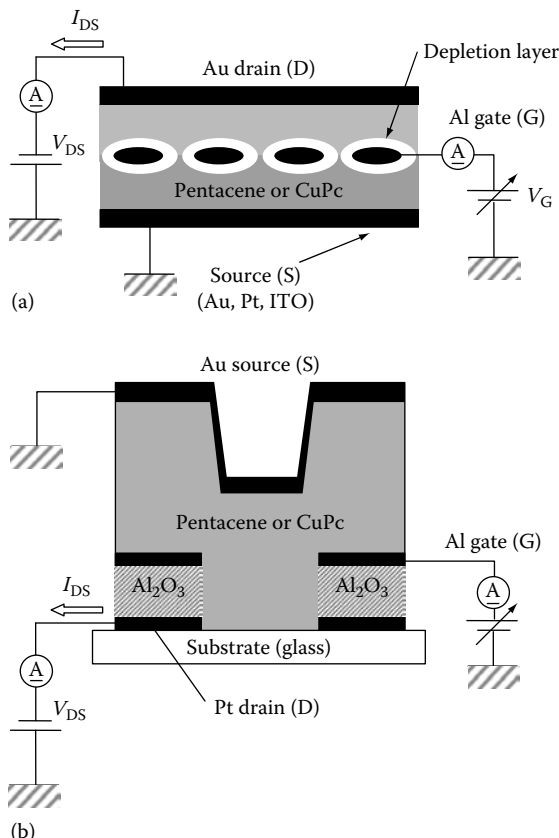
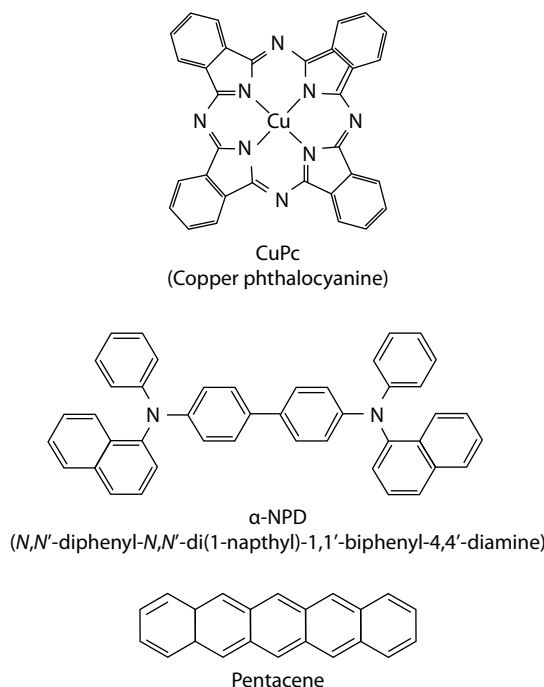


**FIGURE 10.4**

Device structure and circuit diagram of OSITs fabricated by (a) the conventional evaporation technique and (b) colloidal lithography.

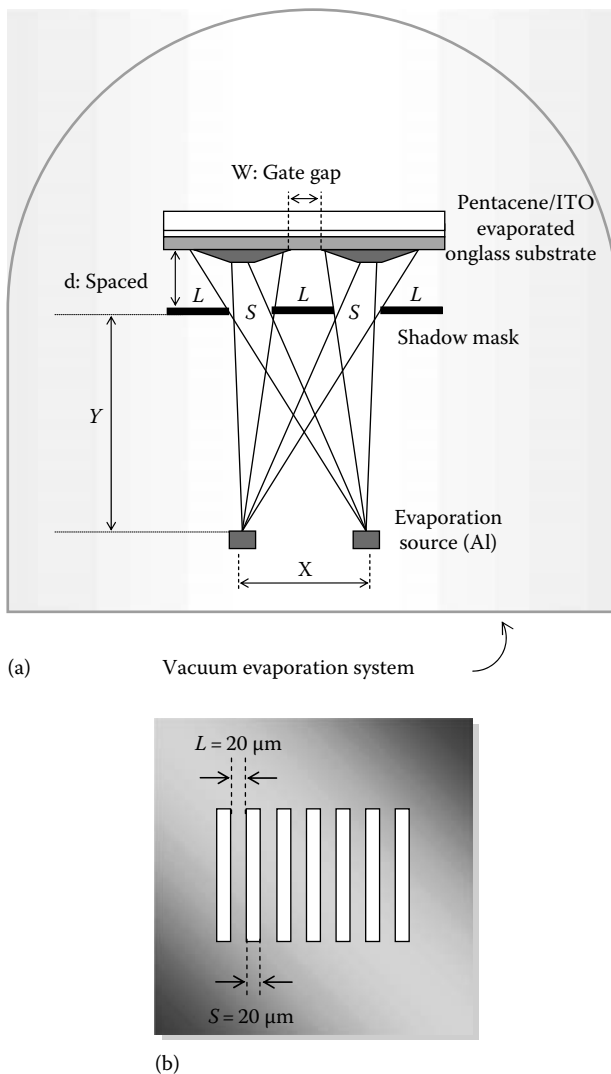
### 10.4.1.1 Shadow Evaporation Technique

Figure 10.5 shows the molecular structures of CuPc, 4,4'-bis[N-(1-naphthyl)-N-phenyl-amino] biphenyl ( $\alpha$ -NPD), and pentacene used in the fabrication of the OSITs. Firstly, an organic semiconductor film with a thickness of approximately 100 nm is deposited on the source electrode (Au or indium tin oxide [ITO])-formed glass substrate. Secondly, a grid-type gate electrode (Al) is formed on the organic film by the shadow evaporation technique, as shown in Figure 10.6. Thirdly, a second organic semiconductor film of approximately 100 nm thickness is deposited. Finally, the drain electrode (Au) is fabricated. Since the introduction of oxygen gas has the positive effect of increasing the carrier concentration of organic semiconductor films and creates a stable Schottky contact with the Al electrode, the vacuum chamber was leaked with air after evaporation of the Al electrode [15,28]. The dimensions and edge features of the grid-type gate Al electrode can be controlled by adjusting the distance of the two evaporation sources ( $d$ ) and the spacer thickness between the sample and evaporation mask ( $L$ ), as shown in Figure 10.6. The effective area of the source/drain electrode was  $0.025\text{ cm}^2$ .



**FIGURE 10.5**

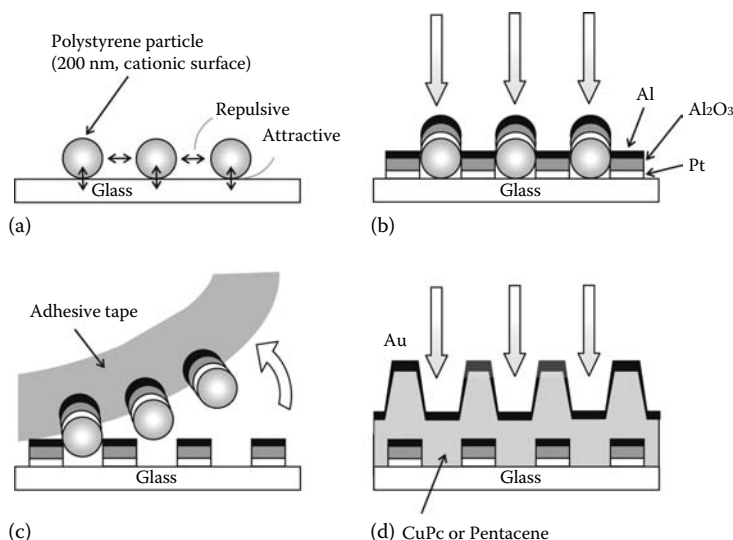
Molecular structures of CuPc,  $\alpha$ -NPD, and pentacene.

**FIGURE 10.6**

Shadow evaporation technique: Schematic of the (a) shadow evaporation method, and the (b) evaporation mask of the formed Al gate electrode.

#### **10.4.1.2 Colloidal Lithography**

Figure 10.7 schematically illustrates the OSIT fabrication process using colloidal lithography. Glass substrates are immersed in an aqueous suspension of nanoparticles resulting in adsorption. A high-performance SIT requires excellent surface coverage without particle aggregation because

**FIGURE 10.7**

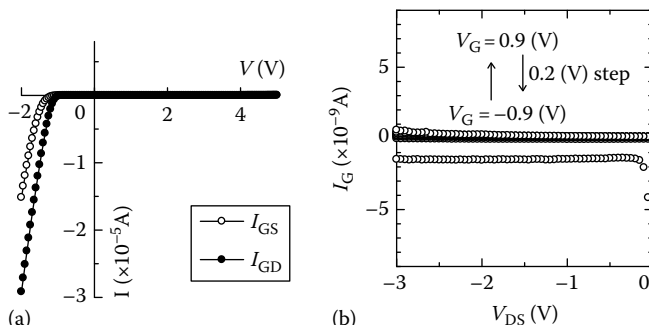
Fabrication process for OSITs using colloidal lithography. (a) Adsorption of polystyrene particles on a glass substrate, (b) deposition of Al, Al<sub>2</sub>O<sub>3</sub>, and Pt layers using the particles as evaporation masks, (c) removal of the particles using adhesive tape, and (d) deposition of the organic semiconductor and Au layers.

the active region of the structure corresponds to the total area of adsorbed particles, while the continuous space between particles is used as the gate electrode in the transistor. Based on this requirement, positively charged polystyrene particles are chosen to exploit the electrostatic interactions between particle surfaces and the substrate (Figure 10.7a). Immersion in a suspension containing a large density of particles improves coverage. However, aggregation is observed after drying the materials. The aggregation of particles on the surface is normally ascribed to capillary forces created by the menisci between particles as water evaporates [32]. Therefore, to suppress particle aggregation and retain control of the particle film structure, the film is heated while in solution. This step is effective in overcoming the capillary forces and keeping the particles in place because the particles are slightly deformed on the surface increasing their contact area and preventing capillary forces from moving the particles [33]. As a result, high-density films are obtained, in which the particles are homogeneously dispersed on the surface. The temperature of the heat treatment (below 90°C) is the highest temperature used throughout the entire process indicating that this method should be generally applicable to polymer substrates. After adsorption of the particles, the bottom electrode (Pt), insulating layer (Al<sub>2</sub>O<sub>3</sub>), and gate electrode (Al) are successively deposited onto the particles by vacuum evaporation (Figure 10.7b). After deposition

of the Pt,  $\text{Al}_2\text{O}_3$ , and Al layers, the particles are selectively removed using adhesive tape, as shown in Figure 10.7c. Because the density of particles is sufficient, the adhesive tape does not contact the flat part of the film. As a result, a large number of nanoholes are formed without destroying the film. The organic semiconductor layer and top electrode (Au) are then deposited on the porous film to complete the OSIT (Figure 10.7d).

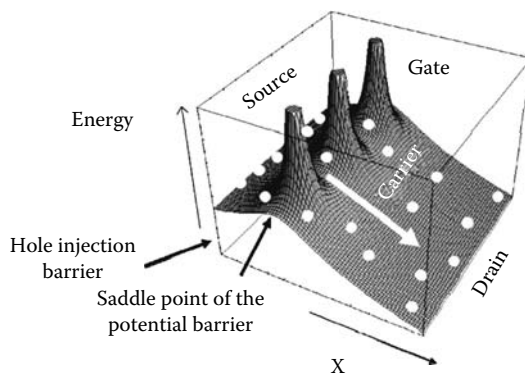
#### 10.4.2 Operational Mechanism of OSITs

The basic characteristics of OSITs can be explained as follows. CuPc,  $\alpha$ -NPD, and pentacene films exhibit p-type semiconducting properties, create an ohmic contact with the Au electrodes, and form a Schottky barrier contact with the Al gate electrode. As an example, experimental data for the case of pentacene OSITs is explained as follows. The current-voltage ( $I$ - $V$ ) characteristics between the gate electrode, and the source and drain electrodes are shown in Figure 10.8a and b. The  $I$ - $V$  curves indicate the rectifying properties, and the forward bias corresponds to the positive voltage applied to the Au electrodes. These static characteristics can be explained by the potential diagram of the OSITs shown in Figure 10.9. The injected hole carriers from the source electrode flow toward the drain electrode through the potential barrier near the gate electrode. The carrier flow is controlled by the potential barrier height depending on the gate voltage ( $V_G$ ). Although current saturation at high source-drain voltage ( $V_{DS}$ ), due to the negative feedback effect of the series channel resistance, is observed in the lateral type OFETs [11], current saturation does not appear in the OSITs. The non-saturating source-drain current ( $I_{DS}$ )- $V_{DS}$  characteristic is typical of SIT operation due to the sufficiently small channel resistance [10].



**FIGURE 10.8**

Current-voltage characteristics of OSITs. (a) Current-voltage characteristics between gate to source and gate to drain electrodes. (b)  $I_G$ - $V_{DS}$  curves of a pentacene OSIT.  $V_G$  was varied from  $-0.9$  to  $0.9 \text{ V}$  in  $0.2 \text{ V}$  steps.

**FIGURE 10.9**

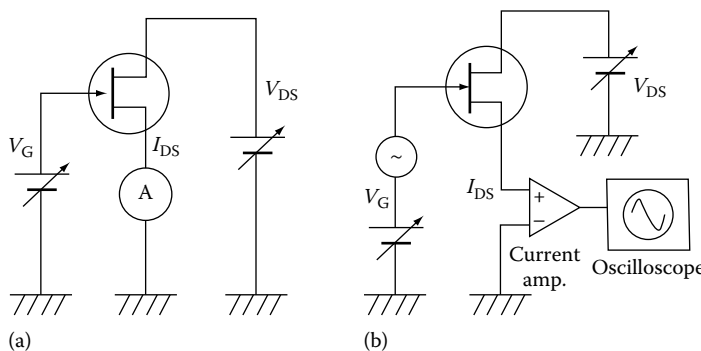
Potential distribution in an OSIT viewed from the source-drain side.

#### 10.4.3 Static and Dynamic Characteristics of OSITs and OFETs

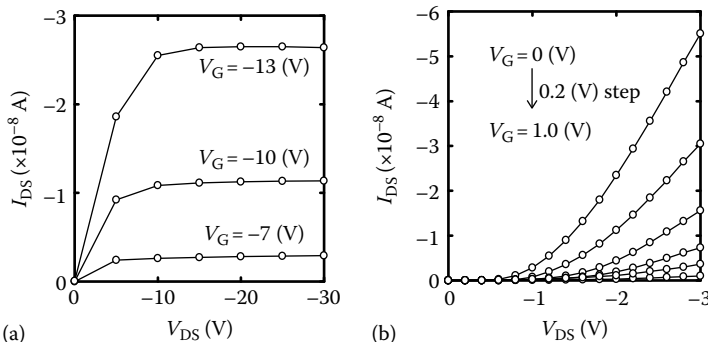
For comparison, lateral-type OFETs based on CuPc were also fabricated. The device structure of the OFETs is schematically shown in Figure 10.2a and the device fabrication process of the OFETs is as follows. As in the case of the OSITs, the OFETs were also fabricated by a standard evaporation technique. The substrate temperature, evaporation rate, total thickness, and background pressure during the evaporation process are room temperature, 2 nm/min, 200 nm, and  $10^{-4}$  Pa, respectively. For the fabrication of the OFETs, interdigitated Au/Cr-source and drain electrodes with 100  $\mu\text{m}$  spacing, 4 mm width, and 30 lines were formed on a highly doped p-type silicon substrate using standard vacuum evaporation and photolithographic techniques. The thickness of the  $\text{SiO}_2$  layer was approximately 200 nm.

Compared with the OFETs, the OSITs have a short channel and large effective area, and therefore a high speed and a large current operation are expected. The characteristics of the  $I_{DS}$  vs.  $V_{DS}$  with the application of a gate voltage ( $V_G$ ) were measured. Static and dynamic characteristics of the SIT were measured using a pA meter/DC voltage source, a function generator, and a digital storage oscilloscope. All measurements were carried out in air at room temperature, and in the dark, in order to prevent the photovoltaic effect of the Schottky barrier contact affecting the SIT characteristics.

Figure 10.10a and b show the electrical measurement systems for the static and dynamic characteristics. Typical static characteristics of the OFETs and OSITs based on CuPc are shown in Figure 10.11a and b, respectively. In both transistors,  $I_{DS}$  is controlled by  $V_G$ . For the OFET, negative gate voltages enhance the channel current, due to the formation of a hole accumulation layer, and the device operates like an enhancement-type transistor. On the other hand, the static characteristics of the OSIT are different when compared with those of the OFET. The operational voltages of  $V_{DS}$  and  $V_G$  for

**FIGURE 10.10**

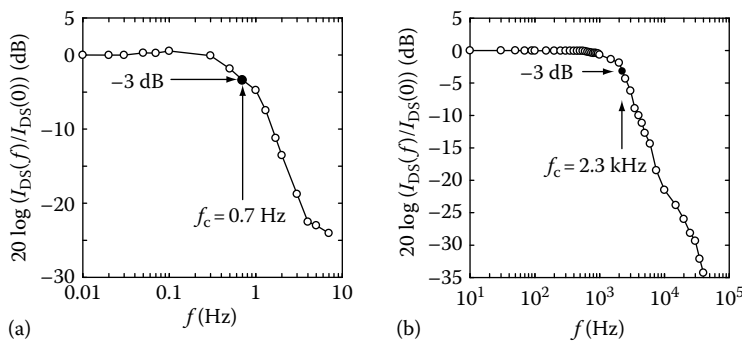
Electrical measurement systems for (a) static and (b) dynamic characteristics.

**FIGURE 10.11**

Static characteristics of (a) lateral-type OFETs and (b) vertical-type OSITs.

the OSIT are rather small compared with those for the OFET. The  $I_{DS}$  of the OSIT is approximately two orders larger than that of the OFET, and the OSIT operates like a depletion-type transistor. The slope of the  $I_{DS}$ - $V_{DS}$  curves for the OSIT increases with increasing  $V_{DS}$  without current saturation. Since the Al gate electrode in the OSIT functions as a Schottky barrier gate, a negative gate voltage, that is a forward bias voltage of the Schottky diode, increases the leakage current through the gate electrode. However, the OSIT operates with negligibly small leakage currents ( $I_{GL} < 10^{-8} \text{ A}$ ) at low negative gate voltages ( $V_G < -0.8 \text{ V}$ ).

Figure 10.12a and b shows the frequency characteristics of the OFET and the OSIT, respectively. In both transistors, modulated  $I_{DS}$  gradually decreases with increasing  $V_G$  frequency. In order to evaluate the decrease of  $I_{DS}(f)$  from the static state value  $I_{DS}(0)$ ,  $20 \log(I_{DS}(f)/I_{DS}(0))$  is plotted in the figure. The cut-off frequency ( $f_C$ ) is defined here as the frequency where  $I_{DS}(f)$  decreases to 3 dB less than the static state  $I_{DS}(0)$ . The  $f_C$  of the OSIT is approximately three orders higher than that of the OFET. The output  $I_{DS}$  shows good coincidence

**FIGURE 10.12**

Frequency characteristics of (a) lateral-type OFETs and (b) vertical-type OSITs.

as can be expected from the static characteristics in Figure 10.11a and b. High-speed operation of the OSIT was observed compared with that for the OFET. It is suggested that the high-speed, low-voltage, and high-current operation of the samples examined here originate from the device structure, that is, the very short channel length and large effective area of the OSIT improve the characteristics of the organic transistors.

Table 10.1 provides a comparison of the device size and performance for both the lateral-type OFET and vertical-type OSIT. In this case, the channel length and effective area of the OFET are evaluated simply as the gap of the source and drain electrodes ( $100\text{ }\mu\text{m}$ ) and the thickness of the CuPc film (200 nm), respectively. On the other hand, the channel length and effective area of the OSIT correspond to the thickness of the CuPc film and the effective area of the top drain electrode. Therefore, the channel length of the OFET is 500 times longer than that of the OSIT, and the effective area of the OFETs is two orders smaller than that of the OSITs. The operational current of the OSIT is approximately two orders larger than that of the

**TABLE 10.1**

Comparison of the Device Size and Device Performance of Lateral-Type OFETs and Vertical-Type OSITs

	Device Size		Device Performance		
	Channel Length ( $\mu\text{m}$ )	Effective Area ( $\text{cm}^{-2}$ )	Voltage (V)	Current (A)	Frequency (Hz)
Lateral-type OFETs	100	$2.4 \times 10^{-4}$	$V_D:25$ $V_G:15$	$2.3 \times 10^{-6}$	0.7
Vertical-type OSITs	0.2	$2.4 \times 10^{-5}$	$V_D:3$ $V_G:1$	$2.4 \times 10^{-6}$	2300
Vertical/lateral	1/500	~100	~1/10	~100	~3000

OFET. The  $f_C$  of the OSIT is approximately 3000 times higher than that of the OFET. These results indicate that device structure, such as the channel length and the effective area, have a significant effect on the device characteristics, and also that the OSITs have excellent device performance.

#### **10.4.4 Improvement in Device Performance**

Further improvements in the characteristics of the OSITs are expected by optimizing the semiconductor materials, controlling the interface states, and optimizing the dimensions of the gate electrode. In general, the frequency characteristics of the transistors strongly depend on the carrier mobilities of the semiconductor materials. It was confirmed that the cutoff frequency for the OSITs based on pentacene fabricated on a glass substrate was around 7 kHz, which is higher than that of the OSITs based on CuPc fabricated on a glass substrate. The results demonstrate that a higher cutoff frequency is achieved by using pentacene, which has a higher carrier mobility. However, the OSITs also have the remaining issue of too low an on/off ratio for use in electronic devices. The on/off ratios of the OSITs strongly affect the carrier injection properties and the gate electrode structure. Carrier injection into the semiconductor material is generally affected by the interface state of the organic semiconductor/source electrode. Therefore, in order to fabricate OSITs with high on/off ratios, it is important to investigate not only the influence of the gate geometry, but also that of the interface state, on the characteristics of the OSITs.

##### **10.4.4.1 Control of Interfaces Related to Carrier Injection**

In this section, the effect of controlling the interface state of the organic semiconductor/source electrode on the characteristics of the OSITs fabricated by the conventional evaporation technique is presented. The device structure of the sample is shown in Figure 10.4a.

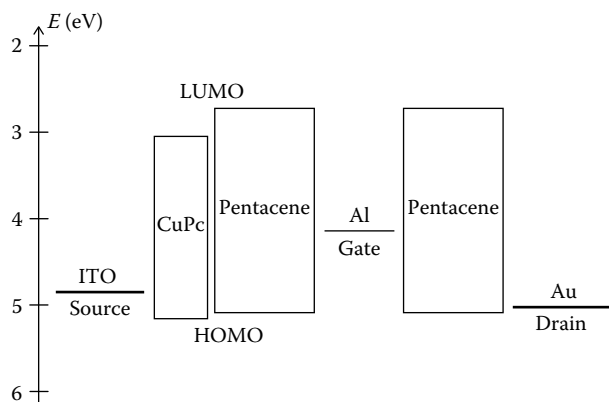
OSITs based on pentacene thin films have been fabricated on ITO formed on glass substrates. It is well known that the work function of ITO is controlled by the method used to clean its surface. OSITs were fabricated based on pentacene thin films with a high-work function ITO of 5.3 eV and a low-work function of 4.2 eV. The effect of the work function of ITO on the static characteristics of the OSITs was investigated using  $I$ - $V$  measurements and ultraviolet photoemission spectroscopy (UPS) [34]. These results provided an important clue, in that the characteristics of the OSITs were strongly associated with the work function of ITO used as a source electrode. In general, the hole injection barrier at the organic semiconductor/metal interface is influenced by the work function of the metal.

Therefore, in order to realize high-performance OSITs, further investigation is required to evaluate the effect of a hole injection barrier at the interface

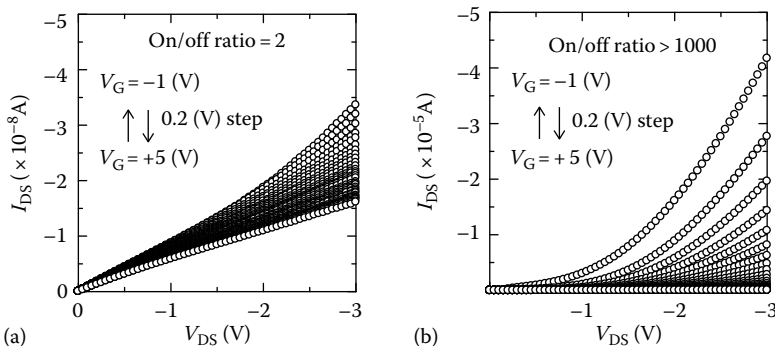
between the pentacene film and source electrode. OSITs based on pentacene films were also fabricated on various electrodes such as ITO, Au, and Pt with different work functions [35]. The obtained results demonstrate that a higher on/off ratio is achieved when a hole injection barrier with a moderate height is formed at the interface. It was found that the control of the hole injection barrier is effective for improving the characteristics of OSITs.

In order to control the interface of pentacene/ITO in the OSITs, a CuPc layer was inserted between pentacene and ITO [36]. It was reported that the electron carrier injection characteristics of OLEDs were improved by a thin insulating layer, such as LiF or  $\text{Al}_2\text{O}_3$ , inserted between the cathode and the organic layers. On the other hand, the hole injection characteristics were also improved by a thin CuPc inserted between the anode (typically ITO electrode) and the organic layers. These results indicate that an inserted layer between the electrodes and the organic layers works to improve the overall characteristics of organic devices. A CuPc layer is well known as a material to improve hole injection into OLEDs [37]. There are many research reports regarding CuPc/ITO systems in OLEDs. Therefore, the effect of an inserted CuPc layer on the characteristics of OSITs was investigated.

A CuPc layer was inserted between ITO as a source electrode and a pentacene thin film as the organic semiconductor layer in the OSIT. A band diagram for the pentacene OSIT with inserted CuPc layer is shown in Figure 10.13. For comparison, OSITs based on pentacene thin films were also fabricated directly on an ITO/glass substrate without the insertion of a CuPc layer. In addition, the dependence of the CuPc layer thickness on the characteristics of the OSITs was also investigated. It was found that the hole injection barrier was affected by the thickness of the CuPc layer, and

**FIGURE 10.13**

Energy levels of organic materials and electrodes for pentacene OSITs fabricated on CuPc/ITO.

**FIGURE 10.14**

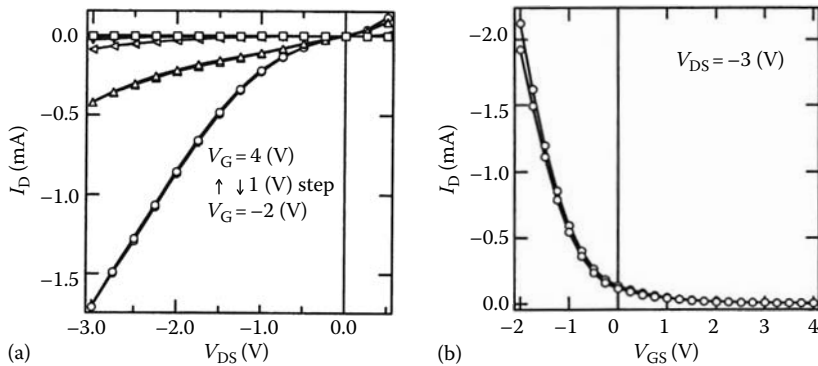
Static  $I_{DS}$ - $V_{DS}$  characteristics of pentacene OSITs (a) on ITO and (b) on CuPc/ITO.

the optimized thickness of the CuPc layer was approximately 1–3 nm for OSITs with a high on/off ratio.

The static characteristics of a pentacene OSIT without a CuPc layer (3 nm thick) and that with a CuPc layer are shown in Figure 10.14a and b, respectively. In this experiment,  $V_{DS}$  was changed continuously from 0 to -3 V, while  $V_G$  was changed from -1 to +5 V in +0.2 V steps. The constant  $I_{DS}$  was controlled by the  $V_G$ .  $I_{DS}$  was found to increase as  $V_{GS}$  decreased from 0 to -1 V, and decreased as  $V_G$  increased from 0 to +5 V. For the OSITs without the CuPc layer, the on/off ratio of  $I_{DS}$  at  $V_{DS} = -3 \text{ V}$  under applied  $V_G$  from -1 (on-state) to +5 V (off-state) was 2. On the other hand, for the OSIT with the CuPc layer, the on/off ratio was approximately 1000, which is two orders of magnitude higher than that of the OSIT without the CuPc layer. In addition, the current value of the OSIT with the CuPc layer was three orders of magnitude higher than that of the OSIT without the CuPc layer.

#### 10.4.4.2 Fabrication of a Gate Electrode with a Nanogap

The characteristics of the OSITs were improved by fabricating the gate electrode with a narrow gap, which was achieved by colloidal lithography [31]. Figure 10.4b shows a cross sectional view and measurement circuit of the OSITs with pentacene or CuPc as the p-type semiconductor material. The effective device area of the CuPc OSIT is  $2.0 \times 2.0 \text{ mm}$ , and 28 million nanotriode cells operate in parallel. In CuPc OSITs containing nanotriode arrays, the thickness of the CuPc layer and the total circumference of all the nanoholes correspond to a channel length of 200 nm and a channel width of ca. 21 m. The static output and transfer characteristics of the CuPc OSITs are shown in Figure 10.15a. The drain current ( $I_D$ ) is well modified by the gate bias ( $V_{GS}$ ). The gate leakage current ( $I_G$ ) is considerably smaller than that of the  $I_D$ , which indicates that the  $I_D$  is not modulated by the leak current from the gate electrode. Therefore, it was confirmed that the CuPc OSITs were operating

**FIGURE 10.15**

(a) Output characteristics of the CuPc OSITs fabricated by colloidal lithography, and (b) the transfer characteristics of the CuPc OSITs.

properly, with a low operating voltage (less than a few volts). The on-state current of the CuPc OSITs was several millamps, and was two orders of magnitude larger than that of conventional OSITs. The current on/off ratio was 470, and the transconductance ( $g_m = dI_D/dV_{GS}$ ) was  $2.0\text{ mS}$  ( $50\text{ mS cm}^{-2}$  when normalized by the device area), as obtained from the transfer characteristics (Figure 10.15a and b). The transconductance is very large for an organic transistor, even though CuPc is not a high-mobility material. The on-state current of the CuPc OSITs increased with increasing  $V_{DS}$ , but the on/off ratio decreased with increasing  $V_{DS}$  because of the greater increase in the off-state current. The on-state current also increased with decreasing  $V_{GS}$ , but  $g_m$  decreased dramatically in the range  $V_{GS} < -2$  V. Therefore, the most suitable CuPc OSIT operating voltage is in the range between  $V_{DS} = -3$  to 0 V and  $V_{GS} = -2$  to 4 V. Note that the  $V_{GS}$  of 4 V is not the critical limit of this transistor, and therefore, the on/off ratio described earlier is not a limiting value. The  $I_D$  of an ideal OSITs must be almost exponentially dependent on  $V_{DS}$  [38], but the  $I_D$  of the CuPc OSIT is linearly dependent on  $V_{DS}$  at higher  $V_{DS}$  values, as shown in Figure 10.15a. It is considered that the series resistance attributed to the low carrier mobility of CuPc affects the static OSIT characteristics.

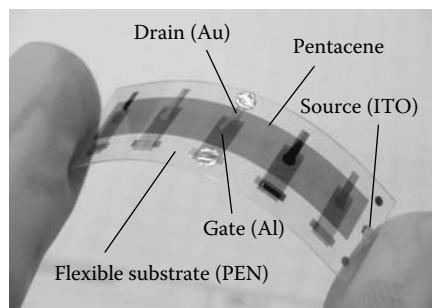
## 10.5 Application to Flexible Sheet Displays

### 10.5.1 Flexible Organic Transistor Based on OSITs

Flexible organic transistors have been attractive for driving electronic devices such as paper-like displays, low-cost identification tags, and flexible photovoltaic cells. These devices may not be fabricated using conventional inorganic materials. In order to commercialize such devices, it is necessary

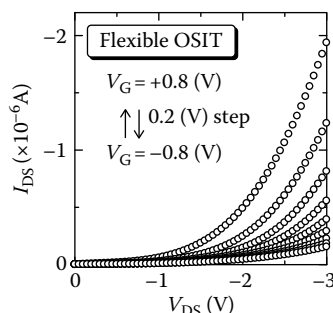
to develop new materials, propose new device processing, and design new device structures.

In this study, the OSIT was fabricated on a flexible plastic substrate using the vacuum evaporation method [17,18]. Pentacene thin film was used as the semiconductor layer and polyethylene naphthalate (PEN) was used as the flexible substrate. The pentacene films were fabricated under a vacuum of  $2 \times 10^{-4}$  Pa. In this case, the estimated gap between the Al gate electrodes was less than 1  $\mu\text{m}$ . For comparison, a pentacene OSIT was also fabricated on an ITO/glass substrate at the same time. Figure 10.16 shows a photograph of the pentacene OSIT fabricated on a PEN film, and Figure 10.17 shows the static characteristics of the flexible OSIT. It was found that the characteristics of the flexible pentacene OSIT were comparable with the non-flexible pentacene OSIT. Figure 10.18 shows the variation of  $I_{DS}$  for the flexible pentacene OSIT under conditions of bending. The variation in the OSITs characteristics is negligible and less than 5% in  $I_{DS}$  when the flexible OSITs is bent to a radius of 10 mm. OLETs can be fabricated by an almost similar procedure to that for OLEDs in flexible displays by replacing glass with plastic substrates.



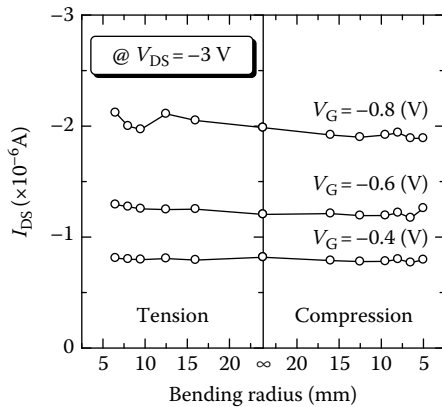
**FIGURE 10.16**

Photograph of a flexible pentacene OSIT.



**FIGURE 10.17**

Static characteristics of the flexible OSITs fabricated on PEN substrates.

**FIGURE 10.18**

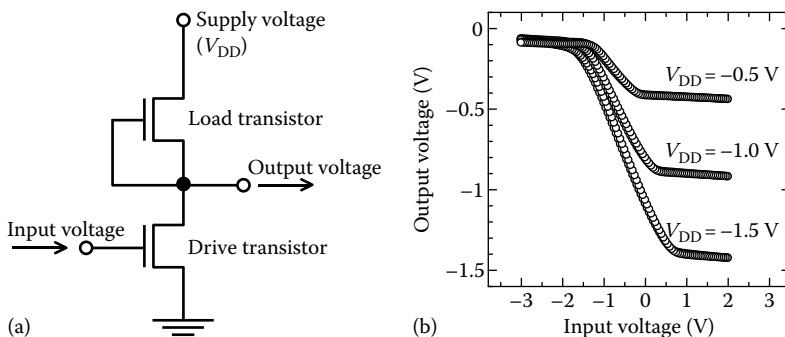
Variation of  $I_{DS}$  for flexible OSITs as a function of the bending radius (compressive and tensile strain).  $I_{DS}$  were measured under various  $V_G$  of  $-0.4$  to  $-0.8$  V at  $V_{DS}$  of  $-3$  V.

### 10.5.2 Organic Logic Devices Based on OSITs

Complementary metal-oxide-semiconductor (CMOS) inverters using organic semiconductors have been used to investigate the fabrication of flexible integrated circuits [39]. However, the operating voltage of CMOSSs based on organic semiconductors [40–50] is higher than that of CMOSSs using inorganic semiconductors because organic semiconductor CMOSSs are composed of OFETs with a lateral-type structure that operate at higher voltages, due to low carrier density and low mobility.

We have studied OSITs with a vertical-type structure in an attempt to overcome the disadvantages of OFETs [15–18, 28, 34–36]. In this study, organic inverters based on pentacene OSITs were fabricated and their characteristics were investigated and compared with those of inverters based on OFETs. In addition, the characteristics of the organic inverters were improved by achieving a higher on/off ratio in the OSITs by the use of the ultrathin CuPc layer as mentioned in Section 10.4.4.1.

Organic inverters consisting of two OSITs were fabricated. For comparison, organic inverters containing two OFETs were also fabricated and their characteristics investigated. The inverter circuit was composed of two p-type organic transistors, a load transistor, and a drive transistor, as shown in Figure 10.19a. For low values of input voltage ( $V_{in}$ ), the drive transistor is in the on-state and the load transistor is in the off-state. As  $V_{in}$  is increased, the drive transistor is gradually turned to the off-state. A further increase in  $V_{in}$  causes the drive transistor to be turned to the off-state and the load transistor turned to the on-state. Eventually, the output voltage ( $V_{out}$ ) reaches the level of the supply voltage ( $V_{DD}$ ).

**FIGURE 10.19**

(a) Schematic of the inverter circuit composed of load and drive transistors, and (b) the transfer characteristics of the OSIT-based inverter.

The inverter transfer characteristics of the organic inverters based on OFETs and OSITs were measured under a variety of bias conditions. Figure 10.19b shows the inverter transfer characteristics of organic inverter based on OSITs. In the OFET-based inverter,  $V_{in}$  was changed continuously from  $-40$  to  $+40\text{ V}$ , while  $V_{DD}$  was varied in the range from  $-10$  to  $-20\text{ V}$ , and the transfer characteristics were measured in each case. Eventually,  $V_{out}$  reached the level of  $V_{DD}$ . In contrast, for the OSIT-based inverter, the  $V_{in}$  was varied from  $-2$  to  $+1\text{ V}$ , while  $V_{DD}$  was varied in the range from  $-0.8$  to  $-1.2\text{ V}$ . However, the eventual value of  $V_{out}$  was smaller than  $V_{DD}$ . These characteristics are thought to be due to the low on/off ratio of the drive and load OSITs. In this case, the on/off ratio of the OSITs used as load and drive transistors were 270 and 370, respectively, at  $V_{DS} = -3\text{ V}$  under applied  $V_G$  from  $-1$  to  $+3\text{ V}$ . To determine the reason for the mismatch in the level of the output voltage, an organic inverter composed of two OSITs with higher on/off ratios was fabricated and the inverter transfer characteristics were measured. The results showed that higher on/off ratios were required in the OSITs acting as load and drive transistors in order to achieve high performance. The results obtained demonstrate that it is possible to decrease the operational voltage of organic inverters from  $\pm 20$  to  $\pm 2\text{ V}$  by the use of two OSITs.

### 10.5.3 Organic Light-Emitting Transistors

Example devices of OLEDs and OLETs are shown schematically in Figure 10.20a and b. The OLETs were combined with the OSITs and OLEDs, which have the OSITs based on  $\alpha$ -NPD and a simple structure similar to the OLEDs [26]. All layers were fabricated on ITO-coated glass substrate using the vacuum evaporation technique at approximately  $10^{-4}\text{ Pa}$ . The substrate temperature was maintained at room temperature during evaporation. The OLET has a grid-type Al gate electrode in the hole-transporting layers of  $\alpha$ -NPD. The grid-type gate electrode was formed using a shadow evaporation mask,

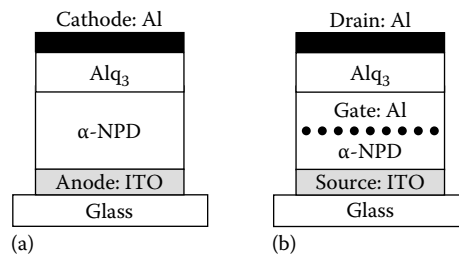
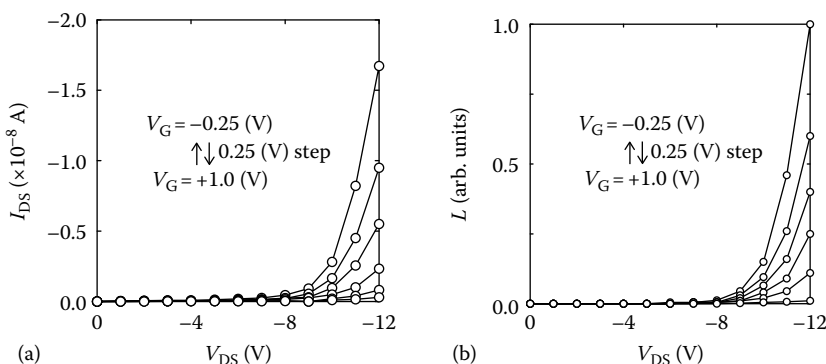


**FIGURE 10.20**  
Cross-sectional structures of (a) OLEDs and (b) OLETs.

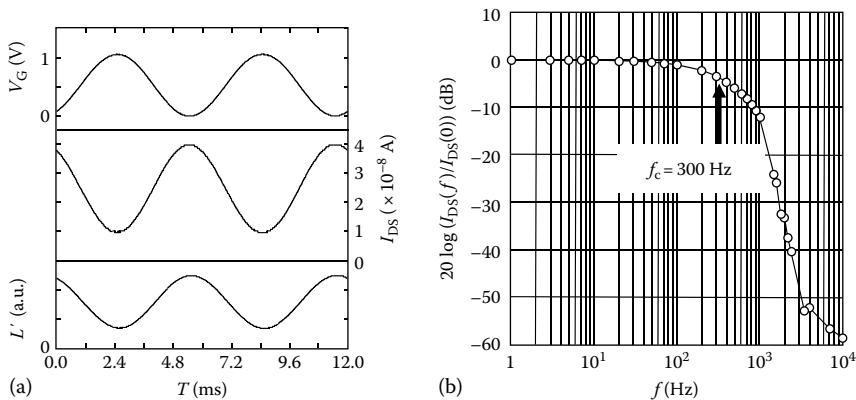
as described in Section 10.4.1.1. The line and space dimensions of the shadow mask are 24 and 18  $\mu\text{m}$ , respectively. Typical thicknesses for the first and second  $\alpha$ -NPD layers are 50 and 30 nm. In this case, tris-(8-hydroxyquinoline) aluminum (Alq<sub>3</sub>, 55 nm) and Al were employed as an emitting layer and top electrode, respectively. The effective electrode area of the OLED and the OLET is approximately 4 mm<sup>2</sup>.

For fabrication of the OLETs, controllability of the grid-type Al gate electrode is important, as with the fabrication of OSITs. In this case, the estimated gate gap,  $W$ , was checked using optical microscopy, and  $W$  was varied between 1 and 24  $\mu\text{m}$ .

Figure 10.21a and b shows the  $I$ - $V$  and luminance–voltage ( $L$ - $V$ ) characteristics of the OLETs as a function of gate voltage,  $V_G$ . The  $I$ - $V$  curve indicates that the Al-slit-gate forms a Schottky barrier to  $\alpha$ -NPD layer, and  $\alpha$ -NPD behaves as a p-type semiconductor. Dynamic characteristics of the OLETs were also measured at room temperature using a silicon photodetector, function synthesizer, and digital storage oscilloscope. The  $I_{DS}$  at a constant  $V_{DS}$  decreases with increasing  $V_G$ . The current is controlled by relatively small  $V_G$  (-1 V) and typical SIT characteristics are obtained for the OLETs. The luminance also varies



**FIGURE 10.21**  
(a)  $I$ - $V$  and (b)  $L$ - $V$  characteristics of OLETs.

**FIGURE 10.22**

Dynamic characteristics of OLETs. (a) Current–luminescence and (b) frequency characteristics.

corresponding to the  $I$ - $V$  characteristics. These results are reasonable because the potential barrier formed by the Schottky gate restricts the current flow from the source to the drain electrodes, and the emitted light is also obstructed by the Al gate electrode (slit gate part in the device structure).

A typical dynamic operation of the OLETs ( $W=5\mu\text{m}$ ) is shown in Figure 10.22. The peak–peak value of the gate voltage and  $V_{DS}$  were  $-0.25$  to  $1.0\text{ V}$  and  $-12$  to  $-15\text{ V}$ , respectively. Luminance intensity,  $L'$ , was measured using a silicon photodiode and were modulated by  $V_G$ . The luminance of the OLET is controlled by gate voltages as low as  $1\text{ V}$ . Excellent dynamic operation at  $60\text{ Hz}$  (Figure 10.22a) and a cutoff frequency of  $0.3\text{ kHz}$  (Figure 10.22b) were obtained.

Future developments of OLETs operating with higher power and speed are expected from the optimization of the device structure, such as the thickness of the organic layers and the dimensions of the gate electrode. In particular, the modulation depth and operational frequency of the OLETs are strongly dependent on the edge features of the gate electrode.

## 10.6 Summary

We have focused on vertical-type organic transistors that operate as SITs. Two types of organic transistors, lateral-type organic transistors (OFETs) and vertical-type organic transistors (OSITs) using CuPc evaporated films were fabricated, and the device performance was measured. Measurement of the static and dynamic characteristics revealed relatively high-current, high-speed, and low-voltage operations for the OSITs. OSITs with a short length between the source, drain, and gate electrodes exhibited improved device

characteristics. Typical SIT operation, with nonsaturating  $I_{DS}$  vs.  $V_{DS}$  characteristics, was observed in the  $V_{DS}$  range measured. It is also expected that the device properties will be improved by controlling the structure of the gate electrode, and by selecting appropriate organic materials with improved electrical characteristics.

There are two important factors to be considered for the improvement of OSIT performance. One factor is the control of the electronic structure, such as the hole injection barrier and band bending at the interface between the organic semiconductor layer and the source electrode. Both high on/off ratio and high current value were achieved for the OSITs by inserting an ultrathin CuPc layer. The experimental results demonstrate that the effect of the ultrathin CuPc layer on the characteristics of OSITs is not only that the hole injection barrier at the interface between pentacene and ITO is decreased, but also that the pentacene film orientation may be controlled. The other factor is fabrication of an Al gate electrode with densified nanoholes, which effectively controls the carrier flow with high current density between the source and drain electrode by the application of the gate voltage.

For the realization of flexible displays based on OSITs, flexible transistors, logic devices, and light-emitting transistors based on OSITs were fabricated. The flexible OSITs exhibited stable electrical characteristics at compressive and tensile strains up to a bending radius of 5 mm. Organic inverters using two OSITs displayed low operational voltage compared to those based on OFETs. The device structures and performance of OLETs combined with OSITs and OLEDs were also investigated. Relatively high luminance modulation with low gate voltage was observed in the OLET by optimizing the gate electrode and layer thicknesses. The results obtained here demonstrate that OSITs are a suitable element for flexible sheet displays.

---

## Acknowledgments

This work was partly supported by the Advanced Organic Device Project contracted by Optoelectronic Industry and Technology Development Association (OITDA) with New Energy and Industrial Organization (NEDO) and the 21st Century COE Program (COE in organic device physics).

---

---

## References

1. Kudo, K., M. Yamashina, and T. Moriizumi. 1984. Field effect measurement of organic dye films. *Jpn. J. Appl. Phys.* 23:130.
2. Dimitrakopoulos, C. D. and P. R. L. Malenfant. 2002. Organic thin film transistors for large area electronics. *Adv. Mater.* 14:99–117.

3. Tsumura, A., H. Koezuka, and T. Ando. 1986. Macromolecular electronic device: Field-effect transistor with a polythiophene thin film. *Appl. Phys. Lett.* 49:1210–1212.
4. Sirringhaus, H., N. Tessler, and R. H. Friend. 1998. Integrated optoelectronic devices based on conjugated polymers. *Science* 280:1741–1744.
5. Dodabalapur, A., Z. Bao, A. Makhija, J. G. Laquindanum, V. R. Raju, Y. Feng, H. E. Katz, and J. Rogers. 1998. Organic smart pixels. *Appl. Phys. Lett.* 73:142–144.
6. Forrest, S. R. 2004. The path to ubiquitous and low-cost organic electronic appliances on plastic. *Nature* 428:911–918.
7. Mori, T. 2008. Molecular materials for organic field-effect transistors. *J. Phys. Condens. Matter* 20:184010.
8. Jurchescu, O. D., M. Popinciuc, B. J. van Wees, and T. T. M. Palstra. 2007. Interface-controlled, high-mobility organic transistors. *Adv. Mater.* 19:688–692.
9. Sze, S. M. and H. K. Gummel. 1966. Appraisal of semiconductor-metal-semiconductor transistor. *Solid State Electron.* 9:751–769.
10. Nishizawa, J., T. Terasaki, and J. Shibata. 1975. Field-effect transistor versus analog transistor (static induction transistor). *IEEE Trans. Electron. Devices* 22:185–197.
11. Bozler, C. O., G. O. Alley, R. A. Murphy, D. C. Flanders, and W. T. Lindley. 1979. Fabrication and microwave performance of the permeable base transistor. *IEEE Tech. Dig. Int. Electron Device Meet.* 384–387.
12. Wright, J. D. 1987. *Molecular Crystals*. Cambridge University Press, Cambridge, U.K.
13. Mott, N. F. and E. A. Davis. 1971. *Electronic Processes in Non-Crystalline Materials*. Oxford University Press, New York.
14. Sze, S. M. 1969. *Physics of Semiconductor Devices*. Wiley, New York.
15. Kudo, K., M. Iizuka, S. Kuniyoshi, and K. Tanaka. 2001. Device characteristics of lateral and vertical type organic field effect transistors. *Thin Solid Films* 393:362–367.
16. Watanabe, Y., H. Iechi, and K. Kudo. 2008. Characteristics of organic inverters using vertical- and lateral-type organic transistors. *Thin Solid Films* 516:2729–2732.
17. Watanabe, Y. and K. Kudo. 2005. Flexible organic static induction transistors using pentacene thin films. *Appl. Phys. Lett.* 87:223505.
18. Watanabe, Y., H. Iechi, and K. Kudo. 2006. Electrical characteristics of flexible organic static induction transistors under bending conditions. *Appl. Phys. Lett.* 89:233509.
19. Van Slyke, S. A., C. H. Chen, and C. W. Tang. 1996. Organic electroluminescent devices with improved stability. *Appl. Phys. Lett.* 69:2160–2162.
20. Parthasarathy, G., P. E. Burrows, V. Khalfin, V. G. Kozlov, and S. R. Forrest. 1998. A metal-free cathode for organic semiconductor devices. *Appl. Phys. Lett.* 72:2138–2140.
21. Huitema, H. E. A., G. H. Gelinck, J. B. P. H. van der Putter, K. E. Kuijk, C. M. Hart, E. Cantatore, P. T. Herwig, A. J. J. M. van Breemen, and D. M. de Leeuw. 2001. Plastic transistors in active-matrix displays. *Nature* 414:599.
22. Sheraw, C. D., L. Zhou, J. R. Huang, D. J. Gundlach, and T. N. Jackson. 2002. Organic thin-film transistor-driven polymer-dispersed liquid crystal displays on flexible polymeric substrates. *Appl. Phys. Lett.* 80:1088–1090.

23. Rogers, J. A., Z. Bao, M. Meier, A. Dodabalapur, O. J. A. Schueller, and G. M. Whitesides. 2000. Printing, molding, and near-field photolithographic methods for patterning organic lasers, smart pixels and simple circuits. *Synth. Met.* 115:5–11.
24. Sirringhaus, H., T. Kawase, R. H. Friend, T. Shimoda, M. Inbasekaran, W. Wu, and E. P. Woo. 2000. High-resolution inkjet printing of all-polymer transistor circuits. *Science* 290:2123–2126.
25. Kudo, K., M. Iizuka, S. Kuniyoshi, and K. Tanaka. 2000. Organic static induction transistor for display devices. *Synth. Met.* 111–112:11–14.
26. Kudo, K. 2005. Organic light emitting transistors. *Curr. Appl. Phys.* 5:337–340.
27. Yang, Y. and A. J. Heeger. 1994. A new architecture for polymer transistors. *Nature* 372:344–346.
28. Kudo, K., D. X. Wang, M. Iizuka, S. Kuniyoshi, and K. Tanaka. 1998. Schottky gate static induction transistor using copper phthalocyanine films. *Thin Solid Films* 331:51–54.
29. Ma, L. and Y. Yang. 2004. Unique architecture and concept for high-performance organic transistors. *Appl. Phys. Lett.* 85:5084–5086.
30. Fujimoto, S., K. Nakayama, and M. Yokoyama. 2005. Fabrication of a vertical-type organic transistor with a planar metal base. *Appl. Phys. Lett.* 87:133503.
31. Fujimoto, K., T. Hiroi, K. Kudo, and M. Nakamura. 2007. High-performance, vertical-type organic transistors with built-in nanotriode arrays. *Adv. Mater.* 19:525–530.
32. Johnson, C. A. and A. M. Lenhoff. 1996. Adsorption of charged latex particles on mica studied by atomic force microscopy. *J. Colloid Interface Sci.* 179:587–599.
33. Rimal, D. S., D. J. Quesnel, and A. A. Busnaina. 2000. The adhesion of dry particles in the nanometer to micrometer-size range. *Colloids Surf. A* 165:3–10.
34. Watanabe, Y., H. Iechi, and K. Kudo. 2006. Effect of ITO surface condition on the characteristics of organic static induction transistors based on pentacene film. *Trans. Mater. Res. Soc. Jpn.* 31(3):593–596.
35. Watanabe, Y., H. Iechi, and K. Kudo. 2007. Improvement in on/off ratio of pentacene static induction transistors by controlling hole injection barrier. *Jpn. J. Appl. Phys.* 46(4B):2717–2721.
36. Watanabe, Y., H. Iechi, and K. Kudo. 2006. Improvement in on/off ratio of pentacene static induction transistors with ultrathin CuPc layer. *Jpn. J. Appl. Phys.* 45(4B):3698–3703.
37. Forsythe, E. W., M. A. Abkowitz, Y. Gao, and C. W. Tang. 2000. Influence of copper phthalocyanine on the charge injection and growth modes for organic light emitting diodes. *J. Vac. Sci. Technol. A* 18:1869–1874.
38. Nishizawa, J. and K. Yamamoto. 1978. High-frequency high-power static induction transistor. *IEEE Trans. Electron Devices* ED-25:314–322.
39. Klauk, H., M. Halik, U. Zschieschang, F. Eder, G. Schmid, and C. Dehm. 2003. Pentacene organic transistors and ring oscillators on glass and on flexible polymeric substrates. *Appl. Phys. Lett.* 82:4175–4177.
40. Brown, A. R., A. Pomp, C. M. Hart, and D. M. de Leeuw. 1995. Logic gates made from polymer transistors and their use in ring oscillators. *Science* 270:972–974.
41. Dodabalapur, A., J. Baumbach, K. Baldwin, and H. E. Katz. 1996. Hybrid organic/inorganic complementary circuits. *Appl. Phys. Lett.* 68:2246–2248.

42. Dodabalapur, A., J. Laquindanum, H. E. Katz, and Z. Bao. 1996. Complementary circuits with organic transistors. *Appl. Phys. Lett.* 69:4227–4229.
43. Klauk, H., D. J. Gundlach, and T. N. Jackson. 1999. Fast organic thin-film transistor circuits. *IEEE Electron Device Lett.* 20:289–291.
44. Lin, Y. Y., A. Dodabalapur, R. Sarpeshkar, Z. Bao, W. Li, K. Baldwin, and V. R. Raju. 1999. Organic complementary ring oscillators. *Appl. Phys. Lett.* 74:2714–2716.
45. Gelinck, G. H., T. C. T. Geuns, and D. M. de Leeuw. 2000. High-performance all-polymer integrated circuits. *Appl. Phys. Lett.* 77:1487–1489.
46. Kane, M. G., J. Campi, M. S. Hammond, F. P. Cuomo, B. Greening, C. D. Sheraw, J. A. Nichols, D. J. Gundlach, J. R. Huang, C. C. Kuo, L. Jia, H. Klauk, and T. N. Jackson. 2000. Analog and digital circuits using organic thin-film transistors on polyester substrates. *IEEE Electron Device Lett.* 21:534–536.
47. Crone, B. K., A. Dodabalapur, R. Sarpeshkar, R. Sarpeshkar, R. W. Filas, Y. Y. Lin, and Z. Bao. 2001. Design and fabrication of organic complementary circuits. *J. Appl. Phys.* 89:5125–5127.
48. Inoue, Y., Y. Sakamoto, T. Suzuki, M. Kobayashi, Y. Gao, and S. Tokito. 2005. Organic thin-film transistors with high electron mobility based on perfluoropentacene. *Jpn. J. Appl. Phys.* 44:3663–3668.
49. Ahles, M., R. Schmechel, and H. V. Seggern. 2005. Complementary inverter based on interface doped pentacene. *Appl. Phys. Lett.* 87:113505.
50. Gundlach, D. J., K. P. Pernstich, G. Wilckens, M. Gruter, S. Hees, and B. Batlogg. 2005. High mobility *n*-channel organic thin-film transistors and complementary inverters. *J. Appl. Phys.* 98:064502.

# 11

---

## *Routes toward High-Efficiency Polymer Solar Cells*

---

Yang Yang, Yan Yao, and Gang Li

### CONTENTS

11.1	Introduction .....	319
11.2	Accurate Efficiency Measurement of Polymer Solar Cells.....	321
11.2.1	Spectral Mismatch Factor.....	322
11.2.2	Spectral Responsivity .....	324
11.2.3	Device Area and Layout.....	326
11.3	Performance Enhancement and Nanomorphology Control in Polymer Solar Cells.....	327
11.3.1	“Thermal Annealing” and “Solvent Annealing” .....	328
11.3.2	Improvement in Absorption.....	329
11.3.3	Improvement in Crystallinity .....	331
11.3.4	Improvement in Nanomorphology .....	331
11.3.5	Improvement in <i>I</i> - <i>V</i> Characteristics .....	335
11.3.6	Improvement in Charge Carrier Mobility.....	336
11.3.7	Improvement in Exciton Generation and Dissociation .....	339
11.4	Novel Device Architectures .....	341
11.4.1	Inverted Polymer Solar Cells.....	341
11.4.2	Laminated Transparent Solar Cells.....	343
11.5	Future Directions .....	345
11.5.1	Low Band-Gap Polymer .....	345
11.5.2	Stacking Solar Cell Structures.....	350
11.5.3	Mixture Solvent Approach .....	351
11.6	Conclusion .....	354
	Acknowledgments .....	355
	References.....	355

---

### 11.1 Introduction

To meet the energy demands of the world in the 21st century, it is necessary to develop affordable renewable energy sources. Today, solar cells based on

organic materials and polymers are considered promising alternatives to their inorganic counterparts. Some of the advantages of organic solar cells are their lightweight, mechanical flexibility, and simple processing as well as easy tunability of chemical properties of the organic materials.<sup>1,2</sup>

Polymeric solar cells, due to easy solution processing, are especially attractive to harness solar energy in a cost-effective way. They are designed based on the phenomenon of photoinduced electron transfer in organic molecules, which is an intensively investigated topic in physics and chemistry.<sup>3</sup> Since the discovery of an efficient photoinduced electron transfer from conjugated polymers to C<sub>60</sub>,<sup>3</sup> significant efforts are underway to improve the efficiency of polymer solar cells to the level of practical applications.<sup>4–6</sup> Device efficiencies around 6% have been reported to date,<sup>7</sup> which is just below the threshold required for commercial development. This also implies that a significant amount of research is required to bring this technology out from the research labs to the market.

In this chapter, we review the recent progress on achieving high efficiency polymer solar cells in the research group at the University of California, Los Angeles. We focus on developing routes from different perspectives toward high efficiency solar cells. It is appropriate to begin by defining the accurate efficiency measuring method. Section 11.2 is an attempt to provide such a method developed for polymer solar cells in collaboration with the National Renewable Energy Laboratory (NREL). We discuss the error sources in the measurements as well as the strategies to minimize their influence. In Section 11.3, we discuss performance enhancement and nanomorphology control in polymer solar cells. It is known that efficiency is strongly related to the processing condition and nanomorphology of the active layer. In the current state-of-the-art bulk heterojunction (BHJ) regioregular (RR) poly(3-hexylthiophene):[6,6]-phenyl-C<sub>61</sub>-butyric acid methyl ester (P3HT:PCBM) blends system, research efforts have led to two highly effective approaches to improve device performance. Comparison between these two approaches is conducted in detail. Section 11.4 covers our efforts on designing novel inverted solar cell architecture and a new low-cost fabrication method by lamination process. Finally, in Section 11.5 we discuss future directions, including but not limited to low band-gap materials, stacking solar cells, and mixture solvent approach.

Before discussing the methods to improve the performance or energy-conversion efficiency of polymer solar cells, it is important to understand the physics that is involved in the conversion of light to electricity in a typical polymer solar cell. The energy conversion, or photovoltaic, process in a polymer solar cell is a multiple step process,<sup>8</sup> which can be described as follows. Step 1—*Incoupling of the photon*: The incoming photons encounter the first interface—glass or plastics—when they hit the device. The reflection losses at the air–substrate interface as well as at each subsequent interface, which depend on the difference between optical refractive indices of the two materials, have to be minimized; Step 2—*Photon absorption*: The incoming photons are then absorbed in the active layer. The absorption spectrum of the active

material should match the solar irradiation for maximum absorption. As a result, low band-gap polymers are highly desired; Step 3—*Exciton formation and migration*: After a photon has been absorbed in the polymer, an exciton is formed. The excitons then diffuse in the material with a characteristic exciton diffusion length ( $L_D$ ) typically of the order of 5–10 nm.<sup>9,10</sup>  $L_D$  depends on the structure of the material and the dielectric properties. The excitons have a finite lifetime and during the diffusion they decay or dissociate through several mechanisms. In order to achieve efficient photovoltaic conversion, the excitons have to be dissociated into free electrons and holes before they decay radiatively, thermally, or vibronically; Step 4—*Exciton dissociation or charge separation*: The most common way to achieve exciton dissociation into free electrons and holes is through photoinduced charge transfer process. The processes that act as counterforce to exciton dissociation are geminate recombination, where separated electrons and holes recombine back to form an exciton, and nongeminate bimolecular recombination, where an electron and a hole from different excitons recombine; Step 5—*Charge transport*: The free charges must then travel through the active layer to reach the electrodes where they can be collected to produce photocurrent. The charge carrier mobilities for both electron and hole therefore play an important role in determining device efficiency. The charge carrier mobility in conjugated polymers is usually very low,<sup>11,12</sup> which makes it necessary to have a thin active layer, which on the other hand reduces the optical absorption; Step 6—*Charge collection*: Finally, the free electrons that reach the electrodes are collected and passed into the outer circuit to generate device photocurrent. The charge collection efficiency depends on the energy level matching at metal–polymer interface, interfacial defects, etc.

---

## 11.2 Accurate Efficiency Measurement of Polymer Solar Cells

As in the case of any new technology that is undergoing rapid progress, standardization is a crucial step for its further development. For healthy development of polymer solar cell technology, it is critical to accurately determine the efficiency values for a fair comparison with results among various research groups. Significant efforts have been made in the past to accurately determine the efficiency of solar cells, and a standard test method has been established.<sup>13,14</sup> Unfortunately, for organic solar cells, these internationally accepted norms are seldom followed at the research level, partially due to lack of awareness of these norms, limited resources, and/or relatively low efficiency. As a result, efficiency values under various testing conditions have been reported in the literature, which makes reliable comparison between data from different research groups very difficult. Some efforts have sought to motivate the organic solar cell community toward adopting standards for accurately

measuring efficiency.<sup>15–17</sup> People have realized pushing the accuracy of measurements to the highest possible level and seeking independent confirmation of results will eventually benefit the whole organic solar cell community.<sup>18</sup>

Here we point out three important factors that need to be carefully examined during the efficiency measurement: spectral mismatch factor, spectral responsivity measurement, and the device area and layout. They are discussed in detail in the following sections. For calibration and measurement purpose, two types of P3HT:PCBM blend solutions were prepared—1:1 wt. ratio (20 mg/mL P3HT) in dichlorobenzene (DCB)<sup>4</sup> and 1:0.8 wt. ratio (10 mg/mL P3HT) in chlorobenzene (CB)<sup>5,19</sup>—to fabricate two types of devices named P3HT:PCBM(DCB) and P3HT:PCBM(CB), respectively. Solar cells were also fabricated with MEH-PPV:PCBM (MEH-PPV: poly(2-methoxy-5-(2'-ethyl-hexyloxy)-1,4-phenylene vinylene) wt. ratio of 1:4 and DCB as solvent<sup>17</sup> and CuPc/C<sub>60</sub>/BCP (CuPc: copper phthalocyanine, and BCP: bathocuproine).<sup>17</sup>

### 11.2.1 Spectral Mismatch Factor

The current reference spectrum adopted by the international terrestrial PV community is given in Standard IEC 60904-3 (*Measurement principles for terrestrial PV solar deices with reference spectral irradiance data*, International Electrotechnical Commission, Geneva) and ASTM Standard G159 (*Standard tables for reference solar spectral irradiances: direct normal and hemispherical on 37° tilted surface*, American Society for Testing and Materials, West Conshacken, PA). The irradiance incident on the PV cell is typically measured with a reference cell. For *I-V* measurements with respect to a reference spectrum, there is a spectral error in the measured  $I_{SC}$  of the PV cell because of the following two reasons: (i) the spectral irradiance of the light source does not match the reference spectrum, which is computer generated, and (ii) the spectral responses of reference detector and test cell are different. This error can be expressed as spectral mismatch correction factor ( $M$ ):<sup>20,21</sup>

$$M = \frac{\int_{\lambda_1}^{\lambda_2} E_{\text{Ref}}(\lambda) S_R(\lambda) d\lambda}{\int_{\lambda_1}^{\lambda_2} E_{\text{Ref}}(\lambda) S_T(\lambda) d\lambda} \frac{\int_{\lambda_1}^{\lambda_2} E_S(\lambda) S_T(\lambda) d\lambda}{\int_{\lambda_1}^{\lambda_2} E_S(\lambda) S_R(\lambda) d\lambda} \quad (11.1)$$

where

$E_{\text{Ref}}(\lambda)$  is the reference spectral irradiance

$E_S(\lambda)$  is the source spectral irradiance

$S_R(\lambda)$  is the spectral responsivity of the reference cell

$S_T(\lambda)$  is the spectral responsivity of the test cell, each as a function of wavelength ( $\lambda$ )

A matched photovoltaic reference cell is typically used as the reference detector and a solar simulator is used as the light source to minimize the deviation

of  $M$  from unity. Once  $M$  is known, the measured photocurrent needs to be scaled by dividing  $M$  to obtain photocurrent under AM 1.5G standard testing condition. For the purpose of light-source calibration for organic solar cell testing, a reference cell with spectral response matching that of the actual test cells is preferred to minimize the spectral error, which is not being numerically corrected for. The spectral responsivities of three reference cells are shown in Figure 11.1a: the unfiltered Si diode shows significant response in the wavelength range of 400–1100 nm; and the response for Si diode with KG5 color filter is exhibited in a wavelength range of 350–700 nm, which is similar to our testing organic cells, making it more suitable for use in calibrating the light

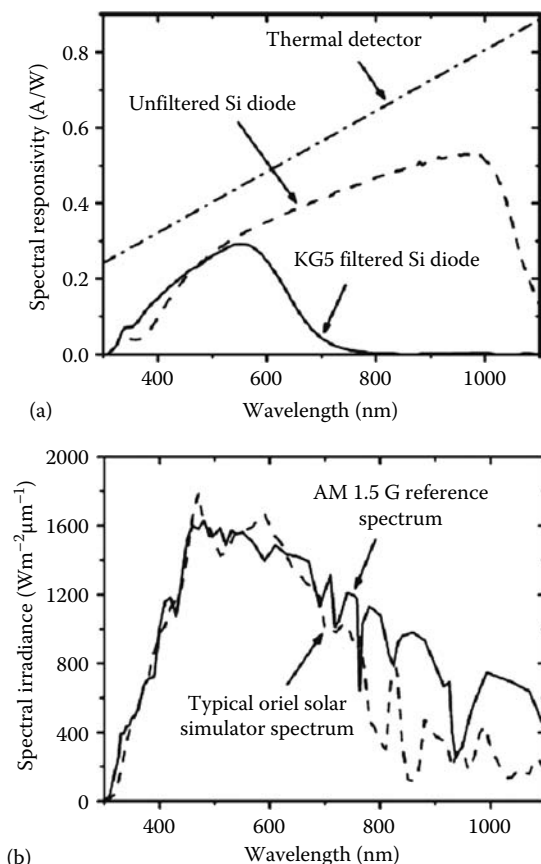


**FIGURE 11.1**

(a) Spectral responsivities of three types of reference cells: Unfiltered monocrystalline Si diode, Si diode with KG5 color filter, and thermal detector. (b) Spectral irradiance data for AM 1.5G reference spectrum (IEC 60904) and the typical source irradiance for an Oriel 150W solar simulator with AM 1.5G filters (obtained from Newport Corporation). Both spectra are plotted for intensities normalized to  $100\text{ mW/cm}^2$ . (Reused from Shrotriya, V. et al., *Adv. Funct. Mater.*, 16, 2016, 2006. With permission.)

intensity of the solar simulator. The reference spectrum used is the AM 1.5G standard spectrum and the source irradiance spectrum is the typical irradiance spectrum for Oriel 150W solar simulator with AM 1.5G filter (Newport Corporation). The reference and source spectra used for calculating  $M$  are shown in Figure 11.1b. The  $M$  values calculated for different test cell/reference cell combinations are summarized in Table 11.1. Using a Si diode with KG5 color filter as a reference cell for light-source calibration has a clear advantage over an unfiltered Si diode and a thermal detector. The mismatch factor values are very close to unity for the samples when a KG5 filtered Si diode is used as the reference cell, whereas the mismatch is 31%–35% for unfiltered Si diode and 33%–37% for thermal detector. It is therefore very important to consider the spectral mismatch and include it in the efficiency calculation.

### 11.2.2 Spectral Responsivity

The spectral responsivity measurements yield the number of collected electrons per incident photon at each wavelength. Hence it is also called incident photon to collected electron (IPCE), or external quantum efficiency (EQE) measurement. IPCE is given as

$$\text{IPCE (EQE)} = \frac{n_e}{n_{ph}} = \frac{I_{SC}}{P_{OPT}} \frac{hc}{\lambda e} \quad (11.2)$$

where

$n_e$  is the number of photoelectrons generated

$n_{ph}$  is the number of incident photons

The spectral responsivity,  $S(\lambda)$ , can be calculated from the IPCE value by

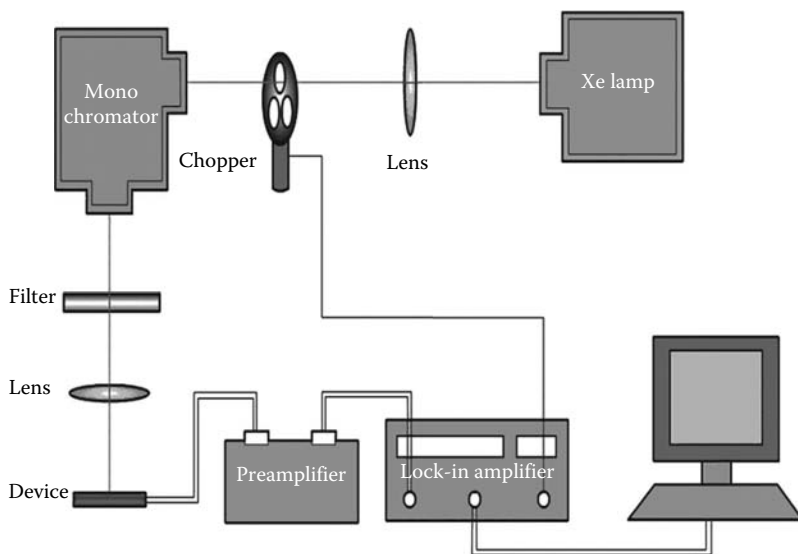
$$S(\lambda) = \frac{q\lambda}{hc} \text{IPCE}(\lambda) \quad (11.3)$$

**TABLE 11.1**

Spectral Mismatch Factors Calculated with Respect to the AM 1.5G Reference Spectrum for Various Test Cell/Reference Cell Combinations

Test Cell Type	Mismatch Factors for Different Reference Cells		
	KG5 Color Filtered	Unfiltered	Thermal Detector
MEH-PPV:PCBM	0.99	1.32	1.35
P3HT:PCBM(CB)	1.01	1.35	1.37
P3HT:PCBM(DCB)	1.01	1.35	1.37
CuPc/C <sub>60</sub> /BCP	0.98	1.31	1.33

Source: Reused from Shrotriya, V. et al., *Adv. Funct. Mater.*, 16, 2016, 2006.  
With permission.

**FIGURE 11.2**

Schematic of IPCE measurement setup.

IPCE measurement is an important method to cross-check with *I-V* measurement to assure the accuracy of efficiency. Integrating solar cell spectral responsivity and solar irradiance reference spectrum gives a good estimate of the photocurrent under short-circuit condition. IPCE is measured under the illumination of incident light from a xenon lamp passing through a grating monochromator with a typical intensity of tens of  $\mu\text{W}$ . The incident beam is chopped with a mechanical chopper and focused on the testing finger of the device. The photocurrent signal is then amplified using a trans-impedance amplifier and detected with a lock-in amplifier. A calibrated crystalline silicon diode is always used as a reference before each measurement. The schematic of a measurement setup is shown in Figure 11.2.

IPCE measurement is typically conducted under the condition of no external electric bias. Sometimes in order to probe the field-dependence of the photocurrent in the testing device, reverse electric bias can be applied through the preamplifier. Because the dark current generated at reverse bias is a DC signal and therefore is excluded by the lock-in amplifier, the dark current will not interfere with the testing photocurrent signal. A lock-in amplifier has high signal-to-noise ratio, which is of crucial importance to achieve accurate IPCE data. In some systems, picoampere meter is used instead of lock-in amplifier. The data collected in this way is not as accurate since the leakage current cannot be excluded and may be counted as photocurrent.

Bias light is typically applied during the IPCE measurement. It has been reported that IPCE shows a significant reduction upon flooding with white light in some organic PV cells.<sup>22</sup> This reduction in IPCE suggests that the device is limited by space-charge build-up in the device and charge recombination is an issue. This can be understood as following: the light bias will induce higher carrier concentration; the increased number of charge carriers increases recombination and hinders carrier transport due to space-charge within the device structure. Hence the IPCE-light bias measurement can also provide information on the charge recombination and transport in the device.

### 11.2.3 Device Area and Layout

To accurately determine the current density through the device, it is crucial to correctly measure the device area. Usually, the device area is chosen as the area defined by the shadow mask used for evaporating the top contact. An important factor that can result in significant errors in the estimation of the area is the shadow effect arising from evaporating successive layers from multiple sources. One such example is the Ca/Al top electrode used in our study. Figure 11.3 shows an optical microscopy image of copper (30 nm) and gold (40 nm) metal layers successively evaporated onto a substrate. The two metals were chosen because the difference in film color makes it easier to see the shadow effect when observed under an optical microscope. For six

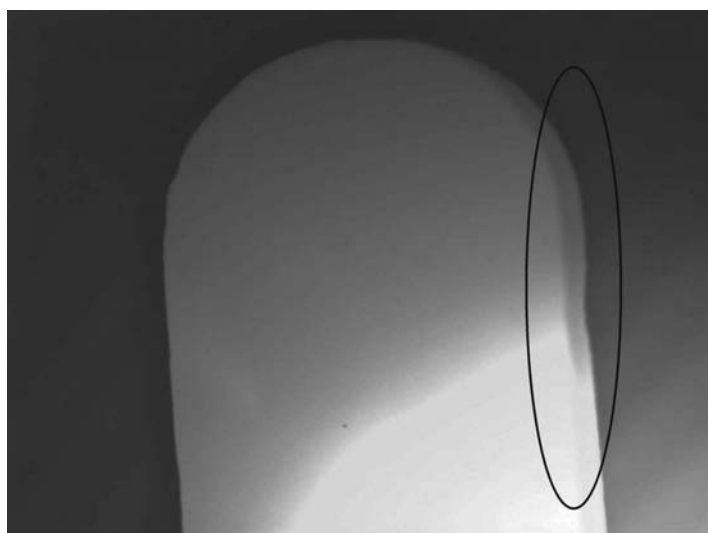


**FIGURE 11.3**

The grayscale optical microscope image of Cu and Au layers evaporated on an ITO substrate to demonstrate the shadow effect. The incomplete overlap of the two metallic films which results in a reduction in the device area is highlighted by the black oval. (Reused from Shrotriya, V. et al., *Adv. Funct. Mater.*, 16, 2016, 2006. With permission.)

different films prepared in this manner, the actual device area (defined by the overlapped area of the Cu and Au films) was  $91\% \pm 3\%$  of the total area. It is clear that the shadow effect can therefore result in up to 12% error in current-density values. However, the shadow effect can be reduced significantly by adjusting the mask orientation in such a way that the device (finger) length direction is parallel to the connecting line between the sources. Hence the device area for each device should be measured separately to correct the values of current density.

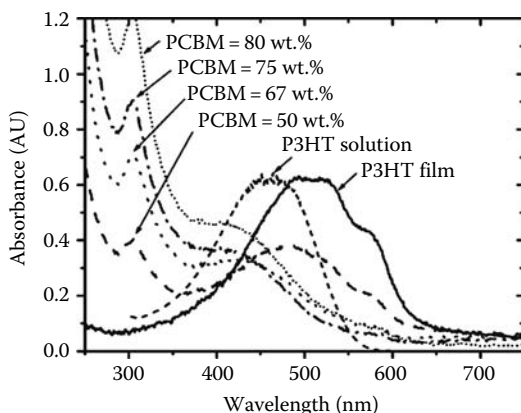
Recently, Cravino et al. have also addressed the importance of device layout (size and shape) on the evaluation of device performance.<sup>23</sup> They emphasized that devices with crossing electrodes and unpatterned organic layers can collect a nonnegligible current from regions usually not considered as part of the photovoltaic element. This fact may lead to an overestimation of the power conversion efficiency (PCE).

---

### 11.3 Performance Enhancement and Nanomorphology Control in Polymer Solar Cells

Significant amount of research has been dedicated to two material systems MDMO-PPV:PCBM<sup>24,25</sup> (MDMO-PPV:poly(2-methoxy-5-(3',7'-dimethyloctyloxy)-1,4-phenylenevinylene)) and RR-P3HT:PCBM, which represent the state-of-the-art polymer solar cell technology. Because there are excellent review papers on the MDMO-PPV:PCBM system in the literature,<sup>26</sup> in this section we will only focus on the recent improvements in RR-P3HT:PCBM system, especially the approaches to optimize the active blend layer for enhancing device efficiency.

The application of RR-P3HT to improve polymer solar cell performance, however, is not straightforward. Figure 11.4 shows the ultraviolet-visible (UV-Vis) absorption spectra for pure RR-P3HT and RR-P3HT:PCBM blend films with different concentrations of PCBM.<sup>27</sup> The films are spin-cast at 3000 rpm for 1 min in a nitrogen filled glove box. The solvent is removed very fast during spin-coating and polymer blend films with very smooth surface are produced. For pure P3HT films the solid-state absorption spectra shows three features—two peaks and one shoulder at the longest wavelength. The first two bands can be attributed to the  $\pi-\pi^*$  transition, whereas the shoulder is due to the interchain interaction. The absorption of the films with increasing amount of PCBM reduces significantly in the visible range, specifically between 450 and 600 nm which is the peak absorption range for RR-P3HT. The modification of the absorption spectra in the films with PCBM can be attributed to the interaction between the polymer chains and the PCBM molecules where the presence of PCBM molecules lowers the interaction among the P3HT chains upon increased disordering in the blend films.<sup>28</sup>

**FIGURE 11.4**

Absorption of RR-P3HT solution and RR-P3HT:PCBM blend films with different weight ratios of PCBM. (Reused from Shrotriya, V. et al., *Chem. Phys. Lett.*, 411, 138, 2005. With permission.)

Since the donor/acceptor (D/A) blend is critical, strategies must be developed to improve light harvesting and to improve charge carrier transport in the RR-P3HT:PCBM system for enhanced polymer solar cell performance. Over the last few years, research efforts have led to two highly effective approaches toward this end. One approach is *thermal annealing* of the polymer:fullerene films or completed devices, and the second is *solvent annealing*. In the following section, we will focus on the two approaches, and shed some light on the whole picture of the P3HT:PCBM system.

### 11.3.1 “Thermal Annealing” and “Solvent Annealing”

While the direct comparison of efficiency among different groups is difficult due to the lack of common measurement standards and missing spectral mismatch correction in most cases, significant improvement in device performance upon thermal annealing in P3HT:PCBM system is clearly the central theme in all the studies. Mild thermal treatment at 55°C was shown to improve the efficiency of P3HT:fulleropyrrolidine solar cells from 0.1% to 0.6% by Camioni et al.<sup>29</sup> Dittmer et al. studied photovoltaic cells with P3HT and a small molecule dye *N,N*-bis(1-ethylpropyl)-3,4:9,10-perylene bis(tetracarboxyl diimide) (EP-PTC) as electron donor and acceptor, respectively.<sup>30</sup> It was observed that thermal annealing at 80°C for 1 h led to highest EQE of 11%, an improvement by a factor of 1.6 compared to an untreated device. In 2003, Padinger et al.<sup>31</sup> reported 3.5% PCE polymer solar cells by annealing RR-P3HT:PCBM blend. The demonstration of this high efficiency stimulated extensive studies on thermal annealing approach and PCE up to 5% were reported.<sup>5,6,19,28,32,33</sup>

However, only a partial recovery of the RR-P3HT absorption in the blend film after thermal annealing (to be discussed in Section 11.3.2) suggests that this approach is not sufficient to fully exploit the potential of RR-P3HT:PCBM system. Additional evidence is the fact that thicker film does not lead to a more efficient device, indicating the existence of the carrier transport bottleneck. These limitations can be overcome through another approach called “solvent annealing.” Instead of recovering the RR-P3HT crystallinity (ordering), which is lost during the fast solvent removing (fast spin-coating) process, this approach aims at maintaining the polymer ordering during the film formation stage. Reducing solvent-removing speed results in self-organization in polymer chains by controlling the active polymer layer growth rate from solution to solid-state. The intrinsic polymer self-organization capability gives higher absorption, higher carrier mobility, and balanced carrier transport. In solvent annealing, high boiling point solvent and low spin speed are chosen and the films were in liquid phase after spin-coating. The films formed by slowly removing the solvent in covered glass Petri dish are referred as slow-grown films, while the fast removal of solvent by heating the spin-cast film gives fast-grown films.

In the following sections, we will discuss and compare the effect of two approaches on absorption, polymer crystallinity, nanomorphology, *I*-*V* characteristics, charge carrier mobility, and exciton generation and dissociation.

### 11.3.2 Improvement in Absorption

Figure 11.5 shows the UV–Vis absorption spectra obtained for P3HT:PCBM thin films before and after annealing at different temperatures (70°C,

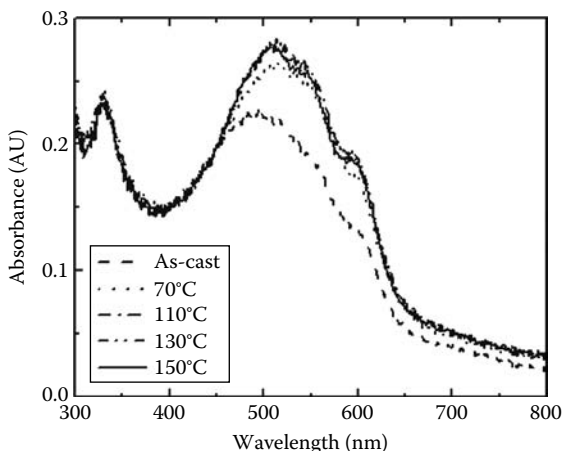


**FIGURE 11.5**

UV–Vis absorption spectra obtained for P3HT:PCBM thin films (80 nm, with PCBM conc. = 50 wt.%) before and after annealing at different temperatures. The annealing time is 10 min for all the films. (Reused from Li, G. et al., *J. Appl. Phys.*, 98, 043704, 2005. With permission.)

110°C, 130°C, and 150°C for 10 min).<sup>33</sup> The absorption enhancement seems to saturate at 110°C after which increasing the annealing temperature has no positive effect on absorbance. Interestingly, annealing the films at 110°C also gives maximum photocurrent in the solar cells fabricated in the same study. Similar phenomena are also reported by Mihailetti et al.<sup>34</sup> Chirvase et al.<sup>28</sup> demonstrated that the absorption of pure RR-P3HT or PCBM shows only a slight change whereas significant enhancement in RR-P3HT absorption is observed in the blend films.

The effect of solvent annealing is shown in Figure 11.6 and compared with thermal annealing. The absorption for the slow-grown film is significantly stronger compared to that of fast-grown film. The three vibronic absorption features are the most prominent reported in the literature, indicating strong interchain–interlayer interaction of RR-P3HT chains, as well as well-maintained polymer ordering in the blend films. After annealing at 110°C for 20 min, the absorbance of fast-grown film shows significant increment and the vibronic features become clearer, indicating a partial recovery of ordering. For the slow-grown film, the absorption spectra shows no significant difference before and after thermal annealing, further strengthening the argument that the slow-grown film already has a high degree of ordering. The absorption of the slow-grown film is a simple addition of the absorption of the two components in the film, which strongly supports the occurrence of phase segregation and the formation of crystalline RR-P3HT domains in the blend film. PCBM absorption is clearly unaffected by solvent-removing speed, which indicates that the driving force of device improvement is self-organization of polymer through solvent annealing process.

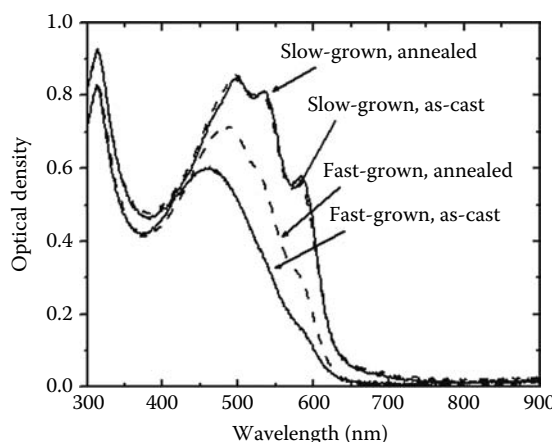


**FIGURE 11.6**

UV-Vis absorption spectra for slow- and fast-grown P3HT:PCBM films, before and after thermal annealing at 110°C for 20 min.

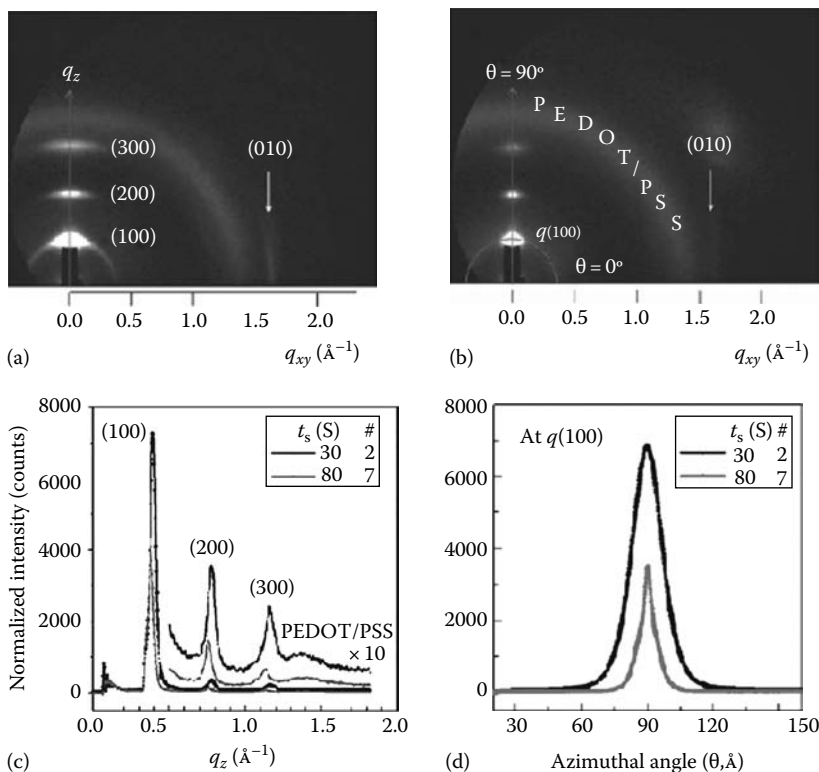
### 11.3.3 Improvement in Crystallinity

The improved long-wavelength absorption of P3HT upon thermal annealing is only one part of the story. Due to the enhanced crystallinity of the polymer film, the hole mobility in P3HT also improves along with enhanced absorption. The improvement in hole mobility plays a significant role in device efficiency improvement, since hole mobility of P3HT donor is comparatively lower than the electron mobility of PCBM, which is recognized as a major bottleneck in device performance. In the nonannealed blend films, the primary peaks are significantly diminished indicating significant reduction in polymer crystallinity. The crystallinity is clearly improved upon thermal annealing. Erb et al.<sup>35</sup> conducted x-ray diffraction (XRD) study on as-cast and thermal annealed RR-P3HT:PCBM (1:2 wt. ratio) films. After thermal annealing a single peak appeared corresponding to the polymer chain *a*-axis orientation (main chain parallel and side chains perpendicular to the substrate), with layer spacing of  $1.61 \pm 0.2$  nm. The mean size of the RR-P3HT crystallites was found to be about 8 nm. In addition to the common observation of enhanced crystallinity in all cases, it was observed that the ordering of RR-P3HT is hampered by the amount of PCBM, which agrees with the UV-Vis absorption spectra. Kim et al.<sup>6</sup> also observed crystallization enhancement after annealing the P3HT:PCBM blend films at 140°C by grazing incidence x-ray diffraction (GIXD) measurements. Erb et al.<sup>35</sup> have also reported enhancement in photoluminescence (PL) of RR-P3HT in the blend films upon thermal annealing, indicating the reduction of interface area between the polymer and the PCBM where the PL quenching occurs. These results are consistent with the improved polymer crystallization where more pure RR-P3HT and PCBM domains are formed. It is worthwhile to mention that while this phase separation reduces exciton dissociation, the improved charge carrier transport in both donor and acceptor phases after thermal annealing offsets the former effect and results in overall improvement in device performance.

In comparison, the overall crystalline structure of RR-P3HT in the solvent annealed RR-P3HT:PCBM 1:1 wt. ratio blend films has been studied with the aid of GIXD analysis using synchrotron source in Brookhaven National Lab.<sup>36</sup> 2D GIXD patterns of the solvent-annealed blend film clearly (Figure 11.7) show the intense reflections of (100) layer and (010) crystals along the  $q_z$  (substrate normal) and  $q_{xy}$  (substrate parallel) axis, respectively, implying that the films have highly ordered edge-on hexyl-side chains and parallel  $\pi$ -conjugated planes of RR-P3HT with respect to the substrate (same as in pure P3HT films).<sup>37,38</sup> The GIXD peaks are much stronger than that based on thermal annealing,<sup>6</sup> indicating superior crystallinity obtained in this approach.

### 11.3.4 Improvement in Nanomorphology

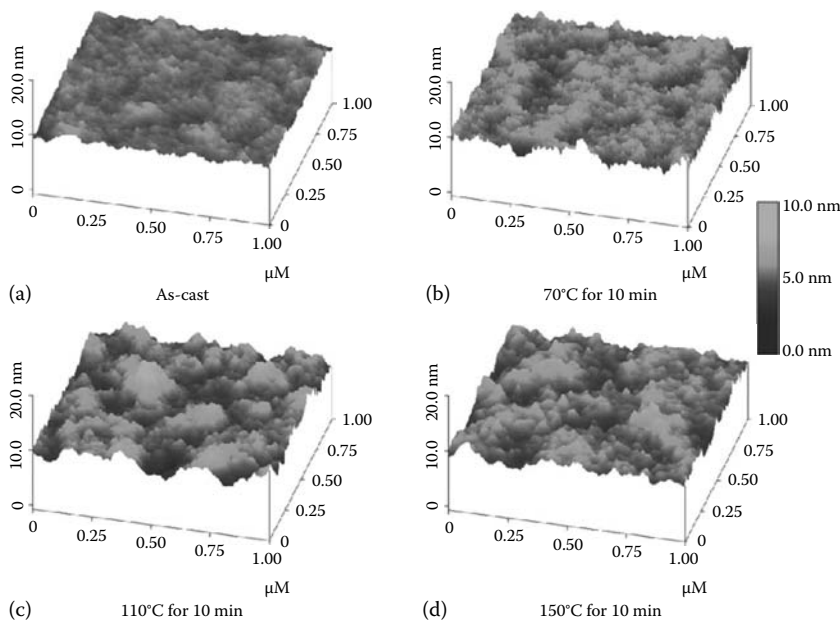
In the BHJ polymer solar cells, efficient exciton dissociation requires large interfacial area between polymer and PCBM. On the other hand, fast charge

**FIGURE 11.7**

2D GIXRD patterns of 1:1 RR-P3HT:PCBM films (spin-coated at 1000 rpm) fabricated with different  $t_s$ : (a) 30 s and (b) 80 s. 1D out-of-plane (c) X-ray and (d) azimuthal scan (at  $q(100)$ ) profiles extracted from (a) and (b). (Reused from Li, G. et al., *Adv. Funct. Mater.*, 17, 1636, 2007. With permission.)

carrier transport requires continuous pathways to be formed and large domains or semicrystalline structures are preferred. Hence the optimum nanomorphology should be a balance between a large interfacial area and continuous pathways for carrier transportation. The morphology of the polymer blend layer reflects the phase separation and plays important roles in determining device performance.<sup>39,40</sup> In this section, we discussed the nanomorphology of the active layer and demonstrated the effects of thermal annealing and solvent annealing in controlling nanomorphology. Without any annealing, devices typically show low efficiency because PCBM is finely dispersed between P3HT chains and suppressed P3HT crystallite formation. To heal the disordered polymer chains, PCBM must be redistributed (demixed) to allow better polymer chain alignment.

Atomic force microscope (AFM) images of the polymer film surface before and after thermal annealing at different temperatures are shown in Figure 11.8.<sup>33</sup> The surface of the as-cast film is very smooth with rms roughness ( $\sigma_{\text{rms}}$ )

**FIGURE 11.8**

AFM height images of the P3HT:PCBM surface (a) before annealing, and after annealing at (b) 70°C, (c) 110°C, (d) 150°C for 10 min. (Reused from Li, G. et al., *J. Appl. Phys.*, 98, 043704, 2005. With permission.)

of 0.377 nm. After undergoing thermal treatment, the  $\sigma_{\text{rms}}$  first increases up to 110°C and then decreases. The film texture also changes after annealing. The film annealed at 110°C shows a much coarser texture with broad hill-like features compared to the other films. Higher film roughness gives higher device efficiency. However, the surface area of the roughest film is only about 0.1% more than that of a completely flat surface. Therefore the increased surface roughness probably does not play any direct role in efficiency improvement. Instead, higher surface roughness is more likely a signature of annealing enhanced ordered structure formation in the polymer film. Higher absorption and increase in the charge carrier mobility due to ordering are the most likely reasons for efficiency enhancement. An increase in surface roughness upon annealing was also observed independently by other groups.<sup>5,19</sup>

In the transmission electron microscopy (TEM) study on the effect of thermal annealing of P3HT:PCBM system, Yang et al.<sup>41</sup> reported that the P3HT crystals grow continuously into longer fibrils upon thermal annealing, as a signature of enhanced polymer crystallinity. Another important observation is the emergence of segregated PCBM crystalline structure after thermal annealing, different from the uniform PCBM distribution in the as-cast film. The PCBM crystalline structure, however, does not grow into large size crystals as observed in MDMO-PPV:PCBM (1:4 wt. ratio)

films upon annealing.<sup>42</sup> Yang et al. suspected that growth of P3HT crystallites forms boundaries to hamper the extensive diffusion of PCBM molecules and their large-scale crystallization. This is especially helpful for the long-term stability of these devices due to the formation of stable film morphology upon thermal annealing. Indeed, the devices show relatively good stability under 70°C for 1000 h illumination.

The effect of solvent annealing on the nanomorphology is more significant. The AFM height and phase images (Figure 11.9) show that slow-grown film (a) has  $\sigma_{\text{RMS}} \sim 9.5 \text{ nm}$ , whereas fast-grown film (b) has very smooth surface with  $\sigma_{\text{RMS}} \sim 0.87 \text{ nm}$ . The rough surface of slow-grown film is most likely a signature of polymer (blend) self-organization which in turn enhances ordered structure formation in the film. The peak to valley height of the slow-grown film is about 100 nm, corresponding to 50% of the mean thickness (210 nm). The phase image of the fast-grown film (d) shows coarse chain-like (fibrillar) features running across the surface. These fibrillar features are assigned to the domains of pure P3HT crystallites. The region between these features is disorder zone, which harbors structural defects like chain ends and folds as wells as tie segments.<sup>43</sup> PCBM molecules suppress the formation of P3HT crystallites in the fast-grown films and most of the film consists of mixed domains which are amorphous in nature. For the slow-grown film (c), the crystalline domains of pure P3HT chains are denser. They have strong tendency of forming an interconnecting network and are distributed more uniformly throughout the film. The separation distance between the features is also less, which suggests tighter packing of P3HT crystallites in the

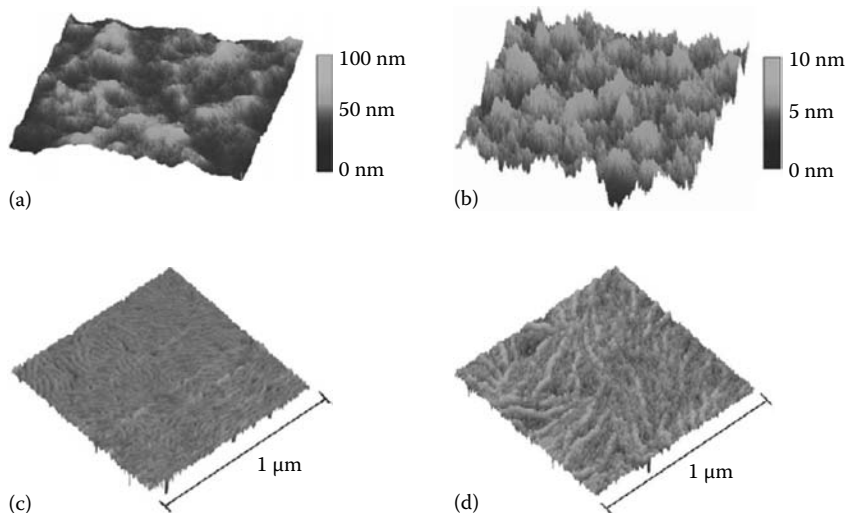


**FIGURE 11.9**

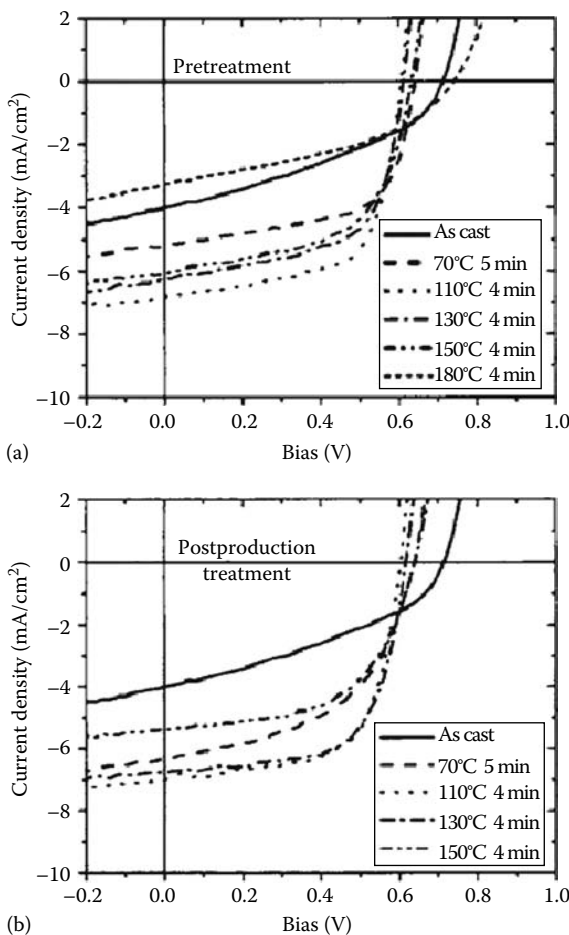
AFM images for different growth rate of polymer active layer. Height images for (a) slow- and (b) fast-grown films. Phase images for (c) slow- and (d) fast-grown films.

slow-grown film. The separation distance between surface features in slow-grown film (~28 nm) is smaller than that in fast-grown film (~55 nm). The crystallite size estimated from AFM phase images matches the results from XRD data on similar films,<sup>35</sup> where mean crystallite size estimated from Scherrer's equation is 10–50 nm. The reduced crystallite size and intercrystallite spacing are believed to be the result of higher ordering. P3HT chains get more time to self-organize into a more ordered structure during very slow growth. As a result, the regions of mixed P3HT/PCBM domains will reduce.

### 11.3.5 Improvement in *I*–*V* Characteristics

For thermal annealed devices, *I*–*V* curves were shown in Figure 11.10 and postannealed device at 110°C for 10 min gives the best performance. For the solvent-annealed devices, as shown in Figure 11.11,  $J_{SC}$  reduces from 9.9 mA/cm<sup>2</sup> in a device with slow-grown highly ordered active layer to 4.5 mA/cm<sup>2</sup> in that with fast-grown active layer, showing the effect of solvent annealing approach. The device series resistance,  $R_{SA}$ , increases from 2.4 to 19.8 Ω·cm<sup>2</sup>, with increasing film growth rate. The FF also decreases from 60.3% to 52.0%. The low  $R_{SA}$  of 2.4 Ω·cm<sup>2</sup> (for slow-grown device) is comparable to that of much thinner devices (~48 nm),<sup>33</sup> underlining the effect of self-organization. Although solvent-annealed films consist of highly ordered polymer chains, which cannot be achieved through thermal annealing, the extra step of annealing the films provides further enhancement in device performance due to different effects. The *I*–*V* curves under illumination for four devices with annealing (at 110°C) times ( $t_A$ ) are shown in Figure 11.11b. All four devices were made from blend films which were slow-grown. Upon annealing,  $J_{SC}$  increases slightly from 9.9 to 10.6 mA/cm<sup>2</sup>, FF increases from 60.3% to 67.4%, and the PCE improves from 3.5% to 4.4%. Under the dark condition, the rectification ratios are close to 10<sup>7</sup> at a bias of 2 V. The reason behind high FF in slow-grown devices is believed to be the significantly large thickness of the active layer. The thickness of the active layer makes it free of pin-holes and microcracks and all devices show very high shunt resistance in the range of 180–640 MΩ as derived from the *I*–*V* characteristics measured under the dark. The ultrahigh shunt resistance reduces the noise equivalent power of the device and makes it ideal for photodetector applications. Moreover, the surface of the active layer becomes smoother upon annealing which enables a very good, defect-free contact with the metal cathode, thereby increasing the FF values.

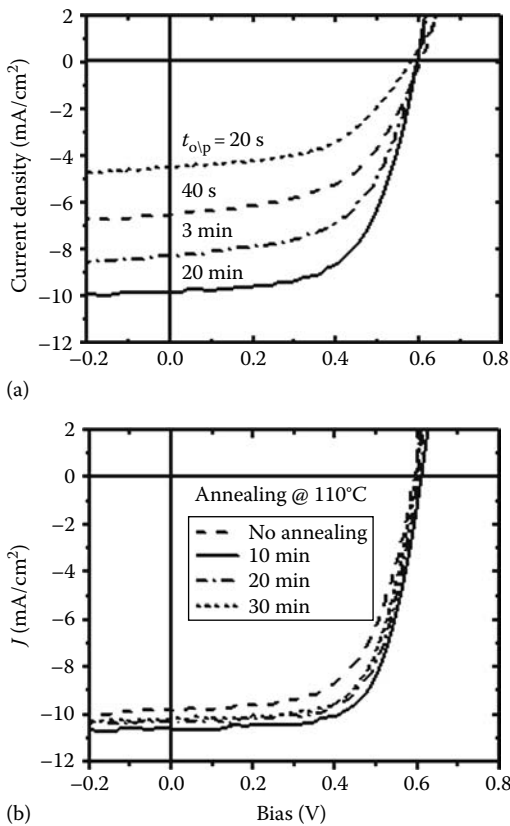
The EQE for the device with fast-grown film shows a maximum of ~19% at a wavelength of 350 nm. On the other hand, for the device with slow-grown film, the EQE maximum increases by more than three times to ~63% at 500 nm (Figure 11.12). This increase in EQE over the wavelength range of 350–650 nm contributes to the increase in the PCE of the devices. The enhancement in EQE clearly originates from two important contributions: an increase in the charge carrier mobility and increased absorption in the active layer.

**FIGURE 11.10**

*I*-*V* characteristics under an illumination of  $100 \text{ mW/cm}^2$  (AM 1.5G) for devices that have undergone annealing (a) pretreatment and (b) postproduction treatment. The different curves represent different annealing temperatures ranging from RT to  $180^\circ\text{C}$ . (Reused from Li, G. et al., *J. Appl. Phys.*, 98, 043704, 2005. With permission.)

### 11.3.6 Improvement in Charge Carrier Mobility

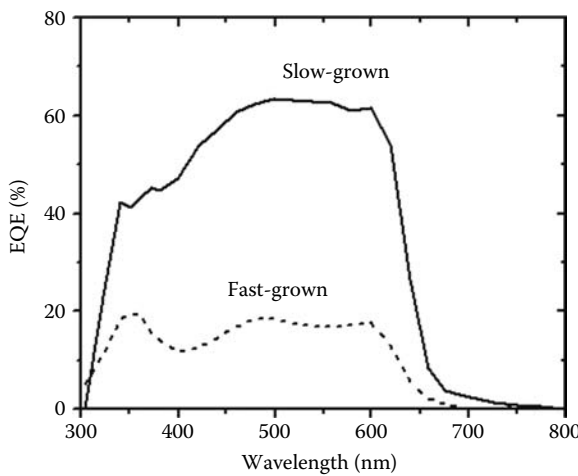
Time-of-flight (TOF) study (Figure 11.13) conducted on slow- and fast-grown films at  $E \sim 2 \times 10^5 \text{ V/cm}$  shows that in slow-grown film both electron and hole transport is nondispersive with  $\mu_e = 7.7 \times 10^{-5}$  and  $\mu_h = 5.1 \times 10^{-5} \text{ cm}^2/\text{V s}$ , whereas for fast-grown film dispersive hole transport and significant reduction in  $\mu_h$  to  $5.1 \times 10^{-6} \text{ cm}^2/\text{V s}$  is observed.<sup>4</sup> The electron mobility increases slightly to  $1.1 \times 10^{-4} \text{ cm}^2/\text{V s}$ . The destruction of ordered structure during fast growth is believed to be the reason. In addition, in the slow-grown film the

**FIGURE 11.11**

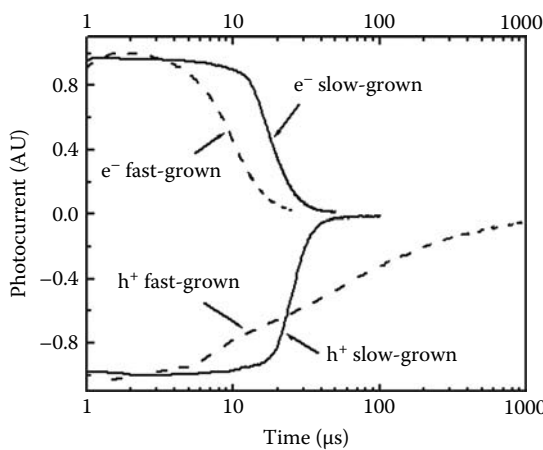
(a)  $I$ - $V$  characteristics under illumination for devices with different film growth rates by varying the solvent evaporation time,  $t_{\text{evp}}$ . (b)  $I$ - $V$  curves for devices with an active layer before and after thermal annealing at 110°C for 10, 20, and 30 min. The active layer thickness was 210 nm and the film growth time was  $t_{\text{evp}} \sim 20$  min.

ratio between electron and hole mobilities is close to unity ( $\mu_e/\mu_h \sim 1.5$ ) resulting in balanced carrier transport in the active layer.

The electron and hole mobilities are also measured by fitting the dark  $J$ - $V$  curves for single carrier devices to space charge limited current (SCLC) model at low voltages,<sup>44</sup> where the current is given by  $J = 9\epsilon_0\epsilon_r\mu V^2/8L^3$ , where  $\epsilon_0\epsilon_r$  is the permittivity of the polymer,  $\mu$  is the carrier mobility, and  $L$  is the device thickness. The hole-only devices using high work function ( $\Phi_F$ ) metal oxide  $\text{MoO}_3$  ( $\Phi_F = 5.3$  eV) to replace Ca, and electron-only devices with low work function  $\text{Cs}_2\text{CO}_3$  to replace poly(3,4-ethylenedioxythiophene)poly(styrenesulfonate) (PEDOT:PSS) in regular solar cell structure are tested with the active layer of P3HT/PCBM obtained by slow and fast growth. For the fast-grown films the mobilities are  $\mu_e \sim 6.5 \times 10^{-8}$  and  $\mu_h \sim 1.9 \times 10^{-9} \text{ m}^2/\text{V s}$ . For slow-grown film the

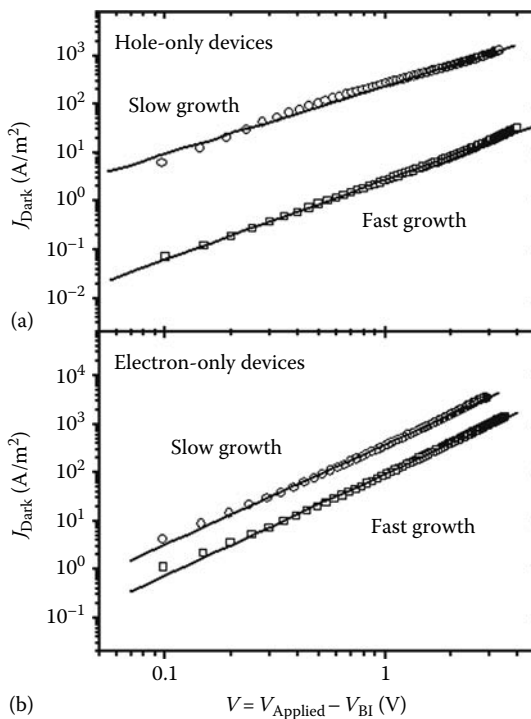
**FIGURE 11.12**

EQE for P3HT:PCBM solar cells for two types of active layers: Slow- and fast-grown. The efficiency maximum for the slow-grown film is  $\sim 63\%$  which is more than three times that of the fast-grown film ( $\sim 19\%$ ).

**FIGURE 11.13**

TOF signals of slow- and fast-grown films plotted on a semilog scale. Films were prepared in the same way as cells in this study with film thickness of about  $1\text{ }\mu\text{m}$ .

electron mobility increases by four times to  $2.6 \times 10^{-7}\text{ m}^2/\text{V s}$ , and the hole mobility increases by about two orders of magnitude to  $1.7 \times 10^{-7}\text{ m}^2/\text{V s}$ . The ratio of electron to hole mobility is about 1.5 (Figure 11.14). Independently, Mihailescu et al. also reported a similar study on device with slow-grown active layer with no further thermal annealing.<sup>45</sup> A hole mobility of  $5.0 \times 10^{-7}\text{ m}^2/\text{V s}$  was derived from the model. This value represents a 33-fold increment

**FIGURE 11.14**

$J$ - $V$  curves in the dark for (a) hole-only and (b) electron-only device for different growth rate. The solid lines represent the fit to the experimental data using SCLC model. (Reused from Shrotriya, V., *Appl. Phys. Lett.*, 89, 063505, 2006. With permission.)

of the RR-P3HT hole mobility compared to the device with optimized thermal annealing only.<sup>34</sup> The high hole mobility leads to balanced electron transport and hole transport, and reduced space-charge accumulation. Active layer thickness over 300 nm does not lower the device fill factor and photocurrent. The superior performance of device with slow-grown active layer over thermally annealed device is attributed to the improved absorption of incoming photons.

### 11.3.7 Improvement in Exciton Generation and Dissociation

The effect of solvent annealing on photocurrent generation in the device has been studied by examining  $I$ - $V$  curves measured in reverse bias under 100 mW/cm<sup>2</sup> simulated AM 1.5G conditions using a method adopted by Mihailescu et al.<sup>46,47</sup> for MDMO-PPV/PCBM system. At large reverse bias ( $V_{\text{EFF}} = V_0 - V > 10$  V), photocurrent ( $J_{\text{PH}}$ ) saturates for both devices with saturation photocurrent ( $J_{\text{SAT}}$ ) of ~125 A/m<sup>2</sup> for the fast- and ~155 A/m<sup>2</sup> for the slow-grown film. The maximum generation rate ( $G_{\text{max}}$ ; given as  $J_{\text{SAT}} = eG_{\text{max}}L$ )

is  $3.5 \times 10^{27} \text{ m}^{-3}\text{s}^{-1}$  and  $4.4 \times 10^{27} \text{ m}^{-3}\text{s}^{-1}$  for the fast- and slow-grown films, respectively, for film thickness  $L=220 \text{ nm}$  (Figure 11.15). Upon changing the growth rate of the film from fast to slow, the  $e-h$  pair generation in the film increases by about 26%, which is attributed to the increased absorption in the slow-grown film as discussed earlier.

Onsager's theory of ion-pair dissociation in weak electrolytes,<sup>48</sup> later modified by Braun,<sup>49</sup> has been used in the system. In fast-grown film, at the short-circuit condition ( $V_{\text{EFF}}=V_0$ ) only 57% of the total photogenerated  $e-h$  pairs dissociate into free carriers, which further reduces to 41% at the maximum power output point ( $V=0.4 \text{ V}$ ). This suggests that more than half of the generated  $e-h$  pairs are lost due to recombination in fast-grown films. On the other hand, the  $e-h$  pair dissociation efficiency of the device with slow-grown film is more than 80% at the short-circuit condition. At the maximum power output bias, the dissociation efficiency is still around 70%. Such high dissociation efficiency numbers clearly demonstrate the effect of self-organization induced ordering in the blend films.

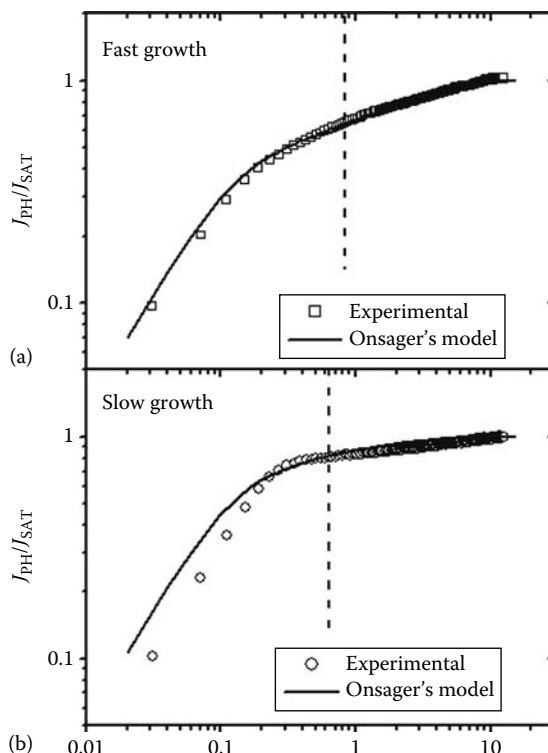


**FIGURE 11.15**

Measured (open symbols) and calculated (solid curves) normalized photocurrent as a function of effective applied bias for (a) fast- (b) slow-grown films. (Reused from Shrotriya, V., *Appl. Phys. Lett.*, 89, 063505, 2006. With permission.)

---

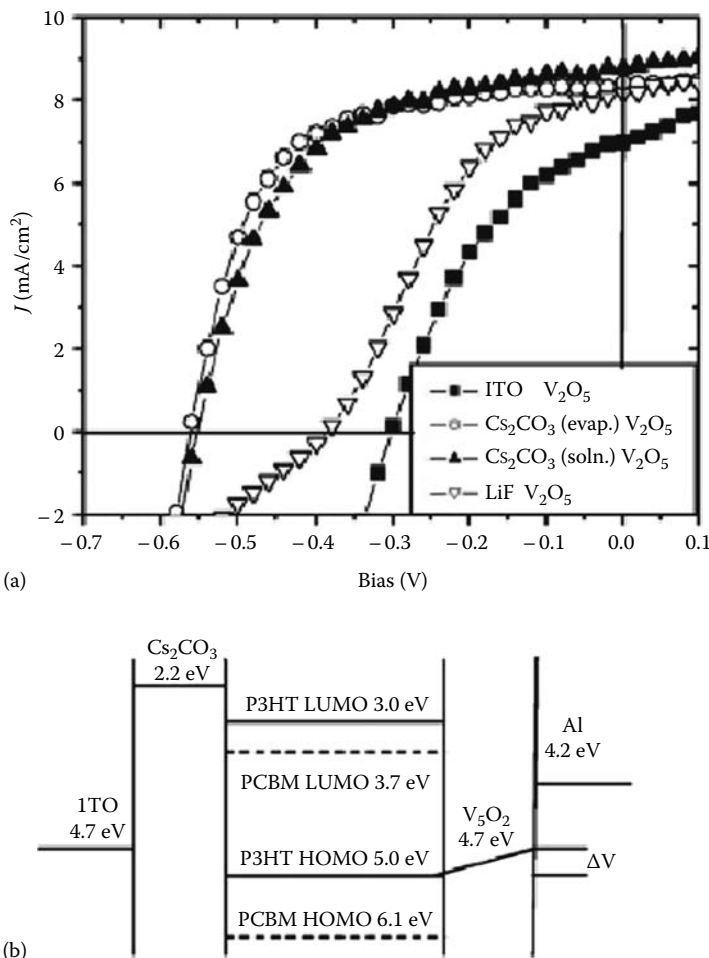
## 11.4 Novel Device Architectures

### 11.4.1 Inverted Polymer Solar Cells

Here we show that the polarity of polymer solar cells can be reversed by changing the position of two interfacial layers: vanadium oxide ( $V_2O_5$ ) layer as hole injection and cesium carbonate ( $Cs_2CO_3$ ) layer as electron injection, independent of the top and bottom electrodes.<sup>50</sup> Since our first demonstration of inverted solar cells, more and more interests have focused on this new architecture. Waldauf et al. demonstrated inverted solar cells with a solution-processed titanium oxide interfacial layer.<sup>51</sup> White et al. developed a solution-processed zinc oxide interlayer as efficient electron extraction contact and achieved 2.58% PCE with silver as a hole-collecting back contact.<sup>52</sup> It is noteworthy to mention that EQE value for inverted solar cells approaches 85% between 500 and 550 nm, which is higher than that of normal polymer solar cells. This is possibly due to (i) the positive effect of vertical phase separation of active layer to increase the selection of electrode and (ii) lower series resistance without the PEDOT:PSS layer.

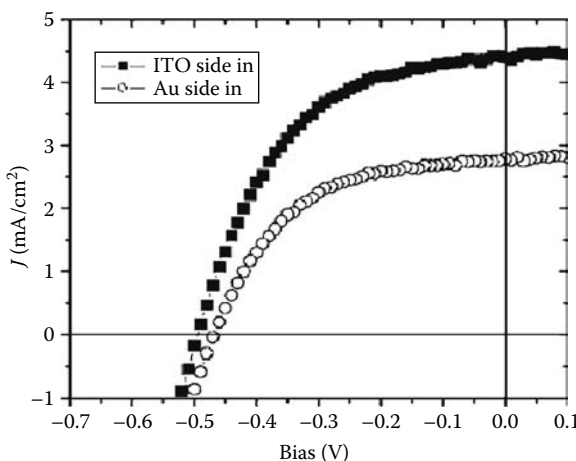
Efficient inverted polymer solar cell can be fabricated with the following device structure: indium tin oxide (ITO)/ $Cs_2CO_3$ /P3HT:PCBM/ $V_2O_5$ /Metal.  $Cs_2CO_3$  is a relatively new interfacial material, which was first reported for organic light-emitting device (OLED) applications by Canon group.<sup>53</sup> Studies on  $Cs_2CO_3$  indicated that during thermal evaporation,  $Cs_2CO_3$  decomposes into cesium oxide. Ultraviolet photoemission spectroscopy (UPS) measurements show a work function of 2.2 eV for thermally evaporated  $Cs_2CO_3$  films.<sup>54</sup>  $V_2O_5$  was also demonstrated to replace P3DOT:PSS as the anodic buffer layer in polymer solar cells.<sup>55</sup> The highest occupied molecular orbital (HOMO) level of thermally evaporated  $V_2O_5$  film was determined by UPS to be 4.7 eV, which is identical to that of ITO.

Figure 11.16a shows  $J$ - $V$  curves for various inverted polymer solar cell structures. The ITO/polymer blend/ $V_2O_5$  (10 nm)/Al inverted solar cell has  $J_{SC} = 6.97 \text{ mA/cm}^2$ ,  $V_{OC} = 0.30 \text{ V}$ , FF = 41.2%, and PCE of 0.66%. This provides evidence for the presence of surface dipoles that enhance the  $V_2O_5$  work function by ~0.3 eV. Based on these results, an efficient inverted polymer solar cell can be achieved with the following structure: ITO/ $Cs_2CO_3$ /polymer blend/ $V_2O_5$ /Al, where  $Cs_2CO_3$  can be either thermally evaporated or spin-coated. The  $J$ - $V$  curves for solar cells with thermally evaporated (1 nm, open circle) and solution-processed (solid triangle)  $Cs_2CO_3$  clearly demonstrate efficient inverted solar cells. The  $J_{SC}$ ,  $V_{OC}$ , and FF are very similar for the evaporated (8.42 mA/cm<sup>2</sup>, 0.56 V, 62.1%) and the solution-processed (8.78 mA/cm<sup>2</sup>, 0.55 V, 56.3%) device. The overall efficiencies are 2.25% and 2.10%, respectively. Recently, we have further optimized the process by annealing the  $Cs_2CO_3$  layer and up to 4.2% efficiency was achieved for inverted polymer solar cells.<sup>56</sup>

**FIGURE 11.16**

(a) Current-voltage characteristics of inverted solar cells. The interfacial layers at ITO/blend and blend/Al interfaces are (i) none,  $\text{V}_2\text{O}_5$  (solid square); (ii)  $\text{Cs}_2\text{CO}_3$  (evaporated),  $\text{V}_2\text{O}_5$  (open circle); (iii)  $\text{Cs}_2\text{CO}_3$  (solution process),  $\text{V}_2\text{O}_5$  (solid triangle); and (iv) LiF,  $\text{V}_2\text{O}_5$  (open inverted triangle). (b) Energy level diagrams for various materials in the inverted solar cells. (Reused from Li, G. et al., *Appl. Phys. Lett.*, 88, 253503, 2006. With permission.)

The energy level diagrams for various inverted configurations are illustrated in Figure 11.16b. Based on above information, we can treat  $\text{V}_2\text{O}_5$  as a hole injection layer with “effective” work function of ~5.0 eV and  $\text{Cs}_2\text{CO}_3$  as an electron injection layer with very low work function, both of which provide ohmic contacts to the active layer. The polarity of the device is decided by the relative positions of these two interfacial layers and is insensitive to the conducting electrodes.

**FIGURE 11.17**

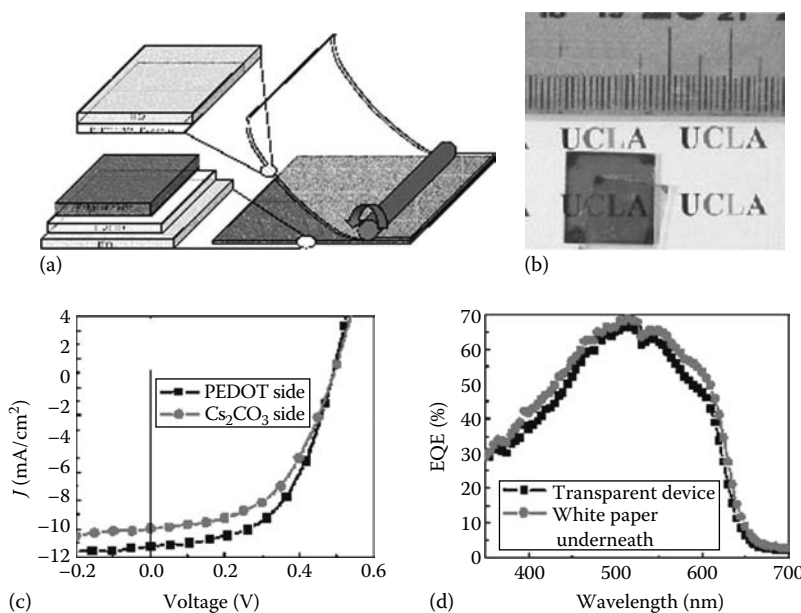
$I$ - $V$  curves for transparent polymer solar cells illuminated from two transparent electrodes—ITO and Au. (Reused from Li, G. et al., *Appl. Phys. Lett.*, 88, 253503, 2006. With permission.)

Transparent polymer solar cells (i.e., polymer solar cells with transparent electrodes) can be easily fabricated based on inverted architecture and have important application in tandem architectures as well. We can form transparent solar cells by replacing the Al top electrode with 12 nm Au in the inverted structure. The  $J$ - $V$  curves for this transparent polymer solar cell, with light incident from ITO and Au side, are shown in Figure 11.17. The difference between the two  $J$ - $V$  curves is due to the partial loss by the reflection and absorption at the semitransparent Au electrode. To provide sufficient electrical conductance, Au layer thickness has to be sufficient and the optical loss at Au electrode becomes significant. However, the inverted solar cell structure has the  $\text{V}_2\text{O}_5$  layer which is not only transparent but also provides effective protection to the polymer layer. A transparent conductive oxides electrode, such as ITO, can therefore be deposited without compromising device performance.

#### 11.4.2 Laminated Transparent Solar Cells

Based on inverted solar cells, we further demonstrated a lamination process using the conductive polymer glue. This method has the advantage of being low-cost, undergoing self-encapsulation, and providing high transparency for various applications. It is potentially easy to be adopted in large area device fabrication through roll-to-roll printing process.

The device fabrication process is illustrated in Figure 11.18a and can be described in the following steps. Step-I is the selection of two transparent substrates coated with a transparent conductor such as ITO, fluorine-doped tin oxide (FTO), or a high conductivity polymer, etc. In Step-II, one substrate

**FIGURE 11.18**

(a) Scheme for the device fabrication; (b) picture of one device; (c)  $I$ - $V$  curve of the device under illumination of  $100 \text{ mW/cm}^2$ ; (d) EQE of device with and without a piece of white paper underneath. (Reused from Huang, J., *Adv. Mater.*, 20, 415, 2008. With permission.)

is coated with a very thin low work function buffer layer ( $\text{Cs}_2\text{CO}_3$ ) to act as the low work function cathode, followed by the coating of polymer active layer. Step-III is the coating of conductive polymer glue to the other transparent substrate. We use a modified conducting polymer PEDOT:PSS as the electronic glue, which is spin-coated to form the adhesive anode. Step-IV is the lamination process: after drying both the substrates, they are laminated together by exerting force so that the two substrates are tightly glued together. During this lamination, a plastic rod with proper hardness rolls the plastic substrate to get rid of the air bubbles. Both substrates are heated at a temperature of  $105^\circ\text{C}$ – $120^\circ\text{C}$  during the lamination process. And then the finished devices are kept on the hotplate for 5–10 min for the final heat treatment. The PEDOT:PSS was purposely modified to become adhesive, so that the two separate films form good contact at the interface, both electronically and mechanically. This adhesive and conductive PEDOT:PSS layer was obtained by doping D-sorbitol into PEDOT:PSS.<sup>57</sup> It has been successfully demonstrated in polymer light-emitting diodes.<sup>57</sup> The 200 nm thick P3HT:PCBM polymer blend film was deposited by the solvent annealing to enhance device efficiency. Either glass or plastic can be used as the transparent substrates. Figure 11.18b shows the picture of an all-plastic solar cell with

device area of  $\sim 40\text{ mm}^2$ . With both cathode and anode being transparent, a semitransparent polymer solar cell is formed. Transparency of around 70% is obtained in the wavelength range where polymer/PCBM has no absorption which makes this device suitable for application in stacking devices to make full use of the solar spectrum.

Figure 11.18c shows the  $I$ - $V$  curve of the device under an illumination of  $100\text{ mW/cm}^2$ . The active area is defined by a mask of  $4\text{ mm}^2$ .  $J_{SC}$  of  $11\text{ mA/cm}^2$  form the ITO/PEDOT:PSS side, and  $10\text{ mA/cm}^2$  from the ITO/ $\text{Cs}_2\text{CO}_3$  side are obtained. Figure 11.18d shows the EQE of the device with or without white paper on the back. The purpose of placing a piece of paper is to reflect the unabsorbed light back to the device for secondary absorption. The maximum EQE obtained is 67% at  $514\text{ nm}$  for the transparent device, which further increases to close to 70% with a paper placed behind.  $V_{OC}$  is  $0.48\text{ V}$ , which is lower than that of regular device ( $0.6\text{ V}$ ), possibly from the reduced work function of PEDOT:PSS by D-sorbital doping<sup>58</sup>, the high resistance of plastic ITO, and/or extra dark current in the unilluminated area. The obtained preliminary power efficiency reaches 3% under AM 1.5 with spectral mismatch correction. Higher solar cell performance is feasible upon further optimization of parameters such as the ITO conductivity, the PEDOT:PSS conductivity, the work functions, etc.

---

## 11.5 Future Directions

### 11.5.1 Low Band-Gap Polymer

One limitation of energy conversion process in plastic solar cells is the limited overlap between the active layer absorption and the solar spectrum. Over 60% of the total solar photon flux is at wavelengths  $\lambda > 600\text{ nm}$ , with approximately 50% in the red and near-infrared spectrum. As a result of poor absorption of current materials, a significant amount of photons have not been utilized and there is still a tremendous room for improvement on device efficiency. A large amount of research efforts has already been devoted to the development of new polymers with band-gaps lower than those of current state-of-the-art RR-P3HT.<sup>59</sup> The absorption edge of RR-P3HT:PCBM film is around  $650\text{ nm}$  and extending the band-gap of polymer to  $900\text{ nm}$  or beyond will increase the photon absorption in the active layer by 100% or more. To improve the efficiency, the energy level offset between the donor polymer and the acceptor has to be minimized while still allowing sufficient energy offset for efficient exciton dissociation. Finally, the polymers with high hole mobility values are desired. Scharber et al.<sup>60</sup> and Koster et al.<sup>61</sup> have independently modeled the energy-conversion efficiency versus band-gap and lowest unoccupied molecular orbital (LUMO) level of donor polymer,

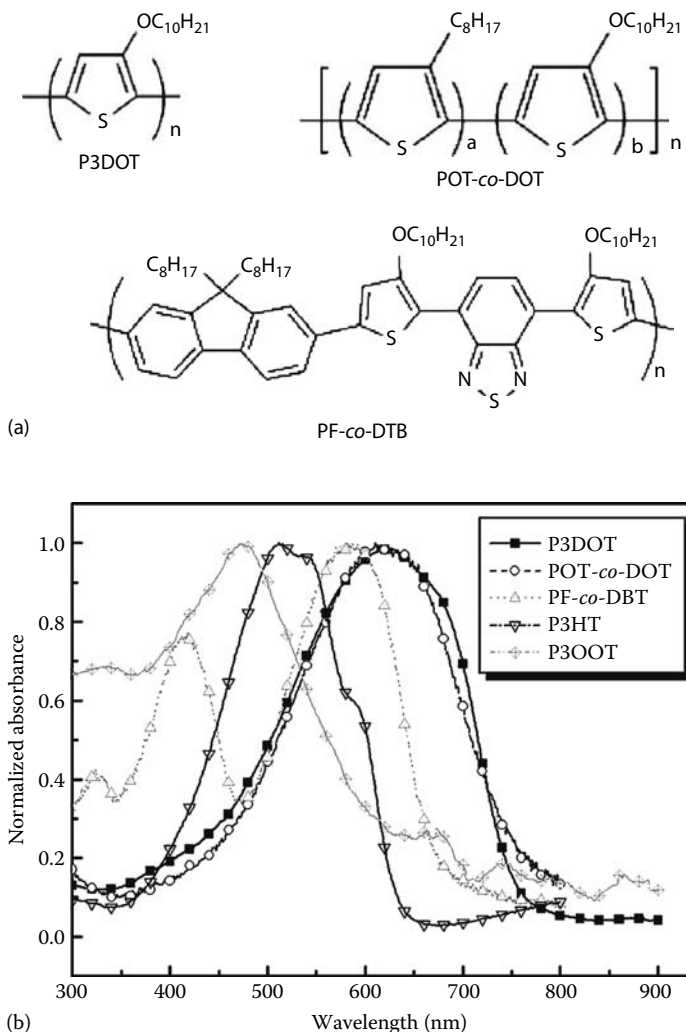
and HOMO level of acceptor. By assuming the high fill factor achieved in RR-P3HT:PCBM system, single layer polymer solar cell with efficiency over 10% under standard reporting condition (SRC) is predicted.

A large amount of research efforts have already been devoted to prepare low band-gap polymers<sup>62–67</sup> and were recently reviewed by Bundgaard and Krebs.<sup>62</sup> Synthetic principles for band-gap control<sup>68</sup> has been established and several promising low band-gap polymer:PCBM systems have been reported.<sup>63–66</sup> It is also realized the following factors are equally important as the band-gap control, and should be addressed simultaneously in the polymer design: LUMO level,<sup>60</sup> charge carrier mobility,<sup>69</sup> absorption profile<sup>70</sup> and extinction coefficient,<sup>71</sup> molecular weight<sup>72</sup> and polydispersity, impurity,<sup>73</sup> and doping.<sup>74</sup> The challenge is to realize all the preferred properties in one polymer.

Two RR copolymers of 3-alkoxythiophene have been synthesized recently.<sup>75</sup> Compared to RR poly(3-alkylthiophenes), the incorporation of an alkoxy group to the 3-position of the thiophene ring yields poly(3-alkoxythiophenes) (P3AOT) with significant red-shift absorption. This may be attributed to both the electron-donating effect of the alkoxy group and the more coplanar conformation of the P3AOT. P3AOT does not have sufficiently high uniformity and environmental stability.<sup>75</sup> Hence two copolymers poly(3-decyloxythiophene-*co*-3-octylthiophene) (POT-*co*-DOT) and poly{(9,9-diptylfluorene)-2,7-diyl-*alt*-[4,7-bis(3-decyloxythien-2-yl)-2,1,3-benzo thiadiazole]-5',5"-diyl} (PF-*co*-DTB) were synthesized.

Figure 11.19 shows the chemical structures of polymers and their optical absorption spectra of thin films. Regiorandom poly(3-octyloxythiophene) (P3OOT) prepared by oxidative polymerization using  $\text{FeCl}_3$ <sup>76</sup> and RR-P3HT are also plotted for comparison. The spectrum of RR POT-*co*-DOT thin film has an absorption maximum at ~621 nm. The band-gap is 1.64 eV, which is lower than that of the regiorandom P3OOT and RR-P3HT due to the RR structure and electron-donating decyloxy side chain. UV-Vis absorption spectrum of PF-*co*-DTB has two absorption peaks at 420 and 581 nm, respectively. The onset of the optical absorption is at about 700 nm. The band-gap is 1.77 eV, which is ~0.14 eV lower than of P3HT. The HOMO and LUMO levels determined using cyclic voltammetry are -4.55 and -2.91 eV for POT-*co*-DOT, and -5.14 and -3.36 eV for PF-*co*-DTB.

Photovoltaic performance has been tested for the two polymers with a layered structure of glass/ITO/PEDOT:PSS/polymer:PCBM blend/LiF/Al. The PCE for POT-*co*-DOT is quite low, due to high dark current or low shunt resistance and low  $V_{\text{OC}}$ . Raising HOMO closer to LUMO of PCBM diminishes the values of  $V_{\text{OC}}$ . However, solar cells made from PF-*co*-DTB exhibits higher PCE with a high value of  $V_{\text{OC}}$  up to 0.76 V. The best obtained performance is from the blend with the wt. ratio of PF-*co*-DTB to PCBM being 1:4. The  $J_{\text{SC}}$  is 4.31 mA/cm<sup>2</sup>,  $V_{\text{OC}}$  is 0.76 V, FF is 48.6%, and PCE is 1.6%. Annealing at 110°C increased the  $V_{\text{OC}}$  from 0.76 to 0.79 V. However, the  $J_{\text{SC}}$  was decreased with no enhancement on the overall PCE.

**FIGURE 11.19**

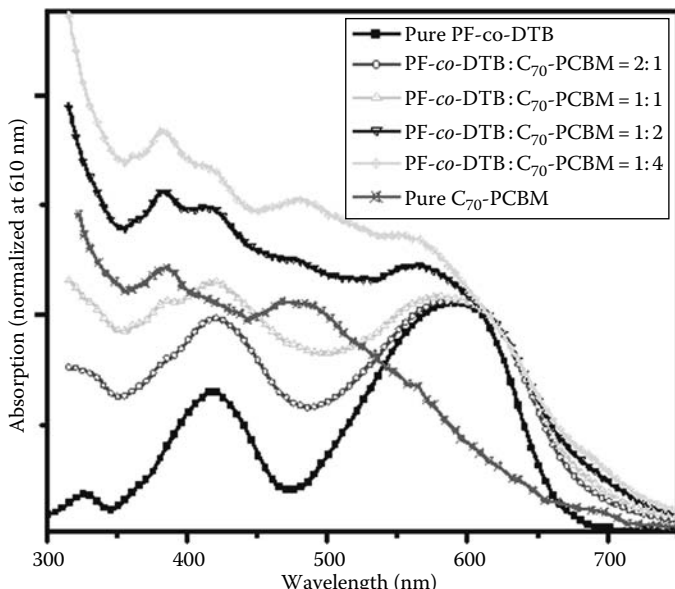
(a) Chemical structures of polymer, (b) UV-Vis absorption spectra of POC-co-DOT, PF-co-DBT, P3HT, and P3OOT thin film. (Reprinted from Shi, C. et al., *J. Am. Chem. Soc.*, 128, 8980, 2006. With permission.)

Many new electron acceptor materials have been tested in the polymer BHJ blend system, including polymer: polymer blend,<sup>77,78</sup> polymer:  $\text{CdSe}$ ,<sup>79,80</sup> polymer: oxide,<sup>81</sup> etc. However, currently they are not as effective as the polymer: PCBM system. To further improve the performance of the promising polymer PF-co-DBT, we work on new fullerene derivative as electron acceptor materials. It is shown up to a large amount of (80 wt%) PCBM is required for optimal performance arising from a strong enhancement of

hole transport in polymer.<sup>82</sup> However, PCBM is not ideal because of its low absorption coefficient in the visible range due to the high structural symmetry forbidden low-energy transitions. We replace PCBM with its higher fullerene analog (6,6)-phenyl-C<sub>70</sub>-butyric acid methyl ester (C<sub>70</sub>-PCBM) and study the effect of C<sub>70</sub>-PCBM blended with low band-gap conjugated polymer PF-*co*-DTB. Both  $J_{SC}$  and FF are increased with no loss in  $V_{OC}$ , which can be attributed to better light absorption and charge transport in the interpenetrating donor/acceptor system.

We have mentioned that the two-band feature of PF-*co*-DTB makes the polymer less efficient in light absorption in the “valley” region between the two peaks. Fortunately, C<sub>70</sub>-PCBM film shows strong absorption in this range and complements PF-*co*-DTB well. As shown in Figure 11.20, when 50 wt.% C<sub>70</sub>-PCBM is added into PF-*co*-DTB, we observe significant absorption enhancement in 430–530 nm and the absorption feature of C<sub>70</sub>-PCBM (370 nm) starts to appear. When more C<sub>70</sub>-PCBM (67–80 wt.%) is added into the polymer, features of C<sub>70</sub>-PCBM (370 and 480 nm) become more pronounced and the blend film shows a near flat absorption profile in contrast to the “two-band” shape absorption of the pure polymer.

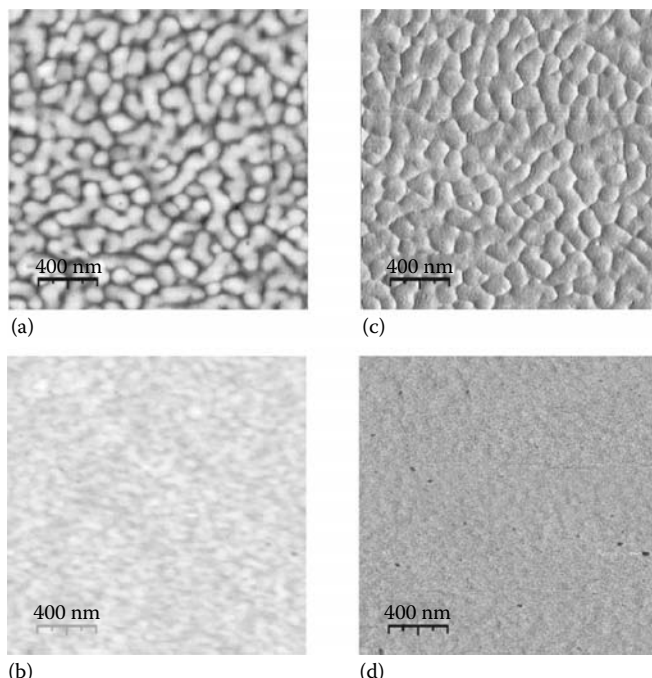
We have shown nanomorphology of the composite layer strongly influences the BHJ photovoltaic performance in RR-P3HT:PCBM system. This is also true for the low band-gap polymer system when C<sub>70</sub>-PCBM is used. Because C<sub>70</sub>-PCBM



**FIGURE 11.20**

UV-Vis absorption spectra of PF-*co*-DTB, C<sub>70</sub>-PCBM and blended film in various ratios. All spectra except pure C<sub>70</sub>-PCBM film are normalized at 610 nm for easy comparison. (Reused from Yao, Y., *Appl. Phys. Lett.*, 89, 153507, 2006. With permission.)

is larger than PCBM and tends to be less soluble, o-dichlorobenzene (ODCB) is used for optimal processing conditions. For example, PCBM:MDMO-PPV solar cells were spun from CB and  $C_{70}$ -PCBM:MDMO-PPV were spun from ODCB.<sup>19,21</sup> Figure 11.21 shows the height and corresponding phase images for the composite PF-*co*-DTB/PCBM film cast from CB, and PF-*co*-DTB/ $C_{70}$ -PCBM film cast from ODCB. To match the conditions used for optimized device preparation, films were prepared under the same conditions, except for top electrode. The height image of PCBM blend film reveals rather uneven surface (root mean square roughness of 4.0 nm) with reproducible phase contrast. Because phase contrast is related to the difference in mechanical property (adhesion, stiffness) of materials, this clearly indicates that the peaks and valleys are of different chemical nature. Separate domains with feature size of ~200–300 nm can be recognized. For comparison,  $C_{70}$ -PCBM blend film reveals a uniform mixing (root mean square roughness of 0.8 nm) of constituents with unobservable phase contrast, indicating excellent miscibility between PF-*co*-DTB and  $C_{70}$ -PCBM. Because the exciton diffusion length in organic materials is typically small (~10 nm), intimate mixture favors exciton separation and therefore higher photocurrent.

**FIGURE 11.21**

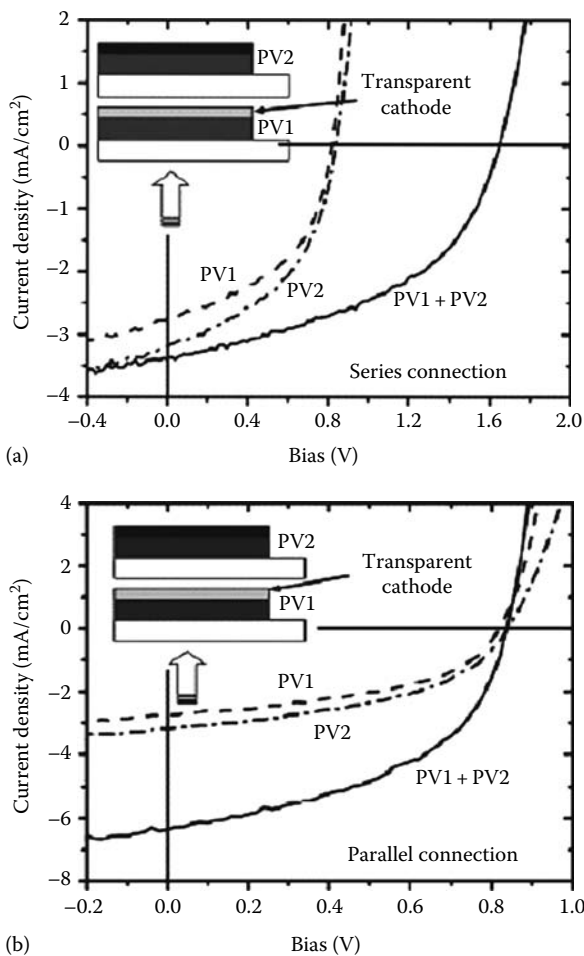
AFM tapping mode height and phase images of (a) and (c) PF-*co*-DTB:PCBM (1:4, w/w) ( $z$  range = 25 nm) and (b) and (d) PF-*co*-DTB: $C_{70}$ -PCBM (1:4, w/w) ( $z$  range = 11 nm) thin films. (Reused from Yao, Y., *Appl. Phys. Lett.*, 89, 153507, 2006. With permission.)

### 11.5.2 Stacking Solar Cell Structures

A single polymer might not be sufficient to make polymer solar cells efficient enough for a useful commercial product. In order to achieve the needed efficiency, the “tandem solar cell” architecture, a multilayer structure that is equivalent to two or more photovoltaic cells in series connection, is needed. Electron–hole pairs generated by photons with energy greater than that of the energy gap, rapidly relax to the respective band edges; thus, the PCE of the two cells in series is inherently better than that of a single cell made from the smaller band-gap material. Recently, Janssen et al. successfully demonstrated double- and triple-junction solution process polymer solar cells.<sup>83</sup> The combination of spin-coating ZnO nanoparticles and neutral pH PEDOT leads to a  $V_{OC}$  of the multiple junction solar cells (2.18 V for a triple-junction device) close to the  $V_{OC}$  summation of the individual cells, indicating the effectiveness of this approach. More recently, Kim et al. use a transparent TiO<sub>x</sub>/PEDOT bilayer as the middle layer in the tandem structure.<sup>7</sup> The TiO<sub>x</sub> layer is fabricated by spin-coating from methanol solution using sol-gel chemistry, and the PEDOT (PH500) is more conducting than PEDOT (4083). The PCE for this tandem cell set a record of more than 6% at illuminations of 200 mW/cm<sup>2</sup>, which was an important step forward on the efficiency.

However, when two subcells are stacked in series, the photocurrent is determined by the cell generating the smaller current. Therefore a current balance (or resistance match) is required between the front and back cell. Another approach is the so-called “stacking solar cell” in which two separate solar cells with transparent electrodes are fabricated and stacked together, with the front and back cell connected in parallel to give a larger short-circuit current. In this case, open-circuit voltage balance, which now becomes the key feature, can be fairly easily achieved. This will significantly increase the number of material systems applicable for efficient utilization of the solar spectrum.

The approach of “stacking solar cell” decouples the fabrication of the front and back cells. The freedom of interconnection is intrinsic and it also enables “parallel connection” in addition to “series connection.” Two separate PV devices can be stacked together to form a multiple-device stacking structure. Both devices are illuminated together using a single source with an intensity of 100 mW/cm<sup>2</sup>. The light from the source is absorbed partially by the first PV device (PV1) and the unabsorbed photons are transmitted through a semitransparent cathode (LiF/Al/Au) to the second device (PV2) where they are absorbed by the second active layer. Both active layers consisted of MEH-PPV/PCBM with the layer thickness of ~70 nm.  $I$ - $V$  curves were measured for the stacked devices connected in series and in parallel, and the results are shown in Figure 11.22. The efficiency can be more than doubled when individual PV cells can be stacked together. Here we used the same active layer for both PV1 and PV2 in order to efficiently absorb the photons that remain unabsorbed from the first active layer. However, this technique can

**FIGURE 11.22**

*I-V* curves for the multiple-device stacked structures where the two cells were connected in (a) series and (b) parallel. Also shown are the *I-V* curves measured for individual cells PV1 and PV2. The stacking sequence for the devices PV1 and PV2 are shown in the inset of both figures. (Reused from Shrotriya, V., *Appl. Phys. Lett.*, 88, 064104, 2006. With permission.)

be extended to use materials with different peak absorption wavelengths in order to increase the total absorption range of the stacked device structure and cover a larger part of the solar spectrum.

### 11.5.3 Mixture Solvent Approach

We have compared thermal annealing approach and solvent annealing approach to modify the nanoscale phase separation in Section 11.3; however,

both methods involve two steps: spin-coating the film and further treatment. Recently the efforts to simplify the process to one single step by using solvent mixtures approach have been reported. Zhang et al. found a significant enhancement in the photocurrent density in polyfluorene copolymer/fullerene blends when introducing a small amount of chlorobenzene into chloroform solvent.<sup>84</sup> Peet et al. reported that adding alkanethiol to P3HT/PCBM in toluene can enhance device performance due to longer carrier lifetime.<sup>85</sup> Alkanethiol is also found effective to achieve the highest efficiency record for low band-gap polymer solar cells.<sup>86</sup> However, few attempts have been made to link the improved performance to the function of the mixture solvent. Several important questions remain unanswered in recent reports: (i) how does the optimized morphology develop during spin-coating process when the additive exists? (ii) What is the function of the additive in the solvent mixture and which properties of additive are relevant for the improvement? (iii) Can we find some alternative mixture solvents to achieve similar function as alkanethiol?

The film formation in the spin-coating process for the polymer/fullerene blend system in the mixture solvent is a complex process because it is a nonequilibrium state that both thermodynamic and kinetic parameters can influence phase separation, and the system contains four components with dissimilar physical/chemical properties. We found the donor/acceptor components in the active layer can phase separate into an optimum morphology during the spin-coating process with the additive.<sup>87</sup> Supported by AFM, TEM, and X-ray photoelectron spectroscopy (XPS) results, a model as well as a selection rule for the additive solvent, and identified relevant parameters for the additive are proposed. The model is further validated by discovering other two additives to show the ability to improve polymer solar cell performance as well.

TEM are used to characterize the lateral phase separation of the active layer. The most pronounced feature compared to samples without octylthiophene (OT) is the appearance of dark clusters in the TEM images and high contrast of these clusters to the background. These clusters are reminiscent of TEM images by Yang et al.,<sup>41</sup> in which PCBM-rich domains were developed during the annealing step. The zoomed-in image shows pronounced fibrillar P3HT crystals, suggesting the crystallinity has been improved compared to pristine film.

To further characterize the active layer in the vertical direction, we conducted XPS measurement on the top and bottom surfaces of the active layer to determine the polymer/fullerene composition. The bottom surface was exposed by using the “floating off” method in water and collected on a TEM grid. The S(2p) peak originates from P3HT and is interpreted as a signature of polymer. Even though PCBM contains oxygen, O(1s) cannot unambiguously be assigned to PCBM due to the air contamination of the sample. Since C(1s) peak represents the total content of P3HT and PCBM, S(2p)/C(1s) peak area ratio hence can be proportionally correlated to the P3HT concentration

**TABLE 11.2**

Area Ratio of S(2p) Peak and C(1s) Peak for the Top and Bottom Surfaces

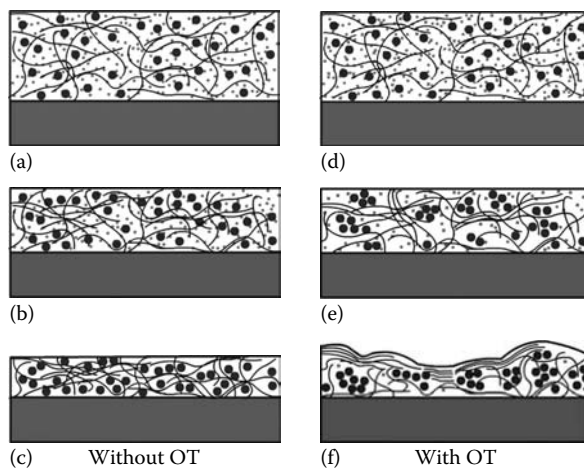
Peak Area Ratio of S(2p)/C(1s)	Top Surface	Bottom Surface
Without 1,8-octanedithiol	0.132	0.130
With 1,8-octanedithiol	0.140	0.106

*Source:* Reused from Yao, Y., *Adv. Funct. Mater.*, 18, 1787, 2008. With permission.

in the blend. Results in Table 11.2 show that S(2p)/C(1s) ratio in the top and bottom surfaces is very close when no OT exists in the solution, indicating a homogeneous distribution of P3HT in the vertical direction. However in the mixture solvent with OT, S(2p)/C(1s) ratio for the top surface is much higher than that of the bottom, suggesting P3HT enriched region in the surface and depleted region in the bottom. The observed vertical phase separation agrees well with other polymer/PCBM systems detected using dynamic TOF-SIMS<sup>88</sup> and UPS<sup>89</sup>. However, an enrichment of polymer at the bottom surface would be expected for better charge collection when PEDOT:PSS-coated ITO is used as substrates. The observed vertical phase separation makes it ideal for an inverted solar cell structure<sup>50</sup> and we recently have achieved more than 72% EQE in inverted device structure.<sup>56</sup>

Combining all the above-mentioned results, we propose a model in Figure 11.23 to explain the results. When P3HT and PCBM are dissolved in DCB, polymer chains extend freely in the solvent and do not interact with PCBM. During spin-coating, when DCB is extracted rapidly, the whole system is quenched into a metastable state and PCBM molecules are finely dispersed between P3HT chains, interrupting the ordering of P3HT chains.<sup>26</sup> This is supported by the blue-shift absorption, smooth AFM morphology and homogeneous TEM images. However, when a small amount of OT is present in the mixture solvent, the situation is different. Because the vapor pressure of DCB is 200 times higher than OT at room temperature, DCB will evaporate much faster than OT during spin-coating, and gradually the concentration of OT increases in the mixture. Due to the limited solubility of PCBM in OT, PCBM will initially form clusters. With a smaller amount of PCBM contained in the solution, P3HT chains are able to self-organize in an easier fashion, supported by our former study.<sup>36</sup> In this way, preformed PCBM clusters not only provide a percolation pathway for better electron transport, but also enable better hole transport in the polymer phase.

According to the proposed model, the additive in the mixture solvent approach should fulfill the following requirements: first, the compound must have lower vapor pressure than that of the primary solvent at room temperature, corresponding to a higher boiling point. Second, the compound must have lower solubility of PCBM than the solvent. Third, the compound must be miscible with solvent. Based on these requirements, we found two new

**FIGURE 11.23**

Proposed model during spin-coating process. Black wire: P3HT polymer chain; Big black dots: PCBM; blue dots: DCB molecules; and red dots: 1,8-octanedithiol molecules. (a–c) correspond to three stages in the spin-coating process when DCB is the sole solvent; (d–f) correspond to three stages in the spin-coating process when octanedithiol is added in DCB. Note the difference of PCBM distribution in the final stage of each case (c) and (f). The total numbers of big black dots are same in all the images. (Reused from Yao, Y., *Adv. Funct. Mater.*, 18, 1787, 2008. With permission.)

additives, di(ethylene glycol)diethyl ether and *N*-methyl-2-pyrrolidone that are effective in the P3HT:PCBM system as well.<sup>87</sup>

## 11.6 Conclusion

Research efforts to increase the efficiency of polymer solar cells conducted at University of California, Los Angles (UCLA) are reviewed in this chapter. The focus is on three broadly defined directions: (i) understanding the underlying physics and device operation mechanisms in polymer solar cells, (ii) optimizing device structure through device engineering, and (iii) understanding morphology of polymer film which governs charge generation and transport in the device. However, research on these novel organic materials and devices is still far from over. The search for ideal materials for efficient photovoltaic conversion continues. The optimization of device structure for maximum performance by device engineering has recently gained momentum. The issue of lifetime and stability associated with organic materials is the biggest obstacle and suitable encapsulation techniques must be developed to bring these devices to commercial market.

---

## Acknowledgments

We thank Vishal Shrotriya and Jinsong Huang for providing help in the preparation of the manuscript. We would like to thank Keith Emery and Tom Moriarty from National Renewable Energy Lab for collaboration on solar cell efficiency measurement. We thank Prof. Qiping Pei at UCLA and Prof. Luping Yu at University of Chicago on providing us low band-gap polymer for the study. We also thank Dr. Hoichang Yang from Rensselaer Polytechnic Institute on GIXRD measurement. Finally, we would like to express our ultimate thanks to the financial support for the past several years on the polymer solar cell devices: Office of Naval Research, Air Force Office of Scientific Research, Solarmer Energy Inc., and University of California Discovery Grant.

---

---

## References

1. C. J. Brabec, V. Dyakonov, J. Parisi, and N. S. Sariciftci, *Organic Photovoltaics: Concepts and Realization*, eds., Springer: Berlin, Germany, 2003.
2. S.-S. Sun and N. S. Sariciftci, *Organic Photovoltaics: Mechanism, Materials, and Devices*, eds., CRC Press: Boca Raton, FL, 2005.
3. N. S. Sariciftci, L. B. Smilowitz, A. J. Heeger, and F. Wudl, *Science* **1992**, 258, 1474.
4. G. Li, V. Shrotriya, J. Huang, Y. Yao, T. Moriarty, K. Emery, and Y. Yang, *Nat. Mater.* **2005**, 4, 864.
5. W. L. Ma, C. Y. Yang, X. Gong, K. Lee, and A. J. Heeger, *Adv. Funct. Mater.* **2005**, 15, 1617.
6. Y. Kim, S. Cook, S. M. Tuladhar, S. A. Choulis, J. Nelson, J. R. Durrant, D. D. C. Bradley, M. Giles, I. McCulloch, C.-S. Ha, and M. Ree, *Nat. Mater.* **2006**, 5, 197.
7. J. Y. Kim, K. Lee, N. E. Coates, D. Moses, T. Q. Nguyen, M. Dante, and A. J. Heeger, *Science* **2007**, 317, 222.
8. N. K. Persson and O. Inganäs, In *Organic Photovoltaics: Mechanisms, Materials, and Devices*, eds. Sun, S.-S. and Sariciftci, N. S., CRC Press: Boca Raton, FL, 2005.
9. P. Peumans, A. Yakimov, and S. R. Forrest, *J. Appl. Phys.* **2003**, 93, 3693.
10. C. J. Brabec, A. Cravino, D. Meissner, N. S. Sariciftci, T. Fromherz, M. T. Rispens, L. Sanchez, and J. C. Hummelen, *Adv. Funct. Mater.* **2001**, 11, 374.
11. M. Pope and C. E. Swenberg, *Electronic Processes in Organic Crystals*, Oxford University Press: Oxford, 1982.
12. H. S. Nalwa, ed., *Handbook of Organic Conductive Molecules and Polymers*, Wiley: New York, 1997.
13. K. Emery and C. Osterwald, In *Current Topics in Photovoltaics*, Volume 3, Academic: London, 1988, ch. 4.

14. K. Emery, In *Handbook of Photovoltaic Science and Engineering*, eds. Luque, A. and Hegedus, S., Wiley: West Sussex, U.K., 2003.
15. J. Rostalski and D. Meissner, *Solar Energy Mater. Solar Cells* **2000**, *61*, 87.
16. J. M. Kroon, M. M. Wienk, W. J. H. Verhees, and J. C. Hummelen, *Thin Solid Films* **2002**, *403–404*, 223.
17. V. Shrotriya, G. Li, Y. Yao, Y. Yang, T. Moriarty, and K. Emery, *Adv. Funct. Mater.* **2006**, *16*, 2016.
18. G. Dennler, *Mater. Today* **2007**, *10*, 56.
19. M. Reyes-Reyes, K. Kim, and D. Carroll, *Appl. Phys. Lett.* **2005**, *87*, 083506.
20. K. Emery, C. Osterwald, T. W. Cannon, D. R. Myers, J. Burdick, T. Glatfelter, W. Czubatyj, and J. Yang, In *Proc. 18th IEEE Photovoltaic Specialist Conf.*, IEEE, New York, 1985.
21. K. Emery and C. Osterwald, *Solar Cells* **1986**, *17*, 253.
22. P. Peumans, S. Uchida, and S. R. Forrest, *Nature* **2003**, *425*, 158.
23. A. Cravino, P. Schilinsky, and C. J. Brabec, *Adv. Funct. Mater.* **2007**, *17*, 3906.
24. S. E. Shaheen, C. J. Brabec, F. Padinger, T. Fromherz, J. C. Hummelen, and N. S. Sariciftci, *Appl. Phys. Lett.* **2001**, *78*, 841.
25. M. M. Wienk, J. M. Kroon, W. J. H Verhees, J. Knol, J. C. Hummelen, P. A. van Hal, and R. A. J. Janssen, *Angew. Chem. Int. Ed.* **2003**, *42*, 3371.
26. H. Hoppe and N. S. Sariciftci, *J. Mater. Chem.* **2006**, *16*, 45.
27. V. Shrotriya, J. Ouyang, R. J. Tseng, G. Li, and Y. Yang, *Chem. Phys. Lett.* **2005**, *411*, 138.
28. D. Chirvase, J. Parisi, J. C. Hummelen, and V. Dyakonov, *Nanotechnology* **2004**, *15*, 1317.
29. N. Camioni, G. Ridolfi, G. C. Miceli, G. Possamai, and M. Maggini, *Adv. Mater.* **2002**, *14*, 1735.
30. J. J. Dittmer, E. A. Marseglia, and R. H. Friend, *Adv. Mater.* **2000**, *13*, 1270.
31. F. Padinger, R. S. Rittberger, and N. S. Sariciftci, *Adv. Funct. Mater.* **2003**, *13*, 85.
32. Y. Kim, S. A. Choulis, J. Nelson, and D. D. C. Bradley, *Appl. Phys. Lett.* **2005**, *86*, 063502.
33. G. Li, V. Shrotriya, Y. Yao, and Y. Yang, *J. Appl. Phys.* **2005**, *98*, 043704.
34. V. D. Mihailetschi, H. Xie, B. de Boer, L. J. A. Koster, and P. W. M. Blom, *Adv. Funct. Mater.* **2006**, *16*, 699.
35. T. Erb, U. Zhokhavets, G. Gobsch, S. Raleva, B. Stuhn, P. Schilinsky, C. Waldauf, and C. J. Brabec, *Adv. Funct. Mater.* **2005**, *15*, 1193.
36. G. Li, Y. Yao, H. C. Yang, V. Shrotriya, G. Yang, and Y. Yang, *Adv. Funct. Mater.* **2007**, *17*, 1636.
37. H. C. Yang, T. J. Shin, L. Yang, K. Cho, C. Y. Ryu, and Z. Bao, *Adv. Funct. Mater.* **2005**, *15*, 671.
38. J. F. Chang, B. Sun, S. W. Brieby, M. M. Nielsen, T. I. Solling, M. Giles, I. McCulloch, and H. Sirringhaus, *Chem. Mater.* **2004**, *16*, 4772.
39. J. Liu, Y. Shi, and Y. Yang, *Adv. Funct. Mater.* **2001**, *11*, 420.
40. H. Hoppe, M. Niggemann, C. Winder, J. Kraut, R. Hiesgen, A. Hinsch, D. Meissner, and N. S. Sariciftci, *Adv. Funct. Mater.* **2004**, *14*, 1005.
41. X. N. Yang, J. Loos, S. C. Veenstra, W. J. H. Verhees, M. M. Wienk, J. M. Kroon, M. A. J. Michels, and R. A. J. Janssen, *Nano Lett.* **2005**, *5*, 579.
42. X. Yang, J. K. J. van Duren, R. A. J. Janssen, M. A. J. Michels, and J. Loos, *Macromolecules* **2004**, *37*, 2151.

43. M. Brinkmann and J. C. Wittmann, *Adv. Mater.* **2006**, *18*, 860.
44. M. A. Lampert and P. Mark, *Current Injection in Solids*, Academic Press: New York, 1970.
45. V. D. Mihailescu, H. Xie, B. de Boer, L. M. Popescu, J. C. Hummelen, and P. W. M. Blom, *Appl. Phys. Lett.* **2006**, *89*, 012107.
46. V. D. Mihailescu, L. J. A. Koster, P. W. M. Blom, C. Melzer, B. de Boer, J. K. J. van Duren, and R. A. J. Janssen, *Adv. Funct. Mater.* **2005**, *15*, 795.
47. V. D. Mihailescu, L. J. A. Koster, J. C. Hummelen, and P. W. M. Blom, *Phys. Rev. Lett.* **2004**, *93*, 216601.
48. L. Onsager, *J. Chem. Phys.* **1934**, *2*, 599.
49. C. L. Braun, *J. Chem. Phys.* **1984**, *80*, 4157.
50. G. Li, C.-W. Chu, V. Shrotriya, J. Huang, and Y. Yang, *Appl. Phys. Lett.* **2006**, *88*, 253503.
51. C. Waldauf, M. Morana, P. Denk, P. Schilinsky, K. M. Coakley, S. A. Choulis, and C. J. Brabec, *Appl. Phys. Lett.* **2006**, *89*, 233517.
52. M. S. White, D. C. Olson, S. E. Shaheen, N. Kopidakis, and D. S. Ginley, *Appl. Phys. Lett.* **2006**, *89*, 143517.
53. T. Hasegawa, S. Miura, T. Moriyama, T. Kimura, I. Takaya, Y. Osato, and H. Mizutani, *Dig. Tech. Papers—Soc. Inf. Disp. Int. Symp.* **2004**, *35*, 154.
54. J. Huang, Z. Xu, and Y. Yang, *Adv. Funct. Mater.* **2007**, *17*, 1966.
55. V. Shrotriya, G. Li, Y. Yao, C.-W. Chu, and Y. Yang, *Appl. Phys. Lett.* **2006**, *88*, 073508.
56. H. Liao, L. Chen, Z. Xu, G. Li, and Y. Yang, *Appl. Phys. Lett.* **2007**, *92*, 173303.
57. J. Ouyang, Y. Yang, *Adv. Mater.* **2006**, *18*, 2141.
58. J. Huang, P. F. Miller, J. S. Wilson, A. J. Mello, J. C. Mello, and D. D. C. Bradley, *Adv. Funct. Mater.* **2005**, *15*, 290.
59. C. Winder and N. S. Sariciftci, *J. Mater. Chem.* **2004**, *14*, 1077.
60. M. C. Scharber, D. Mühlbacher, M. Koppe, P. Denk, C. Waldauf, A. J. Heeger, and C. J. Brabec, *Adv. Mater.* **2006**, *18*, 789.
61. L. J. A. Koster, V. D. Mihailescu, and P. W. M. Blom, *Appl. Phys. Lett.* **2006**, *88*, 093511.
62. E. Bundgaard and F. C. Krebs, *Solar Energy Mater. Solar Cells* **2007**, *91*, 954.
63. C. J. Brabec, C. Winder, N. S. Sariciftci, J. C. Hummelen, A. Dhanabalan, P. A. van Hal, and R. A. J. Janssen, *Adv. Funct. Mater.* **2002**, *12*, 709.
64. F. Zhang, K. Jespersen, C. Björstrom, M. Svensson, M. R. Andersson, V. Sundstrom, K. Magnusson, E. Moons, A. Yartsev, and O. Inganäs, *Adv. Funct. Mater.* **2006**, *16*, 667.
65. D. Mühlbacher, M. Scharber, M. Morana, Z. Zhu, D. Waller, R. Gaudiana, and C. J. Brabec, *Adv. Mater.* **2006**, *18*, 2884.
66. J. Hou, Z. Tan, Y. Yan, Y. He, C. Yang, and Y. Li, *J. Am. Chem. Soc.* **2006**, *128*, 4911.
67. C. J. Brabec, N. S. Sariciftci, and J. C. Hummelen, *Adv. Funct. Mater.* **2001**, *11*, 15.
68. J. Roncali, *Chem. Rev.* **1997**, *97*, 173.
69. P. Schilinsky, C. Waldauf, J. Hauch, and C. J. Brabec, *J. Appl. Phys.* **2004**, *95*, 2816.
70. M. Svensson, F. Zhang, S. C. Veenstra, W. J. H. Verhees, J. C. Hummelen, J. M. Kroon, O. Inganäs, and M. R. Andersson, *Adv. Mater.* **2003**, *15*, 988.
71. M. M. Wienk, M. P. Struijk, and R. A. J. Janssen, *Chem. Phys. Lett.* **2006**, *422*, 488.
72. P. Schilinsky, U. Asawapirom, U. Scherf, M. Biele, and C. J. Brabec, *Chem. Mater.* **2005**, *17*, 2175.

73. F. C. Krebs, R. B. Nyberg, and M. Jorgensen, *Chem. Mater.* **2004**, *16*, 1313.
74. K. T. Nielsen, K. Bechgaard, and F. C. Krebs, *Macromolecules* **2005**, *38*, 658.
75. C. Shi, Y. Yao, Y. Yang, and Q. Pei, *J. Am. Chem. Soc.* **2006**, *128*, 8980.
76. X. Hu and L. Xu, *Polymer* **2000**, *41*, 9147.
77. J. J. M. Halls, C. A. Walsh, N. C. Greenham, E. A. Marseglia, R. H. Friend, S. C. Moratti, and A. B. Holmes, *Nature* **1995**, *376*, 498.
78. C. R. McNeill, A. Abrusci, J. Zaumseil, R. Wilson, M. J. McKiernan, J. H. Burroughes, J. J. M. Halls, N. C. Greenham, and R. H. Friend, *Appl. Phys. Lett.* **2007**, *90*, 193506.
79. N. C. Greenham, X. Peng, and A. P. Alivisatos, *Phys. Rev. B* **1996**, *54*, 17628.
80. W. U. Huynh, J. J. Dittmer, and A. P. Alivisatos, *Science* **2002**, *295*, 2425.
81. W. J. E. Beek, M. M. Wienk, and R. A. J. Janssen, *Adv. Mater.* **2004**, *16*, 1009.
82. C. Melzer, E. J. Koop, V. D. Mihailescu, and P. W. M. Blom, *Adv. Funct. Mater.* **2004**, *14*, 865.
83. J. Gilot, M. M. Wienk, and R. A. J. Janssen, *Appl. Phys. Lett.* **2007**, *90*, 143512.
84. F. Zhang, K. G. Jespersen, C. Bjorstrom, M. Svensson, M. R. Andersson, V. Sundstrom, K. Magnusson, E. Moons, A. Yartsev, and O. Inganäs, *Adv. Funct. Mater.* **2006**, *16*, 667.
85. J. Peet, C. Soci, R. C. Coffin, T. Q. Nguyen, A. Mikhailovsky, D. Moses, and G. C. Bazan, *Appl. Phys. Lett.* **2006**, *89*, 252105.
86. J. Peet, J. Y. Kim, N. E. Coates, W. L. Ma, D. Moses, A. J. Heeger, and G. C. Bazan, *Nat. Mater.* **2007**, *6*, 497.
87. Y. Yao, J. Hou, Z. Xu, G. Li, and Y. Yang, *Adv. Funct. Mater.* **2008**, *18*, 1783.
88. C. Bjorstrom, A. Bernasik, J. Rysz, A. Budkowski, S. Nilsson, M. Svensson, M. R. Andersson, K. O. Magnusson, and E. Moons, *J. Phys: Condens. Matter.* **2005**, *17*, L529.
89. S. K. M. Jonsson, E. Carlegrim, F. Zhang, W. R. Salaneck, and M. Fahlman, *Jpn. J. Appl. Phys.* **2005**, *44*, 3695.
90. V. Shrotriya, Y. Yao, G. Li, Y. Yang, *Appl. Phys. Lett.* **2006**, *89*, 063505.
91. J. Huang, G. Li, Y. Yang, *Adv. Mater.* **2008**, *20*, 415.
92. Y. Yao, C. Shi, G. Li, V. Shrotriya, Q. Pei, Y. Yang, *Appl. Phys. Lett.* **2006**, *89*, 153507.
93. V. Shrotriya, E.H. Wu, G. Li, Y. Yao, Y. Yang, *Appl. Phys. Lett.* **2006**, *88*, 064104.

# 12

---

## *Mixed Molecular Heterojunction Photovoltaic Cells*

---

Jiangeng Xue

### CONTENTS

12.1	Introduction .....	359
12.2	CuPc:C <sub>60</sub> Mixed Heterojunctions .....	361
12.2.1	Structural, Optical, and Electrical Properties of CuPc:C <sub>60</sub> Mixtures .....	361
12.2.2	Device Performance of CuPc:C <sub>60</sub> Mixed Heterojunction Photovoltaic Cells.....	366
12.2.3	Modeling of Mixed HJ Cell Performance .....	370
12.3	CuPc:C <sub>60</sub> Planar–Mixed Heterojunctions .....	373
12.3.1	Concept of Planar–Mixed Heterojunctions.....	373
12.3.2	Dark Current of CuPc:C <sub>60</sub> Planar–Mixed Heterojunction Cells.....	374
12.3.3	Photoresponse of CuPc:C <sub>60</sub> Planar–Mixed Heterojunction Cells.....	376
12.3.4	Modeling the Performance of CuPc:C <sub>60</sub> Planar–Mixed Heterojunction Cells.....	380
12.4	Tandem Cells Based on CuPc:C <sub>60</sub> Planar–Mixed Heterojunctions ...	382
12.4.1	Background of Organic Tandem Cells.....	382
12.4.2	Asymmetric Organic Tandem Cells Based on CuPc–C <sub>60</sub> PM-HJs.....	383
12.5	Conclusions.....	388
	Acknowledgments .....	389
	References.....	389

---

### 12.1 Introduction

In an organic donor–acceptor (D–A) heterojunction (HJ) photovoltaic (PV) cell, the entire PV process consists of four consecutive steps: photon absorption by either donor or acceptor molecules to generate excitons, diffusion of

excitons to the D–A heterointerface, charge transfer at the interface leading to the dissociation of excitons and generation of separated charge carriers, and finally the collection of photogenerated charge carriers at opposite electrodes (Peumans et al., 2003). In bilayer, or planar HJ, organic PV cells, exciton diffusion is generally the limiting step for the overall PV performance (Forrest, 2005). Due to the weak van der Waals-type intermolecular interactions that hold the organic molecules together, the exciton diffusion length  $L_D$  is typically on the order of a few nm (Pope and Swenberg, 1999; Peumans et al., 2003). As an exciton is less likely to reach the interface if it is generated farther from the interface, the exciton diffusion efficiency  $\eta_{ED}$ , or the fraction of excitons reaching the interface (and subsequently dissociate at the interface), decreases with increasing the layer thicknesses. On the other hand, the optical absorption length  $L_A = 1/\alpha$  (where  $\alpha$  is the absorption coefficient) is typically on the order of 50–100 nm. This suggests that there is a critical trade-off between using thicker layers for more efficient light absorption and using thinner layers for a higher  $\eta_{ED}$ .

To circumvent this “exciton diffusion bottleneck” (Forrest, 2005), blends of DA polymers have been used to create an interpenetrating D–A network, resulting in a three-dimensional, spatially distributed D–A interface (Halls et al., 1995; Yu et al., 1995). The high density of interface area in this so-called bulk heterojunction (BHJ) structures effectively reduces the average distance a photogenerated exciton needs to diffuse in order to reach the D–A interface, especially when the phase separation between the two materials leads to domains on the order of the exciton diffusion length, i.e., a few to tens of nm. The BHJ structure was first successfully demonstrated with polymer-polymer (Halls et al., 1995) and polymer–fullerene (Yu et al., 1995) blends using solution processing. For vacuum-deposited small molecules, simultaneous evaporation, or coevaporation, of both DA source materials leading to mixed D–A thin films (also called “mixed HJs”) has also been used to mimic the polymer-based BHJ structure, and efficiencies similar to or even higher than bilayer devices have been achieved (Tsuzuki et al., 2000; Gebeyehu et al., 2003; Peumans et al., 2003; Uchida et al., 2004).

The collection efficiency of photogenerated charge carriers at the electrodes,  $\eta_{CC}$ , is, however, critically dependent on the charge transport properties of the interpenetrating D–A network. The intermixing of DA materials in the BHJ structure may deteriorate the already low carrier mobilities in the organic materials. Due to the significant energy level offsets (typically 0.5–1 eV) at the D–A interface that are necessary to induce exciton dissociation/charge separation, the transport of holes and electrons is separately confined within the DA materials, respectively. Therefore, percolated paths for both molecular species need to exist throughout the photoactive region to efficiently transport the charge carriers toward their respective electrodes; otherwise, trapping and eventually recombination of these charge carriers would amount to a loss in the photocurrent. Such loss is more significant under higher illumination intensities when the concentration of photogenerated charges is

higher, or under a voltage bias approaching closer to the built-in potential, which corresponds to a lower electric field and a longer transit time for carriers in the mixed HJ. In terms of PV device performance, the stronger voltage dependence of the photocurrent results in a reduced fill factor (FF) for the PV cell, which is further reduced at higher illumination intensities. In addition, the short-circuit current density ( $J_{SC}$ ) has a sublinear dependence on the illumination intensity ( $P_O$ ), especially at high  $P_O$ , due to the increased carrier recombination. For example, a mixed zinc phthalocyanine (ZnPc):C<sub>60</sub> PV cell was reported to have a power conversion efficiency of  $\eta_P=3.37\%$ , FF = 0.50, and  $J_{SC}/P_O=0.15\text{ A/W}$  under 0.1 sun ( $P_O=10\text{ mW/cm}^2$ ) solar illumination; but those device parameters were reduced to  $\eta_P=1.04\%$ , FF = 0.33, and  $J_{SC}/P_O=0.063\text{ A/W}$  under 1 sun illumination (Gebeyehu et al., 2003). It is therefore critically important to control the morphological structure of the mixed HJ to allow efficient transport of charge carriers towards the electrodes.

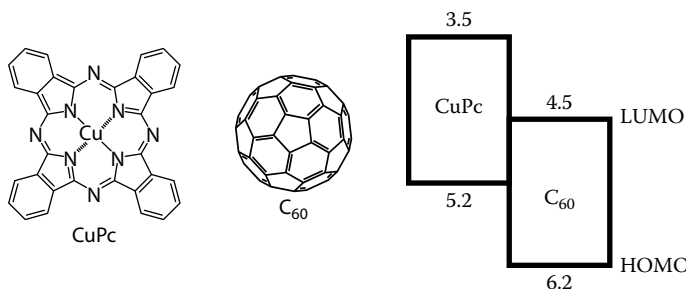
In this chapter, we discuss important work on material processing, characterization, and device performance of mixed molecular HJ PV cells. In Section 12.2, we first describe properties of vacuum codeposited mixtures of copper phthalocyanine (CuPc) and C<sub>60</sub> followed by the performance of PV cells using CuPc:C<sub>60</sub> mixed HJs as the active region. Section 12.3 presents work on planar-mixed HJs (PM-HJs) which combine the advantages of mixed HJs with those of planar HJs. Individual PM-HJ cells were then stacked vertically to form tandem cells to achieve the highest efficiencies, which will be discussed in Section 12.4. Conclusions are presented in Section 12.5.

---

## 12.2 CuPc:C<sub>60</sub> Mixed Heterojunctions

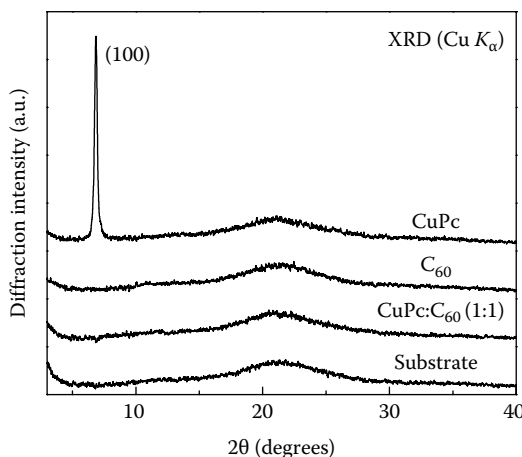
### 12.2.1 Structural, Optical, and Electrical Properties of CuPc:C<sub>60</sub> Mixtures

Free- or metal-base phthalocyanines have been widely studied as donor materials in organic PV cells due to their strong optical absorption and good thermal stability (Tang, 1986; Hiramoto et al., 1991; Peumans et al., 2000; Peumans and Forrest, 2001; Gebeyehu et al., 2003; Peumans et al., 2003; Uchida et al., 2004; Xue et al., 2004a). Fullerenes, such as C<sub>60</sub> and their derivatives, on the other hand, have been used as acceptors for vacuum-deposited or solution-processed organic PV cells (Yu et al., 1995; Peumans and Forrest, 2001; Gebeyehu et al., 2003; Padinger et al., 2003; Uchida et al., 2004; Xue et al., 2004a; Ma et al., 2005; Kim et al., 2007). The molecular structure and the energy level alignment of the highest occupied and lowest unoccupied molecular orbitals (HOMO and LUMO, respectively) at the CuPc-C<sub>60</sub> HJ are shown in Figure 12.1. This D-A material system has been used to fabricate bilayer PV cells with power conversion efficiencies up to 3%-4% (Peumans and Forrest, 2001; Xue et al., 2004a).

**FIGURE 12.1**

Molecular structures of CuPc and C<sub>60</sub>, and the schematic energy level diagram for the CuPc–C<sub>60</sub> HJ. The energies (in eV) for the HOMO and LUMO levels are referenced from the vacuum level.

The x-ray diffraction (XRD) patterns of 100 nm thick neat and mixed CuPc and C<sub>60</sub> films, obtained in the  $\theta$ –2 $\theta$  geometry using a Cu K <sub>$\alpha$</sub>  radiation source, are shown in Figure 12.2 (Xue et al., 2005a). While the neat C<sub>60</sub> film appears to be amorphous (the broad peak centered at  $2\theta = 21^\circ$  is due to diffraction from the glass substrate), the neat CuPc film shows a crystalline diffraction peak at  $2\theta = 6.85^\circ$ , corresponding to an interplanar spacing of  $d = 12.9 \text{ \AA}$  for the (200) Bragg reflection of the  $\alpha$ -CuPc phase (E et al., 2003). The CuPc diffraction peak, however, disappears in the pattern for the 1:1 mixed (by weight) CuPc:C<sub>60</sub> film, suggesting the amorphous nature of the mixed film. A more careful study showed that the CuPc diffraction peak is barely observable in the XRD pattern for a 6:1 mixed CuPc:C<sub>60</sub> film, but completely disappears in the pattern for a 3:1 mixed film (Rand et al., 2005).

**FIGURE 12.2**

XRD patterns for 100 nm thick CuPc, C<sub>60</sub>, and a 1:1 mixed CuPc:C<sub>60</sub> film as well as for the glass substrate, taken in the  $\theta$ –2 $\theta$  configuration using Cu K <sub>$\alpha$</sub>  radiation.

Figure 12.3 shows scanning electron micrographs (SEM) of the neat CuPc and 1:1 mixed CuPc:C<sub>60</sub> film. The neat CuPc film shows a grainy surface typical of polycrystalline films, and the typical grain size is approximately 30–40 nm. The root-mean-square (rms) surface roughness of the film as measured by atomic force microscopy (AFM) is  $R_{\text{rms}} = 5 \text{ nm}$  (Rand et al., 2005). The 1:1 mixed film, on the other hand, is much smoother and nearly featureless under SEM, and the surface roughness is only  $R_{\text{rms}} = 0.5 \text{ nm}$  (Rand et al., 2005). Combined with the XRD results, this suggests that the existence of C<sub>60</sub> molecules in the mixed films reduces the aggregation tendency of CuPc molecules, and no significant phase separation occurs in the mixed films with C<sub>60</sub> concentration greater than approximately 25%.

The intermixing of the molecules also has a strong impact on the optical absorption properties. As shown in Figure 12.4, with increasing C<sub>60</sub> concentration in the mixed CuPc:C<sub>60</sub> films, the relative intensity of the CuPc absorption

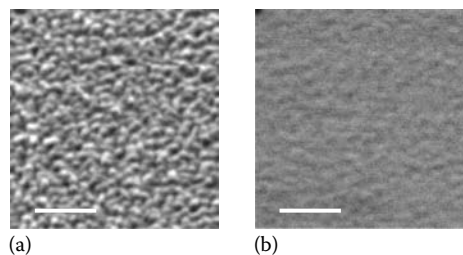


**FIGURE 12.3**

SEM images of (a) CuPc and (b) 1:1 mixed CuPc:C<sub>60</sub> films. The scale bars are 200 nm.

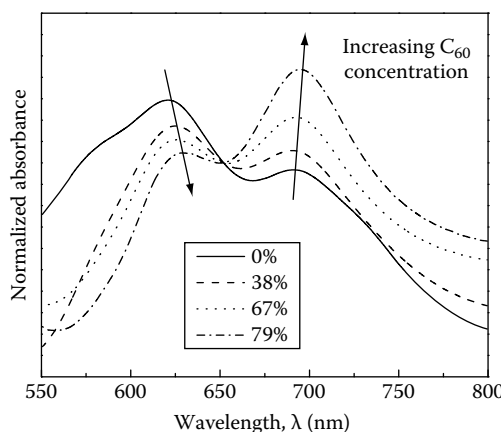


**FIGURE 12.4**

Absorption spectra in the CuPc absorption region for mixed CuPc:C<sub>60</sub> films with varying C<sub>60</sub> concentration.

peak at a wavelength of  $\lambda=695\text{ nm}$  increases accompanied by a decrease in the relative intensity for the CuPc absorption peak at  $\lambda=620\text{ nm}$ . For CuPc, it has been shown that the longer wavelength absorption peak is dominant in the gas phase or in dilute solutions, whereas the shorter wavelength peak results from molecular aggregation (Sielcken et al., 1987; Lenznoff and Lever, 1989). Hence the optical absorption data again show that CuPc molecules have a decreased tendency to aggregate with increasing  $C_{60}$  content in the mixed films.

The carrier mobility in the mixed CuPc: $C_{60}$  films has been obtained by modeling the current density–voltage ( $J$ – $V$ ) characteristics for hole- and electron-only devices using the space-charge-limited current (SCLC) theory (Pope and Swenberg, 1999; Rand et al., 2005), viz.:

$$J = \frac{9}{8} \epsilon \epsilon_0 \mu(E) \theta \frac{V^2}{d^3}, \quad (12.1)$$

where

$\epsilon \approx 3$  is the relative dielectric constant of the organic film

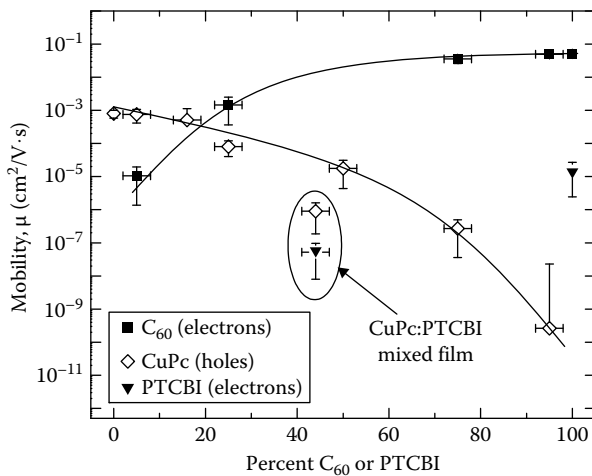
$\epsilon_0$  is the vacuum dielectric constant

$E$  is the electric field

$d$  is the film thickness

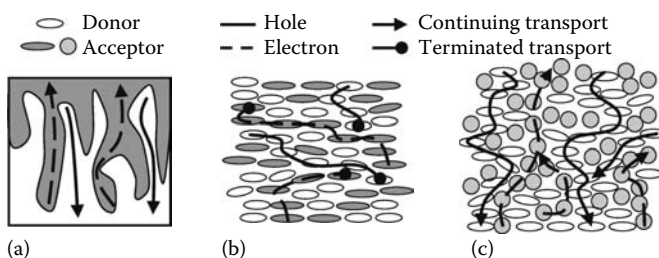
$\mu(E) = \mu_0 \exp(\gamma E^{1/2})$  is the electric field dependent charge carrier mobility according to the Poole–Frankel law, in which  $\mu_0$  is the zero-field mobility and  $\gamma$  is the field activation parameter (Dunlap et al., 1996)

Shown in Figure 12.5 are the electron and hole mobilities at an electric field of  $E = 10^5\text{ V/cm}$  (which roughly corresponds to the field in PV devices at the short-circuit condition) in CuPc: $C_{60}$  mixed films as a function of the acceptor concentration (Rand et al., 2005). For CuPc: $C_{60}$  films, the hole mobility monotonically decreases with increasing  $C_{60}$  concentration, from  $\mu_h = 8 \times 10^{-4}\text{ cm}^2/\text{V}\cdot\text{s}$  in the neat CuPc film to approximately  $\mu_h = 2 \times 10^{-5}\text{ cm}^2/\text{V}\cdot\text{s}$  in the 1:1 mixed film. Conversely, the electron mobility increases with the  $C_{60}$  concentration, from  $\mu_e = 1 \times 10^{-5}\text{ cm}^2/\text{V}\cdot\text{s}$  for the 5%  $C_{60}$  film, to  $\mu_e = 1 \times 10^{-3}\text{ cm}^2/\text{V}\cdot\text{s}$  for the 25%  $C_{60}$  film, and to  $\mu_e = 0.05\text{ cm}^2/\text{V}\cdot\text{s}$  for the neat  $C_{60}$  film (100%  $C_{60}$ ). This behavior can be explained by considering the hopping transport of carriers in these films. Due to the large HOMO/LUMO offsets at the D–A interface, hole and electron transport are separately confined in the donor (CuPc) and acceptor ( $C_{60}$ ) molecules, respectively. As the mean distance between neighboring molecules of the same species in the mixed layer is larger than that in their respective neat films, the hopping mobility for holes among CuPc molecules and electrons among  $C_{60}$  molecules is expected to decrease upon intermixing of CuPc and  $C_{60}$  on the molecular scale.

**FIGURE 12.5**

Electron and hole mobilities, at an electric field of  $E=10^5$  V/cm, in CuPc:C<sub>60</sub> and CuPc:PTCBI mixtures as functions of the acceptor concentration. The solid lines are guides to the eye.

Also shown in Figure 12.5 are the carrier mobilities in the 5:4 mixed CuPc:PTCBI film as well as the electron mobility in the neat PTCBI film. Here PTCBI = 3,4,9,10-perylenetetracarboxylic bis-benzimidazole is a planar-type molecular acceptor that has also been studied in organic PV cells (Tang 1986; Peumans et al., 2000), although the exciton diffusion length is much shorter than that in C<sub>60</sub> (3 vs. 40 nm) (Peumans et al., 2003). From Figure 12.5, it is important to note that the hole mobility in the CuPc:PTCBI film is approximately two orders of magnitude lower than in a CuPc:C<sub>60</sub> film with similar CuPc content. The mobility difference was attributed to the different microstructures of the mixtures resulting from different molecular properties (Rand et al., 2005; Xue et al., 2005a). Figure 12.6a schematically

**FIGURE 12.6**

Microstructures and charge transport scenarios in mixed DA layer: (a) an idealized BHJ; (b) a mixed layer without percolating paths across the entire film; and (c) a mixed layer with somewhat percolating paths across the film.

shows an idealized BHJ structure. With lateral feature sizes on the order of the exciton diffusion lengths (i.e., a few to tens of nm), the BHJ structure ensures a high exciton diffusion efficiency, whereas the interdigitated structure allows efficient transport of charge carriers towards the electrodes. In mixed films consisting of the planar-stacking of DA molecules, such as CuPc:PTCBI, the homogeneous mixing of the two types of molecules results in poorly percolated charge transport paths for both electrons and holes as shown in Figure 12.6b, hence low carrier mobilities in the mixture. For CuPc:C<sub>60</sub> mixtures, even though no crystalline domains exist for the planar-stacking CuPc molecules and the tendency of aggregation is significantly suppressed for both molecular species, as shown in Figure 12.6c, the different molecular shapes (planar for CuPc and spherical for C<sub>60</sub>) may lead to small disordered CuPc and C<sub>60</sub> domains or molecular chains, which provide somewhat percolating paths for charge transport.

### 12.2.2 Device Performance of CuPc:C<sub>60</sub> Mixed Heterojunction Photovoltaic Cells

Shown in Figure 12.7a is the schematic device structure of a CuPc:C<sub>60</sub> mixed HJ PV cell (Uchida et al., 2004). The device was fabricated on a glass substrate precoated with an indium-tin oxide (ITO) transparent anode. A homogeneously mixed CuPc:C<sub>60</sub> layer with a weight ratio of 1:1 was used as the photoactive region. A thin layer of bathocuproine (BCP) was deposited on top of the organic active region to serve as the exciton blocking layer (EBL) (Peumans et al., 2000). A thin (100 Å thick) C<sub>60</sub> layer was inserted between the mixed layer and the BCP EBL, which not only increases the optical field in the mixed layer by displacing it farther from the reflective metal cathode, but also enhances the total absorption of the incident light and contributes to the overall photocurrent.

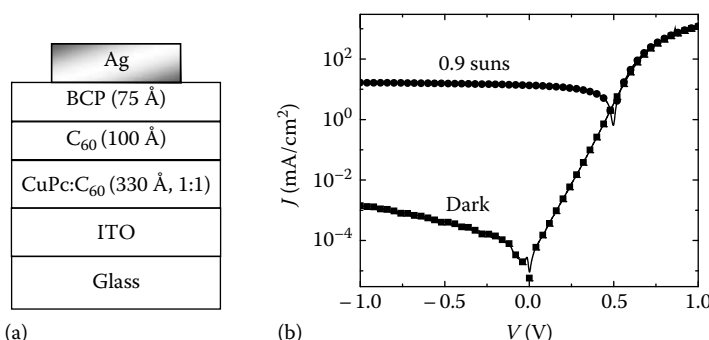


**FIGURE 12.7**

(a) Schematic device structure of a CuPc:C<sub>60</sub> mixed HJ PV cell; (b)  $J$ - $V$  characteristics of the device in the dark and under 0.9 suns of simulated AM1.5 solar illumination.

The  $J$ - $V$  characteristics of this PV device in the dark and under 0.9 suns of simulated AM1.5 solar illumination are shown in Figure 12.7b. The device shows excellent rectifying behavior in the dark with a rectification ratio of approximately  $10^6$  at  $\pm 1$  V, and has a very low leakage current, corresponding to a shunt resistance  $R_{sh} \approx 1 \text{ M}\Omega \cdot \text{cm}^2$ . The dark  $J$ - $V$  characteristics can be well described using the modified diode equation (Sze and Ng, 2007):

$$J_d(V) = J_s \left\{ \exp \left[ \frac{q(V - JR_{SA})}{nkT} \right] - 1 \right\}, \quad (12.2)$$

where

$J_s$  is the reverse-bias saturation current density

$q$  is the electron charge

$n$  is the diode ideality factor

$k$  is Boltzmann's constant

$T$  is the temperature

$R_{SA}$  is the specific series resistance

For the mixed HJ device shown here, we obtained a very low specific series resistance of  $R_{SA} = 0.2 \Omega \cdot \text{cm}^2$ , which is comparable to that of a CuPc-C<sub>60</sub> planar HJ cell and is ultimately limited by the sheet resistance of the ITO anode ( $\sim 15 \Omega/\square$ ) (Xue et al., 2004a). Under 0.9 suns AM1.5 illumination, the device achieved a short-circuit current density of  $J_{SC} = 13.5 \text{ mA/cm}^2$ , an open-circuit voltage of  $V_{OC} = 0.50 \text{ V}$ , and a FF of 0.46, resulting in a power conversion efficiency of  $\eta_P = (3.5 \pm 0.2)\%$  (Uchida et al., 2004).

A comparison of the PV performance of this mixed HJ device (Uchida et al., 2004) and that of a bilayer, planar HJ CuPc-C<sub>60</sub> cell (Xue et al., 2004a) at various illumination intensities is shown in Figure 12.8. The mixed HJ

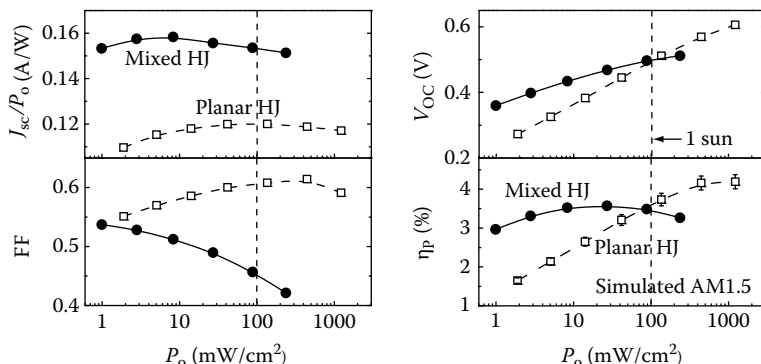
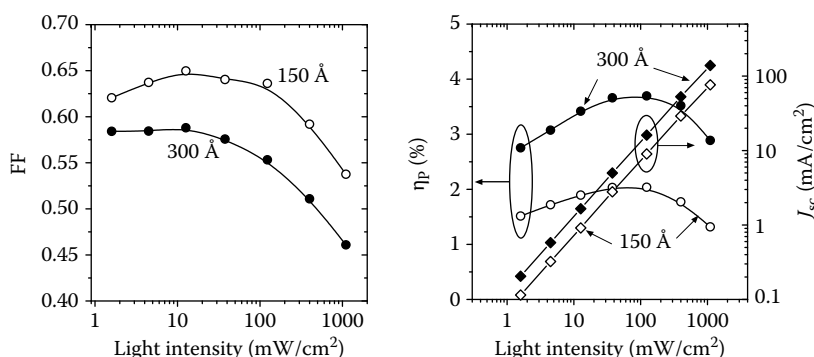


FIGURE 12.8

Comparison of the PV performance of a CuPc:C<sub>60</sub> mixed HJ cell (filled circles) and a CuPc-C<sub>60</sub> planar HJ cell (open squares) at various illumination intensities ( $P_o$ ).

cell has approximately 25% higher  $J_{SC}$  than the planar HJ cell, which is attributed to the better exciton dissociation efficiency in the mixture. However, the lower carrier mobility in the mixture leads to significantly lower FF in the mixed HJ device, especially at high illumination intensities. While the planar HJ device has a very high  $FF \approx 0.6$  at an illumination intensity of around 1 sun (or  $P_O = 100 \text{ mW/cm}^2$ ), the FF of the mixed HJ device monotonically decreases with the increase of  $P_O$ , from  $FF = 0.54$  at  $P_O = 1 \text{ mW/cm}^2$  to  $FF = 0.42$  at  $P_O = 260 \text{ mW/cm}^2$ .  $V_{OC}$  of both devices increases logarithmically with  $P_O$ , although the slope is somewhat different, and is steeper for the planar HJ device. Such a dependence can be explained by considering that  $V_{OC}$ , by definition, is the voltage at which the photocurrent and the dark current cancel each other to yield a zero total current. With increasing  $P_O$ , the photocurrent increases proportionally ( $J_{SC}/P_O$  is nearly constant in the intensity range of interest here), which requires a larger voltage bias to produce the higher dark current to achieve zero total current. Overall, the two devices have similar  $\eta_P \approx 3.5\%$  at 1 sun; however the detailed dependence of  $\eta_P$  on  $P_O$  is very different: the mixed HJ device has a rather constant  $\eta_P$  for  $0.01 \text{ suns} < P_O < 2.6 \text{ suns}$ , whereas  $\eta_P$  of the planar HJ device increases nearly logarithmically with  $P_O$  from below 2% at 0.02 suns to 4.2% at 4–12 suns.

The FF of mixed HJ devices can be improved by reducing the mixed layer thickness. Shown in Figure 12.9 are the performances of two CuPc:C<sub>60</sub> mixed HJ cells with the structures of ITO/CuPc:C<sub>60</sub>( $x$  Å, 1:1)/C<sub>60</sub>(50 Å)/BCP(75 Å)/Ag, where  $x = 150$  or 300 (Xue, 2005). Under approximately 1 sun illumination,  $FF = 0.63$  is achieved for the cell with a mixed layer thickness of 150 Å, compared to  $FF = 0.55$  for the cell with a 300 Å thick mixed layer. With a thinner mixed layer, the lower carrier mobility in mixed layer has a less serious impact on the extraction of photogenerated charge carriers from the active layer. However, the use of a thinner mixed layer leads to



**FIGURE 12.9**

Performance comparison between two mixed HJ cells with different mixed layer thicknesses: ITO/CuPc:C<sub>60</sub>( $x$  Å, 1:1)/C<sub>60</sub>(50 Å)/BCP(75 Å)/Ag.

less efficient absorption of the incident light, and therefore significantly lower  $J_{SC}$ . Hence, the cell with a 300 Å thick mixed layer achieves a maximum  $\eta_P \approx 3.5\%$ , whereas the efficiency is reduced to  $\eta_P \approx 2.0\%$  for the cell with a 150 Å thick mixed layer.

We have also studied the temperature dependence of the performance of mixed HJ cells (Xue, 2005; Xue et al., 2005b). The  $J$ - $V$  characteristics in the dark and under 0.9 suns illumination for a CuPc:C<sub>60</sub> mixed HJ cell in the operating temperature range of 300–380 K are shown in Figure 12.10, whereas the temperature dependencies of the normalized  $\eta_P$  and  $J_{SC}$  for this cell and a planar HJ cell are shown in Figure 12.11. The dark current density for both mixed and planar HJ cells increases with temperature, a typical behavior of a diode

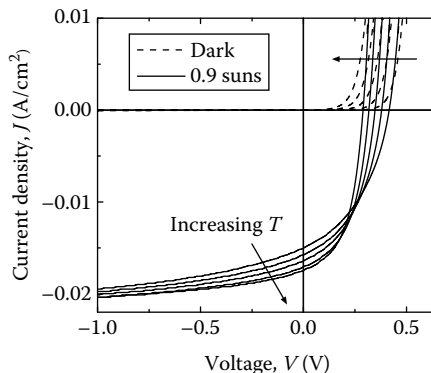


**FIGURE 12.10**

$J$ - $V$  characteristics in the dark and under 0.9 suns of simulated AM1.5 solar illumination at various temperatures for a CuPc:C<sub>60</sub> mixed HJ cell. The arrows indicate the increase of device temperature from 300 to 380 K with an interval of 20 K.

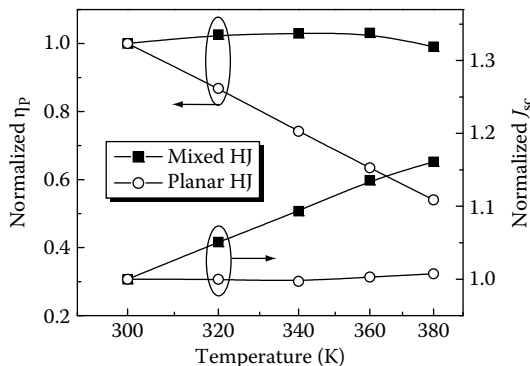


**FIGURE 12.11**

Temperature dependencies of the normalized power conversion efficiency and short-circuit current density for a mixed HJ and a planar HJ cell.

(Sze and Ng, 2007). This leads to a decrease in  $V_{OC}$  with the temperature. For the mixed HJ cell, the short-circuit current density also increases with temperature, suggesting that carrier collection is improved as the thermally activated carrier mobilities in these organic materials are higher at higher temperatures. The power conversion efficiency remains almost unchanged for temperatures up to 380K. For the planar HJ cell,  $J_{SC}$  is unaffected by the temperature (see Figure 12.11) as the carrier collection efficiency remains close to unity in that device. This also suggests that the exciton diffusion process is independent of, or at least is very weakly dependent on, the temperature, which agrees with the results from a previous study on multilayer photo-detectors based on DA HJs (Xue and Forrest, 2004). Since  $V_{OC}$  also decreases with temperature due to the increase in the diode dark current,  $\eta_p$  of the planar HJ decreases with temperature as shown in Figure 12.11.

### 12.2.3 Modeling of Mixed HJ Cell Performance

In a mixed HJ cell, as carrier generation occurs across the entire mixed layer, the carrier concentration gradient is small, leading to a much smaller diffusion component of the photocurrent than the corresponding drift component. Hence the charge transport in a mixed HJ cell may be described by the electron and hole drift lengths, or the mean distances a charge travels in the direction of the electric field before recombination with its counter charge. The drift lengths can be represented as  $l_n = \tau_n \mu_n E$  for electrons and  $l_p = \tau_p \mu_p E$  for holes, where  $\tau_n$  ( $\tau_p$ ) is the electron (hole) lifetime,  $\mu_n$  ( $\mu_p$ ) is the electron (hole) mobility, and  $E$  is the electric field. Following the treatment by Crandall used for  $p-i-n$  a-Si solar cells (Crandall, 1983), we obtain the charge collection efficiency for photogenerated charge carriers within a mixed layer as

$$\eta_{CC} = \frac{L_c}{d_m} \left[ 1 - \exp \left( -\frac{d_m}{L_c} \right) \right], \quad (12.3)$$

where  $d_m$  is the thickness of the mixed layer. Here  $L_c = l_n + l_p$  is the charge collection length, or the characteristic length for transport of photogenerated charge carriers within the mixed layer without experiencing recombination (Crandall, 1983; Xue, 2005; Xue et al., 2005a). From Equation 12.3, clearly we see that  $\eta_{CC} \approx 1$  for  $d_m \ll L_c$ , and  $\eta_{CC} \approx L_c/d_m \ll 1$  for  $d_m \gg L_c$ , suggesting that the mixed layer should be thinner than  $L_c$  to obtain a high  $\eta_{CC}$ .

Due to the electric field dependence of the electron and hole drift lengths, the charge collection length and therefore the charge collection efficiency depend on the applied bias on the PV device. When the applied voltage is  $V < V_{bi}$ , where  $V_{bi}$  is the built-in potential of the device,  $L_c$  can be approximated as

$$L_c \approx (\tau_n \mu_n + \tau_p \mu_p)(V_{bi} - V)/W \approx L_{c0}(V_{bi} - V)/V_{bi}, \quad (12.4)$$

where

$W$  is the depletion width

$L_{c0} = (\tau_n \mu_n + \tau_p \mu_p) V_{bi} / W = L_c |_{V=0}$  is the charge collection length at the short-circuit condition

The photocurrent density in a mixed HJ cell can be expressed as

$$J_{ph}(V) = P_O R_0 \eta_{CC}(V), \quad (12.5)$$

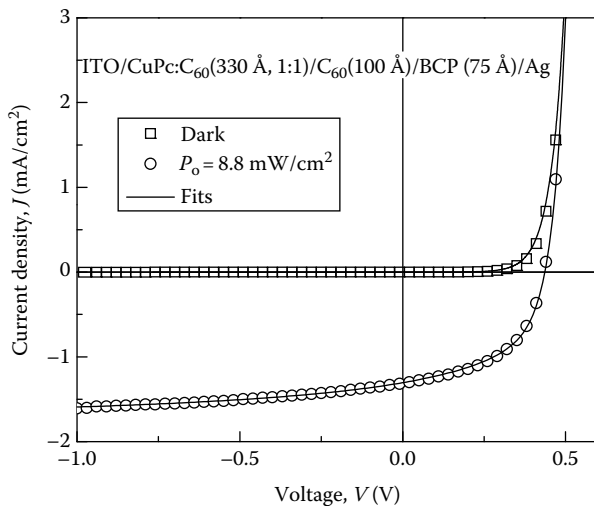
where  $P_O$  is the incident optical power density, and  $R_0 = (J_{ph}/P_O)_{V \rightarrow \infty}$  is the maximum responsivity corresponding to  $\eta_{CC} = 1$ , which can be calculated using the models by Pettersson et al., (1999) and Peumans et al., (2003) by considering both the nonuniform optical field in the active region due to optical interference and exciton diffusion in the homogeneous layers. Using the modified diode equation (Equation 12.2) to describe the dark current density  $J_d(V)$ , we obtain the total current density under illumination as

$$J(V) = J_d(V) + J_{ph}(V) = J_s \left\{ \exp \left[ \frac{q(V - JR_s)}{nkT} \right] - 1 \right\} + P_O R_0 \eta_{CC}(V), \quad (12.6)$$

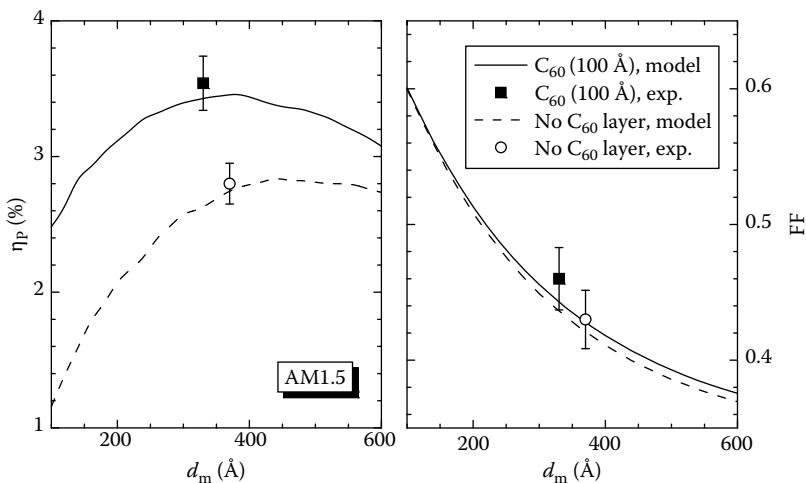
from which the PV cell output parameters ( $J_{SC}$ ,  $V_{OC}$ , FF, and  $\eta_P$ ) can be derived.

Note from Equations 12.3 through 12.5, either a greater  $d_m$  or a shorter  $L_{c0}$  in a mixed HJ PV device leads to a more pronounced voltage dependence of  $\eta_{CC}$ , and consequently a lower FF for the device. It is therefore important to use mixed HJs with high carrier mobilities so that  $L_{c0}$  is comparable to or greater than the optical absorption length to take full advantage of the high  $\eta_{ED}$  in mixed HJs.

Figure 12.12 shows the fitting of the  $J$ - $V$  characteristics in the dark and under simulated AM 1.5 illumination ( $P_O = 8.8 \text{ mW/cm}^2$ ) for a cell with a  $330 \text{ \AA}$  thick active layer of 1:1 mixed CuPc:C<sub>60</sub>, with the following parameters:  $n = 1.6$ ,  $J_s = 20 \text{ nA/cm}^2$ ,  $R_s = 0.22 \Omega \cdot \text{cm}^2$ ,  $R_0 = 0.20 \text{ A/W}$ , and  $V_{bi} = 0.6 \text{ V}$  (Xue, 2005). From the fitting,  $L_{c0} = (450 \pm 50) \text{ \AA}$  is obtained for the 1:1 mixed CuPc:C<sub>60</sub> film, corresponding to  $\eta_{CC} = 70\%$  at  $d_m = 330 \text{ \AA}$  (see Equation 12.3). Using these parameters, we further calculated the performance of mixed HJ cells with different mixed layer thicknesses, either with or without a thin pure C<sub>60</sub> layer in between the mixed layer and the EBL (the function of the pure C<sub>60</sub> layer will be further explained in the following section). As shown in Figure 12.13, the predicted  $\eta_P$  and FF for the two optimized cells agree with the experimental data (Xue, 2005). Moreover, the model predicts an optimal mixed layer thickness of  $d_m = (360 \pm 50) \text{ \AA}$  for the cell with a  $100 \text{ \AA}$  thick C<sub>60</sub> layer, and  $d_m = (450 \pm 50) \text{ \AA}$  for the one without the C<sub>60</sub> layer. Both values are slightly

**FIGURE 12.12**

Comparison of the experimental data (symbols) and model fitting (solid lines) of the  $J$ - $V$  characteristics of a mixed HJ cell in the dark (open squares) and under simulated AM1.5 illumination (open circles).

**FIGURE 12.13**

Model prediction and experimental data for the power conversion efficiency and FF of CuPc: $C_{60}$  mixed HJ cells.

larger than those obtained experimentally (330 Å and 370 Å, respectively). This may be due to the composition variation of the mixed layers across its thickness, which is difficult to maintain at exactly the desired ratio using the vacuum deposition system.

---

## 12.3 CuPc:C<sub>60</sub> Planar–Mixed Heterojunctions

### 12.3.1 Concept of Planar–Mixed Heterojunctions

In the previous section, we have compared performance of small molecule PV cells employing two types of D–A HJ structures: a “planar” HJ formed between pure DA layers, and a “mixed” HJ with DA molecules mixed at the molecular level. The efficiency of a planar HJ cell is limited by the exciton diffusion process as the exciton diffusion length in these organic materials is usually significantly shorter than their optical absorption length, although the charge collection efficiency could approach unity with decent carrier mobilities in these pure layers. For a mixed HJ cell, however, the exciton diffusion efficiency approaches unity as the spatially distributed D–A interface is readily accessible for every exciton generation site. In this case, charge transport through the mixed layer becomes the new bottleneck due to the significantly reduced charge carrier mobilities in the mixed layer compared to those in the respective pure layers.

Due to the limitations of exciton diffusion (in planar HJ cells) or charge transport/collection (in mixed HJ cells), the optimal thickness of the organic active regions in these cells could not be sufficiently large for complete absorption of the incident light. A new type of HJ structure was therefore introduced to combine the advantages of these two types of HJs. The new HJ structure, called “hybrid PM-HJ” (Xue et al., 2005a,b), consists of a mixed layer of the DA molecules sandwiched between pure DA layers. The mixed layer thickness,  $d_m$ , in this PM-HJ structure is less than or comparable to the corresponding charge collection length so that the charge collection efficiency associated with photogenerated charge carriers in this mixed layer is close to unity (see Equation 12.3). The thicknesses of the pure DA layers,  $d_D$  and  $d_A$ , respectively, are less than or comparable to the corresponding exciton diffusion lengths, so that excitons generated in these pure layers have a high probability of reaching the interface with the mixed layer, thereby ensuring a high exciton diffusion/dissociation efficiency. In this way, efficient exciton dissociation and charge carrier generation occurs throughout the mixed layer as well as at the interfaces between the mixed layer and the adjacent pure layers, and the PM-HJ structure has both the high exciton diffusion efficiency of a mixed HJ and the low resistance to charge transport of a planar HJ. Although the individual layers are thinner than in an optimized planar or mixed HJ cell, the total thickness of the active region of a PM-HJ cell is comparable to or greater than the other two types of cells, leading to an equal or greater light absorption efficiency. Table 12.1 compares various performance characteristics of planar, mixed, and PM-HJ cells (Xue, 2005).

Note that similar three-layered structures have been reported previously (Hiramoto et al., 1991, 1992), where 40 nm thick mixed layers of phthalocyanine and perylene derivative molecules were sandwiched between pure

**TABLE 12.1**

Comparisons between the Performances of Optimized Planar, Mixed, and PM-HJ Cells under 1 sun, AM1.5 Solar Illumination

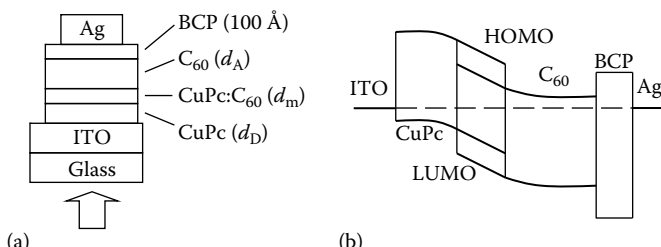
	Planar HJ	Mixed HJ	PM-HJ
Absorption efficiency, $\eta_A$	Good	Fair	Good
Exciton diffusion efficiency, $\eta_{ED}$	Poor	Excellent	Fair
Charge transfer efficiency, $\eta_{CT}$	Excellent	Excellent	Excellent
Charge collection efficiency, $\eta_{CC}$	Excellent	Fair	Excellent
Short-circuit current density, $J_{SC}$	Fair	Good	Good
Fill factor, FF	Excellent	Fair	Excellent
Open-circuit voltage, $V_{OC}$	Good	Good	Good
Power conversion efficiency, $\eta_P$	Good	Good	Excellent

layers. However, the charge collection length in such mixtures is actually very short,  $L_{c0} < 10\text{ nm}$  (Xue et al., 2005b), which leads to  $d_m > 4L_{c0}$  in those devices, and according to Equation 12.3,  $\eta_{CC} < 0.25$ . Hence the advantage of the PM-HJ structure is only realized when the mixed layer is relatively thin, i.e., thinner than the characteristic charge collection length.

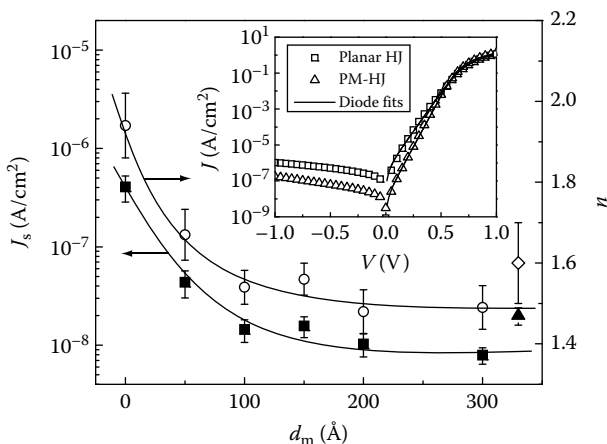
### 12.3.2 Dark Current of CuPc:C<sub>60</sub> Planar–Mixed Heterojunction Cells

The schematic cross section and energy level diagrams of a CuPc:C<sub>60</sub> PM-HJ cell are shown in Figure 12.14. The active region consists of a pure CuPc donor layer, a mixed CuPc:C<sub>60</sub> layer, and a pure C<sub>60</sub> acceptor layer successively deposited on the ITO anode. The thicknesses of these three layers are  $d_D$ ,  $d_m$ , and  $d_A$ , respectively.

The inset of Figure 12.15 shows the  $J$ - $V$  characteristics in the dark for two PV devices based on the CuPc–C<sub>60</sub> material system: a planar HJ cell with  $d_D = 200\text{ \AA}$  and  $d_A = 400\text{ \AA}$  and a PM-HJ cell with  $d_D = 100\text{ \AA}$ ,  $d_m = 200\text{ \AA}$ , and  $d_A = 300\text{ \AA}$ . The CuPc to C<sub>60</sub> ratio in the mixed layer of the PM-HJ cell is 1:1 by weight. Both cells exhibit diode-like characteristics with a high rectification ratio of over 10<sup>6</sup> at  $\pm 1\text{ V}$  and shunt resistances  $> 1\text{ M}\Omega \cdot \text{cm}^2$ . In particular, the PM-HJ device has approximately an order of magnitude lower reverse-bias

**FIGURE 12.14**

(a) Schematic cross section and (b) energy level diagram of a CuPc–C<sub>60</sub> PM–HJ cell.

**FIGURE 12.15**

The fitting results of  $J_s$  (filled squares) and  $n$  (open circles), as a function of  $d_m$ . The solid lines are a guide to the eye. Also indicated are the results ( $J_s$ : filled triangle,  $n$ : open diamond) for a mixed HJ cell. Inset: dark  $J$ - $V$  characteristics for a planar HJ (open squares) and a PM-HJ (open triangles) organic PV cell as well as fits based on the modified diode equation (solid lines).

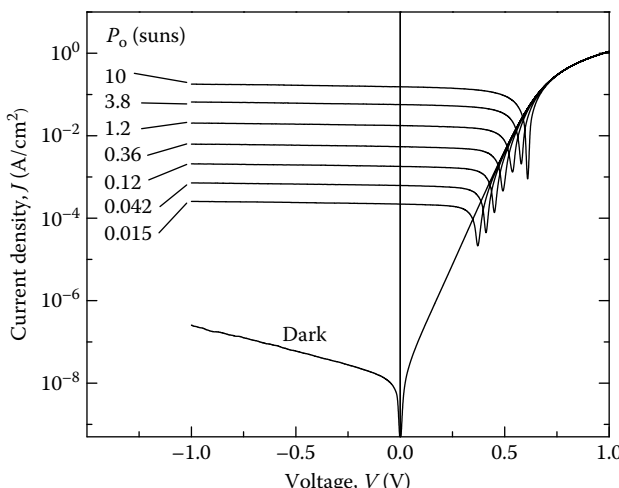
dark current than the planar HJ device. The forward-bias characteristics can again be fit using the modified diode equation (Equation 12.3) (Sze and Ng, 2007), as shown by the solid lines in the inset. Both cells have  $R_{SA} \approx 0.25 \Omega \cdot \text{cm}^2$ ; however, the diode ideality factor is reduced from  $n = 1.94 \pm 0.08$  for the planar HJ cell to  $n = 1.48 \pm 0.05$  for the PM-HJ cell, and the reverse-bias saturation current density is also reduced from  $J_s = (5 \pm 1) \times 10^{-7} \text{ A/cm}^2$  (planar HJ) to  $J_s = (1.0 \pm 0.3) \times 10^{-8} \text{ A/cm}^2$  (PM-HJ). Both  $n$  and  $J_s$  for the PM-HJ cells are dependent on the mixed layer thickness as shown in Figure 12.15. In these PM-HJ cells,  $d_D = d_A - 200 \text{ \AA} = 200 \text{ \AA} - d_m/2$  so that the total thickness of the active region is maintained at 600 Å. As shown in Figure 12.15, with increasing  $d_m$ , both  $n$  (open circles) and  $J_s$  (filled squares) decrease significantly for  $d_m < 100 \text{ \AA}$ , and then tend to saturate to  $n \approx 1.5$  and  $J_s \approx 1 \times 10^{-8} \text{ A/cm}^2$  at  $d_m > 200 \text{ \AA}$ . Also shown are data for the mixed HJ cell with  $d_m = 330 \text{ \AA}$  ( $n$ : open diamond,  $J_s$ : filled triangle) discussed in Section 12.2, which appear to be consistent with the results for the PM-HJ cells.

We attribute the asymptotic dependencies of  $n$  and  $J_s$  on the mixed layer thickness to the reduced charge recombination in the mixed layer as a result of the reduced carrier mobility. In a planar HJ cell, there are significant energy level offsets of  $\sim 1 \text{ eV}$  for both HOMO and LUMO levels at the D-A interface (Peumans and Forrest, 2001), which lead to a negligible diffusion-emission dark current (Sharma and Purohit, 1974). Hence, the dark current in the planar HJ cell is dominated by recombination current in the depletion region, leading to  $n \approx 2$  (Xue et al., 2004a). A closer look at the recombination current reveals that it can be related to the carrier mobility in these organic

semiconductors. Following the Shockley–Hall–Read recombination model, the recombination current is proportional to the carrier thermal velocity (Sze and Ng, 2007), which in turn is proportional to the carrier mobility for disordered semiconductors in which charge carriers are transported via hopping and  $\mu < 1 \text{ cm}^2/\text{V}\cdot\text{s}$  (Paasch et al., 2002). As we have discussed earlier, charge carrier mobilities in the mixed molecular layers are significantly reduced compared to those in pure donor or acceptor layers; therefore we expect that the recombination current in devices containing a mixed layer is significantly reduced compared to that in the planar HJ device which contains only pure layers. In fact, the amount of reduction in  $J_s$  we observe here from  $d_m = 0$  to  $200 \text{ \AA}$ , approximately one and a half order of magnitude, is about the same as the mobility drop in the 1:1 mixed CuPc:C<sub>60</sub> film compared with the pure CuPc (for holes) and C<sub>60</sub> (for electrons) films. With reduced recombination, the diffusion-emission component of the dark current may become appreciable, leading to  $n \approx 1.5$  in cells with a sufficiently thick mixed layer ( $d_m > 200 \text{ \AA}$ ).

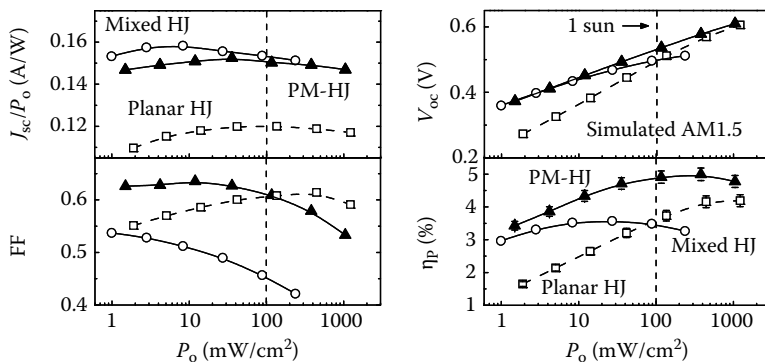
### 12.3.3 Photoresponse of CuPc:C<sub>60</sub> Planar–Mixed Heterojunction Cells

Figure 12.16 shows the  $J$ – $V$  characteristics of a CuPc–C<sub>60</sub> PM-HJ cell in the dark and under various intensities of simulated AM1.5 solar illumination. The donor, mixed, and acceptor layer thicknesses for this cell are  $d_D = 150 \text{ \AA}$ ,  $d_m = 100 \text{ \AA}$ , and  $d_A = 350 \text{ \AA}$ , respectively. Shown in Figure 12.17 are the PV characteristics of this cell (Xue et al., 2005a,b) as compared to the optimized



**FIGURE 12.16**

$J$ – $V$  characteristics of a CuPc–C<sub>60</sub> PM-HJ cell in the dark and under various intensities of simulated AM1.5 solar illumination. The donor, mixed, and acceptor layer thicknesses are  $d_D = 150 \text{ \AA}$ ,  $d_m = 100 \text{ \AA}$ ,  $d_A = 350 \text{ \AA}$ , respectively.

**FIGURE 12.17**

Comparison of the PV performance of a CuPc:C<sub>60</sub> PM-HJ cell (filled triangles), a mixed HJ cell (open circles), and a planar HJ cell (open squares) at various illumination intensities ( $P_o$ ).

planar and mixed HJ cells based on the same D–A material system (Uchida et al., 2004; Xue et al., 2004a). All three cells show a nearly constant responsivity,  $J_{sc}/P_o$ , over the entire range of  $P_o$ . Under simulated 1 sun illumination,  $J_{sc} = (11.8 \pm 0.5)$ ,  $(15.4 \pm 0.7)$ , and  $(15.0 \pm 0.6)$  mA/cm<sup>2</sup> for the planar, mixed, and PM-HJ cells, respectively. As discussed in the previous section, the planar HJ cell has a significantly higher FF than the mixed HJ cell, especially under high illumination intensities, and the lower FF in the mixed HJ cell is attributed to the difficulties of extracting the photogenerated charge carriers from the relatively thick mixed layer (330 Å). For the PM-HJ cell, on the other hand, with a much thinner mixed layer (100 Å), the collection of photogenerated charge carriers is significantly improved, leading to a high FF of 0.6 at 1 sun, approximately the same as that of the planar HJ cell. However, the FF for the PM-HJ cell under more intense illumination does decrease, to 0.53 at  $P_o \approx 10$  suns, due to the low carrier mobilities in the mixed layer.

For all three cells, except at the highest illumination intensities,  $V_{oc}$  increases logarithmically with  $P_o$ , a behavior that has been observed commonly for inorganic *p-n* junction solar cells and can be explained by using the conventional diode theory (Sze and Ng, 2007; Xue et al., 2004a). The slopes of the  $V_{oc}$  vs.  $\log(P_o)$  plots are nearly the same for both the mixed HJ and PM-HJ cells, both smaller than that for the planar HJ device. According to the diode theory (Sze and Ng, 2007; Xue et al., 2004a), such a slope is directly related to the ideality factor of the diodes, and as discussed earlier,  $n \approx 1.5$  for the mixed HJ and PM-HJ cells, whereas  $n \approx 2$  for the planar HJ cell.

Overall, while both the mixed and planar HJ cells have power conversion efficiencies of  $\eta_p \approx 3.5\%$  at 1 sun illumination, the efficiency of the PM-HJ cell is approximately 40% higher, reaching  $\eta_p = (5.0 \pm 0.3)\%$ . The efficiency of the PM-HJ cell is peaked with the illumination intensity in the range of  $1 \text{ sun} \leq P_o \leq 4$  suns, due to interplay of the illumination intensity dependencies of FF and  $V_{oc}$ . At  $P_o < 1$  sun, the FF is nearly constant and the increase

of  $V_{OC}$  with  $P_O$  contributes to the increase of  $\eta_P$ . At  $P_O > 4$  suns, although we still observe the increase of  $V_{OC}$  with  $P_O$ , the significant reduction of FF at such intense illumination levels dictates the drop-off of  $\eta_P$ . Also note that the intensity at which maximum efficiency of the PM-HJ cell is achieved can be adjusted by varying the mixed layer thickness used in the cell. For the PM-HJ cell described above in which  $d_m = 100 \text{ \AA}$ , peak  $\eta_P$  is achieved at  $1 \text{ sun} \leq P_O \leq 4$  suns. With a thicker mixed layer, FF decreases more rapidly with increasing  $P_O$ , leading to  $\eta_P$  peaking at lower intensities; on the other hand, for cells with a very thin mixed layer ( $d_m \leq 50 \text{ \AA}$ ), the cell series resistance ultimately limits FF under intense illuminations, similar to the situation in planar HJ cells (Xue et al., 2004a). For example, for a PM-HJ cell with  $d_m = 150 \text{ \AA}$ ,  $\eta_P$  reaches its maximum at  $0.4 \text{ sun} \leq P_O \leq 1.2$  suns, whereas the peak efficiency is achieved at  $P_O \approx 4\text{--}10$  suns for a cell with  $d_m = 50 \text{ \AA}$  (Xue, 2005).

The external and internal quantum efficiencies,  $\eta_{ext}$  and  $\eta_{int}$ , respectively, of the planar HJ cell and the PM-HJ cell are compared in Figure 12.18 (Xue, 2005; Xue et al., 2005b). The quantum efficiencies are comparable in the region between  $\lambda = 400$  and  $530 \text{ nm}$  where  $C_{60}$  absorption dominates. The efficiencies of the PM-HJ cell, however, are considerably higher than those of the planar HJ cell in the CuPc absorption region, i.e.,  $550 \text{ nm} < \lambda < 750 \text{ nm}$ . This means that mixing the CuPc and  $C_{60}$  molecules within  $50 \text{ \AA}$  of the D-A interface in the planar HJ cell leads to an increase in  $\eta_{int}$  from  $\sim 50\%$  to  $\sim 75\%$  in the CuPc absorption region, while  $\eta_{int}$  remains almost unchanged in the  $C_{60}$  absorption region. This trend is consistent with the different exciton diffusion lengths in CuPc and  $C_{60}$ , which are approximately  $100$  and  $400 \text{ \AA}$ , respectively (Peumans et al., 2003). In the planar HJ cell, the donor layer thickness

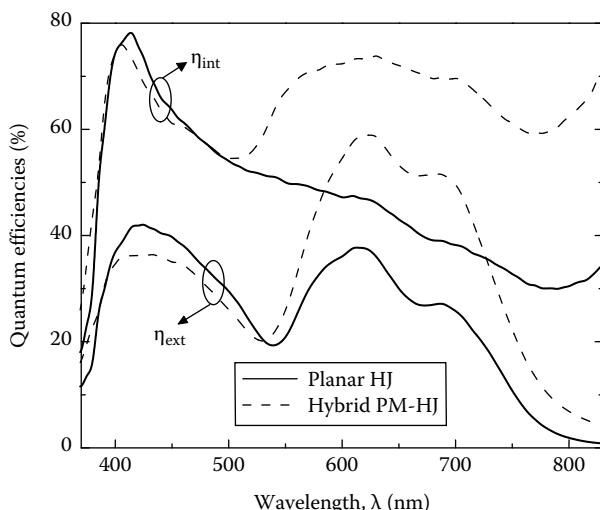


**FIGURE 12.18**

Internal ( $\eta_{int}$ ) and external ( $\eta_{ext}$ ) quantum efficiencies of a PM-HJ and a planar HJ cell.

is twice as much as the exciton diffusion length, while the acceptor layer thickness is approximately the same as the corresponding exciton diffusion length. Hence, exciton diffusion is more of a problem for absorption by the donor molecules than by the acceptor molecules. As we expect the exciton diffusion efficiency to approach unity in the mixed layer, the mixing of the DA molecules therefore leads to a significant increase in  $\eta_{int}$  for absorption by the CuPc molecules. Note that integrating the external quantum efficiencies of the planar and PM-HJ cells with the standard AM1.5 solar spectrum yields  $J_{SC}=9.7$  and  $12.9\text{ mA/cm}^2$ , respectively, which are approximately 15% lower than the experimental data. This is attributed to the deviation of the output spectrum of the Xe-arc solar simulator used in the experiments from the standard AM1.5 solar spectrum.

Shown in Figure 12.19 are the PV performance parameters under 1.2 suns of simulated AM1.5 illumination for a series of PM-HJ cells with varying mixed layer thicknesses. The total thickness of the active region was maintained at  $600\text{ \AA}$  as  $d_D=d_A=200\text{ \AA}-d_m/2=200\text{ \AA}-d_m/2$ , whereas the ratio of CuPc to  $C_{60}$  in the mixed layer was also maintained at 1:1 by weight. While  $V_{OC}$  for these devices mostly remains the same at  $0.52\text{--}0.54\text{ V}$ ,  $J_{SC}$  shows a strong dependence on  $d_m$ . With increasing  $d_m$ ,  $J_{SC}$  at first monotonically increases for  $d_m \leq 200\text{ \AA}$ , consistent with the better exciton diffusion in the mixed layer than in pure layers. For  $d_m > 200\text{ \AA}$ , however,  $J_{SC}$  decreases with the further increase of  $d_m$ , which is attributed to the significantly reduced charge collection efficiency as the thickness approaches the charge collection length. The inferior charge transport properties of the mixed layer as compared with the pure layers also affect the FF of the devices significantly. As seen in Figure 12.19, the FF decreases from  $>0.6$  for devices with  $d_m \leq 100\text{ \AA}$  to only 0.43 for

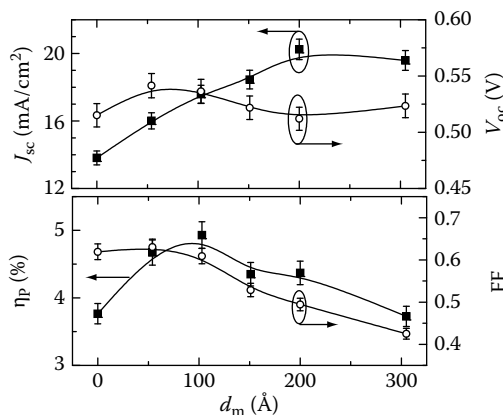


**FIGURE 12.19**

Performance of hybrid PM-HJ cells under 1.2 suns of simulated AM1.5 solar illumination, as functions of the mixed layer thickness  $d_m$ . The thicknesses of the DA layers are  $d_D=200\text{ \AA}-d_m/2$  and  $d_A=400\text{ \AA}-d_m/2$ , respectively.

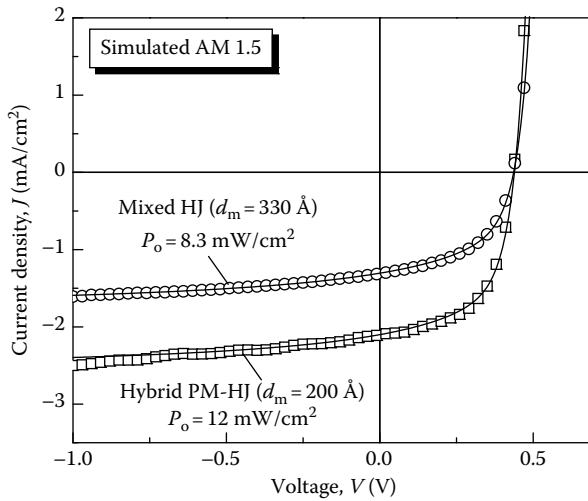
the device with  $d_m = 300 \text{ \AA}$ . Overall, the maximum  $\eta_p \approx 5\%$  was achieved in the device with  $d_m = 100 \text{ \AA}$  ( $d_D = 150 \text{ \AA}$  and  $d_A = 350 \text{ \AA}$ , accordingly).

### 12.3.4 Modeling the Performance of CuPc:C<sub>60</sub> Planar–Mixed Heterojunction Cells

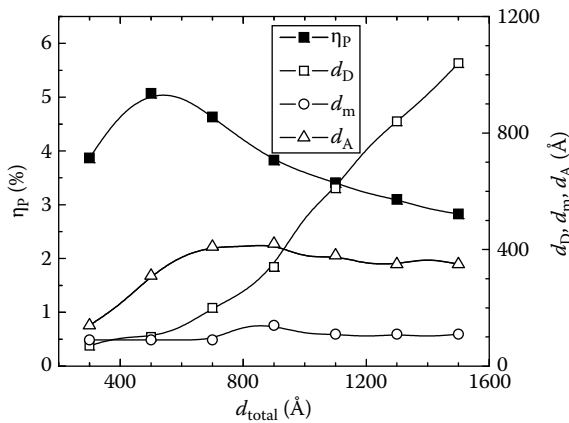
The PM-HJ cells can be modeled in a way similar to that for mixed HJ cells as described in Section 12.2.3 (see Equations 12.3 through 12.6). The main difference is that the concentration of photogenerated charges at the layer interfaces (donor/mixed and mixed/acceptor) would be much higher than that within the mixed layer due to the diffusion of excitons from the bulk of the pure DA layers.  $\eta_{CC}$  expressed in Equation 12.3 represents the average collection efficiency for charges uniformly generated in the mixed layer. In a PM-HJ cell, holes generated at the donor layer/mixed layer interface can be collected at the anode with nearly no losses, i.e.,  $\eta_{CC} \approx 100\%$ . However the holes generated at the mixed layer/acceptor interface have to be transported through the entire mixed layer to reach the pure donor layer and eventually be collected at the anode; therefore, the corresponding collection efficiency for these holes should be lower than that expressed in Equation 12.3. Here, we still use Equation 12.3 to represent the average charge collection efficiency for charges generated everywhere in the active region of a PM-HJ cell. An exact expression can be obtained in a similar fashion as Crandall used for *p*–*i*–*n* a-Si solar cells by self-consistently solving the carrier concentration profile (Crandall, 1983). For PM-HJ cells with thin mixed layers, e.g.,  $d_m < L_{c0}/2$ , the approximation of charge collection efficiency used here only leads to small errors as  $\eta_{CC} \approx 80\%$  is close to unity.

Figure 12.20 shows the fitting of the photoresponse of a PM-HJ cell with  $d_m = 200 \text{ \AA}$  under an illumination intensity of  $P_O = 12 \text{ mW/cm}^2$ . A zero-bias charge collection length of  $L_{c0} = (450 \pm 50) \text{ \AA}$  was obtained from the fitting, which agrees with that obtained from the fitting of the mixed HJ device discussed in Section 12.2.3 (the *J*–*V* characteristics under illumination are also shown here for comparison). Such a charge collection length leads to  $\eta_{CC} \approx 0.8$  for this PM-HJ cell and  $\eta_{CC} \approx 0.7$  for the mixed HJ cell under short-circuit conditions. Also note that the charge collection length is comparable to the optical absorption length ( $L_A = 1/\alpha \approx 600 \text{ \AA}$ , where  $\alpha$  is the absorption coefficient), suggesting the existence of percolating paths for electron and hole transport in the 1:1 mixed CuPc:C<sub>60</sub> layer.

Note that the active layers of the optimized PM-HJ cells described here are fairly thin, at  $600 \text{ \AA}$  in total. For large area production of organic PV devices, it is desirable to use sufficiently thick organic layers between the electrodes to minimize the effect of pinholes and other microscopic structural defects, which would otherwise lead to electrical shorts and lower the device yield. Using the model described earlier, we can simulate the performance of the PM-HJ cells with any combinations of donor, mixed, and acceptor layer thicknesses. Shown in Figure 12.21 is the dependence of the maximum  $\eta_p$  as a

**FIGURE 12.20**

Comparison between model predictions (solid lines) and experimental  $J$ - $V$  characteristics of a PM-HJ cell (open squares) and a mixed HJ cell (open circles) under simulated AM1.5 solar illumination.

**FIGURE 12.21**

Calculated optimized power conversion efficiency (filled squares)  $\eta_p$  and individual layer thicknesses (open symbols) of PM-HJ cells under 1 sun of simulated solar illumination, as functions of the total active layer thickness  $d_{total}$ .

function of the total active layer thickness  $d_{total} = d_D + d_m + d_A$ , as well as the individual layer thicknesses ( $d_D$ ,  $d_m$ , and  $d_A$ ) in optimized structures (Xue et al., 2005b). The efficiency is peaked at approximately 5% with  $d_{total} \approx 500 \text{ \AA}$ , and gradually decreases with a further increase in  $d_{total}$ . Nevertheless,  $\eta_p > 3\%$

is still achieved with  $d_{\text{total}}$  up to 1400 Å. In these optimized structures, it is also interesting to note that  $d_m$  is maintained at approximately 100 Å, while  $d_A$  saturates at 350–400 Å for devices with  $d_{\text{total}} > 600$  Å. The optimized CuPc layer thickness, on the other hand, increases linearly with  $d_{\text{total}}$ . As the exciton diffusion length in CuPc is approximately 100 Å, this suggests that the lowering of  $\eta_P$  for devices with thicker  $d_{\text{total}}$  is mostly due to the extra CuPc layer acting as a filter for the incoming sunlight. Hence, to further improve the efficiency of PM-HJ cells with thick layers, one may use a *p*-doped transparent organic layer (Maennig et al., 2004) to replace that first portion of the CuPc layer, leaving only a ~150 Å thick CuPc film adjacent to the mixed layer.

---

## 12.4 Tandem Cells Based on CuPc:C<sub>60</sub> Planar–Mixed Heterojunctions

### 12.4.1 Background of Organic Tandem Cells

As we discussed in earlier sections, in a planar HJ, there exists a trade-off between the exciton diffusion efficiency and the absorption efficiency of the incident light. For a mixed HJ, the trade-off shifts to between the charge collection efficiency and the light absorption efficiency. The absorption coefficients for typical organic PV materials in their strongly absorptive regions can be as high as  $(1\text{--}2) \times 10^5$  cm<sup>-1</sup>, corresponding to optical absorption lengths of  $L_A \approx 500\text{--}1000$  Å. Hence, an organic active region of 500–1000 Å thick is needed to achieve  $\eta_A > 85\%$  when a reflective electrode is used, or twice the thickness when both electrodes are transparent or semitransparent. However, using thicker layers leads to a lower exciton diffusion efficiency in a planar HJ cell, or a lower charge collection efficiency in a mixed HJ cell. The trade-offs are alleviated to some extent when a mixed layer is sandwiched between pure layers to form the PM-HJ structure as described in the previous section. Nevertheless, the less than perfect exciton diffusion and charge collection in such PM-HJ cells leads to internal quantum efficiencies  $\eta_{\text{int}} < 75\%$  (see Figure 12.18) for an active region of 600 Å thickness.

One means to increase the total absorption of the incident light without reducing the internal quantum efficiency is to stack two or more thin cells in series to form “tandem cells.” This also serves to increase the open-circuit voltage of the PV cell due to the addition of the photovoltage of each individual subcell. Tandem cells have been widely used for inorganic semiconductors to realize the world’s most efficient PV cells so far (King et al., 2007; Geisz et al., 2008), in which multiple semiconductors with different bandgaps are used in the subcells to capture different portions of the solar spectrum (Sze and Ng, 2007). For organic semiconductors, we could also use the tandem cell structure to integrate multiple D–A material systems to broadly

cover the solar spectrum. However, even using the same D-A pairs in all the subcells, organic tandem cells can still provide advantages over a single cell by improving the internal quantum efficiency in each thinner individual subcell.

In the first demonstration of organic tandem cells, a 15 nm thick, semi-transparent Au layer was used to connect the two subcells, which significantly reduces the intensity of light reaching the subcell farther away from the direction of incident light (Hiramoto et al., 1990). Yakimov and Forrest employed an ultrathin (~5 Å nominal thickness) layer of Ag nanoclusters between the subcells to achieve more than doubling in  $\eta_p$  using the D-A material system of CuPc and PTCBI (Yakimov and Forrest, 2002). While a single CuPc/PTCBI cell has a  $\eta_p$  of approximately 1% (Tang, 1986; Peumans et al., 2000), a two-cell tandem device with a Ag nanocluster layer acting as the charge recombination zone (CRZ) in between the subcells yielded a  $\eta_p$  of 2.5% (Yakimov and Forrest, 2002). The Ag nanoclusters do not attenuate the light reaching the second subcell, and were also shown to enhance the local optical field, leading to enhanced absorption of light by organic molecules in their vicinity (Peumans et al., 2003; Rand et al., 2004).

#### 12.4.2 Asymmetric Organic Tandem Cells Based on CuPc-C<sub>60</sub> PM-HJs

The cross section of a two-subcell tandem organic PV cell with CuPc-C<sub>60</sub> PM-HJs is schematically shown in Figure 12.22a, whereas the schematic energy level diagram is shown in Figure 12.22b. The anode and the cathode are ITO and Ag, respectively, with the light incident on the device active region through the transparent ITO electrode. We call the subcell that is nearest to the ITO as the “front (sub)cell” and the subcell nearest the Ag (or farthest away from the direction of incident light) as the “back (sub)cell.” The PV region of each subcell consists of a PM-HJ, or a thin mixed layer of CuPcC<sub>60</sub> sandwiched between pure CuPc donor and C<sub>60</sub> acceptor layers.

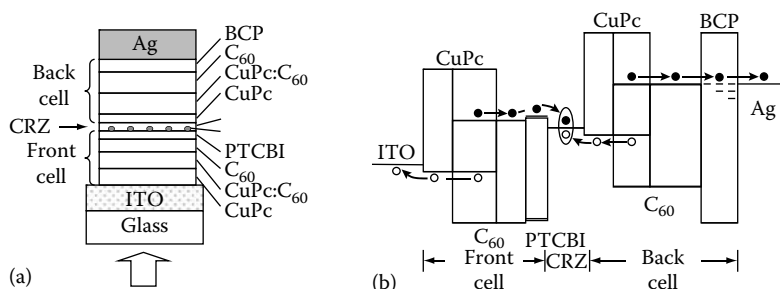


**FIGURE 12.22**

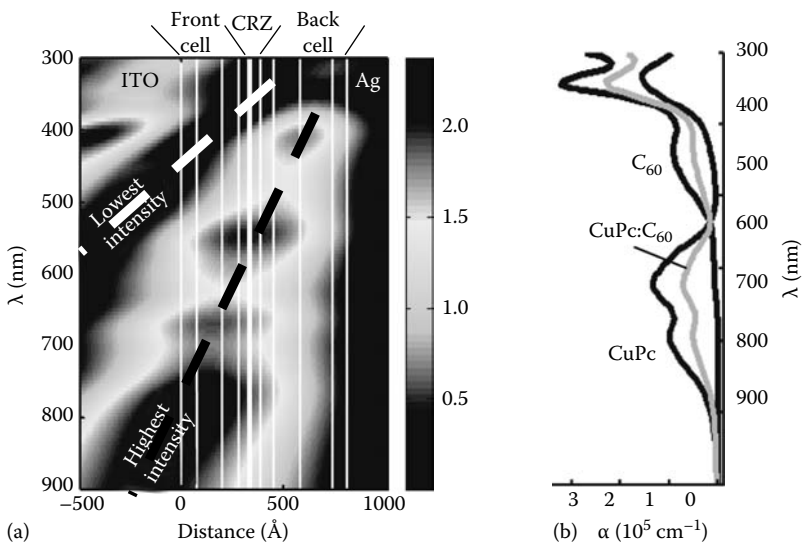
Device structure (a) and schematic energy level diagram (b) of a tandem organic PV cell with CuPc-C<sub>60</sub> planar-mixed molecular HJs.

Thin layers of PTCBI (50 Å thick) and BCP (75 Å thick) are used as the EBL in the front and back subcells, respectively, thereby forming a high efficiency double HJ PV structure (Peumans et al., 2000). A CRZ consisting of Ag nanoclusters (~5 Å average thickness) buried in a 50 Å thick 4,4',4''-tris(3-methyl-phenyl-phenyl-amino)triphenylamine (*m*-MTDATA) *p*-doped with 5 mol% tetrafluoro-tetracyano-quinodimethane (F<sub>4</sub>-TCNQ) (Maennig et al., 2004) was employed to connect the two subcells in series, where electrons generated in the front cell and holes generated in the back cell recombine.

The previously demonstrated CuPc/PTCBI tandem cells had symmetric spectral response from each of the two subcells. However, in organic PV cells, the interference of the incident light and the portion of light reflected by the metal electrode leads to a standing wave of optical field in the organic layers and the maximum optical intensity is achieved at a distance of  $\lambda/4n$  from the organic/cathode interface, where  $\lambda$  is the incident light wavelength and  $n$  is the average refractive index of the intervening organic layers. This suggests that optimal light absorption can be achieved by using an “asymmetric” tandem cell design in which the front cell efficiently absorbing at longer wavelengths and the back cell is tuned for absorption in the shorter wavelengths. This may be achieved by using different D-A material systems in the subcells, with the materials in the front cell absorbing at longer wavelengths. The unique structure of the PM-HJ allows for the realization of the asymmetric configuration even with the same D-A material system for the active layers. Considering that CuPc absorbs strongly between  $\lambda=550$  and 750 nm, and C<sub>60</sub> between  $\lambda=350$  and 550 nm, an asymmetric CuPc-C<sub>60</sub> PM-HJ tandem cell is realized when the front cell has a thicker pure CuPc layer but a thinner pure C<sub>60</sub> layer than the back cell.

Figure 12.23a shows the calculated optical field intensity in a CuPc-C<sub>60</sub> tandem PM-HJ cell as a function of both the distance from the ITO/front cell interface and the wavelength (between 300 and 900 nm) using a transfer-matrix method (Peumans et al., 2003). The thicknesses of all the organic layers in this cell are summarized in Table 12.2. Clearly, the peak optical intensity (depicted by the black dashed line) for the shorter wavelength light is located closer to the reflective Ag cathode. For example, the intensity at  $\lambda=650$  nm, corresponding to the center of the CuPc absorption region (see Figure 12.22b for the absorption spectra of CuPc, C<sub>60</sub>, and the mixed film), is located at approximately 600 Å away from the Ag cathode. As a comparison, the intensity at  $\lambda=450$  nm, around which C<sub>60</sub> absorbs strongly but CuPc does not, peaks at approximately 350 Å away from the Ag cathode. Hence, making the front cell rich in longer wavelength-absorbing material(s), i.e., CuPc in this case, and the back cell rich in shorter wavelength absorbing material(s), i.e., C<sub>60</sub>, leads to increased absorption of the broad solar spectrum. The tandem cell discussed here indeed satisfies such a condition.

Following the modeling of the *J-V* characteristics of each individual PM-HJ cell, we can also model the overall *J-V* characteristics of the tandem cell given that  $J=J_1=J_2$  and  $V=V_1+V_2$ , in which  $J_i$  and  $V_i$  are the current density

**FIGURE 12.23**

Calculated optical field intensity in the spectral range of  $300\text{ nm} \leq \lambda \leq 900\text{ nm}$ , as a function of the distance from the ITO/front cell interface in tandem cell B. (b) Absorption coefficient of CuPc,  $C_60$ , and 1:1 mixed CuPc: $C_60$  in the same spectral range.

**TABLE 12.2**

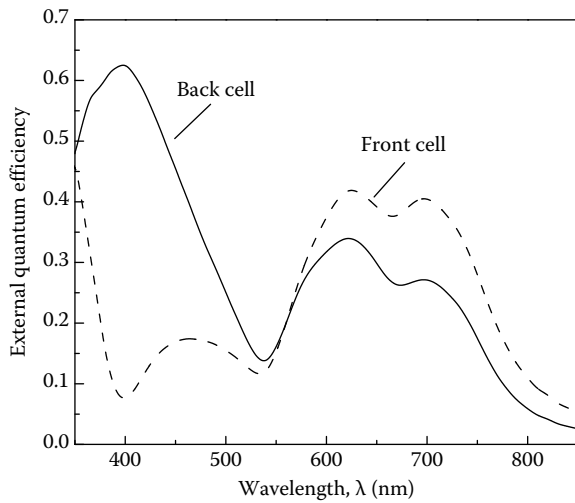
Layer Thicknesses (in Å) of an Asymmetric Tandem Organic PV Cell Based on CuPc– $C_60$  PM-HJs

Front Cell				CRZ		Back Cell			
CuPc	CuPc: $C_60$	$C_60$	PTCBI	Ag	<i>m</i> -MTDATA	CuPc	CuPc: $C_60$	$C_60$	BCP
75	125	80	50	5	50	60	130	160	75

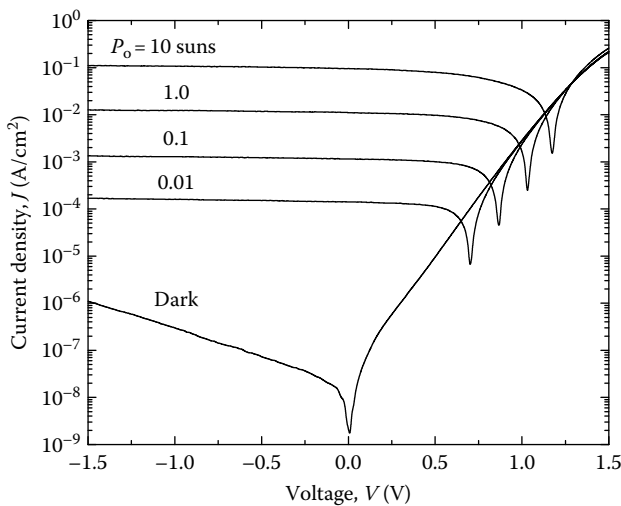
Note: CRZ, charge recombination zone.

and voltage, respectively, for the serially connected subcells ( $i=1$  for the front cell and  $i=2$  for the back cell). Figure 12.24 shows the calculated external quantum efficiency of the subcells (Xue et al., 2004b). In the  $C_60$  absorption region ( $\lambda < 550\text{ nm}$ ), the back cell has a significantly higher external quantum efficiency than the front cell, whereas in the longer wavelength region ( $\lambda > 550\text{ nm}$ ) where CuPc absorption dominates, the front cell has a higher efficiency. Such asymmetric device response is a combination of the interference effect and the asymmetric device structure used here.

The experimental  $J$ – $V$  characteristics of this tandem cell in the dark and under various intensities of simulated AM1.5 illumination are shown in Figure 12.25 (Xue et al., 2004b). Similar to single cells, the dark current of the two-cell tandem device exhibits diode characteristics with a high rectification ratio of  $10^5$ – $10^6$  at  $\pm 1.5\text{ V}$ . By fitting the forward-bias characteristics

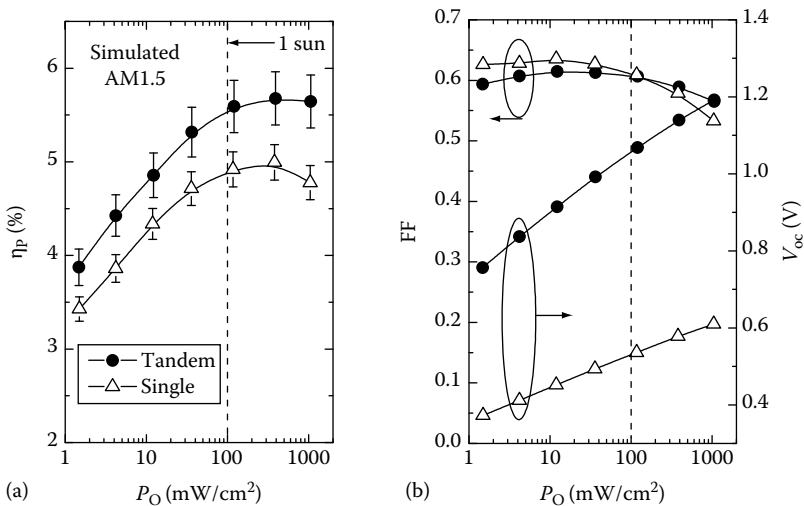
**FIGURE 12.24**

Calculated external quantum efficiencies of the front (dashed line) and back (solid line) subcells of the tandem cell.

**FIGURE 12.25**

$J$ - $V$  characteristics in the dark and under various intensities of simulated AM1.5 solar illumination for an asymmetric organic tandem cell.

to the modified diode equation (Equation 12.2), an ideality factor of  $n=3.2$  was obtained for the tandem cell. Considering that the tandem cell is a serial connection of two subcells, i.e.,  $V=V_1+V_2$ , this corresponds to each subcell having  $n=1.6$ , which is consistent with the results for single PM-HJ

**FIGURE 12.26**

Illumination intensity ( $P_O$ ) dependencies of (a) the power conversion efficiency ( $\eta_P$ ), and (b) the FF and the open-circuit voltage ( $V_{oc}$ ), for the tandem PM-HJ cell, compared to those of the single optimized PM-HJ.

cells discussed above. The series resistance of the tandem cell obtained from the diode fitting is  $R_{SA} = 0.5 \Omega \cdot \text{cm}^2$ , again doubling that of a single cell (Xue et al., 2004b, 2005b).

Figure 12.26 shows the comparison of the PV performance parameters of this tandem cell with those of the optimized single PM-HJ cell under various illumination intensities. The FF of the tandem cell is maintained at around 0.6, similar to that of the single cell, due to the relatively thin mixed layers used in the devices ( $d_m \leq 130 \text{ \AA}$ ). Even at an intense illumination of more than 10 suns, the tandem device still achieves a high FF of 0.56. Furthermore, the tandem cell shows an approximate doubling of the  $V_{oc}$  compared to the single cell as expected from the serial connection of the two subcells. At 1 sun illumination, while  $V_{oc} = 0.53 \text{ V}$  for the single cell, it is 1.05 V for the tandem cell. The maximum  $V_{oc}$  of 1.2 V was achieved from the tandem cell under  $P_O \approx 11$  suns. The short-circuit current density of the tandem cell, however, is only  $J_{SC} = 9.2 \text{ mA/cm}^2$ , significantly lower than that of the single cell, which is approximately 15 mA/cm<sup>2</sup>. This is very different from what was observed earlier for CuPc/PTCBI tandem devices, in which  $J_{SC}$  of the tandem cell was actually higher than that of a single cell. The difference lies in the fact that the single CuPc-C<sub>60</sub> PM-HJ cell is much more efficient than the single CuPc/PTCBI bilayer (planar HJ) cell, and the former absorbs a much greater portion of the incoming light leading to a significant attenuation of the light intensity reaching the back cell. To maintain the same level of current output from the two subcells in series, the layer thicknesses of the front CuPc-C<sub>60</sub>

PM-HJ cell have to be slightly reduced from those in an optimized single cell, resulting in a lower light absorption efficiency by the front cell compared to a single optimized cell. Nevertheless, the reduced layer thicknesses do lead to a higher internal quantum efficiency, and the existence of two subcells in the tandem device compensates the reduced light absorption by each subcell. As a result, a power conversion efficiency of  $\eta_P = (5.7 \pm 0.3)\%$  was obtained from the CuPc–C<sub>60</sub> tandem cell (Xue et al., 2004b; Xue, 2005), which is approximately 15% higher than that of a single optimized cell.

---

## 12.5 Conclusions

In this chapter, we discussed the use of mixed molecular HJs to circumvent the exciton diffusion bottlenecks in organic DA HJ PV cells. With little or no phase separation between the molecular species in the mixture, excitons generated within the active region can all reach a DA interface with very high probability, leading to dissociation of excitons and generation of separated electron and hole pairs. However, the intermixing of two molecular species, especially at the molecular level, presents additional challenges for extracting the photogenerated charge carriers from the active region, since the charge carrier mobility is generally significantly reduced as a result of molecular intermixing. In the CuPc:C<sub>60</sub> DA system, the mobility reduction depends on the detailed mixing ratio between the two materials, and in a 1:1 mixed film, both the electron and hole mobilities are reduced by more than one order of magnitude compared to those in the corresponding pure films (CuPc for holes and C<sub>60</sub> for electrons). Hence, the PV properties of the mixed HJ cells are determined by the trade-off between using a thick layer for sufficient light absorption and using a thin layer for high charge collection efficiency. A PM-HJ was then proposed in which a thin mixed layer was sandwiched between relatively thin pure DA layers, which effectively combines the advantages of the high charge collection efficiency in a planar HJ cell and the high exciton diffusion efficiency of a mixed HJ cell. Using the CuPc:C<sub>60</sub> DA system, a 40% increase in the power conversion efficiency was achieved using this new PM-HJ structure, as compared with a single planar HJ or a single mixed HJ device. Furthermore, two-subcell tandem device structures were implemented with each individual subcell consisting of a PM-HJ structure. Compared with an optimized single cell, the tandem cell achieves a similar FF and doubles the voltage due to the serial connection of the subcells. Even though the short-circuit current is reduced due to the distribution of the incoming light to the two subcells, the reduced layer thicknesses leads to a higher internal quantum efficiency, and an overall 15% increase in the power conversion efficiency was demonstrated, leading to  $\eta_P = 5.7\%$  under 1 sun of simulated AM1.5 solar illumination.

---

## Acknowledgments

The author gratefully acknowledges financial support from the CAREER Program of the National Science Foundation and the Solar Energy Technologies Program of the U.S. Department of Energy for this work.

---

## References

- Crandall, R. S. 1983. Modeling of thin-film solar-cells—Uniform-field approximation. *Journal of Applied Physics* 54 (12):7176–7186.
- Dunlap, D. H., Parris, P. E., and Kenkre, V. M. 1996. Charge-dipole model for the universal field dependence of mobilities in molecularly doped polymers. *Physical Review Letters* 77 (3):542–545.
- E, J. Y., Kim, S., Lim, E. J., Lee, K. J., Cha, D. J., and Friedman, B. 2003. Effects of substrate temperature on copper(II) phthalocyanine thin films. *Applied Surface Science* 205 (1–4):274–279.
- Forrest, S. R. 2005. The limits to organic photovoltaic cell efficiency. *MRS Bulletin* 30 (1):28–32.
- Gebeyehu, D., Maennig, B., Drechsel, J., Leo, K., and Pfeiffer, M. 2003. Bulk-heterojunction photovoltaic devices based on donor–acceptor organic small molecule blends. *Solar Energy Materials and Solar Cells* 79 (1):81–92.
- Geisz, J. F., Friedman, D. J., Ward, J. S., Duda, A., Olavarria, W. J., Moriarty, T. E., Kiehl, J. T., Romero, M. J., Norman, A. G., and Jones, K. M. 2008. 40.8% Efficient inverted triple-junction solar cell with two independently metamorphic junctions. *Applied Physics Letters* 93 (12):123505.
- Halls, J. J. M., Walsh, C. A., Greenham, N. C., Marseglia, E. A., Friend, R. H., Moratti, S. C., and Holmes, A. B. 1995. Efficient photodiodes from interpenetrating polymer networks. *Nature* 376 (6540):498–500.
- Hiramoto, M., Fujiwara, H., and Yokoyama, M. 1991. Three-layered organic solar-cell with a photoactive interlayer of codeposited pigments. *Applied Physics Letters* 58 (10):1062–1064.
- Hiramoto, M., Fujiwara, H., and Yokoyama, M. 1992. p–i–n Like behavior in three-layered organic solar cells having a co-deposited interlayer of pigments. *Journal of Applied Physics* 72 (8):3781–3787.
- Hiramoto, M., Suezaki, M., and Yokoyama, M. 1990. Effect of thin gold interstitial-layer on the photovoltaic properties of tandem organic solar-cell. *Chemistry Letters* 19 (3):327–330.
- Kim, J. Y., Lee, K., Coates, N. E., Moses, D., Nguyen, T. Q., Dante, M., and Heeger, A. J. 2007. Efficient tandem polymer solar cells fabricated by all-solution processing. *Science* 317 (5835):222–225.
- King, R. R., Law, D. C., Edmondson, K. M., Fetzer, C. M., Kinsey, G. S., Yoon, H., Sherif, R. A., and Karam, N. H. 2007. 40% Efficient metamorphic GaInP/GaInAs/Ge multijunction solar cells. *Applied Physics Letters* 90 (18):183516.
- Lenzneroff, C. C. and Lever, A. B. P. 1989. *Phthalocyanines Properties and Applications*. New York: VCH Publishers Inc.

- Ma, W. L., Yang, C. Y., Gong, X., Lee, K., and Heeger, A. J. 2005. Thermally stable, efficient polymer solar cells with nanoscale control of the interpenetrating network morphology. *Advanced Functional Materials* 15 (10):1617–1622.
- Maennig, B., Drechsel, J., Gebeyehu, D., Simon, P., Kozlowski, F., Werner, A., Li, F. et al. 2004. Organic p-i-n solar cells. *Applied Physics A* 79:1–14.
- Paasch, G., Lindner, T., and Scheinert, S. 2002. Variable range hopping as possible origin of a universal relation between conductivity and mobility in disordered organic semiconductors. *Synthetic Metals* 132:97–104.
- Padinger, F., Rittberger, R. S., and Sariciftci, N. S. 2003. Effects of postproduction treatment on plastic solar cells. *Advanced Functional Materials* 13 (1):85–88.
- Pettersson, L. A. A., Roman, L. S., and Inganäs, O. 1999. Modeling photocurrent action spectra of photovoltaic devices based on organic thin films. *Journal of Applied Physics* 86 (1):487–496.
- Peumans, P., Bulovic, V., and Forrest, S. R. 2000. Efficient photon harvesting at high optical intensities in ultrathin organic double-heterostructure photovoltaic diodes. *Applied Physics Letters* 76 (19):2650–2652.
- Peumans, P. and Forrest, S. R. 2001. Very-high-efficiency double-heterostructure copper phthalocyanine/C-60 photovoltaic cells. *Applied Physics Letters* 79 (1):126–128.
- Peumans, P., Uchida, S., and Forrest, S. R. 2003. Efficient bulk heterojunction photovoltaic cells using small-molecular-weight organic thin films. *Nature* 425 (6954):158–162.
- Peumans, P., Yakimov, A., and Forrest, S. R. 2003. Small molecular weight organic thin-film photodetectors and solar cells. *Journal of Applied Physics* 93 (7):3693–3723.
- Pope, M. and Swenberg, C. E. 1999. *Electronic Processes in Organic Crystals and Polymers*, 2nd edn. New York: Oxford University Press.
- Rand, B. P., Peumans, P., and Forrest, S. R. 2004. Long-range absorption enhancement in organic tandem thin-film solar cells containing silver nanoclusters. *Journal of Applied Physics* 96 (12):7519–7526.
- Rand, B. P., Xue, J., Uchida, S., and Forrest, S. R. 2005. Mixed donor–acceptor molecular heterojunctions for photovoltaic applications. I. Material properties. *Journal of Applied Physics* 98 (12):124902.
- Sharma, B. L. and Purohit, R. K. 1974. *Semiconductor Heterojunctions*, B. R. Pamplin (ed.), *International Series of Monographs in the Science of the Solid State*. New York: Pergamon Press.
- Sielcken, O. E., Tilborg, M. M. Van, Roks, M. F. M., Hendriks, R., Drenth, W., and Nolte, R. J. M. 1987. Synthesis and aggregation behavior of hosts containing phthalocyanine and crown ether subunits. *Journal of the American Chemical Society* 109 (14):4261–4265.
- Sze, S. M. and Ng, K. K. 2007. *Physics of Semiconductor Devices*, 3rd edn. Hoboken, NJ: Wiley.
- Tang, C. W. 1986. Two-layer organic photovoltaic cell. *Applied Physics Letters* 48 (2):183–185.
- Tsuzuki, T., Shirota, Y., Rostalski, J., and Meissner, D. 2000. The effect of fullerene doping on photoelectric conversion using titanyl phthalocyanine and a perylene pigment. *Solar Energy Materials and Solar Cells* 61 (1):1–8.
- Uchida, S., Xue, J., Rand, B. P., and Forrest, S. R. 2004. Organic small molecule solar cells with a homogeneously mixed copper phthalocyanine: C-60 active layer. *Applied Physics Letters* 84 (21):4218–4220.

- Xue, J. 2005. Pure and mixed organic thin films and heterojunctions for optoelectronic applications, PhD thesis, Princeton University, Princeton, NJ.
- Xue, J. and Forrest, S. R. 2004. Carrier transport in multilayer organic photodetectors: I. Effects of layer structure on dark current and photoresponse. *Journal of Applied Physics* 95 (4):1859–1868.
- Xue, J., Rand, B. P., Uchida, S., and Forrest, S. R. 2005a. A hybrid planar–mixed molecular heterojunction photovoltaic cell. *Advanced Materials* 17 (1):66–71.
- Xue, J., Rand, B. P., Uchida, S., and Forrest, S. R. 2005b. Mixed donor–acceptor molecular heterojunctions for photovoltaic applications. II. Device performance. *Journal of Applied Physics* 98 (12):124903.
- Xue, J., Uchida, S., Rand, B. P., and Forrest, S. R. 2004a. 4.2% Efficient organic photovoltaic cells with low series resistances. *Applied Physics Letters* 84 (16):3013–3015.
- Xue, J., Uchida, S., Rand, B. P., and Forrest, S. R. 2004b. Asymmetric tandem organic photovoltaic cells with hybrid planar–mixed molecular heterojunctions. *Applied Physics Letters* 85 (23):5757–5759.
- Yakimov, A. and Forrest, S. R. 2002. High photovoltage multiple-heterojunction organic solar cells incorporating interfacial metallic nanoclusters. *Applied Physics Letters* 80 (9):1667–1669.
- Yu, G., Gao, J., Hummelen, J. C., Wudl, F., and Heeger, A. J. 1995. Polymer photovoltaic cells—enhanced efficiencies via a network of internal donor–acceptor heterojunctions. *Science* 270 (5243):1789–1791.



# 13

---

## *Development of Polymer Semiconductors for Field-Effect Transistor Devices in Displays*

---

Rick Hamilton, Martin Heeney, Thomas Anthopoulos,  
and Iain McCulloch

### CONTENTS

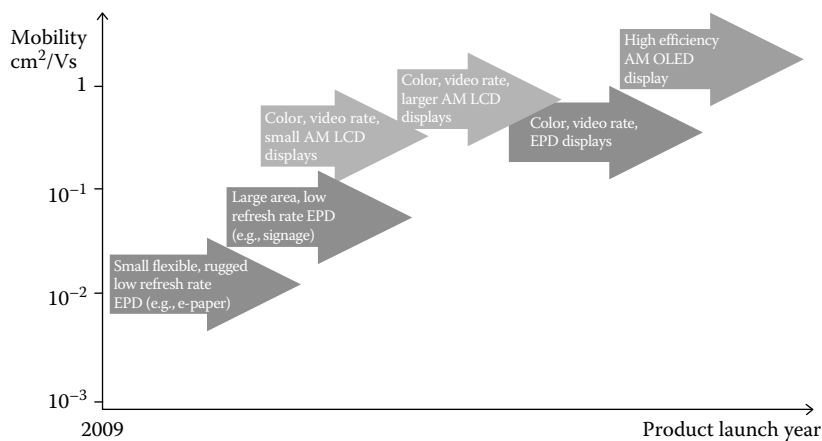
13.1	Organic Transistors in Displays .....	394
13.2	Organic Electronic Device Fabrication .....	395
13.3	Design of Organic Semiconductors.....	397
13.4	Polymerization Synthetic Routes.....	398
13.5	Polymer Conformation Considerations.....	399
13.6	Polymer Semiconductors .....	400
13.6.1	Poly(3-Alkylthiophenes).....	401
13.6.2	Polythiophene Structural Analogs .....	403
13.6.3	Poly(Thieno(3,2- <i>b</i> )Thiophenes .....	404
13.6.4	High Performance Polymer Semiconductors.....	406
13.7	FET Device Fabrication and Characterization.....	411
13.7.1	Electronic Characterization of OFETs .....	411
13.7.2	FET Device Architectures .....	414
13.8	Polymeric, Oligomeric, and Blend OFETs .....	415
13.8.1	Characteristics of Blend Films.....	416
13.8.1.1	Blending of Oligomeric OSC .....	417
13.8.1.2	Blend OFET Preparation and Fabrication.....	418
13.9	Ambipolar Transport in Conjugated Organic Polymers and Transistors.....	419
13.10	Summary.....	424
	Acknowledgments .....	424
	References.....	425

---

### 13.1 Organic Transistors in Displays

The increasingly impressive electrical performance of organic semiconductors is driving the development of solution-based printing processes aimed at low cost fabrication of transistor devices. The most immediate application area will most likely be in active matrix displays, where transistors are used in the backplane circuitry, operating basically as an individual pixel switch. In liquid crystal displays (LCDs) and electrophoretic displays (EPDs), the transistor charges both the pixel and storage capacitor, whereas in an organic light-emitting diode display (OLED), the transistor delivers current to the diode element. Most medium and large size LCDs, i.e., monitor and television displays, employ amorphous silicon as the transistor semiconductor (high resolution displays often require polysilicon), with a charge carrier mobility of the order of  $0.5 \text{ cm}^2/\text{V s}$ . The EPD effect can tolerate a lower performance from backplane transistors and is hence the most compatible with the performance limitations of organic transistors. As the EPD effect is reflective, the pixel transistor can occupy almost the full area underneath the pixel, in contrast to transmissive display effects such as LCD, where the opaque transistors block light from the backlight and therefore must be as small as possible (i.e., the pixel should have a high aperture ratio) to maximize the efficiency. This means that the EPD transistor width ( $W$ ) is maximized and can deliver more current per pixel compensating for low mobility semiconductors. As a result, mobility specifications are in the region of  $0.01 \text{ cm}^2/\text{V s}$  for a device with low refresh rates, low resolution, and small size. Another favorable aspect of the EPD effect is that once the pixel and storage capacitor is charged, no further power is required to retain the image, i.e., it is bistable. Thus the duty cycle load on the transistor is minimized, and subsequently the devices can potentially have longer lifetimes as their operational times are reduced. Increasing the display size and resolution, leading to higher number of rows and columns, faster pixel charging speeds, and consequently higher on-currents translates into higher semiconductor mobility requirements. Figure 13.1 illustrates a simplistic roadmap of display application development in relation to the requirements of the backplane transistors and the timing for commercialization [1].

High performance flexible EPD displays are even further from commercialization than equivalent LCD displays, as the front-plane technology enabling full color and video speed requires much more development. The opportunity to compete with LCD technology may only be possible where lower cost manufacture can be achieved through potentially fewer photolithographic mask steps during the fabrication process, and where product features such as flexibility and ruggedness are desired. Comparing identical resolution and size EPD and LCD panels, although the transistor size of the EPD pixel can be larger, and thus, the corresponding mobility requirements of the transistor should be lower, it is often the case that impurities in the liquid EPD

**FIGURE 13.1**

Commercialization roadmap for organic transistor backplane displays.

cell leads to current leakage, and thus requires higher semiconductor charge carrier mobility than would be predicted. Using an organic transistor to drive an OLED display allows the potential for a complete integrated display fabrication process by high throughput printing techniques such as ink jet or even gravure, thus eliminating the need for the currently expensive mask-based lithographic steps. It is also possible to fabricate OLED devices with transparent cathodes, so-called top-emitting devices, thus allowing the transistor to be located beneath the emissive layer and potentially allow larger transistors per pixel than LCD backplanes with the same pixel size. Typical driving schemes for OLEDs, however, require multiple transistors per OLED pixel, and therefore they need to be smaller than the equivalent EPD, where there needs to be only one transistor per pixel. Whereas both EPD and LCD devices are electrical field driven, an OLED device requires an electrical current to emit light. A higher performance is required from the transistor, not only in terms of mobility, but also in transistor to transistor uniformity, as the current output from the transistor dictates the brightness of the pixel. Compensation driving schemes are often required to prevent nonuniform brightness and color shifts across the display arising from both transistor instabilities and pixel differential aging effects.

## 13.2 Organic Electronic Device Fabrication

Many current prototype device pilot processes fabricate on plastic laminated glass and then delaminate the glass at the end of the process to leave

finished devices on a plastic substrate. Temperature limits for the process are set by both substrate thermal distortion and semiconductor polymorphism and chemical decomposition. In their simplest form, field-effect transistors (FETs) comprise of a source and drain electrode, a semiconductor, dielectric, and a gate electrode. The highest throughput fabrication technique will likely require that each component be additively deposited. Depending on the patterning resolution and layer thickness, there are many possible printing and coating techniques that have been successfully shown to deposit the range of component of the device. As the distance between the source and drain electrodes (the channel length) is the most critical dimension of the device, with short distances providing higher performance, this deposition step requires the highest resolution and is typically the most expensive step. To achieve submicron channel lengths, nanoimprinting [2], high resolution photolithography, soft lithography, or other self-aligned printing techniques [3] can be employed. The shortest channel length transistors have been fabricated by a self-aligned printing technique [4], where droplet repulsion from a surfactant-treated electrode results in adjacent drops separated by the thickness of the surfactant, which acts as the dielectric. The device performance is compromised, however, by the thickness of the dielectric layer that does not scale with the channel length. Photolithography utilizing standard masks and exposure sources can achieve submicron resolution electrode features, but more typically offer channel lengths from 1 to 100 µm with good precision. However this fabrication technique is nonadditive as it requires etching and development steps to pattern the electrodes, and is additionally a batch process, difficult to integrate in roll to roll fabrication. However, the process is well understood, and the equipment is readily available. Although substrates are typically rigid, it is possible to delaminate flexible devices from rigid carrier substrates. Ink jet deposition can achieve a resolution of at least 50 µm, although when integrated with surface prepatteing, which can control and direct droplets by lateral surface energy differences, this resolution can be improved by about an order of magnitude. It is also possible by multiple heads and high nozzle density to increase the potential throughput, such that this process is a viable possibility for roll to roll processing, although there is still engineering challenges ahead to fully optimize this process. Both ink jet and photolithography processes require inks with relatively low viscosities. The low solubility of highly aromatic semiconducting polymers combined with the need to limit polymer molecular weights to optimize electrical performance sets an upper limit for polymer viscosity, in the region of 20 cP, which is compatible with both printing techniques. Conducting inks for electrode deposition often tend to have higher viscosities, and are difficult to deposit by these techniques. Contact printing techniques including gravure, flexo, and offset have all been considered for electrode deposition. The lowest feasible viscosity for gravure printing inks is higher than ink jet, and typically greater than 50 cP, while both flexo and offset require even higher viscosities. From a deposition perspective, this is compatible with some electrode

inks and pastes, but current achievable patterning resolutions from gravure cylinders are typically greater than 50 µm that may not be good enough for high performance devices. For both gate and perhaps dielectric deposition, contact printing is a viable and promising candidate. Wide area-coating techniques such as spray, slot-die, and curtain coating are also possible for deposition of continuous layers of semiconductor or dielectric, which can then be postdeposition patterned by a subsequent process such as direct write laser etching or nanoembossing.

---

### 13.3 Design of Organic Semiconductors

Typically most organic semiconductors are p-type and operate in the accumulation mode in field effect devices. n-Type organic semiconductors are becoming more prevalent, but mobilities often lag behind p-type organics and often poor ambient stability, particularly when in operation is also still an issue. In this chapter, we focus mainly on p-type semiconductors. Organic semiconductors are often broadly classified in terms of their processability, as being either evaporative or solution processable. Polymer semiconductors cannot usually be processed by evaporation, and therefore, when appropriately functionalized, fall within the solution processable category. Small molecule semiconductors, however, can often be either solution or evaporatively processed. The exemplary small molecule semiconductor is pentacene, which can now achieve mobilities as high as  $3.5 \text{ cm}^2/\text{V s}$  for thin film devices [5] as a result of extensive process optimization. The poor solubility of pentacene, however, excludes the possibility of solution patterning of the semiconductor by inexpensive and widely available techniques such as ink jet printing. The introduction of bulky alkynyl silyl groups in the central 6- and 13-positions of the pentacene ring has been shown to significantly improve solubility and oxidative stability by Anthony and coworkers [6–9]. In addition, the substituents dramatically alter the crystalline packing of material resulting in the formation of highly ordered two-dimensional slipped stack arrays in certain derivatives of substituted pentacenes or related dithienoanthracenes. These materials display highly impressive mobilities in excess of  $1 \text{ cm}^2/\text{V s}$  for drop-cast films [8]. However, potential problems still remain, in particular issues relating to interlayer mixing during the solution deposition of subsequent dielectric or encapsulation layers, control of the crystallization process over large substrate areas, and the anisotropic in-plane transport that causes device to device nonuniformity.

Polymeric semiconductors have many attractive features for thin-film transistor (TFT) fabrication. Solution viscosity can be widely tuned (increased) by (increasing) molecular weight opening up the possibility to formulate solutions compatible with high viscosity printing techniques such as gravure

and flexography [10]. The rheological properties of polymer formulations are also advantageous in the fabrication of cohesive, conformal thin films from solution casting processes. Thin film reticulation, which often occurs on drying from solution on a low-energy substrate, can be minimized through the optimization of polymer molecular weight and polydispersity. Fabrication of multilayer device stacks from sequential solution deposition processes requires that each layer is impervious to the solvents and temperatures that are subsequently used during deposition of the next layer. Polymers possess a narrow solubility parameter window and high bulk viscosity which minimizes any diffusivity between layers. They typically can also be exposed to a wider range of solvents while remaining inert, thus expanding the choice of materials and solvents that can be deposited during device formation. Dielectrics can therefore be employed that need to be soluble in this narrow solvent range, which limits choice. The mechanical properties of polymer semiconductors allow compatibility with flexible processing or flexible operation. Relatively isotropic in-plane transport can be achieved from the solution deposition of even highly crystalline polymer semiconductors due to their small thin film crystalline domain sizes (typically tens of nanometers) relative to the transistor channel length. This results in low device to device performance variability, which is particularly important in TFT devices for OLED applications.

---

### **13.4 Polymerization Synthetic Routes**

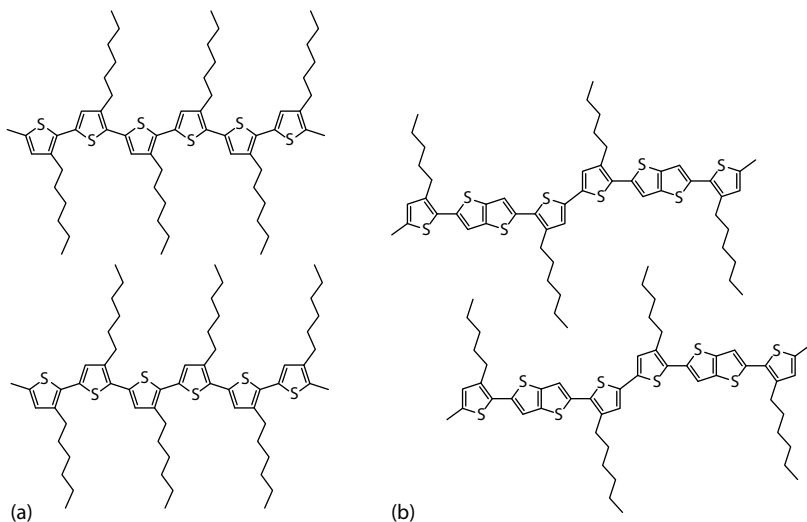
The choice of synthetic route for the preparation of semiconducting polymers derivatives is an important factor in determining the resultant electrical performance. Molecular weight, polydispersity, end groups, and chemical defects in the polymer backbone are all influenced by the choice of synthetic route, and these can have a significant influence on electrical performance. The choice of catalysts and reagents can also lead to the incorporation of impurities that are hard to remove, which also affect performance. Several groups have investigated the influence of molecular weight on transistor performance for various classes of thiophene polymer [11–16]. All studies have shown a beneficial effect on increasing molecular weight, and although a plateau region is typically reached, average molecular weights above 20,000 kDa are usually desirable. At very high molecular weights ( $M_n > 150$  kDa), the high polymer viscosity can hinder crystallization during annealing resulting in a nonoptimal mobility. A systematic study of the influence of polydispersity on charge carrier mobility has not been reported, but high polydispersity would be expected to reduce the crystallinity of the polymer and therefore be detrimental to device performance. Impurities resulting from the synthesis such as catalyst residues can have a deleterious impact on device performance [17],

and removal of these impurities by appropriate purification techniques such as sequestration, washing, or reprecipitation [18] are typically employed. Rather harder to remove are defects which are chemically bound into the polymer backbone, and the best strategy is to minimize defects by the choice and optimization of synthetic route.

---

### 13.5 Polymer Conformation Considerations

As initially demonstrated with small molecules semiconductors [19] there is also a broad correlation between polymer molecular ordering and charge carrier mobility. A FET device transports charge within the plane of the thin film semiconductor, and when devices are operating in the accumulation regime, charge propagates within a thin semiconductor layer of only a few molecules thick at the semiconductor/dielectric interface. Semiconductor molecular packing and ordering at this interface into organized pi-stacked and oriented domains has been shown to lead to improved charge transport. The semiconductor polymer conformation provides the molecular template from which this oriented microstructure assembles. Polymers with thiophene units coupled along the backbone arrange spatially such that the sulfur atoms along the backbone maximize their separation from each other across the short axis of the polymer. This is optimal where the sulfur atoms in adjacent thiophene units arrange in an “anti” configuration across the backbone, as shown in Figure 13.2, and as a result these polymers typically have a long persistence length. The angle formed from the projection of the two bonds that link the thiophene monomer at the 2- and 5-positions is less than 180°. This makes the rotation of the thiophene ring around the long axis of the polymer a cooperative motion requiring rotation of neighboring thiophene units which is not energetically favorable. The coupled thiophene units have the potential to adopt a coplanar conformation, allowing close intermolecular approach between adjacent backbones, stacking together in a face to face (pi-stacked) arrangement. Sheet-like structures are formed from extended interchain  $\pi$  stacking and are vertically separated by the alkyl chains that extend from the backbone forming the crystalline lamella structure observed in polymers such as poly(3-hexylthiophene) (P3HT) and poly(2,5-bis(3-alkylthiophen-2-yl)thieno(3,2-b)thiophene copolymers (pBTTT). The order and spacial density of the side chains as well as the regiosymmetry of the repeat units play a key role in influencing the domain ordering and length-scale. Side chain interdigitation has been shown to facilitate “registration” between pi-stacked vertically adjacent lamellae, thus promoting large three-dimensional domain sizes and improved ordering. Interdigitation can occur only if the side chain attachment density along a polymer chain is low enough to permit chains from the nearest vertical aliphatic layer to occupy the free space between the chains.

**FIGURE 13.2**

(a) Poly(3 hexylthiophene) extended structure showing two vertically adjacent polymer chains, where the close packed density of the side chains prevents interdigitation between backbones and (b) the extended structure of polybialkylthiophene-*co*-thieno[3,2-*b*]thiophene where the wider alkyl side chain attachment distance along the backbone allow interdigitation.

P3HT, for example, has too high a side chain density to permit interdigitation, whereas pBTTT, with larger spacing distance, and ordered side chains, can interdigitate leading to much larger and more ordered domains.

### 13.6 Polymer Semiconductors

Both amorphous and crystalline polymer semiconductors have been widely studied. Amorphous polymers, such as polyarylamines, have demonstrated excellent ambient stability with mobilities of around  $0.005\text{ cm}^2/\text{V s}$  and isotropic in-plane transport achieved in transistors with high work function electrodes and low K dielectrics, with minimal thermal annealing of the semiconductor required [20]. Most high performing semiconducting polymers exhibit a crystalline microstructure, or at least local ordering around the main chain. Polyfluorenes, for example, are rigid rod polymers which can be rendered soluble in organic solvents by appropriate substitution at the bridging C9 position. Alkyl-substituted polyfluorenes can exhibit high temperature liquid crystalline phases which can be exploited to achieve the optimal microstructure in transistor devices [21]. This class of polymer has low lying highest occupied molecular orbital (HOMO)

energy levels leading to poor charge injection in FET devices from other than high work function electrodes, and subsequently poor charge transport. Incorporation of a bithiophene unit to form the alternating copolymer poly(9,9-diethylfluorene-*co*-bithiophene) (F8T2) resulted in an increase in both HOMO energy level (from  $-5.8$  to  $-5.4$  eV) and improved charge transport [22]. Orientation of the polymer backbones can be achieved by a thermal annealing step at the mesophase temperature utilizing a rubbed polyimide alignment layer as substrate [23]. Mobilities of up to  $0.02\text{ cm}^2/\text{V s}$  have been reported for this polymer, with good ambient stability. Attempts to increase mobility by increasing the thiophene content in the backbone were unsuccessful [24]. The highest mobilities measured in solution processed all-polymer FET devices have been exhibited by thiophene containing polymers. The crystalline nature of many functionalized thiophene derivatives contributes to their excellent charge transport properties. The most widely studied semiconducting polymer for charge transport applications is P3HT, and elucidating the structure property relationships for this polymer served as the basis for many of the improved design concepts for later polymers.

### 13.6.1 Poly(3-Alkylthiophenes)

Regioregular (RR) P3HT has emerged as a benchmark semiconducting polymer due to its ready availability, ease of processing from solution, and its promising electrical properties arising from a highly crystalline microstructure. Maximizing the regioregularity and optimizing the molecular weight [11,12] have shown to result in a systematic improvement in charge carrier mobility. The electron rich,  $\pi$ -conjugated, and highly planar backbone contribute to a high HOMO energy level of about  $-4.6$  eV, and a thin film electronic absorption maximum of about 560 nm. Additional fine structure can often be observed at wavelengths greater than the absorption maximum and are attributed to solid state aggregation [25]. This high HOMO energy level is responsible for the oxidative instabilities of P3HT to ambient air and humidity, and encapsulation of the semiconducting layer in devices is usually required. When the H-T regioregularity of P3HT exceeds about 96%, charge carrier mobilities of up to  $0.1\text{ cm}^2/\text{V s}$  have been exhibited in an inert atmosphere [26]. Transistor transfer curves often show a positive threshold voltage which is believed to be due to both slight intrinsic doping of the semiconductor as well as dipole effects from the dielectric. The in-plane electrical properties of these crystalline films are dramatically influenced by many device and fabrication properties. For example, treatment of a bare  $\text{SiO}_2$  dielectric surface with a hydrophobic self-assembled monolayer (SAM) such as octyltrichlorosilane (OTS) [27] results in improved P3HT mobility and higher on-currents. It is believed that a contributing factor to reduce the mobility on bare silicon oxide surface, in addition to the presence of surface trap sites [28], is that the more polar surface can “anchor” polymer chains inhibiting large-scale self-assembly at the critical dielectric–semiconductor

interface. This leads to faster nucleation and a less organized semiconductor microstructure. Particularly on the treated, low energy surface, an annealing step also improves charge carrier mobility, even at temperatures that appear to be lower than the thin film T<sub>g</sub>.

Several groups have examined the role of the side chain in influencing electrical performance of regioregular polyalkylthiophenes. Studies [29,30] suggest that hexyl chains are the optimum length, with a decrease in the charge carrier mobility as the chain length increased. The  $\pi$ - $\pi$  distance is similar across the series [31], so the decrease may be due to an increase in the fraction of insulating side chains in the polymer. If the polymer lamellae are not well aligned in the plane of the substrate and direction of charge flow, hopping or tunneling between the insulating chains may be required. Since the rate of hopping is dependent on distance, longer chains would be expected to show a detrimental effect.

The effect of the bulkiness of the side chain on field effect mobility has also been examined by Bao and Lovinger [31] with the conclusion that nonpolar, linear alkyl chains were optimal for backbone stacking and charge transport. They prepared a series of regioregular polythiophenes containing bulky or highly polar-substituted end groups. These showed low degrees of crystallinity and ordering, and poor field effect mobilities of around  $10^{-6}$  cm<sup>2</sup>/V s. The introduction of a chiral alkyl side chain was shown to maintain crystallinity, but to increase the  $\pi$ - $\pi$  stacking distance to 4.3 Å (vs. 3.8 Å for P3HT). A reduction in FET charge carrier mobility of about one order of magnitude was observed. Low molecular weight, highly regioregular P3HT (~5 kDa) is highly crystalline, with a rod-like microstructure observed by atomic force microscopy (AFM) measurements, in which the rod width does not exceed the length of the polymer chains. Higher molecular weight, P3HT (>30 kDa), with similar regioregularity is less crystalline with small nodule-like crystallites. The low molecular weight films, although more crystalline, exhibit lower mobilities. It appears that the higher molecular weight P3HT has better defined and more connected grains, whereas the low molecular weight P3HT has more defined grain boundaries [11]. An enhanced out of plane twisting in low molecular weight polymer backbone conformation has also been proposed as an explanation for the difference in mobility [32]. The deviation from planarity decreases the effective conjugation length and reduces the efficiency of charge hopping. A study in the high mobility regime has correlated increasing molecular weight with increasing crystalline quality within domains, with fewer chain ends per domain or “nanoribbon” as well as the possibility for individual polymer chains to bridge between domains at high molecular weight [13]. However, at high molecular weights (>~50 kDa) there is an increase in crystalline disorder, possibly due to slower crystallization kinetics. The sensitivity of P3HT morphology development on the processing solvent and conditions has also been recognized. Higher boiling solvents allow the self-assembly of crystalline domains to occur in a more organized and controlled timeframe [33] leading to improved electrical performance. More recently this approach has been developed to demonstrate that even

low regioregularity P3HT, when fabricated from very high boiling point solvents such as trichlorobenzene can achieve high charge carrier mobilities. The solvent evaporation rate, controlled by spin casting from solution at different spinning rates [34], was also shown to influence the orientation of the backbone plane with respect to the substrate. A low evaporation rate promoted a more edge-on orientation, which is more optimal for charge transport. Similarly, dip-coating techniques have been utilized to fabricate highly ordered thin film layers that show mobilities up to  $0.2\text{ cm}^2/\text{V s}$  [35].

### 13.6.2 Polythiophene Structural Analogs

Chemical modification of polythiophene backbone structures has been used [36] to generate controlled changes in both the backbone conformation and microstructure, as well as modification of the electronic energy levels of the molecular orbitals. Head to head regiopositioning of alkyl groups in adjacent thiophene units along a polythiophene leads to significant steric interactions and a resultant twist between the planes of adjacent thiophene rings. This not only reduces the  $\pi$  orbital overlap, but prevents a closely packed pi-stacked lamella microstructure, thus inhibiting crystallization. The reduced  $\pi$  orbital overlap significantly lowers the HOMO energy level, therefore improving ambient stability.

Alternative approaches to improve polymer ambient stability by increasing the ionization potential have utilized electron poor comonomers in the polymer backbone. Electron deficient six-membered rings, such as 1,2-pyrazine [37] or perfluorobenzene [38], have also been introduced into the backbone. These are able to planarize the backbone through the formation of intrachain S–N or S–F bonding interactions. Increases in ionization potential can therefore be attributed solely to an electron-withdrawing effect. Ambient stabilities were not reported, but charge carrier mobilities were on the order of  $10^{-3}\text{ cm}^2/\text{V s}$ .

Donor–acceptor (D–A) type polymers utilizing a range of acceptor monomers have been reported by several groups [39], initially designed for use as photovoltaic materials. When suitable electron acceptors are incorporated, strong intramolecular orbital hybridization can occur between D–A units allowing the polymers to exhibit small bandgaps. In this case, the polymer tends to adopt the HOMO energy level of the donor unit, and the lowest unoccupied molecular orbital (LUMO) of the acceptor [39]. Polymers incorporating thieno(3,4-*b*)pyrazine have been reported with moderate charge carrier mobilities [40]. However, high off-currents in the devices suggested unintentional doping by the ambient atmosphere. Copolymers of unsubstituted thiophene and thiadiazole have also been reported, with moderate charge carrier mobilities [41]. Due to the lack of solubilizing substituents, transistor devices were prepared from strongly acidic trifluoroacetic acid solutions, into which the basic thiadiazole groups could be dissolved. Soluble, crystalline copolymers of alkylated thiazole and thiophene have also been reported [42] with charge carrier mobilities up to  $0.0025\text{ cm}^2/\text{V s}$ , although ambient stability was not reported. More recently a copolymer of benzothiadiazole

and cyclopenta(2,1-*b*;3,4-*b*)dithiophene was reported that exhibited FET mobilities of  $0.02\text{ cm}^2/\text{V s}$ .

An alternative approach reported by Frechet and coworkers [43] was to introduce the electron-withdrawing ester group as a substituent on a thiophene polymer backbone. This served to increase the ionization potential in comparison to the simple alkyl chain substituent analogs, with the additional benefit of increasing solubility. The polymer still exhibited crystalline morphology with charge carrier mobilities up to  $0.06\text{ cm}^2/\text{V s}$  in top contact mode, slightly lower than the analogous alkyl analog [44], but the polymers exhibited much improved ambient operation.

Bauerle and coworkers first reported a regiosymmetric thiophene oligomer with a 3,3'''-dialkyl-quaterthiophene repeat unit which exhibited a strong tendency for self-organization through interdigitation of the solubilizing alkyl chains [45,46]. Polymers based upon the same unit, poly(3,3'''-dialkyl-quaterthiophenes) (PQT), were later reported that could also form highly ordered thin film structures with FET charge carrier mobilities up to  $0.14\text{ cm}^2/\text{V s}$  [44]. Annealing of the polymer within its liquid crystalline mesophase was beneficial to the formation of ordered films [47]. Furthermore, the additional conformational freedom of the unalkylated bithiophene monomer was attributed as the reason for reduced conjugation along the thiophene backbone leading to a modest increase of  $0.1\text{ eV}$  in ionization potential over P3HT. Nevertheless this was reported to sufficiently impart a significant improvement in ambient stability, with transistors operating for over 1 month in ambient air. The same group reported that a terthiophene derivative also exhibited good air stability, with a mobility of  $0.01\text{ cm}^2/\text{V s}$  [48].

The copolymers of thieno(2,3-*b*)thiophene were designed such that when coupled in the 2,5 position a fully conjugated pathway between coupled units is not possible, thus reducing the conjugation length and therefore reducing the HOMO energy level, thereby increasing ambient stability. Crystalline copolymers with 4,4'-dialkyl-2,2'-bithiophene (referred to as poly(bithiophene-crossconjugated thiophene) [pBTCT]) were prepared by Stille coupling with alkyl chain lengths from C8 to C12 [49]. The pBTCT polymer series were reported to exhibit a  $0.4\text{ eV}$  lowering of the HOMO energy level in comparison to P3HT [49] and transistor devices showed only very minor changes in transfer characteristics when measured over a storage period of up to 2 months in air, with values of up to  $0.04\text{ cm}^2/\text{V s}$  with corresponding ON/OFF ratios around  $10^6$  in air.

### 13.6.3 Poly(Thieno(3,2-*b*)Thiophenes)

Poly(2,5-bis(3-alkylthiophen-2-yl)thieno(3,2-*b*)thiophene)copolymers (pBTTT) were reported [50] with high charge carrier mobilities. This has been attributed to the large crystalline domains formed by the assembly of the planar conjugated backbones into closely pi-stacked sheet-like lamellae, and subsequent orientation of these domains in the plane of the substrate, hence

giving rise to excellent charge transport. PBTETT is an alternating A-B-A-B copolymer of thieno(3,2-*b*)thiophene and 4,4-dialkyl 2,2-bithiophene. Both monomers are centrosymmetric, and on polymerization, the repeat unit has a rotational symmetry along the polymer long axis. In addition, the optimal conformation of the backbone has an all-antisulfur orientation across the backbone short axis with a resultant regularity in spacing between alkyl side chains. This helps facilitate optimal backbone and side chain packing and leads to a highly ordered microstructure as illustrated in Figure 13.3. The delocalization of electrons from the thienothiophene aromatic unit into the backbone is less favorable than from a single thiophene ring, due to the larger resonance stabilization energy of the fused ring over the single thiophene ring. This reduced delocalization along the backbone, as well as the reduced inductive electron donation from the fewer alkyl chains per repeat unit causes a lowering of the polymer HOMO level compared to P3HT, and therefore improved ambient stability.

The polymer can be oriented with the backbone long axis in the plane of the substrate, and the thiophene ring plane oriented orthogonal to the substrate plane with the appropriate surface treatment. It has been shown [51] from both spectral ellipsometry and near edge x-ray absorption fine structure spectroscopy (NEXAFS), that on annealing, the lamella lie almost exactly in the plane of the substrate, and that the backbone conjugated plane is tilted with respect to the lamella plane. The alkyl side chains also appear, from polarized IR measurements, to be well ordered in a transconfiguration, and are tilted to the backbone. Significant side chain interdigitation has also been identified [52], a process that, due to the symmetry of the repeat units, can be facilitated by a simple rotation round the backbone axis, unlike P3HT. The combination of the spacing density between adjacent alkyl chains on the polymer backbone, and the tilt angle of the side chains facilitates this interdigitation,

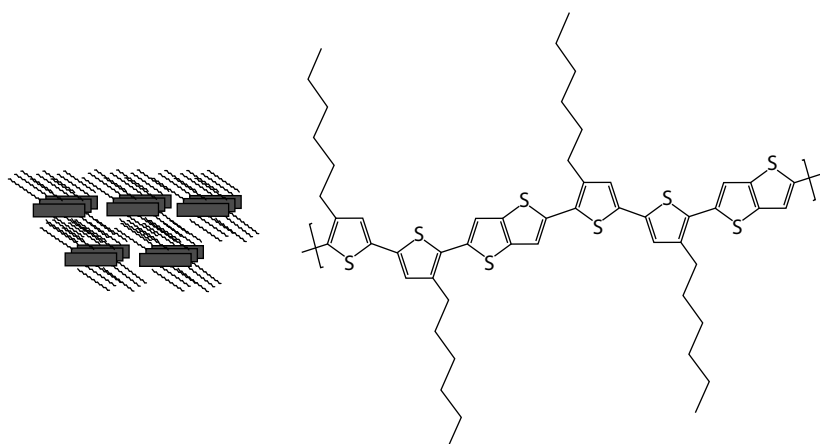


**FIGURE 13.3**

Three-dimensional registration of lamella formed from planar pBTTT backbones pi stacking.

which “registers” the lamella layers. In thin film form, large lateral domains of dimensions in the micron length-scale, comprised of many polymer chains in length can be developed. Very thin films (20–30 nm) were also observed to have terrace-like topography, in which the height of each step correlates well to the cross-sectional width of the polymer backbone and tilted side chains. Very recently, high resolution transmission electron spectroscopy (TEM) data now suggests that these domains are comprised of clusters of nanocrystallites, although the reason that these appear to form a molecularly flat surface remains unexplained. The presence of both side chain ordering and interdigitation are in contrast to that of regioregular P3HT, in which the side chains were concluded [53] to be “liquid like,” and noninterdigitated as observed by polarized Fourier transform infrared (FTIR). This improved crystallinity and ordering manifests as improved charge carrier mobility in FET devices.

Organic field effect transistor (OFET) devices have been fabricated from pBT<sub>TTT</sub> polymer solutions and hole mobility values of up to 0.8 cm<sup>2</sup>/V s were reported in a nitrogen atmosphere. These values approach that of high performing evaporated small molecule devices and are comparable to amorphous silicon. In bottom gate, bottom-contact devices, in which the active semiconductor layer is the exposed top surface, the effect of different ambient conditions has been evaluated. Exposure to unpurified, ambient air in which the humidity is ~50%, results in an initial increase in the off-current of the device. In filtered, low humidity air, transistor devices remain very stable over time.

Further improvements in ambient stability were achieved through the introduction of alkyl side chains at the 3- and 6-positions of the thieno(3,2-*b*) thiophene by a Negishi coupling of an alkyl zinc halide with 3,6-dibromo-thieno(3,2-*b*)thiophene. Copolymers of 3,6-dialkylthieno(3,2-*b*)thiophene with both unsubstituted thiophene and bithiophene comonomers gave rise to liquid crystalline polymers, with high charge carrier mobility. The bithiophene copolymer, for example, had a highly crystalline thin film microstructure, although AFM images reveal crystalline domain sizes of less than tens of nanometers on OTS functionalized substrates, dimensions that do not approach the micron scale domains of pBT<sub>TTT</sub> fabricated under identical conditions. Even as-cast films are highly ordered, PAT2T has a less planar backbone conformation than pBT<sub>TTT</sub>, which is also supported by the hypsochromic  $\lambda_{\text{max}}$  shift in the solid state UV spectra of about 15 nm. This reduced planarity may also contribute to the slightly increased ionization potential of 0.05 eV as measured by ultraviolet photoelectron spectroscopy (UPS). Bottom-gate transistor devices exhibited charge carrier mobilities of up to 0.2 cm<sup>2</sup>/V s and were remarkably stable in fully ambient conditions in the dark. The monothiophene copolymer also exhibited high charge carrier mobility, in this case up to 0.3 cm<sup>2</sup>/V s in nitrogen.

### 13.6.4 High Performance Polymer Semiconductors

The molecular unit benzodithiophene was incorporated into semiconducting polymer structures [54] and when alkylated in the 4- and 8-positions

then copolymerized with a dialkylbithiophene, mobilities of about  $0.2\text{ cm}^2/\text{V s}$  were reported [55] and devices appeared to be reasonably air stable. These polymers seemed to form a self-assembled aggregated microstructure on solvent evaporation, and thus did not require an extended thermal annealing to promote good transport. The closely packed alkylated chain density around the backbone prevents the possibility of side chain interdigitation, and only a high temperature mainchain melt is observed on heating.

Copolymers of the conjugated aromatic unit, *N*-alkyldithienopyrrole, with alkylated thiophenes (DTP-co-THs) were prepared [56] and high charge carrier mobility measured. Although the monomer units had a planar conformation, the authors concluded that polymer thin films were amorphous, but could possess “long range pi connectivity”). Charge carrier mobilities of around  $0.1\text{ cm}^2/\text{V s}$  were demonstrated. The high electron density of the thiophene rings, coupled with the electron donation of the nitrogen on the pyrrole, contribute to raising the HOMO energy level of these polymers. Devices were measured under argon, and even in this environment, the ON/OFF ratios were suboptimal indicating the possibility of doping and ambient instabilities.

Copolymers of the fused monomer cyclopentabithiophene and benzothiadiazole (CDT-BTZ) were designed and synthesized as both donor–acceptor hybridized polymers with a low band gap for solar cells [57], and their non-branched analogs with improved molecular ordering were shown to exhibit high charge transport in OFET devices [58]. Although the bridging carbon on the cyclopentabithiophene is  $\text{sp}^3$  hybridized and therefore the alkyl chains project out of the plane of the planar, fused monomer, good ordering was achieved as evidenced by both the highly crystalline two-dimensional grazing incidence wide angle x-ray diffraction patterns, and the highly textured AFM images. Interestingly, when a subsequent rigorous purification process was employed for both monomers, higher molecular weight polymer was achieved. TFT devices were then fabricated with this higher molecular weight polymer by a dip-coating process to optimize molecular orientation, and a very large charge carrier mobility of over  $1\text{ cm}^2/\text{V s}$  can be achieved. The highest mobilities were achieved in the dip-coated direction with an approximate anisotropy of a factor of 2.

Copolymers of dithienosilole and thiophenes (TS6T2) were synthesized and the hole mobilities reported of a bithiophene analog reached values approaching  $0.1\text{ cm}^2/\text{V s}$  [59]. Although the influence of silicon in silole conjugated systems on the molecular orbital energy levels is primarily to stabilize the LUMO [60], it was observed that there was no n-type mobility. However, modest stabilization of the HOMO level also arises from silicon introduction, and the ambient air stability of these polymers was very much improved in comparison to P3HT.

Exploitation of the push–pull effect of the conjugated pyrrolo[3,4]pyrrole monomer unit afforded ambipolar charge transport polymers where the dipolar nature of the fused pyrrole units and the planar thiophene comonomers lead to a highly aggregated, pi-stacked conformation, even when the

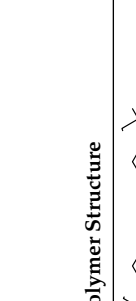
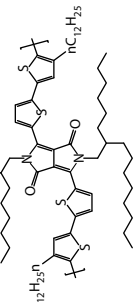
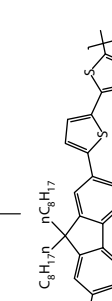
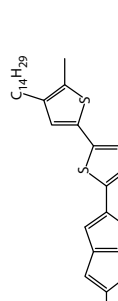
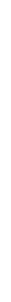
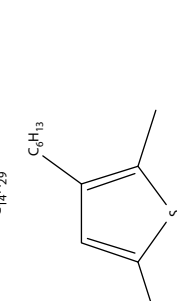
alkylthiophene monomers were coupled with the alkyl chains projecting in a head-to-head link, which typically led to a conformational twist and loss of planarity and aggregation. With appropriate electrodes, chosen to optimize charge injection, the ambipolar nature of the polymer BBDTDP1 was employed in a light-emitting transistor device [61]. Hole mobilities of around  $0.1\text{ cm}^2/\text{V s}$  were obtained on more standard bottom gate devices.

Extending the pBTTT design concept that has previously illustrated the beneficial effects of fused conjugated ring systems to increase backbone stiffness through the reduction of the conformational freedom for out of plane rotations, a highly fused polymer tetrathienothiophene co bithiophene (P2TDC13FT4) was reported with high charge carrier mobility [62]. Although the alkyl side chain incorporation density was quite low, and the alkyl chains were linear, solubility of the polymer surprisingly did not seem to present a particular problem. Another example of high performance fused thiophene cobialkylthiophenes is the dithienothiophene analog (PBTDT-12) of pBTTT which was reported to exhibit mobilities of up to  $0.3\text{ cm}^2/\text{V s}$  [55].

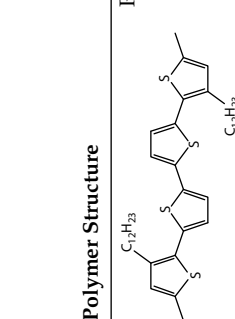
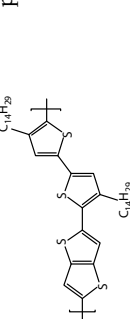
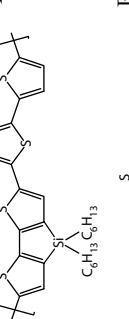
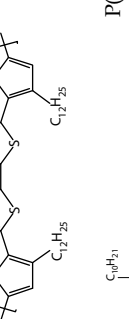
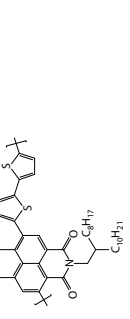
The indenofluorenebis(dicyanovinylene) core unit, with the high electron-withdrawing cyano groups was copolymerized via Stille coupling with a tail to tail alkyl-substituted bithiophene monomer, and the resultant polymer (TIFDMT) was reported to exhibit excellent electron mobility [63]. The dicyanovinyl functionality acts to planarize the indenofluorene ring structure, which may help backbone aggregation, and indeed thin films exhibit highly crystalline textures. Electron mobilities of up to  $0.16\text{ cm}^2/\text{V s}$  were reported from devices employing top-contact Au electrodes.

Acenaphtho[1,2-*b*]thieno[3,4-*e*]pyrazine was coupled in the 2- and 5-positions with alkylthiophene units, then copolymerized with a branched fluorene comonomer (ACTP-F) [64]. The thienopyrazine unit being electron withdrawing has a hybridized molecular orbital with the electron donation components of the conjugated polymer backbone, thus promoting a low band gap, light absorbing functionality suitable for solar cell applications. The highly planar acenaphtho[1,2-*b*]thienopyrazine unit coupled with coplanar alkyl thiophenes is likely to promote an aggregated microstructure, which promotes charge carrier mobilities of up to  $0.17\text{ cm}^2/\text{V s}$ .

Recently a high mobility n-type polymer (P(ND12OD-T2)), based on N-alkylated naphthalene diimide repeat units, was reported [65] with good ambient stability. On optimizing the device architecture, the choice of dielectric and channel length, an electron mobility of up to  $0.85\text{ cm}^2/\text{V s}$  was achieved representing a significant improvement on the benchmark values for n-type polymers. The LUMO level is stabilized by the electron-withdrawing diimide functionality facilitating both electron injection and operational stability, while the planarity of the naphthalene diimide and the bithiophene comonomers helped to promote a highly pi-stacked and crystalline morphology responsible for the high charge carrier mobility. Swallow tail type alkyl chain branching from the imide functionality ensures good polymer solubility.

Polymer Structure	Polymer Acronym	Charge Carrier Mobility (cm <sup>2</sup> /V s)	Reference	Polymer Structure	Polymer Acronym	Charge Carrier Mobility (cm <sup>2</sup> /V s)	Reference
	PTAA	0.005	[20]		BBTDPP1	0.1 (h) 0.1 (e)	[61]
	F8T2	0.02	[23]		CDT-BTZ	1.4	[58]
	pBTCT	0.1	[49]			0.2	[54,55]
	P3HT	0.2	[35]		DTP-co-THs	0.1	[56]

(continued)

Polymer Structure	Polymer Acronym	Charge Carrier Mobility (cm <sup>2</sup> /V s)	Reference	Polymer Structure	Polymer Acronym	Charge Carrier Mobility (cm <sup>2</sup> /V s)	Reference
	PQT	0.1	[44]		pBTITT	0.6	[50]
	TS612	0.1	[59]		PBTDT-12	0.3	[55]
	P(ND12OD-T2)	0.85 (e)	[65]		PATxT	0.1 (e) 0.2 (n = 2)	[66]
	P(TD13FT4)	0.3	[62]		ACTP-F	0.2	[64]

## 13.7 FET Device Fabrication and Characterization

General screening and the characterization of new polymer materials is achieved with FETs fabricated on highly doped crystalline silicon substrates. Using the n-doped silicon wafer as a common gate electrode and the thermally grown (typically 320 nm thick) oxide layer as a gate insulator, gold source-drain electrodes are then thermally evaporated and lithographically etched to produce an accurate and reproducible bottom gate device array. The electrode spacing or channel lengths of the devices on the array are set between 2.5 and 100  $\mu\text{m}$ . A range of channel lengths facilitates the identification of morphological and device specific effects, which will have an impact on the mobility measurement [67]. One such case could be monocrystalline domains spanning a short channel, which usually results in a higher than expected mobility measurement when compared with a long channel. Contact resistance will also have an influence in channel length variation studies, which is seen as a drop in the measured mobility for short channels due to the contact resistance assuming a greater proportion of the overall device resistance.

Having a large number of these device templates available for device fabrication enables efficient screening of new materials: spin-coating or even drop casting a solution of the polymer (typically 10 mg of polymer per mL of dichlorobenzene) to be tested on the silicon substrate will yield an array of devices, which can be tested with minimal further processing. To achieve the optimum mobility measurement though, it is necessary to modify the polar surface of the  $\text{SiO}_2$ . Hydrophobic SAMs, hydrocarbon chains with a silanated end group, such as OTS or hexamethyldisilazane (HMDS), have been reported to improve mobility by orders of magnitude, possibly through lowering of the surface energy of the gate dielectric and removal of residual surface water and other polar groups prior to deposition of the polymer [68]. The SAMs may also induce microstructural changes, which orientate the polymer lamellae at the critical interface to allow easier transport through the device accumulation layer [69].

### 13.7.1 Electronic Characterization of OFETs

When bias is applied to the gate contact, charges accumulate in the transistor channel adjacent to the polymer-insulator interface to a thickness of a few nm. The charge density in the channel and hence its conductivity is controlled by the gate bias. Since the polymer layers are not intentionally doped, charges need to be injected from the metal electrodes. Poor physical contact between organic layer and injecting electrodes as well as high Schottky barrier can result in significant contact resistance effects in transistor current-voltage characteristics. In operation, transistor current is carried in a thin region (~5 nm) next to the gate insulator [70] and is very sensitive to both molecular order and quality of semiconductor-dielectric interface.

Hopping dominated transport in polymer films is influenced by charge density induced by the gate in the FET channel resulting in effective gate voltage dependence of charge carrier mobility [67]. For a simplified analysis of FETs this dependence can be left out, especially if mobility is only weakly dependent on the gate bias. Qualitative behavior of organic transistors can be described using inorganic TFT models [71], where source–drain current is expressed as

$$I_{\text{sd}}^{\text{lin}} = \frac{WC_0}{L} \mu^{\text{lin}} \left[ (V_g - V_0) V_{\text{sd}} - \frac{V_{\text{sd}}}{2} \right] \quad \text{Linear regime} \quad (13.1)$$

$$I_{\text{sd}}^{\text{sat}} = \frac{WC_0}{2L} \mu^{\text{sat}} (V_g - V_0)^2 \quad \text{Saturation regime} \quad (13.2)$$

where

$W$  is the channel width

$L$  is the channel length

$C_0$  is the capacitance of unit area of insulating layer

$V_g$  is the gate voltage

$V_{\text{sd}}$  is the source–drain voltage

$V_0$  is the transistor turn-on or threshold voltage

In the linear regime, when  $V_{\text{sd}} \ll (V_g - V_0)$ ,  $I_{\text{sd}}^{\text{lin}}$  is directly proportional to  $V_g$  (for a fixed  $V_{\text{sd}}$ ) or to  $V_{\text{sd}}$  (for a fixed  $V_g$ ). In the saturation regime, where  $V_{\text{sd}} > (V_g - V_0)$ ,  $I_{\text{sd}}^{\text{sat}}$  is constant, independent of  $V_{\text{sd}}$ , and quadratic with  $V_g$ .

Field effect mobility is usually calculated in linear regime using Equation 13.3 assuming weak dependence of mobility on gate voltage:

$$\left( \frac{\partial I_{\text{sd}}^{\text{lin}}}{\partial V_g} \right)_{V_{\text{sd}}} = \frac{WC_0}{L} \mu^{\text{lin}} V_{\text{sd}} \quad (13.3)$$

However, in the presence of significant contact resistance, device mobility calculated in the saturation regime gives better indication of the material mobility (at corresponding charge density) due to lowered contact resistance values at higher drain voltages [67]. The quadratic dependence of the saturation source–drain current requires that the second derivative with respect to gate voltage be taken in order to derive a saturation mobility measurement:

$$\left( \frac{\partial^2 I_{\text{sd}}^{\text{sat}}}{\partial V_g^2} \right)_{V_{\text{sd}}} = \frac{WC_0}{L} \mu^{\text{sat}} \quad (13.4)$$

It is important to note that blindly taking the second derivative of the source-drain current and deriving a mobility value without checking whether the data is reasonable can be misleading, particularly if the material is to be used to fabricate a useful FET device.

A better approach is to plot the square root of the source-drain current,  $\sqrt{I_{sd}^{\text{sat}}}$ , against gate voltage,  $V_g$ . If the device is functioning within the assumptions of the TFT model, it should be possible to fit a straight line to the above threshold region of the plot. The slope line can then be used to derive the saturation mobility:

$$\mu^{\text{sat}} = 2 \text{slope}^2 \frac{L}{WC_0} \quad (13.5)$$

While the  $x$ -intercept of the line can be used to define the turn-on or threshold voltage,  $V_0$  can depend on various factors including unintentional doping of organic layer and trapped charges at the gate insulator. Figure 13.4 shows a typical transfer plot for an OFET device displaying near-ideal quadratic dependence of drain current on gate voltage. Plotting the square root of the

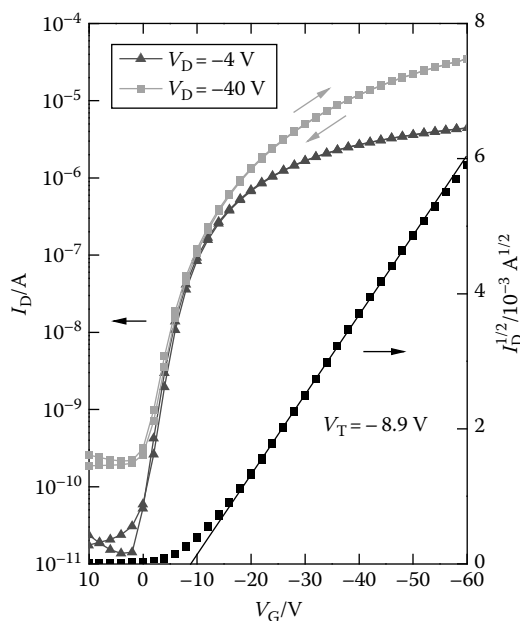


**FIGURE 13.4**

Linear and saturation currents for a typical organic FET showing minimal hysteresis and near ideal behavior. The right axis shows the square root of saturation current, which enables a linear fit to derive the saturation mobility from the gradient and the turn-on voltage from  $x$ -intercept.

drain current allows unambiguous determination of saturation mobility and threshold voltage.

### 13.7.2 FET Device Architectures

In the early days of organic electronic materials testing, OFETs were typically deposited on doped-Si substrates, which acted as the common bottom gate and the thermally grown  $\text{SiO}_2$  used as the gate dielectric. In order to attain a better electrical contact, the source–drain electrodes were evaporated through a shadow mask as the top-contact source and drain. Known as the “staggered” structure, this type of “top-contact” OFET configuration was not easily transferable to commercial scale devices as the electrodes cannot be readily patterned for channel lengths smaller than  $20\text{ }\mu\text{m}$  since organic semiconductors are frequently sensitive to the solvents/chemicals used in the photolithographic patterning or printing of the top source and drain electrodes [72,73]. A more attractive structure is a bottom-contact configuration in which patterned source and drain electrodes are first deposited followed by deposition of the semiconducting layer over the entire substrate. Here, careful selection or treatment of the source–drain electrodes is required so that a good contact is achieved and contact resistance is minimized. Two types of bottom-contact structures denoted by gate electrode position are shown in Figure 13.5:

- A bottom-gate structure in which the gate electrode is at the bottom of all organic layers and source and drain electrodes (often called a “coplanar” structure) [72].
- A top-gate structure in which the gate electrode is on top of all organic layers [74].

The top-gate geometry has several advantages for large-area OFET fabrication as the dielectric layer can act as a barrier layer to radical species in the environment such as ozone that can seriously degrade otherwise air stable

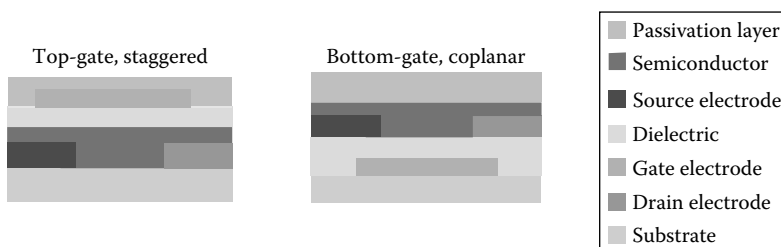


**FIGURE 13.5**

Schematic (not to scale) of typical top-gate staggered and bottom-gate coplanar device structures used in OFETs.

organic semiconductor (OSC) performance. However, the top-gate device structure presents its own set of challenges to fabricate since it requires successive semiconductor/dielectric/top-gate electrode deposition without compromising the layer below and requires good contact between the bottom source/drain electrodes and the organic semiconductor.

The primary requirement, when fabricating top-gate OFET devices, is that the OSC layer remains intact during subsequent coating of the overlying dielectric layer. This limits the choice of dielectric material to those that dissolve in what is known as an orthogonal solvent system. The generally higher solubility of small molecule OSC materials presents an acute limitation in solvent choice as even those in which the material appears sparingly soluble will still disrupt the dielectric OSC interface enough to greatly reduce performance.

---

### 13.8 Polymeric, Oligomeric, and Blend OFETs

The pursuit of an economically viable technology that enables large-area flexible displays [75,76] as well as ubiquitous cheap electronics such as radio-frequency identification tags [77,78] has been sought for over a decade and has tended to focus on two solution depositable approaches: soluble, highly crystalline small molecules, or oligomeric [9,79–82] materials and easily processable, better film forming polymeric [26,50,83] materials.

The potential for crystalline organic semiconductors has been demonstrated by devices fabricated from single crystal structures, which can exhibit impressive levels of performance. For example hole carrier mobilities ( $\mu_{\text{FET}}$ ) for vacuum deposited pentacene of  $5 \text{ cm}^2/\text{V s}$  have been reported [84], while for single crystal pentacene and rubrene values of 7 and  $15 \text{ cm}^2/\text{V s}$  have been observed [85,86]. However, vacuum evaporation will not offer sufficient technological and commercial advantage while the careful, slow growth, and manipulation of molecular crystals does not lend itself to low-cost, high volume manufacturing process [87]. There has been significant progress in the development of polycrystalline oligomeric and polymeric semiconductors deposited from solution, but it remains a challenge to combine the generally good processing characteristics with the high crystalline order required to obtain high values of charge carrier mobility. While localized high crystalline order in thin films has been demonstrated, extending this across large areas and a large number of different discrete devices is still problematic.

By functionalizing oligomers such as pentacene with solubilizing groups, the crystallinity of the solution-deposited film can be maintained leading to the highest headline field effect mobilities for solution processed devices [88,89]. Although impressive, these peak mobility values generally come at the expense of high device-to-device variation due to the difficulty in

controlling the number of crystal domain boundaries within the channel of a field effect device. This makes large-area deposition via printing difficult [90,91], while high solubility makes finding orthogonal solvents for further solution processing a considerable constraint [92]. Polymers, however, demonstrate excellent device uniformity [93] and solution rheology, which make them ideal for large-area printing [75], but have not yet demonstrated the required high mobility to make them truly useful in commercial devices [94].

Combining the high mobility of crystalline small molecules with the device uniformity of polymers is a very attractive option and has been approached in a number of ways. These include increasing the crystallinity of a polymer, such as p3HT [50], by introducing rigid units into the polymer backbone and creating regiosymmetric monomers. Polymer-small molecule blends have previously been investigated [95,96] in an attempt to produce ambipolar devices but rather than enhancing performance, the blending in these experiments appeared to diminish the peak electron and hole mobility of each component. Using a blend of small molecules and polymer to enhance the performance and improve deposition has been described in the patent literature [97,98]. By blending a soluble, highly crystalline p-type small molecule OSC with an inert or semiconducting polymer, significant enhancement in performance is claimed.

Blending of the soluble analogs of pentacene, TIPS-pentacene [7], and diF-TESADT [80,99] with both inert and semiconducting polymers has been demonstrated with significant success [100]. Organic thin-film transistors (OTFTs) fabricated from soluble blends of polymer and small molecule were cast by spin-coating, which appeared to show preferential vertical phase separation of the two components: the oligomeric component, due to its lower surface energy and higher solubility migrates to the interface allowing large crystals to form within the channel region of the device.

### 13.8.1 Characteristics of Blend Films

Several factors should be considered when determining whether to use an oligomer–polymer blend. As the two components often have very different molecular weights and typically different surface energy, this will encourage the lower surface energy component to the regions of high surface energy difference, i.e., the substrate–film interface and the film–air interface. This can be used to great advantage in OFETs as the majority of charge transport occurs in the thin, <5 nm, accumulation layer created at the gate insulator interface under gate bias. If the high mobility oligomeric component prefers to migrate to the gate insulator interface, the proportion of generally expensive OSC material can be reduced dramatically by dilution with a larger proportion of cheaper, excellent film forming polymer material. This principle has been demonstrated to excellent effect in the work of Goffri et al. [101], where the proportion of OSC in an inert polymer

matrix was reduced to as low as 3% by weight without significant loss in OFET performance.

### 13.8.1.1 Blending of Oligomeric OSC

Blending of small molecule (oligomeric) OSCs with lower performance or even inert organic polymers in order to promote easier processing and reduced device variation was initially thought to decrease the device performance because the polymer “dilutes” the current density [102,103]. This turned out to be too simplistic an explanation and researchers subsequently found that polymers with low permittivity dielectric constant could maintain the required performance when mixed with highly crystalline OSCs [20,104]. The permittivity of the polymers used in the blending experiments was shown to influence the charge carrier mobility due to dipolar disorder of a higher dielectric constant material. Therefore, low dielectric constant materials such as poly- $\alpha$ -methylstyrene could, when blended with crystalline oligomeric OSC materials, enhance film morphology while maintaining the high charge mobility.

The advantages of such an approach are seen as improved formulation scope for printing, improved cost effectiveness, and greater control over the morphology of the organic semiconductor active layer. Initial studies on OFETs comprising amorphous poly(triarylamine)s (PTAA)s blended with polystyrene showed that mobility was retained down to 50 wt% of PTAA with correspondingly reduced device hysteresis [97].

Blends of rubrene with ultrahigh molecular weight amorphous polystyrene and a glass inducing phenyl-substituted oligoacene have been reported [105] to exhibit mobilities of  $0.7 \text{ cm}^2/\text{V s}$  and on/off ratios  $>10^6$ . When cast from solution, the blends are amorphous but when annealed at temperatures  $>180^\circ\text{C}$  controlled crystallization of rubrene occurs. Additionally, when regioregular P3HT is blended with amorphous polystyrene and cast and dried at  $125^\circ\text{C}$  it shows good mobility down to 50 wt% P3HT. However, when semicrystalline polystyrene and high density polyethylene (HDPE) are used mobility is retained down to 10 and 1 wt% P3HT, respectively when cast and dried at  $125^\circ\text{C}$  [101]. The use of crystalline–crystalline semiconductor–insulator blends is therefore a useful strategy for yielding higher performing cost effective materials with improved environmental and mechanical properties.

Small molecule materials developed for OFET applications require slightly different treatment of the polymers. The tendency of small molecules to crystallize and form highly ordered domains is the foundation of their success in high performance solution processable devices. For fabrication of top-gate polymer-based OFETs, it is essential that the semiconducting layer remains intact during the spin coating of the overlying dielectric layer. This requirement severely limits the applicable solvent and materials combinations.

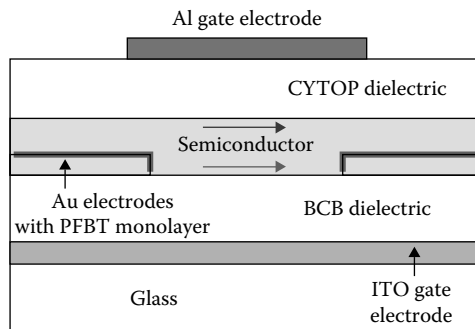
Controlling the phase separation in the direction perpendicular to the substrate to form bilayer structures should be an effective way to diminish this effect because it allows retention of the connectivity of the semiconducting layer in the channel region. To this end, organic-semiconductor/dielectric-polymer blends with vertical phase separation have been used to fabricate TFTs with low operating voltage [74] or with improved environmental stability [106] at high semiconductor concentration ( $\geq 40\%$ ).

### **13.8.1.2 Blend OFET Preparation and Fabrication**

To achieve the best compromise between peak device performance and consistent device-to-device performance crystalline oligomeric materials such as TIPS-pentacene and diF-TESADT can be blended with an amorphous inert polymer such as poly( $\alpha$ -methyl styrene) in a 1:1 weight ratio. This mixture is then dissolved in a high boiling point solvent such as tetralin at a concentration of 4% solids by weight to solvent. This solution should then be vigorously shaken or stirred for several hours at room temperature or under modest heat of 50°C to ensure all solid material has completely dissolved. To guarantee device consistency, it may also be prudent to filter the semiconducting ink before deposition.

Top- and bottom-gate transistors can be fabricated on glass, silicon, or plastic substrates provided they are prepared appropriately. Substrates should be cleaned thoroughly by sonication in a detergent solution (DECON 90), rinsed with deionized water, and dried with a stream of dry nitrogen. For a bottom-gate device, the clean glass or plastic is coated with patterned metal or indium tin oxide (ITO) to form the gate electrode. Divinyltetramethyldisiloxane bis-benzocyclobutane (BCB) is an UV and heat curable insulator with a low dielectric constant, which can be spin coated on top of the gate and polymerized to ensure that it is not washed away or even partially dissolved in the subsequent solution processing steps. The solution is spin coated at 1500 rpm for 60 s before being UV cured and then heat cured at 300°C to form the bottom-gate dielectric. Gold source and drain electrodes of ca. 40 nm thick can be evaporated and then lithographically etched to yield channel lengths of 1  $\mu$ m, but 50  $\mu$ m or more are typical with evaporation through a shadow mask alone. To ensure a low contact resistance, the effective electrode work function can be modified by the application of a SAM layer. Gold typically has a work function of  $-4.8$  eV [107] whereas the HOMO of the hole transporting materials considered here is typically  $-5.1$  eV. This difference will present an energy barrier to hole injection; thus the gold surface is modified by immersion in a  $5 \times 10^{-3}$  mol L $^{-1}$  solution of pentafluorobenzene thiol (PFBT) in isopropanol for 5 min and then rinsed with pure isopropanol.

The semiconducting layer is spin coated from a solution using a dual spin speed: initially 500 rpm for 10 s to spread the material across the substrate, then increased to 2000 rpm for 20 s to drive off the solvent and provide the

**FIGURE 13.6**

Schematic of dual gate device. The red arrow indicates the accumulation channel for the coplanar bottom-gate structure, using BCB as the insulator for ITO gate. The green arrow indicates the channel that will accumulate charge in the event of bias being applied to the aluminum top gate electrode forming a staggered device structure.

final active layer thickness of ca. 70 nm. Any remaining solvent is then evaporated by drying at 100°C for 1 min in air or, because the film is particularly vulnerable to radical attack in the drying phase, dried in a dry nitrogen glove box for 15 min.

After the deposition of the OSC layer on a bottom-gate structure, the devices can now be tested. It may be prudent to apply a barrier film to protect the film from radical attack and thus, there are not many more processing steps required to then continue to a top-gate device structure. Indeed, an excellent test of a blend OSC is to test it in a dual gate device, shown in Figure 13.6. CYTOP is a fluoro-polymer insulator with a very low dielectric constant of 2.1, which has the property of protecting against radical attack, is soluble in an orthogonal solvent that will not dissolve the underlying OSC and thus provides an excellent top-gate insulator. Spin coating a layer of CYTOP as received from Asahi Glass at 2000 rpm for 60 s and drying in an oven or on a hot plate at 100°C for 20 min typically provides a 900 nm layer of the fluorocarbon polymer, which acts as top-gate insulator after evaporation of the gate electrodes.

### 13.9 Ambipolar Transport in Conjugated Organic Polymers and Transistors

Ambipolar organic semiconductors are materials that are able to transport both holes and electrons. Despite the fact that ambipolarity was long predicted to be a generic property of organic conjugated materials (i.e., small-molecules and polymers) the first ambipolar polymer transistors have

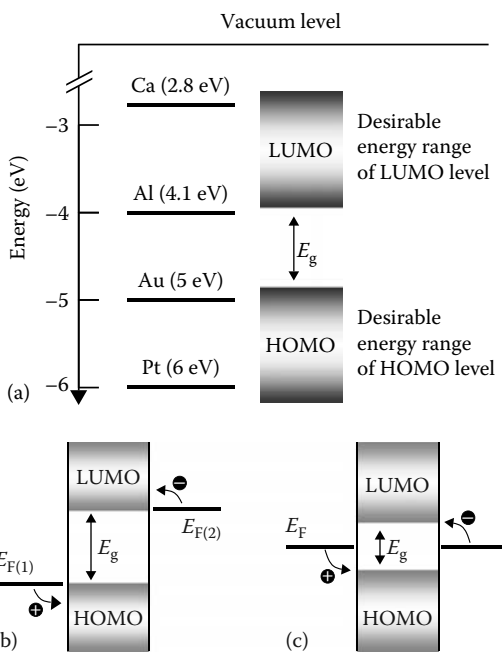
been reported only recently [108]. Ambipolarity is an interesting material property both for fundamental research and technological applications. In recent years, ambipolar transport has been exploited for the fabrication of bifunctional OFETs [108,109], and microelectronics [110,111], a field particularly relevant to optical displays [112]. The majority of ambipolar organic transistors demonstrated to date are based on bulk heterojunction systems where an electron transporting (n-channel) material is mixed with a hole transporting (p-channel) one, either via solution blending or coevaporation. Other device architectures such as bilayer ambipolar organic transistors based on the p/n-channel heterostructure concept have also been demonstrated [108]. Realization of ambipolar organic OFETs based on a single semiconductor, on the other hand, has been proven to be more difficult mainly due to the poor environmental stability of electron transport [113] and inadequate device engineering. This is the reason why ambipolar organic transistors based on a single compound have remained elusive [111,114–116].

For the design and fabrication of ambipolar OFETs, there are several materials and device parameters that need to be taken into consideration. From the materials side, for example, accessible HOMO and LUMO levels are of utmost importance. The electron and hole mobilities needs to be balanced, i.e., HOMO and LUMO should be fully delocalized while the chosen gate dielectric has to provide a trap-free semiconductor–insulator interface for both type of carriers. When selecting source and drain electrode materials, on the other hand, compatibility between the energy levels of the semiconductor with the corresponding Fermi energy ( $E_F$ ) of the injecting electrodes should be sought. Figure 13.7a shows the HOMO and LUMO energy ranges accessible by common metal electrodes and provides a rough guide for the design of ambipolar OFETs. Based on this designing rule, two different approaches can be adopted for the fabrication of ambipolar transistors. One approach is to use dissimilar source–drain electrode materials as shown in Figure 13.7b while the second is based on the use of narrow bandgap polymers in combination with suitable symmetric electrodes with a Fermi level located at the midgap of the semiconductor.

The different operating regimes of an ambipolar transistor are shown in Figure 13.8a. Under certain biasing conditions, the channel current in an ambipolar transistor can be approximated by an equivalent circuit comprising of two unipolar, i.e., a p-channel and an n-channel, transistors connected in parallel as depicted in Figure 13.8b.

Smits et al. have derived analytical equations that describe transistor operation under ambipolar and unipolar regimes [110]. The model has been successfully employed for the study of ambipolar organic transistors based on a narrow bandgap conjugated molecule, and more recently for the description of light-emitting organic transistors [117].

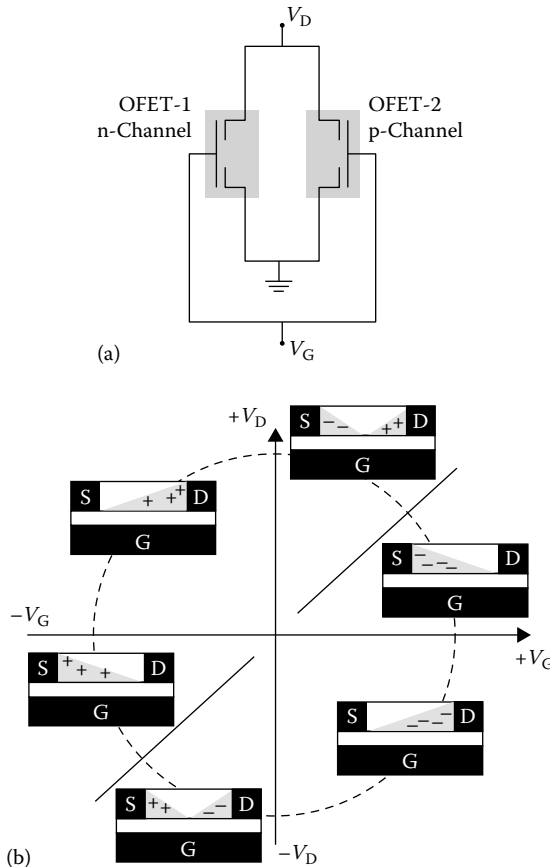
The first demonstration of a polymer-based ambipolar OFET was reported in 1996 by Tada et al. [118]. In this early study, the workers used the polymeric

**FIGURE 13.7**

(a) Desirable HOMO and LUMO energy levels as determined by the Fermi levels of several commonly used metal electrodes. (b) Ambipolar injection in an organic semiconductor employing two dissimilar electrodes. (c) Ambipolar injection in a narrow-gap organic semiconductor employing a single type of metal electrode with a Fermi level located at the midgap.

semiconductor (i.e., poly(3-alkylthiophene) shown in Figure 13.9a) as the hole transporting medium and blended it with a fluorescent dye, namely, *N,N'*-bis(2,5-DI-*tert*-butylphenyl)-3,4,9,10-perylene dicarboximide (see Figure 13.9b), as the electron transporter. It was not until 2003 when Meijer et al. demonstrated the first single component polymer-based ambipolar transistors [114]. This was achieved using the low bandgap (1.55 eV) polymer poly(3,9-di-*t*-butylindeno[1,2-b] fluorene) (PIF) shown in Figure 13.9c. Since then ambipolar transistors based on numerous conjugated polymer semiconductors have been demonstrated [108]. Based on these findings, it is now widely accepted that in general organic conjugated materials are intrinsically as good electron transporters as they are hole transporters [119].

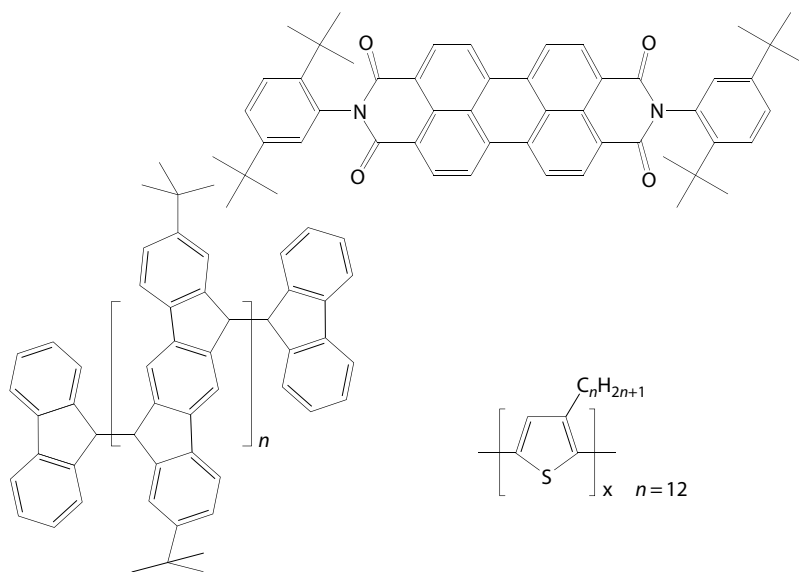
Ambipolar charge transport in conjugated organic materials is interesting not only for basic studies but also for its technological implications. One technology that could benefit from it is large area microelectronics for display applications. To date, there are two demonstrated technologies for the fabrication of such organic integrated circuits. These are (i) the unipolar [112] (Figure 13.10a) and (ii) the complementary logic (Figure 13.10b) [120]. Unipolar circuit architectures consist of unipolar (i.e. p-, or n-channel)

**FIGURE 13.8**

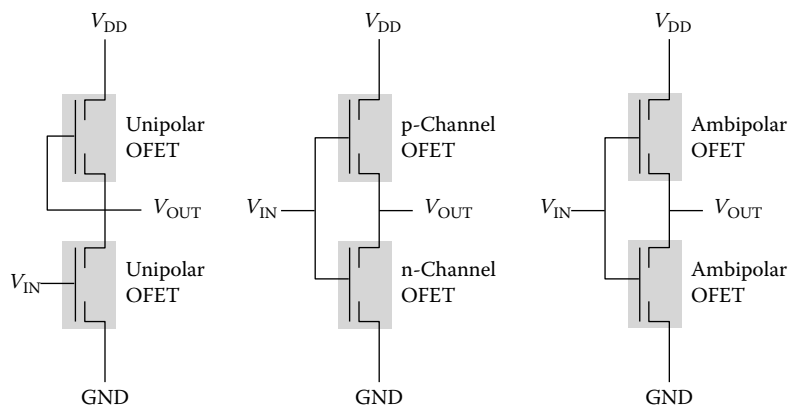
- (a) Operating regimes of an ambipolar transistor as a function of drain and gate biasing.  
 (b) Equivalent circuit of an ambipolar transistor comprising two, i.e., a p- and n-channel, transistors connected in parallel.

transistors and are simple to fabricate since they require a single high work-function metal (e.g., gold) and a single type semiconductor. Despite their simplicity, unipolar circuits have poor performance exhibiting low noise margin, low manufacturing yield, and high power consumption. In order to improve their performance, more sophisticated architectures are usually employed [112].

Despite the significant benefits such an approach increases circuit complexity. Complementary architectures [120], adopted from silicon microelectronics, can provide a solution to this bottleneck with major advantages in circuit performance including large noise margin, robustness, and low power dissipation. Unlike silicon technology, however, fabrication of discrete organic n- and p-channel transistors with lateral dimensions of few

**FIGURE 13.9**

Chemical structure of (a) poly(3-alkylthiophene), (b)  $N,N'$ -bis(2,5-di-*tert*-butylphenyl)-3,4,9,10-perylene dicarboximide, and (c) poly(3,9-di-*t*-butylindeno[1,2-*b*]fluorene).

**FIGURE 13.10**

Circuitry of voltage inverters (i.e., NOT gates) based on different logic architectures. (a) A unipolar voltage inverter, (b) a complementary logic inverter, and (c) a complementary-like voltage inverter.

micrometers, typically required for large-scale integration, is still very challenging. An alternative and promising route toward robust organic integrated circuits is the use of the complementary-like approach based solely on ambipolar transistors [116]. The circuitry of a complementary-like

inverter is shown in Figure 13.10c. Depending on the biasing conditions the circuit can operate both on the first and third quadrant of the output vs. input plot without any alteration in the circuit functionality, a unique characteristic of the technology. Research effort around the world is focusing on the development of new ambipolar organic semiconductors with improved carriers mobilities.

---

### **13.10 Summary**

Semiconducting polymers are attractive candidates for organic electronic transistor devices, due to their potential for low cost processing and increasing electrical performances. Molecular design principles have been employed in the identification of high performing polymers and several illustrations of this were highlighted in the chapter. Highly crystalline, well-ordered, and -oriented polymer thin film microstructures have been shown to be necessary to achieve optimal semiconducting electrical properties. The optimization of synthetic routes and purification techniques, as well as the appropriate polymer molecular weights, processing conditions, choice of solvent, surface treatments, and dielectric interfaces are all important to achieve incremental device performance improvements. Challenges remain however to further improve stability when exposed to the combination of oxygen, humidity, and light, and to tailor the solubility of these aromatic materials to processing friendly solvents. Manipulation of the HOMO energy level of the conjugated backbone was shown to be an effective strategy to improve stability. With the promising advances in the understanding of the morphological and molecular origins of optimal electrical performance made by many groups in recent years, there is an exciting potential for further improvements.

---

### **Acknowledgments**

The authors would like to thank the following colleagues and collaborators for their valuable contributions to the chapter: Maxim Shkunov, David Sparrowe, Weimin Zhang, Steve Tierney, Clare Bailey, Warren Duffy, Kristijonas Genevicius, Joe Kline, Michael Chabinyc, Dean DeLongchamp, Eric Lin, Lee Richter, Alberto Salleo, Mike Toney, Patrick Brocorens, Wojciech Osikowicz, Jui-Fen Chang, Henning Sirringhaus, and Masayoshi Suzuki.

---

## References

1. Y.-L. Loo, I. McCulloch, *MRS Bull.* 2008, **33**, 653.
2. J. Z. Wang, J. Gu, F. Zenhausern, H. Sirringhaus, *Appl. Phys. Lett.* 2006, **88**, 133502/1.
3. Y.-Y. Noh, N. Zhao, M. Caironi, H. Sirringhaus, *Nat. Nanotechnol.* 2007, **2**, 784.
4. C. W. Sele, T. von Werne, R. H. Friend, H. Sirringhaus, *Adv. Mater.* (Weinheim, Ger.) 2005, **17**, 997.
5. T. Kelley, L. Boardman, T. Dunbar, D. Muyres, M. Pellerite, T. Smith, *J. Phys. Chem. B* 2003, **107**, 5877.
6. C. D. Sheraw, T. N. Jackson, D. L. Eaton, J. E. Anthony, *Adv. Mater.* (Weinheim, Ger.) 2003, **15**, 2009.
7. J. E. Anthony, D. L. Eaton, S. R. Parkin, *Org. Lett.* 2002, **4**, 15.
8. M. M. Payne, S. R. Parkin, J. E. Anthony, C. C. Kuo, T. N. Jackson, *J. Am. Chem. Soc.* 2005, **127**, 4986.
9. J. E. Anthony, J. S. Brooks, D. L. Eaton, S. R. Parkin, *J. Am. Chem. Soc.* 2001, **123**, 9482.
10. D. Lawrence, J. Kohler, B. Brollier, T. Claypole, T. Burgin, *Printed Org. Mol. Electron.* 2004, 161.
11. R. J. Kline, M. D. McGehee, E. N. Kadnikova, J. Liu, J. M. J. Fréchet, M. F. Toney, *Macromolecules* 2005, **38**, 3312.
12. A. Zen, J. Pflaum, S. Hirschmann, W. Zhuang, F. Jaiser, U. Asawapirom, J. P. Rabe, U. Scherf, D. Neher, *Adv. Func. Mater.* 2004, **14**, 757.
13. J.-F. Chang, J. Clark, N. Zhao, H. Sirringhaus, D. W. Breiby, J. W. Andreasen, M. M. Nielsen, M. Giles, M. Heeney, I. McCulloch, *Phys. Rev. B: Condens. Matter Mater. Phys.* 2006, **74**, 115318/1.
14. R. Hamilton, C. Bailey, W. Duffy, M. Heeney, M. Shkunov, D. Sparrowe, S. Tierney, I. McCulloch, R. J. Kline, D. M. DeLongchamp, M. Chabinyc, *Proc. SPIE Int. Soc. Opt. Eng.* 2006, **6336**, 633611/1.
15. R. Pokrop, J.-M. Verilhac, A. Gasior, I. Wielgus, M. Zagorska, J.-P. Travers, A. Pron, *J. Mater. Chem.* 2006, **16**, 3099.
16. J.-M. Verilhac, R. Pokrop, G. LeBlevennec, I. Kuliszewicz-Bajer, K. Buga, M. Zagorska, S. Sadki, A. Pron, *J. Phys. Chem. B* 2006, **110**, 13305.
17. F. C. Krebs, R. B. Nyberg, M. Jorgensen, *Chem. Mater. ASAP*.
18. C. E. Garrett, K. Prasad, *Adv. Synth. Catal.* 2004, **346**, 889.
19. C. D. Dimitrakopoulos, D. J. Mascaro, *IBM J. Res. Dev.* 2001, **45**, 11.
20. J. Veres, S. D. Ogier, S. W. Leeming, D. C. Cupertino, S. M. Khaffaf, *Adv. Func. Mater.* 2003, **13**, 199.
21. M. Knaapila, R. Stepanyan, B. P. Lyons, M. Torkkeli, A. P. Monkman, *Adv. Func. Mater.* 2006, **16**, 599.
22. H. Sirringhaus, T. Kawase, R. H. Friend, T. Shimoda, M. Inbasekaran, W. Wu, E. P. Woo, *Science* 2000, **290**, 2123.
23. H. Sirringhaus, R. J. Wilson, R. H. Friend, M. Inbasekaran, W. Wu, E. P. Woo, M. Grell, D. D. C. Bradley, *Appl. Phys. Lett.* 2000, **77**, 406.
24. D. J. Brennan, Y. Chen, S. Feng, J. P. Godschalx, G. E. Spilman, P. H. Townsend, S. R. Kisting, M. G. Dibbs, J. M. Shaw, D. M. Welsh, J. L. Miklovich, D. Stutts, *Mater. Res. Soc. Symp. Proc.* 2004, **814**, 1.

25. P. J. Brown, D. S. Thomas, A. Kohler, J. S. Wilson, J.-S. Kim, C. M. Ramsdale, H. Sirringhaus, R. H. Friend, *Phys. Rev. B: Condens. Matter Mater. Phys.* 2003, **67**, 064203/1.
26. H. Sirringhaus, P. J. Brown, R. H. Friend, M. M. Nielsen, K. Bechgaard, B. M. W. Langeveld-Voss, A. J. H. Spiering, R. A. J. Janssen, E. W. Meijer, P. Herwig, D. M. de Leeuw, *Nature* 1999, **401**, 685.
27. A. Salleo, M. L. Chabinyc, M. Yang, R. Street, *Appl. Phys. Lett.* 2002, **81**, 4383.
28. L.-L. Chua, J. Zaumseil, J. F. Chang, E. C.-W. Ou, P. K.-H. Ho, H. Sirringhaus, R. H. Friend, *Nature* 2005, **434**, 194.
29. A. Babel, S. A. Jenekhe, *Synth. Met.* 2005, **148**, 169.
30. A. Zen, M. Saphiannikova, D. Neher, U. Asawapirom, U. Scherf, *Chem. Mater.* 2005, **17**, 781.
31. Z. Bao, A. J. Lovinger, *Chem. Mater.* 1999, **11**, 2607.
32. A. Zen, P. J. S. Hirschmann, W. Zhuang, F. Jaiser, U. Asawapirom, J. P. Rabe, U. Scherf, D. Neher, *Adv. Func. Mater.* 2004, **14**, 757.
33. J. F. Chang, B. Sun, D. W. Breiby, M. M. Nielsen, T. I. Sölling, M. Giles, I. McCulloch, H. Sirringhaus, *Chem. Mater.* 2004, **16**, 4772.
34. D. M. DeLongchamp, B. M. Vogel, Y. Jung, M. C. Gurau, C. A. Richter, O. A. Kirillov, J. Obraztsov, D. A. Fischer, S. Sambasivan, L. J. Richter, E. K. Lin, *Chem. Mater.* 2005, **17**, 5610.
35. G. Wang, J. Swensen, D. Moses, A. J. Heeger, *J. Appl. Phys.* 2003, **93**, 6137.
36. I. McCulloch, C. Bailey, M. Giles, M. Heeney, I. Love, M. Shkunov, D. Sparrowe, S. Tierney, *Chem. Mater.* 2005, **17**, 1381.
37. T. Yasuda, Y. Sakai, S. Aramaki, T. Yamamoto, *Chem. Mater.* 2005, **17**, 6060.
38. D. J. Crouch, P. J. Skabara, J. E. Lohr, J. J. W. McDouall, M. Heeney, I. McCulloch, D. Sparrowe, M. Shkunov, S. J. Coles, P. N. Horton, M. B. Hursthouse, *Chem. Mater.* 2005, **17**, 6567.
39. J. Roncali, *Chem. Rev. (Washington, DC)* 1997, **97**, 173.
40. Y. Zhu, R. D. Champion, S. A. Jenekhe, *Macromolecules* 2006, **39**, 8712.
41. T. Yamamoto, M. Arai, H. Kokubo, S. Sasaki, *Macromolecules* 2003, **36**, 7986.
42. T. Yamamoto, H. Kokubo, M. Kobashi, Y. Sakai, *Chem. Mater.* 2004, **16**, 4616.
43. A. R. Murphy, J. Liu, C. Luscombe, D. Kavulak, J. M. J. Fréchet, R. J. Kline, M. D. McGehee, *Chem. Mater.* 2005, **17**, 4892.
44. B. S. Ong, Y. Wu, P. Liu, S. Gardner, *J. Am. Chem. Soc.* 2004, **126**, 3378.
45. P. Baeuerle, T. Fischer, B. Bidlingmeier, A. Stabel, J. P. Rabe, *Angew. Chem., Int. Ed. English* 1995, **34**, 303.
46. R. Azumi, G. Gotz, T. Debaerdemaeker, P. Bauerle, *Chem. Eur. J.* 2000, **6**, 735.
47. N. Zhao, G. A. Botton, S. Zhu, A. Duft, B. S. Ong, Y. Wu, P. Liu, *Macromolecules* 2004, **37**, 8307.
48. Y. Wu, P. Liu, S. Gardner, B. S. Ong, *Chem. Mater.* 2004, **17**, 221.
49. M. Heeney, C. Bailey, K. Genevicius, M. Shkunov, D. Sparrowe, S. Tierney, I. McCulloch, *J. Am. Chem. Soc.* 2005, **127**, 1078.
50. I. McCulloch, M. Heeney, C. Bailey, K. Genevicius, I. MacDonald, M. Shkunov, D. Sparrowe, S. Tierney, R. Wagner, W. Zhang, M. L. Chabinyc, R. J. Kline, M. D. McGehee, M. F. Toney, *Nat. Mater.* 2006, **5**, 328.
51. D. M. DeLongchamp, R. J. Kline, E. K. Lin, D. A. Fischer, L. J. Richter, L. A. Lucas, M. Heeney, I. McCulloch, J. E. Northrup, *Adv. Mat.* 2007, **19**, 833.
52. R. J. Kline, D. M. DeLongchamp, D. A. Fischer, E. K. Lin, L. J. Richter, M. L. Chabinyc, M. F. Toney, M. Heeney, I. McCulloch, *Macromolecules* 2007, **40**, 7960.

53. M. C. Gurau, D. M. Delongchamp, B. M. Vogel, E. K. Lin, D. A. Fischer, S. Sambasivan, L. J. Richter, *Langmuir* 2007, 23, 834.
54. M. Heeney, C. Bailey, S. Tierney, W. Zhang, I. McCulloch. US Patent 7,524,922.
55. J. Li, F. Qin, C. M. Li, Q. Bao, M. B. Chan-Park, W. Zhang, J. Qin, B. S. Ong, *Chem. Mater.* 2008, 20, 2057.
56. J. Liu, R. Zhang, G. Sauve, T. Kowalewski, R. D. McCullough, *J. Am. Chem. Soc.* 2008, 130, 13167.
57. J. Peet, J. Y. Kim, N. E. Coates, W. L. Ma, D. Moses, A. J. Heeger, G. C. Bazan, *Nat. Mater.* 2007, 6, 497.
58. H. N. Tsao, D. Cho, J. W. Andreasen, A. Rouhanipour, D. W. Breiby, W. Pisula, K. Müllen, *Adv. Mater.* 2009, 21, 209.
59. G. Lu, H. Usta, C. Risko, L. Wang, A. Facchetti, M. A. Ratner, T. J. Marks, *J. Am. Chem. Soc.* 2008, 130, 7670.
60. C. Risko, G. P. Kushto, Z. H. Kafati, J. L. Bredas, *J. Chem. Phys.* 2004, 121, 9031.
61. L. Burgi, M. Turbiez, R. Pfeiffer, F. Bienewald, H. J. Kirner, C. Winnewisser, *Adv. Mater.* 2008, 20, 2217.
62. H. H. Fong, V. A. Pozdin, A. Amassian, G. G. Malliaras, D.-M. Smilgies, M. He, S. Gasper, F. Zhang, M. Sorensen, *J. Am. Chem. Soc.* 2008, 130, 13202.
63. H. Usta, A. Facchetti, T. J. Marks, *J. Am. Chem. Soc.* 2008, 130, 8580.
64. H. A. Becerril, N. Miyaki, M. L. Tang, R. Mondal, Y.-S. Sun, A. C. Mayer, J. E. Parmer, M. D. McGehee, Z. Bao, *J. Mater. Chem.* 2009, 19, 591.
65. H. Yan, Z. Chen, Y. Zheng, C. Newman, J. R. Quinn, F. Dotz, M. Kastler, A. Facchetti, *Nature* 2009.
66. I. McCulloch, M. Heeney, M. Chabiny, D. DeLongchamp, R. J. Kline, M. Colle, W. Duffy, D. Fischer, D. Gundlach, B. Hamadani, R. Hamilton, L. Richter, A. Salleo, M. Shkunov, D. Sparrowe, S. Tierney, W. Zhang, *Adv. Mater.* 2009, 21, 1091.
67. G. Horowitz, *J. Mater. Res.* 2004, 19, 1946.
68. H. Sirringhaus, N. Tessler, R. H. Friend, *Science* 1998, 280, 1741.
69. D. H. Kim, Y. D. Park, Y. S. Jang, H. C. Yang, Y. H. Kim, J. I. Han, D. G. Moon, S. J. Park, T. Y. Chang, C. W. Chang, M. K. Joo, C. Y. Ryu, K. W. Cho, *Adv. Func. Mater.* 2005, 15, 77.
70. Y. Roichman, Y. Preezant, N. Tessler, *Phys. Status Solidi A: Appl. Res.* 2004, 201, 1246.
71. S. M. Sze, *Physics of Semiconductor Devices*, Wiley, New York, 1987.
72. R. A. Street, A. Salleo, *Appl. Phys. Lett.* 2002, 81, 2887.
73. J. F. Yuan, J. Zhang, J. Wang, X. J. Yan, D. H. Yan, W. Xu, *Appl. Phys. Lett.* 2003, 82, 3967.
74. L. L. Chua, P. K. H. Ho, H. Sirringhaus, R. H. Friend, *Adv. Mater.* 2004, 16, 1609.
75. C. D. Dimitrakopoulos, P. R. L. Malenfant, *Adv. Mater.* (Weinheim, Ger.) 2002, 14, 99.
76. R. H. Reuss, B. R. Chalamala, A. Moussessian, M. G. Kane, A. Kumar, D. C. Zhang, J. A. Rogers, M. Hatalis, D. Temple, G. Moddel, B. J. Eliasson, M. J. Estes, J. Kunze, E. S. Handy, E. S. Harmon, D. B. Salzman, J. M. Woodall, M. A. Alam, J. Y. Murthy, S. C. Jacobsen, M. Olivier, D. Markus, P. M. Campbell, E. Snow, *Proc. IEEE* 2005, 93, 1239.
77. S. Steudel, S. De Vusser, K. Myny, M. Lenes, J. Genoe, P. Heremans, *J. Appl. Phys.* 2006, 99, 114519.

78. S. Steudel, K. Myny, V. Arkhipov, C. Deibel, S. De Vusser, J. Genoe, P. Heremans, *Nat. Mater.* 2005, **4**, 597.
79. J. E. Anthony, J. Gierschner, C. A. Landis, S. R. Parkin, J. B. Sherman, R. C. Bakus, *Chem. Commun.* 2007, 4746.
80. D. J. Gundlach, J. E. Royer, S. K. Park, S. Subramanian, O. D. Jurchescu, B. H. Hamadani, A. J. Moad, R. J. Kline, L. C. Teague, O. Kirillov, C. A. Richter, J. G. Kushmerick, L. J. Richter, S. R. Parkin, T. N. Jackson, J. E. Anthony, *Nat. Mater.* 2008, **7**, 216.
81. K. C. Dickey, T. J. Smith, K. J. Stevenson, S. Subramanian, J. E. Anthony, Y. L. Loo, *Chem. Mater.* 2007, **19**, 5210.
82. K. P. Weidkamp, A. Afzali, R. M. Tromp, R. J. Hamers, *J. Am. Chem. Soc.* 2004, **126**, 12740.
83. D. J. Crouch, P. J. Skabara, M. Heeney, I. McCulloch, S. J. Coles, M. B. Hursthouse, *Chem. Commun. (Cambridge, U.K.)* 2005, 1465.
84. T. W. Kelley, D. V. Muyres, P. F. Baude, T. P. Smith, T. D. Jones, in *Symposium on Organic and Polymeric Materials and Devices held at the 2003 MRS Spring Meeting* (Ed.: P. Blom), Materials Research Society, San Francisco, CA, 2003, p. 169.
85. S. F. Nelson, Y. Y. Lin, D. J. Gundlach, T. N. Jackson, *Appl. Phys. Lett.* 1998, **72**, 1854.
86. V. C. Sundar, J. Zaumseil, V. Podzorov, E. Menard, R. L. Willett, T. Someya, M. E. Gershenson, J. A. Rogers, *Science* 2004, **303**, 1644.
87. V. Subramanian, P. C. Chang, J. B. Lee, S. E. Molesa, S. K. Volkman, in *10th THERMINIC Workshop*, Sophia Antipolis, France, 2004, p. 742.
88. S. K. Park, J. E. Anthony, T. N. Jackson, *IEEE Electron. Device Lett.* 2007, **28**, 877.
89. S. Subramanian, S. K. Park, S. R. Parkin, V. Podzorov, T. N. Jackson, J. E. Anthony, *J. Am. Chem. Soc.* 2008, **130**, 2706.
90. D. Guo, T. Miyadera, S. Ikeda, T. Shimada, K. Saiki, *J. Appl. Phys.* 2007, **102**, 023706.
91. R. L. Headrick, S. Wo, F. Sansoz, J. E. Anthony, *Appl. Phys. Lett.* 2008, **92**, 063302.
92. H. Yan, M. H. Yoon, A. Facchetti, T. J. Marks, *Appl. Phys. Lett.* 2005, **87**, 183501.
93. B. H. Hamadani, D. J. Gundlach, I. McCulloch, M. Heeney, *Appl. Phys. Lett.* 2007, **91**, 243512/1.
94. M. Berggren, D. Nilsson, N. D. Robinson, *Nat. Mater.* 2007, **6**, 3.
95. A. Babel, J. D. Wind, S. A. Jenekhe, *Adv. Func. Mater.* 2004, **14**, 891.
96. Y. Hayashi, H. Kanamori, I. Yamada, A. Takasu, S. Takagi, K. Kaneko, *Appl. Phys. Lett.* 2005, **86**, 052104.
97. B. A. Brown, J. Veres, R. M. Anemian, R. T. Williams, S. D. Ogier, S. W. Leeming, in *PCT Int. Appl.* (Avecia Limited, U.K.), WO, 2005, p. 68.
98. S. D. Ogier, J. Veres, M. Zeidan, in *PCT Int. Appl.* (Merck Patent G.m.b.H., Germany), WO, 2007, p. 46.
99. S. K. Park, C. C. Kuo, J. E. Anthony, T. N. Jackson, in *IEEE International Electron Devices Meeting 2005, Technical Digest*, IEEE, New York, 2005, p. 113.
100. J. Smith, R. Hamilton, M. Heeney, D. M. de Leeuw, E. Cantatore, J. E. Anthony, I. McCulloch, D. D. C. Bradley, T. D. Anthopoulos, *Appl. Phys. Lett.* 2008, **93**, 253301/1.
101. S. Goffri, C. Muller, N. Stingelin-Stutzmann, D. W. Breiby, C. P. Radano, J. W. Andreasen, R. Thompson, R. A. J. Janssen, M. M. Nielsen, P. Smith, H. Sirringhaus, *Nat. Mater.* 2006, **5**, 950.

102. A. Babel, S. A. Jenekhe, *J. Phys. Chem. B* 2003, **107**, 1749.
103. J. S. Liu, E. Sheina, T. Kowalewski, R. D. McCullough, *Angew. Chem.: Int. Edn.* 2001, **41**, 329.
104. A. Babel, S. A. Jenekhe, *Macromolecules* 2004, **37**, 9835.
105. N. Stingelin-Stutzmann, E. Smits, H. Wondergem, C. Tanase, P. Blom, P. Smith, D. De Leeuw, *Nat. Mater.* 2005, **4**, 601.
106. A. C. Arias, F. Endicott, R. A. Street, *Adv. Mater.* 2006, **18**, 2900.
107. P. A. Anderson, *Phys. Rev.* 1959, **115**, 550.
108. J. Zaumseil, H. Sirringhaus, *Chem. Rev. (Washington, DC)* 2007, **107**, 1296.
109. J. Zaumseil, R. H. Friend, H. Sirringhaus, *Nat. Mater.* 2006, **5**, 69.
110. E. C. P. Smits, T. D. Anthopoulos, S. Setayesh, E. van Veenendaal, R. Coehoorn, P. W. M. Blom, B. de Boer, D. M. de Leeuw, *Phys. Rev. B* 2006, **73**, 205316.
111. T. D. Anthopoulos, C. Tanase, S. Setayesh, E. J. Meijer, J. C. Hummelen, P. W. M. Blom, D. M. de Leeuw, *Adv. Mater.* 2004, **16**, 2174.
112. G. H. Gelinck, H. E. A. Huitema, E. Van Veenendaal, E. Cantatore, L. Schrijnemakers, J. Van der Putten, T. C. T. Geuns, M. Beenhakkers, J. B. Giesbers, B. H. Huisman, E. J. Meijer, E. M. Benito, F. J. Touwslager, A. W. Marsman, B. J. E. Van Rens, D. M. De Leeuw, *Nat. Mater.* 2004, **3**, 106.
113. T. D. Anthopoulos, G. C. Anyfantis, G. C. Papavassiliou, D. M. de Leeuw, *Appl. Phys. Lett.* 2007, **90**, 122105.
114. E. J. Meijer, D. M. de Leeuw, S. Setayesh, E. van Veenendaal, B. H. Huisman, P. W. M. Blom, J. C. Hummelen, U. Scherf, J. Kadam, T. M. Klapwijk, *Nat. Mater.* 2003, **2**, 834.
115. T. D. Anthopoulos, D. M. de Leeuw, E. Cantatore, P. van't Hof, J. Alma, J. C. Hummelen, *J. Appl. Phys.* 2005, **98**.
116. T. D. Anthopoulos, S. Setayesh, E. Smits, M. Colle, E. Cantatore, B. de Boer, P. W. M. Blom, D. M. de Leeuw, *Adv. Mater.* 2006, **18**, 1900.
117. E. C. P. Smits, S. Setayesh, T. D. Anthopoulos, M. Buechel, W. Nijssen, R. Coehoorn, P. W. M. Blom, B. de Boer, D. M. de Leeuw, *Adv. Mater.* 2007, **19**, 734.
118. K. Tada, H. Harada, K. Yoshino, *Jpn. J. Appl. Phys. Part 2: Lett.* 1996, **35**, L944.
119. J. Cornil, J.-L. Bredas, J. Zaumseil, H. Sirringhaus, *Adv. Mater.* (Weinheim, Ger.) 2007, **19**, 1791.
120. B. Crone, A. Dodabalapur, Y. Y. Lin, R. W. Filas, Z. Bao, A. LaDuca, R. Sarpeshkar, H. E. Katz, W. Li, *Nature* 2000, **403**, 521.



# **Part IV**

# **Applications**



# 14

---

## *OLED Materials and Device Architectures for Full-Color Displays and Solid-State Lighting*

---

**Tukaram K. Hatwar, Marina E. Kondakova,  
David J. Giesen, and Jeffrey P. Spindler**

### CONTENTS

14.1	Introduction .....	434
14.2	Basics of OLED Devices .....	435
14.2.1	Performance Metrics.....	435
14.2.2	Materials and Architectures.....	439
14.3	Current Status of Fluorescent Red, Green, Blue, and White OLED Devices .....	443
14.3.1	Performance of Red Fluorescent OLED Devices .....	444
14.3.2	Performance of Green Fluorescent OLED Devices .....	445
14.3.3	Performance of Blue Fluorescent OLED Devices.....	447
14.3.4	Displays Based on Patterned Red, Green, and Blue Emitters .....	449
14.3.5	Architectures and Performance of White OLED Devices.....	450
14.3.5.1	Progress in Simple Two-EML-Layer Architecture of White OLEDs.....	450
14.3.5.2	Multilayer White Structures.....	451
14.3.5.3	Obtaining a Stabilized Blue Using White Emission .....	453
14.3.6	Tandem OLED Devices .....	456
14.3.6.1	Tandem Device Architecture .....	456
14.3.6.2	White Tandem Devices .....	457
14.3.6.3	High-Efficiency White Tandem Devices.....	458
14.3.6.4	High-Efficiency and High-Color-Temperature Tandem Whites.....	461
14.3.7	White OLED Devices for Display Applications.....	463
14.3.8	White OLED Devices for Lighting Applications .....	463

14.4	Architectures and Materials for Phosphorescent OLED Devices.....	466
14.4.1	Brief Introduction to Emission Mechanism in Phosphorescent OLED Devices.....	466
14.4.2	Device Architectures and Performance of Monochromatic Phosphorescent OLED Devices.....	468
14.4.2.1	Architectures and Performance of Red Phosphorescent OLED Devices.....	468
14.4.2.2	Architectures and Performance of Green Phosphorescent OLED Devices.....	477
14.4.2.3	Architectures and Performance of Blue Phosphorescent OLED Devices.....	488
14.4.3	White OLED Devices Based on Phosphorescent Emitters...	491
14.4.3.1	Single-Stack White OLED Devices Incorporating Phosphorescent Emitters .....	491
14.4.3.2	Tandem White Devices with Phosphorescent Emitters .....	496
14.5	Future Outlook.....	499
	Acknowledgments .....	499
	References.....	499

---

## 14.1 Introduction

Efficient organic thin-film electroluminescence was discovered in the 1970s and forms the basis of a new generation of flat-panel display technology. A device based on this phenomenon is called an organic light-emitting diode (OLED). The rapid pace of technological development in OLEDs directed toward display applications, such as notebook PCs and TVs, is driven largely by the substantial revenue opportunity in this market segment.<sup>1–7</sup> For a large market penetration, however, active-matrix OLED (AMOLED) display performance should meet or exceed power efficacy, lifetime, color gamut, resolution, and display luminance specifications in order to be competitive with the well-established LCD and PDP technologies. This requires careful selection of OLED materials, device architecture, manufacturing methods, and backplane technology. OLEDs also represent the future of a vast array of completely new lighting applications.<sup>8–10</sup> By combining color with shape, OLEDs will create a new way of decorating with solid-state lighting. At the same time, OLEDs offer the potential to become even more efficient than fluorescent light bulbs.

In this chapter, we will review the progress in performance of small-molecule OLED materials and architectures, the backbone technologies for high-quality displays. Significant progress has been made in developing device architectures based on both fluorescent and phosphorescent materials, however, major challenges remain in improving the performance of red (R), green (G), blue (B), and white (W) OLEDs for both displays and lighting.<sup>11,12</sup>

All of the device architectures discussed in this chapter are for bottom-emission devices using a transparent substrate (light is emitted through the anode and glass substrate) but are also suitable for top-emission devices using a transmissive cathode and opaque anode. The basics of OLED devices will be discussed in Section 14.2, including typical performance metrics and the names and functions of various materials and layers. We will review the advanced architectures and current status of red-, green-, or blue-emitting OLED devices based on fluorescent materials in Section 14.3.

White-emitting OLED devices will also be discussed in Section 14.3. White OLED technology has attracted much attention in recent years because of its potential to become the preferred emission format for both displays and lighting applications. The consideration of white OLEDs with integrated color filters on thin-film transistor (TFT) substrates for manufacturing large-area AMOLED displays is mainly due to expected high yield and low unit manufacturing cost because of the avoidance of costly precision shadow masks. We will discuss highly efficient and stable single-stack white OLEDs that have been reported based upon fluorescent, phosphorescent, and combinations of fluorescent and phosphorescent (hybrid) emitters. In addition, we will describe advanced multistacked structures where similar or different emitting units are connected through a transparent charge-generating layer, providing further improvements in device performance.<sup>13,14</sup>

The luminous efficiency of OLEDs can be improved further by use of phosphorescent emissive materials. Incorporated into OLED devices starting in the 1990s, phosphorescent dopants have a potential to achieve 100% internal quantum efficiency.<sup>15,16</sup> We will describe materials and architecture developments of phosphorescent OLED devices in Section 14.4. Finally, we discuss the future outlook of the OLED technology in Section 14.5.

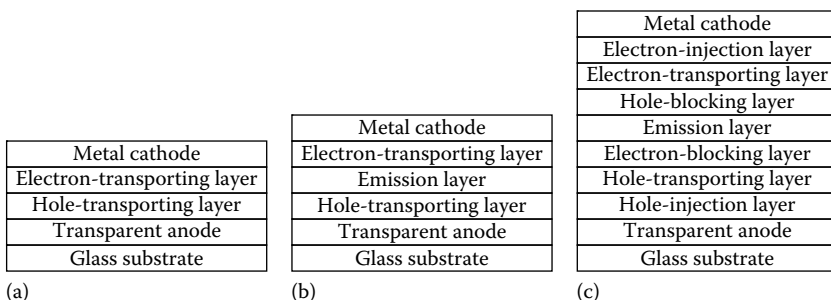
---

## 14.2 Basics of OLED Devices

This section covers the background information for OLED devices that applies to both fluorescent and phosphorescent devices. In addition, materials and architectures specific to fluorescent devices are discussed. Phosphorescent structures are described in Section 14.4.

### 14.2.1 Performance Metrics

An OLED is an electronic device that emits light in response to an applied potential. At its most basic, as shown in Figure 14.1a, an OLED consists of a substrate and one or more layers of organic material sandwiched between two electrodes. When a potential is applied to the device, the anode injects

**FIGURE 14.1**

OLED device structures: (a) bilayer OLED; (b) trilayer OLED; and (c) multilayer OLED.

holes into the organic material and the cathode injects electrons. The oppositely charged holes and electrons migrate toward each other under the influence of the applied electric field.<sup>1,2</sup> When a hole and electron meet, they recombine according to Equation 14.1:



In Equation 14.1,  $A^+$  represents the hole or cation,  $A^-$  represents the electron or anion,  $A_0$  is a ground state molecule, and  $A^*$  is a molecule in an excited state.  $A^+$  and  $A^-$  can be molecules of the same material or different materials. Subsequent to the recombination,  $A^*$  can radiatively relax back to the ground state, losing a photon of light. In some OLED devices,  $A^*$  relaxes by energy transfer to a second molecule, B, creating an excited molecule,  $B^*$ , which can then emit a photon of light.

There are four main performance metrics by which an OLED device is typically described: drive voltage, efficiency, lifetime, and color. The drive voltage, usually referred to as simply voltage, is the voltage that must be applied in order to achieve light emission of the desired intensity. Some important factors that affect the voltage are the built-in potential between the electrodes, the energy barriers for charge injection from the electrodes, and the electric field that is needed to drive charge carriers between and through the organic layers. In practice, the voltage in a well-constructed device approaches the energy of the emitted photon of light.<sup>17</sup>

The efficiency of a device is the measure of the amount of light output relative to the amount of energy input or electrical current generated.<sup>18</sup> The most common measure of efficiency has historically been candelas of light per ampere of current (cd/A). This measure weighs photons of light based on the photopic response curve of the human eye, so photons of light near 555 nm give the highest cd/A efficiency. A second measure of efficiency is external quantum efficiency (EQE).<sup>18</sup> EQE is given as a percent and is the ratio of photons of light that emit externally to the device to the number

of electrons (or holes) injected into the device. The number of photons that emit externally to the device is given by Equation 14.2:

$$n_{\text{external}} = n_{\text{electrons}} \cdot \eta_{\text{recombination}} \cdot \eta_{\text{spin}} \cdot \eta_{\text{internal}} \cdot \eta_{\text{outcoupling}} \cdot 100\% \quad (14.2)$$

where

$n_{\text{electrons}}$  is the number of electrons injected into the device

$\eta_{\text{recombination}}$  is the fraction of electrons that recombine with holes—as opposed to becoming trapped or reaching the anode

$\eta_{\text{spin}}$  is the fraction of recombination events that yield an excited state of the appropriate spin for light emission

$\eta_{\text{internal}}$  is the quantum yield of photons of light per recombination event and depends on the competing radiative and nonradiative decay rates of the materials in the recombination zone

$\eta_{\text{outcoupling}}$  gives the fraction of emitted light photons that escape the device

Due to the statistics of spin recombination—25% singlet and 75% triplet states<sup>19–21</sup>— $\eta_{\text{spin}}$  is generally accepted to be 0.25 for fluorescent emitters and 1.0 for phosphorescent emitters. However, it has been shown recently<sup>22–24</sup> that the triplet states formed as the result of recombination can subsequently undergo a triplet–triplet annihilation (TTA) process that forms additional singlet states, thus boosting  $\eta_{\text{spin}}$  to as high as 0.40 for fluorescent materials.  $\eta_{\text{outcoupling}}$  is significantly less than 1.0 because many photons are lost to cavity modes, become trapped in the glass, are absorbed by various species in the device, or wasted through other pathways. It has long been assumed that  $\eta_{\text{outcoupling}}$  is ~0.20,<sup>25</sup> however, recent reports of EQE values of 30%<sup>26,27</sup> would imply a value of  $\eta_{\text{outcoupling}}$  no less than 0.30 in some OLED devices.  $\eta_{\text{outcoupling}}$  can be even higher when measures are taken to aid the outcoupling of the light from the device through microcavities or light extraction layers. Some EQE measurements also place the device inside an integrating sphere so that the light trapped and piped through the glass substrate can be captured.<sup>18</sup> All results in this chapter are given without  $\eta_{\text{outcoupling}}$  enhancements unless specified. Taking into account the historical assumptions for the values in Equation 14.2, EQE should be capped at 5% for fluorescent emitters and 20% for phosphorescent emitters. Using the higher values of 0.40 for  $\eta_{\text{spin}}$  and 0.30 for  $\eta_{\text{outcoupling}}$ , EQE should be capped at 12% for fluorescent emitters and 30% for phosphorescent emitters when no light extraction techniques are used. Literature reports of EQE values of about 10% for fluorescent green emitters<sup>28</sup> support these higher limits. Some caution must be applied when examining EQE values, however, as EQE is often calculated from a measurement of light emitted normal to the device, and then an assumption is made that the angular dependence of the emission is Lambertian. This assumption is not always true.<sup>18</sup> Finally, efficiency is also often given as

power efficacy, lumens per Watt (lm/W). This is typically calculated from the cd/A efficiency. Assuming Lambertian emission, Equation 14.3 gives the conversion between lm/W and cd/A.

$$\text{lm}/\text{W} = (\text{cd}/\text{A}) \cdot \pi / \text{voltage} \quad (14.3)$$

The luminance of an OLED device at a constant current density drops over time. This drop in luminance can be due to, among other reasons, chemical reactions that occur in the device, the deterioration of the interfaces between the metal electrodes and the organic layers, or changes in the film quality of the organic materials. The lifetime, or operational stability, of an OLED device is defined as the number of hours required for the luminance at a given current density to drop to half the luminance of the fresh device. Lifetime defined thusly is often abbreviated as  $T_{50@X}$ , where X gives the conditions under which the device was faded. Typical conditions are at the current density required to generate 1000 nits initial luminance or at a current density of  $80 \text{ mA/cm}^2$ . Lifetime is usually inversely exponential with current density, so doubling the current density often causes a drop of a factor of 3–4 in lifetime. High current densities can cause even stronger drops in lifetime due to internal heating of the devices.

The final performance metric, color, is typically given as 1931 CIE<sub>x,y</sub> values.<sup>29</sup> These values reduce an entire emission spectrum to two numbers that describe the emission color as perceived by the human eye. National Television Standards Committee (NTSC) specifications of CIE<sub>x,y</sub> are (0.67, 0.33) for red, (0.21, 0.71) for green, and (0.14, 0.08) for blue. There are actually many different shades of color referred to as white, but typical values for a white are around (0.33, 0.33). One common white point, D65, has CIE<sub>x,y</sub> values of (0.31, 0.33). Two more additional color metrics are color rendering index (CRI) and %NTSC color gamut. CRI is a measure of how well various colors are reproduced under a given white light compared to a reference white spectrum. If a white spectrum is missing or has very few photons of a particular color, that color will not be well reproduced under that white light. CRI > 80 is desirable for solid-state lighting applications. %NTSC color gamut is a metric defined for display devices with separate red, green, and blue pixels. For these devices, %NTSC color gamut is the area of the triangle formed by the red, green, and blue CIE<sub>x,y</sub> coordinates of the device divided by the area of the triangle formed by the NTSC standard values given above, expressed as a percent—having a color gamut equal to or greater than 100% NTSC is very desirable in a display.<sup>30</sup>

Several other performance metrics beyond the four described above are important when designing OLED devices. The rise in the drive voltage with age can cause the power consumption of a device to increase and the lifetime to decrease over time, and can even cause catastrophic device failure. Too much change in the color of the device with current is an issue

for both display and solid-state lighting. This is particularly a problem for solid-state lighting because the resulting color shift cannot be rectified in drive electronics, and lighting that changes color when dimmed or brightened is undesirable. For a display, changes in the OLED color with current can cause a change in the white balance of the display across its dynamic range, but these changes can potentially be compensated for with drive electronics. Of course, any color change with age of the device should also be kept within acceptable limits so the color balance of the display does not change, or is not noticeable, over time.

#### 14.2.2 Materials and Architectures

The organic electroluminescent unit placed between the anode and the cathode is generally comprised of an organic hole-transporting layer (HTL) and an organic electron-transporting layer (ETL). The structure of this device is shown in Figure 14.1a. The HTL assists in the injection of holes from the anode and provides hole transport toward the ETL, while the ETL assists in the injection of electrons from a metal cathode and electron transport toward the HTL. The holes and electrons recombine at the HTL|ETL interface. In order to increase efficiency and operational stability, improved layer structures such as the three-layer organic electroluminescent structure shown in Figure 14.1b have been disclosed. It contains an organic emission layer (EML) placed between the HTL and the ETL, designated HTL|EML|ETL.<sup>1,31</sup> The EML commonly includes at least one host material doped with an emitting material. To reduce voltage, the materials for the HTL, ETL, and EML are selected so that the energy barriers for charge injection from both transport layers into the EML are as small as possible. In order to further reduce voltage, and increase efficiency and operational stability, the architecture of the three-layer structure can become more complex through the addition of functional layers such as a hole-injection layer (HIL), an electron-injection layer (EIL), a hole-blocking layer (HBL), an electron-blocking layer, or an exciton-blocking layer (EBL). An example of such a device is shown in Figure 14.1c. The HIL can serve to improve the film formation property of subsequent organic layers and to facilitate the injection of holes into the HTL. The same is true for the metal cathode|ETL interface where introduction of an EIL helps to improve injection of electrons. The hole-, electron-, and exciton-blocking layers serve to confine these species to the EML for most efficient recombination and emission.

Introduction of a material into an OLED can affect the performance of the device in regions that are remote from the new material. For example, a new electron-injection material (EIM) can make electron injection from the cathode more facile, thus causing the electrons to drive further into the device. This can cause the recombination zone to move to a more (or less) favorable location. Alternatively, a highly efficient dopant might also be a charge trap or transporter, which can lead to an expansion or contraction of the

recombination zone with associated positive or negative consequences for operational stability. As a result, a material introduced to change one performance metric can also have (un)intended consequences on all of the other metrics. Therefore, when developing a new material, it is important to keep in mind not only the desired property of the new material, but also how all of the properties of the new material will interact with the properties of all of the other materials in the device.

Hole-transporting materials (HTM) have relatively low ionization potentials (IP).<sup>32</sup> The IP is defined as the energy required to remove an electron from the highest occupied molecular orbital (HOMO) of a substance. It can be measured, for instance, by photoelectron spectroscopy or obtained from electrochemical oxidation potentials in solution. It is also preferable that the HTM have sufficiently high hole drift mobilities. Various classes of materials have been used in the HTL, for example, starburst amorphous molecules,<sup>32</sup> spirocompounds,<sup>33</sup> triarylamines, and tetraarylbenzidines are representative classes of well-known HTMs. The structure of the most commonly used HTM, 4,4'-bis[N-(1-naphthyl)-N-phenylamino]biphenyl (NPB), is shown in Figure 14.2.

Electron-transporting materials (ETM) should have a suitable electron affinity (EA), defined as the negative of the energy released or absorbed by an atom or a molecule (X) upon attachment of an electron to form the negative ion ( $X^-$ ). EA can be measured, for example, by laser photoelectron spectroscopy, and correlates with the lowest unoccupied molecular orbital (LUMO) energy level. The LUMO levels can be estimated from potentials of reversible electrochemical reduction in solution or calculated from the HOMO energy and the optical band gap. ETM should also have high electron drift mobility to transport electrons. Commonly used ETM materials are metal-chelated oxinoid compounds, phenanthrolines, and anthracene derivates.<sup>1,17,34</sup> Examples of well-known compounds are tris(8-hydroxy-quinolinato)aluminum (Alq), 4,7-diphenyl-1,10-phenanthroline (Bphen), and 2-phenyl-9,10-di(2-naphthyl) anthracene (PADN).<sup>17</sup> However, devices with Bphen as the ETM usually exhibit poor operational stability. Recently, devices comprising novel phenanthroline derivatives in the ETL with improved lifetime have been reported.<sup>35</sup> Modification of the ETL to more complex architectures has shown many performance benefits. For example, mixtures of two-ETM in the ETL have

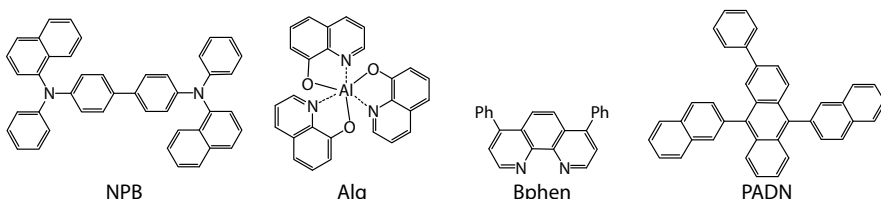


**FIGURE 14.2**

Common HTM and ETM used in OLEDs.

shown to give lower drive voltage and improved lifetime.<sup>36</sup> Also, splitting the ETL into multiple layers that have different LUMO levels was found to be beneficial for lowering the drive voltage, and increasing the lifetime and efficiency.<sup>37,38</sup>

Hole injection from the anode into the HTL depends upon the energy barrier at this interface. The higher the barrier, the larger the voltage required to induce injection. Therefore, in order to reduce the barrier (i.e., increase anode work function) and facilitate hole injection, for the typical anode material, indium tin oxide (ITO), various treatments of the surface are used, such as oxygen ( $O_2$ ) plasma treatment<sup>39</sup>; UV/ozone treatment<sup>40</sup>; treatment with polymerization of  $CHF_3$ <sup>41</sup>; and  $CF_4/O_2$  plasma treatment.<sup>42</sup> The surface of ITO can also be modified by deposition of a thin layer of various hole-injection materials (HIM), such as copper phthalocyanine (CuPc),<sup>3</sup> poly(3,4-ethylene dioxythiophene) (PEDOT),<sup>43</sup> organosilane ( $CH_3O)_3\text{-Si-C}_3H_7NH_2$ ,<sup>44</sup> and many others. Use of an HIM between ITO and the HTL allows for achieving significant improvements in device stability and efficiency.<sup>3,33,44</sup>

The IP of a HIM is generally lower (i.e., easier to oxidize) than the IP of an HTM. This stair-step architecture promotes facile hole injection from the ITO to the EML via the HIL and HTL layers. Importantly, in addition to voltage reduction, use of an HIL in OLED devices also decreases the rise of drive voltage during their operation at constant current density, perhaps by strengthening the interface between the metal electrode and the organic HTM. Therefore, development of HIMs is a subject of intense research.<sup>45–47</sup> At present, a different type of HIM with a high IP and extremely high EA is broadly used in OLED devices. This type of HIM is such a strong electron acceptor that holes and electrons are formed at the HIM|HTL interface even in the absence of an electric field. A common HIM of this type is dipyrrazino[2,3-f:2',3'-h]quinoxalinehexacarbonitrile (DQHC) and the structure is shown in Figure 14.3.<sup>45</sup>

Some known EIM are reactive low work function materials, such as LiF and  $LiO_2$ , that can modify reactive cathodes such as aluminum,<sup>48</sup> thus improving charge injection from the cathode into the ETL.<sup>49</sup> Kido et al. have used low work function metals such as Li and cesium doped into the ETL instead of using the thin layer of alkaline metal as a separate EIL.<sup>50</sup>

Instead of using injection layers, an alternative approach to achieving low voltage and high-efficiency devices is through the use of p-i-n technology.<sup>51–53</sup> Doping of a strong electron acceptor into a HTM (p-type doping) and a strong electron donor into an ETM (n-type doping) greatly increases conductivity in both transporting layers. As a result, electric field strengths in the charge-transporting layers are low, and voltage drops across even relatively thick layers are small. Birnstock et al. reported that at  $10^{-5}$  S/cm

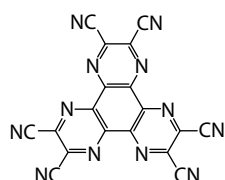


**FIGURE 14.3**  
Chemical structure of DQHC, a HIM.

conductivity of HTL and ETL, the voltage drop across a 100 nm thick layer is only 0.1 V at 100 mA/cm<sup>2</sup>.<sup>53</sup> This p-i-n technology makes it possible to achieve ohmic contacts between a doped charge-transport layer and an electrode regardless of existing energy barriers at the interfaces. Because charge carriers can tunnel from the electrodes through narrow space-charge regions into the transport layers, no injection-enhancing materials are necessary. Additionally, thin blocking layers of undoped HTM or ETM are usually inserted between the EML and the doped charge-transporting layers to confine excitons to the EML, to balance injection of charge carriers in the emission zone, and, in some cases, to prevent quenching of excitons by exciplexes possibly formed at interfaces. The electrical doping of charge-transport layers is also reported to improve device stability. The physics of molecular doping and its application to OLEDs and solar cells is reviewed in detail elsewhere.<sup>52</sup>

Host materials for the EML perform multiple duties and so have the most stringent requirements for molecular properties. A good host material will have a low barrier to injection and good transport of both holes and electrons. Low injection barriers to both charges will promote recombination throughout the bulk of the host material rather than at one or the other interface. Bulk recombination is preferable to interfacial recombination because interfacial recombination is more subject to efficiency quenching and material degradation by interactions with adjacent dissimilar materials. This low barrier requirement puts limits on both the HOMO and the LUMO of the host, limiting the choices of materials. In addition to low charge-injection barriers, host materials must not undergo any excited state chemistry because the host frequently is the A\* species in Equation 14.1. In addition, the host must not form an exciplex with the emitting dopant nor form an excimer with itself that quenches the dopant. The host should also have a slow nonradiative decay rate so as not to waste host-based A\* states before energy transfer to the dopant. Finally, the host must have a wider band gap than the dopant so that it does not quench the dopant emission. Because of all of the requirements on the host material, some architectures use multiple materials as mixed hosts in the EML in order to avoid one material having to satisfy both the HOMO and LUMO requirements—this will be discussed in Section 14.4. Typical host materials will be shown in Sections 14.3 and 14.4.

Initially, emitting dopants were all fluorescent materials, and fluorescent materials remain a major development focus to this day. Fluorescent materials emit light by relaxing from their lowest singlet excited state, S<sub>1</sub>, to their ground state—also a singlet—S<sub>0</sub>. S<sub>1</sub> on the dopant can be created when excitons formed on a host molecule during recombination transfer their energy to the dopant or by direct recombination on a charge-trapping or -transporting dopant molecule. Emission from an excited singlet state is spin-allowed and occurs with high quantum yield in many organic molecules. However, as mentioned above, 75% of excitons formed by hole–electron recombination

are triplets rather than singlets. Transition from any triplet state  $T_x$  to the ground state,  $S_0$ , is formally spin-forbidden and involves a nonradiative process in typical organic molecules. When it does occur, emission from a triplet state is referred to as phosphorescence and is discussed in more detail in Section 14.4.

Materials with high quantum yield of fluorescence are known across the entire visible spectrum, enabling the utilization of red, green, and blue colors for RGB display applications. In addition to high fluorescence quantum yield, several other characteristics are preferable in dopant molecules. For unfiltered displays using red, green, or blue emitters, a narrow emission band is useful to achieve the desired color and color gamut. When the dopant emission is combined with a color filter, a narrow emission band is also useful for maintaining high efficiency, as less of the emission spectrum is filtered out. Naturally, for solid-state lighting the opposite is true—wide band emitters help improve the CRI of the lighting device. Dopants can also be used as charge traps or transporters in the EML. Using the dopant as the carrier for one type of charge removes a requirement for the host molecule, widening the available choices of host materials. Whether the dopant traps or transports charge depends mainly on the dopant concentration. Common fluorescent dopant molecules will be presented in more detail in Section 14.3.

All materials within an OLED structure should meet several basic physical and optical requirements. When traditional vapor deposition techniques are used to deposit thin films, all materials should be thermally stable for sublimation. Also, with the exception of dopants, and possibly injection materials used only in very thin layers, all OLED materials should form amorphous films that are morphologically and thermally stable. Finally, OLED materials present in large quantities—hosts and transport materials—should also have little or no absorption in the light emission region.

The performance characteristics of an OLED device, such as luminance efficiency, drive voltage, operational stability, and color are governed by the often subtle interplay of the host, dopant, blocking, transport, injection, and electrode material properties. Therefore, development of advanced materials is crucial for fabrication of high-performance OLEDs, and implementation of these materials in advanced architectures that take advantage of new material properties is equally critical.

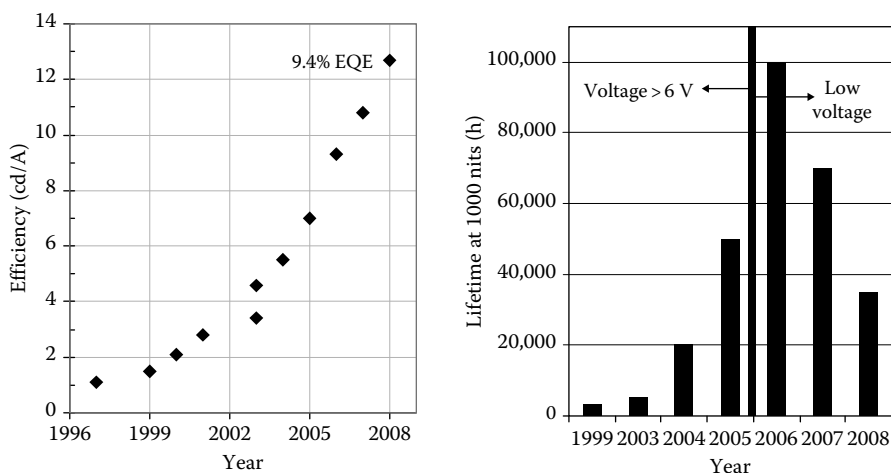
---

### 14.3 Current Status of Fluorescent Red, Green, Blue, and White OLED Devices

In the following sections, we will review the status of fluorescent OLED devices of red, green, blue, and white colors.

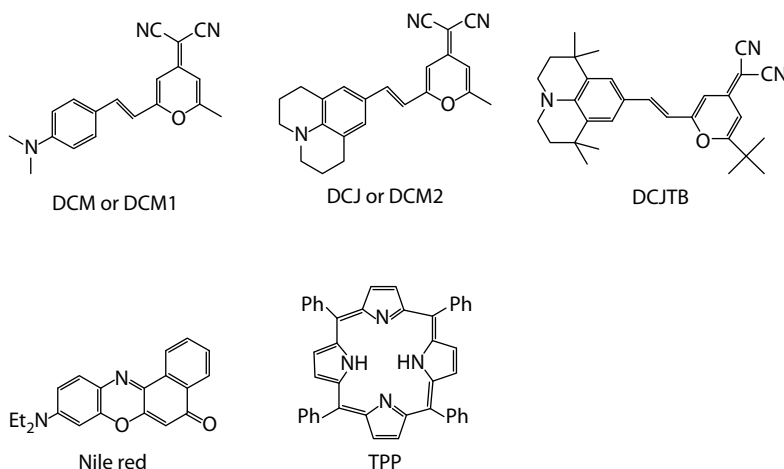
### 14.3.1 Performance of Red Fluorescent OLED Devices

Figure 14.4 shows the performance history of red fluorescent OLED devices developed at Eastman Kodak Company. From 1997 through 2005, the devices used DCJTB (Figure 14.5) as the emitting dopant and ALQ as the ETM. Increases in 2003 through 2005 came about through the use of a mixed host in the EML with one material serving as the hole-transporting moiety and the other serving as the electron-transporting moiety.<sup>54</sup> Because the



**FIGURE 14.4**

Red efficiency and lifetime improvement at Eastman Kodak Company as a function of year. Data at 20 mA/cm<sup>2</sup>.



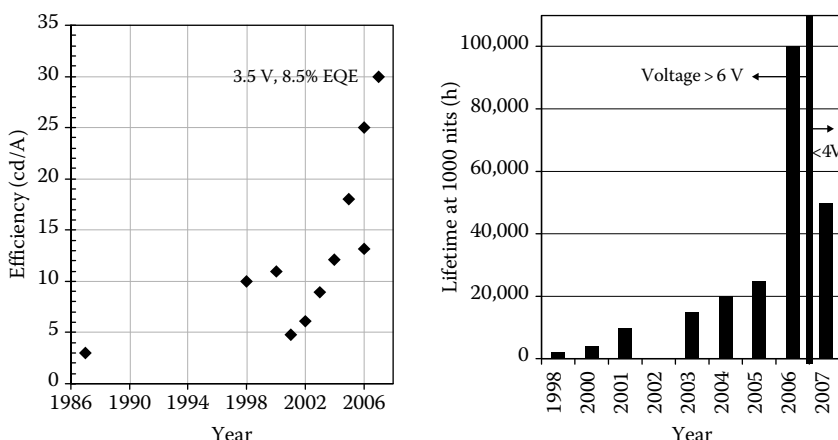
**FIGURE 14.5**

Structures of typical red fluorescent emitters.

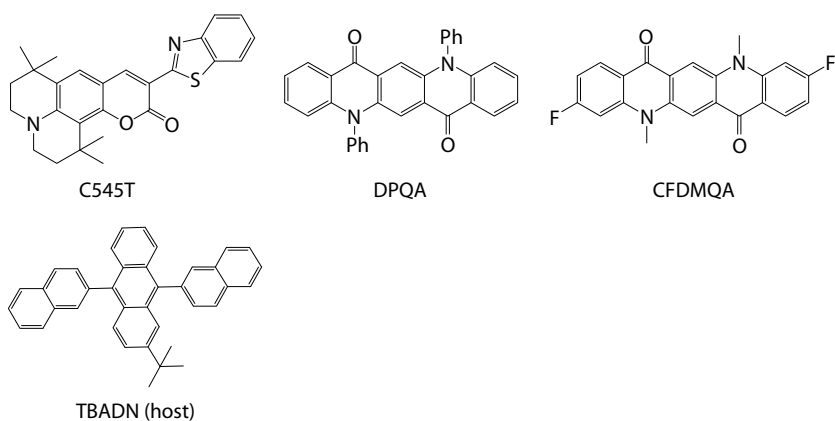
mixed-host system puts less restriction on the host materials, host materials could be chosen to have better spectral overlap with the dopant, allowing for better energy transfer from the host to the dopant.<sup>55,56</sup> This eventually doubled the efficiency from 3.4 to 7 cd/A. Additionally, the operational stability of the device was dramatically improved, with  $T_{50@1000\text{ nits}}$  improving from about 5,000 to about 50,000 h over that period of time.<sup>57</sup> This mixed-host concept was extended to a doping of polycyclic aromatic hydrocarbons into Alq or a 2-*t*-butyl-9,10-di(2-naphthyl)anthracene (TBADN)-type host to yield extremely long lifetimes for red and green devices.<sup>58</sup> Aziz et al. has also used a mixture of NPB and Alq in the light-emitting layer to increase device stability.<sup>59</sup> The use of mixed hosts in developing high efficiency and low voltage phosphorescent devices<sup>60</sup> will be discussed in Section 14.4. The improved stability that is due to the use of a mixture of materials in the hole-transport or emission layer has been ascribed to the expansion of the recombination zone. Beginning in 2006, device performances plotted in Figure 14.4 use a more highly efficient dopant, Kodak OLED material RD 3. Also in 2006, devices used an ETL consisting of a mixture of two materials that gave better overall performance than simple Alq.<sup>61</sup> These two advances combined to give a jump in efficiency from 7 to 9.3 cd/A and a reduction in voltage from over 7 to 4.5 V. In 2007, the use of a new EIM as well as a different combination of host and ETL materials increased the performance to 10.8 cd/A and decreased the voltage below 4 V at 20 mA/cm<sup>2</sup>. Finally, in 2008, a new material in the mixed EML host and new ETL materials increased the efficiency to 12.7 cd/A, or 9.4% EQE. In addition to the above results, Nishimura et al. have reported on a red-emitting (0.67, 0.33) system with 11.4 cd/A and  $T_{50@1000\text{ nits}}$  of 160,000 h.<sup>62</sup> Using their p-i-n structure, Birnstock et al. have demonstrated a low voltage fluorescent device with the following metrics at 1000 nits: 2.5 V, 10 cd/A, 8.5% EQE, CIE<sub>xy</sub> of (0.66, 0.34), and  $T_{50@500\text{ nits}}$  of 150,000 h.<sup>53</sup> In addition to increases in efficiencies and reductions in voltages, extrapolated values of  $T_{50@1000\text{ nits}}$  exceeding 1,000,000 h at lower efficiency for red OLED devices have also been reported.<sup>23,58,63</sup> Detailed reviews of fluorescent emitters are given elsewhere.<sup>64,65</sup>

### 14.3.2 Performance of Green Fluorescent OLED Devices

Figure 14.6 shows the performance history of green fluorescent OLED devices at Kodak. The first device published by Tang and Van Slyke had no emitting dopant and its luminance efficiency was below 2 cd/A.<sup>1</sup> C545T was the first commonly used green dopant. Figure 14.7 shows its structure along with other common green fluorescent materials. The efficiency of the green devices increased from the original 2 to 11 cd/A using C545T and a mixed host consisting of Alq and TBADN in 2000. In 2001, a new class of emitters, quinacridones, was introduced that offered substantially improved lifetimes. The increased lifetime came at a trade-off, however: the efficiency was lower than that of the C545T devices. In 2004, reformulation of the C545T

**FIGURE 14.6**

Green color efficiency and lifetime improvement at Kodak as a function of year. Data at 20 mA/cm<sup>2</sup>.

**FIGURE 14.7**

Structures of green fluorescent emitters and hosts.

devices with a new mixed-host material gave not only a slight increase in efficiency to 12.2 cd/A, but a factor of 4 increase in device lifetime. In 2005, the use of an improved HIM led to a 50% increase in efficiency to 18 cd/A. Introduction of the highly efficient EK-GD403 dopant in 2006 increased the efficiency to 25.4 cd/A and  $T_{50@1000 \text{ nits}}$  to 100,000 h. In 2007 changing the ETL and the EIL to new materials increased the efficiency again to 30 cd/A (8.5% EQE) and reduced the voltage from 7 to 3.7 V. The improved efficiency and voltage came at some cost to lifetime, which decreased to 50,000 h. Because this lifetime is considered sufficient for any display or lighting application,

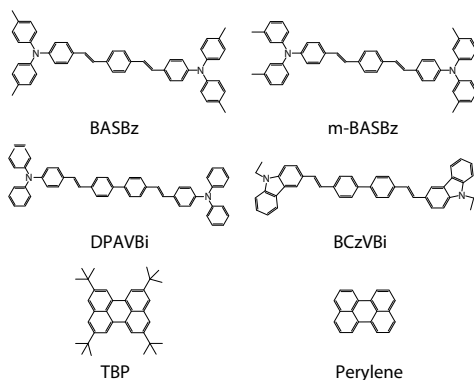
**TABLE 14.1**Fluorescent Device Performance Measured at 1000 cd/m<sup>2</sup>

Device Color	Drive Voltage (V)	Color (CIE <sub>x,y</sub> )	Efficiency (cd/A)	EQE (%)	$T_{50}$ (h)	Refs.
Red	4.2	0.66, 0.34	11.4	9.1	>100,000	36
Red	4.3	0.67, 0.33	11.4	9.0	160,000	66
Green	3.7	0.25, 0.65	30.0	8.5	50,000	71
Blue	3.4	0.14, 0.13	7.3	6.6	3,000	36
Blue	4.0	0.14, 0.18	11.0	8.1	5,000	80
White	3.7	0.31, 0.33	14.3	6.4	50,000	36
White	3.3	0.29, 0.33	16.0	7.0	20,000	37, 70
White	3.8	0.37, 0.43	19.5	8.4	70,000	62

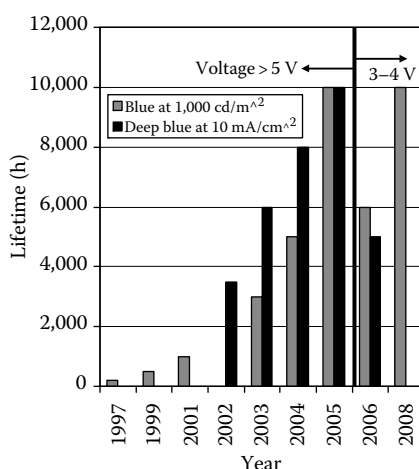
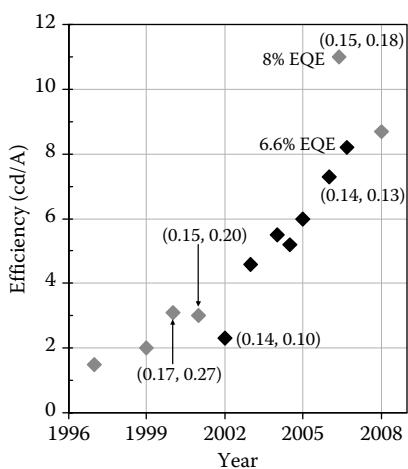
this trade-off is acceptable. Since 2005, Noh et al. has reported efficient green OLEDs with luminous yield of 34 cd/A, power efficacy of 34 lm/W, 3 V and CIE<sub>x,y</sub> color coordinates of (0.31, 0.64).<sup>45</sup> Yamada et al. has reported a solution-coated small-molecule green OLED device with 29 cd/A efficiency and  $T_{50@1000\text{ nits}}$  of 60,000 h.<sup>46</sup> Performance data for green OLEDs obtained at Kodak are shown in Table 14.1.

### 14.3.3 Performance of Blue Fluorescent OLED Devices

Recently, much effort has been directed toward the improvement of OLED blue emission color, efficiency, and lifetime.<sup>62,66,67</sup> The lifetime of a full-color OLED display is mainly determined by the lifetime of a color subpixel that has the shortest lifetime, and this subpixel is typically the blue subpixel. Blue color is also utilized to generate white light in combination with other colors for displays that use a combination of white light and color filters. While deep blue emissive dopants give RGB displays with the widest color gamut and suffer less luminance loss to color filters in white displays, they must be driven at higher current densities to achieve the same candela luminance levels as blue dopants that are shifted to longer wavelengths, and higher current densities lead to higher power consumption and shorter lifetimes. Thus, the choice of blue dopant typically leads to a trade-off between color, efficiency, and lifetime characteristics that affects the overall display performance. Because of this, improving the lifetime and luminance of blue OLEDs will have a large impact on display applications as well as on organic solid-state lighting applications. Some of the commonly used blue dopants are shown in Figure 14.8. Figure 14.9 shows the performance improvement of blue OLEDs at Kodak as a function of time. The first blue dopant was perylene, and blue OLEDs incorporating this dopant gave luminance efficiency of <2 cd/A with CIE<sub>x,y</sub> color coordinates of (0.16, 0.20). In 2000, Kodak introduced a blue dopant, BD 1, with efficiency ~3 cd/A.<sup>34</sup> In 2002, a deep blue dopant, Kodak OLED material BD 3, with excellent deep-blue

**FIGURE 14.8**

Structures of various blue fluorescent emitters.

**FIGURE 14.9**

Blue color efficiency and lifetime improvement at Kodak as a function of year. Numbers in parentheses are CIE<sub>x,y</sub> values. Black points have CIE<sub>y</sub> values below 0.17, grey points have CIE<sub>y</sub> points above 0.17. Data at 20 mA/cm<sup>2</sup>.

chromaticity ( $\text{CIE}_{x,y} = (0.15, 0.12)$ ) was introduced. The deeper blue color caused a drop in cd/A efficiency to 2.3 cd/A. Small changes in the chemical structure of the host material doubled the luminous yield to 4.6 cd/A in 2003 and then 5.2 cd/A in 2004. Also in 2004, an improved ETL material lowered the voltage from over 7 to 3 V. By 2006, improved ETL and EIL materials had increased the efficiency to 7.3 cd/A. In 2007, a change to the ETL material further increased the efficiency to 8.2 cd/A (6.6% EQE). Also in 2006, a

new blue dopant, EK9, was introduced.<sup>68</sup> This dopant is not as deep blue as material BD 3, CIE<sub>x,y</sub> are (0.14, 0.19), but the devices show higher efficiency (11 cd/A, 8% EQE) and also longer lifetime.<sup>68</sup> Several other novel dopants were invented that provide excellent chromaticity and efficiency. For deep blue dopants with CIE<sub>x,y</sub> values below (0.17, 0.17), Nishimura et al. have reported a device with 6.5 cd/A, 5.8% EQE, CIE<sub>x,y</sub> (0.14, 0.13), and  $T_{50@1000\text{ nits}}$  of 11,000 h.<sup>62</sup> Novaled AG has also demonstrated a deep blue device with characteristics of 3.5 V, 6.1 cd/A, 5.0% EQE, CIE<sub>x,y</sub> (0.14, 0.15), and  $T_{50@500\text{ nits}}$  of 10,000 h.<sup>69</sup> For light blue dopants with CIE<sub>y</sub> values > 0.17, Nishimura et al. have reported 8.4 cd/A, CIE<sub>x,y</sub> (0.13, 0.21), and  $T_{50@1000\text{ nits}}$  of 50,000 h.<sup>62</sup> Kondakov has also shown a sky blue (cyan) dopant with 3.7 V, 15.9 cd/A, 9.1% EQE, and CIE<sub>x,y</sub> (0.15, 0.26).<sup>24</sup>

Table 14.1 lists the data for best-performing red, green, blue, and white devices developed at Kodak. The reference is given for each of the devices. From the above discussion, it should be clear that voltage, efficiency, and lifetime improvements that led to the results in Table 14.1 came from modifications to most of the layers within the device, from the HIL, to the EML host(s) and dopants, ETL, and EIL. Improvements came in the form of both changes in architecture and new high-performance materials. This highlights the very cooperative nature of materials in OLED devices—the various materials in an OLED device should not be thought of as individual entities that can be replaced independently of each other but, instead, as entire systems that should be co-optimized together.

#### 14.3.4 Displays Based on Patterned Red, Green, and Blue Emitters

Full-color passive- and AMOLED displays have been demonstrated using red-, green-, and blue-emitting pixels that are typically patterned by the use of shadow masking. The shadow-masking technique uses a very thin metal mask to define the appropriate deposition regions on the substrate so that different materials can be deposited for each color pixel. The use of individual monochrome emitters provides a high display power efficacy and good color gamut—about 80% NTSC<sub>x,y</sub> with the proper OLED emitters. However, shadow masking does have three significant drawbacks. First, having separate masking steps for each color pixel increases the process time and therefore the cost for each display unit. Second, high defect rates reduce manufacturing yield, again increasing unit manufacturing cost. These defects are created both by thermal expansion of the mask, causing misalignment with the pixel pattern, and by repeated mask contact with the substrate, causing physical damage to the OLED stack. Finally, the difficulty of depositing through very small apertures and the thermal and physical instability of large masks preclude the use of shadow-masking techniques for very small, high-resolution displays and for displays larger than about Gen 4 sized glass—about 730 mm × 920 mm. Nevertheless, the first full-color AMOLED-based on commercial product, the Kodak EasyShare LS633 zoom

digital camera, was fabricated using the shadow-masking technique. These displays (2.2" diagonal, QCIF format) were mass-produced on a Gen 1 line— $300 \times 400$  mm substrate glass—and yield issues were resolved by careful control of the shadow mask fabrication, shadow mask alignment, and other processes.<sup>72</sup> Another drawback of RGB pixilated displays unrelated to manufacturing technique is that the display color balance is difficult to maintain over time because the emitting materials are different for each color and degrade at different rates. These difficulties with shadow-mask patterning and RGB devices led to the investigation of alternative techniques such as a white emitter with color filters for making a full-color display.

#### **14.3.5 Architectures and Performance of White OLED Devices**

As stated earlier, recent interest in developing white OLEDs is due in part to the manufacturing advantage of fabricating AMOLED displays without the use of shadow masks. Arguably, the most important factor that will determine whether OLED displays are widely adopted is manufacturing unit cost. This prompted Kodak and Sanyo Electric to investigate white OLED emission with RGB color filters for the demonstration of a 14.7" full-color display in 2002.<sup>73–76</sup> In this format, the white emitter is applied over the entire display surface and the red, green, and blue emission results from the color filter array that is formed on the backplane prior to the OLED layer depositions. This format is suitable for the higher-generation substrate sizes required for large display manufacturing.

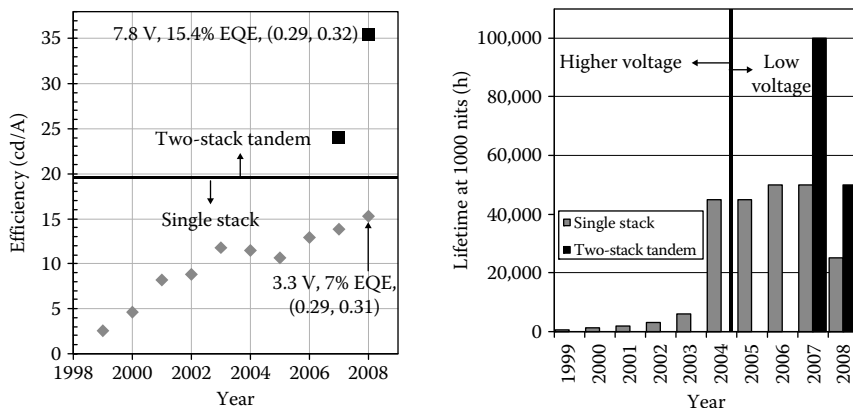
Over the following years significant progress has been made both in the architecture and the performance of the white OLEDs. Figure 14.10 shows a white structure that is similar to those used for producing monochrome colors such as red, green, or blue, except that it contains two light-emitting layers, yellow and blue. The details of this structure have been discussed in earlier publications.<sup>77,78</sup> White emission is obtained by adjusting the ratio of emissions from the adjacent blue- and yellow-emitting layers by varying layer thicknesses, or by using multiple cohosts and/or codopants in both the yellow and blue emissive layers. The yellow dopants are often rubrene derivatives while efficient blue dopants are used in the blue EML.

##### **14.3.5.1 Progress in Simple Two-EML-Layer Architecture of White OLEDs**

Figure 14.11 shows the progress at Kodak in performance of simple two-layer single-stack white structures based on fluorescent hosts and dopants incorporated into a two-emission layer yellow|blue (Y|B) configuration. The performance has continuously been improved, culminating in

Cathode:1000 Å(Al)
EIL:5 Å(LiF)
ETL:350 Å
Blue EML:200 Å
Yellow EML:200 Å
HTL:1200 Å
HIL:100 Å
Anode:600 Å(ITO)
Glass substrate

**FIGURE 14.10**  
White device architecture: (Y/B structure).

**FIGURE 14.11**

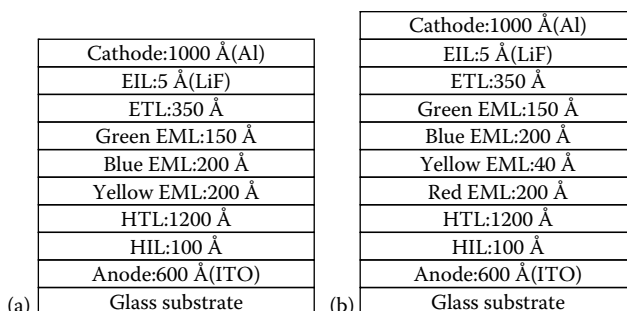
White color efficiency improvement at Kodak as a function of year. Data at 20 mA/cm<sup>2</sup>.

a low-voltage (<4 V), highly efficient (14 cd/A), and stable (~50,000 h lifetime) device, as discussed recently.<sup>76,77</sup>

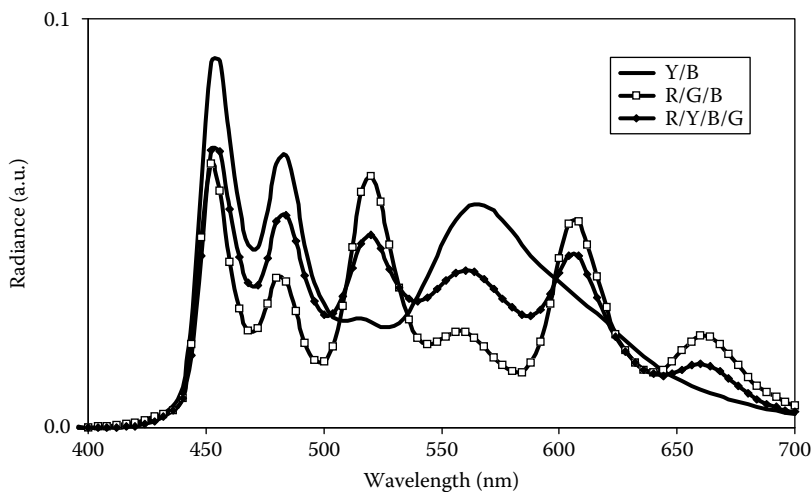
#### 14.3.5.2 Multilayer White Structures

The Y/B white structure described above has good efficiency and excellent operational stability but is deficient in green emission, however. To correct for this deficiency, a three-emitting-layer structure (R/B/G) was created by replacing or supplementing the yellow-emitting layer with red- and green-emitting layers.<sup>79</sup> Such structures are shown in Figure 14.12.

The emission spectra for these three white architectures are shown in Figure 14.13 (R/G/B). Use of this RGB architecture results in improved color gamut when the white OLED spectrum is transmitted through color filters, due to both the presence of a well-defined green emission band and the deep-red emission at 610 nm. Unfortunately, the efficiency was compromised

**FIGURE 14.12**

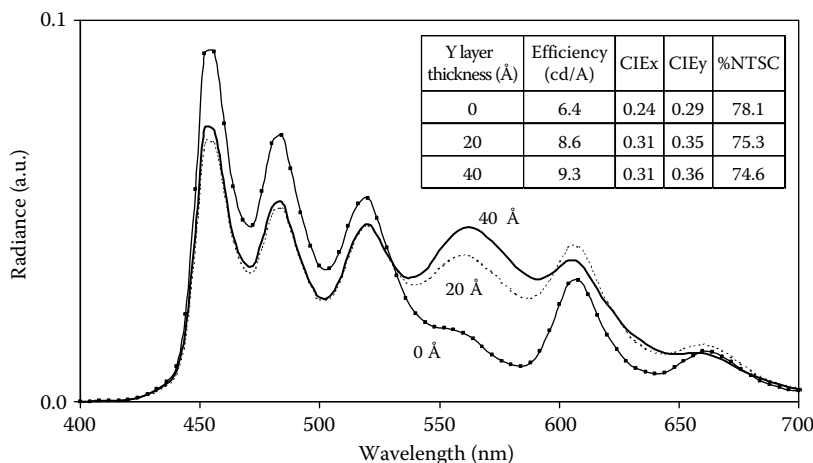
Multilayer white structures of OLED devices.

**FIGURE 14.13**

Electroluminescent spectra for two-layer (Y/B), three-layer (R/G/B), and four-layer (R/Y/B/G) white OLEDs. (Reproduced from Spindler, J.P. and Hatwar, T.K., *SID Int. Symp. Dig. Tech. Papers*, 38, 89, 2007. With permission.)

with this structure ( $7.2\text{cd}/\text{A}$ , compared to over  $10\text{cd}/\text{A}$  for the Y/B device). A significant efficiency improvement was achieved with the insertion of a yellow-emitting layer between the red- and blue-emitting layers. The spectrum for this device is shown in Figure 14.14 (R/Y/B/G), and the cross section is shown in Figure 14.12b. In this four-layer R/Y/B/G configuration, the efficiency was improved to  $9.3\text{cd}/\text{A}$ . As shown in Figure 14.14, the thickness of the yellow layer is critical for achieving higher efficiency and maintaining a high color gamut. It is generally thought that the emission from the various layers results from energy transfer from the blue excited states created during the charge recombination event. Understandably, the layer thicknesses are critical for maintaining the appropriate emission balance from the individual layers. For example, the optimum Y layer thickness is in the range of  $20\text{--}40\text{\AA}$ . Within this range, the efficiency is maximized while still maintaining adequate red and green emission peaks to ensure good color gamut. With a thicker Y layer, the color gamut is reduced for two reasons: first, the red dopant in the EML is not excited, resulting in a much lower red emission intensity; and second, the green color purity is reduced as more yellow emission is allowed to pass through the green color filter.

The white structures described above have excellent operational luminance, voltage stability, and color stability as the device ages during operation. With operation at a constant current, the extrapolated lifetime with an initial luminance of 1000 nits is approximately  $50,000\text{h}$ . Most recently, Nishimura et al. has shown operational stability of  $70,000\text{h}$  at 1000 nits and efficiency of  $19.6\text{cd}/\text{A}$ .<sup>62</sup> It is noteworthy that white OLEDs have higher

**FIGURE 14.14**

Effect of yellow layer thickness in the four-layer (R/Y/B/G) white OLED structure. (Reproduced from Spindler, J.P. and Hatwar, T.K., *SID Int. Symp. Dig. Tech. Papers*, 38, 89, 2007. With permission.)

stability than other component colors such as blue, yellow, or green, even though the layer architecture is the same for all of the devices of these component colors.<sup>73</sup> Although the blue layer is separately very unstable, the two-layer white OLED using the blue and yellow layers adjacent to each other provides a very stable device. As described earlier, white emission results from the mixing of blue and yellow emissions from adjacent layers, as a result of energy transfer from blue to yellow. This also creates an emission zone that is widely distributed in both the yellow and blue EML. The spreading of the emission zone is the most probable cause of improved stability and efficiency.<sup>72</sup> Also, because of the energy transfer from blue to yellow, both emitters decrease at the same rate and the ratio of blue to yellow emissions remains the same. This provides a stable color as a function of aging time.

#### **14.3.5.3 Obtaining a Stabilized Blue Using White Emission**

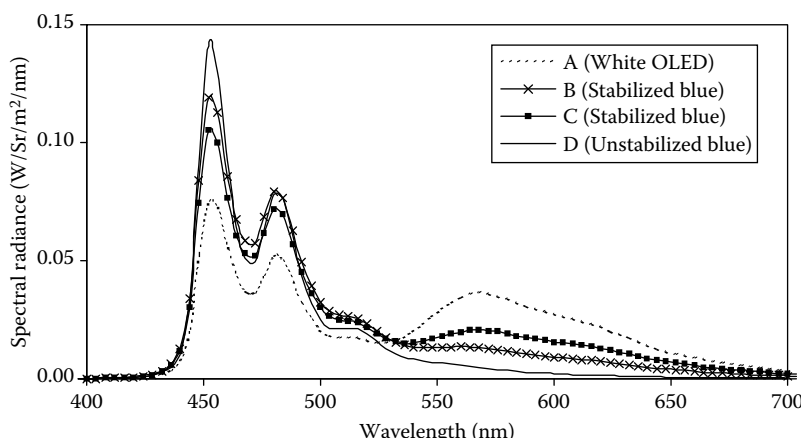
As was pointed out earlier, blue is often the weakest link in the white OLED structure and needs improvement both in efficiency and stability. A novel architecture has been developed to obtain a stable blue color by using a similar format to the high-stability white devices.<sup>78</sup> To this end, it was found that a stable blue emission could be obtained by using a “white” structure if the blue emission is decoupled from the yellow emission by the introduction of a thin, nonemitting buffer layer between these two layers. This non-emitting buffer layer consists of a HTM (such as NPB) and an ETM (such as EK-BH121). Figure 14.15 shows the stabilized blue device structure. The

thickness and composition of the buffer layer determine the transporting characteristics and thus the color, efficiency, and stability of the blue OLEDs. The typical thickness of the buffer layer was between 50 and 100 Å, and the composition of the NPB + EK-BH121 mixed layer can be varied between 25% and 75%. Figure 14.16 shows the spectra of devices with and without a buffer layer. The device without a buffer layer emits white with CIE<sub>x,y</sub> of (0.31, 0.31), whereas the resultant stabilized blue device with a buffer layers emits between CIE<sub>x,y</sub> of (0.19, 0.20) with efficiency 6.1 cd/A and CIE<sub>x,y</sub> of (0.23, 0.23) with 7.3 cd/A. For comparison, a blue OLED using BD 3, the same dopant that was used in the stabilized OLED, has 7.5 cd/A luminance efficiency and color CIE<sub>x,y</sub> of (0.15, 0.18).<sup>80</sup> Figure 14.17 shows the luminance efficiency as a function of current density for the three devices. Additional device characteristics are summarized in Table 14.2.

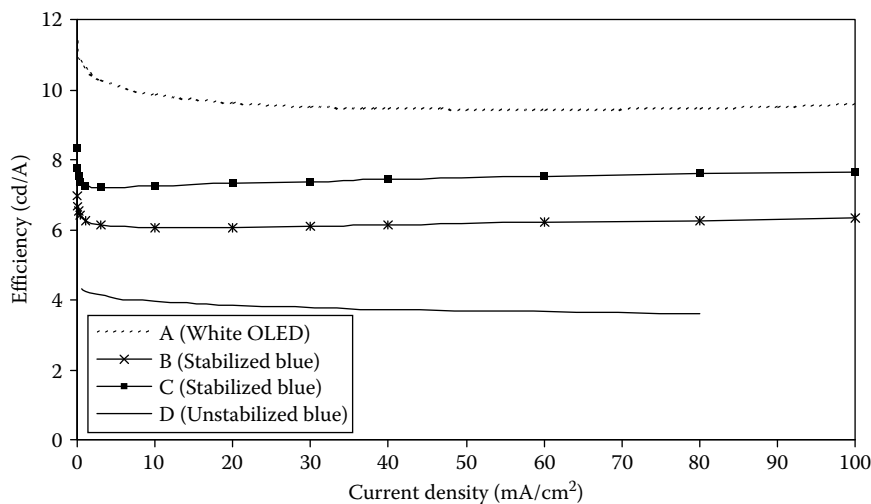
Cathode:1000 Å (Al)
ETL:300 Å (Alq + Bphen + Li)
Blue EML:300 Å (EK-BH12 + BD 3)
Buffer Layer:50–200 Å (NPB + EK-BH121)
Yellow EML:200 Å (NPB + EK121 + 2% YD3)
HTL:1100 Å (NPB)
HIL:100 Å (EK13)
Anode:600 Å (ITO)
Glass substrate

**FIGURE 14.15**

Device structure of the stabilized OLED.

**FIGURE 14.16**

Spectra for devices A–D in Table 14.2. (Reproduced from Hatwar, T.K. and Spindler, J.P. *SID Int. Symp. Dig. Tech. Papers*, 39, 814, 2008. With permission.)

**FIGURE 14.17**

Luminance efficiency as a function of current density for devices A–D in Table 14.2.

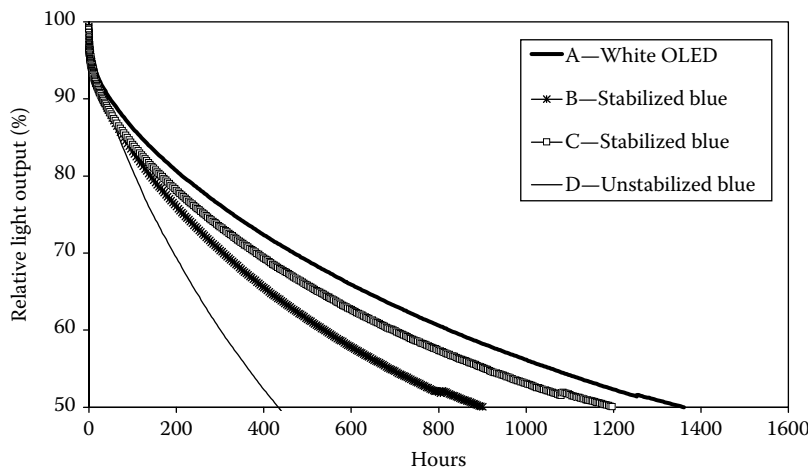
**TABLE 14.2**

Properties of Stabilized Blue Comparison Devices Measured at  $20 \text{ mA}/\text{cm}^2$

	Device A White	Device B Stabilized Blue	Device C Stabilized Blue	Device D Unstabilized Blue
EML structure <sup>a</sup>	Y   B	Y   buffer   B	Y   buffer   B	B
Buffer layer	NA	100 Å (NPB + 50% EK-BH121)	100 Å (NPB + 75% EK-BH121)	NA
Drive voltage (V)	5.9	5.7	5.9	4.5
Efficiency (cd/A)	9.6	6.1	7.3	3.8
EQE (%)	4.6	3.9	4.3	3.2
Color (CIE $x,y$ )	0.31, 0.31	0.19, 0.20	0.23, 0.23	0.15, 0.14
$T_{50} @ 80 \text{ mA}/\text{cm}^2$ (h)	1360	900	1200	400

<sup>a</sup> Device structure: Glass/ITO/HIL/HTL/EML/ETL/Al. Y, yellow EML, B, blue EML.

Although a high-purity blue color is difficult to achieve by this method, the stability improvement is nonetheless dramatic. Figure 14.18 shows the comparison of the operational stability of the white device A and the stabilized blue OLEDs B and C measured at  $80 \text{ mA}/\text{cm}^2$  constant current density. It is clear that the stabilized blue devices have very high half-life times, 900 and 1200 h, respectively; and in particular, the device C's lifetime is very comparable to the white OLED device D's lifetime of 1360 h. The device B and C lifetimes are significantly higher than the conventional blue OLED (~400 h) at the same operational current density.<sup>73</sup>

**FIGURE 14.18**

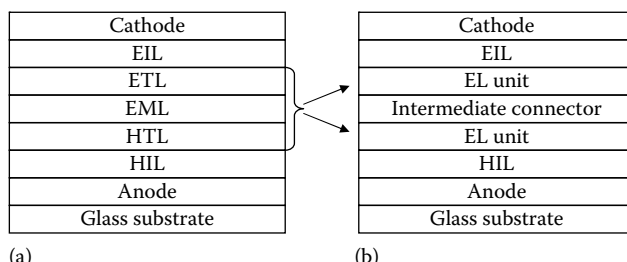
Lifetime at a current density of  $80\text{ mA/cm}^2$  for devices A–D in Table 14.2.

### 14.3.6 Tandem OLED Devices

#### 14.3.6.1 *Tandem Device Architecture*

Recently, a tandem (or stacked) OLED structure was developed in order to improve luminous efficiency and to increase lifetime. This was accomplished by vertically stacking several individual electroluminescent (EL) units, each of which comprise a HTL|EML|ETL, and driving the entire device with a single power source.<sup>13,14,81–84</sup> The schematic structure of the tandem device is shown in Figure 14.19.

In a stacked OLED having  $N$  EL units ( $N > 1$ ), the luminous efficiency ( $\text{cd/A}$ ) can be about  $N$  times as high as that of a conventional OLED containing only one EL unit (the drive voltage will also be about  $N$  times as high as that of the conventional OLED). Therefore, the stacked OLED needs only about  $1/N$

**FIGURE 14.19**

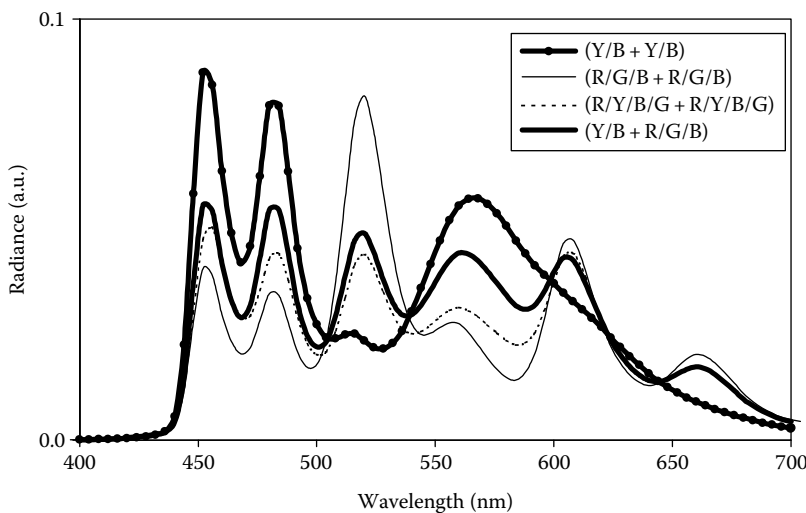
Comparison schematics of (a) single-stack conventional OLED and (b) two-stack tandem architectures.

the current density used in the conventional OLED to obtain the same luminance, resulting in an operational lifetime at least  $N$  times that of the conventional OLED. Alternatively, the tandem OLED can achieve a luminance  $N$  times higher than that of the conventional OLED (driven at the same current density) while maintaining about the same lifetime. In a tandem OLED, all of the EL units are electrically connected in series by inserting an intermediate connector (or connecting unit) between adjacent EL units. The intermediate connector plays an important role in tandem OLEDs. It can be formed using a metal/metal (or metal oxide) bilayer, organic/metal (or metal oxide) bilayer or organic/organic bilayers.<sup>85</sup> In particular, the use of organic/organic intermediate connectors that can be formed using thermal evaporation methods with relatively low evaporation temperatures were found to be the most beneficial. Tandem device structures have been demonstrated for red, green, blue, and white devices. For example, tandem blue OLEDs have achieved 20 cd/A ( $\text{CIE}_{x,y} = 0.14, 0.18$ ) and 38 cd/A ( $\text{CIE}_{x,y} = 0.15, 0.42$ ) with EQEs higher than 11%.<sup>81</sup> At an initial luminance of 1000 cd/m<sup>2</sup>, the drive voltage of the devices can be less than 6.5 V, and the operational lifetime ( $T_{50}$ ) of the devices is estimated to be greater than 10,000 h. Similar to the effect of injection and transport materials in a conventional OLED device, the selection of materials for the intermediate connector has a significant impact on the electroluminescence performance of the tandem OLEDs.

The tandem architecture has been found to be very useful for tuning the color of the white OLEDs for both display and lighting applications, where tandems of the same or different white-emitting units can be connected through a semiconducting p-n junction. In the following section, we will describe the white tandems for display applications developed at Eastman Kodak Company.

#### 14.3.6.2 White Tandem Devices

There are many ways in which tandem devices can be constructed to emit white light. Each stack in the tandem can emit a monochrome color such as red, yellow, green, or blue, so that the overall tandem emits white light. Alternatively, each stack of the tandem can emit white light. In this case, the stacks can contain similar layer structures and materials or different layer structures and materials. In the latter case, two different "shades" of white can be emitted to give the desired white for the overall tandem. And, of course, any strategy along the continuum between individual monochrome stacks and identical white stacks can be explored. We have investigated the various configurations in order to understand the trade-offs that exist between efficiency and color gamut. The spectra for the different tandem structures are shown in Figure 14.20. The highest efficiency combination is a two-stack Y/B structure, but this structure also has the poorest color gamut due to the lack of a green emission peak. It has been found that the best overall performance can be achieved by using configurations that provide a combination

**FIGURE 14.20**

Emission spectra of the white tandem devices with various EL units. (Reproduced from Spindler, J.P. and Hatwar, T.K., *SID Int. Symp. Dig. Tech. Papers*, 38, 89, 2007. With permission.)

of yellow emission along with green and red emission peaks, such as the two-stack, four-layer structure ( $R/Y/B/G + R/Y/B/G$ ) and the  $Y/B + R/G/B$  combination. In these configurations, the  $Y$  emission provides high efficiency, and the separate  $R$  and  $G$  layers provide high gamut. Additionally, in these structures the blue, green, and red emission peaks have been designed, through appropriate material selection as well as layer structure, to match the color filter optical characteristics. This results in an improved gamut relative to the repeat  $Y/B$  structure. Note that the yellow emission corresponds with the peak of the eye sensitivity and therefore contributes to a higher luminous efficiency white, which is very important for the  $W$  (unfiltered) subpixel in an RGBW display.

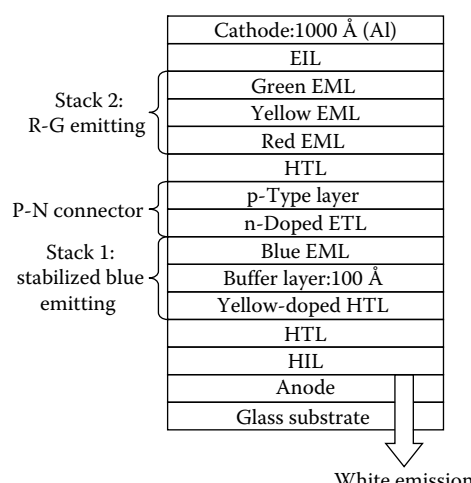
#### **14.3.6.3 High-Efficiency White Tandem Devices**

Although stability could be obtained by the tandem structures where each EL stack is white-emitting, it is difficult to obtain high efficiency. The primary reason for the low efficiency is the fact that it is nearly impossible to optimally position both of the identical emitting zones within the OLED structure with respect to the reflective cathode. Taking this into consideration, the following section describes the fabrication of an efficient and highly stable tandem white device.

A two-stack tandem white OLED was fabricated using the above-described stabilized blue-emitting unit (HTL|yellow EML|buffer layer|blue

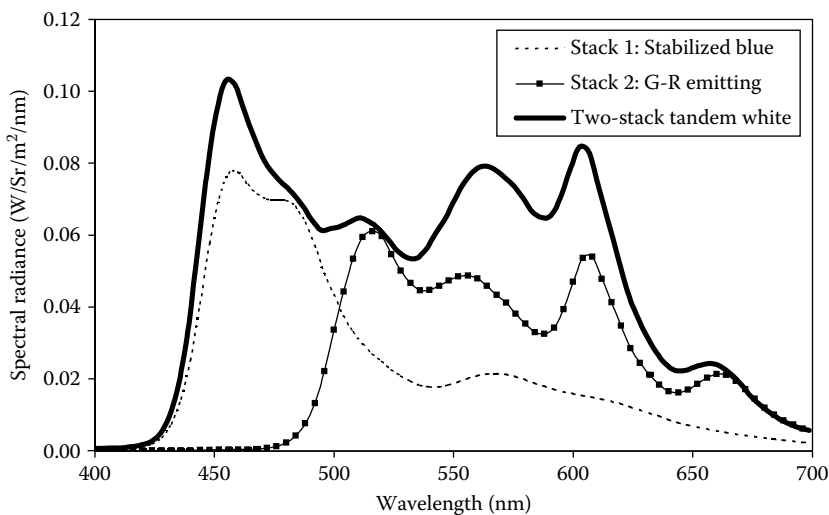
EML|ETL) for stack 1, and a G-R-emitting unit (HTL|red EML|yellow EML|green EML|ETL) for stack 2 with an optically transparent P-N connector.<sup>86,87</sup> The host/dopant combinations for each of the emitting layers were as follows: The red layer used NPB as host, EK-BH121 as a cohost, and Kodak OLED material RD 3 as dopant; the yellow layer used NPB as host, EK-BH121 as cohost, and Kodak OLED material YD 3 as dopant; in the green layer EK-BH109 is used as a host for EK-GD403 green dopant; and the blue layer used EK-BH121 as host and EK9 as dopant. Figure 14.21 shows the device architecture of this two-stack tandem, where one of the stacks is a stabilized blue-emitting EL unit and the other stack is an R/Y/G-emitting unit. Overall composite emission shows a pure white color near the target D65 white point. The spectra of the stabilized blue OLED, R/Y/G-emitting OLED, and two-stack tandem white OLEDs are shown in Figure 14.22. Figure 14.23 shows the luminance efficiency as a function of current density for the two-stack tandem and the individual stacks. The efficiency of the tandem is very close to a summation of the efficiencies of the two individual stacks; this efficiency was obtained by the proper optical tuning of the two individual stacks with respect to the cathode reflector. The performance of the individual stack and the two-stack tandem is summarized in Table 14.3.

The tandem structure demonstrates an operational stability of 1000 h, whereas the stabilized blue stack and the G-R-emitting stack have stabilities of 1300 and 1200 h, respectively, at 80 mA/cm<sup>2</sup>. The slightly lower stability of the tandem at the same current density is primarily due to the p-n connecting layer. The estimated lifetimes at 1000 cd/m<sup>2</sup> in Table 14.3 show that a high-efficiency tandem OLED with a very high operational

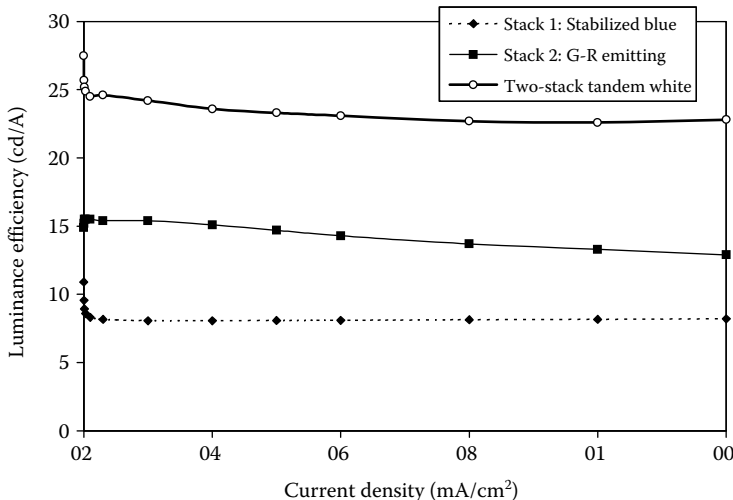


**FIGURE 14.21**

Schematic of two-stack tandem white OLED using stabilized blue in stack 1 and R-G emitters in stack 2.

**FIGURE 14.22**

Spectra of the individual stacks and the resulting white OLED. (Reproduced from Hatwar, T.K. and Spindler, J.P. *SID Int. Symp. Dig. Tech. Papers*, 39, 814, 2008. With permission.)

**FIGURE 14.23**

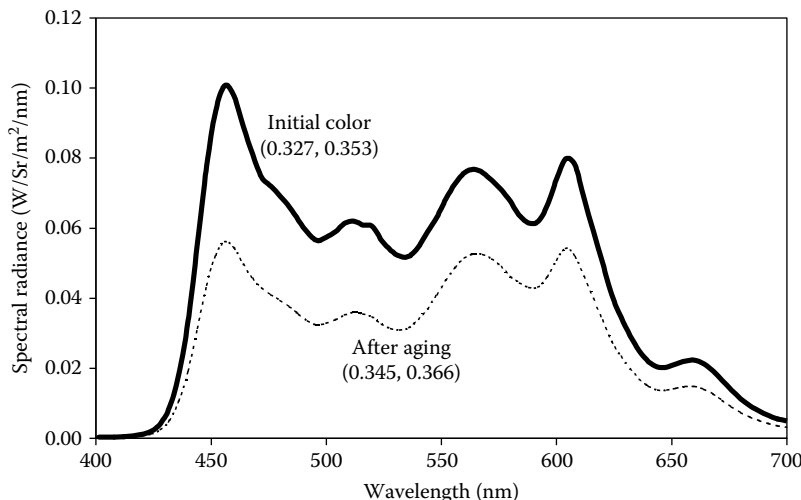
Luminance efficiency as a function of current density for stack 1, stack 2, and the two-stack tandem white.

stability is obtained by using the two different high-efficiency stacks of complementary colors.

Another important feature of the two-stack tandem is the high stability of the color as a function of current density and operational aging. Figure 14.24

**TABLE 14.3**Device Properties Measured at 20 mA/cm<sup>2</sup>

	Blue Emitting Stack 1	Green-Red Emitting Stack 2	White Emitting Two-Stack Tandem
Drive voltage (V)	4.0	5.4	9.3
Efficiency (cd/A)	8.1	15.1	23.6
EQE (%)	4.6	5.5	10.2
Color (CIE <sub>x,y</sub> )	0.23, 0.24	0.41, 0.54	0.33, 0.35
$T_{50@80\text{mA/cm}^2}$ (h) <sup>a</sup>	1,300	1,200	1,000
$T_{50@1000\text{nits}}$ (h) <sup>a,b</sup>	25,000	53,000	150,000

<sup>a</sup> Measured using DC drive.<sup>b</sup> Estimated by extrapolation from higher current density lifetime measurements.**FIGURE 14.24**

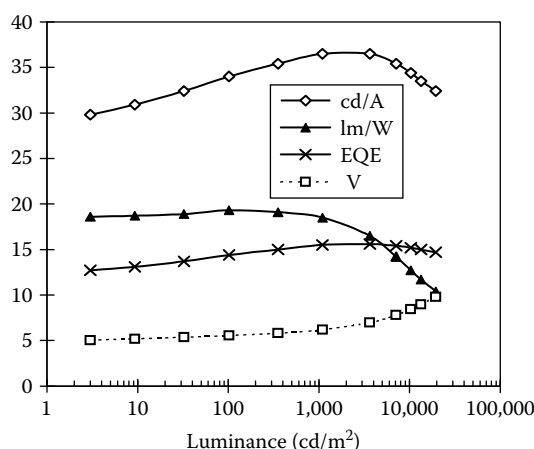
Effect of aging on the white spectrum. The device was operated continuously at 80 mA/cm<sup>2</sup> DC and 40°C. (Reproduced from Hatwar, T.K. and Spindler, J.P. *SID Int. Symp. Dig. Tech. Papers*, 39, 814, 2008. With permission.)

shows the white spectrum before and after operating a device at 40°C and 80 mA/cm<sup>2</sup> DC. The color is very stable over time, with a shift of about 0.02 CIE<sub>x,y</sub> at 50% initial luminance. Clearly, both the stacks of the tandem are very stable over the lifetime of the device, and differential aging of the tandem structure is not an issue of concern.

#### 14.3.6.4 High-Efficiency and High-Color-Temperature Tandem Whites

Although the luminance efficiency for the tandem device structure shown in Figure 14.21 was sufficiently high, the higher voltage resulted in lower

power efficacy ( $10.7\text{ lm/W}$ ). Also, the white point was near the  $6500\text{ K}$  color temperature. Currently available LCD and PDP TV displays typically have higher color temperature in the  $6,500\text{--}10,000\text{ K}$  range, which requires a significant amount of blue emission in the white spectrum. Although a display color temperature of  $10,000\text{ K}$  can be achieved using a white emitter with  $6500\text{ K}$  white color, the display's lifetime will be significantly reduced because the blue pixel will be required to be driven excessively. For this purpose, new materials and architectures were introduced to decrease the drive voltage and increase the efficiency of the two-stack tandem while obtaining a higher color temperature.<sup>87</sup> With the combination of a high-efficiency blue-emitting stack and a yellow-green-emitting stack, a pure white color with a color temperature of  $8500\text{ K}$  and  $\text{CIE}_{x,y}$  of  $(0.28, 0.33)$  was achieved. New ETM were used in both the n-type connector layer and the ETL, resulting in higher efficiency and lower voltage. EK-BH121 and EK-BH109 were used in the emission layers along with EK9 (blue), EK-GD403 (green), and Kodak OLED material YD3. Figure 14.25 shows the performance of the two-stack tandem white OLED device. At  $1000\text{ cd/m}^2$ , this device achieved very high luminance efficiency of  $36.5\text{ cd/A}$  at a low drive voltage of  $6.16\text{ V}$ , resulting in a high power efficacy of  $18.6\text{ lm/W}$ . This is remarkable for a stacked OLED with a cool white color, because the high proportion of blue in the emission spectrum reduces the  $\text{cd/A}$  and  $\text{lm/W}$  efficiency compared to a warmer white with the same overall EQE. The EQE for this cool white device was  $15.5\%$ . This is the highest power efficacy reported to date for a two-stack fluorescent tandem OLED with cool white color and without outcoupling enhancement.  $T_{50@1000\text{ nits}}$  of this device was  $\sim 50,000\text{ h}$ , somewhat lower than the tandem structures described in the previous sections. Figure 14.11 shows a comparison of white tandem versus single-stack OLED performance.

**FIGURE 14.25**

Performance of two-stack tandem white OLED.

### 14.3.7 White OLED Devices for Display Applications

The white tandem structures described previously can be used to prepare full-color displays. In fact, the Sanyo Xacti HD1 digital camcorder incorporated a 2.2" diagonal white-based RGBW OLED display. This commercialized product clearly demonstrated the viability of white OLED emission for a full color display. Kodak and other companies have also demonstrated full-color displays in sizes ranging from 8" to 40" using a-Si TFT backplanes.<sup>58</sup> In particular, Kodak demonstrated the manufacturability of full-color AMOLED prototypes with an a-Si backplane (14.1") using an in-line pilot manufacturing system equipped with advanced linear sources to deposit a tandem white structure. This prototype incorporating commercially available LCD color filters is shown in Figure 14.26a and features a color gamut of 76% NTSC<sub>x,y</sub>.<sup>86</sup> While a well-tuned white OLED spectrum can achieve good color gamut of 70%–80% with typical LCD TV color filters, it is difficult to increase the color gamut further without improving the OLED emission spectrum due to the fairly broad nature of commercially available LCD color filters. To this end, a set of narrow band color filters was developed that achieve greater than 100% NTSC ratio when combined with the tandem white OLED emission.<sup>79</sup> The tandem architecture and the narrow band color filters were incorporated into a prototype AMOLED display on an LTPS Si substrate and was demonstrated at the SID2008 exhibition. Figure 14.26b shows a prototype picture frame with this AMOLED display. This display demonstrates the effectiveness of tandem, unpatterned white RGBW OLED technology with color filters for the fabrication of full-color AMOLED displays.

### 14.3.8 White OLED Devices for Lighting Applications

With the recent advances in performance, white OLEDs are being considered for lighting applications.<sup>88–90</sup> For lighting, high efficiency and stable

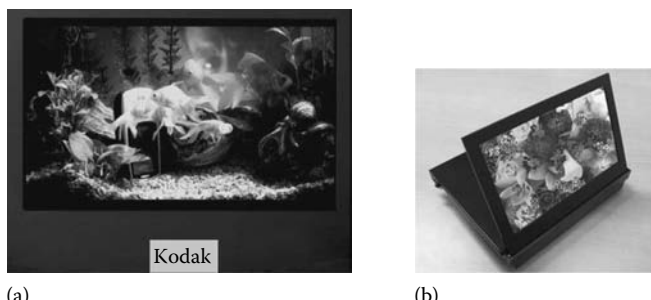


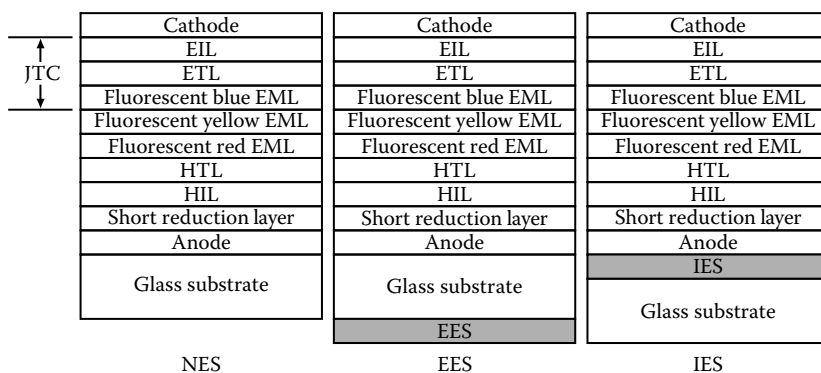
**FIGURE 14.26**

Display prototypes fabricated using white tandem technology: (a) 14.1" display using a-Si backplane and commercial LCD color filters; (b) 8" display using LTPS Si backplane and Kodak's narrow band color filters giving >100% color gamut.

single-stack white OLEDs have been reported based upon fluorescent, phosphorescent, and combinations of fluorescent and phosphorescent (hybrid) emitters. The fluorescent devices are typically more stable than phosphorescent devices; however, white phosphorescent structures have been demonstrated to be more efficient. In this section we will review fluorescent white for lighting applications.

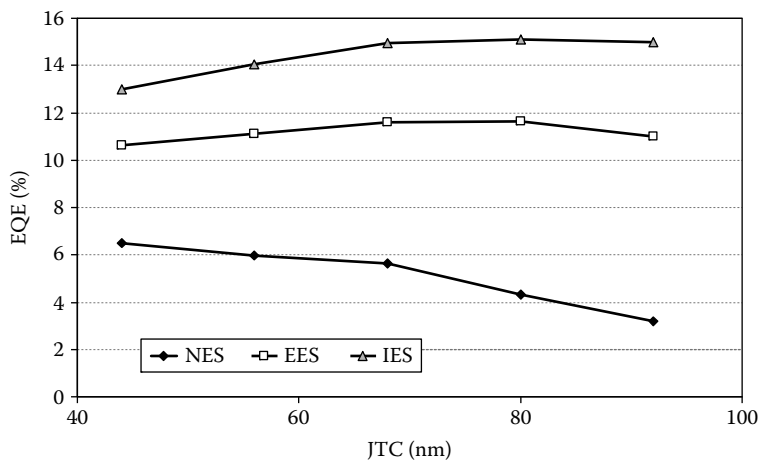
The key requirements for lighting are different than for display applications. For lighting, white OLEDs must have high power efficacy (>30lm/W at 1000 nits), long lifetime (50,000 h @ 1000 nits), and CRI>80.<sup>90</sup> One of the key opportunities for improving OLED device efficiency is to improve the light extraction efficiency. Because of the high refractive index (~1.8) of the emitting organic layers and the glass substrate (~1.5), most of the internally generated light is trapped within the device and only a small fraction (~20%–30%) exits. The internally generated light is distributed between several different modes and details of the emission loss and light-trapping mechanism have been described elsewhere.<sup>90</sup> The efficiency of the OLED devices can be greatly improved if the trapped light can be altered in direction to allow it to exit the structure, and there have been many reported methods to improve light extraction efficiency. These can essentially be divided into two types of structures: the external extraction structure (EES), where the extraction enhancement structure is coated on the free surface of the glass substrate and the internal extraction structure (IES), where an extraction enhancement structure is inserted between the substrate and the cathode, usually between the substrate and the anode. Both EES and IES were implemented with white OLEDs for lighting applications and the device architectures are shown in Figure 14.27.

It was found that the EQE of the above structures depends on the distance between the emission junction, i.e., the interface between the blue-emitting



**FIGURE 14.27**

Schematics of the device architectures, comparing devices with no extraction structure (NES), an EES, and an IES. (Reproduced from Tyan, Y.-S. et al., *SID Int. Symp. Dig. Tech. Papers*, 39, 933, 2008. With permission.)

**FIGURE 14.28**

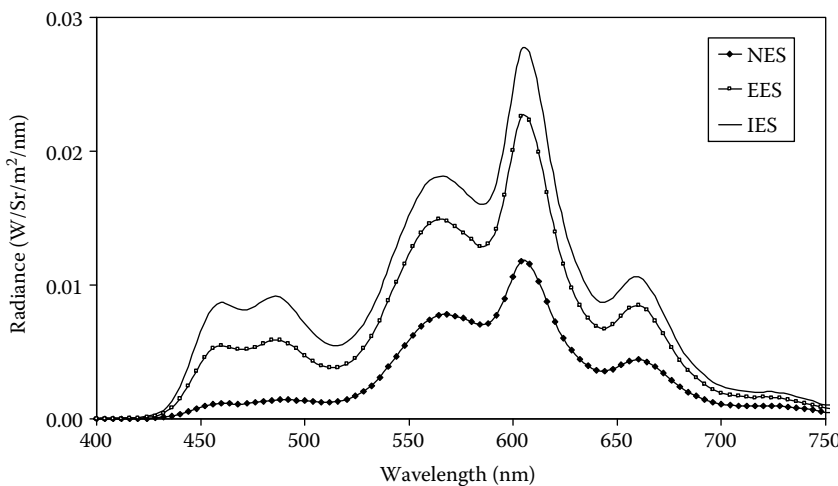
Dependence of EQE on JTC for the devices shown in Figure 14.27. Data acquired at a current density of  $3\text{ mA/cm}^2$ . (Reproduced from Tyan, Y.-S. et al., *SID Int. Symp. Dig. Tech. Papers*, 39, 933, 2008. With permission.)

layer and the yellow-emitting layer (where most of the excitons are generated), and the cathode. This is defined as the junction-to-cathode (JTC) distance. Figure 14.28 shows the measured EQEs as a function of JTC. Three curves, a, b, and c, shown in Figure 14.28, correspond to the three types of structures, NES, EES, and IES, respectively. The maximum EQE observed for the NES device was about 6.5% with a JTC of about 45 nm. The peak EQE observed for the EES device approached 11.7% at a JTC of 80 nm, and a further increase in EQE (15.1%) was realized with the IES device at 70–80 nm JTC. This remarkable 2.3X improvement in EQE results from extracting the light generated within the OLED structure that is otherwise lost to internal reflections. Table 14.4 lists the performance parameters of the best devices of each type. Figure 14.29 shows the spectra of the devices with 68 nm JTC in each series. It is clear that the EES and IES devices provide very high power efficacies at the luminance level that is required for lighting applications.

**TABLE 14.4**

Device Properties Measured at  $3\text{ mA/cm}^2$

	EQE (%)	Efficiency (cd/A)	Luminance (nits)	Color (CIE $x,y$ )	Drive Voltage (V)	Power Efficacy (lm/W)	EQE Enhancement Over NES
NES	6.5	16.5	495	0.44, 0.44	2.8	18.3	1
EES	11.7	26.8	804	0.46, 0.42	2.9	28.7	1.9
IES	15.1	33.4	1002	0.43, 0.40	3.1	33.8	2.3

**FIGURE 14.29**

Electroluminescent spectra of the devices shown in Figure 14.27, at  $3\text{ mA/cm}^2$  and at a JTC of 68 nm. (Reproduced from Tyan, Y.-S. et al., *SID Int. Symp. Dig. Tech. Papers*, 39, 933, 2008. With permission.)

## 14.4 Architectures and Materials for Phosphorescent OLED Devices

### 14.4.1 Brief Introduction to Emission Mechanism in Phosphorescent OLED Devices

Phosphorescent (i.e., triplet) organic light-emitting diodes have very high EQEs,<sup>15,16</sup> and have been a subject of intense research and development activity worldwide. The realization of required luminous and power efficiencies, as well as long operational lifetime, will enable phosphorescent OLED application in various displays for consumer electronics and as solid-state lighting sources.

As described in Section 14.2, the light-emitting layer consists of a host material and a dopant. The host material is usually responsible for charge transport, and the dopant is responsible for emission of light and may also play a role in charge transport. Phosphorescent OLED devices comprise triplet dopants, i.e., typically  $4\text{d}^6$  and  $5\text{d}^6$  transition metal complexes emitting from a triplet metal-to-ligand charge transfer (MLCT) state or a ligand-based  ${}^3(\pi-\pi^*)$  excited state mixed with an MLCT state.<sup>91,92</sup> The most efficient and commonly used phosphorescent emitters are cyclometalated iridium(III) complexes.<sup>93-95</sup> The Ir(III) compounds exhibit high photoluminescent quantum yields and short lifetimes of triplet excited states, which makes them particularly desirable for application as emissive dopants in OLED devices.

Changing the chemical structure of the cyclometalating ( $C^N$ ) ligand allows easy control of the color of phosphorescent emission. Efficient phosphorescent OLEDs with various Ir(III)-based dopants emitting in a wide range of colors from deep red to deep blue have been demonstrated and will be discussed in the following sections.

When voltage is applied to a phosphorescent OLED, electrons and holes injected from electrodes recombine in the EML, creating singlet and triplet excited states (excitons) in a ratio of 1:3 (see Section 14.2). The excited states can initially be formed on the host, in which case the phosphorescent dopants can harvest both triplet and singlet excitons by Dexter and Förster energy transfer mechanisms, respectively.<sup>20,96,97</sup> In addition to the energy transfer mechanism, the excitons can also be formed directly on a triplet emitter molecule as a result of charge carrier trapping followed by recombination with an oppositely charged charge carrier.<sup>98</sup> It is believed that phosphorescent OLEDs operating by the charge-trapping mechanism are more efficient relative to devices with the energy transfer mechanism because energy transfer from the host to the dopant may not be 100% efficient, therefore reducing the luminous yield.<sup>98</sup> In contrast with fluorescent dopants that can only emit from singlet excited states (Section 14.2.1), a phosphorescent molecule with large spin-orbit coupling not only can emit using triplet excitons, but can also efficiently emit using singlet excitons formed during recombination by converting the singlet excitons to triplet excitons via intersystem crossing. Thus, the phosphorescent emitters can theoretically capture four times more excited states than fluorescent dopants—yielding high-efficiency OLEDs.

The development of highly efficient triplet OLEDs requires a proper matching of the energy levels of the emitter and host materials. In a phosphorescent OLED, it is highly preferable that the lowest triplet state of the host be energetically above that of the dopant so that triplet excitons reside preferentially on the dopant. As the triplet energy ( $E_T$ )—the difference in energy between  $S_0$ , the ground state, and  $T_1$ , the lowest triplet state—of the dopant increases, it becomes progressively more difficult to find suitable stable hosts with even higher triplet energy levels. A suitable single-component (“neat”) host is a wide band gap material and typically presents a substantial barrier to the injection of holes, or electrons, or both. An analogous problem exists with fluorescent OLEDs, but it is much more severe for phosphorescent OLEDs. For typical molecules, the band gap—the difference between the HOMO and LUMO energies as determined by oxidation/reduction potentials, gas-phase IPs, and EAs or other methods—is larger or comparable to  $S_1$ , the lowest singlet excited state.  $S_1$  in turn is higher in energy than  $T_1$ . This means that a molecule with a given triplet energy will usually have a larger band gap than a molecule with an  $S_1$  state of the same given energy. Thus, complex architectures of EML(s) and material formulations for blocking and charge-transporting layers are required to construct devices with low energy barriers for charge injection into the light-emitting layer.

Much progress has been made in the development of phosphorescent OLED technology in recent years. The understanding of device physics and material properties as well as studies of degradation mechanisms in the devices lead to the design of novel architectures and the optimization of charge carrier balance. In the following sections we will focus on reviewing advanced architectures of bottom-emission phosphorescent OLED devices of all three colors. The performance of white phosphorescent OLEDs also will be discussed. We should note that for many triplet OLEDs performance metrics are often reported without the disclosure of device architectures or materials used. We will focus mainly on reviewing advanced architectures and performance parameters of phosphorescent OLEDs that are described in the open literature.

#### **14.4.2 Device Architectures and Performance of Monochromatic Phosphorescent OLED Devices**

##### **14.4.2.1 Architectures and Performance of Red Phosphorescent OLED Devices**

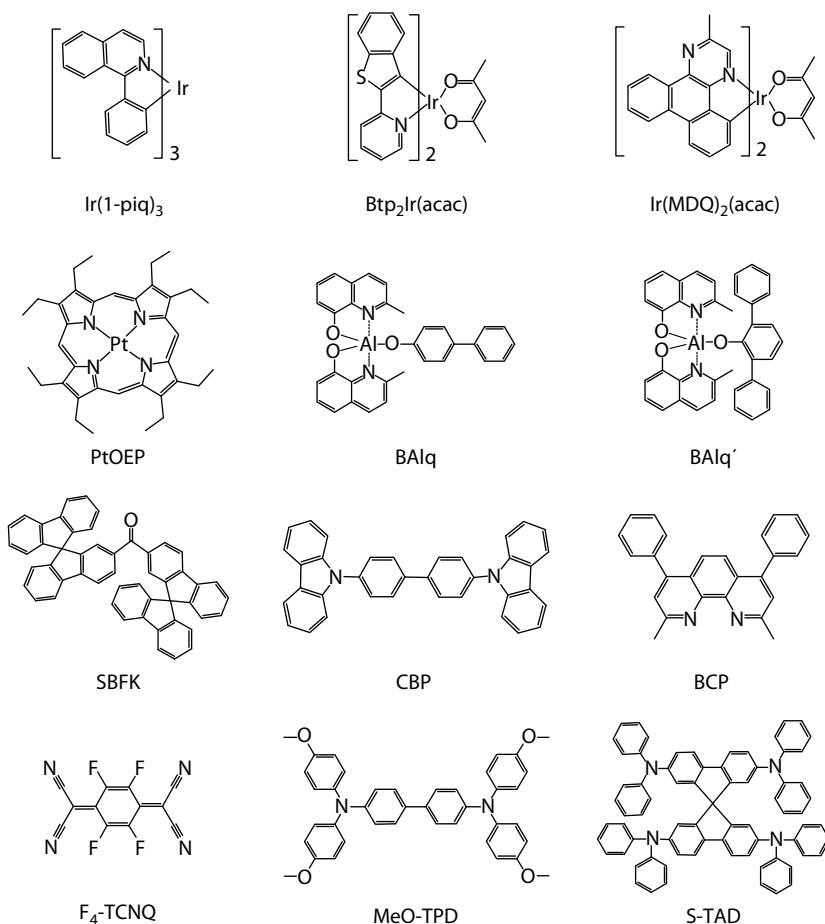
At the early stage of phosphorescent OLED development, red triplet devices often employed a conventional architecture—HTL, EML, and ETLs were placed between the electrodes. Additionally, a HBL was often inserted between the EML and the ETL. The general structure of a red phosphorescent OLED is shown in Figure 14.30. The device may also include a HIL and an exciton/electron-blocking layer (EBL) placed on the anode side of the EML. The effect of the blocking layers on device performance and criteria for material selection for the layers in triplet OLEDs will be discussed in Section 14.4.2.2. The structures of materials commonly used in red phosphorescent OLEDs are shown in Figure 14.31.

A red phosphorescent OLED containing 2,3,7,8,12,13,17,18-octaethyl-21H23H-phorphine platinum(II) (PtOEP) emitter doped into a 4,4'-*N,N'*-diphenyl-biphenyl (CBP) host and an HBL of 2,9-dimethyl-4,7-diphenyl-1,

Cathode:Al
EIL
ETL
HBL
Red emission layer
HTL
Anode:ITO
Glass substrate

**FIGURE 14.30**

Structure of the conventional red phosphorescent OLED with a single EML.

**FIGURE 14.31**

Chemical structures of materials used in red and orange phosphorescent OLEDs.

10-phenanthroline (BCP) was reported by O'Brien et al.<sup>99</sup> The OLED showed 2.2% EQE at 100 cd/m<sup>2</sup> (~0.01 mA/cm<sup>2</sup>). The low efficiency was attributed to the formation of long-lived triplet excited states (~50–80 μs) of the PtOEP participating in nonradiative decay processes.<sup>100</sup> The reduction of efficiency resulting from TTA was observed at high currents.<sup>15,91,101</sup> Substitution of the PtOEP with tris-cyclometalated Ir complexes with much shorter phosphorescence lifetimes, such as, bis-(2-(2-benzo[4,5-a]thienyl)pyridinato-N,C<sup>3'</sup>) iridium(acetylacetone) (i.e., Btp<sub>2</sub>Ir(acac)) (~4 μs) improved device efficiency.<sup>100</sup> The observed EQE was 7% at 0.01 mA/cm<sup>2</sup>, and the device emitted orange-red light with CIEx,y color coordinates of (0.68, 0.32).

Steady progress in the development of high-performance red phosphorescent OLEDs has been made since then. Currently, one of the commonly used deep red phosphorescent emitters is *fac*-tris(1-phenyl-isoquinolinato-N,C<sup>2</sup>) iridium(III) ( $\text{Ir}(\text{1-piq})_3$ ).<sup>102,103</sup> In nitrogen-saturated toluene solution at room temperature, the material exhibits efficient red phosphorescence with an emission maximum of 620 nm, phosphorescent quantum yield ( $\Phi_{\text{PL}}$ ) of 26%,<sup>102</sup> and triplet excitons lifetime of  $2.8 \mu\text{s}$ . A larger value (54%) for  $\Phi_{\text{PL}}$  of  $\text{Ir}(\text{1-piq})_3$  was reported by Okada et al.<sup>104</sup> Tsuji et al. demonstrated efficient long-lived red phosphorescent OLEDs by doping  $\text{Btp}_2\text{Ir}(\text{acac})$  into bis(2-methyl-8-quinolinato)-4-(phenyl-phenolato)aluminum (BAIq).<sup>105</sup> The devices had the following layer structure: ITO (110 nm)|NPB(80 nm)|BAIq + 7 wt.%  $\text{Btp}_2\text{Ir}(\text{acac})$  (30 nm)|Alq (30 nm)|Li<sub>2</sub>O (0.5 nm)|Al (100 nm). Because BAIq is a well-known ETM with a relatively deep HOMO level (6.02 eV),<sup>106</sup> recombination in the devices is very likely to occur near the NPB|EML interface. Thus, an HBL is not required in the devices. At  $2.5 \text{ mA/cm}^2$ , the red triplet OLED shows  $179 \text{ cd/m}^2$ , 8.6% EQE, 6.5 V, and CIE<sub>x,y</sub> of (0.680, 0.319). The operational stability of the device with the BAIq host was 13,000 h at  $180 \text{ cd/m}^2$ , about four times longer compared to the lifetime of the red triplet devices with a carbazole host in the EML. The modification of ligand(s) of the BAIq and use of a different, more advanced red emitter provided by Universal Display Corporation made it possible to improve device efficiency further, to 12% EQE, with only a slight change of CIE coordinates.<sup>105</sup> Most importantly, use of the improved red emitter led to a significant increase of operational lifetime—the red phosphorescent OLEDs showed 30,000 h measured at an initial luminance of  $700 \text{ cd/m}^2$ .

The p-i-n technology allows one to develop OLED devices with low drive voltage, high efficiency, and excellent operational stability. A brief description of the technology is given in Section 14.2.2. Extremely stable efficient red triplet OLEDs with electrically doped transport layers have been reported by Meerheim et al.<sup>107</sup> The devices had the following layer structure: ITO (90 nm)|MeO-TPD + 4% F<sub>4</sub>-TCNQ (75 nm)|NPB (10 nm)|NPB + 20 wt.%  $\text{Ir}(\text{1-piq})_3$  (20 nm)|Bphen (10 nm)|Bphen + Cs (45 nm)|Al (100 nm), where MeO-TPD is *N,N,N',N'*-tetrakis(4-methoxyphenyl)-benzidine, and F<sub>4</sub>-TCNQ is 2,3,5,6-tetrafluoro-7,7,8,8-tetracyanoquinodimethane. This five-layer device architecture is a representative example of a p-i-n OLED (Figure 14.32).

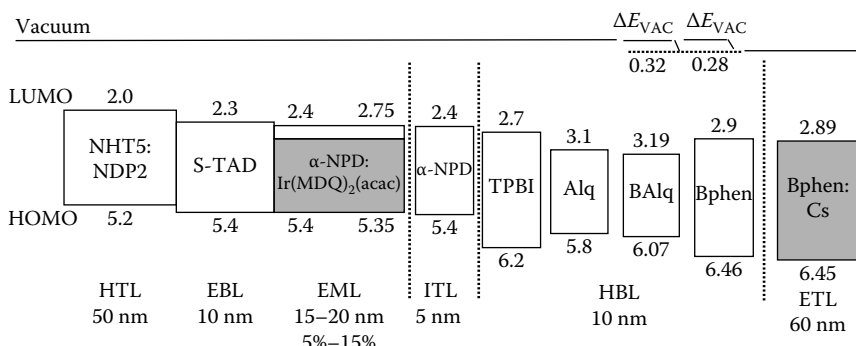
Cathode:Al
n-Doped ETL
HBL ETL
Red emission layer
EBL
p-Doped HTL
Anode:ITO
Glass substrate

**FIGURE 14.32**

Schematic structure of p-i-n red phosphorescent OLED with electrically doped charge-transporting layers.

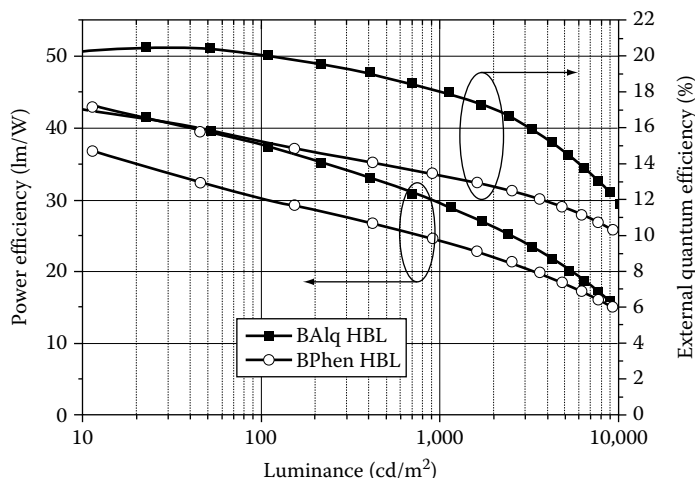
At  $100\text{ cd/m}^2$ , the device shows 8.8% EQE at 3.2 V with chromaticity coordinates of (0.68, 0.32). When the p-doped layer of (MeO-TPD + 4%  $\text{F}_4\text{-TCNQ}$ ) is substituted with an advanced p-type doped HTL such as Novaled AG OLED materials NHT-5+NDP-2, 12.4% EQE and 3 V were observed. The operational lifetime of devices with (MeO-TPD + 4%  $\text{F}_4\text{-TCNQ}$ ) HTL exceeds 11,000 h at  $500\text{ cd/m}^2$ . Replacement of Bphen with chemically stable BAQ in the HBL resulted in a remarkable 133X improvement of operational lifetime. The extrapolated lifetime for the red triplet OLED with BAQ in the HBL surpasses 1,000,000 h at  $500\text{ cd/m}^2$ .<sup>108</sup>

The effect of a hole-blocking material on electron injection and exciton distribution in the red phosphorescent OLEDs was investigated in detail by Meerheim et al.<sup>108,109</sup> In the study, Ir(piq)<sub>3</sub> was replaced with the efficient orange-red-emitting material bis(2-methyldibenzo-[f,h]quinoxaline)(acetylacetone)iridium(III) ( $\text{Ir}(\text{MDQ})_2(\text{acac})$ ),<sup>110</sup> which was doped into the NPB host in an amount of 10%. BAQ, Bphen, Alq, and 2,2',2''-(1,3,5-phenylene)tris[1-phenyl-1H-benzimidazole] (TPBI) were used in the HBL. An EBL of 2,2',7,7'-tetrakis-(N,N-diphenylamino)-9,9'-spirobifluorene (S-TAD) was inserted between the p-doped HTL and the EML. The device structure and energy levels of the materials used are shown in Figure 14.33. Device performances are summarized in Figure 14.34. As can be seen from the material's LUMO data, there are insignificant energy barriers for electron injection from the n-doped Bphen layer to BAQ or Alq HBLs. The device with BAQ in the HBL shows excellent performance metrics: 32 cd/A, 20% EQE, 2.4 V, 37.5 lm/W, and CIE<sub>x,y</sub> of (0.63,0.37) at  $100\text{ cd/m}^2$  (Figure 14.34). EQE is lower (15%) and drive voltage is slightly higher for the red devices with Bphen in the HBL. It is believed that when Bphen is used in the HBL the recombination zone is concentrated in a narrow zone near the EML|HBL interface. One of the possible explanations of reduced efficiency observed



**FIGURE 14.33**

Energy levels and layer structures of the red p-i-n OLEDs with various materials in the HBL and electrically doped transport layers. Indicator layer (ITL) was used as optional interlayer, which served only as sensor for exciton distribution. (From Meerheim, R. et al., *J. Appl. Phys.*, 104, 0145510, 2008. With permission.)

**FIGURE 14.34**

EQE and power efficacy as a function of luminance for red p-i-n OLEDs with different materials in the HBL. (From Meerheim, R. et al., *J. Appl. Phys.*, 104, 0145510, 2008. With permission.)

in the devices with HBL of Bphen may be a quenching of red emission by anion-radicals of Bphen.

The operational lifetime of 30,200 h at  $1000 \text{ cd}/\text{m}^2$  was reported for the devices with the BAHQ HBL while devices with Bphen and TPBI in HBL degraded almost 50 times faster. The improved operational stability of BAHQ devices was attributed to a number of factors: favorable charge carrier balance achieved with BAHQ, possible widening of the recombination zone due to electron transport by the red emitter, and chemical stability of BAHQ. Degradation mechanisms of Bphen and TPBI in the HBL were investigated, and several possible degradation pathways have been identified, such as interaction between Bphen and TPBI with emitter molecules and formation of stable, positively charged dimers of Bphen that can act as electron traps and exciton quenchers.<sup>111,112</sup>

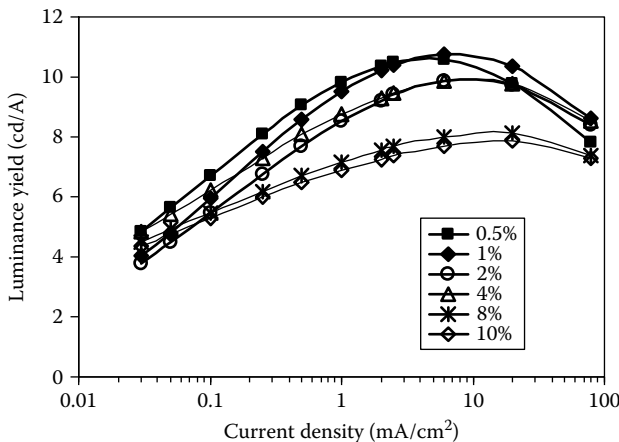
It is generally believed that OLED devices with a broad recombination zone occurring away from organic interfaces show higher luminous efficiency and longer lifetimes.<sup>113</sup> One reason may be the spatial separation of the excited states from charges trapped and prevention/reduction of triplet exciton-polaron quenching (TPQ) and TTA at the interfaces.<sup>23</sup> Extension of the recombination zone in phosphorescent OLEDs can be achieved, for example, by using a single bipolar transporting host material,<sup>102,114,115</sup> a mixture of electron- and hole-transporting compounds in the EML, or graded doped EML.<sup>116</sup> An alternative device concept is to use a phosphorescent dopant at sufficient concentration to transport electrons and/or holes and participate directly in the recombination process.<sup>117</sup> This mechanism will be discussed in Section 14.4.2.3. Mixed-host architecture has been used often in fluorescent

OLEDs to improve the efficiency, voltage, and operating lifetime,<sup>45,118,119</sup> but relatively few studies have been conducted on mixed-host phosphorescent OLEDs.<sup>106,120–123</sup> In the last several years our research was focused on developing high-efficiency triplet OLEDs of three primary colors using mixed-host materials in the EML.<sup>60,106,124,125</sup>

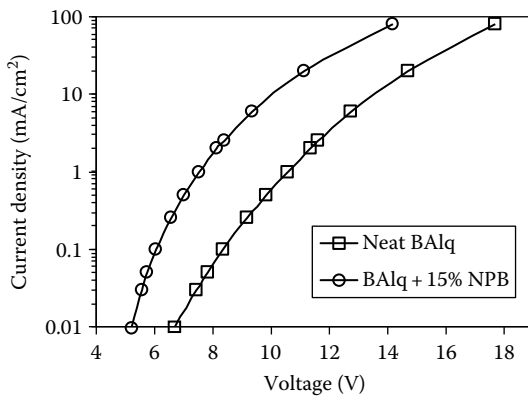
The properties of the host material generally determine device performance. Depending on the charge-transporting properties of the host, recombination can occur at the interface with the blocking layer or in the bulk of the EML. A bipolar host can promote bulk recombination, but can also lead to a situation where the recombination occurs at both the EML|HTL and EML|ETL interfaces, in particular, when the electric field and the mobility of charge carriers in the EML are high.<sup>126</sup>

A key requirement of the phosphorescent host-dopant combination is that the lowest triplet state of the host should be energetically above that of the dopant, so that triplet excitons of the dopant are not quenched by the host. High-energy dopants require even higher energy hosts. A high triplet energy material very often has a large band gap, i.e., a deep HOMO and/or shallow LUMO level. The result is typically a large barrier to charge injection into the emitting layer and a tendency to unipolar conduction and/or a high drive voltage. As was mentioned before, a phosphorescent emitter can be used in high concentrations to allow for charge transport and direct formation of excitons on the dopant, eliminating electrical excitation of the wide band-gap host.<sup>117</sup> However, this approach might result in lower efficiency because of concentration quenching<sup>127,128</sup> and not solve the high voltage problem. In a mixed host, however, the large host band gap issue is mitigated, because the overall HOMO and LUMO belong to different materials. Thus, each material may have a high triplet energy, while the HOMO and the LUMO of the mixture can be favorable for charge injection. As a result, triplet devices with mixed host show very high luminous efficiency and reduced drive voltage. For example, we have demonstrated efficient red phosphorescent OLEDs with EML consisting of a mixture of BAQ as electron-transporting and NPB as hole-transporting cohosts for Ir(1-piq)<sub>3</sub>, and compared their performance to that of red devices with a neat BAQ host material.<sup>106,124</sup> The mixed-host device structure was ITO (25 nm)|CFx (1 nm)|NPB (115 nm)|BAQ + 15% NPB + x% Ir(1-piq)<sub>3</sub> (35 nm)|BAQ (10 nm)|Alq (40 nm)|Mg:Ag (200 nm). While observed luminous yields (9–11 cd/A) were very similar for both neat and mixed-host red phosphorescent OLEDs, the use of the mixed host significantly reduced the drive voltage, resulting in an advantage in power efficiency (Figures 14.35 and 14.36). Codoping of the hole-transporting NPB into a BAQ host clearly increases hole current in the EML, reducing voltage. Ir(1-piq)<sub>3</sub> contributes to hole transport also: holes hop between the emitter molecules. The best performance characteristics in the red phosphorescent OLEDs were observed when the EML consisted of 81% BAQ, 15% NPB, and 4% Ir(1-piq)<sub>3</sub>.

Use of a derivative of BAQ with modified ancillary ligand (BAQ') in place of "regular" BAQ was found to improve the luminous efficiency in the red

**FIGURE 14.35**

Dependence of luminance yield upon current density for varied  $\text{Ir}(1\text{-piq})_3$  concentration in devices having the structure ITO (25 nm)|CFx (1 nm)|NPB (115 nm)|BAIq + 15% NPB +  $x\%$   $\text{Ir}(1\text{-piq})_3$  (35 nm)|BAIq (10 nm)|Alq (40 nm)|Mg:Ag (200 nm). (Reprinted from Deaton, J.C. et al., *Inorg. Chim. Acta*, 361, 1020, 2008. With permission.)

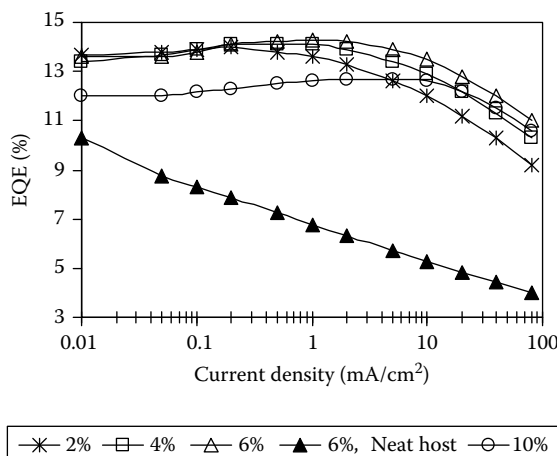
**FIGURE 14.36**

Current density as a function of voltage for devices with neat and mixed EML. Organic layers: NPB (115 nm)|host(s) + 4%  $\text{Ir}(1\text{-piq})_3$  (35 nm)|BAIq (10 nm)|Alq (40 nm). Anode and cathode are ITO|CFx and Mg:Ag. (Reprinted from Deaton, J.C. et al., *Inorg. Chim. Acta*, 361, 1020, 2008. With permission.)

devices. The structure of BAIq' is given in Figure 14.31. The red phosphorescent OLEDs containing 6% of the  $\text{Ir}(1\text{-piq})_3$  doped into a cohost mixture of BAIq' and 15% NPB with a LiF/Al cathode at 1  $\text{mA}/\text{cm}^2$  (6.6 V) showed 11.6  $\text{cd}/\text{A}$ , 13.3% EQE, and CIE<sub>xy</sub> of (0.667, 0.320). The mixed host red device has good operational stability. The  $T_{50}$  was estimated to be about 80,000 h at 500  $\text{cd}/\text{m}^2$ .

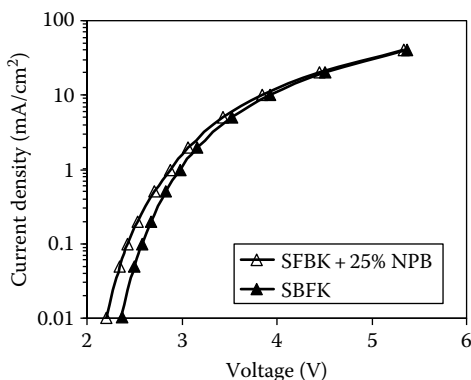
The selection of the mixed-host components can have a strong effect on device performance. We have substituted bis(9,9'-spirobifluorene-2-yl) ketone (SBFK) for BAQ as electron-transporting cohost in the mixed EML and in the blocking layer and fabricated red phosphorescent OLEDs with the following structure: ITO (25 nm)|CFx (1 nm)|DQHC (10 nm)|NPB (105 nm)|SBFK + 25% NPB +  $x\%$  Ir(1-piq)<sub>3</sub> (35 nm)|SBFK (10 nm)|ETL (40 nm)|LiF (0.5 nm)|Al (100 nm). A thin layer of DQHC was used as a HIL, and a bilayer of PADN (30 nm)|Bphen (10 nm) was used as ETL. Device performance is summarized in Figures 14.37 and 14.38.

All SBFK + NPB mixed-host devices are significantly more efficient than the neat-host control device. At 2 mA/cm<sup>2</sup> (230 cd/m<sup>2</sup>), the mixed-host device with 6% Ir(1-piq)<sub>3</sub> shows 14.2% EQE, 3.1 V, 11.6 cd/A, 11.7 lm/W, and a CIE<sub>x,y</sub> of (0.675, 0.324). The mixed-host devices exhibit very flat dependence of efficiency on current density, independent of dopant concentration and the EQE does not decrease below 11% in the luminance range of 1–2000 cd/m<sup>2</sup>. In contrast, the red phosphorescent OLED with a neat SBFK host reaches a maximum luminance yield at the lowest current density and then EQE decreases rapidly as current density increases (Figure 14.37). In comparison to BAQ + 15% NPB red triplet OLED where the drive voltage at 1 mA/cm<sup>2</sup> was about 3 V lower compared to the voltage of the neat BAQ host devices (Figure 14.36), the drive voltages of SBFK + NPB and neat SBFK devices are practically the same (Figure 14.38). At 100 cd/m<sup>2</sup> (~1 mA/cm<sup>2</sup>) the SBFK + NPB + 10% Ir(1-piq)<sub>3</sub> device has a drive voltage of 2.8 V, which is



**FIGURE 14.37**

EQE as a function of current density and concentration of the Ir(1-piq)<sub>3</sub> for red phosphorescent OLED with neat SBFK or mixed SBFK + NPB host. Device structure: ITO (25 nm)|CFx (1 nm)|DQHC (10 nm)|NPB (105 nm)|SBFK + 25% NPB +  $x\%$  Ir(1-piq)<sub>3</sub> (35 nm)|SBFK (10 nm)|PADN (30 nm)|Bphen (10 nm)|LiF (0.5 nm)|Al (100 nm). The EML of a neat-host device consists of SBFK + 6% Ir(1-piq)<sub>3</sub>.

**FIGURE 14.38**

Current density as a function of drive voltage for red phosphorescent OLEDs with neat SBFK and mixed SBFK+NPB hosts. Concentration of  $\text{Ir}(\text{l-piq})_3$  is 6%. See Figure 14.37 captions for device structures.

comparable to the drive voltage of a state-of-the-art red p-i-n phosphorescent OLEDs described above.<sup>107–109</sup>

We attribute the observed low voltage to extremely efficient electron injection from Bphen to PADN and then to SBFK. LUMO levels of the materials were estimated from electrochemical measurements in acetonitrile/toluene (1:1) solution mixture containing 0.1 M tetrabutylammonium tetrafluoroborate and are as follows: –2.88 eV for SBFK, –2.66 eV for PADN, and –2.55 eV for Bphen.<sup>125</sup> We should note that irreversible reduction was observed for Bphen; therefore, the LUMO level may be higher than the reported value by more than 0.3 eV.<sup>129</sup> From the comparison of the LUMO levels of the materials used, it can be concluded that there is no barrier for electron injection from Bphen to PADN and to the electron-transporting cohost (SBFK) of the mixed EML. Recombination in the mixed-host SBFK+NPB devices most likely extends to the bulk of the EML, perhaps reaching the EML|HBL interface. Because SBFK has a very deep HOMO level (no oxidation was observed within the solvent window), a relatively large concentration of the NPB is necessary to achieve advantageous charge and exciton distribution in the EML. The exciton-blocking layer of SBFK placed on the cathode side of the mixed EML is required to maintain high efficiency. We observed that omission of the blocking layer led to significant drop of the luminous yield. The triplet energy of the PADN (~1.8 eV) is much lower than that of  $\text{Ir}(\text{l-piq})_3$  (2.1 eV), thus, the PADN acts as a sink for triplet excitons when recombination takes place at close proximity to the EML|PADN interface. The mixed-host SBFK+25% NPB devices exhibit good operational stability— $T_{90}$ , defined as the time required to lose 10% of the initial luminance, is measured to be 2000 h at 1000 cd/m<sup>2</sup>.

Good OLED performance, even in devices with advanced architectures, cannot be achieved without the use of efficient and stable phosphorescent

**TABLE 14.5**

UniversalPHOLED Red and Green Commercial Materials in Bottom-Emission Devices

PHOLEDs Color	CIE Color Coordinates	EQE (%)	Luminous Efficiency (cd/A)	Lifetime to 50% $L_0$ (h)	Initial Luminance (cd/m <sup>2</sup> )	Initial Voltage (V)
Deep red	(0.67, 0.33)	21	21	80,000	1000	4.3
	(0.66, 0.34)	19	22	200,000	1000	2.8
Red	(0.64, 0.36)	21	28	500,000	1000	2.8
Green	(0.36, 0.60)	16	58	100,000	1000	2.8
	(0.38, 0.59)	19	67	250,000	1000	4.6

emitters. Universal Display Corporation is developing state-of-the-art proprietary dopants emitting in the broad range of colors. Performance metrics are shown in Table 14.5.<sup>130</sup> Deep-red-emitting phosphorescent OLEDs at 1000 cd/m<sup>2</sup> exhibit 21% EQE, 4.3 V, and 80,000 h of operational lifetime. Low-voltage red phosphorescent OLEDs show remarkable performance: 19% EQE and 200,000 h of lifetime.

It is clear from the discussion in this section that red phosphorescent OLEDs show excellent device efficiency and operational lifetime and are consequently good candidates for application as red pixels in OLED displays.

#### 14.4.2.2 Architectures and Performance of Green Phosphorescent OLED Devices

As the triplet energy of the dopant increases, architectural designs and material requirements for phosphorescent OLEDs become more complex. As a general rule, hosts or cohosts for green phosphorescent emitters should have triplet energies exceeding 2.5 eV.<sup>131</sup> In green phosphorescent OLEDs, the insertion of high-energy (i.e.,  $E_T > 2.5$  eV) exciton-blocking layers to confine triplet excited states to the EML is also necessary for achieving high efficiency. Additionally, the redox properties of the materials used in charge-transport, exciton-blocking, and light-emitting layers should be carefully matched to avoid large energy barriers for charge injection, which can lead to high voltages.

Very high-efficiency phosphorescent OLEDs with EQE ranging from 8% to 19% were realized using tris(2-phenyl-pyridine)iridium (III) ( $\text{Ir}(\text{ppy})_3$ ) and bis(2-phenyl-pyridine)(acetylacetone)iridium(III) ( $\text{Ir}(\text{ppy})_2(\text{acac})$ ) as green emitters doped into various host materials.<sup>16,132,133</sup> The high efficiency achieved in the devices was attributed to exciton formation directly on a dopant molecule and confinement of excitons to the EML. It is very desirable that in addition to having exciton-blocking properties (i.e., triplet energy of exciton blocker exceeds that of a phosphorescent emitter), the materials used

in the EBL should also prevent leakage of charge carriers from the EML. A thin electron/exciton-blocking layer is generally placed on the anode side of the EML; in order to block electrons the LUMO level of an electron-blocking material should lie higher (i.e., be less negative) than the LUMO level of the electron-transporting component of the EML. In addition to the energy requirement, the suitable EBL materials should also have hole-transporting properties.<sup>134,135</sup> A hole/exciton-blocking layer is generally placed on the cathode side of the EML; in order to block holes, materials used in the HBL should have a HOMO level deeper than the hole-transporting host, cohost, and emitter.<sup>135</sup>

Carbazoles are the most often used neat-host materials for Ir(ppy)<sub>3</sub>. Triplet energy and transport properties of this class of materials can be tuned by derivatization of the phenyl rings or the carbazole group.<sup>136</sup> Green phosphorescent OLEDs comprising the CBP host doped with Ir(ppy)<sub>3</sub> have been extensively studied.<sup>16,114,127,128,137,138</sup> CBP is reported to have bipolar transporting properties.<sup>114</sup> Adachi et al. established that the process responsible for phosphorescence of Ir(ppy)<sub>3</sub> in the CBP host starts with the trapping of holes on the Ir(ppy)<sub>3</sub> dopant, followed by recombination with a free electron.<sup>114</sup> CBP is much harder to oxidize than Ir(ppy)<sub>3</sub> as the HOMO of CBP lies in the range of 6.0–6.3 eV, while the HOMO level of Ir(ppy)<sub>3</sub> is 5.4–5.6 eV.<sup>125,135</sup> Therefore, holes are predominantly transported by hopping between Ir(ppy)<sub>3</sub> molecules. As doping concentration increases, the recombination zone shifts from the HTL|EML interface toward the bulk of the EML, and the insertion of an HBL becomes necessary to retain high efficiency.

Various high triplet energy ETM such as phenanthrolines and benzimidazoles have been tested in the HBL in CBP + Ir(ppy)<sub>3</sub> green phosphorescent OLEDs.<sup>135,137,138</sup> However, use of these materials usually resulted in poor device stability. In contrast, green triplet OLEDs with BAQ in the HBL demonstrated long lifetimes (*vide infra*). Similar results were reported for red phosphorescent OLEDs (see Section 14.4.2.1).

The hole-blocking properties of BAQ or BAQ' in the HBL in CBP + Ir(ppy)<sub>3</sub> devices have been questioned recently.<sup>106</sup> An IP of BAQ estimated by UPS is 6.05 eV,<sup>106</sup> which is comparable to that of CBP. Hence, BAQ most likely blocks holes transported by Ir(ppy)<sub>3</sub> but not by CBP. BAQ cannot act as an exciton-blocking material for CBP + Ir(ppy)<sub>3</sub> devices because its triplet energy is lower than the triplet energy of Ir(ppy)<sub>3</sub>. The reported triplet energies of BAQ and Ir(ppy)<sub>3</sub> are 2.36<sup>106</sup> and 2.54 eV,<sup>125</sup> respectively. Triplet energies of other useful materials are listed in Table 14.6. It was established that the recombination zone in CBP + Ir(ppy)<sub>3</sub> is spread throughout the EML; as a result of triplet exciton quenching by BAQ, the green phosphorescent OLEDs with BAQ in the HBL exhibit lower efficiencies compared to that of devices with high-energy materials in the HBL, for example, TPBI or BCP.<sup>136,137</sup> However, the main advantage of the BAQ HBL in green phosphorescent OLEDs is significantly longer operational lifetime. Later, high-triplet-energy aromatic hydrocarbons were used to replace BAQ in green triplet devices.<sup>139</sup> Use of

**TABLE 14.6**

Triplet Energies of Materials Used in Green and Red Phosphorescent OLEDs

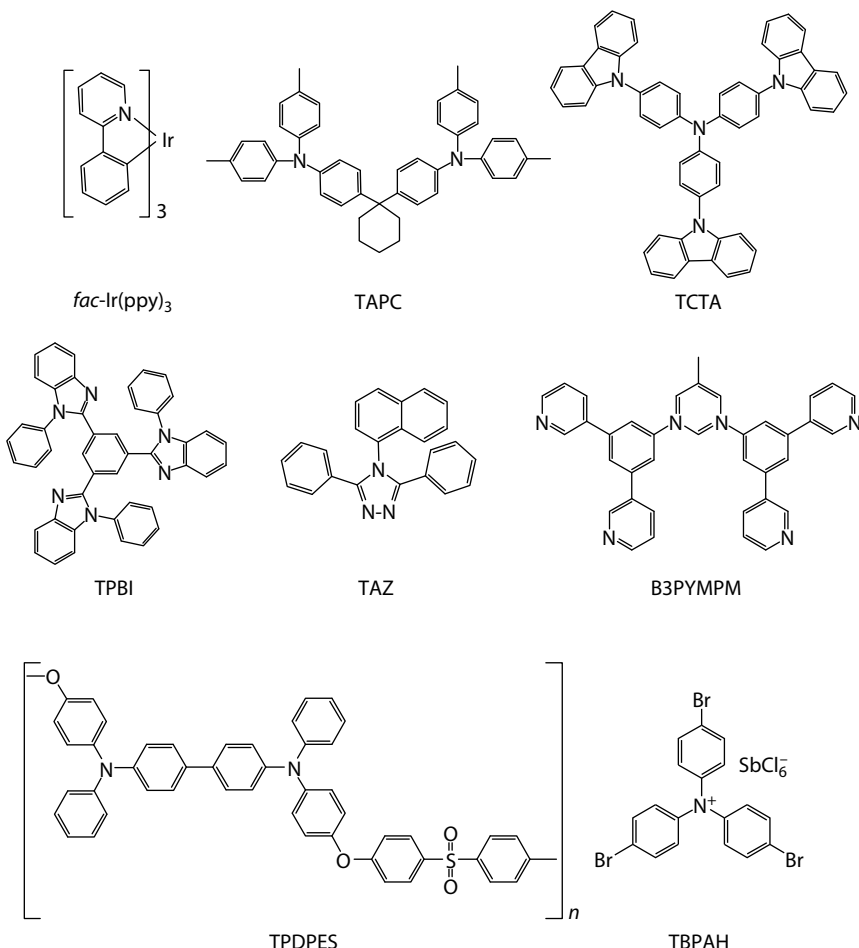
Compound	Triplet Energy ( $E_T$ ), eV	
	Experimental $E_T$	DFT $E_T$
Alq	2.19	2.11
BAlq'	2.31	2.21
Bphen	2.59	2.64
CBP	2.61	2.67
NPB	2.41	2.50
PADN		1.82
SBFK	2.62	2.49
TAPC	2.95	2.96
TBADN	1.81	1.86
TCTA	2.86	2.85
TPBI	2.74	2.69
Ir(1-piq) <sub>3</sub>	2.06	2.12
Ir(ppy) <sub>3</sub>	2.49	2.54

*Note:* The energy values are obtained from phosphorescence spectra measured at 77K. The triplet energies of the dopants were estimated from adsorption and emission spectra in degassed ethylacetate solution at room temperature. Density-function theory (DFT) was used to calculate  $E_T$  values.<sup>125</sup>

these materials improved not only luminous yield by more than 20% but also operational lifetime by 30% over the devices with BAlq.

Extremely high-efficiency green phosphorescent OLEDs were reported recently by Tanaka et al.<sup>26</sup> The EML consisted of CBP host doped with 8% of Ir(ppy)<sub>3</sub>. A novel high-triplet-energy ETM bis-4,6-(3,5-di-3-pyridylphenyl)-2-methylpyrimidine (B3PYMPM) was used in the ETL (for material structures see Figure 14.39). Poly(arylene ether sulfone)-containing tetraphenylbenzidine (TPDPES) doped with 10% tris(4-bromo-phenyl) ammonium hexachloroantimonate (TBPAH) was used as a p-type doped HTL. A thin EBL of 1,1-bis[4-[N,N-di-(p-tolyl)amino]phenyl]cyclohexanone (TAPC) was placed between the EML and the HTL. Thus, in this device configuration the triplet excitons were confined entirely to the EML.

The novel ETM B3PYMPM was reported to have high electron mobility and relatively low LUMO level. The combination of these properties led to effective electron injection and transport from the cathode into the ETL of B3PYMPM. TAPC used in EBL on the anode side of the EML is a well-known HTM with a high triplet energy of 2.89 eV<sup>26</sup> and a hole mobility of at least  $7 \times 10^{-3}$  cm<sup>2</sup>/V·s.<sup>140</sup> Thus, extremely efficient charge-transporting materials

**FIGURE 14.39**

Structures of materials used in green phosphorescent OLEDs.

were used in the triplet OLED. The device exhibited green phosphorescence with an emission maximum of 514 nm corresponding to an emission of Ir(ppy)<sub>3</sub>. The emission was confirmed to be Lambertian. At 100 cd/m<sup>2</sup> the observed EQE was 29%. At 1000 cd/m<sup>2</sup> the performance characteristics were as follows: 26% EQE, 2.9 V, 107 lm/W. Device lifetime data were not given.

Conventional phosphorescent OLEDs with CBP host in the EML and stable materials in blocking layers usually show better stability compared to triplet OLEDs with other host materials.<sup>137–139</sup> Nevertheless, it was established that chemical mechanism of degradation in the CBP + Ir(ppy)<sub>3</sub> devices is linked to homolytic cleavage of C–N bonds in CBP and includes several key steps such as the formation of CBP excited states, homolytic dissociation and formation

of radicals, followed by irreversible radical additions and disproportionation reactions.<sup>141,142</sup> Several products of the reactions were identified as nonradiative recombination centers as well as luminescence quenchers of Ir(ppy)<sub>3</sub>, the formation of which contributes to efficiency loss. In addition to CBP host degradation, the degradation of the Ir(ppy)<sub>3</sub> was also observed.

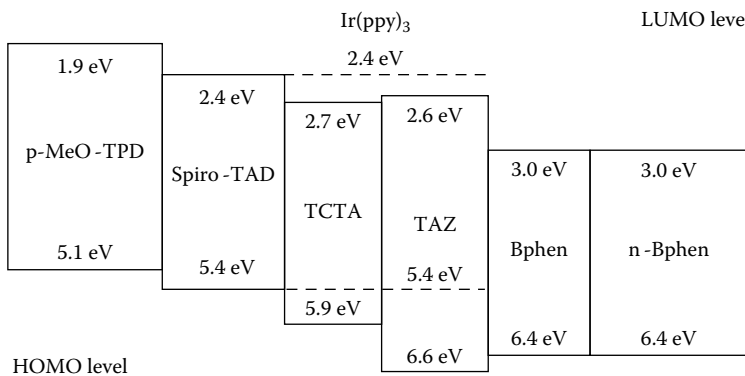
Green phosphorescent OLEDs often include a conventional EML with a neat bipolar-transporting host material. An alternative architecture is a double emission EML (D-EML) introduced by Zhou et al.<sup>143</sup> The general device structure is shown in Figure 14.40. The materials of the two light-emitting layers carry only holes or electrons, respectively. Hence, much of the recombination in these devices probably occurs exactly at the junction between the two EMLs. This feature may adversely affect the device lifetime because only a few molecules are responsible for generating excited states and if degradation involves these excited states, a higher concentration of degradation products resides at the interface. Assuming that the degraded species quench excited states and are continuously formed during operation, a higher and higher fraction of the excited states will be quenched with time, resulting in the observed decrease in efficiency. Although no degradation products have been clearly identified and the exact mechanism of the observed instability is unclear, it is also speculated that the instability may be associated with various quenching processes, such as TTA, TPQ, and quenching of triplet excitons by exciplexes formed between host materials with different charge-transporting properties. As was mentioned previously, these quenching processes may be lessened to a certain degree by the use of the phosphorescent emitter in sufficient concentrations so that the emitter participates in charge transport in both EMLs, therefore extending the recombination zone and shifting it away from the EML1|EML2 interface. The concentration of quenching sites is reduced, leading to a more stable structure.

Very efficient phosphorescent OLEDs with a D-EML and p- and n-doped charge-transporting layers have been demonstrated.<sup>144,145</sup> Their device structure is presented in Figure 14.41. The hole-transporting part of the D-EML consists of 4,4',4''-tris(carbazolyl)-triphenylamine (TCTA) doped

Cathode:Al
n-Doped ETL
HBL ETL
EML2:ET host + emitter
EML1:HT host + emitter
EBL
p-Doped HTL
Anode:ITO
Glass substrate

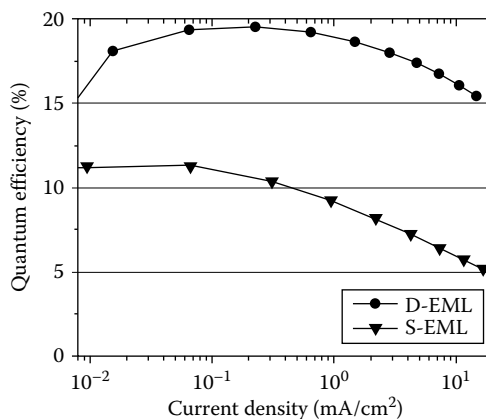
**FIGURE 14.40**

Schematic structure of a phosphorescent OLED with double emission EML and electrically doped charge-transporting layers.

**FIGURE 14.41**

Device structure of D-EML p-i-n OLED and the proposed energy level diagram. Anode and cathode are ITO and Al. (From He, G. et al., *Appl. Phys. Lett.*, 85, 3911, 2004. With permission.)

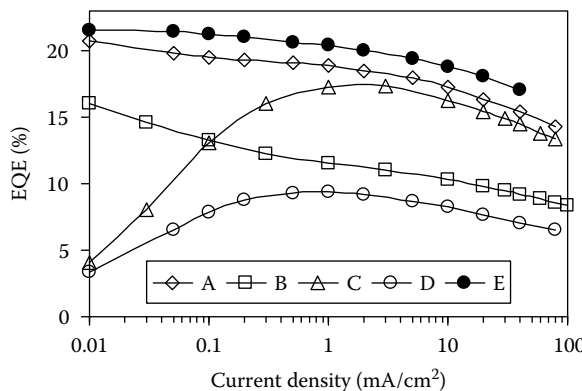
with 8% Ir(ppy)<sub>3</sub>; and the electron-transporting EML comprises 3-phenyl-4-(1'-naphthyl)-5-phenyl-1,2,4-triazole (TAZ) host doped with the same amount of Ir(ppy)<sub>3</sub>. At 1000 cd/m<sup>2</sup> this device shows 62.4 cd/A, 3.2 V, and 61.1 lm/W.<sup>146</sup> A maximum EQE of 19.5% corresponding to a power efficacy of 77 lm/W was obtained at 100 cd/m<sup>2</sup>. The efficiency of green phosphorescent OLEDs with a double emission layer is significantly higher than the EQE of the green devices with single-emission EML (S-EML) as shown in Figure 14.42 (no TAZ layer). In the S-EML device, recombination occurs

**FIGURE 14.42**

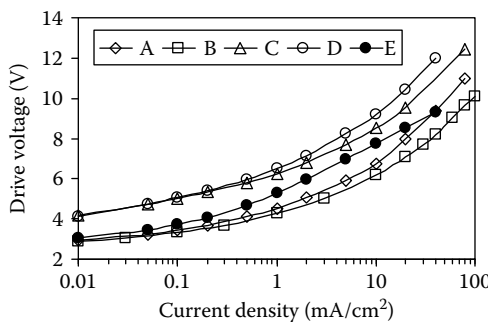
EQE as a function of current density for D-EML and S-EML devices. Structure of D-EML is shown in Figure 14.41; S-EML has the following structure of the layers: ITO|MeO-TPD+2% F<sub>4</sub>-TCNQ (100 nm)|Spiro-TAD (10 nm)|TCTA + 8 wt.% Ir(ppy)<sub>3</sub> (20 nm)|Bphen (10 nm)|Bphen + Cs (50 nm)|Al (100 nm). (From He, G. et al., *Appl. Phys. Lett.*, 85, 3911, 2004. With permission.)

at the narrow region at the EML|Bphen interface. Because of the large difference in HOMO levels of TCTA and Bphen, holes accumulate at the TCTA|Bphen interface.<sup>144</sup> In addition to TTA, triplet excitons formed in this region may be quenched by the anion-radicals of Bphen and cation radicals of TCTA. Also, it was established that TCTA and Bphen form an exciplex with a fluorescence maximum of 460 nm.<sup>145,147</sup> The triplet energy of the exciplex is unknown; however, most likely the  $E_T$  is below 2.5 eV. In this case, triplet excitons of Ir(ppy)<sub>3</sub> are quenched by Dexter energy transfer mechanisms between Ir(ppy)<sub>3</sub> and the exciplex, causing an efficiency decrease. Use of advanced p- and n-type doped charge-transporting layers, such as NHT-5:NDP2 and NET-5:NDN-1, respectively, in devices with D-EML and an outcoupling foil attached to a glass substrate, allows realization of extremely efficient green phosphorescent OLEDs with the following performance metrics: 95 cd/A, 116 lm/W, 2.6 V at 1000 cd/m<sup>2</sup>.<sup>148</sup>

We have demonstrated efficient low-voltage green phosphorescent OLEDs with mixed EML. The relative hole- and electron-transporting properties of the mixed host can be optimized by varying the ratio of the components. The low voltage does not require doping of the charge-transport layers. To demonstrate the advantage in the performance of green phosphorescent OLEDs with a mixed host over conventional devices with a neat host, four sets of devices were made having the following structures—(A) and (B): ITO (25 nm)|CF<sub>x</sub> (1 nm)|NPB (95 nm)|EBL ( $A=10$  nm,  $B=0$  nm)|TPBI + TCTA + Ir(ppy)<sub>3</sub> (35 nm)|BALq' (10 nm)|Alq (40 nm)|LiF (0.5 nm)|Al (100 nm), and (C) and (D): ITO (25 nm)|CF<sub>x</sub> (1 nm)|NPB (95 nm)|EBL ( $C=10$  nm,  $D=0$  nm)|CBP + Ir(ppy)<sub>3</sub> (35 nm)|BALq' (10 nm)|Alq (40 nm)|LiF (0.5 nm)|Al (100 nm). CBP was an example of a neat host, and TPBI (64%) + TCTA (30%) were used as electron- and hole-transporting cohosts. The green phosphorescent dopant Ir(ppy)<sub>3</sub> was present at 6% in each case. A 10 nm exciton/electron-blocking layer of TCTA was used to confine triplet excitons to the EML in devices A and C. The EBL was omitted in devices B and D. Device performance is summarized in Figures 14.43 and 14.44. Both mixed-host devices (A, B) demonstrated substantially higher luminous efficiencies than the neat-host controls (C, D), especially at low current densities. Codoping of a hole-transporting component TCTA into the TPBI host increases hole current in the EML; therefore, devices A and B have significantly lower drive voltage compared to devices C and D. As is shown in Figure 14.44, the use of the mixed EML decreases the drive voltages by as much as 2 V. For the most efficient mixed-host device (A), the EQE reaches 20.8% at 0.01 mA/cm<sup>2</sup> and exceeds ~14% throughout the entire range of current density. The power efficacies at 1000 cd/m<sup>2</sup> are 41.6 and 24.5 lm/W for the mixed-host devices (A, B) and 30.2 and 13.1 lm/W for the neat-host controls (C, D). The use of an EBL also improves the EQE and power efficacy without voltage change. Similarly significant advantages in the performance of mixed-host over neat-host devices were observed for blue phosphorescent OLEDs.<sup>125</sup> The only difference between devices A (or B) and C (or D) is the use of the conventional neat host in one (C, D) and the

**FIGURE 14.43**

EQE as a function of current density for green phosphorescent OLEDs with mixed TPBI + TCTA and neat CBP host. Device structures for A–D: ITO (25 nm)|CF<sub>x</sub>|X|BALq'(10 nm)|Alq (40 nm)|LiF (0.5 nm)|Al (100 nm), where (A) X = NPB (95 nm)|TCTA (10 nm)|TPBI + TCTA + Ir(ppy)<sub>3</sub> (35 nm); (B) X = NPB (105 nm)|TPBI + TCTA + Ir(ppy)<sub>3</sub> (35 nm); (C) X = NPB (95 nm)|TCTA (10 nm)|CBP + Ir(ppy)<sub>3</sub> (35 nm); (D) X = NPB (105 nm)|CBP + Ir(ppy)<sub>3</sub> (35 nm); (E): ITO (25 nm)|CF<sub>x</sub> (1 nm)|NPB (85 nm)|TCTA (10 nm)|TPBI + TCTA + 10% Ir(5'-ph-ppy)<sub>3</sub> (35 nm)|TPBI (10 nm)|Alq (40 nm)|LiF (0.5 nm)|Al (100 nm).

**FIGURE 14.44**

Drive voltage as a function of current density for green phosphorescent OLEDs with mixed TPBI + TCTA and neat CBP host. See Figure 14.43 captions for formulations.

mixed host in the other (A, B). The significantly lower drive voltage can be attributed to more facile injection of charge carriers into the EML as a consequence of its higher HOMO and lower LUMO levels, leading to a smaller voltage drop across the mixed-host EML. The compatibility of these transport levels with required triplet energy of the host is a consequence of the fact that the overall HOMO and LUMO reside on different molecules. In the mixed-host system (TPBI + TCTA) holes hop through the TCTA sites and electrons hop through the TPBI sites. Holes can be also injected directly from the EBL of TCTA into the Ir(ppy)<sub>3</sub> HOMO level (this process is energetically

favorable). It is expected that the trapped holes will recombine with anion radicals of TPBI, producing excited states of Ir(ppy)<sub>3</sub>. As is clearly shown, TPBI + TCTA + Ir(ppy)<sub>3</sub> devices provide very high luminous yield. Further improvement in luminous yield is attained by replacement of Ir(ppy)<sub>3</sub> with Ir(5'-ph-ppy)<sub>3</sub> in this device structure, with an EQE reaching 22% at low current density (see device E, Figure 14.43).

It is generally believed that the use of high triplet energy ETM with deep HOMO levels is required for maintaining high efficiency. As was discussed in the beginning of this section, many hole-blocking materials are known to be very unstable and their application in OLED devices is not practical. We have reduced the drive voltage of mixed-host phosphorescent OLEDs significantly, without the need for Li doping, by replacing the high triplet energy HBL with a simple ETL|EIL combination. Because of the ability to change location of the recombination zone in mixed-host devices, the selection of an ETM for the ETL was based entirely on its electron injection and transport properties without regard to its triplet energy. We investigated a number of different materials in ETL|EIL in the general device structure: ITO|CF<sub>x</sub>|NPB (95 nm)|TCTA (10 nm)|TPBI + 30% TCTA + 6% Ir(ppy)<sub>3</sub> (35 nm)|ETL ((50-X) nm)|EIL (X nm)|LiF|Al. The device data are shown in Figures 14.45 and 14.46. The devices display similar efficiencies, both in trend and in magnitude, except for the device with Alq ETL. The device with a 50 nm Alq ETL exhibits a lower luminous efficiency as expected. Insertion of a 10 nm layer of TPBI between the mixed EML and the Alq layer increases EQE from 16.9% to 18.7% without significant changes in drive voltage. At 1000 cd/m<sup>2</sup> the

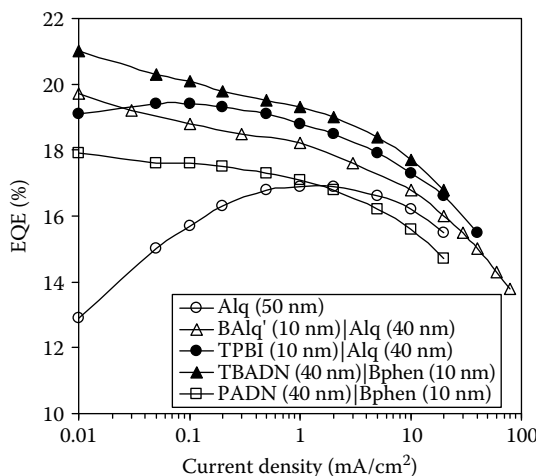
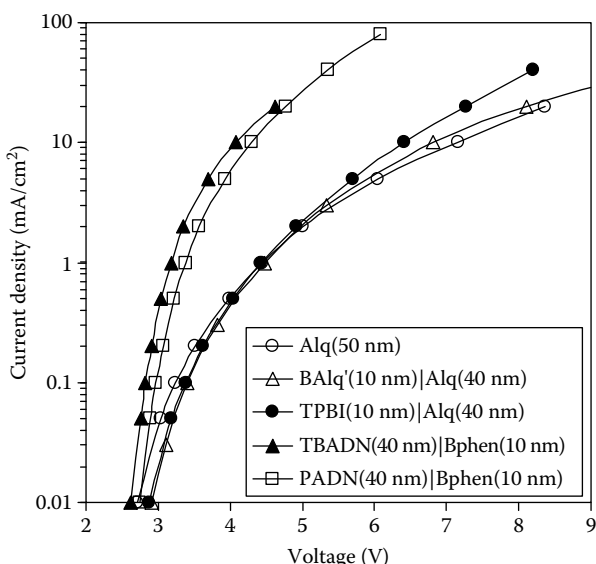


**FIGURE 14.45**

EQE as a function of current density for green phosphorescent OLED devices with mixed EML and various ETLs (see legend). Organic layers: NPB (95 nm)|TCTA (10 nm)|TPBI + 30%TCTA + 6%Ir(ppy)<sub>3</sub> (35 nm)|ETLs. Anode and cathode are always ITO|CF<sub>x</sub> and LiF|Al. CIE coordinates are all in the ranges (0.296–0.308, 0.625–0.634).

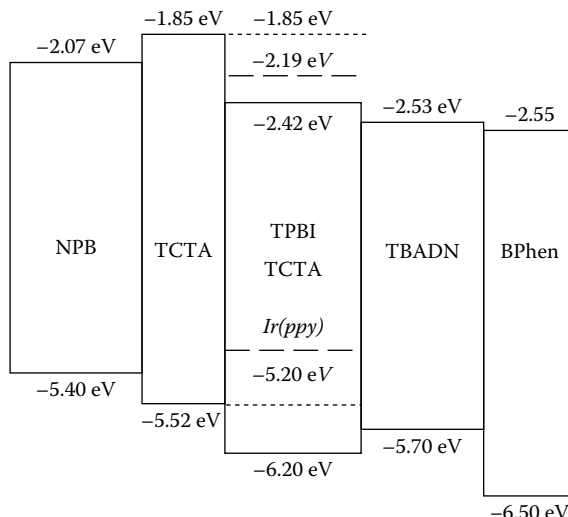
green triplet OLED with TPBI|Alq in ETL|EIL shows performance metrics of 18.7% EQE, 44.7 lm/W, 4.9 V, CIE<sub>x,y</sub> (0.30, 0.63). For all devices with a 40 nm Alq layer adjacent to the cathode, the drive voltages are similar, as shown in Figure 14.46.

Remarkably, the use of a low triplet energy anthracene such as TBADN in the ETL further increases the luminous yield and greatly reduces the drive voltage compared to BAQ'|Alq or TPBI|Alq. The devices with PADN|Bphen ETL also exhibit low drive voltages, however, device efficiency is lower than that of TBADN|Bphen. For TBADN|Bphen devices, improvement in voltage ranges from  $\geq 1.3$  V at  $1\text{ mA/cm}^2$  to  $\geq 2.7$  V at  $20\text{ mA/cm}^2$  over voltages of TPBI|Alq devices. Largely as a result of the reduced drive voltage, the power efficacy at  $1000\text{ cd/m}^2$  is higher than that of for the phosphorescent OLEDs with Alq-based ETLs (64 versus 37–45 lm/W). These effects are, most likely, results of facile electron injection from the TBADN into the mixed EML. As can be seen from Figure 14.47, there is a relatively small energy barrier for charge injection from TBADN into TPBI. Facile electron injection and transport should concentrate the recombination zone toward the hole-injecting side of the EML where the triplet excitons are not subject to quenching by the low triplet energy material in the ETL. The green phosphorescent OLED device with TBADN|Bphen in ETL|EIL shows performance metrics at  $1000\text{ cd/m}^2$  ( $\sim 1.5\text{ mA/cm}^2$ ) of 19.1% EQE, 64 lm/W, 3.2 V, CIE<sub>x,y</sub> (0.30, 0.63). The LUMO level of PADN was estimated to be  $-2.66\text{ eV}$ , thus the energy barrier for electron injection from PADN to TPBI is about  $0.23\text{ eV}$ , which is larger than the injection barrier from TBADN to TPBI ( $0.11\text{ eV}$ ). This manifests in



**FIGURE 14.46**

Current density as a function of voltage for green phosphorescent OLED devices with mixed EML and various ETL (see legend). For organic layer structures see Figure 14.45 captions.

**FIGURE 14.47**

Device structure and energy level diagram of green phosphorescent OLED with mixed EML and TBADN|Bphen ETL. HOMO energies were obtained as IPs by UPS spectroscopy or as electrochemical oxidation potentials by cyclic voltammetry. LUMO values were estimated from solution-determined redox data. Unless otherwise noted, redox processes were reversible. No reduction was observed for TCTA within solvent window, LUMO of TCTA is significantly higher than the shown value. Irreversible reduction was observed for Bphen: LUMO may be up to 0.3 eV higher.<sup>125</sup>

slightly higher drive voltage in devices with PADN|Bphen compared to TBADN|Bphen OLEDs and is likely responsible for somewhat lower efficiency. The mechanism could involve a reduced electron current across the EML|PADN interface, possibly combined with an accumulation of negative charge in this vicinity.

For a detailed investigation of the operation mechanism and location of the recombination zone in green and blue mixed-host phosphorescent OLEDs, we refer to our paper.<sup>125</sup> We established that the recombination zone in the device with mixed EML and an advanced ETL (i.e., TBADN|Bphen) is concentrated only within ~10 nm of the EBL. For this reason, the ETL does not need to have hole- or triplet-blocking properties. The location of the recombination zone in the devices can be easily adjusted by varying the concentrations of the cohosts, therefore, it is possible to significantly reduce operational voltage via simple changes in the architecture of the ETL and EIL without sacrificing EQE not only in green but also in blue phosphorescent OLEDs.

Although the efficiency of the mixed-host green triplet OLEDs is superior to those with the neat-host CBP, the operational stability of these devices is inferior. The half-life ( $T_{50}$ ) of the device NPB|TCTA|TPBI + 30%TCTA + 6%*Ir(ppy)<sub>3</sub>*|TPBI|Alq|LiF|Al at 1000 cd/m<sup>2</sup> is only 200 h. The probable cause is the known instability of TPBI. Device lifetime can be improved by replacing TPBI with more stable host materials and using more stable emitters, such

as  $\text{Ir}(5'\text{-ph-ppy})_3$ . For example, use of SBFK in place of TPBI in the mixed EML and HBL improves the lifetime of  $\text{Ir}(\text{ppy})_3$  devices by nearly 11 times without significant loss of luminous efficiency. Replacement of  $\text{Ir}(\text{ppy})_3$  with  $\text{Ir}(5'\text{-ph-ppy})_3$  in the mixed SBFK + TCTA EML further improves  $T_{50}$  by three times. Thus, half-life of the device  $\text{NPB}|\text{TCTA}|\text{SBFK} + 30\% \text{TCTA} + 6\% \text{Ir}(5'\text{-ph-ppy})_3|\text{SBFK}|\text{Alq}|\text{LiF}|\text{Al}$  at  $1000 \text{ cd/m}^2$  is 6500 h.

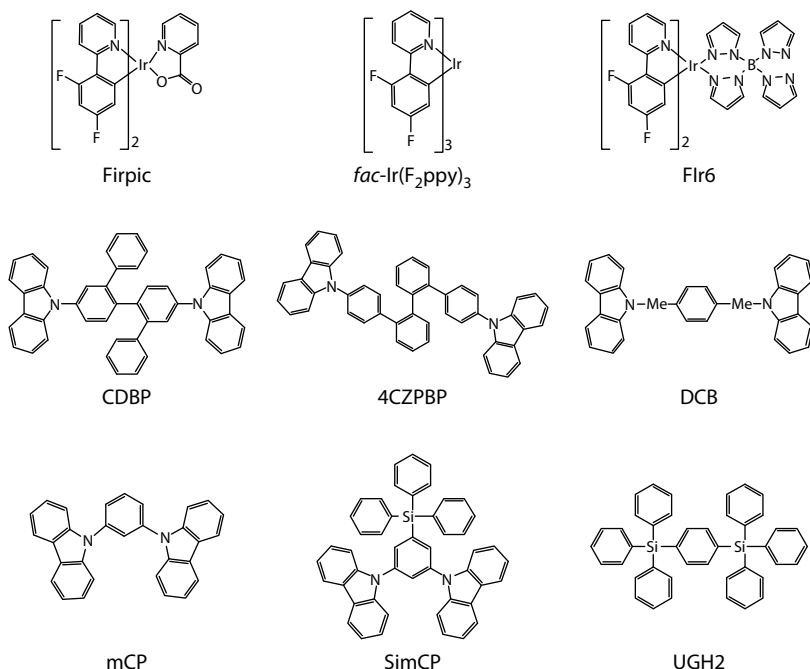
TCTA, TPBI, and SBFK were used as model cohost materials to demonstrate that mixed EML architecture offers a significant advantage in device performance compared to the conventional neat-host devices and can be used as an alternative approach to the design of triplet OLEDs. The most important feature of this architecture is that the simple variation of the cohosts ratio “tunes up” the location of recombination in the mixed EML, allowing simplification of required properties of the materials used in phosphorescent OLEDs.

#### **14.4.2.3 Architectures and Performance of Blue Phosphorescent OLED Devices**

Blue phosphorescent OLEDs place the most stringent demands on the energy levels of the host, frequently resulting in limited efficiency and/or high drive voltage. Development of blue triplet OLEDs, especially those emitting deep-blue light with high efficiency and with sufficient device lifetimes, has proven to be a challenging task. However, this area of research is of great interest and importance. So far, there are very few reports on the development of novel blue triplet dopants and their application in blue phosphorescent OLEDs.<sup>117,149–152</sup>

Figure 14.48 shows the common materials used in blue triplet devices. The most widely used efficient blue-green phosphorescent dopant is  $[(4,6\text{-difluorophenyl})\text{pyridinato-N,C}^2](\text{picolinato})\text{iridium(III)}$  (FIrpic). Phosphorescence with an emission maximum at 472 nm and device CIE $x,y$  color coordinates of about (0.16, 0.37) are typical.<sup>151</sup> Triplet energy of this dopant is estimated to be 2.7 eV.<sup>135,151</sup> When doped into a high-energy host (mCP,  $E_T$  is 2.9 eV<sup>151</sup>), the photoluminescence quantum yield of FIrpic is 99%.<sup>127,128</sup> Thus, to obtain high luminous yield in the blue-green phosphorescent OLED devices, the triplet energy of a suitable host material should exceed 2.7 eV. Otherwise, endothermic energy transfer from the host to the dopant material takes place, leading to low-efficiency devices.<sup>149</sup> Blue phosphorescent OLEDs containing a 4,4'-bis(9-carbazolyl)-2,2'-dimethyl-biphenyl (CDBP),<sup>150</sup> 1,3-di-(9-carbazolyl)benzene (mCP),<sup>151,152</sup>  $N,N$  CDBP-dicarbazolyl-1,4-dimethane-benzene (DCB),<sup>153</sup> and 3,5-bis(9-carbazolyl)tetraphenylsilane (Si<sub>m</sub>CP)<sup>152</sup> as high-energy neat hosts for FIrpic were reported. The maximum EQEs observed were in the range of 7.5%–14.4%, corresponding to the power efficacies of 8.9–11.9 lm/W.

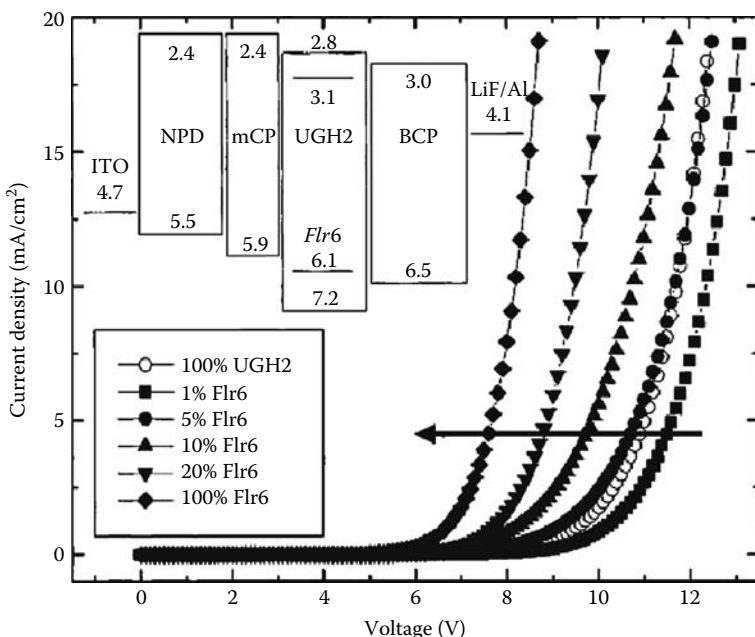
As was mentioned above, a high energy (large band gap) host material most likely transports predominantly only one type of charge carrier. A different approach to the selection of a blue triplet host is to use wide band gap compounds that serve as an inert matrix.<sup>117,154</sup> In this case, holes or electrons are

**FIGURE 14.48**

Material structures used in blue phosphorescent OLEDs.

trapped and transported through the EML by the emitter if its concentration is sufficiently high. Exciton formation occurs directly on the dopant molecule. Diphenyldi(*o*-tolyl)silane (UGH1) and *p*-bis(triphenylsilyl)benzene (UGH2) were used as wide band gap hosts for a deep-blue bis(4',6'-difluorophenylpyridinato)tetrakis(1-pyrazolyl)borane (FIr6) emitter.<sup>117</sup> The dopant was used at 10 wt %. Maximum EQE of 8.8% and power efficacy of 11 lm/W were achieved at 22.5 and 6.2 mA/cm<sup>2</sup>, respectively, for the device with UGH1 host. The blue phosphorescent OLED with UGH2 host exhibited 11.6% EQE and 13.9 lm/W at 9.9 and 5.6 mA/cm<sup>2</sup>. Device lifetime data were not given.

Figure 14.49 shows the dependence of current density on voltage and concentration of the dopant for UGH2:FIr6-based blue phosphorescent OLED. A thin layer of mCP was used to confine triplet excitons to the EML and block electrons. From redox data and voltage analysis, the authors conclude that FIr6 traps and transports both holes and electrons while UGH2 serves as an inert matrix host. However, it was established that in the absence of the FIr6, UGH2 is capable of electron transport. According to estimated HOMO-LUMO energy levels of materials used, the energy barrier for hole injection from mCP into UGH2 is 1.3 eV, while the energy barrier for hole injection from mCP to FIr6 is only 0.2 eV; therefore hole transport by FIr6 is more favorable. The LUMO level of FIr6 lies below that of UGH2, thus

**FIGURE 14.49**

Current density–voltage characteristics for ITO|NPD (40 nm)|mCP (15 nm)|UGH2:*x*%Flr6 (25 nm)|BCP(40 nm)|LiF (0.5 nm)|Al (50 nm) OLEDs. The arrow points in the direction of increasing Flr6 concentration. Inset: Proposed energy level scheme for the device under zero applied bias. (From Holmes, R.J. et al., *Appl. Phys. Lett.*, 83, 3818, 2003. With permission.)

resulting in electron-trapping properties of the dopant. As can be seen from Figure 14.49, the highest voltage is observed in the blue triplet OLED with 1% of Flr6. At small concentrations, the dopant traps electrons effectively, voltage decreases with an increase of the emitter concentration. Thus, higher concentrations of Flr6 provide a pathway for injection and transport of electrons throughout the EML.

Extremely efficient blue phosphorescent OLEDs with novel high triplet energy host and charge-transport materials were demonstrated by Tanaka et al.<sup>155</sup> The architecture of the device was conventional: the neat-host EML was placed between high energy transporting layers. For the emitting layer, 2,2'-bis(4-carbazolylphenyl)-1,1'-biphenyl (4CZPB) host material was doped with 13% of Flrpic. TPDPES doped with 10% TBPAH was used as a p-type doped HTL<sup>128,155</sup> and a high energy EBL of bis[4-(*p,p'*-ditolylamino)-phenyl] diphenylsilane (DTASI) was placed between the p-doped HTL and the EML. The ETM was tris[3-(3-pyridyl)-mesityl]borane (3TPYMB) with a reported electron mobility of about 10<sup>-5</sup> cm<sup>2</sup>/V/s. At 100 cd/m<sup>2</sup> the blue phosphorescent OLED shows 21% EQE and power efficacy of 39 lm/W; at 1000 cd/m<sup>2</sup> the luminous yield reaches 25 cd/A, and the drive voltage is ~5 V. The 20% EQE translates to nearly 100% of the internal quantum efficiency for the blue

triplet. The device stability was not discussed, but based upon other work, it is probably low.

The development of an efficient blue or deep-blue phosphorescent emitter with long operational lifetime has been a very challenging task. Ir(III) complexes containing carbene-based C<sup>N</sup> cyclometalated ligand(s) with emission at about 407 nm have been characterized.<sup>156,157</sup> Deep-blue-emitting OLED devices employing UGH2 host and these dopants in the EML were fabricated and the observed EQE was 2.7%.<sup>157</sup> Such low EQE can be attributed to an unoptimized device structure and underestimation that is due to instrumental difficulties in measuring the intensity of deep-blue emission. The stability was not reported. For other work on blue phosphorescent emitters we refer to the literature.<sup>158,159</sup> Significant advancements have been reported by Nakayama et al.<sup>160</sup> Molecular structures of the sky-blue emitters are not disclosed yet, but device performance has been reported<sup>161</sup> and blue phosphorescent OLED with a KMBD-342 emitter doped into Konica Minolta's proprietary host material shows blue phosphorescence with an emission maximum of 472 nm, 17% EQE, 42 cd/A, and 16,000 h of lifetime at an initial luminance of 300 cd/m<sup>2</sup>. This performance is one of the best reported for blue triplet OLEDs.

#### 14.4.3 White OLED Devices Based on Phosphorescent Emitters

As described in Sections 14.3.5 to 14.3.8, white-emitting OLED devices are of great interest for application as a solid-state lighting sources, backlights for LCDs, and AMOLED displays incorporating color filters to form the R, G, B emission. Although white OLEDs based on fluorescent dopants gave power efficacies of about 34 lm/W for single-stack structures with an internal extraction layer (Section 14.3.8) and 19 lm/W for two-stack tandems (Section 14.3.6.4), these values are insufficient to meet the challenges of the ever-increasing threshold set by both display and lighting industries. In fact, current benchmarks for efficacy and lifetime targets for SSL are set at 50 lm/W and 10,000 h at 1000 cd/m<sup>2</sup>, respectively. With technology development, luminous efficacies in excess of 85–90 lm/W for fluorescent-based lamps are expected. The U.S. Department of Energy targets an efficacy of 150 lm/W for commercial OLED luminaires to be achieved by 2015. Certainly, this high efficiency in OLEDs cannot be achieved without the use of phosphorescent OLED technology. As was discussed in the previous sections, use of phosphorescent emitters can provide significantly higher efficiencies and red and green triplet OLEDs now show acceptably long operational lifetimes.<sup>108,130</sup>

##### 14.4.3.1 Single-Stack White OLED Devices Incorporating Phosphorescent Emitters

Device architectures of white OLEDs using phosphorescent emitters can be similar to the architectures described in Section 14.3.5. The white color can be generated by the simultaneous emission of light from multiple emitters in

the correct proportions. A one-stack white OLED may include a single EML with multiple emitters, or several EMLs emitting three primary or two complementary colors to produce white light. The single-stack device generally provides a lower drive voltage compared to tandems or multistack OLEDs, however, it may be difficult to adjust the emission color in a one-stack white OLED by changing only one EML without affecting overall device performance. Maintaining color stability with fade is also challenging: different emitters age with different fade rates, especially when fluorescent and phosphorescent emitters are incorporated in the same device. Tandem structure, although more complicated to fabricate, generally provides enhanced stability over a one-stack format. Tandem white structures with phosphorescent emitters are described in Section 14.4.3.2.

White devices comprising phosphorescent emitters in the light-emitting layers were demonstrated by D'Andrade et al.<sup>162</sup> Three emitting materials—2 wt% iridium(III) bis(2-phenyl quinolyl-N,C<sup>2</sup>) acetylacetone (PQIr) providing red emission, green-emitting 0.5 wt% Ir(ppy)<sub>3</sub>, and deep-blue emitter FIr6 present at 20 wt%—were doped simultaneously in a wide band gap UGH2 host material. Triplet excitons were confined to the EML by the use of TCTA and TPBI in the blocking layers on the anode and cathode side of the triple-doped EML, respectively. Additionally, the use of TCTA and TPBI facilitates injection of both holes and electrons into FIr6. It is believed that excitation of the blue dopant and subsequent energy transfer to the green and red emitters is a dominant mechanism for white emission in devices. The efficiency of the FIr6 dopant limited the EQE of the white device. The highest EQE is observed at lower currents (about 10% at 0.01 mA/cm<sup>2</sup>) and then decreases as the current density is increased. At 10 mA/cm<sup>2</sup> the EQE is 6.7%. Measured at the same current density, an EQE of 10% is observed for an analogous blue phosphorescent OLED.<sup>117</sup> The lower efficiency of the triple-doped white OLED can be attributed to inefficient energy transfer from the blue dopant to Ir(ppy)<sub>3</sub> and PQIr as well as possible concentration quenching of FIr6 when used at 20 wt%. The white phosphorescent OLED has a power efficacy of >20 lm/W at 1000 cd/m<sup>2</sup>.

Another example of a white phosphorescent OLED with triple-doped EML was demonstrated recently.<sup>163</sup> The device architecture was similar to that described above; however, the material structures used were not disclosed. At 1000 cd/m<sup>2</sup> the white triplet OLED showed 25 lm/W, CRI index of 78, and CIE<sub>x,y</sub> of (0.39, 0.44). At 100 cd/m<sup>2</sup>, the device power efficacy reached 30 lm/W, and with outcoupling enhancement the total power efficacy increased to 51 lm/W.

Nakayama et al. reported highly efficient and stable single-stack white phosphorescent OLEDs<sup>160,161</sup> based on blue triplet emitter KMBD-342 described in Section 14.4.2.3. Yellow-green (YD-85) and red (RD-61) dopants used in the device were provided by Universal Display Corporation. The device layer structure was as follows: Light outcoupling film|ITO|HIL|HTL|green EML|red EML|blue EML|HBL|n-doped ETL|Al. At 1000 cd/m<sup>2</sup> the performance

metrics are 34% EQE, 64lm/W, 3.6 V, CIE<sub>x,y</sub> of (0.37, 0.42), color temperature of 4500K, and 10,000h lifetime. Without the light outcoupling film, the EQE was 20%.

Most recently, a very efficient and stable white triplet OLED with a simplified architecture was developed by D'Andrade et al.<sup>164</sup> The device structure is shown in Figure 14.50 and comprises two EMLs where blue, yellow, and red phosphorescent emitters were doped into the same host material. Relatively large concentrations of the blue and yellow emitters were used—18% and 30%, respectively. The red dopant (0.5%) was codeposited into the orange EML simultaneously with the yellow triplet emitter. Recombination is believed to take place at the interface between the EMLs, and generation of white emission occurs by an energy transfer mechanism. At 1000cd/m<sup>2</sup>, the device shows remarkable performance with 15.3% EQE, 34.2 cd/A, 6.3 V, and 16 lm/W. With outcoupling enhancement, the power efficacy increases to 30lm/W. The emission has warm white color with the CIE<sub>x,y</sub> color coordinates are (0.45, 0.46). Very good operational stability is reported—the extrapolated lifetime is estimated to be 200,000 h at 1000cd/m<sup>2</sup>.

The development of white phosphorescent OLEDs is severely limited by the absence of efficient deep-blue phosphorescent emitters with an operational lifetime suitable for commercial applications. Therefore, OLEDs combining blue fluorescent emitters with longer wavelength-emitting phosphorescent dopants have been considered as an alternative to achieving high efficiencies in white devices. Fluorescent and phosphorescent dopants can be incorporated into the EML(s) of a single-stack OLED, or they may be used in fluorescent and phosphorescent EMLs of individual EL units in stacked devices, as was reported by Murano and Birnstock.<sup>165,166</sup> Note that the use of a fluorescence-emitting layer severely limits the efficiency of the white OLED because of the waste of 75% of the triplet excitons formed during recombination in this layer. An alternative approach to attain high efficiency while still including fluorescent materials is through a triplet-harvesting mechanism involving migration of triplet excitons out of the blue fluorescent EML into a phosphorescent EML. Devices employing

LiF/Al
LG201 (30 nm)
Host1 (5 nm)
Host1:blue (25 nm)
Host1:yellow:red (30 nm)
LG101 (10 nm)
ITO (120 nm)
Glass

**FIGURE 14.50**

Schematic of white phosphorescent OLED device with six organic materials. (Reproduced from D'Andrade, B. et al., *SID Int'l. Symp. Dig. Tech. Papers*, 39, 940, 2008. With permission.)

such triplet harvesting can, in principal, achieve an internal quantum efficiency of 100% by confining recombination in a fluorescent EML and converting the resulting singlet excitons to blue light, while forcing the triplet excitons formed at recombination in the fluorescent layer to diffuse into a nearby phosphorescent EML where one or more phosphorescent dopants harvest and convert these triplet excitons to light.<sup>167–169</sup> This approach to white emission generation opens a completely new way of white OLED development.

We demonstrated highly efficient white OLED devices based on this concept.<sup>169</sup> We refer to the devices as hybrid-harvesting OLEDs (HHOLEDs). Harvesting OLED devices entails extremely complex material requirements and architecture designs. In particular, a high triplet energy host material must be used in the blue fluorescent light-emitting layer to sensitize both fluorescence and phosphorescence. Also, the blue fluorescent dopant cannot trap triplet excitons formed in the blue EML and the charge-transport layers should have sufficient triplet energy to block triplet exciton migration in undesirable directions. Additionally, the triplet emitter must not have charge-trapping properties, otherwise, recombination will take place on the phosphorescent dopant instead of on the blue singlet emitter, which will result in loss of blue photons and reduced efficiency. Following these requirements, blue fluorescent and yellow phosphorescent light-emissive layers separated by an appropriate spacer layer were combined in a single-stack architecture, as shown in Figure 14.51. The device is designed so that electrons are blocked from reaching the blue EML, and recombination is most likely to occur at the blue EML|spacer interface. The thickness of the organic layers was optimized to achieve an efficient blue fluorescence. The blue EML consists of a CBP host doped with Kodak's proprietary blue singlet dopant. The spacer layer prevents Förster energy transfer from the blue EML to the yellow emitter while allowing the diffusion of triplets into the yellow EML by Dexter energy transfer. These energy transfer processes likely occur over different length scales, hence, the spacer layer thickness can be optimized so that there is little quenching of the blue emission, yet there is

Cathode:Al (1000 Å)
EIL:LiF (5 Å)
ETL:Bphen (370 Å)
Yellow emission layer:(100 Å)
Spacer:(80 Å)
Blue emission layer:(50 Å)
EBL:TCTA (100 Å)
HTL:NPB (750 Å)
Anode:ITO (250 Å)
Glass substrate

**FIGURE 14.51**

Schematic structure of the white hybrid harvesting OLED.

appreciable emission from the yellow EML. For efficient transfer of triplet excited states from the blue EML to the yellow EML, host materials were selected so that the triplet energy of the blue host (CBP) exceeds the triplet energies of the phosphorescent host and the spacer material. The structure of the *fas*-Bis(2-phenylpyridyl)(2-pyridylcoumarin)iridium(III) yellow emitter is shown in the inset of Figure 14.52. An exciton-blocking layer of TCTA was used to prevent loss of triplets to the HTL. The spectrum of a blue|yellow (B|Y) device is shown in Figure 14.52, where emission from both light-emissive layers is observed. The B|Y hybrid device exhibits an EQE of 15.8% at a current density of  $0.01\text{ mA/cm}^2$ , which decreases gradually as the current increases. At  $1000\text{ cd/m}^2$  ( $3.2\text{ mA/cm}^2$ ), the performance metrics are 13.6% EQE, 3.8 V, 30.1 lm/W, 34.8 cd/A, and CIE $x,y$  of (0.317, 0.364). All of these results are without optical outcoupling enhancement. The color change with current is not significant;  $\Delta\text{CIE}u'v'$  is 0.0088 in the range of current densities from 0.05 to  $80\text{ mA/cm}^2$ .

The triplet-harvesting mechanism was confirmed by efficiency analysis of the B|Y device spectra. A blue fluorescent (BF) device was constructed similarly to the B|Y except that the phosphorescent emitter was omitted. The blue portion of the spectrum (380–512 nm) of the BF device exhibits 4.9% EQE, indicating very efficient fluorescence. Figure 14.52 shows that devices B|Y and BF have nearly identical spectral radiance for the blue component of the electroluminescence. Thus, fluorescence remained the same while the addition of the phosphorescent dopant to the BF device resulted in the appearance

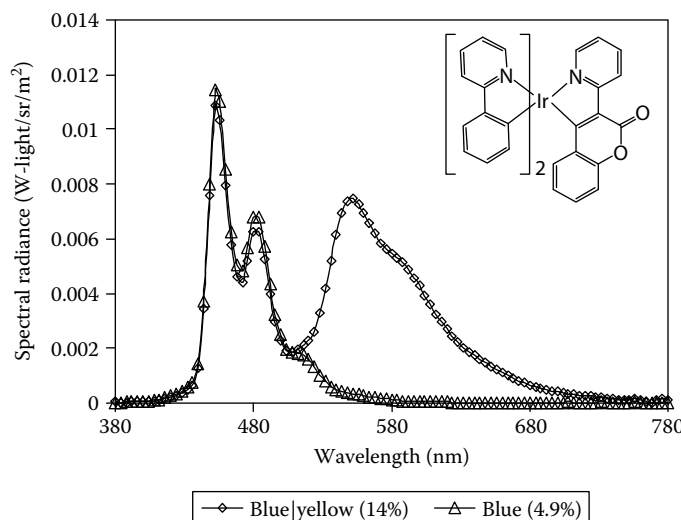


**FIGURE 14.52**

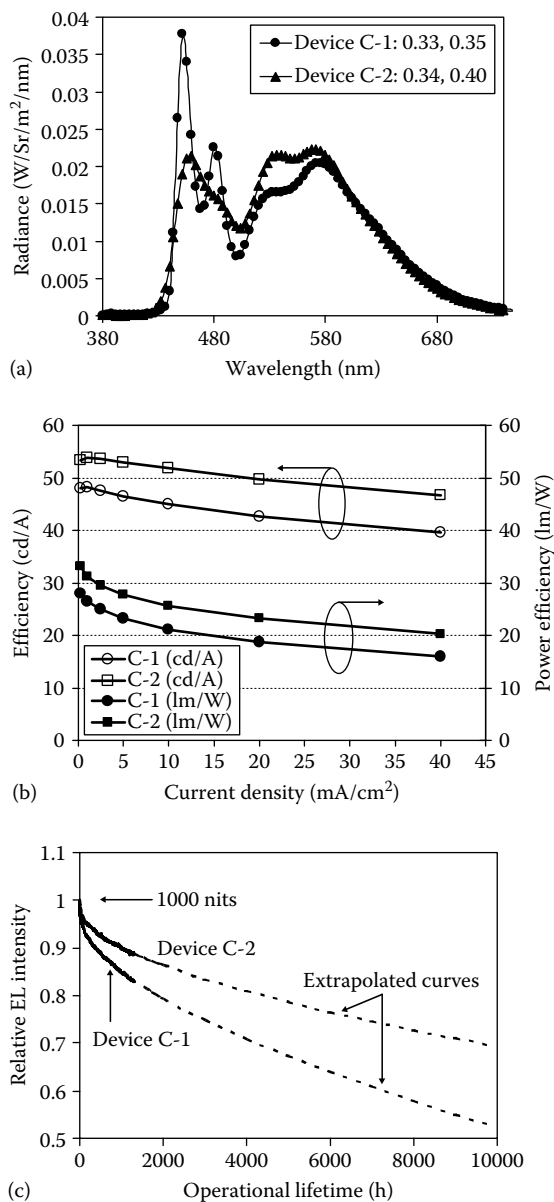
Spectra of blue|yellow (B|Y) harvesting hybrid and blue fluorescent OLEDs. Blue device has the same structure as B|Y except that the yellow phosphorescent emitter is omitted. Data are taken at  $1\text{ mA/cm}^2$ . Inset: Structure of the yellow phosphorescent dopant.

of yellow phosphorescence. These data show that the triplet excitons are captured by the yellow triplet dopant without affecting utilization of the singlet excitons for blue fluorescence in the B|Y device. The hypothesis of triplet migration in the B|Y device was further proven by several physical methods, such as time-resolved electroluminescence and magnetic field effect on the electroluminescence.<sup>169</sup> The results will be described elsewhere.

The B|Y HHOLED shows excellent color characteristics. Transmission curves of color filter materials developed by Eastman Kodak Company<sup>68</sup> were mathematically applied to the B|Y spectrum. Modeling shows that the  $\text{CIE}_{x,y}$  of the red and blue resulted from the emission spectrum cascaded through color filters lie practically on the locus, indicating highly saturated color. The color gamut of the B|Y device using the Kodak color filters is 97% NTSC, which is sufficient for display application. Alternatively, a white-harvesting device can be realized by combining the blue fluorescent emitter and proper proportions of green and red phosphorescent emitters. Harvesting devices having nonwhite emission may also be useful when combined with additional fluorescent or phosphorescent elements in series in the stacked OLED. Other studies conducted on the hybrid white OLED devices can be found in Refs. [170–172].

#### **14.4.3.2 Tandem White Devices with Phosphorescent Emitters**

High-efficiency OLEDs can be realized by the use of a tandem architecture—multiple EL units are connected by charge-generating layers, as was described in Section 14.3.6. Light-emitting layers of the EL units may include only phosphorescent emitters, or fluorescent and phosphorescent dopants can also be combined in the EML of a single stack, or, alternatively, singlet and triplet emitters can be used in the EMLs of separate EL units. The latter devices are called hybrid OLEDs. Note that compared to hybrid harvesting devices, these architectures are not designed to utilize the 75% of triplets generated in the fluorescent EML for light emission. Stacked architectures offer several important advantages, including being significantly more efficient compared to single-stack OLEDs, it is easier to adjust device color, and, most importantly, tandem OLEDs generally exhibit longer operational lifetimes. This said, single-stack devices generally are competitive in power efficiency. Efficient white hybrid OLEDs were realized by mixing both fluorescent and phosphorescent emitters in the emission layers of two- and three-stack devices.<sup>173</sup> A simpler approach to maintain efficiency and stability in white OLEDs is the usage of a blue fluorescent EL unit in a separate stack connected with a phosphorescent EL unit of a complementary color. Liao et al. demonstrated efficient white tandem OLED devices including a fluorescent blue EL unit and a phosphorescent green and red (or orange) EL unit using this approach.<sup>174</sup> In Figure 14.53, devices C-1 and C-2 differ only by the fluorescent emitter used in the blue

**FIGURE 14.53**

Spectra (a), efficiency–current characteristics (b), and operational lifetimes (c) of tandem white hybrid devices. (Reproduced from Liao, L.-S. et al., *SID Int. Symp. Dig. Tech. Papers*, 39, 818, 2008. With permission.)

EML while the phosphorescent orange-emitting stack was the same for both devices. As shown, high luminous yield, power efficacy, good color gamut, and satisfactory device lifetime were attained. At 1000cd/m<sup>2</sup> device C-1 has the following performance: 22% EQE, 50 cd/A, 25lm/W, 6.2 V, CIEx,y of (0.33, 0.35), and 10,000 h of operational stability. The performance metrics of device C-2 are 23% EQE, 57 cd/A, 30lm/W, 5.9 V, CIEx,y of (0.34, 0.40), and 30,000 h of lifetime. With the hybrid approach, a significantly higher efficiency can be attained in white OLEDs compared to fluorescent-based devices. At present, the operational stability of the hybrid white OLEDs is inferior to lifetimes of the tandem devices with all fluorescent materials; however, further improvements are expected as new materials and architectures are implemented.

A three-stack tandem white hybrid OLED with separate monochromatic EL units (fluorescent blue, phosphorescent green, and a phosphorescent red) connected in series was reported by Murano et al.<sup>165</sup> Electrically doped charge-transport layers were included in the device structure. This three-organic-stack architecture allowed the R, G, B stacks to be placed in their optimal optical positions in order to achieve the best efficiency. At 1000cd/m<sup>2</sup> the devices exhibit 16.3 lm/W, CIEx,y coordinates of (0.35, 0.37), and CRI of 95. The efficiency was reported without optical outcoupling enhancement. Further modification of the three-stack architecture and use of the advanced p-dopant NDP-9 in the HTL and n-type dopant NDN-26 in the ETL of NET-18 led to dramatic improvements in device performance.<sup>166</sup> The red and green phosphorescent EMLs were placed at the first and second optical maximum, respectively, and the blue fluorescent EML of the singlet EL unit was placed in the third maximum (the blue EL stack is the closest to the anode). Measured with an outcoupling enhancement film at 1000cd/m<sup>2</sup>, the devices show 38lm/W, CIEx,y of (0.43, 0.43), and CRI of 90. The white emission is suitable for SSL application. The performance characteristics obtained without an outcoupling enhancement foil are as follows: 28lm/W, CIEx,y (0.39, 0.42). Most importantly, the operational stability of the white hybrid OLED exceeds 100,000 h. The triple-stack white hybrid OLED shows flat dependence of EQE on luminance; even at 10,000 nits the power efficacy does not decrease below 30lm/W.

In summary, various architectures of white-emitting OLED devices incorporating phosphorescent emitters have been demonstrated. Mechanism of white-emission generation depends on the device structure. All of these devices show significantly higher luminous efficiencies compared to fluorescent white OLEDs. Recently obtained data show that hybrid single- and multistacked white devices are capable of exhibiting sufficiently long operational stability. This approach to white OLED design has a potential to become a main technology for the development of OLED displays and SSL products.

## 14.5 Future Outlook

Considerable progress has been made in developing the materials and architecture for R, G, B, and W emitting devices. High efficiency, lifetimes exceeding 10 years for some colors, and color gamut equivalent to 100% NTSC<sub>x,y</sub> have been demonstrated and this has enabled the fabrication of full-color displays a reality. Evidence of the considerable progress made in the OLED technology is clearly evident by the tremendous interest shown by the display and lighting manufacturers. Future trends in OLED development include large-area displays suitable for television screens, computer monitors, and flexible displays. However, to impact these display market segments, AMOLED panels must be competitively priced with identically sized AMLCD and PDP TVs. Another area of focused activity will be on solid-state lighting applications. White OLEDs have already surpassed the power efficacy of fluorescent lamps and OLED panels can become a premier low-cost lighting technology. Certainly, there are challenges to make the product cost competitive. Continuous progress in improving the power efficiency and lifetime and reducing the manufacturing cost are required to meet these challenges.

---

## Acknowledgments

The authors acknowledge the help and contributions of several colleagues who were instrumental in developing OLED technology at Eastman Kodak Company. They include S. A. Van Slyke, C. W. Tang, Y.-S. Tyan, W. J. Begley, L. S. Liao, M. L. Ricks, M. J. Helber, R. H. Young, R. J. Vargas, K. P. Klubek, D. Y. Kondakov, J. C. Deaton, V. V. Jarikov, T. D. Pawlik, X. Ren, C. T. Brown, T. L. Royster, and B. Owczarczyk. The authors also thank A. Pletean, R. S. Cupello, D. L. Comfort, D. A. Prosperi, R. L. Winter, D. J. Neill, and D. R. Arnold for device fabrication and testing.

---

## References

1. Tang, C. W. and Van Slyke, S. A. 1987. Organic electroluminescence diodes. *Appl. Phys. Lett.* 51:913.
2. Tang, C. W., Van Slyke, S. A., and Chen, C. H. 1989. Electroluminescence of doped organic thin films. *J. Appl. Phys.* 65:3610.
3. Van Slyke, S. A., Chen, C. H., and Tang, C. W. 1996. OLED devices with improved stability. *Appl. Phys. Lett.* 69:2160.

4. Rajeswaran, G., Itoh, M., Boroson, M. et al. 2000. Active matrix low temperature poly-Si TFT/OLED full color displays: development status. *SID Intl. Symp. Dig. Tech. Papers* 31:974.
5. Wakimoto, T., Murayama, R., Nagayama, K., Okuda, Y., Nakada, H., and Tohma, T. 1996. Organic LED dot-matrix display. *SID Intl. Symp. Dig. Tech. Papers* 27:849.
6. Tsujimura, T., Kobayashi, Y., Murayama, K. et al. 2003. A 20-inch OLED display driven by super-amorphous-silicon technology. *SID Intl. Symp. Dig. Tech. Papers* 34:6.
7. Chung, K. H. and Lee, K. Y. 2005. Alternative approach to large size AMOLED HDTV. *SID Intl. Symp. Dig. Tech. Papers* 36:956.
8. Tsao, J. (ed.). 2002. *Organic Light Emitting Diodes (OLEDs) for General Illumination, Update 2002, An OIDA Technology Roadmap*. [http://www.netl.doe.gov/ssl/PDFs/Report%20led%20November%202002a\\_1.pdf](http://www.netl.doe.gov/ssl/PDFs/Report%20led%20November%202002a_1.pdf) (Accessed September 5, 2008).
9. Duggal, A. R., Foust, D. F., Nealon, W. F. et al. 2004. OLEDs for lighting: New approaches. *Proc. SPIE* 5214:241.
10. Kido, J., Hongawa, H., Okuyama, K. et al. 1994. White light-emitting organic electroluminescent devices using the poly(N-vinylcarbazole) emitting layer doped with three fluorescent dyes. *Appl. Phys. Lett.* 64:815.
11. Ghosh, A. and VanSlyke, S. A. 2006. OLEDs: The challenges ahead. *Inform. Display* 26:2.
12. Chung, J. C., Jung, J., Choi, B. et al. 2006. Is AMOLED TV ready to enter the battle for large screen FPD dominance. *Inform. Display* 22:12.
13. Liao, L.-S., Klubek, K. P., and Tang, C. W. 2004. High-efficiency tandem organic light-emitting diodes. *Appl. Phys. Lett.* 84:167.
14. Matsumoto, T., Nakada, T., Endo, J. et al. 2003. Multi-photon organic EL device having charge generation layer. *SID Intl. Symp. Dig. Tech. Papers* 34:979.
15. Baldo, M. A., O'Brien, D. F., You, Y. et al. 1998. Highly efficient phosphorescent emission from organic electroluminescent devices. *Nature* 395:151.
16. Baldo, M. A., Lamansky, S., Burrows, P. E. et al. 1999. Very high-efficiency green organic light-emitting devices based on electrophosphorescence. *Appl. Phys. Lett.* 75:4.
17. Jarikov, V. V., Kondakov, D. Y., and Brown, C. T. 2007. Efficient and extremely long-lived organic light emitting diodes based on dinaphthylperylene. *J. Appl. Phys.* 102:104908.
18. Forrest, S. R., Bradley, D. D. C., and Thompson, M. E. 2003. Measuring the efficiency of organic light-emitting devices. *Adv. Mater.* 15:1043.
19. Brown, A. R., Pichler, K., Greenham, N. C., Bradley, D. D. C., Friend, R. H., and Holmes, A. B. 1993. Optical spectroscopy of triplet excitons and charged excitations in poly(*p*-phenylenevinylene) light-emitting diodes. *Chem. Phys. Lett.* 210:61.
20. Baldo, M. A., O'Brien, D. F., Thompson, M. E. et al. 1999. Excitonic singlet-triplet ratio in a semiconducting organic thin film. *Phys. Rev. B* 60:14442.
21. Wohlgemann, M., Tandon, K., Mazumdar, S., Ramasesha, S., and Vardeny, Z. V. 2001. Formation cross-sections of singlet and triplet excitons in  $\pi$ -conjugated polymers. *Nature* 409:494.
22. Kondakov, D. 2007. Characterization of triplet-triplet annihilation in OLED based on anthracene derivatives. *J. Appl. Phys.* 102:114504.

23. Reineke, S., Walzer, K., and Leo, K. 2007. Triplet-exciton quenching in organic phosphorescent light-emitting diodes with Ir-based emitters. *Phys. Rev. B* 75:125328.
24. Kondakov, D. 2008. Role of triplet-triplet annihilation in highly efficient fluorescent devices. *SID Intl. Symp. Dig. Tech. Papers* 39:617.
25. Bulović, V., Khalfin, V. B., Gu, G., Burrows, P. E., Garbuzov, D. Z., and Forrest, S. R. 1998. Weak microcavity effects in organic light-emitting devices. *Phys. Rev. B* 58:3730.
26. Tanaka, D., Sasabe, H., Li, Y.-J. et al. 2007. Ultra high efficiency green organic light-emitting devices. *Jpn. J. Appl. Phys.* 46:L10.
27. Watanabe, S., Ide, N., and Kido, J. 2007. High-efficiency green phosphorescent organic light-emitting devices with chemically doped layers. *Jpn. J. Appl. Phys.* 46:1186.
28. Okumoto, K., Kanno, H., Hamada, Y., Takahashi, H., and Shibata, K. 2006. Green fluorescent organic light-emitting device with external quantum efficiency of nearly 10%. *Appl. Phys. Lett.* 89:063504.
29. Smith, T. and Guild, J. 1931. The C.I.E. colorimetric standards and their use. *Trans. Opt. Soc.* 33:73.
30. Sluyterman, S. 2006. The NTSC color triangle is obsolete, but no one seems to know. *Inform. Display* 24:8.
31. Adachi, C., Tokita, S., Tsutsui, T. et al. 1998. Organic electroluminescent device with three-layer structure. *Jpn. J. Appl. Phys.* 27:L713.
32. Shirota, Y. and Kageyama, H. 2007. Charge carrier transporting molecular materials and their applications in devices. *Chem. Rev.* 107:953.
33. Sagari, T. P. I., Spehr, T., Siebert, A. et al. 2007. Spiro compounds for organic optoelectronics. *Chem. Rev.* 107:1011.
34. Shi, J., Chen, C., and Klubek, K. P. 1999. Organic electroluminescent elements for stable blue electroluminescent devices. U.S. Patent 5,972,247.
35. Klubek, K. P. and Kondakov, D. Y. 2007. Improving operating lifetime of blue OLEDs with phenanthroline-based electron transport materials. *SID Intl. Symp. Dig. Tech. Papers* 38:1290.
36. Begley, W. J. and Hatwar, T. K. 2006. Novel electron-transporting layer for lowering drive voltage and improving the efficiency of OLED devices. *SID Intl. Symp. Dig. Tech. Papers* 37:942.
37. Begley, W. J. and Hatwar, T. K. 2007. High performance organic electron injecting and transporting layers for R, G, B and white OLEDs. *SID Intl. Symp. Dig. Tech. Papers* 38:1286.
38. Royster, T., Ricks, M., and Kondakov, D. 2007. Performance of highly efficient electron transporting materials. *SID Intl. Symp. Dig. Tech. Papers* 38:41.
39. Wu, C. C., Wu, C. I., Sturm, J. C. et al. 1997. Surface modification of indium tin oxide by plasma treatment: An effective method to improve the efficiency, brightness, and reliability of organic light emitting diodes. *Appl. Phys. Lett.* 70:1348.
40. Mason, M. G., Hung, L. S., Tang, C. W. et al. 1999. Characterization of treated indium-tin-oxide surfaces used in electroluminescent devices. *J. Appl. Phys.* 86:1688.
41. Hung, L. S., Zheng, L. R., and Mason, M. G. 2001. Anode modification in OLED by low frequency plasma polymerization of CHF<sub>3</sub>. *Appl. Phys. Lett.* 78:673.

42. Chan, I. M. and Hong, F. C. N. 2003. Plasma treatment of indium tin oxide anodes in carbon tetrafluoride ( $\text{CF}_4$ )/oxygen ( $\text{O}_2$ ) to improve the performance of organic light-emitting diodes. *Thin Solid Films* 444:254.
43. Kim, J. S., Granström, M., Friend, R. H. et al. 1998. Indium-tin oxide treatments for single- and double-layer polymeric light emitting diodes: The relation between the anode physical, chemical, and morphological properties and device performance. *J. Appl. Phys.* 84:6859.
44. Wang, X., Rundle, P., Bale, M., and Mosley, A. 2003. Improved operating lifetime of phosphorescent OLED by novel anode coating. *Synth. Met.* 137:1051.
45. Noh, J. K., Kang, J. B., and Kim, J. S. 2008. Inverted OLED. *SID Intl. Symp. Dig. Tech. Papers* 39:212.
46. Chen, S.-F. and Wang, C.-W. 2004. Influence of the hole injection layer on the luminescent performance of organic light-emitting diodes. *Appl. Phys. Lett.* 85:765.
47. Yamada, T., Tsubata, Y., Sekine, C., and Ohnishi, T. 2008. Recent progress in light-emitting polymers for full color OLEDs. *SID Intl. Symp. Dig. Tech. Papers* 39:404.
48. Mason, M. G., Tang, C. W., Hung, L.-S. et al. 2001. Interfacial chemistry of  $\text{Alq}_3$  and LiF with reactive metals. *J. App. Phys.* 89:2756.
49. Hung, L. S., Tang, C. W., Mason, M. G. et al. 2001. Application of an ultrathin LiF/Al bi-layer in OLED surface emitting diode. *Appl. Phys. Lett.* 78:544.
50. Endo, J., Matsumoto, T., and Kido, J. 2002. Organic electroluminescent devices having metal complexes as cathode interface layer. *Jpn. J. Appl. Phys.* 41:L800.
51. Pfeiffer, M., Leo, K., Zhou, X. et al. 2003. Doped organic semiconductors: Physics and application in light emitting diodes. *Org. Electron.* 4:89.
52. Walzer, K., Maennig, B., Pfeiffer, M. et al. 2007. Highly efficient organic devices based on electrically doped transport layers. *Chem. Rev.* 107:1233.
53. Birnstock, J., Canzler, T., Hofmann, M. et al. 2008. PIN OLEDs-improved structures and materials to enhance device lifetime. *J. Soc. Inf. Display* 16:221.
54. Young, R. H., Shi, J., and Tang, C. W. 2004. Organic light emitting diode devices with improved luminance efficiency. U.S. Patent, 6,720,090.
55. Chen, H., Tang, C. W., Shi, J. et al. 1997. Improved red dopants for organic EL devices. *Macromol. Symp.* 125:49.
56. Hamada Y., Kanno, H., and Tsujioka, T. 1999. Red organic light-emitting diodes using an emitting assist dopant. *Appl. Phys. Lett.* 75:1682.
57. Hatwar, T. K., Brown, C. T., Cosimescu, L. et al. 2004. Development in OLED formulations with improved efficiency and stability. *Proc. SPIE* 5519:1.
58. Jarikov, V. V., Vargas, J. R., Kondakov, D. Y., Young, R. H., Klubek, K. P., and Liao, L.-S. 2007. Improving operating lifetime of organic light-emitting diodes with perylene and derivatives as aggregating light-emitting-layer additives. *SID Intl. Symp. Dig. Tech. Papers* 38:1188.
59. Aziz, H., Popovic, Z. D., Hu, N.-X., Hor, A.-M., and Xu, G. 1990. Degradation mechanism of small molecule-based organic light-emitting devices. *Science* 283:1990.
60. Kondakova, M. E., Deaton, J. C., Kondakov, D. Y. et al. 2007. High-efficiency low-voltage phosphorescent OLED devices with mixed host. *SID Intl. Symp. Dig. Tech. Papers* 38:837.
61. Krishnamurthy, S., Brown, C. T., Vargas, J., Cosimescu, L., Kondakov, D., and Alessi, P. 2003. New generation of OLED materials. *Paper presented at the 23rd International Display Research Conference*, September 16–18, Phoenix, AZ.

62. Nishimura, K., Kawamura, M., Jinde, Y. et al. 2008. The improvement of white OLED's performance. *SID Intl. Symp. Dig. Tech. Papers* 39:1971.
63. Birnstock, J., Canzler, T., Hofmann, M. et al. 2007. PIN OLEDs-improved structures and materials to enhance device lifetime and ease mass production. *SID Intl. Symp. Dig. Tech. Papers* 30:1193.
64. Mitschke, U. and Bauerle, P. 2000. The electroluminescence of organic materials. *J. Mater. Chem.* 10:1471.
65. Hing, L. S. and Chen, C. H. 2002. Recent progress of molecular organic electroluminescent materials and devices. *Mat. Sci. Eng. R* 39:143.
66. Kuma, H., Jinde, J., Kawamura, M. et al. 2007. Highly efficient white OLEDs using RGB fluorescent materials. *SID Intl. Symp. Dig. Tech. Papers* 38:1504.
67. Helber, M., Ricks, M., and Cosimescu, L. 2005. Highly efficient and stable blue OLED systems. *SID Intl. Symp. Dig. Tech. Papers* 36:863.
68. Helber, M., Alessi, P., Burbury M. et al. 2007. Color filter formulations for full color OLED displays: High color gamut plus improved efficiency and lifetime. *SID Intl. Symp. Dig. Tech. Papers* 38:1022.
69. Novaled. 2008. *OLED & Organic Electronics Solution Provider. Data presented at SID 2008 exhibition*, Los Angeles, CA.
70. Eastman Kodak Company. 2008. *Enabling the OLED industry. Data Presented at SID 2008 Exhibition*, Los Angeles, CA.
71. Ricks, M., Vargas, J. R., Klubek, K. P. et al. 2007. Efficient, long-lifetime OLED host and dopant formulations for full-color displays. *SID Intl. Symp. Dig. Tech. Papers* 38:830.
72. Hatwar, T. K. and Spindler, J. P. 2008. Development of white OLED technology for application in full-color displays and solid state lighting. In *Luminescent Materials and Applications*, A. Kitai (ed.), John Wiley & Sons, Hoboken, NJ, pp. 111–159.
73. Hatwar, T. K., Young, R. H., and Rajeswaran, G. 2001. White OLEDs with excellent stability and manufacturability. *Paper Presented at the 21st International Display Research Conference Asia Display/IDW'01*, Nagoya, Japan.
74. Mameno, K., Suzuki, K., Ichikawa, S. et al. 2002. Active matrix full color OLED displays with high efficiency white OLEDs and ON-chip color filters. *Abstracts of the 8th IUMRS International Conference on Electronic Materials G-06*, June 10–14, 2002, Xian, China.
75. Hatwar, T. K., Spindler, J. P., Ricks, M. L. et al. 2004. High efficiency white OLEDs based on small molecule. *Proc. SPIE*, 5214:233.
76. Hatwar, T. K., Spindler, J. P., and Van Slyke, S. A. 2004. High performance white OLEDs for full color displays. *Paper Presented at the 12th International Workshop on Inorganic and Organic Electroluminescence and International Conference on the Science and Technology of Emissive Displays and Lighting*, Toronto, Canada.
77. Hatwar, T.K., Spindler, J. P., Ricks, M. L. et al. 2004. White OLED structures optimized for RGB and RGBW formats. *Paper Presented at the 24th International Display Research Conference ASIA Display*, Daegu, Korea.
78. Hatwar, T. K. and Spindler, J. P. 2008. Novel approach to stabilize blue OLEDs and fabrication of high efficiency tandem white OLEDs for large-area display applications. *SID Intl. Symp. Dig. Tech. Papers* 39:814.
79. Spindler, J. P. and Hatwar T. K. 2007. Development of tandem white architecture for large-sized AMOLED displays with wide color gamut. *SID Intl. Symp. Dig. Tech. Papers* 38:89.

80. Liao, L.-S., Klubek, K. P., Helber, M. J., Cosimescu, L., and Comfort, D. 2007. High efficiency tandem blue OLEDs. *SID Intl. Symp. Dig. Tech. Papers* 38:1197.
81. Kanno, H., Hamada, Y., Nishimura, K., et al. 2006. High efficiency stacked organic light emitting diodes employing  $\text{Li}_2\text{O}$  as a connecting layer. *Jpn. J. Appl. Phys.* 45:9219.
82. Guo, F. and Ma, D. 2005. White OLEDs based on tandem structures. *Appl. Phys. Lett.* 87:173510.
83. Kanno, H., Holmes, R. J., Sun, Y., Cohen, S. K., and Forrest, S. R. 2006. White stacked electrophosphorescent OLEDs employing  $\text{MoO}_3$  as a charge generation layer. *Adv. Mater.* 18:339.
84. Liao, L.-S., Slusarek, W., Hatwar, T. K., Ricks, M., and Comfort, D. 2008. Tandem OLED using hexaazatriphenylene hexacarbonitrile in the intermediate connector. *Adv. Mater.* 20:324.
85. Spindler, J. P., Hatwar, T. K., Miller, M. E. et al. 2005. Lifetime and power enhanced RGBW displays based on white OLEDs. *SID Intl. Symp. Dig. Tech. Papers* 36:36.
86. Hatwar, T. K., Spindler, J. P., Vargas, J. R. et al. 2007. Advances in white OLED tandem architectures for next generation AMOLED displays. *IMID 2007 Digest*. 231.
87. Spindler, J. P. and Hatwar, T. K. 2008. High efficiency tandem white based on fluorescent emitters. *Paper Presented at the 28th International Display Research Conference*, Orlando, FL.
88. Duggal, A. R., Shiang, J. J., Foust, D. F., Turner, L., Nealon, W., and Borscheller, J. 2005. Large area white OLEDs. *SID Intl. Symp. Dig. Tech. Papers* 36:28.
89. Duggal, A. R., Shiang, J. J., Foust, D. F., and Heller C. M. 2002. OLEDs for illumination quality white. *Appl. Phys. Lett.* 80:3470.
90. Tyan, Y.-S., Rao, Y., Wang, J. S., Kesel, R., Cushman, T. R., and Begley, W. J. 2008. Fluorescent white OLED devices with improved light extraction. *SID Intl. Symp. Dig. Tech. Papers* 39:933.
91. Adachi, C., Thompson, M. E., and Forrest, S. R. 2002. Architectures for efficient electrophosphorescent organic light emitting devices. *IEEE J. Select. Top. Quantum Electron.* 8:372.
92. Yersin, H. and Finkenzeller, W. J. 2008. Triplet emitters for organic light-emitting diodes: Basic properties. In *Highly Efficient OLEDs with Phosphorescent Materials*, H. Yersin (ed.), Wiley-VCH Verlag, Weinheim, Germany, pp. 1–97.
93. Lamansky, S., Djurovich, P., Murphy, D. et al. 2001. Highly phosphorescent bis-cyclometalated iridium complexes: synthesis, photophysical characterization, and use in organic light emitting diodes. *J. Am. Chem. Soc.* 123:4304.
94. Tamayo, A. B., Alleyne, B. D., Djurovich, P. I. et al. 2003. Synthesis and characterization of facial and meridional tris-cyclometalated iridium(III) complexes. *J. Am. Chem. Soc.* 125:7377.
95. Djurovich, P. I. and Thompson, M. E. 2008. Cyclometalated organometallic complexes as emitters in electrophosphorescent devices. In *Highly Efficient OLEDs with Phosphorescent Materials*, H. Yersin (ed.), Wiley-VCH Verlag, Weinheim, Germany, pp. 131–183.
96. Baldo, M. A. and Forrest, S. R. 2000. Transient analysis of organic electrophosphorescence: I. Transient analysis of triplet energy transfer. *Phys. Rev. B* 62: 10958.

97. Baldo, M. and Segal, M. 2005. Phosphorescence as a probe of exciton formation and energy transfer in organic light emitting diodes. In *Physics of Organic Semiconductors*, W. Brüttig (ed.), Wiley-VCH Verlag, Weinheim, Germany, pp. 257–269.
98. Yersin, H. 2004. Organometallic triplet emitters for OLED application. Controlling of emission properties by chemical variation. *Proc. SPIE* 5214:124.
99. O'Brien, D. F., Baldo, M. A., Thompson, M. E. et al. 1999. Improved energy transfer in electrophosphorescent devices. *Appl. Phys. Lett.* 74:442.
100. Adachi, C., Baldo, M. A., and Forrest, S. R. 2001. High-efficiency red electrophosphorescence devices. *Appl. Phys. Lett.* 78:1622.
101. Baldo, M. A., Adachi, C., and Forrest, S. R. 2000. Transient analysis of organic electrophosphorescence. II. Transient analysis of triplet-triplet annihilation. *Phys. Rev. B* 62:10697.
102. Tsuboyama, A., Iwawaki, H., Furigori, M. et al. 2003. Homoleptic cyclometalated iridium complexes with highly efficient red phosphorescence and application to organic light-emitting diodes. *J. Am. Chem. Soc.* 125:12971.
103. Tsuboyama, A., Okada, S., and Ueno, K. 2008. Highly efficient red-phosphorescent iridium complexes. In *Highly Efficient OLEDs with Phosphorescent Materials*, H. Yersin (ed.), Wiley-VCH Verlag, Weinheim, Germany, pp. 163–183.
104. Okada, S. and Ueno, K. 2005. Substituent effect of Ir complexes. *Paper Presented at IDMS Conference*, Taiwan.
105. Tsuji, T., Kawami, S., Miyaguchi, S. et al. 2004. Red-phosphorescent OLEDs employing bis(8-quinolinato)-phenolato-aluminum (III) complexes as emission-layer hosts. *SID Intl. Symp. Dig. Tech. Papers* 35:900.
106. Deaton, J. C., Place, D. W., Brown, C. T. et al. 2008. The blue aluminum and gallium chelates for OLEDs. *Inorg. Chim. Acta* 361:1020.
107. Meerheim, R., Walzer, K., Pfeiffer, M. et al. 2006. Ultrastable and efficient red organic light emitting diodes with doped layers. *Appl. Phys. Lett.* 89:061111-1.
108. Meerheim, R., Scholz, S., Olthof, S. et al. 2008. Influence of charge balance and exciton distribution on efficiency and lifetime of phosphorescent organic light-emitting devices. *J. Appl. Phys.* 104:0145510.
109. Meerheim, R., Scholz, S., Schwartz, G. et al. 2008. Efficiency and lifetime enhancement of phosphorescent organic devices. *Proc. SPIE* 6999:699917-1.
110. Duan, J.-P., Sun, P.-P., and Cheng, C.-H. 2003. New iridium complexes as highly efficient orange-red emitters in organic light-emitting diodes. *Adv. Mater.* 15:224.
111. Scholz, S., Corten, C., Walzer, K. et al. 2007. Photochemical reactions in organic semiconductor thin films. *Org. Electron.* 8:709.
112. Scholz, S., Meerheim, R., Walzer, K. et al. 2008. Chemical degradation mechanisms of organic semiconductor devices. *Proc. SPIE* 6999:69991B-1.
113. Varikov, V. V., Young, R. H., Vargas, J. R. et al. 2006. Operating longevity of organic light-emitting diodes with perylene derivatives as aggregating light-emitting-layer additives: Expansion of the emission zone. *J. Appl. Phys.* 100:094907.
114. Adachi, C., Kwong, R., and Forrest, S. R. 2001. Efficient electrophosphorescence using a doped ambipolar conductive molecular organic thin film. *Org. Electron.* 2:37.
115. Lee, J.-H., Tsai, H.-H., Leung, M.-K. et al. 2007. Phosphorescent organic light-emitting devices with ambipolar oxadiazole host. *Appl. Phys. Lett.* 90:243501.

116. Chwang, A. B., Kwong, R. C., and Brown, J. J. 2003. Graded mixed-layer OLEDs. *Proc. SPIE* 4800:55.
117. Holmes, R. J., D'Andrade, B. W., Forrest, S. R. et al. 2003. Efficient, deep-blue organic electrophosphorescence by guest charge trapping. *Appl. Phys. Lett.* 83:3818.
118. Popovic, Z. D., Aziz, H., Tripp, C. P. et al. 1998. Improving the efficiency of organic light emitting devices by using mixed emitting layers. *Proc. SPIE* 3476:68.
119. Popovic, Z. D. and Aziz, H. 2002. Reliability and degradation of small molecule-based organic light-emitting devices (OLEDs). *IEEE J. Select. Top. Quantum Electron.* 8:362.
120. Kwong, R., Hack, M. G., Zhou, T. et al. Highly stable and efficient OLEDs with a phosphorescent-doped mixed layer architecture. U.S. Patent 6,803,720 B2.
121. Anthopoulos, T. D., Markham, J. P. J., Namdas, E. B. et al. 2003. Highly efficient single layer dendrimer light-emitting diodes with balanced charge transport. *Appl. Phys. Lett.* 82:4824.
122. Kim, S. H., Jang, J., Lee, J. Y. et al. 2007. Relationship between host energy levels and device performances of phosphorescent organic light-emitting diodes with triplet mixed host emitting structure. *Appl. Phys. Lett.* 91:083511.
123. Kim, S. H., Jang, J., Yook, K. S. et al. 2008. Triplet host engineering for triplet exciton management in phosphorescent organic light-emitting diodes. *J. Appl. Phys.* 103:054502.
124. Brown, C. T., Deaton, J. C., Place, D. W. et al. 2005. Host materials for orange and red phosphorescent OLEDs. *SID Intl. Symp. Dig. Tech. Papers* 36:850.
125. Kondakova, M. E., Pawlik, T. D., Young, R. H. et al. 2008. High-efficiency low-voltage phosphorescent OLED devices with mixed host. *J. Appl. Phys.* 104: 094501.
126. Pawlik, T. D., Kondakova, M. E., Giesen, D. J. et al. 2008. Charge carriers and triplets in OLED devices studied by electrically detected magnetic resonance. *SID Intl. Symp. Dig. Tech. Papers* 39:613.
127. Kawamura, Y., Goushi, K., Brooks, J. et al. 2005. 100% phosphorescence quantum efficiency of Ir(III) complexes in organic semiconductor films. *Appl. Phys. Lett.* 86:071104.
128. Kawamura, Y., Brooks, J., Brown, J. J. et al. 2006. Intermolecular interaction and a concentration-quenching mechanism of phosphorescent Ir(III) complexes in a solid film. *Phys. Rev. Lett.* 96:017404-1.
129. Andrieux, C. P., Le Gorande, A., and Saveant, J.-M. 1992. Electron transfer and bond breaking. Examples of passage from a sequential to a concerted mechanism in the electrochemical reductive cleavage of arylmethyl halides. *J. Am. Chem. Soc.* 114:6892.
130. Universal Display Corporation. 2008. Features and performance of PHOLEDs. [www.universaldisplay.com/default.asp?contentID=604](http://www.universaldisplay.com/default.asp?contentID=604) (accessed August 20, 2008).
131. Van Dijken, A., Brunner, K., Börner, H. et al. 2008. High-efficiency phosphorescent polymer LEDs. In *Highly Efficient OLEDs with Phosphorescent Materials*, H. Yersin (ed.), Wiley-VCH Verlag, Weinheim, Germany, pp. 311–328.
132. Adachi, C., Baldo, M. A., Forrest, S. R. et al. 2000. High efficiency organic electrophosphorescent devices with tris(2-phenyl-pyridine)Iridium doped into electron-transporting materials. *Appl. Phys. Lett.* 77:904.

133. Adachi, C., Baldo, M. A., Thompson, M. E. et al. 2001. Nearly 100% internal phosphorescence efficiency in organic light emitting device. *J. Appl. Phys.* 90:5048.
134. Goushi, K., Kwong, R., Brown, J. J. et al. 2004. Triplet exciton confinement and unconfinement by adjacent hole-transport layers. *J. Appl. Phys.* 95:7798.
135. Adamovich, V. I., Cordero, S. R., Djurovich, P. I. et al. 2003. New charge-carrier blocking materials for high efficiency OLEDs. *Org. Electron.* 4:77.
136. Brunner, K., Van Dijken, A., Börner, H. et al. 2004. Carbazole compounds as host materials for triplet emitters in organic light-emitting diodes: tuning the HOMO level without influencing the triplet energy in small molecules. *J. Am. Chem. Soc.* 126:6035.
137. Watanabe, T., Nakamura, K., Kawami, S. et al. 2001. Optimization of driving lifetime durability in organic LED devices using Ir complex. *Proc. SPIE* 4105:175.
138. Kwong, R. C., Nugent, M. R., Michalski, L. et al. 2002. High operational stability of electrophosphorescent devices. *Appl. Phys. Lett.* 81:162.
139. Hack, M., Weaver, M. S., and Adamovich, V. 2005. Status and potential for phosphorescent OLED technology. *Proc. SPIE* 5961:596102-1.
140. Borsenberger, P. M., Pautmeier, L., and Richert, R. 1991. Hole transport in 1,1-bis(di-4-tolylaminophenyl)cyclohexane. *J. Chem. Phys.* 94:8276.
141. Kondakov, D. Y., Lenhart, W. C., and Nichols, W. F. 2007. Operational degradation of organic light-emitting diodes: Mechanism and identification of chemical products. *J. Appl. Phys.* 101:024512.
142. Kondakov, D. Y., Pawlik, T. D., Nichols, W. F., and Lenhart, W. C. 2008. Free-radical pathways in operational degradation of OLEDs. *J. Soc. Inf. Display* 16:37.
143. Zhou, X., Qin, D. S., Pfeiffer, M. et al. 2002. High-efficiency electrophosphorescent organic light-emitting diodes with double light-emitting layers. *Appl. Phys. Lett.* 81:4070.
144. He, G., Pfeiffer, M., Leo, K. et al. 2004. High-efficiency and low-voltage p-i-n electrophosphorescent organic light-emitting diodes with double-emission layers. *Appl. Phys. Lett.* 85:3911.
145. He, G., Schneider, O., Qin, D. et al. 2004. Very high-efficiency and low-voltage phosphorescent organic light-emitting diodes based on p-i-n junction. *Appl. Phys. Lett.* 95:5773.
146. He, G., Walzer, K., Pfeiffer, M. et al. 2004. Ultra high efficiency electrophosphorescent p-i-n OLEDs with double emission layers. *Proc. SPIE* 5519:42.
147. Jarikov, V. V. 2008. Exciplexes and excimers in fluorescent organic light-emitting diodes. Unpublished data.
148. Birnstock, J., Lux, A., Ammann, M. et al. 2006. Novel materials and structures for highly-efficient, temperature-stable, and long-living AM OLED displays. *SID Intl. Symp. Dig. Tech. Papers* 37:1866.
149. Adachi, C., Kwong, R. C., Djurovich, P. et al. 2001. Endothermic energy transfer: A mechanism for generating very efficient high-energy phosphorescent emission in organic materials. *Appl. Phys. Lett.* 79:2082.
150. Tokito, S., Iijima, T., Suzuri, Y. et al. 2003. Confinement of triplet energy on phosphorescent molecules for highly-efficient organic blue-light-emitting devices. *Appl. Phys. Lett.* 83:569.
151. Holmes, R. J., Forrest, S. R., Tung, Y.-J. et al. 2003. Blue organic electrophosphorescence using exothermic host-guest energy transfer. *Appl. Phys. Lett.* 82:2422.

152. Yeh, S.-J., Wu, M.-F., Chen, C.-T. et al. 2005. New dopant and host materials for blue-light-emitting phosphorescent organic electroluminescent devices. *Adv. Mater.* 17:285.
153. Lei, G., Wang, L., and Qui, Y. 2004. Improved performance of electrophosphorescent organic light-emitting diodes by graded doped emissive layer. *Jpn. J. Appl. Phys.* 43:L1226.
154. Thompson, M. E. and Forrest, S. R. 2004. Materials and devices for blue phosphorescence based organic light emitting diodes. U.S. Patent application US 2004/0155238 A1.
155. Tanaka, D., Agata, Y., Takeda, T. et al. 2007. High luminous efficiency blue organic light-emitting devices using high triplet excited energy materials. *Jpn. J. Appl. Phys.* 46:L117.
156. Sajoto, T., Djurovich, P. I., Tamayo, A. et al. 2005. Blue and near-UV phosphorescence from iridium complexes with cyclometalated pyrazolyl or N-heterocyclic carbene ligands. *Inorg. Chem.* 44:7992.
157. Thompson, M. E., Li, J., Tamayo, A. et al. 2005. Color tuning dopants for electrophosphorescent devices: Towards efficient blue phosphorescence from metal complexes. *SID Intl. Symp. Dig. Tech. Papers* 36:1058.
158. Dedeian, K., Shi, J., Forsythe, E. et al. 2007. Blue phosphorescence from mixed cyano-isocyanide cyclometalated iridium(III) complexes. *Inorg. Chem.* 46:1603.
159. Ren, X., Tyan, Y.-S., Madaras, M. et al. 2008. High-efficiency long-lifetime phosphorescent OLED devices based on electron-trapping iridium(III) complexes. *SID Intl. Symp. Dig. Tech. Papers* 39:864.
160. Nakayama, T., Hiyama, K., Furukawa, K. et al. 2008. Development of a phosphorescent white OLED with extremely high power efficiency and long lifetime. *J. Soc. Inf. Display* 16:231.
161. Nakayama, T., Hiyama, K., Furukawa, K. et al. 2007. Development of a phosphorescent white OLED with extremely high power efficiency and long lifetime. *SID Intl. Symp. Dig. Tech. Papers* 38:1018.
162. D'Andrade, B. W., Holmes, R. J., and Forrest, S. R. 2004. Efficient organic electrophosphorescent white-light-emitting device with triple doped emissive layer. *Adv. Mater.* 16:624.
163. D'Andrade, B. W., Tsai, J.-Y., Lin, C. et al. 2007. Efficient white phosphorescent organic light-emitting devices. *SID Intl. Symp. Dig. Tech. Papers* 38:1026.
164. D'Andrade, B., Esler, J., Lin, C. et al. 2008. Extremely long lived white phosphorescent organic light emitting devices with minimum organic materials. *SID Intl. Symp. Dig. Tech. Papers* 39:940.
165. Murano, S., Burghart, M., Birnstock, J. et al. 2005. Highly efficient white OLEDs for lighting applications. *Proc. SPIE* 5937:59370H/1.
166. Birnstock, J., He, G., Murano, S. et al. 2008. White stacked OLED with 35 lm/W and 100,000 hours lifetime at 1000 cd/m<sup>2</sup> for display and lighting application. *SID Intl. Symp. Dig. Tech. Papers* 39:822.
167. Sun, Y., Giebink, N. C., Kanno, H. et al. 2006. Management of singlet and triplet excitons for efficient white organic light-emitting devices. *Nature* 440:908.
168. Deaton, J. C., Kondakova, M. E., Kondakov, D. Y. et al. 2007. Triplet exciton diffusion in hybrid fluorescent/phosphorescent OLEDs. *SID Intl. Symp. Dig. Tech. Papers* 38:849.

169. Kondakova, M. E., Giesen, D. J., Deaton, J. C. et al. 2008. Highly efficient fluorescent/phosphorescent OLED devices using triplet harvesting. *SID Intl. Symp. Dig. Tech. Papers* 39:219.
170. Schwartz, G., Fehse, K., Pfeiffer, M. et al. 2006. Highly efficient white organic light emitting diodes comprising an interlayer to separate fluorescent and phosphorescent regions. *Appl. Phys. Lett.* 89:083509.
171. Schwartz, G., Walzer, K., Pfeiffer, M. et al. 2006. Highly efficient white organic light emitting diodes combining fluorescent and phosphorescent emitter systems. *Proc. SPIE* 6192:61920Q-1.
172. Lee, J.-I., Chu, H. Y., Yang, Y. S. et al. 2007. Harvest of triplet excitons in fluorescence emission layer based on a wide band gap host of TcTa for efficient white organic light emitting diodes. *Proc. SPIE* 6655:665501-1.
173. Kanno, H., Giebink, N. C., Sun, Y. et al. 2006. Stacked white organic light-emitting devices based on a combination of fluorescent and phosphorescent emitters. *Appl. Phys. Lett.* 89:023503.
174. Liao, L.-S., Ren, X., Begley, W. J. et al. 2008. Tandem white OLEDs combining fluorescent and phosphorescent emission. *SID Intl. Symp. Dig. Tech. Papers* 39:818.



# 15

---

## *Organic Light-Emitting Diodes and Photodetectors for Optical Communication*

---

Yutaka Ohmori

### CONTENTS

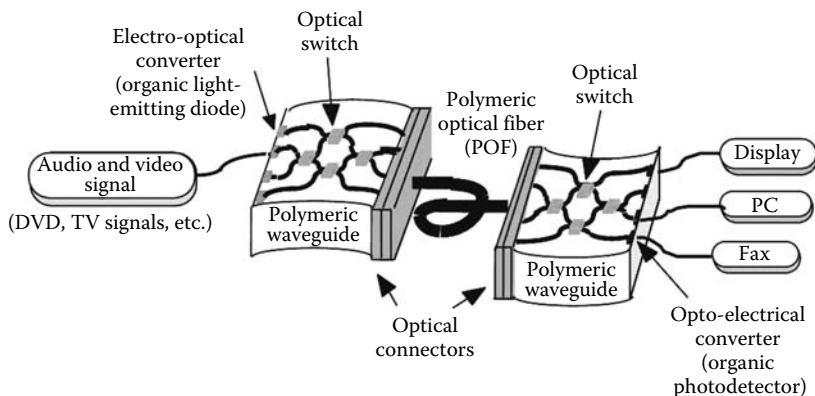
15.1	Introduction .....	511
15.2	Device Fabrication Process .....	512
15.3	Discussions for OLEDs Fabricated by Vacuum and Solution Process .....	516
15.4	Discussions for OPDs Fabricated by Vacuum and Solution Process .....	521
15.5	Summary.....	526
	Acknowledgments .....	527
	References.....	527

---

### 15.1 Introduction

Organic light-emitting diodes (OLEDs) utilizing fluorescent dyes [1–3] or conducting polymers [4,5] have attracted great interest because of their advantages in thin-film flat-panel display or illumination use. An additional advantage is that they are simple for fabrication on various kinds of substrates, including polymeric substrates, and can be formed by solution process. Further, OLEDs have a high potential for use in the next generation of information technology system, in particular for signal processing and optical sensing systems with flexible devices for mobile use [6]. Organic photodetectors (OPDs) utilizing organic materials are useful being light in weight and easy to handle in the fabrication process and due to the fact that the wavelength can be selected by choosing organic materials with suitable absorption wavelength. Prof. Forrest's group demonstrated a high-speed response of multilayer OPDs under the irradiation of a red single-pulsed intense laser light [7].

On the other hand, polymeric waveguide devices have attracted great attention with regard to their use for optical interconnection with high-speed transmission and flexible optical circuits. The combination of polymeric waveguide,

**FIGURE 15.1**

Schematic of polymeric optical integrated device fabricated on polymeric waveguide. OLEDs and OPDs are directly fabricated on a polymeric waveguide. (From Ohmori, Y. et al., *IEEE J. Selected Top. Quantum Electron.*, 10, 70, 2004. With permission.)

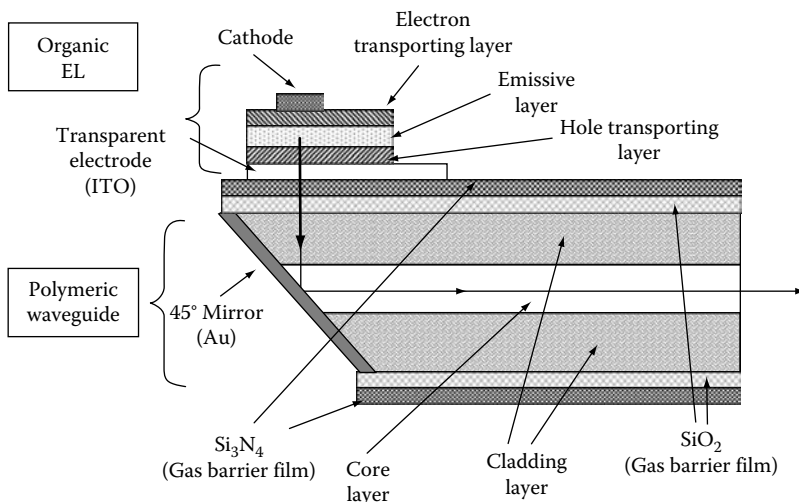
OLED, and OPD will realize a polymeric optical integrated devices [6]. A schematic of polymeric optical integrated devices is shown in Figure 15.1. Audio and visual signals are converted to optical signals by OLEDs and transmitted through polymeric optical waveguide and optical fibers connected by optical connectors. On the other hand, optical signals are received by OPDs through polymeric waveguide and converted to electrical video and audio signals.

In this chapter, we discuss the characteristics of OLEDs fabricated by vacuum and solution process and their application in optical communication. We also discuss the characteristics of OPDs fabricated by vacuum and by solution process. The mechanism of device performance and the application to optical communication is also discussed.

## 15.2 Device Fabrication Process

OLEDs with various emissive materials including red, yellow, green, and blue light emission have been investigated. The organic layers for OLEDs and OPD were vacuum deposited by organic molecular beam deposition (OMBD) at a background pressure of  $10^{-5}$  Pa. Along with the substrates used for the experiments, polymeric and glass substrates were used for comparison. Polymeric waveguide films were used as a substrate; however, polyimide films were also employed as polymeric materials because they have high thermal stability.

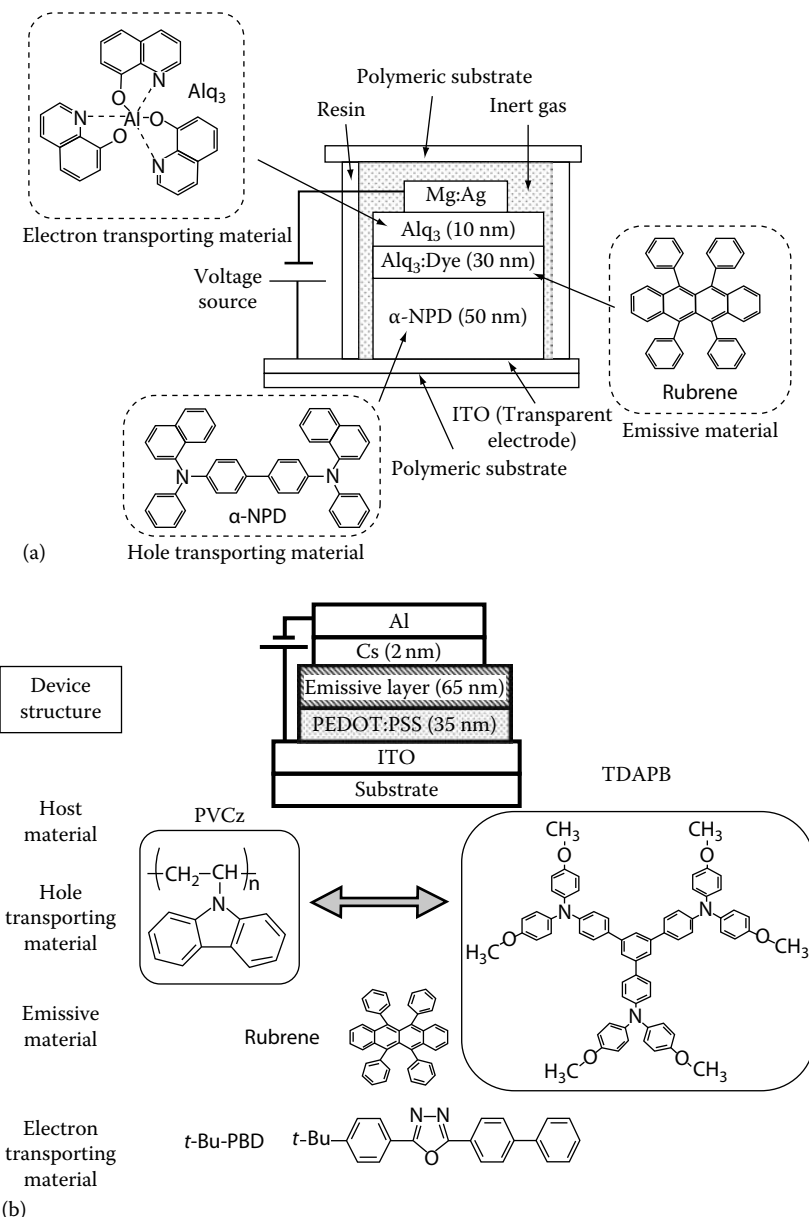
A schematic of the OLED fabricated on the polymeric waveguide substrate is shown in Figure 15.2. The output light from the OLED was introduced perpendicular to the substrate, using 45° cut mirror. Since one of the edges of the polymeric waveguide is cut in 45°, which serves as a mirror, the

**FIGURE 15.2**

Schematic of the device structure of OLEDs fabricated on polymeric waveguide. Polymeric waveguide film is used as a substrate.

optical output from the OLED is introduced to the waveguide. Both sides of the polymeric waveguide are covered with thin film of silicone oxide  $\text{Si}_2\text{O}$  and silicone nitride  $\text{Si}_3\text{N}_4$  films. This prevents oxide and humid gases from penetrating into organic layers and to stick the indium-tin-oxide (ITO) electrode to the polymeric waveguide substrate. In order to improve the reflection at the  $45^\circ$  cut mirror, gold metal is deposited. The output light from the OLED (active area:  $100\text{ }\mu\text{m}$  in square) through the transparent anode is reflected at the  $45^\circ$  cut mirror and is led to the core of the waveguide. The ITO anode was fabricated by using a face-centered type sputtering system (Thin-Film Process Soft Inc., Japan). Using this, we can obtain high-quality ITO film without annealing process of the deposited film. The ITO film has a resistivity in the order of the  $4 \times 10^{-4} \Omega \text{ cm}$ . The polymeric waveguide (typical core size:  $70\text{ }\mu\text{m}$  in square) is connected to the polymeric optical fiber (typical core size:  $62.5\text{ }\mu\text{m}$  in diameter), and the output light from the fiber is led to the photodetectors. For a polymeric waveguide [8], deuterated-poly(methylmethacrylate) (d-PMMA) and ultraviolet (UV)-cured epoxy resin for core and cladding layers of the polymeric waveguide were used, respectively. The polymeric waveguide has a square core size of  $70\text{ }\mu\text{m}$ . A graded-index multimode silica optical fiber with a core size of  $200\text{ }\mu\text{m}$  and length of  $100\text{ m}$  was used for optical transmission experiments.

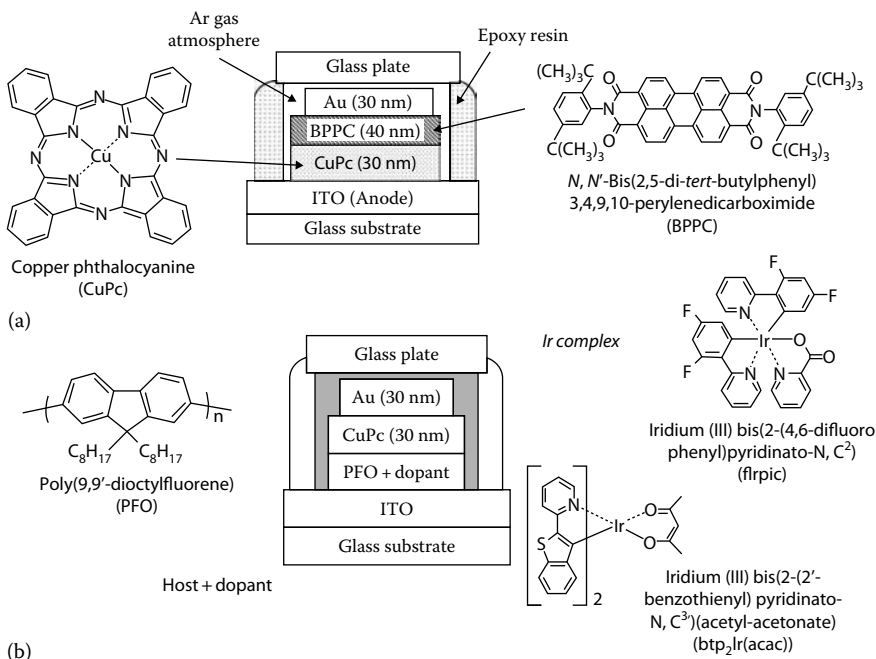
The application of the proposed polymeric optical integrated devices will be used for local area network (LAN) for home use or for short-distance interconnections. For the use of the polymeric waveguide and the organic devices, i.e., OLED and OPD, the transmission speed will be in the range of several hundreds megahertz. In Figure 15.3, schematic of OLEDs fabricated by vacuum [9] and solution processes [10] are shown. A typical vacuum

**FIGURE 15.3**

Device structure of OLEDs and the materials used for the devices. (a) Device structure of vacuum processed device and the materials used for the device and (b) device structure of solution processed device and the molecular structure for the devices.

processed OLED, which is shown in Figure 15.3a, consists of ITO-coated polymeric substrate with buffer layers with thin layers of silicone oxide and silicone nitride multilayers, hole transporting layer of 4, 4'-bis[N-(1-naphthyl)-N-phenyl-amino]-biphenyl ( $\alpha$ -NPD), emissive layer (doped type or undoped type), electron transporting layer of 8-hydroxquinoline aluminum ( $\text{Alq}_3$ ), terminated with cathode of silver-containing magnesium (Mg:Ag). As a dopant of the emissive layer, 5,6,11,12-tetraphenylnaphthacene (rubrene) or 5,10,15,20-tetraphenyl-21H,23H-porphine (TPP) molecules were doped in  $\text{Alq}_3$ . In order to reduce the straight capacitance of the diode, the active size of the device was employed as small as  $0.01\text{ mm}^2$ . After the deposition of the organic layers and the metal electrode, the OLEDs are sealed in an inert gas (Ar gas). Highly emissive OLEDs fabricated by solution process are also fabricated and discussed. Two kinds of host materials are tested for OLED fabricated by spin coating method, which is shown in Figure 15.3b. The device consists of poly(ethylenedioxythiophene):poly(styrenesulfonicacid)(PEDOT:PSS) as a hole transporting layer, emissive layer of mixed materials and terminated with cesium and silver. The layer thickness for PEDOT:PSS and emissive layer are 35 and 65 nm, respectively. Two kinds of host materials for the emissive layer, methoxy-substituted 1,3,5-tris[4-(diphenylamino) phenyl]benzene (TDAPB), and poly(*n*-vinylcarbazole) (PVCz) were employed, and were prepared by spin coating method. 2-(4-biphenyl)-5-(4-*tert*-butylphenyl)-1,3,4-oxadiazole (*t*-Bu-PBD) and rubrene were mixed as electron transporting and emissive materials, respectively. The molar ratio for the emissive layer is as follows: TDAPB: *t*-Bu-PBD: rubrene = (100:72:1.65 wt%), PVCz: *t*-Bu-PBD: rubrene = (100:72:1.65 wt%). The device structure and the molecular structure used for the experiments are shown in Figure 15.3b.

For vacuum processed OPDs [11–13], the device was fabricated onto an ITO-coated glass substrate by OMBD at a background pressure of  $10^{-5}\text{ Pa}$  similar to the fabrication process of OLEDs. The device consists of the heterostructure of copper phthalocyanine (CuPc) and *N,N'*-bis(2,5-di-*tert*-butylphenyl) 3,4,9,10-perylenediacarboximide (BPPC) as a p-type and an n-type material, respectively. CuPc film has high sensitivity and stability in air, and it shows a strong absorption band at the wavelength range of 550–780 nm, whereas BPPC shows an absorption band in the range of 400–550 nm. The thickness of CuPc layer was set at 30 nm, which corresponds to the exciton diffusion length in the photogenerated layer. As an electrode, 30 nm thick Au was deposited on the BPPC layer. The device was covered by a glass plate in Ar gas atmosphere to prevent oxidation of the organic layers. The active area of the device was fixed at  $0.01\text{ mm}^2$ , in order to reduce the influence of the RC time constant. For devices fabricated by solution process, poly(9,9-dioctylfluorene) and a phosphorescent iridium derivative, (iridium (III) bis(2-(4,6-difluorophenyl) pyridinato-N,C<sup>2</sup>) (FIrpic), or iridium (III) bis(2-(2'-benzothienyl) pyridinato-N,C<sup>3</sup>) (acetylacetone) (btp<sub>2</sub>Ir(acac)), were used as a host and a dopant material, respectively. The materials were dissolved in 1,2,4-trichlorobenzene

**FIGURE 15.4**

Device structure of OPDs and the materials used for the devices. (a) Device structure of vacuum processed device and the materials used for the device and (b) device structure of solution processed device and the molecular structure for the devices.

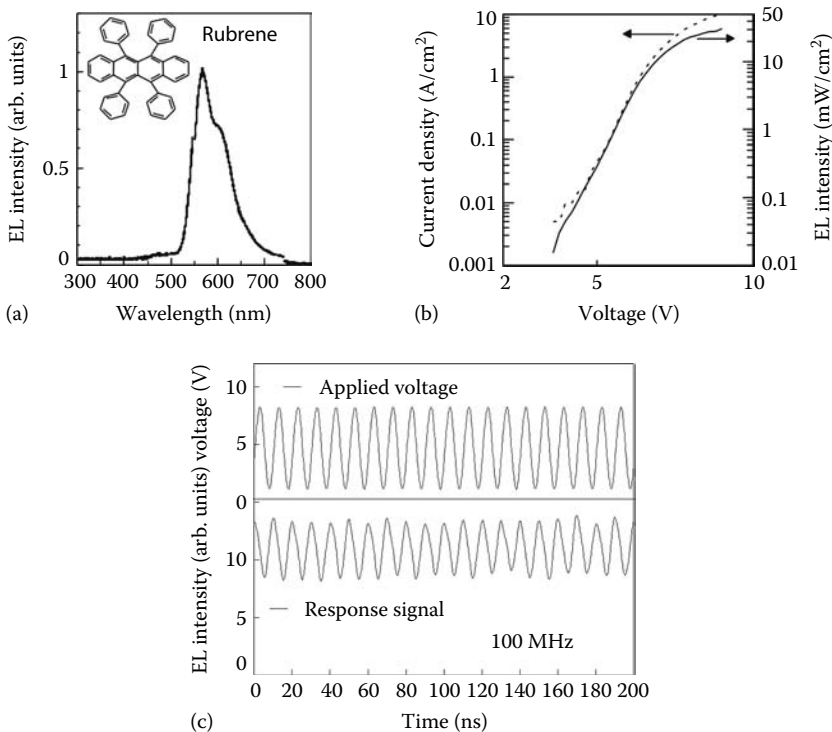
or chloroform solution and the organic layers were fabricated by spin coating method similar to the OLEDs. The active area of the device was fixed at  $0.03\text{ mm}^2$ . The device structure and the materials used in the experiments are shown in Figure 15.4a and b for vacuum and solution processed devices, respectively.

### 15.3 Discussions for OLEDs Fabricated by Vacuum and Solution Process

First, OLEDs fabricated by vacuum process are discussed. Four kinds of OLEDs fabricated by OMBD are discussed and the emission characteristics are summarized. There are two types of organic materials for OLEDs: one for undoped type such as  $\alpha$ -NPD and  $\text{Alq}_3$ , and the other is for doped type such as rubrene and porphine derivative (TPP), which are doped in a carrier transporting material. In case of a device in which  $\alpha$ -NPD is

the emissive layer, the device consists of an ITO-coated glass substrate, 60-nm-thick  $\alpha$ -NPD as a hole transporting and emissive layer, 5 nm thick 4,4'-bis(carbazol-9-yl)-biphenyl (CBP), 10-nm-thick 2,9-dimethyl-4,7-diphenyl-1,10-phenanthroline (BCP) as hole blocking layers, and 15-nm-thick Alq<sub>3</sub> as an electron transporting layer, and is terminated with a silver-containing magnesium (Mg:Ag) cathode. The device emits clear blue emission centered at about 435 nm, and the emission intensity reaches to a maximum intensity of 40 mW/cm<sup>2</sup> at an injection current density of 6 A/cm<sup>2</sup>. The clear light pulses were created by direct modulation of the OLED with an active area of 0.01 mm<sup>2</sup> under the applied pulse of 100 MHz. Second device is made with an emissive material of Alq<sub>3</sub>. The device consists of an ITO-coated glass substrate, 50 nm thick  $\alpha$ -NPD as a hole transporting layer, and 50 nm thick Alq<sub>3</sub> as an emissive and electron transporting layer, and is terminated with a silver-containing magnesium (Mg:Ag) cathode. The device emits clear green emission centered at about 520 nm. The emission intensity reaches 30 mW/cm<sup>2</sup> at an injection current density of 6 A/cm<sup>2</sup>. However, the modulation frequency is limited to 60 MHz due to the fluorescence lifetime of Alq<sub>3</sub> [14], which has more than 10 ns lifetime. The third device consists of rubrene doped in Alq<sub>3</sub> layer as an emissive layer. The emission spectra of OLED with 9.1 vol% of rubrene doped in Alq<sub>3</sub> layer are shown in Figure 15.5a. The device consists of 50 nm thick  $\alpha$ -NPD as a hole transporting layer, 30 nm thick rubrene doped in Alq<sub>3</sub> as an emissive layer and 10-nm-thick Alq<sub>3</sub> as an electron transporting layer, and is terminated with Mg:Ag cathode. The device emits clear yellow emission centered at about 560 nm. The emission intensity reaches to 30 mW/cm<sup>2</sup> at a current density of 5 A/cm<sup>2</sup>. The modulation characteristics will be discussed in the later paragraph. The fourth device is for red light-emitting device, which consists of 50 nm thick  $\alpha$ -NPD as a hole transporting layer, 30 nm thick TPP doped in Alq<sub>3</sub> as an emissive layer, 10 nm thick BCP layer as a hole blocking layer, and a 10 nm thick Alq<sub>3</sub> layer as an electron transporting layer, and is terminated with a Mg:Ag cathode. The mole fraction of TPP is 1 wt%, and it is sufficient for emitting red light. The emission spectra have two peaks centered at 650 and 720 nm. The modulation frequency reaches 100 MHz. However, the emission intensity is rather poor compared with other materials due to the poor emission efficiency, and the maximum emission intensity is 3 mW/cm<sup>2</sup> at a current density of 5 A/cm<sup>2</sup>.

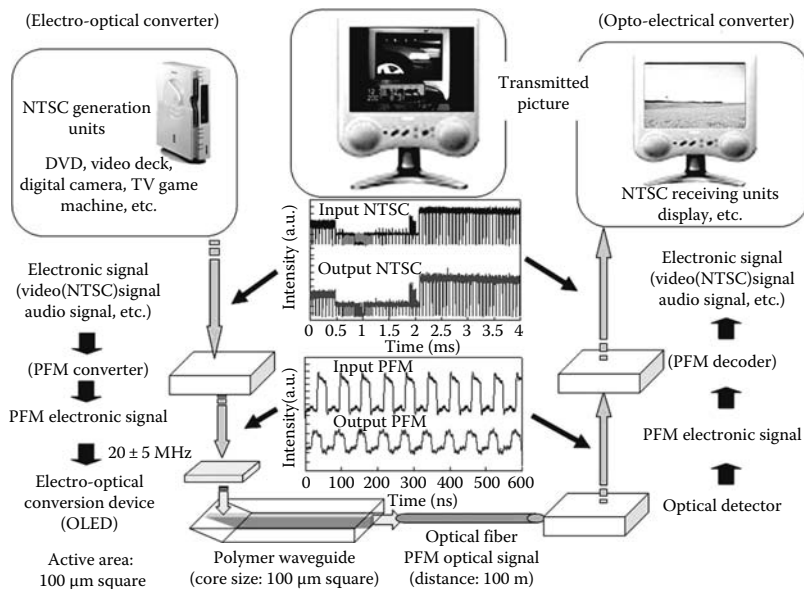
Four kinds of OLEDs fabricated by OMBD are discussed, and the emission characteristics are summarized. In Figure 15.5a, emission spectrum of the OLED is shown. The device emits yellow emission centered at about 560 nm. The emission characteristics of the OLED fabricated on a polymeric substrate, i.e., polyimide substrate, shows similar characteristics to that on a glass substrate. In Figure 15.5b, current density–applied voltage and the emission intensity–applied voltage characteristics are shown. The emission intensity reaches 30 mW/cm<sup>2</sup> at an applied voltage of 8 V, and a current density of 10 A/cm<sup>2</sup>. The modulation characteristics are shown in Figure 15.5c, as a reference with the applied voltage.

**FIGURE 15.5**

Emission characteristics of OLED with rubrene doped in  $\text{Alq}_3$  emissive layer. (a) Emission spectrum and the molecular structure of rubrene. (From Ohmori, Y. et al., *IEEE J. Selected Top. Quantum Electron.*, 10, 70, 2004. With permission.) (b) Current–voltage and EL intensity–voltage characteristics of OLEDs, and (c) EL output signal at 100 MHz directly modulated by pulsed voltage application. (From Ohmori, Y. et al., *IEEE J. Selected Top. Quantum Electron.*, 10, 70, 2004. With permission.)

As is shown in Figure 15.5c, the OLED with rubrene doped in  $\text{Alq}_3$  layer shows 100 MHz modulation when a 8 V pulse voltage is applied to the OLED, and the modulation ratio of output light is about 30%. In order to enhance the response speed of the OLED, it is effective to apply bias voltage to the OLED in addition to the pulsed voltage. The response speed of more than 100 MHz was obtained by applying lower pulsed voltage with a bias voltage, which is less than the turn-on voltage of the OLED. In the experiments shown here, the response speed is limited by the experimental systems.

The proposed polymeric optical integrated devices can be applicable to electro-optical conversion devices [15,16] for transmitting high modulation signals in LANs, such as home networks and car LAN. Using the rubrene-doped OLED with an active size of  $0.015\text{ mm}^2$  as electro-optical conversion devices, optical transmission experiments were demonstrated as shown in Figure 15.6. The video and audio signals are converted to National Television Standards Committee (NTSC) signals, and the signals are modulated by

**FIGURE 15.6**

Schematic of optical transmission systems utilizing OLEDs and OPDs as an electro-optical and an opto-electrical converter, respectively. Converted and transmitted signals are shown before and after transmission of the organic devices.

pulse frequency modulation (PFM), in which the pulse width is kept constant and the pulse generation cycle is modulated, in order to ensure the error-free transmission. The baseband frequency of PFM signals is kept at 20 MHz. The transmission signals have a bandwidth of the video and audio signals from 50 Hz to 4.2 MHz, and 60 Hz to 10 kHz, respectively. Typical PFM signals have a carrier wave of 20 MHz signals modulated by 5 MHz as shown in Figure 15.6. The PFM-converted signals are applied to the OLED and the optical signals emitted from the OLED are transmitted through polymeric waveguide with a 45° cut mirror. The waveguide is connected through the connectors to the standard multimode optical fiber with core size of 200 μm and length of 100 m. After transmission of 100 m, the clear transmitted signals are obtained as shown in Figure 15.6, since the clear NTSC signals are reproduced using the optical transmission system of OLED. We can obtain clear moving picture after transmission over 100 m using the optical transmission system with the OLED [6]. These results show that the OLED can be used as electro-optical conversion devices for the optical link.

Next, OLEDs for optical transmission systems fabricated by solution process are discussed. Two kinds of hole transporting materials are tested for the host materials. As is shown in Figure 15.7a, the OLED with TDAPB emit higher emission intensity at low driving voltage compared with that of PVCz in EL intensity. This comes from the higher hole transport properties in

TDAPB than that in PVCz, and the higher energy transfer properties between host materials and emissive materials. Pulse response characteristics are shown in Figure 15.7b for a device with 100  $\mu\text{m}$  circle active layer which was driven by a 10  $\mu\text{s}$  repetition voltage pulse. Symbols are for rise time ( $\blacktriangle$ ) and decay time ( $\blacksquare$ ) in Figure 15.7b. The result shows that the device with TDAPB shows faster response compared to that with PVCz at the same driving voltage. Since the device with TDAPB has lower turn-on voltage than that with PVCz, it coincides with the carrier conduction in the emissive layer.

Using the device with TDAPB as a light source for electro-optical conversion, moving picture signals are successfully transmitted using 5 m long polymeric optical fiber with 1 mm in diameter [10]. The results show that the device fabricated by wet process can be also used as a light source for the polymeric integrated device.

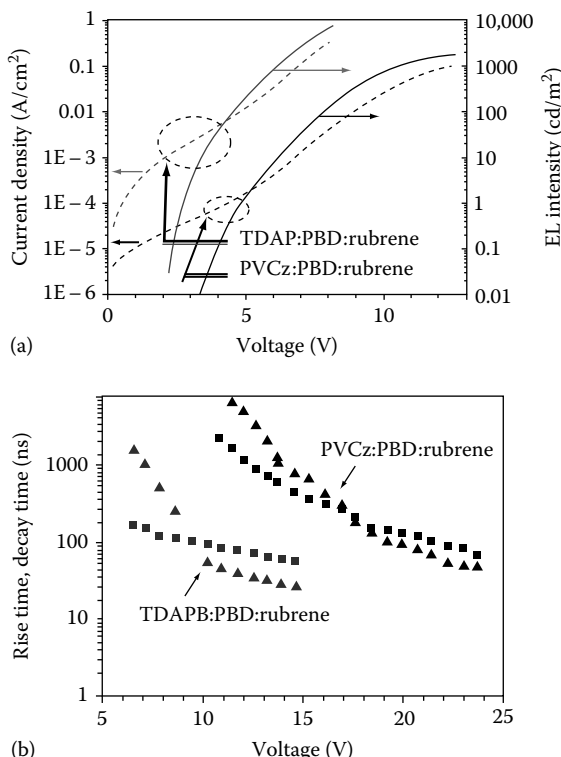


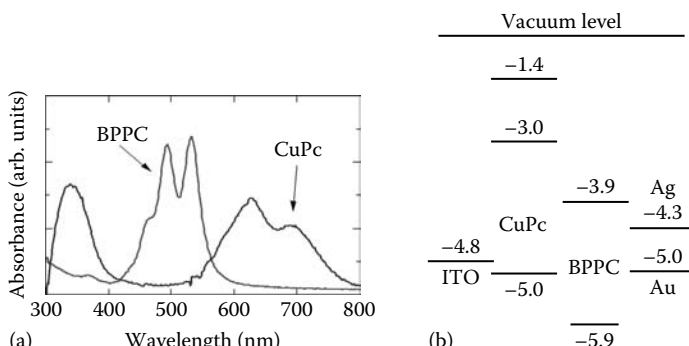
**FIGURE 15.7**

Emission characteristics and the response time of OLED with two kinds of host materials. The device consists of ITO/PEDOT:PSS (35 nm)/emissive layer (65 nm)/Cs (2 nm)/Al. (a) Current-voltage and EL intensity–voltage characteristics of OLEDs with rubrene doped in TDAPB and PVCz for host materials. (b) Rise time and decay time of OLEDs under pulsed voltage application. Symbols are for rise time ( $\blacktriangle$ ) and decay time ( $\blacksquare$ ), respectively. (From Kajii, H. et al., *IEICE Trans. Electron.*, E87-C(12), 2059, 2004. With permission.)

## 15.4 Discussions for OPDs Fabricated by Vacuum and Solution Process

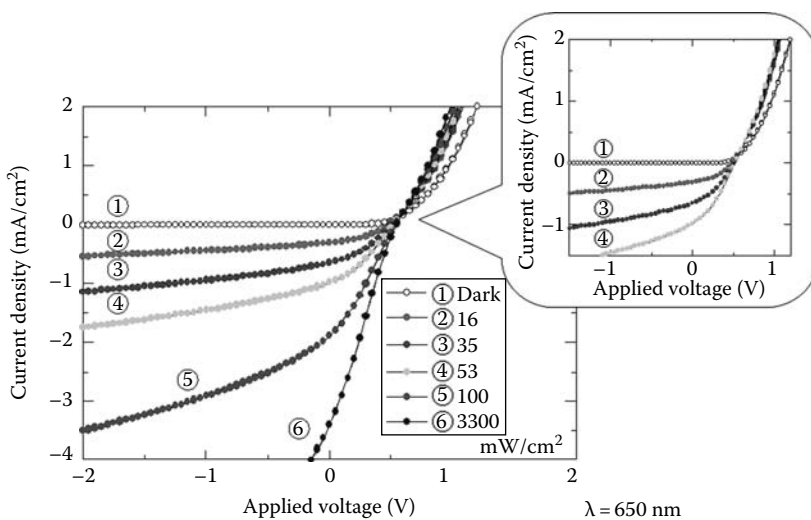
First, the OPDs fabricated by vacuum process are discussed [11–13]. Figure 15.8a shows the absorption spectra of CuPc and BPPC, which are used in photoabsorbing and carrier generation layers in a photodetector fabricated by OMBD similar to the OLED fabricated by vacuum process. The absorption band in the green and yellowish light regions attributes to the BPPC layer, whose absorption band exists in the range of 450–550 nm. On the other hand, an absorption band in red light region corresponds to CuPc with an absorption band of 550–750 nm. In the case of red light illumination, photocarriers are generated in the CuPc layer and the photogenerated carriers are recombined at the interface of the CuPc and the BPPC layer, and results in the photocurrent. Energy band diagram is estimated by the absorption and the emission spectrum of the CuPc and BPPC. The highest occupied molecular orbital (HOMO) levels are estimated by the photoemission spectrum. The energy band diagram of the OPD with CuPc and BPPC are summarized in Figure 15.8b.

Current–voltage ( $I$ – $V$ ) characteristics of an OPD which consists of ITO (150 nm)/CuPc (30 nm)/BPPC (40 nm)/Au (30 nm) has been examined under dark and red laser diode (LD) with the emission wavelength of  $\lambda = 650$  nm irradiated at a different light intensity from 0 to 3.3 W/cm<sup>2</sup>. The active area of the device was fixed at 0.01 mm<sup>2</sup>.  $I$ – $V$  characteristics at a reverse bias condition show a good rectifying characteristic under dark condition, and gradual increase with applying voltage under a red light irradiation, which is shown in Figure 15.9. The photocurrent density is shown at a different irradiation intensity in which the photocurrent attributes to the absorption



**FIGURE 15.8**

Optical characteristics and the energy band diagram of CuPc and BPPC. (a) Absorption spectra of CuPc and BPPC for vacuum deposited device and (b) energy band diagram of the single heterostructured CuPc and BPPC OPD.

**FIGURE 15.9**

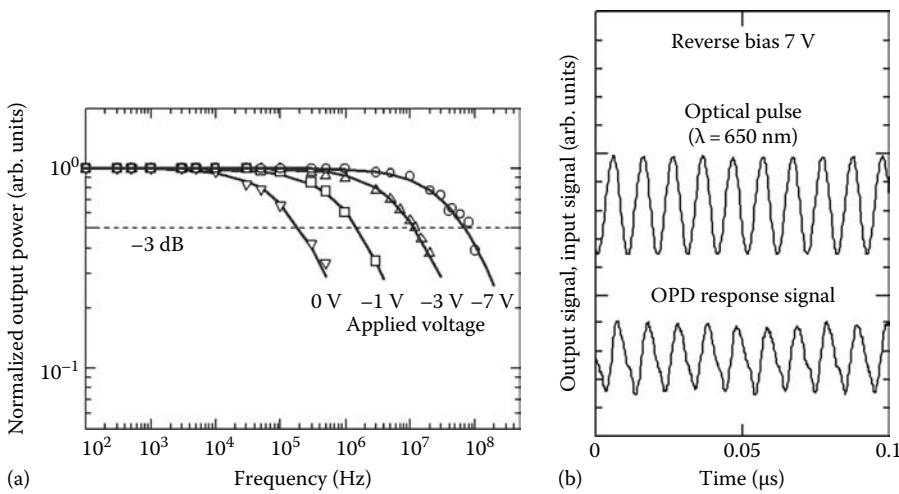
Current–voltage characteristics of an OPD which consists of ITO (150 nm)/CuPc (30 nm)/BPPC (40 nm)/Au (30 nm) under dark and red laser light ( $\lambda=650\text{ nm}$ ) irradiation.

in the CuPc layer rather than in the BPPC layer from the result of photoabsorption spectra. With increasing light intensity, the photocurrent under reverse bias condition increases proportionally to the irradiated light. Photoinduced carriers at CuPc layer are proportional to the light intensity, and recombine at the interface of the BPPC layer result in the photocurrent. As the reverse bias voltage increases, the photogenerated carriers drift toward the opposite side depending on the polarity of charged carriers by the applied electric field in the CuPc and BPPC layers, and recombine at the interface of the layers. With increasing applied field, the photocurrent increases proportional to the applied electric field within the drift length of the photogenerated carriers at an applied electric field, and then saturates at the applied field.

The response speed of OPD was evaluated in the frequency range up to 100 MHz using a sinusoidal modulated laser ( $\lambda=650\text{ nm}$ ). The results obtained at the reverse bias of 0.0, 1.0, 3.0, and 7.0 V are shown in Figure 15.10a. As the reverse bias is increased, the response increases toward the high-speed regions. The intensity of output power  $P$  of OPD, which depends on the frequency  $f$  is described as

$$P = \frac{P_0}{1 + j(f/f_c)} \quad (15.1)$$

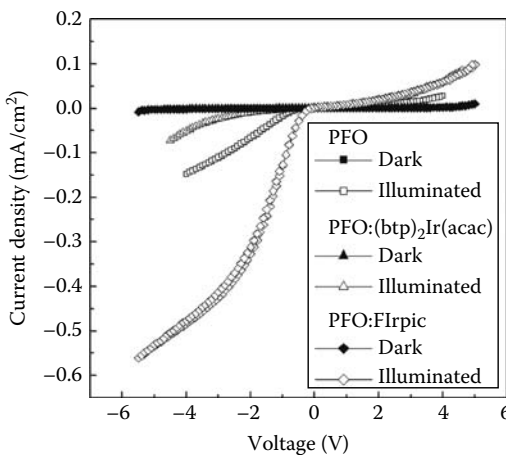
where  $P_0$  and  $f_c$  are the output power intensity at lower frequency and the cut-off frequency, respectively. Solid lines show the calculation results under

**FIGURE 15.10**

Frequency responses under pulsed light illumination in reverse bias conditions and optical signal modulation at 100 MHz. (a) Frequency responses under pulsed light illumination in various reverse bias fields. Solid lines show the calculation results under the reverse bias using Equation 15.1. (b) Optical signal output at 100 MHz sinusoidal modulated laser light ( $\lambda=650$  nm) illumination. (From Morimune, T. et al., *IEEE Photon. Technol. Lett.*, 18, 2602, 2006. With permission.)

reverse bias using Equation 15.1, and dashed line shows the guide of  $-3$  dB. From the result shown in Figure 15.10b, the cut-off frequency was estimated to be 70 MHz at the reverse bias of 7 V. The clear response pulses at 100 MHz were generated [13] using sinusoidal modulated laser ( $\lambda=650$  nm), as shown in Figure 15.10b. The result of high-speed response of the OPD indicates a possibility of the OPD to be used in optical communication for detecting moving picture signals. The OPD can be used as a photodetector of optical moving picture signals and a clear picture was obtained using OPD as a photodetector in optical fiber communication.

Next, the fabrication and characteristics of OPDs by solution process have been discussed. Poly(9,9-diptylfluorene) (PFO) is one of blue light-emitting materials and is used in organic electroluminescent devices [6]. In this experiment, PFO is used as a host material of solution processed photodetectors. Current–voltage ( $I$ – $V$ ) characteristics of an OPD which consists of ITO (150 nm)/PFO with iridium derivatives (30 nm)/CuPc (30 nm)/Au (30 nm) under dark and violet light by xenon (Xe) arc lamp  $\lambda=380$  nm irradiation are shown in Figure 15.11 for three kinds of solution processed devices. The active area of the device was fixed at  $0.03\text{ mm}^2$ . Three kinds of devices are shown for PFO, PFO with Flrpic, and PFO with  $(\text{btp})_2\text{Ir}(\text{acac})$ . The device structure and the materials used in this experiment are shown in Figure 15.4b. Flrpic and  $(\text{btp})_2\text{Ir}(\text{acac})$  are dissolved in PFO utilizing 1,2,4-trichlorobenzene as a solvent. The concentration of the iridium derivatives are 6 wt% to the PFO. After forming the

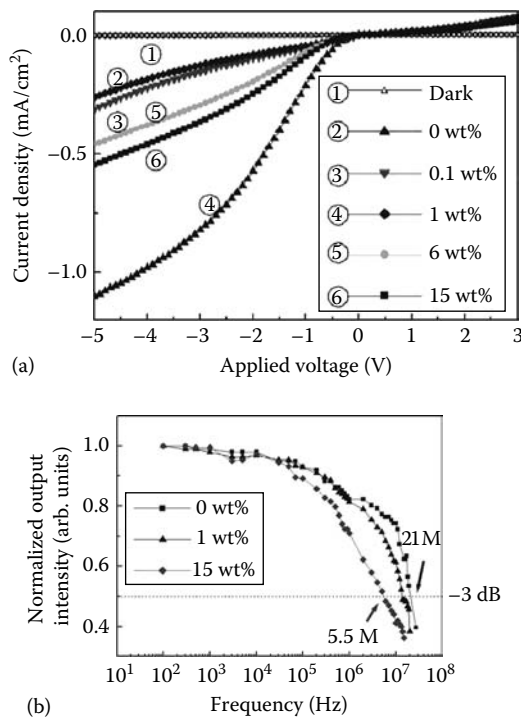
**FIGURE 15.11**

Current–voltage characteristics of an OPD which consists of ITO (150 nm)/PFO with iridium derivatives (30 nm)/CuPc (30 nm)/Au (30 nm) under dark and violet light by Xe arc lamp ( $\lambda=380\text{ nm}$ ) irradiation. Three kinds of devices are shown for PFO, PFO with Flrpic, and PFO with (btp)<sub>2</sub>Ir(acac). Closed and open symbols show photocurrent in dark and illuminated conditions, respectively.

photoabsorption layer by spin coating method, the device is heated at 80°C in order to degas the solvent. Finally, the device is sealed in an inert gas (Ar gas) with epoxy resin to avoid oxidization of the active layer.

The device shows photosensitive characteristics and the photocurrent increases as increasing the reverse bias. The nondoped PFO device shows larger photocurrent than PFO with (btp)<sub>2</sub>Ir(acac) device, whereas, less than PFO with Flrpic. PFO has lowest unoccupied molecular orbital (LUMO) and HOMO levels at -3.1 and -6.0 eV below vacuum level, respectively. Flrpic has LUMO and HOMO levels at -3.3 and -6.0 eV, respectively. On the other hand, (btp)<sub>2</sub>Ir(acac) has less energy band gap than these materials and the LUMO and HOMO levels at -3.2 and -5.1 eV, respectively. Flrpic in PFO enhances photogeneration in the photoabsorption layer, whereas (btp)<sub>2</sub>Ir(acac) enhances recombination of the photogenerated carriers in the photoabsorbed layer due to the less energy band gap of the doped material.

Figure 15.12a shows the current–voltage characteristics of an OPD which consists of PFO with Flrpic (60 nm) with various concentrations of Flrpic in PFO under dark and violet light by Xe arc lamp  $\lambda=380\text{ nm}$  irradiation. Flrpic was dissolved in PFO utilizing chloroform as a solvent. Five kinds of devices in different concentration are fabricated and tested for OPDs with 0–15 wt% of Flrpic in PFO. The highest photoresponse shows for the device with 1 wt% Flrpic doped in PFO. The other concentration shows increased photoresponse as increasing the concentration of Flrpic. The reason is not clear at this stage of experiment why the photoresponse is not in the order

**FIGURE 15.12**

Current-voltage characteristics and frequency response characteristics of an OPD which consists of PFO with FlIrpic (60 nm). (a) Current-voltage characteristics of an OPD with various concentrations of FlIrpic in PFO under dark and violet light by Xe arc lamp  $\lambda=380$  nm illumination. Five kinds of devices are shown for OPD with 0–15 wt% of FlIrpic in PFO, (b) frequency responses under pulsed light illumination for different concentrations of FlIrpic in reverse bias voltage at  $-5$  V. A sinusoidal modulated laser light ( $\lambda=408$  nm) of  $1.5\text{ W/cm}^2$  is illuminated.

of FlIrpic concentration, however, the mixture of 1% is the best for the carrier transport in the photoabsorbing layer.

In Figure 15.12b, the photoresponse of OPD was evaluated in the frequency range up to 100 MHz using a sinusoidal modulated laser ( $\lambda=408$  nm) for a different concentration of FlIrpic doped in PFO. As the concentration increases, the photoresponse of the photodiode decreases. The highest photoresponse was obtained for the device with nondoped PFO device. Since iridium complex has a large triplet state in the relaxation process, the slow component is the reason why the response speed becomes slow as the concentration of FlIrpic increases.

For an application of opto-electrical conversion device, a vacuum deposited OPDs with CuPc and BPPC was used to receive the transmitted signal through optical fiber in the application of transmitting image signals. Since

the OPDs have a bandwidth of about 100 MHz, the OPDs are used for optical communication devices with short distances and multimode paths. Using the system, transmission of high-quality NTSC video signals over a standard multimode optical fiber were tested. A red LD was used to generate optical pulses as an optical signal generation process. This system employs PFM, in which the pulse width is kept constant and the pulse generation cycle was varied, to ensure error-free transmission. The base band frequency of PFM and the typical PFM modulation frequency of the carrier wave were 4.5 and 5.3 MHz, respectively. It can be noted that the output NTSC signal was in agreement with the input NTSC signals, and the results show that OPDs can be used as opto-electrical conversion devices for transmitting moving picture signals [12].

---

## 15.5 Summary

In summary, high-speed operation of OLEDs fabricated by vacuum and solution process is discussed as a light source for the polymeric optical integrated device. Both the OLEDs with low molecular and polymeric materials can be used as a light source for transmitting moving picture signals. The OLED with rubrene doped in Alq<sub>3</sub> as an emissive layer emits more than 30 mW/cm<sup>2</sup>. As for modulation speed, the OLEDs with rubrene doped in Alq<sub>3</sub> and TPP doped in Alq<sub>3</sub> show more than 100 MHz with direct modulation of voltage pulse. However, in the case of the OLED with Alq<sub>3</sub> as an emissive layer, the modulation frequency limited to 60 MHz due to the fluorescence lifetime of the material. We found that the fluorescence lifetime of the emissive material is one of the determinant factors for the modulation speed of OLED. A clear moving picture can be obtained through a polymeric waveguide and an optical fiber utilizing OLED as an electro-optical conversion device. We demonstrate that an OLED fabricated on a polymeric waveguide can be applicable as an electro-optical conversion device for short range optical LAN.

The fabrication and characteristics of OPDs fabricated by vacuum process and solution process have been discussed. The carrier generation and the charge transfer in a single heterostructured OPD have been discussed for vacuum processed device utilizing phthalocyanine derivative and perylene derivative. A cut-off frequency of 70 MHz was observed under reverse bias of 7 V and clear response pulses at 100 MHz were demonstrated using a sinusoidal modulated laser light ( $\lambda=650\text{ nm}$ ). For solution processed OPDs, poly(9,9-dialkylfluorene) doped with iridium derivative are discussed. The moving picture signals can be detected through the OPDs and the OPDs can be demonstrated to be used as a photodetector for optical communication use.

---

## Acknowledgments

This research was supported by Dr. H. Kajii, Mr. T. Taneda, and Dr. M. Kaneko (Osaka University) for the experiments and discussions of OLEDs. The author thanks Dr. H. Kajii, Dr. T. Morimune, and Mr. T. Hamasaki (Osaka University) for the experiments and discussions on OPDs. The author also thanks Dr. M. Hikita and Dr. H. Takenaka (NTT Advanced Technology) for the experiments and discussions of polymeric waveguide. The author expresses his sincere thanks to Prof. K. Yoshino, Prof. M. Ozaki, and Prof. A. Fujii (Osaka University) for discussions and supports for the experiments.

This research was partially supported financially by the Ministry of Education, Culture, Sports, Science and Technology in Japan (MEXT) under a Grant-in-Aid for Scientific Research (A) #20246058, under a grant for the Osaka University Global COE Program, Center for Electronic Devices Innovation, and a Grant in Aid of Special Coordination Funds for Promoting Science and Technology. It also partially supported financially by Support Center for Advanced Telecommunications Technology Research, Foundation (SCAT).

---

---

## References

1. C. W. Tang, S. A. Vanslyke, and C. H. Chen, Electroluminescence of doped organic thin films, *J. Appl. Phys.*, 65(9), 3610–3616 (1989).
2. M. A. Baldo, S. Lamansky, P. E. Burrows, M. E. Thompson, and S. R. Forrest, Very high-efficiency green organic light-emitting devices based on electrophosphorescence, *Appl. Phys. Lett.*, 75(1), 4–6 (1999).
3. C. Adachi, M. A. Baldo, M. E. Thompson, and S. R. Forrest, Nearly 100% internal phosphorescence efficiency in an organic light emitting device, *J. Appl. Phys.*, 90(10), 5048–5051 (2001).
4. J. H. Burroughes, D. D. C. Bradley, A. R. Brown, R. M. Marks, K. Mackay, R. H. Friend, P. L. Burns, and A. B. Holmes, Light emitting diodes based on conjugated polymers, *Nature*, 347(6293), 539–541 (1990).
5. Y. Ohmori, M. Uchida, K. Muro, and K. Yoshino, Blue electroluminescent diodes utilizing poly(alkylfluorene), *Jpn. J. Appl. Phys.*, 30(11B), L1941–L1943 (1991).
6. Y. Ohmori, H. Kajii, M. Kaneko, K. Yoshino, M. Ozaki, A. Fujii, M. Hikita, and H. Takenaka, Realization of polymeric optical integrated devices utilizing organic light emitting diodes and photo detectors fabricated on a polymeric waveguide, *IEEE J. Selected Top. Quant. Electron.*, 10(1), 70–78 (2004).
7. P. Peumans, P. V. Bulovic, and S. R. Forrest, Efficient high-bandwidth organic multiplayer photodetectors, *Appl. Phys. Lett.*, 76(26), 3855–3857 (2000).
8. M. Hikita, S. Tomaru, K. Enbutsu, N. Ooba, R. Yoshimura, M. Usui, T. Yoshida, and S. Imamura, Polymeric optical waveguide films for short-distance optical interconnects, *IEEE J. Selected Top. Quant. Electron.*, 5(5), 1237–1242 (1999).

9. H. Kajii, T. Tsukagawa, T. Taneda, K. Yoshino, M. Ozaki, A. Fujii, M. Hikita, S. Tomaru, S. Imamura, H. Takenaka, J. Kobayashi, and F. Yamamoto, Transient properties of organic electroluminescent diodes using 8-hydroxyquinoline aluminum doped with rubrene as an electro-optical conversion device for polymeric integrated devices, *Jpn. J. Appl. Phys.*, 41(4B), 2746–2748 (2002).
10. H. Kajii, K. Takahashi, Y. Hino, and Y. Ohmori, Organic light emitting diode using starburst molecule doped with rubrene fabricated by wet-processing for application on an electro-optical conversion device, *IEICE Trans. Electron.*, E87-C(12), 2059–2063 (2004).
11. T. Morimune, H. Kajii, and Y. Ohmori, High speed organic photodetectors using heterostructure with phthalocyanine and perylene derivative, *Jpn. J. Appl. Phys.*, 45(1B), 546–549 (2006).
12. T. Morimune, H. Kajii, and Y. Ohmori, Frequency response properties of organic photo-detectors as opto-electrical conversion devices, *IEEE J. Display Technol.*, 2(2), 170–174 (2006).
13. T. Morimune, H. Kajii, and Y. Ohmori, Photo-response properties of a high-speed organic photo-detector based on copper phthalocyanine under red light illumination, *IEEE Photon. Technol. Lett.*, 18(24), 2602–2604 (2006).
14. C. Hosokawa, H. Tokailin, H. Higashi, and T. Kusumoto, Transient behavior of organic thin film electroluminescence, *Appl. Phys. Lett.*, 60(10), 1220–1222 (1992).
15. H. Kajii, K. Takahashi, J.-S. Kim, and Y. Ohmori, Study of the transient electroluminescence process using organic light-emitting diode with a partial doping layer, *Jpn. J. Appl. Phys.*, 45(4B), 3721–3724 (2006).
16. J.-S. Kim, H. Kajii, and Y. Ohmori, Characteristics of optical response in red organic light-emitting diodes using two dopant system for application to the optical link devices, *Thin Solid Films*, 499(1–2), 343–348 (2006).

# 16

---

## *Organic Light-Emitting Diodes in Chemical and Biological Sensors*

---

Ruth Shinar, Yuankun Cai, and Joseph Shinar

### CONTENTS

16.1 Introduction .....	529
16.2 Structurally Integrated OLED/Sensing Component Modules.....	531
16.3 Examples of Analyte Monitoring .....	532
16.3.1 Gas-Phase and Dissolved Oxygen.....	532
16.3.2 Multianalyte Sensing .....	537
16.4 Advantages and Challenges Related to the OLED-Sensing Platform.....	540
16.5 OLED/Sensing Component/Photodetector Integration .....	543
16.6 Summary and Concluding Remarks .....	546
References.....	546

---

### 16.1 Introduction

This chapter overviews recent developments in photoluminescence (PL)-based chemical and biological sensors, where an array of organic light-emitting diode (OLED) pixels, integrated with a sensor film, serves as the excitation source.

Sensitive and reliable sensors are important in many areas including environmental, medical, food and water safety, homeland security, and the chemical industry. Ideally, such sensors should also be low cost, compact, easy to fabricate, user friendly, fast in response, and suitable for high throughput monitoring of complex samples. Despite significant expansion in the field of chemical and biological sensors, their development, in particular that of field-deployable devices for monitoring multiple analytes, remains a challenge. Several viable options to encounter this challenge, which are under different stages of development, are based on organic electronics. These options include, e.g., organic thin-film transistors (OTFTs), as well as PL-based sensors with small-molecular OLEDs (SMOLEDs) or polymer LEDs (PLEDs) as

the excitation source. Currently, the use of organic-based photodetectors for monitoring analyte-induced changes in the PL intensity or decay time of the sensor component is also being explored.

OTFT-based sensors are promising devices with the potential to alleviate shortcomings of available sensors that are often bulky, costly, and require long sampling and data analysis periods.<sup>1</sup> OTFT sensors with different active layers are suitable for detecting various analytes. They are sensitive and reproducible and can track analyte-induced changes in, e.g., the bulk conductivity of an organic thin film, the field-induced conductivity, the transistor threshold voltage, and the field-effect mobility.<sup>2</sup> Combinatorial sensor arrays can be designed for analyte mixtures by manipulating the active layer's chemistry or morphology.<sup>1</sup> However, high specificity remains an open issue.<sup>3</sup> Importantly, devices with nanoscale channel length, whose operating mechanism differs from that of sensors with microscale dimensions (where the channel length is significantly larger than the grain size of the active layer), are very promising. Such devices exhibit strong analyte-induced increases in the drain current.<sup>1</sup>

Like the OTFT-based sensors, OLED-based photoluminescent chemical and biological sensors are very promising, as the field of PL-based and other optical chemical and biological sensors has been growing steadily.<sup>4–11</sup> Such sensors require a luminescent sensing component, whose PL is affected by the analyte, a light source that excites that PL, a photodetector (PD), a power supply, a signal processor, and a display or telemetry (for remote control) component. Compact light sources such as diode lasers and LEDs typically require intricate design (optical fibers, couplers, lens, mirrors, etc.) for incorporation in a compact device.<sup>12</sup> In contrast, we have recently demonstrated that OLEDs are promising light sources for a *uniquely simple* structurally integrated PL-based sensor platform<sup>13–26</sup> that includes miniaturized sensor arrays for high throughput, multianalyte analysis.

Multianalyte detection in a single sample has been reported extensively using electrochemical,<sup>27,28</sup> piezoelectric,<sup>29,30</sup> electrical resistance,<sup>31,32</sup> and optical<sup>10,11,33–39</sup> methods. The sensor arrays were fabricated by photolithography and soft lithography,<sup>28,32,40–42</sup> inkjet-, screen-, and pin-printing,<sup>38–43</sup> and photodeposition.<sup>10,34,44,45</sup> These techniques involve labor-intensive multistep fabrication and image analysis and pattern-recognition codes. The monochromatic or multicolor OLED excitation platform in (micro)arrays would drastically simplify fabrication and reduce cost.

Other developments, though still in early stages, appear promising for a field-deployable, diverse next-generation sensing platform. Such developments include the use of an integrated poly(paraphenylene vinylene) (PPV)-based PLED excitation source for microscale fluorescence detection<sup>26</sup>; an orthogonal detection geometry was employed to eliminate the need for optical filters. PLEDs were also used as integrated excitation sources in microscale capillary electrophoresis.<sup>46</sup> A polyfluorene PLED was integrated with a capillary electrophoresis device, which enabled detection of

separations of fluorescein and 5-carboxy-fluorescein with detection limits comparable to those obtained using a conventional mercury lamp as the excitation source. Blue-to-red PLEDs can be easily fabricated from solution and integrated with chip structures, and are therefore advantageous for portable devices. Further improvement of the PLEDs and the additional integration with thin-film organic PDs should yield multianalyte microfluidic systems for point-of-care applications. Indeed, the development of such PDs for microscale chemiluminescence assays was also reported.<sup>47</sup> The PDs, which were easy to fabricate, were based on copper phthalocyanine (CuPc)-C<sub>60</sub> and were used for monitoring a peroxyoxalate-based chemiluminescence reaction in a poly(dimethylsiloxane) (PDMS) microfluidic system. Steps toward the development of modular polymer-based microarray sensors, using both an OLED excitation source and an organic PD were also reported recently.<sup>48</sup>

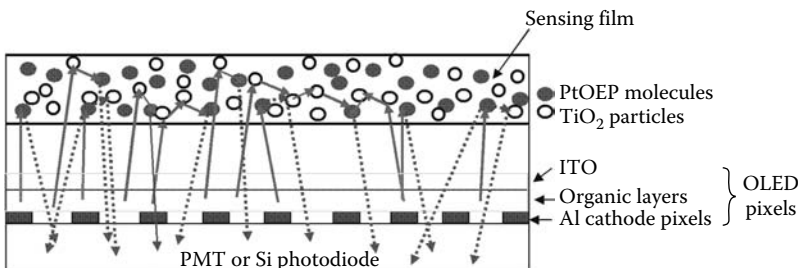
---

## 16.2 Structurally Integrated OLED/Sensing Component Modules

The SMOLEDs we fabricated (by vacuum thermal evaporation) for sensor development<sup>49</sup> consisted of an indium tin oxide (ITO)-coated glass anode substrate, organic hole- and electron-transporting layers (HTL and ETL, respectively), an emitting layer, and a metal cathode. Their thickness, excluding the substrate, was <0.5 μm. The structure and fabrication procedure of the SMOLEDs underscores their unique simplicity, versatility, and eventual low cost and ease of fabrication.<sup>49,50</sup> Their performance has improved dramatically over the past decade,<sup>51–55</sup> and they are proliferating in commercial products.<sup>54,55</sup> They are inherently advantageous as low-voltage,<sup>51–55</sup> miniaturizable,<sup>56</sup> and flexible light sources<sup>57</sup>; electrophosphorescent red-to-green OLEDs with external quantum efficiencies (EQEs)  $17 \leq \eta_{\text{ext}} \leq 20\%$ <sup>58</sup> and blue OLEDs with  $\eta_{\text{ext}} \approx 11\%$ <sup>54</sup> have been reported. Importantly for sensors, OLEDs can be operated at an extremely high brightness, and for micro- or nanoarray applications, 43–170 nm diameter OLED arrays were demonstrated recently.<sup>59</sup> Therefore, OLEDs are an attractive new platform for development of integrated multi-analyte (micro)sensor arrays.

Our recent studies demonstrated the viability of the structurally integrated OLED array/sensing film, where these components are fabricated on two separate glass slides that are attached back-to-back. This uniquely simple geometry eliminates the need for optical fibers, lens, and mirrors, resulting in a compact and potentially very low-cost OLED/sensor film module.<sup>13–21</sup> The close coupling of the excitation source with the sensor film also enables operation at relatively low power.

The PD, typically a photomultiplier tube (PMT) or a Si photodiode, is positioned either in front of the sensing film and sample volume (“front

**FIGURE 16.1**

Basic structure of an integrated OLED pixel array/luminescent sensor film module in the “back detection” geometry. The green solid arrows represent the OLED’s electroluminescence (EL); the red dotted arrows are the PL. An oxygen-sensitive dye and titania particles are embedded in the sensor film. The titania particles act as a scattering medium, increasing the absorption of the EL by the dye, strongly enhancing the PL. (From Zhou, Z. et al., in *Chemical and Biological Sensors for Industrial and Environmental Security*, Sedlacek III, A.J. et al. (Eds.), SPIE Conference Proceedings, vol. 5994, SPIE, Bellingham, WA, 2005, 59940E-1. With permission.)

detection”) or behind the OLED array (“back detection”; see Figure 16.1 for a basic scheme of this design). In this configuration, the PD collects the PL that passes through the gaps between the OLED pixels. Back-detection provides an obvious route for the additional integration of the PD with the integrated OLED-sensing element module, as the resulting sensor probe, which consists of the OLEDs, the sensing elements, and the PDs, is very compact when using <2 mm thick surface-mounted Si photodiodes. The small OLED pixel array also enables fabrication of compact multiple sensor arrays, with easily fabricated single- or multicolor OLED arrays.

Similar to inorganic LEDs, the cost of OLEDs and OLED arrays will drop to a disposable level, and will therefore enable the realization of field-deployable, compact, low cost, user-friendly, and autonomous sensors.

### 16.3 Examples of Analyte Monitoring

#### 16.3.1 Gas-Phase and Dissolved Oxygen

The most extensive efforts to develop the OLED-based sensor platform have focused on PL-based gas-phase and dissolved O<sub>2</sub> (DO) sensors. Such sensors, which have been studied for many years, are based on the efficient quenching of the PL of dyes such as Ru complexes and Pt or Pd porphyrins by collisions with O<sub>2</sub> molecules<sup>4–9,60–69</sup>; the sensitivity to O<sub>2</sub> is due to the nearly unique triplet nature of the ground state of O<sub>2</sub>. In an ideal homogeneous matrix, the O<sub>2</sub> concentration [O<sub>2</sub>] is related to the steady-state PL intensity  $I$  and the PL decay time  $\tau$  by the Stern–Volmer (SV) equation:

$$I_0/I = \tau_0/\tau = 1 + K_{SV}[O_2] \quad (16.1)$$

where

$I_0$  and  $\tau_0$  are the unquenched values

$K_{SV}$  is a temperature- and film-dependent constant

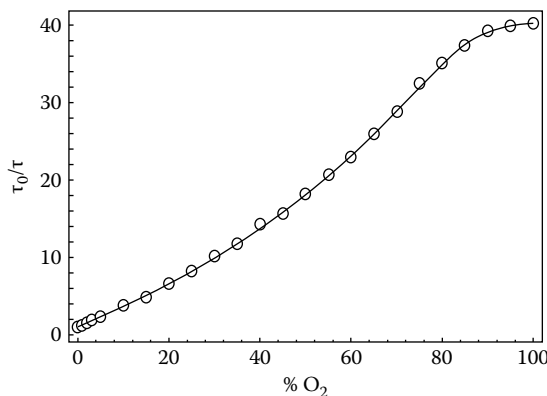
Despite the numerous reports, extensive studies of optical O<sub>2</sub> sensors are still ongoing to improve performance, reduce cost and size, and develop an O<sub>2</sub> sensor for *in vivo* applications.<sup>70</sup> The large market for O<sub>2</sub> sensors also drives these efforts. The development of field-deployable, compact, low-cost monitors such as those based on OLEDs is therefore highly attractive for gas-phase and DO monitoring in various biological, medical, environmental, and industrial applications.<sup>60–72</sup>

The fabrication of the OLED arrays, by thermal vacuum evaporation, was described previously.<sup>16,20,49,73–75</sup> In brief, following cleaning and a 3–5 min treatment in a UV ozone treatment, the ~100 nm thick ITO-coated glass was loaded onto the thermal vacuum evaporator, which was pumped to a background pressure of ~2 × 10<sup>-6</sup> torr. Then 5 nm of CuPc (a hole-injecting layer, which is also believed to reduce the surface roughness of the ITO<sup>76</sup>) followed by 50 nm of the common *N,N'*-diphenyl-*N,N'*-bis(1-naphthyl phenyl)-1,1'-biphenyl-4,4'-diamine (NPD) HTL, were deposited on the ITO. For the green OLEDs with peak emissions at ~535 and ~545 nm that were fabricated to excite Pt octaethylporphyrin (PtOEP) and its Pd analog PdOEP, respectively, the ~40 nm thick emitting layer and ETL were Alq<sub>3</sub> and rubrene-doped Alq<sub>3</sub>, respectively. In all cases, an 8–10 Å CsF or LiF buffer layer was deposited on the organic layers,<sup>77,78</sup> followed by the ~150 nm thick Al cathode. The total thickness of the OLEDs, excluding the glass mechanical support, was thus <0.5 μm.

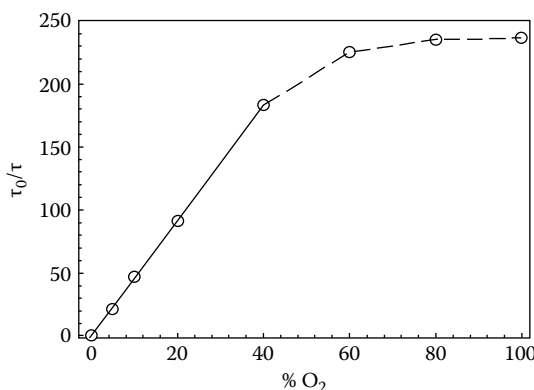
Structurally integrated Alq<sub>3</sub> OLED-based sensors with PtOEP and PdOEP embedded in polystyrene (PS) yielded the highest sensitivities in monitoring gas-phase O<sub>2</sub> and DO in water, ethanol, and toluene.<sup>20</sup> The gas-phase and DO sensors were evaluated extensively. In the gas-phase, the detection sensitivity is defined as  $S_g \equiv \tau_0/\tau(100\% O_2)$ ; in solution,  $S_{DO}$  is defined as the ratio of  $\tau$  measured in a deoxygenated solution to that of an oxygen-saturated solution (i.e., a solution in equilibrium with a pure O<sub>2</sub> atmosphere).

For an O<sub>2</sub>-sensitive dye in solution and for the solid matrix of the [blue OLED]/[Ru dye-based sensor film], the predicted linear SV dependence was confirmed.<sup>17,79</sup> However, deviations of SV plots from linearity are common (see Figures 16.2 and 16.3).

Changing the preparation conditions of the sensing film can also affect the linearity of the SV plot. Figure 16.4 shows a linear gas-phase plot obtained for a film prepared from a solution with a 1:10 PtOEP:PS ratio.  $S_g \sim 30$  is somewhat lower than the  $S_g \sim 40$  shown in Figure 16.2, whose plots were nonlinear.<sup>20</sup>

**FIGURE 16.2**

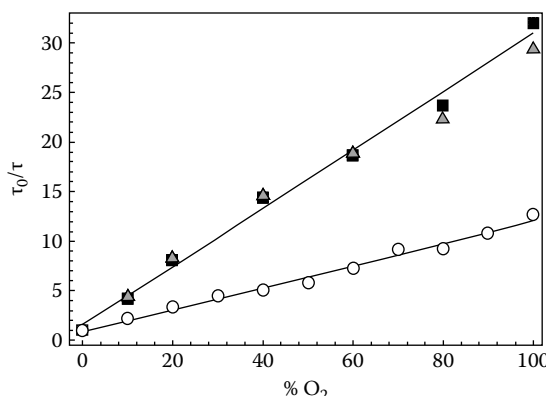
Example of an SV plot (see Equation 16.1) for gas-phase O<sub>2</sub> at 23°C obtained for a PtOEP:PS. (From Shinar, R. et al., *Anal. Chim. Acta*, 568, 190, 2006.)

**FIGURE 16.3**

The SV plot (see Equation 16.1) for gas-phase O<sub>2</sub> at 23°C, obtained from a drop-cast PdOEP:PS film excited by a rubrene-doped Alq<sub>3</sub> OLED. Note that the SV plot is linear only up to ~40% O<sub>2</sub>. (From Shinar, R. et al., *Anal. Chim. Acta*, 568, 190, 2006. With permission.)

Figure 16.4 also demonstrates the performance of the DO sensors in water. The detection sensitivity was ~12.5. In solution, the value of  $\tau_0 \sim 85\text{ }\mu\text{s}$  is shorter than the  $\sim 95\text{ }\mu\text{s}$  value measured in the gas-phase;  $\tau$  in O<sub>2</sub>-saturated water was  $\sim 8.9\text{ }\mu\text{s}$ . The relatively short  $\tau_0$  is probably due to the incomplete deoxygenation of the solvent and/or solvent-related PL quenching.<sup>69</sup> Through improvements in the PtOEP-doped PS films, we have recently improved  $S_{DO}$  from ~12.5 (Figure 16.4) to ~14, which is among the highest values reported to date.

The OLED-based sensors were tested in the  $23^\circ\text{C} \leq T \leq 60^\circ\text{C}$  temperature range.  $\tau$  generally decreases with increasing  $T$ , due to increased dynamic quenching,<sup>20,61</sup> but in the porphyrins that change is slight.<sup>80</sup> Indeed, the

**FIGURE 16.4**

Linear Stern–Volmer plots obtained for gas-phase O<sub>2</sub> at 23°C (■) and 55°C (△) for a PtOEP:PS film prepared by drop casting 50 μL of a solution containing 1 mg/mL PtOEP and 10 mg/mL PS, and SV plot for DO in water (○). (From Shinar, R. et al., *Anal. Chim. Acta*, 568, 190, 2006. With permission.)

temperature dependence of the SV plots was minimal, as only small reductions in  $\tau_0$  and  $\tau(100\% \text{ O}_2)$  were observed with increasing  $T$ . For example, for one film  $\tau_0$  decreased from ~91 to ~84 μs with  $S_g$  varying from ~36.5 to ~37.5.

The stability of the OLED/sensor film module was monitored over 30 days,  $\tau$  was measured in air using the Alq<sub>3</sub>/PtOEP:PS module. It slowly decreased from  $20.2 \pm 0.1$  to  $19.7 \pm 0.05$  μs, i.e., the relative error in the measurement decreased with time, from ~0.5% to ~0.25%. These and later results demonstrated that the lifetime of this sensor module is well beyond 30 days.

To monitor O<sub>2</sub> levels accurately and reliably over the entire 0%–100% O<sub>2</sub> range, PtOEP- and PdOEP-based sensors would be used simultaneously. Alternatively, by using different films prepared under different conditions (e.g., PS:dye ratio, film thickness), different SV plots and detection sensitivities are expected. For example, a simple array could consist of 2–4 Alq<sub>3</sub> OLED pixels exciting a 1:10 PtOEP:PS film, which exhibits near linear SV plot over the whole 0%–100% range (see Figure 16.4), and 2–4 rubrene-doped Alq<sub>3</sub> OLED pixels exciting a PdOEP:PS film, that is very sensitive to low levels of O<sub>2</sub> and exhibits a linear behavior up to ~40% O<sub>2</sub> (Figure 16.3).<sup>20</sup>

In summary, the results on the OLED-based O<sub>2</sub> sensor demonstrate the promise of the OLED-based chemical and biological sensor platform. The ease of OLED fabrication and unique simplicity of the structurally integrated OLED/sensing component result in compact modules, which are expected to be inexpensive and suitable for real-world applications. The results described earlier also demonstrate the advantages of monitoring the oxygen via the PL decay time, and the promise of the OLED pixel platform for developing sensor arrays for multiple analyses of a single analyte or for detection of multiple analytes, as shown in Section 16.3.2.

To improve the response of the dye-doped oxygen sensor films, we developed an approach to enhance the PL of the O<sub>2</sub> sensing films through doping with titania (TiO<sub>2</sub>) particles (see Figure 16.1). The index of refraction  $n$  of titania is ~2.8 over most of the visible range, so its dielectric contrast with the surrounding PS network, where  $n \sim 1.5$ , is high. Therefore, the titania particles reflect much of the light incident on them, resulting in efficient scattering of the incident EL into the dye-doped polymer matrix and a consequent increase in the optical path length of the EL in the film. This increased optical path length results in an increased absorption of the EL by the dye.<sup>22</sup>

To dope the sensor films with titania, we used common DuPont 360 nm-diameter titania particles. When excited by an OLED, the dye PL intensity increased up to ~10-fold, depending on the TiO<sub>2</sub> concentration and the excitation source. However, the enhanced PL is attributed to enhanced light scattering not only by the embedded particles, but possibly by voids (whose  $n = 1$ ), generated by the titania, as well.

The titania particles can also result in an increase in the PL outcoupling, reducing waveguiding to the film edges (Figure 16.1).

As an example of the effect of titania, Figure 16.5 shows the PL decay curves of PtOEP:PS, with and without titania, excited by Alq<sub>3</sub> OLEDs, in water in a 100% Ar environment and in O<sub>2</sub>-saturated water at room temperature. The strong enhancement in the PL intensity is clearly seen. The stronger PL increases the signal-to-noise (S/N) ratio without affecting the response time or the long-term stability of the sensor films (the particles,

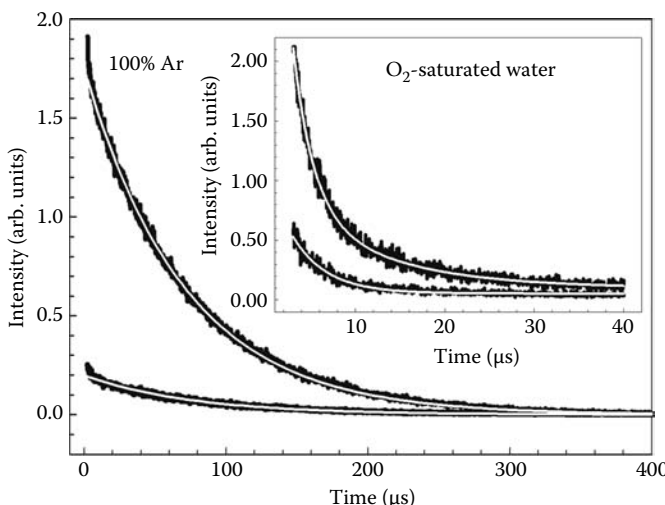


**FIGURE 16.5**

The PL decay curves in Ar- (and, in the inset, O<sub>2</sub>-) saturated solutions for PtOEP:PS with 360 nm diameter TiO<sub>2</sub> nanoparticles (upper curves) and without TiO<sub>2</sub> (lower curves). The white curves seen inside the experimental decay curves are the exponential (in Ar) and biexponential (in O<sub>2</sub>) fits. (From Zhou, Z. et al., *Adv. Func. Mater.*, 17, 3530, 2007. With permission.)

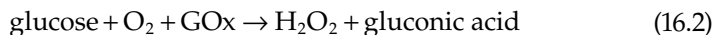
however, affect  $\tau$ , independently of their concentration). Consequently, the improved S/N improves the O<sub>2</sub> limit of detection (LOD), allows shortened data acquisition times, and allows lower-intensity excitation sources, thus reducing potential dye photobleaching. Lowering the OLED intensity also increases its own lifetime.

### 16.3.2 Multianalyte Sensing

As mentioned in Section 16.1, sensor arrays for multianalyte detection in a single sample have been studied extensively using various techniques that frequently involve labor-intensive multistep fabrication, complex image analysis, and pattern-recognition codes.<sup>10,11,27–45</sup> The OLED-based sensing platform presents an opportunity to develop compact structurally integrated multianalyte sensor arrays, which would be uniquely simple in their design and fabrication process. The individually addressable OLED pixels could be single- or combinatorial multicolor blue-to-red arrays.<sup>81</sup> OLED pixels of nanometer size, reported recently,<sup>59</sup> should be suitable for future sensor micro/nanoarrays for a wide range of applications.

The OLED-based multianalyte sensor was built on the preceding successful integration of the OLED/O<sub>2</sub> sensor. The analytes, present in a single sample, were DO, glucose, lactate, and ethanol, demonstrating also the viability of the platform for bioanalytes. These analytes are of clinical, health, industrial, and environmental importance. For demonstrating the sensing of the multiple analytes, the measurements were performed in sealed cells, where the O<sub>2</sub>-sensitive dye, embedded in a PS film, formed the base of reaction cells. Analyte mixtures were added to such cells, each containing a buffered solution of an enzyme that specifically oxidizes glucose, ethanol, or lactate. The total volume of the filled cells was 100–200 µL. Sealed cells were used due to the more complex responses observed in a cell open to air, where a relatively constant supply of oxygen is available.<sup>19</sup> Additionally, measurements in sealed cells resulted in a low ~0.01–0.02 mM LOD for each of the latter three analytes. We note that our previous studies demonstrated also the OLED-based platform for measuring glucose, where the enzyme, like the O<sub>2</sub>-sensitive dye, was embedded in a solid thin film, rather than dissolved in solution. In other reports, the excitation sources in similar PL-based glucose biosensors have included Ar<sup>+</sup> lasers operated at 20–40 mW,<sup>7</sup> Hg lamps,<sup>30</sup> or a fluorometer equipped with a 150 W Xe lamp.<sup>82</sup> The glucose concentration,  $c_{\text{Gl}}$ , was usually monitored via changes in  $I$ .

As a specific example, glucose sensing relies on its enzymatic oxidation by glucose oxidase (GOx) (see Equation 16.2);  $c_{\text{Gl}}$  can be determined by analyzing the reaction products,<sup>33</sup> or by measuring  $I$  or  $\tau$  of the oxygen-sensitive dye,<sup>30</sup> coembedded with GOx in a thin film (e.g., sol–gel) or dissolved in solution.



In the presence of glucose, the PL quenching of the O<sub>2</sub>-sensitive dye is reduced (i.e.,  $I$  and  $\tau$  increase) due to O<sub>2</sub> consumption during the enzymatic oxidation.<sup>7,80,82,83</sup> A similar reaction in the presence of lactate oxidase (LOx) or alcohol oxidase (AOx) describes lactate or ethanol oxidation, respectively.

Using the OLED sensor array, the analytes can be monitored in sequence, using a single PD. Simultaneous detection, using several films, can be achieved by using a compatible small-size array of Si-based PDs. Comparable results were obtained using both approaches. The sensors were operated in the back-detection geometry and  $\tau$  mode and the measurements were performed in sealed cells, where there is no supply of DO beyond the initial concentration. Then calibration curves are obtained by noting that if the initial analyte concentration [analyte]<sub>initial</sub> is smaller than the initial DO concentration [DO]<sub>initial</sub>, and the analyte conversion into products is complete, the final DO concentration [DO]<sub>final</sub> is given by

$$[\text{DO}]_{\text{final}} = [\text{DO}]_{\text{initial}} - [\text{analyte}]_{\text{initial}} \quad (16.3)$$

The SV equation becomes, accordingly

$$I_0/I = \tau_0/\tau = 1 + K_{\text{SV}} \times \{[\text{DO}]_{\text{initial}} - [\text{analyte}]_{\text{initial}}\} \quad (16.4)$$

Thus,  $1/\tau$  will ideally be linear in the initial analyte concentration, yielding  $K_{\text{SV}}$ , which, as expected, was found to be film-dependent. Note that Equation 16.4 is valid for measurements performed with containers open to air as well, if the oxidation reaction is much faster than the in-diffusion of gas-phase oxygen.

The validity of Equation 16.4 was confirmed in analyses of single analytes. Figure 16.6 shows an example of monitoring ethanol in a sealed cell at ~22°C.

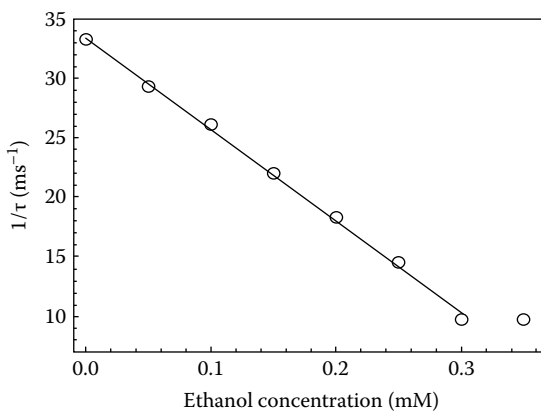


**FIGURE 16.6**

1/ $\tau$  vs. ethanol concentration. The reaction was performed in a sealed cell at 22°C. The enzyme concentration was 75 units/mL.

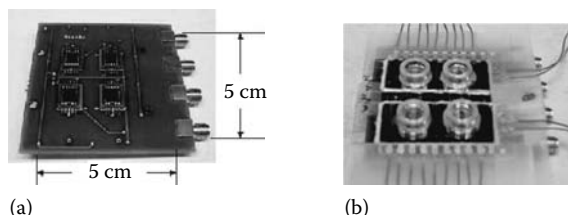
The PL decay time was measured 5 min after addition of the analyte to the buffered enzyme solution. We note that the oxidation reactions of the above analytes were slow and, as expected, depended on the enzyme concentration. As seen,  $1/\tau$  vs. the ethanol concentration is linear over a concentration range of 0–0.3 mM.

The ~0.25 mM limit of the dynamic range (corresponding to the ~8.6 ppm DO level in equilibrium with air at ~23°C) corresponds to the diluted analyte in the final test solution. Hence, higher initial analyte concentrations, which cover the concentration range of medical/industrial interest, can be used.

Figure 16.7 shows the design of the multianalyte sensor array in the back-detection geometry. The array includes (1) the Alq<sub>3</sub>-based  $2 \times 2\text{mm}^2$  OLED pixels (not shown), defined by the overlap between the mutually perpendicular ITO and Al stripes (we note that there is no cross talk between the pixels), (2) the  $5 \times 5\text{mm}^2$  Si photodiodes assembled in an array compatible with the OLED pixel array and located underneath it, and (3) the reaction cells, whose base is the PtOEP:PS film, on top. As mentioned, three of these reaction cells contained each an enzyme that specifically catalyzes the oxidation of one of the analytes. Two OLED pixels were used for each of the four analytes.

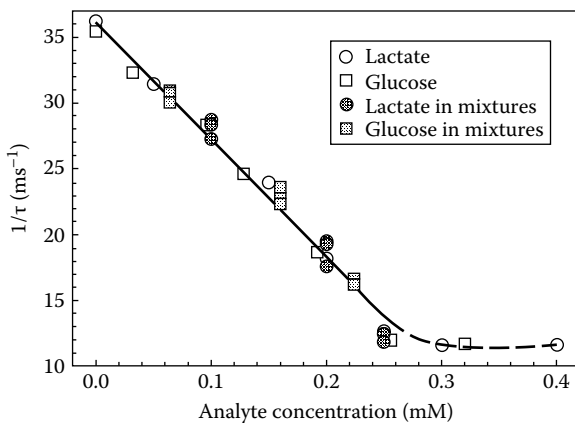
Using the setup of Figure 16.7, mixtures of the four analytes were analyzed simultaneously, with the output of each PD corresponding to a different analyte. We note that various Si-based PD arrays with rectangular 1–4 mm<sup>2</sup> elements are available commercially (from, e.g., Hamamatsu) and can be used in conjunction with OLED arrays for monitoring a larger number of analytes.

Figure 16.8 shows a calibration curve obtained by monitoring lactate and glucose separately, together with data points obtained from simultaneous measurements of these analytes in mixtures. As seen, a universal linear calibration curve is obtained for comparable films for glucose, lactate, and ethanol, and the calibration line fits the modified SV equation (Equation 16.4) well. That is, for comparable sensor films, the data for all three analytes can be presented by a single line, with  $\tau$  being independent of the analyte, whether glucose, lactate, or ethanol, due to the similar oxidation reactions and the actual monitoring of the DO level.



**FIGURE 16.7**

The sensor array designed for four analytes: (a) the Si photodiode array and (b) the complete structure in the back-detection geometry, with four reaction cells, whose base is a PtOEP:PS film, on top of the OLED array. ((b) From Cai, Y. et al., *Sens. Actuators B*, 134, 727, 2008. With permission.)

**FIGURE 16.8**

$1/\tau$  vs. analyte concentration. The reactions were performed in a sealed cell at 23°C. The gray data points represent the analytes in mixtures. (From Cai, Y. et al., *Sens. Actuators B*, 134, 727, 2008. With permission.)

No interference between the analytes was observed and the reaction for a given analyte occurred only in the presence of the specific corresponding enzyme. The presence of the three analytes at varying total concentrations did not affect  $\tau$  for each of the analytes at a given concentration. The deviations of the individual values from the average were <2%. As a typical example, in the presence of LOx,  $\tau$  for 0.1 and 0.2 mM lactate varied from 45.3 to 46.1  $\mu$ s and from 68.0 to 69.1  $\mu$ s, respectively, in the presence of any combination of 0.15 or 0.35 mM ethanol and 0.15 or 0.35 mM glucose.

The multianalyte sensor was operated also sequentially. In that case the OLED pixels associated with the different analytes are lit sequentially, monitoring separately each of the analytes in mixtures.<sup>19</sup> A single PD was used when utilizing this approach, and the results were comparable to those obtained in the simultaneous measurements.

To summarize, the results show that the use of the compact OLED-based sensor array is a viable approach for simultaneous monitoring of these multiple analytes. As described later, work is in progress to develop more compact sensors, where additionally  $\mu$ m-thick thin-film PD arrays, such as those based on amorphous or nanocrystalline Si (nc-Si), are structurally integrated with the OLED/sensing component module.<sup>21</sup>

#### 16.4 Advantages and Challenges Related to the OLED-Sensing Platform

Recent developments, some of which were described above, demonstrated the viability of the OLED-based sensing platform for chemical and biological

analytes. The advantages of the OLEDs as excitation sources include their high brightness, design flexibility, suitability for glass or plastic substrates, and consequently, compatibility with microfluidic architectures. Moreover, OLED arrays are easily fabricated and integrated with the sensor component, and their pixels can be individually addressed to eventually generate low cost, miniaturized sensor arrays for monitoring multiple analytes. Importantly, OLEDs can be operated in a pulsed mode, and as the EL decay time of fluorescent OLEDs (as opposed to phosphorescent OLEDs) is typically  $<100\text{ ns}$ , they can be used in suitable instances in the  $\tau$  mode, which eliminates the need for frequent sensor calibration and optical filters. We note also that the constantly improving long-term stability of OLEDs with improved fabrication and encapsulation methods will increase the utility of the OLED-sensing platform.

The PtOEP and PdOEP dyes, used in the examples provided above, have a large Stokes shift; their absorption bands peak at  $\sim 380\text{ nm}$  and  $\sim 535\text{--}545\text{ nm}$  (the latter suitable for excitation with the Alq<sub>3</sub>-based OLEDs), while their emission peaks at  $\sim 640\text{ nm}$ . This attribute enables their successful use not only in the  $\tau$  mode, but also in the  $I$  mode, as the OLED EL tail at the PL wavelength is minimal.

Another example of a successful OLED-based sensor is that of hydrazine (N<sub>2</sub>H<sub>4</sub>).<sup>18</sup> Hydrazine, a highly toxic and volatile compound, is used in NASA space shuttles as a powerful monopropellant, and it is also a common precursor in the synthesis of some polymers, plasticizers, and pesticides. The American Conference of Governmental Industrial Hygienist has recommended that the threshold limit value (TLV) for hydrazine exposure (i.e., the time-weighted average concentration of permissible exposure within a normal 8 h workday) be lowered from 100 to 10 ppb in air; a level of 56 ppm is considered an immediate life-threatening level.<sup>84</sup> The OSHA-recommended skin exposure limit is 0.1 ppm.<sup>85</sup>

The PL-based hydrazine sensor is based on the reaction between N<sub>2</sub>H<sub>4</sub> and anthracene 2,3-dicarboxaldehyde (ADA).<sup>18,86</sup> While the reactants are not emissive, the reaction product can be excited at 476 nm by a blue 4,4'-bis(2,2'-diphenylvinyl)-1,1'-biphenyl (DPVBi)-based OLED<sup>18,74,75</sup> to emit at 549 nm; the signal is proportional to the N<sub>2</sub>H<sub>4</sub> level. The OLEDs used were operated in a dc or pulsed mode with a forward bias of 9–20 V or up to 35 V, respectively. The PD was a PMT. The LOD of hydrazine was  $\sim 60\text{ ppb}$  in 1 min, i.e., roughly equivalent to 1 ppb in 1 h. That is, the LOD using this system exceeds the OSHA requirements by a factor of  $\sim 80$ .

In other instances, where analyte-sensitive dyes with a narrower Stokes shift are utilized, the contribution of the long-wavelength EL tail to the background can be large, reducing the detection sensitivity and deteriorating the LOD. An example for that behavior is that of a sensor for anthrax lethal factor (LF), which is one of the three proteins of the anthrax toxin secreted by the live *Bacillus anthracis* bacterium. The development of a compact, field-deployable, and low-cost sensor for prompt, on-site detection of

such bacteria is obviously highly desirable. As a first step toward this goal, we tested an OLED-based sensor for anthrax LF. The sensor is based on the cleavage of certain peptides by LF.<sup>87–89</sup> Such a peptide is labeled by a fluorescence resonance energy transfer (FRET) donor–acceptor pair, with the donor on one side of the cleavage site and the acceptor on the other side. As the LF cleaves the peptide, and the two cleaved segments are separated, the PL of the donor, previously absorbed by the acceptor, becomes detectable by the photodetector.

A suitable peptide with a rhodamine-based dye as the donor and a Molecular Probes QSY7 dark quencher as the acceptor was synthesized.<sup>18</sup> Preliminary results using green ITO/CuPc/NPD/Alq<sub>3</sub>/CsF/Al OLEDs biased at 28 V indicated that for 25 nM LF and varying levels of the peptides, at 37°C the PL change reached its maximal value of ~100% after an incubation time of ~15 min and a peptide concentration of ~40 μM. This overall PL change is relatively low (a ~16-fold increase in the PL excited by a laser was reported by Cummings et al.<sup>87</sup>), probably due to the broad EL spectrum of the Alq<sub>3</sub> OLED and the small Stokes shift of only ~20 nm between the absorption and emission peaks of the rhodamine dye. Indeed, using a green inorganic LED with a 530 nm bandpass filter, and a 550 nm long pass filter in front of the PMT, resulted in an increase by a factor of 6 in the PL following peptide cleaving by LF.<sup>90</sup>

To that end, other donor–acceptor pairs are being examined, together with microcavity OLEDs with narrower EL bands, such as that shown in Figure 16.9. Other approaches to reduce the contribution of the EL tail are under investigation. These include the use of orthogonal detection, or polaroids, which are at 90° to each other, above the OLED and in front of the PD.<sup>91</sup>

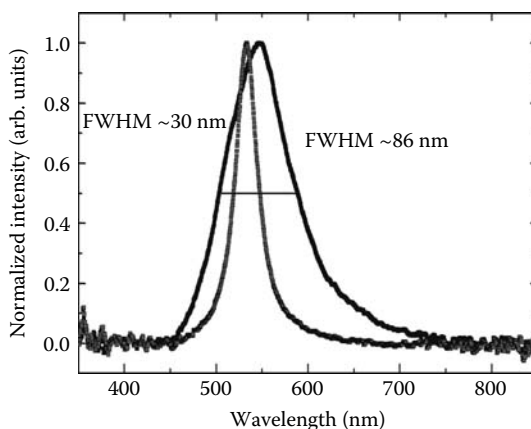


**FIGURE 16.9**

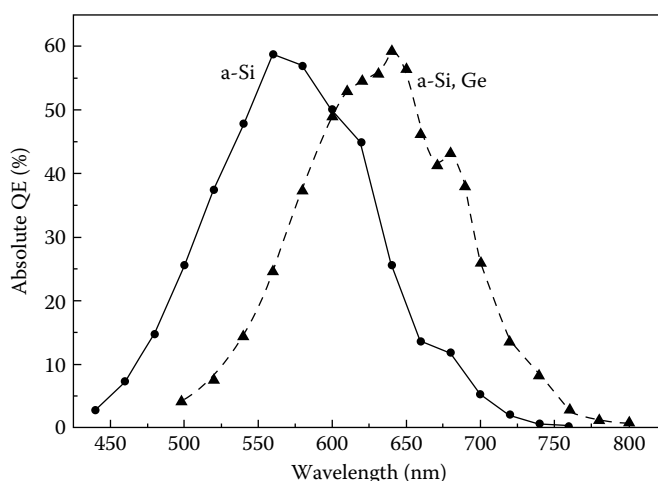
Microcavity Alq<sub>3</sub>-based OLED with reduced EL band width. (From Shinar, J. and Shinar, R., *J. Phys. D: Appl. Phys.*, 41, 13301, 2008. With permission.)

## 16.5 OLED/Sensing Component/Photodetector Integration

To enhance the structural integration of the different components of the OLED-based sensor platform, efforts are underway to evaluate a fully integrated platform, where the PD is a p-i-n or n-i-p structure based on thin films of hydrogenated amorphous Si (a-Si:H) and related materials, or nanocrystalline Si (nc-Si).<sup>21</sup> These efforts focus on the oxygen sensors described above.

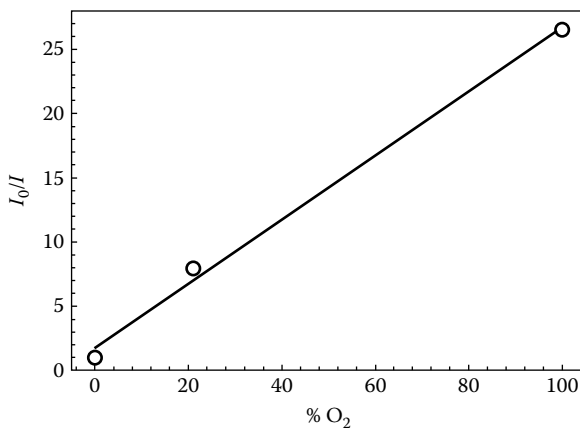
Similar to the OLEDs, the thin-film Si-based PDs are also fabricated on glass or plastic substrates. The PDs were first tuned to reduce their sensitivity to the OLED excitation (peaking at ~540 nm) and enhance it at the emission wavelengths of PtOEP and PdOEP (~640 nm). For this purpose, a-Si:H and a-(Si,Ge):H PDs were evaluated by measuring their quantum efficiency (QE) vs. wavelength.<sup>21</sup> Figure 16.10 shows the QE spectra of electron cyclotron resonance (ECR)-deposited a-Si:H- and a-(Si,Ge):H PDs. As seen, the latter are preferred due to their better match with the dyes' PL, and lower response at the EL band. However, a-(Si,Ge):H PDs were inferior due to their higher dark current and slower speed.

Initial results using the three-component integrated sensor resulted in small responses due to the broad EL band, and the relatively large PD dark current ( $1.5 \times 10^{-8}$  A/cm<sup>2</sup>). Improved OLEDs and PDs increased the detection sensitivity  $S$  to ~7 using an Alq<sub>3</sub> excitation source, a PtOEP:PS film, and an n-i-p a-(Si,Ge)-based PD.  $S \sim 26$  was obtained for the PdOEP:PS film, as shown in Figure 16.11. The dark current in an n-i-p device, where the p layer is grown last, was reduced, due to elimination of boron diffusion from the p layer to the i layer during growth.<sup>92,93</sup>



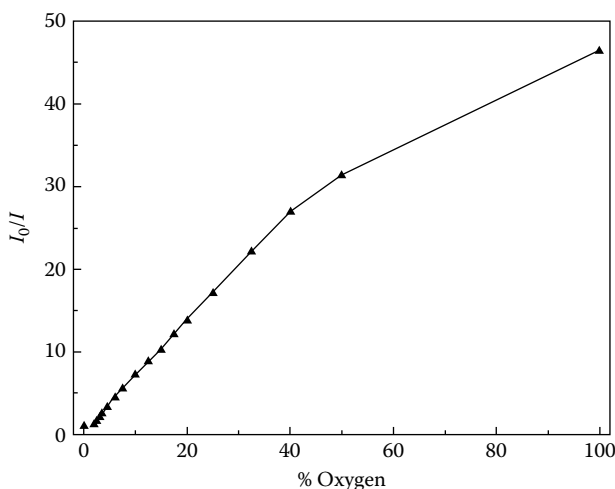
**FIGURE 16.10**

The QE vs. wavelength of ECR-grown a-Si- and a-(Si,Ge) PDs. (From Ghosh, D. et al., *J. Non-Crystal. Sol.*, 354, 2606, 2008. With permission.)

**FIGURE 16.11**

SV plot for a gas-phase O<sub>2</sub> sensor with structurally integrated Alq<sub>3</sub>/PdOEP:PS/thin-film PD.

As shown in Figure 16.12, a higher sensitivity,  $S \sim 47$ , was achieved for an integrated sensor of [coumarin-doped Alq<sub>3</sub> OLED]/[PdOEP-doped PS sensor film]/[VHF-grown SiC/a-Si/nc-Si ( $p^+$  layer):nc-Si ( $i$  layer) PD]. This higher sensitivity was achieved in part by shielding the electromagnetic noise stemming from the pulsed OLED.<sup>93</sup> Though this sensitivity is still lower than that obtained using a PMT (see Figure 16.3), it still demonstrates the promise of the three-component integrated platform. However,

**FIGURE 16.12**

$I_0/I$  vs. gas-phase O<sub>2</sub> concentration using the three-component integrated OLED/PdOEP:PS/nc-Si-based PD. (From Ghosh, D. et al., *J. Non-Cryst. Sol.*, 354, 2606, 2008. With permission.)

when using the thin-film PD, the sensor was operated successfully only in the *I* mode, since the response time of the detection circuit was long. The shortest response time,  $\sim 250\text{ }\mu\text{s}$ , was obtained for the nc-Si-based PD. This response time is too slow to enable monitoring oxygen in the  $\tau$  mode, which is clearly advantageous over the intensity mode. Therefore, current efforts focus on elucidating the factors that affect the speed of these PDs, in the hope that they will lead to faster PDs. For example, it was recently observed that the PDs' speed is affected by the device structure, with boron diffusion from the  $p^+$  to the *i* layer during growth resulting in a reduced speed. Incorporating a SiC buffer layer and a superstrate structure, where the  $p^+$  layer was grown last, resulted in an increase in the speed. The effects of Ge, nanocrystallinity and grain passivation, bandgap, defect states, as well as the illumination wavelength, and reverse bias are also being considered. Additionally, efforts are centered on improving the design of the sensor and the PD, as well as devising approaches to block the EL tail at  $\lambda > 600\text{ nm}$ . The goal is to reduce the dark current of the PD by a factor  $> 100$  and the EL tail at the PL emission band by a factor  $> 4$ . Potentially faster organic photodetectors may be suitable for the  $\tau$  mode of operation.<sup>94</sup>

The long-term goal is to develop the OLED-sensing platform for monitoring multiple analytes using sensor arrays, eventually miniaturized, with integrated OLED pixel and PD arrays. As demonstrated, single-color OLEDs are suitable for multianalyte detection. The use of multicolor OLED pixels, such as those fabricated combinatorially<sup>74,76</sup> and shown in Figure 16.13, are also being examined for use in sensing applications with different colors of probes.

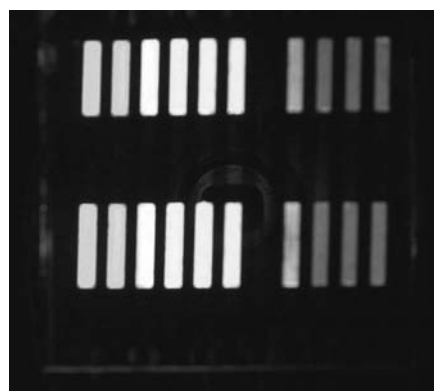


**FIGURE 16.13**

An OLED array with blue-to-red EL pixels that can potentially be used in multianalyte sensor arrays utilizing different probes. (From Cheon, K.O. and Shinar, J., *Appl. Phys. Lett.*, 83, 2073, 2003. With permission.)

---

## 16.6 Summary and Concluding Remarks

This review demonstrated the advantages of the structurally integrated OLED-based platform for luminescent chemical and biological sensors, which include their ease of fabrication, unique simplicity of integration with the sensing elements, consequent potential low cost and field deployability, and promise as efficient light sources in sensor (micro)arrays for detection of multiple analytes in microfluidic architectures. The viability of this compact platform was demonstrated for gas-phase and dissolved oxygen, hydrazine, and simultaneous monitoring of the bioanalytes, O<sub>2</sub>, glucose, lactate, and ethanol. Initial results on efforts to integrate a thin-film Si PD with an integrated OLED/oxygen sensor film were also described. These results are promising but require additional improvement. If successful, they could lead to badge-size monitors.

The oxygen and multianalyte sensors were operated in a pulsed mode; the phosphorescent PL decay-time  $\tau$ , which is much longer than the EL lifetime, yielded the analyte concentration. This mode of operation is strongly preferred over intensity measurements, because it eliminates the need for frequent sensor calibration and optical filters, as  $\tau$  is independent of moderate changes in the sensing film, light source intensity, and background light.

Some current and future directions to enhance this platform include: (1) the fabrication of microcavity, stacked, and/or graded junction phosphorescent OLEDs. The latter would be narrower band, more efficient, and longer-lived than the conventional fluorescent OLEDs, respectively. Their narrow EL spectra could be tailored to the absorption spectrum of the sensing element, resulting in drastic improvement of the sensor platform. (2) Development of the platform for various biological sensors, notably sensors for food-borne pathogens, which are a major ongoing issue in the global food supply chain. (3) Improvement of nc-Si-based thin-film PDs to shorten their response time and evaluation of organic PDs for structural integration with the OLED/sensing element module.

---

## References

1. L. Wang, D. Fine, D. Sharma, L. Torsi, and A. Dodabalapur, Nanoscale organic and polymeric field-effect transistors as chemical sensors, *Anal. Bioanal. Chem.* **384**, 310–321 (2006).
2. L. Torsi, A. Dodabalapur, L. Sabbatini, and P. G. Zambonin, *Sens. Actuators B* **67**, 312 (2000).
3. M. C. Tanese, L. Torsi, G. M. Farinola, L. Valli, O. Hassan Omar, G. Giancanec, E. Ieva, F. Babudri, F. Palmisano, F. Naso, and P. G. Zambonin, in *Organic-Based Chemical and Biological Sensors*, Edited by R. Shinar and G. G. Malliaras, *SPIE Conf. Proc.* vol. **6659**, 66590A-1 (SPIE, Bellingham, WA, 2007).

4. O. S. Wolfbeis, L. Weis, M. J. P. Leiner, and W. E. Ziegler, *Anal. Chem.* **60**, 2028 (1988).
5. B. H. Weigl, A. Holobar, W. Trettnak, I. Klimant, H. Kraus, P. O'Leary, and O. Wolfbeis, *J. Biotech.* **32**, 127 (1994).
6. P. Hartmann and W. Ziegler, *Anal. Chem.* **68**, 4512 (1996).
7. Z. Rosenzweig and R. Kopelman, *Sens. Actuators B* **35–36**, 475 (1996).
8. B. D. MacCraith, C. McDonagh, A. K. McEvoy, T. Butler, G. O'Keeffe, and V. Murphy, *J. Sol-Gel Sci. Technol.* **8**, 1053 (1997).
9. A. K. McEvoy, C. M. McDonagh, and B. D. MacCraith, *Analyst* **121**, 785 (1996).
10. V. K. Yadavalli, W.-G. Koh, G. J. Lazur, and M. V. Pishko, *Sens. Actuators B* **97**, 290 (2004).
11. M. Vollprecht, F. Dieterle, S. Busche, G. Gauglitz, K.-J. Eichhorn, and B. Voit, *Anal. Chem.* **77**, 5542 (2005).
12. E. J. Cho and F. V. Bright, Optical sensor array and integrated light source, *Anal. Chem.* **73**, 3289 (2001).
13. W. Aylott, Z. Chen-Esterlit, J. H. Friedl, R. Kopelman, V. Savvateev, and J. Shinar, U.S. Patent No. 6,331,438 (December 2001).
14. V. Savvate'ev, Z. Chen-Esterlit, C.-H. Kim, L. Zou, J. H. Friedl, R. Shinar, J. Shinar, and R. Kopelman, *Appl. Phys. Lett.* **81**, 4652 (2002).
15. B. Choudhury, R. Shinar, and J. Shinar, in *Organic Light Emitting Materials and Devices VII*, Edited by Z. H. Kafafi and P. A. Lane, *SPIE Conf. Proc.* **5214**, 64 (2004).
16. B. Choudhury, R. Shinar, and J. Shinar, *J. Appl. Phys.* **96**, 2949 (2004).
17. R. Shinar, B. Choudhury, Z. Zhou, H.-S. Wu, L. Tabatabai, and J. Shinar, in *Smart Medical and Biomedical Sensor Technology II*, Edited by Brian M. Cullum, *SPIE Conf. Proc.* **5588**, 59 (2004).
18. Z. Zhou, R. Shinar, B. Choudhury, L. B. Tabatabai, C. Liao, and J. Shinar, in *Chemical and Biological Sensors for Industrial and Environmental Security*, Edited by A. J. Sedlacek III, S. D. Christensen, R. J. Combs, and T. Vo-Dinh, *SPIE Conf. Proc.* vol. **5994**, 59940E-1 (SPIE, Bellingham, WA, 2005).
19. R. Shinar, C. Qian, Y. Cai, Z. Zhou, B. Choudhury, and J. Shinar, in *Smart Medical and Biomedical Sensor Technology III*, Edited by B. M. Cullum and J. C. Carter, *SPIE Conf. Proc.* vol. **6007**, 600710-1 (SPIE, Bellingham, WA, 2005).
20. R. Shinar, Z. Zhou, B. Choudhury, and J. Shinar, *Anal. Chim. Acta* **568**, 190 (2006).
21. R. Shinar, D. Ghosh, B. Choudhury, M. Noack, V. L. Dalal, and J. Shinar, *J. Non Crystal. Solids* **352**, 1995 (2006).
22. Z. Zhou, R. Shinar, A. J. Allison, and J. Shinar, *Adv. Func. Mater.* **17**, 3530 (2007).
23. Y. Cai, R. Shinar, Z. Zhou, C. Quain, and J. Shinar, *Sensors & Actuators B* **134**, 727 (2008).
24. J. Shinar and R. Shinar, *J. Phys. D: Appl. Phys.* **41**, 133001 (2008).
25. S. Camou, M. Kitamura, J.-P. Gouy, H. Fujita, Y. Arakawa, and T. Fujii, *Proc. SPIE* **4833**, 1 (2002).
26. O. Hofmann, X. Wang, J. C. deMello, D. D. C. Bradley, and A. J. deMello, *Lab Chip* **5**, 863 (2005).
27. H. Frebel, G.-C. Chemnitius, K. Cammann, R. Kakerow, M. Rospert, and W. Mokwa, *Sens. Actuators B* **43**, 87–93 (1997).
28. M. S. Wilson and W. Nie, *Anal. Chem.* **78**, 2507–2513 (2006).
29. I. Sugimoto, M. Nakamura, and H. Kuwano, *Sens. Actuators B* **10**, 117–122 (1993).

30. E. T. Zellers and M. Han, *Anal. Chem.* **68**, 2409 (1996).
31. M. S. Freund and N. S. Lewis, *Proc. Natl. Acad. Sci. U.S.A.* **92**, 2652–2656 (1995).
32. A. Carbonaro and L. Sohn, *Lab Chip* **5**, 1155 (2005).
33. C. A. Rowe, L. M. Tender, M. J. Feldstein, J. P. Golden, S. B. Scruggs, B. D. MacCraith, J. J. Cras, and F. S. Ligler, *Anal. Chem.* **71**, 3846–3852 (1999).
34. T. A. Dickinson, J. White, J. S. Kauer, and D. R. Walt, *Nature* **382**, 697 (1996).
35. D. R. Walt, T. Dickinson, J. White, J. Kauer, S. Johnson, H. Engelhardt, J. Sutter, and P. Jurs, *Biosens. Bioelectron.* **13**, 697–699 (1998).
36. K. L. Michael, L. C. Taylor, S. L. Schultz, and D. R. Walt, *Anal. Chem.* **70**, 1242–1248 (1998).
37. M. D. Marazuela and M. C. Moreno-Bondi, *Anal. Bioanal. Chem.* **372**, 664–682 (2002).
38. E. J. Cho and F. V. Bright, *Anal. Chem.* **74**, 1462 (2002).
39. E. J. Cho, Z. Tao, E. C. Tehan, and F. V. Bright, *Anal. Chem.* **74**, 6177 (2002).
40. S. P. A. Fodor, R. P. Rava, X. C. Huang, A. C. Pease, C. P. Holmes, and C. L. Adams, *Nature* **364**, 555–556 (1993).
41. M. Chee, R. Yang, E. Hubbell, A. Berno, X. C. Huang, D. Stern, J. Winkler, D. J. Lockhart, M. S. Morris, and S. P. A. Fodor, *Science* **274**, 610–614 (1996).
42. G. McGall, J. Labadie, P. Brock, G. Wallraff, T. Nguyen, and W. Hinsberg, *Proc. Natl. Acad. Sci. U.S.A.* **93**, 13555–13560 (1996).
43. V. Lemmo, J. T. Fisher, H. M. Geysen, and D. J. Rose, *Anal. Chem.* **69**, 543–551 (1997).
44. L. Li and D. R. Walt, *Anal. Chem.* **67**, 3746 (1995).
45. Y.-H. Liu and T. H. Pantano, *Anal. Chim. Acta* **419**, 215–225 (2000).
46. J. B. Edel, N. P. Beard, O. Hofmann, D. D. C Bradley, and A. J. deMello, *Lab Chip* **4**, 136 (2004).
47. O. Hofmann, P. Miller, P. Sullivan, T. S. Jones, J. C. deMello, D. D. C. Bradley, and A. J. deMello, *Sens. Actuators B* **106**, 878 (2005).
48. R. Sharpe, P. Rensing, G. van Heck, B. Allard, M. Koetse, N. Meulendijks, P. Kruijt, M. Tijdink, R. de Zwart, S. van Veen, and H. Schoo, in *Organic-Based Chemical and Biological Sensors*, Edited by R. Shinar and G. G. Malliaras, *SPIE Conf. Proc.* vol. **6659**, 665908-1 (SPIE, Bellingham, WA, 2007).
49. J. Shinar and V. Savvate'ev, in *Organic Light-Emitting Devices: A Survey*, Edited by J. Shinar, Chap. 1 (Springer Verlag, New York, 2003).
50. J. Shinar, Editor, *Organic Light-Emitting Devices: A Survey* (Springer Verlag, New York, 2003).
51. C. Adachi, M. A. Baldo, S. R. Forrest, S. Lamansky, M. E. Thompson, and R. C. Kwong, *Appl. Phys. Lett.* **78**, 1622 (2001).
52. C. Adachi, R. C. Kwong, P. Djurovich, V. Adamovich, M. A. Baldo, M. E. Thompson, and S. R. Forrest, *Appl. Phys. Lett.* **79**, 2082 (2001).
53. R. H. Friend, R. W. Gymer, A. B. Holmes, J. H. Burroughes, R. N. Marks, C. Taliani, D. D. C. Bradley, D. A. Dos Santos, J. L. Brédas, M. Lögdlund, and W. R. Salaneck, *Nature* **397**, 121 (1999).
54. [www.universaldisplay.com](http://www.universaldisplay.com)
55. [www.cdt.co.uk](http://www.cdt.co.uk)
56. [www.emagincorp.com](http://www.emagincorp.com)
57. G. Gustafsson, Y. Cao, G. M. Treacy, F. Klavetter, N. Colaneri, and A. J. Heeger, *Nature* **357**, 447 (1992); C. C. Wu, S. D. Theiss, G. Gu, M. H. Lu, J. C. Sturm, S. Wagner, and S. R. Forrest, *IEEE Electron Device Lett.* **18**, 609 (1997); H. Kim, J. S.

- Horwitz, G. P. Kushto, Z. H. Kafafi, and D. B. Chrisey, *Appl. Phys. Lett.* **79**, 284 (2001); E. Guenther, R. S. Kumar, F. Zhu, H. Y. Low, K. S. Ong, M. D. J. Auch, K. Zhang, and S. J. Chua, in *Organic Light-Emitting Materials and Devices V*, Edited by Z. H. Kafafi, *SPIE Conf. Proc.* vol. **4464**, p. 23 (SPIE, Bellingham, WA, 2002); T.-F. Guo, S.-C. Chang, S. Pyo, and Y. Yang, in *Organic Light-Emitting Materials and Devices V*, Edited by Z. H. Kafafi, *SPIE Conf. Proc.* vol. **4464**, p. 34 (SPIE, Bellingham, WA, 2002).
58. C. Adachi, M. A. Baldo, M. E. Thompson, and S. R. Forrest, *J. Appl. Phys.* **90**, 5048 (2001).
59. J. G. C. Veinot, H. Yan, S. M. Smith, J. Cui, Q. Huang, and T. J. Marks, *Nano Lett.* **2**, 333–335 (2002); F. A. Boroumand, P. W. Fry, and D. G. Lidzey, *Nano Lett.* **5**, 67 (2005); H. Yamamoto, J. Wilkinson, J. P. Long, K. Bussman, J. A. Christodoulides, and Z. H. Kafafi, *Nano Lett.* **5**, 2485 (2005).
60. W. Trettnak, W. Gruber, F. Reininger, and I. Klimant, *Sens. Actuators B* **29**, 219 (1995).
61. D. B. Papkovsky, G. V. Ponomarev, W. Trettnak, P. O'Leary, *Anal. Chem.* **67**, 4112 (1995).
62. Z. Rosenzweig and R. Kopelman, *Anal. Chem.* **67**, 2650 (1995).
63. S.-K. Lee and I. Okura, *Anal. Commun.* **34**, 185 (1997).
64. C. McDonagh, B. D. MacCraith, and A. K. McEvoy, *Anal. Chem.* **70**, 45 (1998).
65. D. Garcia-Fresnadillo, M. D. Marazuela, M. C. Moreno-Bondi, G. Orellana, *Langmuir* **15**, 6451 (1999).
66. Y. Amao, K. Asai, T. Miyashita, and I. Okura, *Polym. Adv. Technol.* **11**, 705 (2000).
67. Y. Amao, *Microchim. Acta* **143**, 1 (2003).
68. Y.-E. L. Koo, Y. Cao, R. Kopelman, S. M. Koo, M. Brasuel, and M. A. Philbert, *Anal. Chem.* **76**, 2498 (2004).
69. R. N. Gillanders, M. C. Tedford, P. J. Crilly, and R. T. Bailey, *Anal. Chim. Acta* **502**, 1 (2004).
70. P. A. S. Jorge, P. Caldas, C. C. Rosa, A. G. Oliva, and J. L. Santos, *Sens. Actuators B* **103**, 290 (2004).
71. C. Preininger, I. Klimant, and O. S. Wolfbeis, *Anal. Chem.* **66**, 1841 (1994).
72. Y. Amao, T. Miyashita, and I. Okura, *Analyst* **125**, 871 (2000).
73. V. Savvate'ev, J. H. Friedl, L. Zou, J. Shinar, K. Christensen, W. Oldham, L. J. Rothberg, Z. Chen-Esterlit, and R. Kopelman, *Appl. Phys. Lett.* **76**, 1501 (2000).
74. K. O. Cheon and J. Shinar, *Appl. Phys. Lett.* **81**, 1738 (2002).
75. G. Li and J. Shinar, *Appl. Phys. Lett.* **83**, 5359 (2003).
76. L. Zou, V. Savvate'ev, J. Booher, C.-H. Kim, and J. Shinar, *Appl. Phys. Lett.* **79**, 2282 (2001).
77. L. S. Hung, C. W. Tang, and M. G. Mason, *Appl. Phys. Lett.* **70**, 152 (1997).
78. S. E. Shaheen, G. E. Jabbour, M. M. Morell, Y. Kawabe, B. Kippelen, N. Peyghambarian, M.-F. Nabor, R. Schlaf, E. A. Mash, and N. R. Armstrong, *J. Appl. Phys.* **84**, 2324 (1998).
79. Z. J. Fuller, D. W. Bare, K. A. Kneas, W.-Y. Xu, J. N. Demas, and B. A. DeGraff, *Anal. Chem.* **75**, 2670 (2003).
80. X. Lu and M. A. Winnik, *Chem. Mat.* **13**, 3449 (2001).
81. K. O. Cheon and J. Shinar, *Appl. Phys. Lett.* **83**, 2073 (2003).
82. O. S. Wolfbeis, I. Oehme, N. Papkovskaya, and I. Klimant, *Biosens. Bioelectron.* **15**, 69 (2000).

83. H. Xu, J. W. Aylott, and R. Kopelman, *Analyst* **127**, 1471 (2002).
84. American Conference of Governmental Industrial Hygienists (ACGIH). 1999 TLVs and BEIs. Threshold Limit Values for Chemical Substances and Physical Agents, Biological Exposure Indices (Cincinnati, OH, 1999). See also <http://www.epa.gov/ttn/atw/hlthef/hydrazin.html#ref12>
85. National Institute for Occupational Safety and Health (NIOSH). Pocket Guide to Chemical Hazards. U.S. Department of Health and Human Services, Public Health Service, Centers for Disease Control and Prevention (Cincinnati, OH, 1997), <http://www.cdc.gov/niosh/npg/npg.html>
86. S. Rose-Pehrsson and G. E. Collins, U.S. Patent 5,719,061 (Feb. 17, 1998).
87. R. T. Cummings, S. P. Salowe, B. R. Cunningham, J. Wiltsie, Y. W. Park, L. M. Sonatore, D. Wisniewski, C. M. Douglas, J. D. Hermes, and E. M. Scolnick, *Proc. Nat. Acad. Sci. U.S.A.* **99**, 6603 (2002).
88. F. Tonello, P. Ascenzi, and C. Montecucco, *J. Biol. Chem.* **278**, 40075 (2003).
89. B. E. Turk, T. Y. Wong, R. Schwarzenbacher, E. T. Jarrell, S. H. Leppla, R. J. Collier, R. C. Liddington, and L. C. Cantley, *Nat. Struct. Mol. Biol.* **11**, 60 (2004).
90. Z. Zhou, R. Shinar, L. Tabatabai, C. Liao, and J. Shinar, unpublished results.
91. E. Kraker, A. Haase, B. Lamprecht, G. Jakopic, C. Konrad, and S. Köstler, Integrated organic electronic based optochemical sensors using polarization filters, *Appl. Phys. Lett.* **92**, 033302 (2008).
92. D. Ghosh, R. Shinar, V. Dalal, Z. Zhou, and J. Shinar, *J. Non-Crystal. Sol.* **354**, 2606 (2008).
93. D. Ghosh, R. Shinar, Y. Cai, Z. Zhou, V. L. Dalal, and J. Shinar, in *Organic-Based Chemical and Biological Sensors*, Edited by R. Shinar and G. G. Malliaras, *SPIE Conf. Proc.* vol. **6659**, 66590E-1 (SPIE, Bellingham, WA, 2007).
94. P. Peumans, V. Bulovic', and S. R. Forrest, *Appl. Phys. Lett.* **76**, 3855 (2000).

---

# Index

---

## A

Absorption, polymer solar cell  
UV-Vis absorption spectra, 329  
vibronic features, 330

Active-matrix OLED (AMOLED),  
463, 491

Admittance spectroscopy (AS)  
DISCLC and, 64  
measurement, 78–79, 94, 95  
phenylamine-based compounds,  
97–99  
signal, 99

AFM, *see* Atomic force microscopy

Alcohol oxidase ( $\text{AO}_x$ ), 538

Alkali doping and modeling  
dependence, energy-level, 156  
emission wavelength conversion,  
150–151  
energy-level shift, 154–155  
Fermi level, 157–158  
Lorentzian distribution, 157  
LUMO intensity, 152–153  
UPS and IPES spectra, 151–152  
XPS spectra, 153–154

Amorphous organic semiconductor  
charge injection mechanism  
approaches, 68  
energy band diagram, 69  
interface dipole layer, 70

charge transport mechanism  
Einstein relation, 66  
GDM, 67–68  
hopping motion, 65–66

devices application, single-layer  
OLED  
NPB, 102–104  
perylene doping, 104–106

energy gap, melting points and  
mobilities, 63–64

measurement, experimental  
techniques  
admittance spectroscopy, 78–79  
current-voltage ( $JV$ ), 76–77

DISCLC, 77–78  
OTFTs, 74–76  
TOF, 71–74

phenylamine-based compounds  
bipolar transport, 82–93  
description, 79–82  
nearly ohmic hole injection,  
94–102

$\sigma$  and  $\pi$ -bonds, 64–65

AS, *see* Admittance spectroscopy

Asymmetric organic tandem cell  
external quantum efficiencies, 386  
illumination intensity, 387  
layer thicknesses, 385  
optical intensity, 384  
single cell, 387–388  
subcells, 383

Atomic force microscopy (AFM)  
images  
height and phase, 334  
tapping mode, 173  
topographic, 245  
measurements, 402  
optical detection mechanism, 147

## B

Bipolar transport  
electron mobilities, 90–91  
hole mobilities, TOF and OTFTs  
discrepancy factors, 89  
features, 83  
higher energetic disorder, 88  
NPB and, 84–85  
output characteristics, 85–86  
transport parameters, 87

microscopic explanation, 91–93  
sample preparations, 82–83

Blend film  
OFETs  
charge transport, 416–417  
preparation and fabrication,  
418–419

- oligomeric OSC blending  
advantages, 417  
phase separation, 418
- Boltzmann constant, 42, 66, 68, 112
- C**
- Chapman–Enskog equation, 34, 38
- Charge carrier mobility, polymer solar cell  
electron mobility, 336  
hole mobility, 338–339  
slow-and fast-grown films, 338  
work function, 337
- Clausius–Clapeyron equation, 31
- Colloidal lithography  
aggregation, 301  
nanoholes, 302  
OSIT fabrication process, 300–301
- Color rendering index (CRI)  
three-stack tandem, 498  
true-wide band emitters, 443  
white OLED, 464
- Complementary metal-oxide-semiconductor (CMOS), 311
- Concentric hemispherical analyzer (CHA), 188
- Copper phthalocyanine (CuPc)  
absorption spectra, 521  
aromatic rings, 153  
electronic structure, 152  
interface dipole, 150  
layer, thickness, 515  
OPDs, 525  
photoinduced carriers, 522  
UPS and IPES spectrum, 145
- CRI, *see* Color rendering index
- Crystallinity, polymer solar cells, 331
- D**
- Dark-injection space-charge-limited current (DISCLC)  
measurement  
experimental techniques, 73  
phenylamine-based compounds, 96–97  
structure, 77  
transient current, 78
- D-EML, *see* Double emission EML
- Density functional theory (DFT), 92, 93, 162, 163
- Density of states (DOS), 87, 89
- Devices interfaces, OLED  
electronegativity model  
concept extension, 194–195  
work function *vs.*, 189–194
- experimental techniques, 187–188
- implication  
ambipolar OFETs, 203–204  
stacked organic light-emitting diode, 204–207
- O/O heterojunctions  
 $\text{Alq}_3/\text{CuPc}$  substrate effect, 196–199  
energy-level alignment, 199–203  
vacuum-level alignment, 195–196
- semiconductors structures  
molecular-level alignment, 183–184  
space charges and built-in potential, 184–185  
surface properties, 183
- traditional concepts  
 $\text{Alq}_3\text{-on-Mg}$ , 185–186  
metal work function, 186–187  
Schottky–Mott model, 187  
vacuum-level discontinuity, 185
- DFT, *see* Density functional theory
- Diffusion-limited aggregation (DLA), 174, 175
- DISCLC, *see* Dark-injection space-charge-limited current (DISCLC) measurement
- DLA, *see* Diffusion-limited aggregation
- Double emission EML (D-EML)  
device structure, 482  
hole-transporting part, 481
- E**
- EBL, *see* Exciton-blocking layer
- EES, *see* External extraction structure
- EIL, *see* Electron-injection layer
- EIM, *see* Electron-injection material
- Electroluminescence (EL)  
emission spectra, 276  
spectra, intensity

- angular distributions, 283  
microcavity device, 279  
symbols and lines, 282  
top-emitting OLED, 286–287
- Electronegativity model, metal/organic concept extension  
carrier-injection barriers, 195  
ITO, 194–195  
schematic energy, 186  
vs. work function  
Alq<sub>3</sub>/metal, 190–191  
barrier heights, 189–190  
charge transfer, 193–194  
 $\phi_h$  and  $X_M$ , 192  
metal/inorganic semiconductor interfaces, 191–192  
parameter values, 194  
vacuum-level discontinuity, 189  
validity, 193
- Electron-injection layer (EIL), 485, 486
- Electron-injection material (EIM), 441, 445
- Electron-transporting layer (ETL)  
conductivity, 442  
doped, device structure, 250  
EML, 245  
film preparation, 248  
host, 249  
QDs, 256  
role, 446
- Electron-transporting materials (ETM)  
BAIq, 470  
electron affinity, 440  
use, 462, 485
- Electrophoretic displays (EPDs), 394–395
- Emissive layer (EML)  
electron injection barrier, 245  
EQE, 253  
hole injection barrier, 250, 252  
PEDOT:PSS and, 254
- EQE, *see* External quantum efficiency
- ETL, *see* Electron-transporting layer
- ETM, *see* Electron-transporting materials
- Exciton-blocking layer (EBL)  
p-doped HTL and the EML, 471  
TAPC, 479
- External extraction structure (EES)  
and IES, 464  
peak EQE, 465
- External quantum efficiency (EQE);  
*see also* Incident photon to collected electron (IPCE)  
B|Y hybrid device, 495  
D-EML and S-EML devices, 482  
dependence, 465  
FIr<sub>6</sub> dopant, 492  
green phosphorescent OLEDs, 484  
tandem blue OLEDs, 457
- F**
- Fabry–Perot formulation  
cavity mode, 269–270  
conventional bottom-emitting, 268–269  
field redistribution, 267–268  
luminance maximization, 268
- Fermi–Dirac distribution, 156
- FETs, *see* Field-effect transistors
- Fick's law, 36
- Field-effect transistors (FETs)  
device architectures  
OSC layer, 415  
top-gate and bottom-gate structure, 414
- OFETs, electronic characterization  
gate bias, 411  
source-drain current, 412–413  
threshold voltage, 413–414
- Flexible organic transistor  
electronic devices, 309–310  
pentacene OSITs, 310–311
- Fluorescence resonance energy transfer (FRET), 542
- Fluorescent OLED device  
blue triplet  
dopant, 449  
host material, 448  
lifetime and luminance, 447  
performance improvement, 447–448
- full-color and AMOLED  
drawback, 450  
shadow-masking technique, 449

- green triplet  
efficiency and lifetime  
improvement, Kodak, 445–446  
performance data, 447  
structure, 445, 446
- red triplet  
mixed-host concept, 445  
performance and structure, 444
- white triplet  
blue emission, 453–456  
multilayer structure, 451–453  
two-EML-layer architecture, 450–451
- Full width at half maximum (FWHM), 164–165
- G**
- Gas-phase and dissolved oxygen detection sensitivity, 534  
gas-phase, O<sub>2</sub>, 534–535  
PL decay curves, 536–537  
stability, OLED/sensor, 535  
SV equation and plot, 532–534  
UV ozone treatment, 533
- Gaussian disorder model (GDM), 67–68, 87, 93
- Gilch polymerization, 5
- Glucose oxidase (GO<sub>x</sub>), 537
- H**
- HBL, *see* Hole-blocking layer
- Heck reaction, 5
- Heterojunctions  
mixed (*see* Mixed heterojunction, CuPc:C<sub>60</sub>)  
photovoltaic cell (*see* Mixed molecular heterojunction, photovoltaic cell)
- HHOLEDs, *see* Hybrid-harvesting OLEDs
- Highest occupied molecular orbital (HOMO)  
BP2T film, 168  
definition, 65  
energy
- gap, 4  
levels, 8, 102, 143  
separation, 68–69, 145
- gap state, 153
- hopping rate, 92
- interface levels, 169–170
- intramolecular excitons, 116  
*vs.* LUMO, 148, 467
- organic molecules, 142
- High-resolution electron energy loss spectroscopy (HREELS), 143
- HIL, *see* Hole-injection layer
- Hole-blocking layer (HBL)  
BALq, 478  
Ir(ppy)<sub>3</sub> lifetime, 488
- Hole-injection layer (HIL)  
*vs.* LUMO energy level, 467  
SBFK, 476
- Hole mobilities, TOF and OTFTs  
discrepancy factors, 89  
features, 83  
higher energetic disorder, 88  
NPB and, 84–85  
output characteristics, 85–86  
transport parameters, 87
- Hole-transporting layer (HTL)  
conductivity, 442  
materials, hole injection barrier, 250  
multilayer, 251  
operational lifetime, 471  
PFCB-based cross-linkable HTMs  
cyclic voltammetry (CV), 252  
TCTA, 253–254  
trifluorovinyl aromatic ether, 251–252
- p-type doped, 490
- styrene-based cross-linkable HTMs  
PEDOT:PSS, 254–256  
TCTA, 256
- Hole-transporting materials (HTMs)  
blocking layers, 442  
cross-linkable  
advantage, 251  
QDs and LEDs, 257
- HTL, cross-link  
perfluorocyclobutane-based, 251–254  
styrene-based, 254–256
- IP, 441

- OLED application, 63  
PA compounds, 80  
*HOMO*, *see* Highest occupied molecular orbital  
HTL, *see* Hole-transporting layer  
HTMs, *see* Hole-transporting materials  
Hybrid-harvesting OLEDs (HHOLEDs), 494, 496  
HYI, *see* Hyperfine interaction  
Hyperfine interaction (HYI)  
  intermolecular excited states, 120  
  magnetic interaction, 118
- I**
- IES, *see* Internal extraction structure  
Incident photon to collected electron (IPCE)  
  charge recombination, 326  
  measurement setup, 325  
  value, 324  
Indium tin oxide (ITO)  
  and Ag, 272  
  anode glass substrates, 266  
  bottom-emitting OLED, 268  
  glass  
    efficiency characteristics, 274  
    structure, 273  
  hole injection barrier, 250, 252, 253  
PEDOT:PSS, 254  
use, 249–250  
work function, 252  
Interface engineering, OLED  
  cathode and emission layer  
    neutral surfactants, 248–249  
    PFN-OH, 246–247  
    PLEDs, 247–248  
    poly(ethylene glycol) (PEG)-based  
      neutral surfactants, 245  
    P<sub>12</sub>TE, 245–246  
    turn-on voltage, 248  
    vaporphase deposition, 244  
    work-function metals, 244–245  
  emission layer and anode  
    HTL, hole injection, 250–251  
    ITO, hole injection, 249–250  
    perfluorocyclobutane-based  
      cross-linkable HTMs, 251–254  
    QDs and LEDs, 256–258  
    styrene-based cross-linkable  
      HTMs, 254–256  
Internal extraction structure (IES), 464  
Intersystem crossing (ISC)  
  electron-hole pairs, 117  
  internal magnetic interaction, 116, 118  
  ionpair model, 119  
  perturbation, 113  
  polaron-pair and excitonic states, 114  
  singlet and triplet exciton ratios, 115  
Intrinsic degradation and homolytic reactions, OLED  
  characteristics, 213  
  chemical analysis  
    HPLC technique, 235  
    organic materials quantities, 234  
    products identification and structure, 236–237  
    quantitative evaluations, products, 233–234  
    TAPC chemical conversion, 235–236  
  chemical processes, 215  
  Coulombic character, 213–214  
  durability, 211  
  electric field profiling  
    aging experiments, 227–228  
    charge densities evaluation, 226–227  
    space charge, 228–229  
  extrinsic degradation, 212  
  instability, 211–212  
  matrix uniqueness, 214–215  
  molecular structures, 216  
  photoluminescence  
    Alq cation-radicals, 232–233  
    charge carrier recombination, 230  
    luminescence quenching, 229–230  
    models, 231–232  
    quencher concentrations estimation, 230–231  
    usefulness, 233  
  voltammetry (*see* Voltammetry, intrinsic degradation)  
Inverse photoemission spectroscopy (IPES)  
  LUMO onset, 152

- structure and spectrum, 144  
UPS and, 145, 154, 169
- Inverted polymer solar cell  
current–voltage characteristics, 342  
fabrication, 341  
transparent, 343
- Ionization potentials (IP)  
BAIQ, 478  
defined, 440
- IP, *see* Ionization potentials
- IPCE, *see* Incident photon to collected electron
- IPES, *see* Inverse photoemission spectroscopy
- ISC, *see* Intersystem crossing
- ITO, *see* Indium tin oxide
- ITO/PEDOT/polymer/Al devices  
characteristics, 16–17  
EL spectra, 14  
PLED performance, 19
- J**
- Junction-to-cathode (JTC), 465–466
- K**
- Kelvin probe, 143, 148  
Knudsen number, 42
- L**
- Laminated transparent solar cell  
device fabrication process, 343–344  
EQE, 345
- Laser diode (LD), 521, 526
- LEDs, *see* Light-emitting diodes
- LiF insertion layer  
Au/LiF/Alq interface, 166  
HOMO, 165  
organic optoelectronic devices, 161  
simple band bending, 163  
symmetric molecular structure, 164
- UPS spectra evolution, 161–162  
XPS evolution, 162–163
- Light-emitting diodes (LEDs), 256–258
- Logic devices, organic  
CMOS, 311  
inverter transfer characteristics, 312
- Low band-gap polymer  
chemical structures, 347  
copolymers, 346  
energy level offset, 345  
fullerene derivative, 347–348  
height and phase images, 349  
light absorption, 348
- Low-energy electron diffraction (LEED), 143
- Low-energy electron microscopy (LEEM), 143
- Lowest unoccupied molecular orbital (LUMO)  
definition, 65  
energy gap, 4  
levels, 8, 10  
separation, 68  
evolution, 153  
Fermi level, 145  
and HOMO, 442  
HOMO energy-level alignment, 148  
hopping rate, 92  
intramolecular excitons, 116  
Lorentzian distribution, 157  
organic molecules, 142
- M**
- Magnetic field effects (MFEs)  
definition, 111–112  
electroluminescence  
electrofluorescence-based, 127–129  
electrophosphorescence-based, 129–132  
spintronic devices applications, 126
- electron and hole capture, 112–113
- intersystem crossing and  
intramolecular states  
energy levels, polaron, 114
- ISCs, field-dependent and  
independent, 115
- polaron pairs, 113
- magnetoresistance  
bulk charge density, 133  
charge transport-based, 135–136  
electrical injection current, 132  
excited states-based, 133–135

- photocurrent  
channels and dependence, 123–124  
emission characteristics, 122  
PCBM doping, 124–125  
photovoltaic channels, 121  
polaron pairs and excitons, 125  
positive and negative components, 124  
singlet and triplet states, 123
- photoluminescence  
intermolecular excited states, 118–121  
intramolecular excited states, 116–118  
photon absorption, 115  
spin selection rule, 116
- Magnetic field effects of  
electroluminescence (MFEL)  
electrofluorescence-based  
light-emitting singlet exciton ratio, 127  
primary and secondary types, 128  
process, 131  
singlet-triplet ISC, 129
- electrophosphorescence-based  
intermolecular SOC process, 130–131  
triplet emission, 129–130
- issues, 127
- spintronic devices applications, 126
- Magnetic field effects of photocurrent (MFPC)  
channels and dependence, 123–124  
emission characteristics, 122  
*vs.* PCBM doping, 124–125  
photovoltaic channels, 121  
polaron pairs and excitons, 125  
positive and negative components, 124  
singlet and triplet states, 123
- Magnetic field effects on  
photoluminescence (MFPL)  
intermolecular excited states  
electron-hole separation, 120  
energy transfer and migration, 118  
singlets and triplets, 118–119  
Zeeman splitting, 119
- intramolecular excited states  
HOMO and LUMO, 116  
TTA-generated delayed fluorescence, 117–118  
Zeeman splitting, 117
- Magnetoresistance (MR), MFEs  
bulk charge density, 133  
charge transport-based, 135–136  
electrical injection current, 132  
excited states-based  
generation and tuning, 134–135  
magnetic field-sensitive channels, 133  
singlet polaron-pair ratio, 134
- Marcus theory, 65
- Metal-induced gap states (MIGSs), 184, 189
- Metal-to-ligand charge transfer (MLCT), 466
- Metal/vacuum interface representation, 186
- MFEL, *see* Magnetic field effects of electroluminescence
- MFEs, *see* Magnetic field effects
- MFPC, *see* Magnetic field effects of photocurrent
- MFPL, *see* Magnetic field effects on photoluminescence
- Microcavity effect, OLEDs  
Fabry–Perot formulation  
emission function, 269–270  
field redistribution, 267–268  
 $G_{\text{int}}$  calculation, 270  
optical structure and characteristics, 267  
organic emitter, 268–269
- interference, weak microcavity bottom-emitting structure, 266, 272  
dipole frequencies, 273–275  
EL characteristics, 275–276  
radiation, 273  
tandem, implication, 276
- microlens  
brightness and color saturation, 289  
cd/A and external quantum efficiencies, 287–288

- EL spectra, relative intensities, 286–287
- image blurring and pixel, 288–289
- narrow emission spectra, 284–285
- without top-emittance, 285–286
- resonant wavelength influence
- cd/A and quantum efficiencies, 283, 284
  - color shift, 282–283
  - considerations, 279–280
  - device structure, 280–281
  - EL spectra symbols and lines, 281–282
  - emission characteristics, 281
- rigorous electromagnetic modeling, 270–272
- two metal mirrors, microcavity
- fabrication, 277
  - luminance enhancement, 277–279
  - optical characteristics
    - comparison, 280
    - structures, 276–277  - top-emitting *vs.* optimized structure, 279
- Mixed heterojunction, CuPc:C<sub>60</sub>
- cell performance modeling
  - electron and hole drift lengths, 370
  - experimental data, 372
  - total current density, 371
- photovoltaic cell, performance
- J–V characteristics, 367
  - mixed layer, 368–369
  - power conversion efficiency, 370
  - schematic device structure, 366
  - temperature dependence, 369
  - zero total current, 368
- structural, optical and electrical properties
- carrier mobility, 364–365
  - diffraction peak, 362
  - mixed films, 363
  - mobility difference, 365
  - organic PV cells, 361
  - percolated paths, 366
- Mixed molecular heterojunction, photovoltaic cell
- charge carriers, 360–361
- exciton diffusion, 360
- mixed HJs, CuPc:C<sub>60</sub>
- device performance, 366–370
  - performance modeling, 370–372
  - structural, optical and electrical properties, 361–366
- PM-HJs, CuPc:C<sub>60</sub>
- dark current, 374–376
  - exciton diffusion/dissociation efficiency, 373
  - performance modeling, 380–382
  - photoresponse, 376–380
  - tandem cells, 382–388
- MLCT, *see* Metal-to-ligand charge transfer
- Monte-Carlo simulation
- Alq<sub>3</sub> films patterning, 45–46
  - chamber pressure effects, 46–47
  - DLA-type monolayers, 174
  - experimental validation
    - hybrid VTE-OVPD resolution limits, 54–55
    - interference microscopy method, 52
    - mask-to-substrate separation, 50–51
    - organic thin films, 50
    - OVPD, shadow mask, 53–54
    - SEM and AFM, 51  - mask thickness and separation, 47–48
  - shape optimization, mask, 48–50
- Mott–Gurney rule, 100
- Mott–Schottky rule, 69–70
- Multianalyte sensing
- analyte array design, 539
  - DO concentration, 538
  - donor–acceptor pairs, 542
  - ethanol concentration, 538–539
  - GOx, 537–538
  - linear calibration curve, 539–540
  - microcavity, OLED, 542
  - sealed cells, 537
- N**
- Nanomorphology, polymer solar cell
- crystallite size, 335
  - exciton dissociation, 331–332

- solvent annealing, 334  
thermal annealing, 332–333  
Navier–Stokes equations, 35, 36, 37  
Near edge X-ray absorption fine structure (NEXAFS), 143  
Nearly ohmic hole injection  
    admittance spectroscopy, 97–99  
    current-voltage characteristics, 95  
    DISCLC measurement, 96–97  
    sample preparations, 94–95  
    using PEDOT, PSS, 96, 99–101  
NPB excitation, 239–240  
*N*-phenylaminobiphenyl (NPB)  
    and Alq, light-emitting layer, 445  
    Ir(1-piq)<sub>3</sub>, 473  
    and SBFK, 475, 476
- O**
- OFETs, *see* Organic field-effect transistors  
OLETs, *see* Organic light-emitting transistors  
OMBD, *see* Organic molecular beam deposition  
OPDs, *see* Organic photodetectors  
Organic field-effect transistors (OFETs)  
    CMOS, 311  
    complementary logic circuit, 203  
    current flow, 294–295  
    electronic characterization  
        gate bias, 411  
        linear and saturation currents, 413  
        saturation mobility, 412–413  
        source-drain current, 412  
        threshold voltage, 413–414  
    F16CuPc-on-CuPc junction, 203–204  
    lateral-type  
        current flow, 295  
        structure, 296  
    organic inverters, 311–312  
polymer, oligomeric and blend  
    blend films, 416–419  
    crystalline organic  
        semiconductors, 415  
    high mobility, 416  
static and dynamic characteristics  
    device fabrication process, 303  
frequency, 304–305  
size and performance, 305  
top-gate geometry, 414–415  
Organic light-emitting diode (OLED)  
    device  
    fluorescent  
        blue, 447–449  
        full-color and AMOLED, 449–450  
        green, 445–447  
        red, 444–445  
        white, 450–456  
materials and architecture  
    fluorescence quantum yield, 443  
    host materials, 442–443  
    HTL, EML and ETL, 439  
    IP, HTM and ETM, 440  
    p-i-n technology, 441–442  
performance metrics  
    drive voltage and efficiency, 436–437  
    emission color, 438–439  
    structure, 435–436  
phosphorescent  
    blue, 488–491  
    emission mechanism, 466–468  
    green, 477–488  
    red, 468–477  
    white, 491–498  
tandem  
    display applications, 463  
    lighting applications, 463–466  
    structure, 456–457  
    white, 457–462  
Organic light-emitting transistors (OLETs)  
    dynamic characteristics, 313–314  
    fabrication, 313  
    grid-type gate electrode, 312–313  
Organic molecular beam deposition (OMBD), 512, 515–517, 521  
Organic/organic (O/O) heterojunction  
    energy-level alignment  
        electronic structures, 199  
        Fermi levels, 199–200, 203  
        formation mechanism, 200–201  
        work function, 201–203

- Organic photodetectors (OPDs)  
 current-voltage characteristics, 521, 524–525  
 device structure, 516  
 optical communication, 523  
 polymeric waveguide, 512  
 response speed, 522
- Organic semiconductor (OSC)  
 carrier-injection barriers, 195  
 conductive doping, 272  
 electronic structures, 183–185  
 Fermi level, 200–201
- Organic SITs (OSITs)  
 definition, 295  
 device performance improvement  
   gate electrode fabrication, 308–309  
   interfaces control, 306–308  
 fabrication  
   colloidal lithography, 300–302  
   gate electrode, 298  
   shadow evaporation technique, 299–300  
 flexible organic transistors  
   electronic devices, 309–310  
   pentacene, 310–311  
 logic devices, organic  
   CMOS, 311  
   inverters, 311–312  
 operational mechanism  
   current-voltage characteristics, 302  
   potential distribution, 303  
 pentacene  
   evaporated films, 296–297  
   films, 306–307  
   static characteristics, 308  
 static and dynamic characteristics  
   device size and performance, 305–306  
   frequency characteristics, 304–305  
   vs. OFETs, 303
- Organic thin-film transistors (OTFTs)  
 anlyte, 529  
 configurations, 75  
 hole mobilities, 83  
 measurements, 64  
 output characteristics, 75–76, 86
- Organic vapor-phase deposition (OVPD)  
 concept, 28
- evaporation and vapor pickup,  
 carrier gas  
 quantitative analysis, 30–31  
 source cell structure, 29–30  
 volumetric flow rate, 32
- film deposition  
 gas flow rate, 38  
 organic vapor concentration, 37  
 stagnant boundary layer, 36–37
- geometries deposition, patterning  
 continuous medium assumption, 42–43  
 diffusive transport, 41–42  
 experimental validation, 50–55  
 gas transport modeling, 43–44  
 Monte-Carlo simulation, 44–50  
 VTE ballistic transport, 39–41
- vapor transport  
 flow field and temperature  
 distribution, 36  
 hydrodynamic and thermal  
 boundary, 35  
 laminar flow assumption, 34  
 Reynolds number, 33
- OSC device interface  
 alkali doping and modeling  
 dependence, energy-level, 156  
 emission wavelength conversion, 150–151  
 energy-level shift, 154–155  
 Fermi level, 157–158  
 HOMO evolution, 151  
 Lorentzian distribution, 157  
 LUMO intensity, 152–153  
 XPS spectra, 153–154
- band bending  
 Debye length, 170–171  
 device performance, 167  
 spectral changes,  $F_{16}CuPc/BP2T$ , 168–169
- Bloch waves, 141–142
- dipole, metal/organic  
 CuPc on Au spectra, 149–150  
 energy-level alignment, 148
- doping-induced energy-level shift  
 summarization curves, 159–160  
 UPS spectra evolution, 158–159
- experimental techniques  
 AFM structure, 147

- electrical measurements, 142  
energy separation, 145  
HOMO energy levels, 143  
PES and IPES structure, 144  
SPM techniques, 146  
fundamental process, 142  
growth mode and modeling  
  adsorbate-substrate interaction, 171–172  
  height correlation function, 174–175  
Monte Carlo simulation, 173–174  
pentacene thin films, 173  
roughness exponent, 175
- LiF insertion layer  
  HOMO, 165  
  organic optoelectronic devices, 161  
  simple band bending, 163  
  symmetric molecular structure., 164  
UPS spectra evolution, 161–162  
valence energy-level, 166  
XPS evolution, 162–163  
occupied and unoccupied energy levels, 141–142
- OTFTs, *see* Organic thin-film transistors
- OVPD, *see* Organic vapor-phase deposition
- P**
- $\pi$ -Conjugated polymer, OLEDs  
  HOMO-LUMO energy gap, 3–4  
  PFV derivatives (*see* Poly(9,9-dialkylfluorenyl-2,7-vinylene) (PFV))  
  PPV derivatives (*see* Poly(*p*-phenylenevinylenes) (PPVs))
- Penning spectroscopy, 143
- Per-fluorocyclobutane (PFCB), 251–254
- PES, *see* Photoemission spectroscopy
- PFM, *see* Pulse frequency modulation
- PF model, *see* Poole-Frenkel (PF) model
- PFV, *see* Poly(9,9-dialkylfluorenyl-2,7-vinylene)
- Phenylamine-based compound  
  bipolar transport  
  electron mobilities, 90–91
- hole mobilities, TOF and OTFT measurements, 83–90  
microscopic explanation, 91–93  
sample preparations, 82–83  
chemical structures, 81  
hole injection capabilities, 80–81  
hole-transporting properties, 85  
merits, 80  
ohmic hole injection  
  admittance spectroscopy, 97–99  
  current-voltage characteristics, 95  
  DISCLC measurement, 96–97  
  sample preparations, 94–95  
  using PEDOT:PSS, 96, 99–101
- Phosphorescent OLED device  
  blue triplet  
    architecture, 490–491  
    current density dependence, 489–490  
    deep-blue emitter, 491  
    material structure, 488–489  
  emission mechanism  
    band gap, 467  
    Ir(III) compounds, 466–467  
  green triplet  
    BAIq HBL, advantage, 478–479  
    carbazoles, 478  
    D-EML, 481–482  
    drive voltage, 483–484  
    energy level diagram, 486–487  
    EQE density, D-EML and S-EML, 482–483  
    high-energy efficiency, 477–478  
    hole-blocking materials, 485  
    HOMO and LUMO levels, 484  
    lifetime, 487–488  
    material structure, 479–480  
    recombination zone location, 487  
    TBADN|Bphen, 486  
    TCTA and triplet excitons, 483  
    triplet energy, 479
- red triplet  
  BAIq' structure, 468–469  
  drive voltage function, 475–476  
  efficiency reduction, 469  
  energy levels, p-i-n, 471  
  EQE and power efficacy, 471–472  
  Ir(1-piq)<sub>3</sub>, 470, 473  
  layer structure, 470–471

- luminance yield dependence, 473–474
- LUMO and HOMO levels, 476
- mixed-host mechanism, 472–473
- operational lifetime, 472
- performance metrics, 477
- SBFK+NPB mixed-host, 475
- white triplet
- single-stack, 491–496
  - tandem, 496–498
- Photodetector integration
- higher sensitivity, S~47, 544
  - multicolor OLED pixels, 545
  - QE vs. ECR wavelength, 543
  - shortest response time, 545
  - SV plot, gas-phase O<sub>2</sub>, 543–544
- Photodetectors, optical communication
- device fabrication process
    - OLEDs structure, 514
    - OPDs structure, 516
    - polymeric waveguide, 512–513
    - spin coating method, 515  - OLEDs, vacuum and solution process
    - direct modulation, 517
    - emission characteristics, 517–518
    - hole transporting materials, 519–520
    - intensity-voltage characteristics, 520
    - transmission systems, 518–519  - vacuum and solution process, OPDs current-voltage characteristics, 522, 524–525
  - fabrication and characteristics, 523
  - frequency responses speed, 521–522
  - LUMO and HOMO levels, 524
  - optical characteristics, 521
  - photoresponse, 525
  - pulse generation cycle, 526
- Photoemission spectroscopy (PES)
- experimental techniques, 187–188
  - structure, 144
  - surface sensitivity, 145
  - techniques, 143
- Photoluminescence (PL)
- absorption spectra, 11
  - biological sensors, 529
  - description
    - experiments, 230–233
    - non emissive energy trap, 229–230
    - solid-state, 229  - emission spectrum, 17
  - polymer-emitting layer, 10
  - quantum efficiency, 12
- Photoluminescence excitation (PLE), 15
- PL, *see* Photoluminescence
- Planar-mixed heterojunctions (PM-HJs), CuPc:C<sub>60</sub>
- charge collection length, 374
  - dark current
    - fitting results, 375
    - layers, 374
    - recombination current, 375–376  - exciton diffusion/dissociation efficiency, 373
  - organic tandem cell
    - Ag nanoclusters, 383
    - asymmetric, 383–388
    - semiconductors, 382–383
    - trade-off shifts, 382  - performance modeling
    - average charge collection efficiency, 380
    - exciton diffusion length, 382
    - optimized power conversion efficiency, 381
    - organic layers, 380–381  - photoresponse
    - diode theory, 377
    - illumination intensity, 377–378
    - J–V characteristics, 376
    - mixed layer thickness, 379–380
    - quantum efficiencies, 378–379
- Planck's constant, 66
- PLE, *see* Photoluminescence excitation
- PLEDs, *see* Polymer light-emitting diodes
- PMMA, *see* Poly(methyl methacrylate)
- Poisson's equation
- carrier mobilities, 79
  - charge density and electric field strengths, 226
- ETL–HTL interface, 219

- Poly(3-alkylthiophenes)  
evaporation rate, 403  
regioregularity, 401  
side chains, 402
- Poly(3-hexylthiophene) (P3HT)  
amorphous polystyrene, 417  
higher and lower molecular weight,  
402  
regioregularity, 401
- Poly(9,9-dialkylfluorenyl-2,7-vinylene)  
(PFV)  
optical and electroluminescence  
properties, 20  
synthesis and characterization  
chemical structures, 8  
dialkyl side chains, 9
- Poly(dialkylfluorenes) (PFs), 4
- Poly(methyl methacrylate)  
(PMMA)  
blend forms, 130  
injection  
bipolar, 134  
blocking, 135  
hole, 128  
TPD and BBOT, 120
- Poly(*p*-phenylenevinylenes) (PPVs)  
optical and electroluminescence  
properties  
absorption spectrum, 14  
asymmetric and color-tunable, 13  
EL and PL spectra, 18  
ITO/PEDOT/polymer/Al  
devices, 16  
LUMO energy level, 10  
maximum absorption spectra, 9  
PLE spectra, 15  
PL quantum efficiency, 12  
sharper emission colors, 11
- synthesis and characterization  
alkyloxyphenoxy-substituted,  
5–6  
molecular design, 5  
oxadiazole-substituted, 7  
PDOT-substituted, 7–8  
silylphenyl-substituted, 6–7
- Poly(thieno(3,2-*b*)thiophenes)  
ambient stability, 406  
chain interdigitation, 405–406
- planar conjugated backbones,  
404–405
- three-dimensional registration, 405
- Poly[9,9-bis(6'-(diethanolamino)hexyl)-  
fluorene] (PFN-OH), 246–247
- Polymerization methods, 5
- Polymer light-emitting diodes (PLEDs)  
applications, 5  
current density *vs.* luminous  
efficiency, 248  
electron-injection material,  
246–247  
electron-transport layer, 18  
EL spectra, 19  
hole-injecting layer, 246  
luminance efficiency, 4, 6  
Oxa-PPV performance, 17  
power efficiency *vs.* voltage, 249  
solvent-induced erosion, 250
- Polymer semiconductor development,  
FETs  
ambipolar transport  
HOMO and LUMO levels,  
420–421  
operating regimes, 422  
organic conjugated materials,  
419–420  
technological implications,  
421–422  
voltage invert circuitry, 423
- amorphous and crystalline, 400
- charge carrier mobility and  
structure, 409–410
- device fabrication and  
characterization  
architecture, 414–415  
OFETs, 411–414
- high performance  
benzodithiophene, 406–407  
copolymers, 407  
electron mobilities, 408
- mobilities, 401
- organic electronic device fabrication  
contact printing, 396–397  
prototype device, 395–396
- organic semiconductor design  
pentacene, 397  
solution viscosity, 397–398

- organic transistor  
 EPD effect, 394  
 OLEDs, 395
- poly(3-alkylthiophenes)  
 evaporation rate, 403  
 regioregularity, 401  
 side chains, 402
- poly(thieno(3,2-*b*)thiophenes)  
 ambient stability, 406  
 interdigitation, 405–406  
 planar conjugated backbones,  
 404–405  
 three-dimensional registration,  
 405
- polymer conformation  
 P3HT extended structure, 400  
 thiophene units, 399
- polymeric, oligomeric and blend  
 OFETs  
 blend films, 416–419  
 crystallinity, 415–416  
 hole carrier mobilities, 415
- polymerization  
 impurities, 398–399  
 molecular weight, 398
- polythiophene  
 charge carrier mobilities, 404  
 ionization potential, 403
- Polymer solar cell, high efficiency  
 device architecture, solar cells  
 inverted polymer, 341–343  
 laminated transparent, 343–345
- efficiency measurement  
 device area and layout, 326–327  
 spectral mismatch factor, 322–324  
 spectral response, 324–326  
 standardization, 321
- low band-gap polymer  
 chemical structures, 347  
 copolymers, 346  
 energy level offset, 345  
 fullerene derivative, 347–348  
 height and phase images, 349
- mixture solvent approach  
 area ratio, 353  
 film formation, 352  
 spin-coating process model, 354  
 thermal and solvent annealing,  
 351–352
- performance enhancement  
 absorption, 329–330  
 charge carrier mobility, 336–339  
 crystallinity, 331  
 exciton generation and  
 dissociation, 321, 339–340  
*I*–*V* characteristics, 335–336  
 nanomorphology, 331–335  
 RR-P3HT, 327–328  
 thermal and solvent annealing,  
 328–329
- stacking  
 current balance, 350  
*I*–*V* curves, 351
- Poly[2-methoxy-5-(2'-ethylhexyloxy)-  
 1,4-phenylenevinylene]  
 (MEHPPV), 123, 124
- Poly(3,4-ethylenedioxythiophene)/  
 polystrenesulfo-nic acid  
 (PEDOT:PSS), 9, 18, 20, 94–101
- Polythiophene  
 copolymers, 404  
 polymer ambient stability, 403
- Poole-Frenkel (PF) model, 67
- Power conversion efficiency (PCE)  
 EQE, 335  
 polymer solar cells, 328
- PPVs, *see* Poly(*p*-phenylenevinylenes)
- Pulse frequency modulation (PFM),  
 519, 526
- Q**
- Quantum dots (QDs), 256–258
- R**
- Reflection infrared spectroscopy (RIRS),  
 143
- Rigorous electromagnetic modeling  
 emission characteristics, 270–271  
 radiation field, 271–272
- S**
- Scanning electron micrograph (SEM),  
 40, 51, 54, 55
- Scanning probe microscopy (SPM), 143,  
 146

- Scanning tunneling microscopy (STM), 143, 146, 147
- Schottky barrier formation, 149
- Schottky–Mott model
- metal/organic interfaces, 183–185, 187
  - O/O heterojunctions, 187
- Secondary ion mass spectroscopy (SIMS), 143
- S-EML, *see* Single-emission EML
- Sensor, chemical and biological
- advantages and challenges, OLED hydrazine, 541
  - analyte monitoring
    - gas-phase and dissolved oxygen, 532–537
    - multianalyte sensing, 537–540  - detection methods, 530
  - photodetector integration
    - higher sensitivity, 544
    - multicolor OLED pixels, 545
    - QE *vs.* ECR wavelength, 543
    - shortest response time, 545
    - SV plot, gas-phase O<sub>2</sub>, 543–544  - PLED, 530–531
  - sensing component modules/OLED structure
    - back-detection geometry, 532
    - Si photodiode, 531–532
    - SMOLED structure and fabrication procedure, 531
- Shadow mask
- OVPD and patterning, diffusive transport
  - geometrical parameters, 42
  - hydrodynamic boundary layer, 41
- VTE ballistic transport
- mean free path, 39
  - process structure, 40
- Single-emission EML (S-EML), 482
- Single-stack white OLED device
- B|Y harvesting hybrid and BF, 495–496
  - color stability, 492
  - fluorescent emitters, 493–494
  - layer structure, 492–493
  - red dopant, 493
- SITs, *see* Static induction transistors
- Small-molecular OLEDs (SMOLEDs), 529, 531
- Solvent annealing, polymer solar cell
- mild thermal treatment, 328
  - self-organization, 329
- Source measure unit (SMU), 76
- Spectral mismatch factor, polymer solar cell
- irradiance, 322
  - reference cell, spectral responses, 323
  - Si diode, 324
- Spin coating method, 515, 524
- Spin-orbital coupling (SOC), 113, 116–119, 121, 127, 129, 130
- Stacked OLEDs
- tandem, device performance, 205–207
  - units
    - connecting, 204–205
    - emitting, 205
- Static induction transistors (SITs)
- high-performance, 300–301
  - OSITs (*see* Organic SITs)
  - static and dynamic characteristics, 303
- Stern–Volmer (SV) equation, 532–533
- Substituted bis(9,9'-spirobifluorene-2-yl) ketone (SBFK)
- HOMO level, 476
  - and NPB, 475
  - use, TPBI, 488
- Suzuki coupling, 5
- T**
- Tandem OLED device
- lighting applications, white
  - EES and IES, 464
  - EQE dependence, JTC, 464–465
  - luminance level, 465–466
  - structure
    - intermediate connector, 457
    - single-and two-stack, 456
- white triplet
- display applications, 463
  - feature, two-stack, 460–461
  - higher color temperature, 461–462
  - high *vs.* low efficiency, 458

- individual and two-stack performance, 459, 461  
luminance efficiency, 459–460  
two-stack Y/B structure, 457–458
- TAPC homolytic dissociation reaction, 239
- TCTA, *see* Tris(carbazolyl)-triphenylamine
- TFT, *see* Thin-film transistor
- Thermal annealing, polymer solar cell  
mild thermal treatment, 328  
self-organization, 329
- Thin-film transistor (TFT)  
characteristics, 85  
configuration, 88  
substrates, AMOLED display, 435  
technique, 75  
*vs.* TOF mobilities, 89
- Threshold limit value (TLV), 541
- Time-of-flight (TOF)  
configuration, 71–72  
data interpretation, 71  
hole mobilities, 85  
technique, 82  
transient signal, 74, 83–84
- TLV, *see* Threshold limit value
- TOF, *see* Time-of-flight
- TPQ, *see* Triplet exciton-polaron quenching
- Triplet exciton-polaron quenching (TPQ), 472, 481
- Triplet-triplet annihilation (TTA)  
definition, 116  
efficiency reduction, 469  
spin flip mechanism, 117  
and TPQ, 472, 481  
and triplet-charge reaction, 127
- Tris(carbazolyl)-triphenylamine (TCTA), 253–254, 256, 481, 483
- TTA, *see* Triplet-triplet annihilation
- Tunneling theory, 132
- U**
- Ultraviolet photoemission spectroscopy (UPS)  
cutoff evolution, 149  
differential curve, 159
- features, 152  
vacuum-level shift, 148  
XPS and, 143, 165
- V**
- Vacuum-level alignment (VLA) model, 148
- Vacuum thermal evaporation (VTE)  
ballistic transport, 39–40  
limitations, 28  
*vs.* OVPD techniques, 39  
source-to-substrate distance, 50
- Vertical-type field-effect transistors,  
*see* Static induction transistors (SITs)
- Vertical-type organic transistor  
flexible sheet display application  
flexible organic transistor, 309–311  
OLETs, 312–314  
organic logic devices, 311–312
- OFETs  
performance, 294  
static and dynamic characteristics, 303–306
- organic transistors  
device structure, 296  
groups, 295  
optoelectronic elements, 297
- OSITs  
device performance improvement, 306–309  
fabrication process, 298–302  
operational mechanism, 302–303  
static and dynamic characteristics, 303–306
- SITs, 295  
structures, 297
- Voltammetry, intrinsic degradation  
capacitive component, 218–219  
conductive component, 217–218  
fixed charge density, 220–221  
fluorescent and phosphorescent spanning, 225–226

- internal fixed charge, 219–220  
negative fixed charge, 221  
NPB|Alq device  
    electron traps, 224–225  
    positive charge, luminance,  
        222–223  
    transition voltage, 221–222  
transition voltage, 220  
VTE, *see* Vacuum thermal evaporation
- W**  
Wittig reaction, 5
- X**  
X-ray photoemission spectroscopy (XPS)  
    core-level intensities, 151–152  
    doped electrons, 157
- Y**  
Yamamoto coupling reaction, 5
- Z**  
Zeeman splitting effect, 113, 114, 117, 119,  
    120, 126





# ORGANIC ELECTRONICS

## Materials, Processing, Devices and Applications

In the near future, organic semiconductors may be used in a variety of products, including flat-screen TVs, e-book readers, and third-generation organic photovoltaics applications, to name just a few. While organic electronics has received increased attention in scientific journals, those working in this burgeoning field require more in-depth coverage of the subject.

Considering the rapid development in this field, ***Organic Electronics: Materials, Processing, Devices and Applications*** is a long-overdue assessment of state-of-the-art technology in organic electronics. This valuable reference harnesses the insight of various experts in the field, who contribute entire chapters on their area of specialty, covering chemistry and materials, fundamental physics, device processing, fabrication, and applications.

**Coverage includes cutting-edge advances in:**

- Organic vapor phase deposition to fabricate organic nanostructures
- Organic semiconductor device physics
- Organic thin film and vertical transistors
- Organic photovoltaic cells
- OLED technologies for flat panel displays and lighting

With its detailed discussion of the latest developments in the field of organic semiconductor materials and devices, this versatile book is ideally suited as a reference tool for scientists, engineers, and researchers or as an overview for those new to the field. In either capacity, its broad range of material will serve as a base for the further development of new sciences and technologies in this area.

72900



**CRC Press**  
Taylor & Francis Group  
an **informa** business  
[www.crcpress.com](http://www.crcpress.com)

6000 Broken Sound Parkway, NW  
Suite 300, Boca Raton, FL 33487  
270 Madison Avenue  
New York, NY 10016  
2 Park Square, Milton Park  
Abingdon, Oxon OX14 4RN, UK

[WWW.CRCPRESS.COM](http://WWW.CRCPRESS.COM)

ISBN: 978-1-4200-7290-7

90000



9 781420 072907